DESIGN, SYNTHESIS, AND EVALUATION OF CHEMICAL TOOLS FOR THE STUDY OF TRANSGLUTAMINASE 2 AND FACTOR XIII

Eric Gates

A Thesis Submitted in Partial Fulfillment
of the Requirements for the Degree of

Doctorate in Philosophy in Chemistry

Department of Chemistry and Biomolecular Sciences

Faculty of Science

University of Ottawa

Supervisor: Jeffrey W. Keillor

Examining Board: Robert N. Ben, PhD, Chemistry and Biomolecular Sciences
Christopher N. Boddy, PhD, Chemistry and Biomolecular Sciences
Adam J. Shuhendler, PhD, Chemistry and Biomolecular Sciences

External Examiner: Andrew A. Beharry, PhD, Chemistry, University of Toronto

October 2023

ABSTRACT

The mammalian transglutaminases (TGases) are a family of eight active and one catalytically inactive calcium dependent enzymes, primarily responsible for crosslinking proteins. Two isozymes within this family with strong therapeutic interest in humans are transglutaminase 2 (TG2) and factor XIII (FXIII). TG2, or tissue transglutaminase, is a multifunctional enzyme ubiquitously expressed and capable of traditional transamidation activity as well as G-protein activity. TG2 is also present both in intracellular and extracellular localizations resulting it being implicated in numerous physiological diseases including Celiac disease, fibrosis, and cancer. Plasma soluble FXIII is a key regulator in the blood coagulation cascade responsible for crosslinking fibrin to form a rigid, insoluble, clot network and is thus associated with hemophilia when activity is low, or venous thrombosis if overactive. Cellular localized FXIII has further been implicated in the activity of macrophages, chondrocytes, and osteocytes.

The content of this thesis develops a broad range of tools to study these two critical enzymes. In our study of FXIII we developed novel peptidic inhibitors and tailored the scaffold to produce a highly reactive fluorescent probe. The probe, KM93, effectively labelled FXIIIa *in cellulo* and enabled fundamental localization studies of this enzyme in bone marrow macrophages. Our work with TG2 developed isozyme selective inhibitors that specifically targeted extracellular TG2, with the lead now referred to as NCEG2. We then further modified this scaffold to produce a cell permeant fluorescent probe (aka NCEG-RHB), a propargylated inhibitor, and several active site directed proteolysis targeting chimeras (PROTACs). Through the use of both cell impermeable inhibitors as well as permeant versions we were able to conclude that intracellular TG2 is responsible for the proliferation and migration of cancer cells. The final tool disclosed within this thesis is a novel fluorogenic activity assay substrate, APH7, which is the highest affinity synthetic

TG2 substrate published to date. APH7 aided in us uncovering an unreported enzymatic hysteresis with TG2's catalytic activity, while also being an extremely reliable, sensitive, and reactive synthetic activity substrate. All of the tools presented within this thesis have already been applied to fundamental studies of TGases and are continuing to aid the field in their respective TGase investigations.

DEDICATION

This thesis is dedicated to everyone who is listed in the acknowledgements section below; however, I would also like to extend it specifically to my grandfather Robert (Bob) S. McLeod. After completing his undergraduate degree in 1941 as a Beaverbrook Scholar at UNB in Math and Chemistry, he like many other individuals of his age, enlisted with the 8th Canadian Hussars (Princess Louise's) regiment and served during WWII. Upon completion of his overseas service in 1945, he was highly encouraged to enroll in a PhD (Chemistry) by Prof. Frank J. Toole, who at that time was the dean of arts and science at UNB. Although it seemed as though my grandfather thoroughly enjoyed the sciences, he did not end up pursuing a PhD at the age of 25 and instead continued working as a farmer, the Veteran's Land Administration Atlantic Director, in the militia, and as a devout community volunteer.

My family just recently learned this fact about my late grandfather through a plethora of archived handwritten letters he had kept in storage, including the letters from Prof. Toole himself. This all came to light after I had enrolled and started my own PhD, but I can't help to think about how I unbeknownst followed the footsteps he had formed for himself but didn't take at that time. Since he continued his over 50 years of community service and did not pursue a PhD in Chemistry, this thesis is also for him.

ACKNOWLEDGEMENTS

On paper, this degree will be completed by the submission of this excessively long (sorry committee members) text document along with various grades in courses and program requirements. What will not be included on the diploma or within this document, aside from this very short section, is mention of the extraordinary people who have helped guide, encourage, and support me throughout. Although I will try to keep this section brief, I would like everyone to know that even if you are not mentioned by name, your positive impact on me during these years could easily be written out and double the length of this document; the memories, laughs, drinks, trips, conferences, etc. are moments I will cherish for the rest of my life, thank you.

To my committee members (Prof. Beharry, Prof. Ben, Prof. Boddy, and Prof. Shuhendler), thank you for agreeing to examine this thesis. I appreciate you taking the time out of your busy schedules to help me complete this degree and continue my journey. Prof. Boddy and Prof. Shuhendler, thank you also for your wisdom, project advice, and laughs on MRN2; you both are incredible scientists working on even more incredible science. Having you on my committee since beginning my studies at uOttawa has been extremely influential on my development as a scientist. To Prof. Eisler and mentor David Cameron at UNB, thank you for showing me the ropes in research and synthetic chemistry during my honours project; I still use many of the skills I learned!

To the amazing current and previous scientists I have had the opportunity to work with in the Keillor Research Group (in no order… Nicole, Sydney, Karine, Kelvin, Ernest, Nancy, Beth, Jane, Kyle, Neda, Cata, Sarah, Nick, Adrien, Kian, Stéphane, Mégan, Janique, Tara, Brenna, Namita, Pauline, Alana, Sarah (again), Sammir, Daniel, Lavleen, Jess, and Francis) thank you for the support and encouragement, I could not think of a better team to be a part of. The discussions in the office/at F&S, Keillor group bingo boards, and TG2 expression weeks are moments I cherish

and thank you all for; you've truly helped me grow (ok, I guess I don't cherish the TG2 expression weeks, but the memories are still there)! Nick Cundy, thank you especially for helping me survive the countless lockdowns/lonely days in the lab during the pandemic and becoming a significantly better chemist through your awe-inspiring expertise (or at least I think I'm moderately better). I will forever be upset that we couldn't convince you to stay in Canada, but I hope I did at least convince you that the East Coast is the best coast. I looked up to and still look up to you as a human and scientist, so thank you for your mentorship during our short (but marvellous) stint together.

André, Mike, and Nick (Calvert), I will save you from reading an extremely drawn-out paragraph about the all the memories, laughs, screaming matches (sorry MRN2 office co-workers), fishing trips, and beers we've had over the years which were some of the brightest days of this degree. I will instead give you an expletive filled version in person to save everyone else from reading it. With that being said however, thank you all so much for the brotherhood we've formed over these few years! Being able to come to work and see some of my best friends will forever bring a smile to my face and still makes me feel at home.

To my family (Mom, Dad, Erin, Meg, Thomas, Allie, Jake, and everyone else present or who are no longer with us) and friends back home thank you for all of the consistent and steadfast support, even though I fail to accurately explain what I do on a regular basis. The trips home, out west, to the cottage, and skiing over the years were breaks to disconnect and feel at home around you all and were exactly what I needed every time. Furthermore, thank you for all that you've done including raising me from a little gremlin to somewhat less of a gremlin, but now older. Cam, Chris, and Drew, thank you for the FaceTimes, casino nights, Smuggs trips, and Canada Post boxes with excellent selections of East Coast brews. You guys have stood by my side since my time at UNB and your encouragement is truly valued.

To Rachael, thank you for the continuous, unwavering, and faithful support during my PhD. Coming home to you and Young Caroles will always bring a smile to my face and warm my heart – no matter how much I screwed up in the lab that day. I apologize that when you ask how my day was, I give you probably the most nondescriptive answer in "I did chemistry/kinetics/writing today", but if you ask anyone from our lab, they will vouch that it is an accurate description. The memories and life we've lived in Ottawa will without a doubt be one of the greatest chapters in our lives and I can't wait to see what the future holds for us.

And finally, to Jeff (no I didn't forget about you). To this day when prospective students email me asking for my opinion on the KRG and you as a supervisor, I still tell them I think I've hit the jackpot. You continuously go above and beyond as a supervisor, mentor, and friend, to ensure all of your students feel supported (in science AND in life) and are able to achieve their full potential. We do not thank you enough for how much you do for all of us whether it is explaining an equation derivatization, brainstorming new projects/going down rabbit holes, reading a myriad of documents, or writing countless reference letters, so please take a second to pat yourself on the back, you deserve it! I still question how you are able to manage so many roles at the same time, while still being an incredible person, but at this point I think I have to chalk it up to you just being that good. (Also please extend my thanks to Jody, the Christmas and pool party meals and cocktails are always some of my favourite events of the year!)

Thank you to all of you… To my family and friends who have no idea what a transglutaminase or amide bond is, feel free to stop reading at this point… I can assure you it will not be as interesting as when I pitched it to you and we both will save ourselves some head scratching/googling.

Table of Contents

ABSTRACT ii
DEDICATION iv
ACKNOWLEDGEMENTS v
Table of Contents viii
List of Tables xiii
List of Figures xiv
List of Symbols, Nomenclature or Abbreviations xvii
Chapter 1: Introduction 1
1.1. Enzymes 1
1.2. Small Molecule Tools 1
1.3. Transglutaminases 3
1.3.1. Keratinocyte Transglutaminase (TG1) 5
1.3.2. Tissue Transglutaminase (TG2) 6
1.3.3. Epidermal Transglutaminase (TG3) 7
1.3.4. Prostate Transglutaminase (TG4) 8
1.3.5. Transglutaminase 5 (TG5) 8
1.3.6. Transglutaminase 6 (TG6) 9
1.3.7. Transglutaminase 7 (TG7) 9
1.3.8. Factor XIII (FXIII) 9
1.3.9. Erythrocyte Membrane Protein Band 4.2 (Band 4.2) 10
1.4. Human Transglutaminase 2 11
1.4.1. Human Transglutaminase 2: Physiological Roles 13
1.4.2. Human Transglutaminase 2: Substrates, Probes, and Inhibitors 14
1.5. Human Factor XIII 16
1.5.1. Human FXIII: Physiological Roles 17
1.5.2. Human FXIII: Substrates, Probes, and Inhibitors 18
1.6. Enzyme Inhibition 20
1.7. Proteolysis Targeting Chimeras (PROTACs) 21
1.8. Thesis Overview and Goals 24
1.9. Chapter 1 References 26

Chapter 2: Peptidic Inhibitors and a Fluorescent Probe for the Selective Inhibition and Labelling of Factor XIIIa Transglutaminase 43
2.1. Introduction to the Research Article Presented Within this Chapter 43
2.2. Author Contributions 44
2.3. Copyright 44
2.4. Abstract 44
2.5. Introduction 45
2.6. Results and Discussion 49
2.6.1. Structure Design 49
2.6.2. Synthesis 53
2.6.3. Kinetic Evaluation 54
2.6.4. Irreversible Labelling of Purified FXIIIa by SDS-PAGE 64
2.6.5. Labelling of FXIIIa in Bone Marrow Macrophages 65
2.7. Conclusions 67
2.8. Materials and Methods 68
2.8.1. Kinetic Evaluation of FXIIIa Inhibition 68
2.8.2. Kinetic Evaluation of TG2 Inhibition 69
2.8.3. Determination of Type of Inhibition 70
2.8.4. Analysis of In Vitro Kinetic Data 71
2.8.5. Fluorescent Labelling of FXIIIa by SDS-PAGE 73
2.8.6. Synthesis of Peptidic Inhibitors, Small Molecule Inhibitors, and Fluorescent Probe 73
2.8.7. Cellular Labelling and Microscopy of FXIIIa 74
2.9. Supplementary Materials 76
2.10. Author Contributions 79
2.11. Funding 79
2.12. Institutional Review Board Statement 79
2.13. Informed Consent Statement 79
2.14. Data Availability Statement 79
2.15. Conflicts of Interest 80
2.16. References 80
2.17. Disclaimer/Publisher's Note 90
Appendix to Chapter 2 91

Chapter 3: Cell Impermeable Inhibitors Confirm That Intracellular Human Transglutaminase 2 Is Responsible for the Transglutaminase-Associated Cancer Phenotype 174
3.1. Introduction to the Research Article Presented Within this Chapter 174
3.2. Author Contributions 175
3.3. Copyright 176
3.4. Abstract 176
3.5. Introduction 177
3.6. Results 179
3.6.1. Design 179
3.6.2. Synthesis 180
3.6.3. Kinetics 185
3.6.4. Isozyme Selectivity 189
3.6.5. Pharmacokinetic Properties 189
3.6.6. Fluorescent Labelling 190
3.6.7. Evaluation of Cancer Cell Proliferation and Migration 191
3.6.8. Pull-Down of TG2 from *E. coli* Lysate 193
3.7. Materials and Methods 195
3.7.1. Chemical Synthesis 195
3.7.2. Molecular Docking of Compounds 16, 18, and 29 into TG2 Active Site 195
3.7.3. rhTG2 Inhibition Assay 195
3.7.4. TGase Isozyme Selectivity 196
3.7.5. Fluorescent Labelling of Purified rhTG2 197
3.7.6. SH-SY5Y Fluorescent Microscopy 198
3.7.7. Cell Proliferation Assay 199
3.7.8. Real-Time Cell Migration Assay 200
3.7.9. HaCaT and SCC-13 Cell Staining 200
3.7.10. Pull-Down of rhTG2 from *E. coli* Lysate 201
3.8. Conclusions 202
3.9. Supplementary Materials 203
3.10. Author Contributions 203
3.11. Funding 203
3.12. Institutional Review Board Statement 203
3.13. Acknowledgments 203
3.14. Informed Consent Statement 204

3.15. Data Availability Statement 204
3.16. Conflicts of Interest 204
3.17. References 204
3.18. Disclaimer/Publisher's Note 213
Appendix to Chapter 3 214
Chapter 4: High Affinity Fluorogenic Substrate for Tissue Transglutaminase Reveals Enzymatic Hysteresis 273
4.1. Introduction to the Research Article Presented Within this Chapter 273
4.2. Author Contributions 274
4.3. Copyright 275
4.4. Abstract 275
4.5. Introduction 276
4.6. Materials and Methods 279
4.6.1. Synthesis 279
4.6.2. Standard Curve Protocol 282
4.6.3. Kinetic Assay Protocol 282
4.6.4. Michaelis-Menten Fitting 283
4.6.5. Isozyme Selectivity Protocol 283
4.6.6. Enzymatic Inhibition Assay 284
4.6.7. Fluorescence Quenching Assay 285
4.6.8. Covalent Binding Kinetics Characterization by RapidFire-MS 286
4.7. Results and Discussion 288
4.7.1. Design 288
4.7.2. Synthesis 289
4.7.3. Kinetics 290
4.7.4. Application to Irreversible Inhibition 292
4.7.5. TG2 Exhibits Enzymatic Hysteresis 296
4.7.6. Substrate-Free Inhibition Profile 299
4.8. Conclusions 301
4.9. Supporting Information 302
4.10. Accession Codes 303
4.11. Funding 303
4.12. Notes 303
4.13. References 304

Appendix to Chapter 4 308
Chapter 5: Towards TG2 Active Site Directed PROTACs 321
5.1. Introduction 321
5.2. Results and Discussion 323
5.2.1. Design 323
5.2.2. Synthesis 324
5.2.3. Kinetic Evaluation 328
5.3. Conclusions and Future Work 330
5.4. Chapter 5 References 332
Appendix to Chapter 5 338
Chapter 6: Conclusions and Future Perspectives 403
6.1. Chapter 2: Peptidic Inhibitors and a Fluorescent Probe for the Selective Inhibition and Labelling of Factor XIIIa Transglutaminase 403
6.1.1. Conclusion to Chapter 2 403
6.1.2. Future Perspectives to Chapter 2 404
6.2. Chapter 3: Intracellular Human Transglutaminase 2 is Responsible for the Transglutaminase-Associated Cancer Phenotype 404
6.2.1. Conclusion to Chapter 3 404
6.2.2. Future Perspectives to Chapter 3 405
6.3. Chapter 4: High Affinity Fluorogenic Substrate for Transglutaminase 2 Reveals Pattern Consistent with Enzymatic Hysteresis 405
6.3.1. Conclusion to Chapter 4 405
6.3.2. Future Perspectives to Chapter 4 406
6.4. Chapter 5: Towards TG2 Active Site Directed PROTACs 407
6.4.1. Conclusion to Chapter 5 407
6.4.2. Future Perspectives to Chapter 5 407

List of Tables

Table 2.1. Structural classification of peptidic FXIIIa inhibitors. The linker length (n methylene units) and warhead are presented along with an alphabetical nomenclature system for noting the distances of the electrophilic carbon (E+ C) and carbonyl carbon (CO C) from the peptide backbone. For example, a designation of d implies that the feature is present at the δ carbon, the 3rd carbon atom away from the backbone's a/α-carbon. 57
Table 2.2. Kinetic parameters, inhibition modes, and isozyme selectivity of acrylamide-, α-chloroacetamide, and α,β-unsaturated methyl ester-bearing peptidic inhibitors of FXIIIa inhibitors with varying linker lengths. Data were determined using distinct continuous activity assays for FXIIIa and TG2 detailed in the Materials and Methods section. 58
Table 2.3. Kinetic parameters and isozyme selectivity of small molecule FXIIIa inhibitors with various N-terminal acidic groups, C-terminal hydrophobic units, and central warhead amino acid residues. Data were determined using distinct continuous activity assays for FXIIIa and TG2 detailed in the Materials and Methods section. 62
Table 3.1. Kinetic data for cell impermeable inhibitors, fluorescent probes, and propargyl inhibitor. 188
Table 3.2. Representative pharmacokinetic properties for cell impermeable inhibitors 17 and 18. 190
Table 4.1. Relative comparison of the k_{cat}, K_M, and k_{bkg} (background hydrolysis rate constant) for three TG2 activity substrates (50 mM MOPS, 7 mM $CaCl_2$, 25 ˚C, pH 6.9). 290
Table 4.2. Inhibitor efficiency values determined for AA9 and 8 when using various activity substrates under continuous assay experimental conditions.[a] 300
Table 5.1. Approximate TG2 inhibition efficiency values of active site targeted PROTACs.... 330

List of Figures

Figure 1.1. Chemical structure of small molecule therapeutics warfarin, rivaroxaban, and aminocaproic acid used in the treatment of thrombosis and hemophilia. 2
Figure 1.2. Transglutaminase dependent formation of Nε(ɣ-glutaminyl)lysine bonds between two peptide substrates. Figure adapted from Keillor *et al. Bioorganic Chemistry* (2014).[15] 4
Figure 1.3. General catalytic cycle of transglutaminases exhibiting the transamidation, hydrolysis, and isopeptidase activities. Figure adapted from Keillor *et al. Bioorganic Chemistry* (2014).[15] 5
Figure 1.4. Structural representation of TG2's mutually exclusive conformations. A) Closed conformation with GTP binding site (magenta) exposed and substrate binding site disrupted (blue). B) Open conformation with substrate binding site (blue) formed and GTP binding site (magenta) fractured. C) Closed conformation stabilized with GTP (green) binding (PDB: 4PYG). D) Open conformation stabilized by irreversible inhibitor (cyan) binding (PDB: 2Q3Z). Figure adapted from McNeil *et al. European Journal of Medicinal Chemistry* (2022).[18] 6
Figure 1.5. Cartoon representation of the two conformations of hTG2 which are regulated allosterically by Ca^{2+} or GTP. The N-terminal β-sandwich in blue, catalytic core in green, β-barrel1 in red, and C-terminal β-barrel2 in yellow. 13
Figure 1.6. Scaffolds of new era Keillor hTG2 targeted irreversible inhibitors with associated inhibitor efficiency values.[18,69,71] 15
Figure 1.7. A representation of the hydrolysis activity assay substrate N-Cbz-L-Glu(ɣ-p-nitrophenyl ester)Gly (AL5) reacting with hTG2, which leads to the release of p-nitrophenol and can be observed by a spectrophotometer at 405 nm. 16
Figure 1.8. Cartoon representation of two step FXIII activation. 17
Figure 1.9. Cleavage and mechanism of isopeptidase A101 TGase activity assay. 19
Figure 1.10. General mechanism of proteasomal degradation of a protein of interest by PROTACs. 21
Figure 1.11. Structure of two clinical candidate PROTACs pioneered by Arvinas. 23
Figure 2.1. Chemical structures of Zedira's ZED1301 [33], ZED2360 [41], ZED3197 [22], Merck's imidazolium inhibitor 16 [39], and Keillor's TG2 targeted small molecule inhibitor NM72 [42]. 48
Figure 2.2. Design of the peptidic FXIIIa inhibitor series with various linker lengths and electrophilic warhead functionalities. 50
Figure 2.3. Design approach for small-molecule inhibitors of FXIIIa, based on a known low potency TG2 "inhibitor 17" and driving selectivity for FXIIIa with N-terminal acids and C-terminal hydrophobic groups [42,46]. 52
Figure 2.4. Design of fluorescent probe for FXIIIa tethered to the optimised inhibitor structure. 53
Figure 2.5. Representative kinetic traces and data fitting for TGase inhibition assays. (A) Raw blank-subtracted kinetic traces of FXIIIa activity with substrate A101 and increasing concentrations of reversible inhibitor 47 (0, 1, 2, 5, 10 μM). (B) Dixon plot fitting of initial rates of FXIIIa activity versus inhibitor concentration divided by alpha for inhibitor 47 to obtain K_i. (C) Raw blank subtracted kinetic traces of FXIIIa activity with substrate A101 and increasing concentrations of irreversible inhibitor 23 (0, 50, 100, 150, 200 μM). (D) Linear regression of saturation fitting of k_{obs} versus inhibitor concentration divided by alpha for irreversible inhibitor 23 to obtain a ratio of k_{inact}/K_I. (E) Saturation fitting of k_{obs} versus inhibitor concentration for

irreversible inhibitor 46 displaying inhibition saturation kinetics to extract both k_{inact} and K_I parameters. 55
Figure 2.6. Structure of the rhodamine B incorporated FXIIIa probe 93 (aka KM93)..... 64
Figure 2.7. Immunofluorescence visualization of the labelling of FXIIIa by KM93 in murine bone marrow macrophages (BMM). Cells were incubated with 20 µM KM93 for 48 h in microscopy chamber slides. At the endpoint, cells were fixed and stained or treated with sheep anti-human FXIII-A antibody, followed by a secondary antibody, donkey anti-sheep AlexaFluor®-488 detection (green, Panel (B)). Nuclei were visualised with DAPI staining (blue). KM93 was visualised at 568 nm (red, Panel (A)). All cells were positive for FXIIIa, incorporation of KM93 into cells was clear and the probe colocalized with FXIII-A (Panel C and yellow arrows, inset Panel (D)). A subset of the macrophages did not incorporate the probe, despite the presence of FXIII-A (white arrows, Panel (C)), indicating that the enzyme may not be active in these specific macrophages. Some cells also showed strong red fluorescence but weak green fluorescence, giving the appearance of little colocalization, despite both probe and enzyme being present at these cellular compartments (red arrows, Panel (C)). White magnification bar represents 20 µm. 66
Figure 3.1. Previous libraries of inhibitors giving rise to the scaffold disclosed in this work [32]. 180
Figure 3.2. Representative kinetic data for inhibitors. Data shown for compound 17 with (A) time-dependent inactivation of TG2 (blank subtracted), (B) fitting of observed first-order rate constants to a hyperbolic model for saturation kinetics, (C) linear regression of lowest concentration rate constants, and (D) double reciprocal fitting of the data shown in B..... 186
Figure 3.3. (A) Cell microscopy of SH-SY5Y cells incubated with 30 µM 29 (NCEG-RHB) (red) for 30 min and nucleus stained with Hoechst (blue). (B) Cell microscopy of SH-SY5Y cells differentiated with 20 µM retinoic acid for 4 days, incubated with 30 µM 29 (NCEG-RHB) (red) for 30 min and nucleus stained with Hoechst (blue)..... 191
Figure 3.4. Treatment of cancer cells with cell-permeable and cell-impermeable inhibitors. (A) HaCaT and SCC-13 are epidermis-derived cutaneous squamous cell carcinoma cells that were treated for 10 h with NCEG-RHB prior to imaging using a spinning disc confocal microscope. NCEG-RHB localization is detected adjacent to the nuclei (N) in both cell types and is indicated by red arrows. The HaCaT cell cultures were also stained for 15 min with MitoTracker Green before imaging. MitoTracker Green detects mitochondria membrane proteins inside the cell and the labelling is indicated by green arrows. White scale bars = 100 µm. (B) SCC-13 cells treated with cell-impermeable inhibitor 18 (NCEG2) and cell-permeable inhibitors NC9, AA9, and NCEG-RHB. Scale bars represent 50 µm; (*) p value < 0.001 (C) HaCaT cells treated with cell-impermeable inhibitor 18 (NCEG2) and cell-permeable inhibitors NC9 and AA9. Scale bars represent 50 µm; (*) p value < 0.001. (D) MDA-MB-436 cells treated with cell-impermeable 18 (NCEG2) and with cell-permeable inhibitors NC9, AA9 and NCEG-RHB. Experiments were carried out in triplicate and are represented as average ± SD of the percentage of living cells; (**) p value < 0.01. 193
Figure 3.5. SDS-PAGE analysis of SH-SY5Y cell lysate. Left panel, Coomassie stain of protein standards and raw lysate. Right panel, fluorescence visualization of lysate and 30 µM NCEG-RHB. 270
Figure 4.1. Rational design incorporating the key elements of the lead inhibitor scaffold (AA9) and the previous activity substrates for TG2. 288

Figure 4.2. Kinetic traces and fittings for APH7 with TGases. (A) Raw kinetic traces of the reaction of APH7 with TG2. (B) Saturation fitting of initial rates versus [APH7]. 290
Figure 4.3. Inhibition of TG2 with the irreversible inhibitor AA9. (A) Raw kinetic traces obtained using chromogenic substrate AL5. (B) Linear region of saturation plot of observed rate constants obtained with AL5 vs [AA9]. (C) Raw kinetic traces were obtained using fluorogenic substrate APH7. (D) Linear region of saturation plot of observed rate constants obtained with APH7 vs [AA9]. (E) Raw kinetic traces using fluorogenic substrate ZFBC. (F) Linear region of saturation plot of observed rate constants obtained with ZFBC vs [AA9]. (G) Raw kinetic traces using fluorescently quenched substrate A101. (H) Linear region of saturation plot of observed rate constants obtained with A101 vs [AA9]. 292
Figure 4.4. Structure of AL5 structural mimic inhibitor 8 [Z-Lys(Acryl)-Gly-OH]. 294
Figure 4.5. TG2 activity measured by 5 µM fluorescent substrate APH7 pre- and post-spiking with a further 5 µM APH7. Initial rates were calculated by linear regression of the first 200s. 295
Figure 4.6. (A) Irreversible inhibition of TG2 by AA9 in the presence of varied concentrations of reporter substrate APH7. Fitting was simplified by using the fixed value of k_{inact} = 2.28 min^{-1}, measured for the data set showing the highest degree of saturation (at 1.0 µM APH7). (B) Graphical representation of the effect of [APH7] on the observed K_I values measured in panel A. The line fitted through the data points represents a binding isotherm, reflecting saturation of the conformational effect of APH7. 297
Figure 4.7. (A) Time-dependent covalent modification of TG2 by AA9, in the absence of reporter substrate. (B) Saturation kinetic analysis of the associated rate constants of inactivation by AA9. (C) Time-dependent covalent modification of TG2 by inhibitor 8, in the absence of reporter substrate. (D) Saturation kinetic analysis of the associated rate constants of inactivation by inhibitor 8. 299
Figure 5.1. Design strategy for the active site targeted TG2 PROTACs, stemming from previous work on chemical biology research tools. 323
Figure 5.2. Synthetic scheme to generate VHL TG2 PROTACs 9-12. 324
Figure 5.3. Synthetic scheme to generate lenalidomide TG2 PROTACs 17-20. 325
Figure 5.4. Synthetic scheme for the Fmoc deprotection of the IAP ligand to yield free amine 22. 326
Figure 5.5. Synthetic scheme to generate IAP TG2 PROTACs 31-34. 327
Figure 5.6. Simplification of inhibition saturation equation to estimate k_{inact}/K_I. 329

List of Symbols, Nomenclature or Abbreviations

α – Alpha value, when in the context of inhibition kinetics, $\alpha = 1 + [S]/K_M$
ACN – Acetonitrile
AcOH – acetic acid
Ac_2O – acetic anhydride
Acryl – Acrylamide
BME – 2-Mercaptoethanol
Boc – *tert*-Butyloxycarbonyl protecting group
Cbz – Carboxybenzyl protecting group
$CDCl_3$ – Deuterated chloroform
COU – Coumarin
CRBN – Cereblon E3 ligase
DAPI – 4′,6-diamidino-2-phenylindole
DCC – Dicyclohexylcarbodiimide
DC_{50} – Half-maximal degradation concentration
D_{max} – Maximal percentage of degradation
DCM – Dichloromethane
DIBAL – Diisobutylaluminium hydride
DIC – Diisopropylcarbodiimide
DIPEA – Diisopropylethylamine
DMAP – 4-dimethylaminopyridine
DMEM – Dulbecco's Modified Eagle Medium
DMF – Dimethylformamide
DMSO – Dimethyl sulfoxide
d_6-DMSO – Deuterated dimethyl sulfoxide
EDC HCl – 1-(3-Dimethylaminopropyl)-3-ethylcarbodiimide hydrochloride
EtOAc – Ethyl acetate
Et_3N – Triethylamine
Et_2O – Diethyl ether
E3L – E3 ligase
FBS – Fetal bovine serum
FITC – Fluorescein isothiocyanate
Fmoc – Fluorenylmethyloxycarbonyl protecting group
FXIII – Factor XIII
GDP – Guanosine diphosphate
GSH – Glutathione
GTP – Guanosine triphosphate
HATU – 1-[Bis(dimethylamino)methylene]-1H-1,2,3-triazolo[4,5-b]pyridinium 3-oxide hexafluorophosphate
HBTU – 2-(1H-Benzotriazole-1-yl)-1,1,3,3-tetramethyluronium hexafluorophosphate
HOBt – Hydroxybenzotriazole
HPLC – High-performance liquid chromatography
Hünig's base – Diisopropylethylamine
[I] – Inhibitor concentration

IC_{50} – Half-maximal inhibitory concentration
K_D – Dissociation constant
K_I – Irreversible inhibitor dissociation constant
K_i – Reversible inhibitor dissociation constant
k_{inact} – Rate constant of inactivation
k_{obs} – Observed rate constant
K_M – Michaelis-Menten constant
LCMS – Liquid chromatography–mass spectrometry
Log P – Partition coefficient
Log D – Distribution coefficient
MeOD – Deuterated methanol (CD_3OD)
MeOH – Methanol
MOPS – 3-(N-morpholino)propanesulfonic acid
MS – Mass spectrometry
NMP – N-Methyl-2-pyrrolidone
NMR – Nuclear magnetic resonance
PAMPA – Parallel artificial membrane permeability assay
PBS – Phosphate-buffered saline
PD – Pharmacodynamic
PK – Pharmacokinetic
PROTAC – Proteolysis targeting chimera
RA – *trans*-retinoic acid
RHB – Rhodamine B
[S] – Substrate concentration
SAR – Structure activity relationship
SDS – Sodium dodecyl sulfate
SDS-PAGE – Sodium dodecyl sulfate–polyacrylamide gel electrophoresis
SPPS – Solid-phase peptide synthesis
TCEP – Tris (2-carboxyethyl) phosphine
TEA - Triethylamine
TFA – Trifluoroacetic acid
TG or TGase – Transglutaminase
THF – Tetrahydrofuran
TRIS – 2-Amino-2-hydroxymethyl-propane-1,3-diol
VHL – von Hippel-Lindau E3 ligase
V_{max} – Maximal reaction rate
7-HC – 7-hydroxycoumarin (umbelliferone)

Chapter 1: Introduction

1.1. Enzymes

Enzymes are proteins that play an enormous and important role in biological systems. These proteins catalyze chemical reactions *in vivo* without being consumed by accelerating the rate of reaction in their active site by increasing the chemical reactivity, stabilizing the transition state, decreasing the distance between two potential substrates, and diminishing the required activation energy. For a simple chemical reaction that could take months, years, or millennia to occur naturally, enzymes can facilitate the reaction with extremely high substrate specificity and perform a stereoselective reaction in a fraction of a second, making them essential for life.[1] Enzymes can catalyze various reactions. Kinases catalyze phosphorylation, oxidases induce oxidations, hydrolases facilitate hydrolysis, and covalent bond formation is catalyzed by enzymes like transglutaminases. Without the reaction catalysis of enzymes, every imaginable physiological process may never occur due to the extensive amount of time needed to elicit each chemical reaction. Even if the time barrier was removed, the correct stereochemical product may still never be generated because without an enzyme it could be energetically unfavourable. Understanding the full role of these proteins has become an immense field of research as the ability to control and fine tune biological systems relies upon these proteins.

1.2. Small Molecule Tools

Small molecules have become one of the more desirable tools to study enzymatic function and location, and then subsequently developed into targeted therapeutics.[2–4] These molecules, due to their minimal molecular weight of typically less than 900 Da, can be easily tailored for

permeability, polarity, affinity, and reactivity in a straightforward synthetic approach with distinct functional groups. Apart from peptidomimetic and peptidic molecules, small molecules offer a unique opportunity to avoid the host's native proteasome and increase the half-life of potential drugs, or probes *in vivo*. The majority of current therapeutics prescribed by physicians are small molecules that have been designed to exert a profound physiological effect.[5] The application of small molecules can even be seen in pharmaceutical drugs relevant to thrombosis and hemophilia such as warfarin, rivaroxaban, and aminocaproic acid (Figure 1.1). Each of these small molecules is a designed therapeutic that has proven to be extremely useful and potent in treating either thrombosis with an anticoagulant like warfarin or rivaroxaban, or hemophilia by using an antifibrinolytic agent like aminocaproic acid.

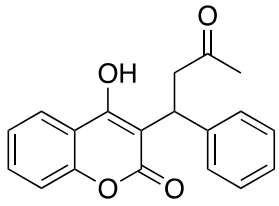

Warfarin

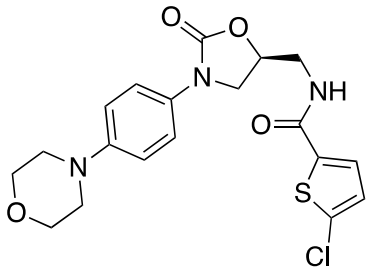

Rivaroxaban

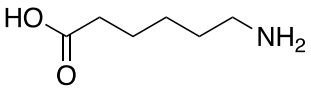

Aminocaproic acid

Figure 1.1. Chemical structure of small molecule therapeutics warfarin, rivaroxaban, and aminocaproic acid used in the treatment of thrombosis and hemophilia.

The ability to transform these molecules into high affinity probes and inhibitors by fine tuning their binding characteristics exemplifies their great role in understanding biological systems and cascades.[6] Instead of relying on the whole native substrate for a specific binding site, using structure activity relationship (SAR) and docking studies, small molecules can dispense with all of the unnecessary functional groups and bulk from the substrate to dramatically increase affinity and interact only with the protein's required binding residues, thereby forming a tight interaction. This process can yield synthetic molecules that are bound even more tightly to the protein than the native substrate. Incorporating cargo onto these scaffolds can further increase the scope of application for these tools from simple inhibitors to fluorescent probes, chemical labels, or localization specific inhibitors. These binding characteristics and modularity are the reason many chemists attempt to centre their medicinal chemistry and biochemistry research projects around these small molecule scaffolds to study specific proteins or enzymes of interest.

1.3. Transglutaminases

Transglutaminases (TGases) are a family of nine calcium dependent isozymes with the primary function of performing post-translational protein modifications. These enzymes crosslink specific protein substrates by introduction of an N^{ε}(ɣ-glutaminyl)lysine linking bond (Figure 1.2). Designated TG1 through TG7, Factor XIII, and erythrocyte membrane protein band 4.2; the role of these enzymes plays a part in numerous biological functions such as cell signalling, cell structure, and extracellular matrix structure.[7–9] Their physiological roles have also elucidated their promising properties as important anticancer, thrombosis, and fibrosis therapeutic targets.[10–14] One defining sequence that allows eight of these enzymes (TG1-TG7, FXIII) to be grouped together is the five conserved Gly-Gln-Cys-Trp-Val residues surrounding the catalytic cysteine.

Transglutaminases go through a cysteine dependent transamidation by utilizing the conserved catalytic triad in their active site consisting of cysteine, histidine, and aspartate residues. These enzymes can also perform two other biologically relevant tasks; hydrolysis of glutamines or an isopeptidase activity to cleave peptide bonds following the opposite direction in the transamidation scheme (Figure 1.3).

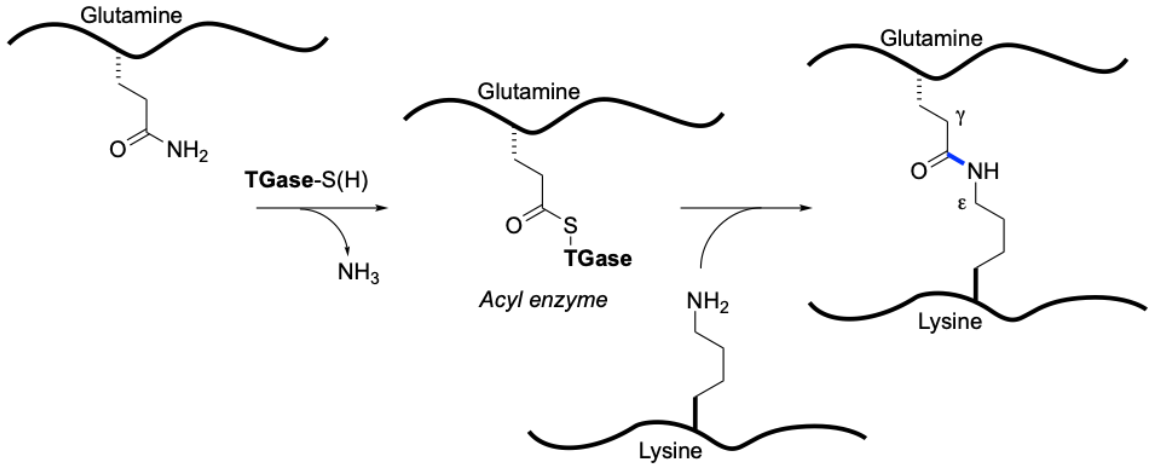

Figure 1.2. Transglutaminase dependent formation of Nε(γ-glutaminyl)lysine bonds between two peptide substrates. Figure adapted from Keillor *et al. Bioorganic Chemistry* (2014).[15]

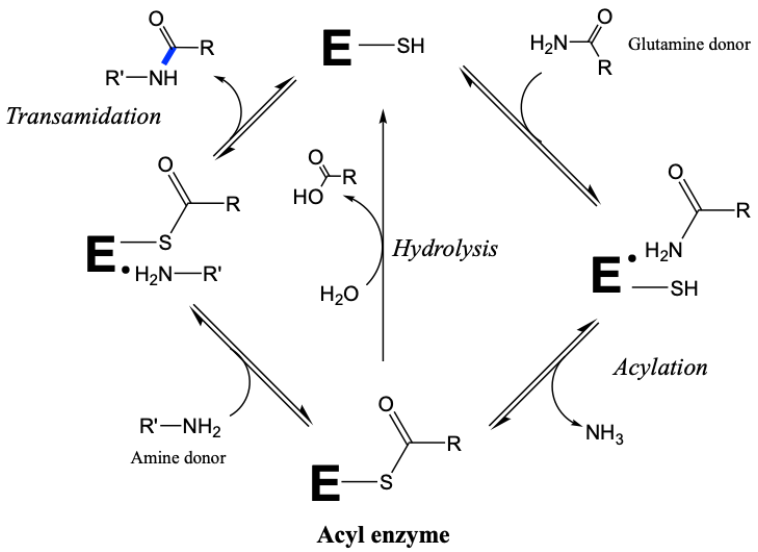

Figure 1.3. General catalytic cycle of transglutaminases exhibiting the transamidation, hydrolysis, and isopeptidase activities. Figure adapted from Keillor *et al. Bioorganic Chemistry* (2014).[15]

1.3.1. Keratinocyte Transglutaminase (TG1)

Transglutaminase 1, or keratinocyte transglutaminase, is a TGase that is predominantly found in keratinocytes and is responsible for generating the cell's cornified envelope in the epidermis.[16] Although the crystal structure of TG1 has not been solved to date, TG1 is a 90-kDa enzyme that is tethered to the plasma membrane and crosslinks multiple substrates just inside the plasma membrane of the keratinocyte to form the cornified envelope.[8] Uncontrolled TG1 activity is associated with lamellar ichytosis, a disorder that affects the cornification of hair and the epidermis.[17]

1.3.2. Tissue Transglutaminase (TG2)

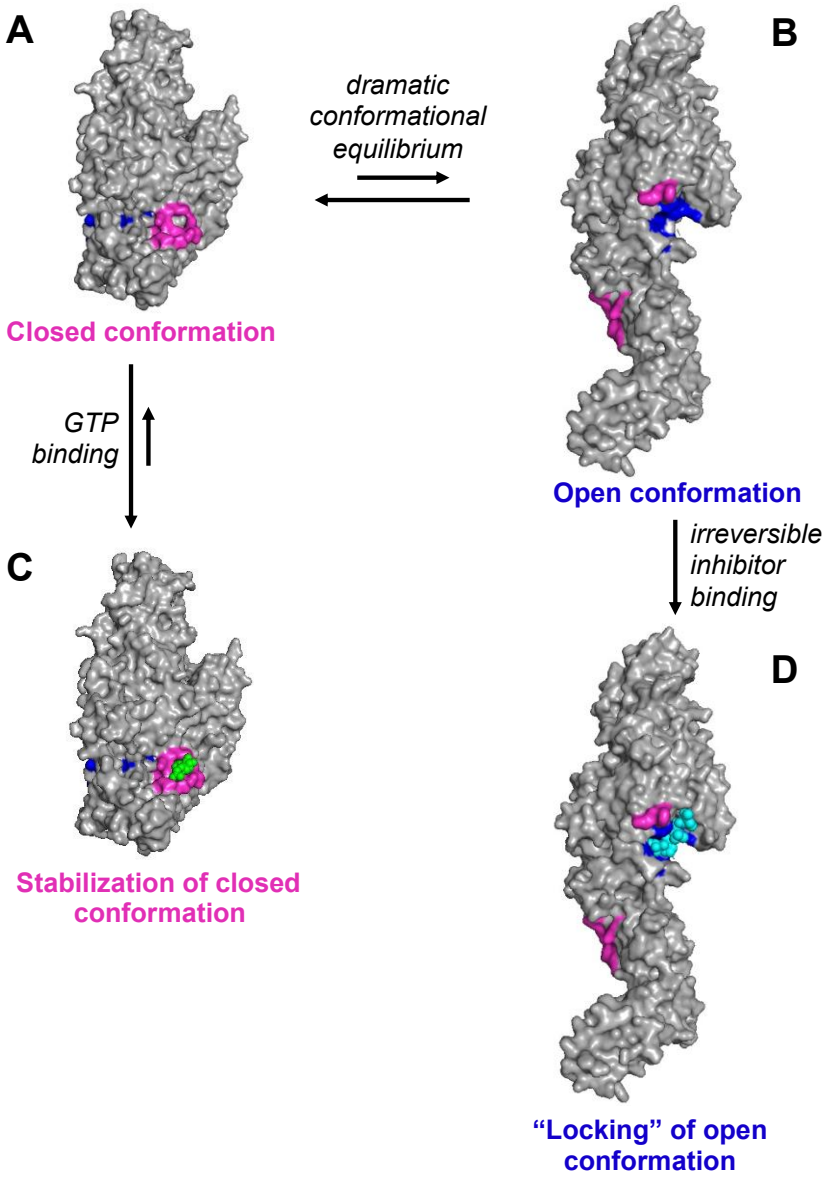

Figure 1.4. Structural representation of TG2's mutually exclusive conformations. A) Closed conformation with GTP binding site (magenta) exposed and substrate binding site disrupted (blue). B) Open conformation with substrate binding site (blue) formed and GTP binding site (magenta) fractured. C) Closed conformation stabilized with GTP (green) binding (PDB: 4PYG). D) Open conformation stabilized by irreversible inhibitor (cyan) binding (PDB: 2Q3Z). Figure adapted from McNeil *et al. European Journal of Medicinal Chemistry* (2022).[18]

Tissue Transglutaminase, or TG2, is a 78-kDa TGase that is one of the broadest functioning and promiscuous TGases known. TG2, as can be inferred from its name, is found throughout tissues in mammals. TG2 has two main biologically relevant activities, the first being the normal transamidation activity and the second being a G-protein function important in cell signalling.[19] These two activities, however, act in a completely independent and discrete manner and are regulated by the environment surrounding the enzyme, mainly the Ca^{2+} concentration. To facilitate transamidation activity, TG2 adopts an open conformation in which the GTP binding site is abolished by dispersal of the residues that form it, whereas during G-protein activity, the enzyme adopts a closed conformation in which the catalytic active site tunnel is occluded and inaccessible (Figure 1.4). Being one of the best studied TGases, TG2 has been hypothesized to play roles in numerous pathological disorders such as cancer, tissue scarring, and even neuron survival.[20–22] Human TG2 is one of the main enzymes of interest in this thesis and will be disused in greater detail in Chapter 1.4.

1.3.3. Epidermal Transglutaminase (TG3)

Similar to TG1, epidermal transglutaminase is also associated with the epidermis. This TGase is found in the cytosol of keratinocytes in the superficial layers of the epidermis. The main difference between TG3 and TG1 is that TG3 requires proteolytic cleavage to become active.[23] TG3 is expressed as a zymogen and not until cleavage by a protease does it become active in 50-kDa and associated 27-kDa fragments referred to as TG3a. TG3a will then crosslink its typical substrates in the keratinocyte, which consist of the intermediate filaments of keratin and trichohyalin.[8,24] As with TG2, it is hypothesized that TG3 undergoes a distinct GTPase function or crosslinking depending on the concentration of Ca^{2+} and GTP. It is also of interest that upon

binding of Mg^{2+} in place of one Ca^{2+} ion, the active site channel is closed and inhibits the crosslinking activity.[23,25] TG3 activity is required for proper hair development and unregulated activity can contribute to hair thinning or non-celiac disease gluten sensitivity, dermatitis herpetiformis.[26,27]

1.3.4. Prostate Transglutaminase (TG4)

Transglutaminase 4, or prostate transglutaminase, is a 77-kDa TGase that was discovered by analysis of the human prostate cDNA in the 1990s.[28] The full role and substrates scope of TG4 remains to be uncovered; however, some evidence does suggest a link between TG4 activity and an aggressive form of prostate cancer. TG4 is suggested to enhance the epithelial-mesenchymal transition of prostate cancer cells and aid in the progression of the disease.[11,29–31] As new discoveries are made regarding this TGase's full biological behaviour, TG4 may be identified as a highly promising anti-prostate cancer therapeutic target.

1.3.5. Transglutaminase 5 (TG5)

Transglutaminase 5 is one of the lesser known TGases. Research is lacking in terms of its full physiological role; however, it is known to be associated with the epidermis like TG1 and TG3. The known protein substrates for TG5 are loricrin, involucrin, and SP3, which can all be found in the epidermis and aid in skin integrity.[8] TG5's pathological role in humans has been hypothesized to have a role in epidermal cell-cell adhesion. This is due to the finding that inactivation of TG5 by genetic mutation results in acral peeling skin syndrome.[32]

1.3.6. Transglutaminase 6 (TG6)

Transglutaminase 6 is also one of the more recently discovered TGases with the gene cluster first being identified in 2001[33] and the primary location and identity of the TGase uncovered in 2013.[34] Like TG2, TG6 can be regulated by Ca^{2+} and GTP suggesting that it may as also have dual activities as a protein post-translational modifier and as a cell signalling protein. Since the discovery, TG6 has been primarily found in the testes and the central nervous system. Some studies have suggested that TG6 has a function in nervous system development and also motor function,[34] but much remains to be understood regarding this TGase.

1.3.7. Transglutaminase 7 (TG7)

Transglutaminase 7 is one of the least studied TGases at this time. Research is especially lacking in terms of TG7's full physiological role and function. TG7 was first hypothesized by the discovery of sequence homology to other TGase members, but the main location, structure, and physiological substrates of the enzyme remain to be uncovered. Some evidence has suggested higher expression of TG7 in the testes, lungs, and brain, but ubiquitous expression has also been observed in some cases.[8,35] To date there has been no association between TG7 and any known physiological disorders.

1.3.8. Factor XIII (FXIII)

Factor XIII, also referred to as plasma transglutaminase due to its role in the blood coagulation cascade, is one of the TGases currently under extensive investigation as its broad physiological role is progressively uncovered. FXIII exists as both a cellular form and as a plasma form, with the cytosolic form being found throughout the body especially in astrocytes, platelets, chondrocytes, placenta, dermal dendritic cells, synovial fluid, macrophages, and osteocytes.[35] The

plasma FXIII is a heterotetrametric TGase consisting of two catalytic A subunits and two carrier B subunits. As seen with TG3, FXIII typically requires proteolytic cleavage by thrombin of an activation peptide on the A subunit and Ca^{2+} to become fully active. The platelet form of FXIII is smaller in size due to its lack of the carrier B subunits; however, activation is still achieved by thrombin mediated cleavage and Ca^{2+}. Plasma FXIII's main physiological function is to act as the last step in the blood coagulation cascade and crosslink fibrin D regions and attach antiplasmin proteins to form a rigid clot network. Cellular FXIII is hypothesized to aid in chondrocyte differentiation, platelet function, and bone growth.[36] Given that human FXIII is one of the enzymes of interest featured in this thesis, it will be discussed in greater detail in Chapter 1.5.

1.3.9. Erythrocyte Membrane Protein Band 4.2 (Band 4.2)

Erythrocyte Membrane Protein Band 4.2 (Band 4.2) is the most unique TGase in the isozyme family. Band 4.2 does have structural homology to the rest of the TGase family, which led to it being grouped into the TGase family; however, it lacks the key catalytic cysteine residue in the active site. Band 4.2, therefore, does not show any known catalytic TGase function due to the mutation of the cysteine with an alanine. Furthermore, the catalytic triad necessary for TGase activity (His-Cys-Asp) is missing.[37] Looking back at the TGase defining sequence (Gly-Gln-Cys-Trp-Val), band 4.2 has four of the five conserved residues, and 27% similarity in a 639-amino acid overlap of the sequence of the FXIII A subunit.[38] This enzyme is primarily found in the red blood cell membrane cytoskeleton and although it lacks classic TGase activity, the protein does play a key role in membrane integrity, and cell signalling.[8] Band 4.2 deficiency has been shown to have pathological relevance as it results irregular red blood cell shape, or spherocytosis.[39]

1.4. Human Transglutaminase 2

Human tissue transglutaminase (hTG2) is one of the most well studied and understood enzymes in the transglutaminase family. Since the initial discovery of the TGase enzyme in the 1950s, research on hTG2 began overtaking investigation of the rest of the TGases in the 1980s and TG2 has become one of the most targeted enzymes for study and therapeutic intervention.[40] As a 78-kDa enzyme, hTG2 is the most ubiquitously expressed and widely distributed TGase in the human body. It is also the transglutaminase predominantly studied by the Keillor Research Group, who have developed potent and selective irreversible inhibitors, probes, and activity assays for hTG2. As mentioned in earlier sections, select TGases have the classical crosslinking function, as well as a guanosine nucleotide binding role – TG2, TG3, TG5, and TG6 are all hypothesized to act as guanosine nucleotide binding proteins,[41–44] which may allow them to act as a unique G-protein in cells. hTG2 is also the only of these guanosine nucleotide binding TGases that has been crystallized in two conformations; one open transamidation conformation[45] and one closed guanosine nucleotide binding conformation.[41]

The structure of hTG2 also sets it apart from the rest of the TGases. hTG2 is composed of four distinct domains: An N-terminal β-sandwich, an α/β-catalytic core, and two C-terminal β-barrels. As the name suggest, the catalytic core contains the catalytic triad and active site tunnel responsible for the TGase crosslinking activity. As aforementioned, hTG2 also has a separate activity from the crosslinking activity which is as a GTPase. The guanosine nucleotide binding function of transglutaminases was initially discovered using guinea pig liver transglutaminase in the 1980s.[46] The GTP binding site of hTG2 has been mapped on to the first of the β-barrels located proximally to the catalytical core.[47] It has also been shown that mutation of an arginine residue in the binding site abolishes guanosine nucleotide binding, and actually promotes the crosslinking

activity.[48] A crystal structure of the GTP bound state was also obtained in 2014.[41] hTG2 has six Ca^{2+} ion binding sites all located on its core domain and it has been shown that using site directed mutagenesis the transamidation activity is abolished – highlighting the Ca^{2+} requirement for crosslinking activity.[47] The binding of Ca^{2+} is a low enthalpy event indicating that this provides the stabilization necessary to maintain the active site of the catalytic core.[19]

Activation of hTG2 is controlled allosterically and is intuitively correlated to which distinct function the TGase will display. One of the defining characteristics of hTG2 that separates it from the other TGases is the great hinge-like conformational change depending on hTG2's activity. In low calcium concentrations as commonly found in intracellular conditions, the calcium binding sites on hTG2 will remain vacant shifting the enzyme's dynamic equilibrium toward the closed, GTP binding conformation (Figure 1.4). However, upon exposure to calcium, such as in the extracellular environment, hTG2 can preferentially adopt an open conformation. The open conformation can also be regulated through the redox state of two vicinal cysteines.[49] The two C-terminal β-barrel domains will be forced away from the enzymatic core and open the active site tunnel, thereby allowing the transamidation function to commence. The allosteric regulation of this enzyme allows it to generally be thought of as intracellular hTG2 operating as a G-protein cell signalling protein, whereas the extracellular hTG2 will perform the classical TGase functions of hydrolysis of glutamines, transamidation, and isopeptidic cleavage; although it is important to note that these two localizations do not rigidly define hTG2's activity or conformation.

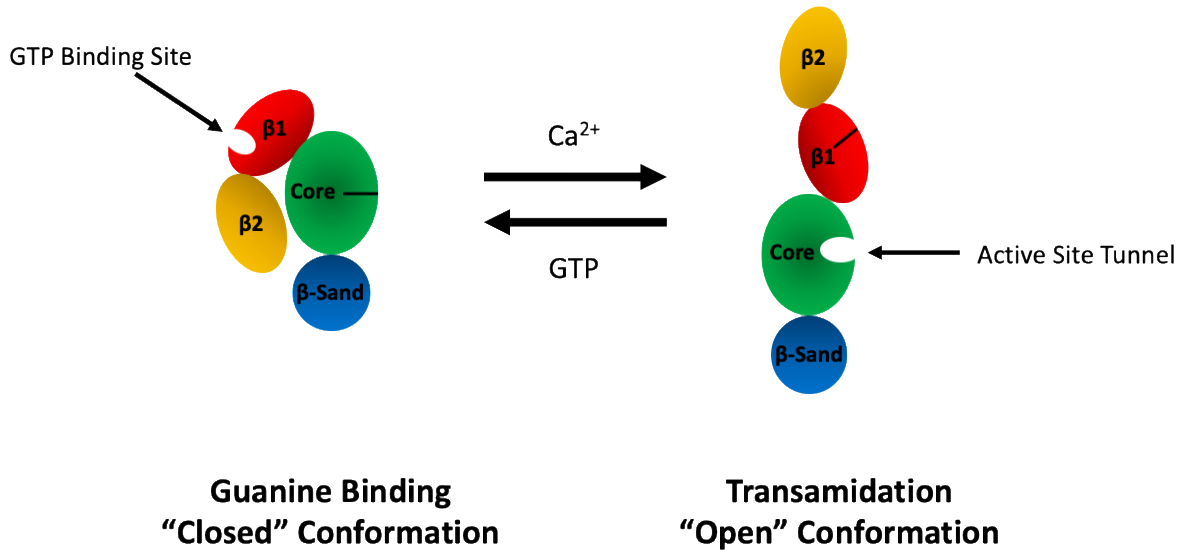

Figure 1.5. Cartoon representation of the two conformations of hTG2 which are regulated allosterically by Ca^{2+} or GTP. The N-terminal β-sandwich in blue, catalytic core in green, β-barrel1 in red, and C-terminal β-barrel2 in yellow.

1.4.1. Human Transglutaminase 2: Physiological Roles

Having two different physiological functions in vivo, the physiological roles and prevalence of hTG2 in disease states continue to be discovered each year. They can be grouped into two categories, the first being the intracellular signal transduction G-protein roles, and the second based on the crosslinking role as seen in the extracellular matrix. In early hTG2 research, it was believed that most of the pathologies associated with hTG2 were relating to its transamidation and hydrolysis, or deamidation, activity; however, as hTG2 research continues to expand, more and more studies have uncovered pathologies relating to the G-protein and cell signalling activities as well. hTG2 has been implicated in a number of disease states including cancer, celiac disease, fibrosis, and neurodegenerative diseases.[50]

1.4.2. Human Transglutaminase 2: Substrates, Probes, and Inhibitors

Some of the early work into TGases was to uncover potential substrates and inhibitors targeting these crosslinking enzymes. Due to its ubiquitous expression and various localizations, hTG2's glutamine and lysine bearing substrate scope is enormous. Among the many substrates, probes, and inhibitors of hTG2, those that are most relevant to this thesis are those designed by Keillor and Zedira GmbH. Keillor's early work focused on optimizing the purification and expression of hTG2 and elucidating the catalytic mechanism of guinea pig liver transglutaminase. Keillor's research has since progressed into probes, assays, and medicinal chemistry projects for hTG2.[51–56]

Various peptidomimetic, synthetic, and targeted antibodies have been developed for hTG2.[57] In terms of small molecule synthetic inhibitors, reversible and irreversible inhibitors have also been uncovered to have a great amount of specificity and in terms of the irreversible inhibitors, reactivity. These inhibitors have extremely diverse scaffolds with a reactive warhead positioned to be proximal to the catalytic cysteine residue. Common warheads attached to targeted irreversible inhibitors are epoxides,[58] 6-diazo-5-oxo-norleucine (DON),[59] acrylamides,[56] chloromethyl ketones,[54] and various α,β-unsaturated carbonyls[52] all with the goal to synthetically mimic either the natural lysine or glutamine residues.[57] A noteworthy inhibitor, ZED1227, developed by Zedira GmbH, has progressed into Phase IIb clinical trials for celiac disease as well as liver fibrosis.[60,61] The Griffin, Löser, and CHDI groups have also published potent inhibitors of hTG2, either focused entirely on a small molecule scaffold or on a more peptidomimetic approach akin to Keillor's current work.[62–68] Recent efforts by Keillor has uncovered three distinct and interesting scaffolds (Figure 1.6). NM72 was designed through the desire to increase the overall PK profile and become more drug-like, compared to the previous lead AA9, while not sacrificing affinity.[18] JA38 a spaced

version of AA9 revealed a dramatic increase in potency versus TG2, but the increased efficacy failed to correlated *in vivo*.[69] Finally, a SAR focused solely on the warhead residue in 2022 built off work conducted by both Griffin[62] and Keillor[70], and uncovered a substantial increase in k_{inact}/K_I, with LM-7j, but sacrificed isozyme selectivity.[71]

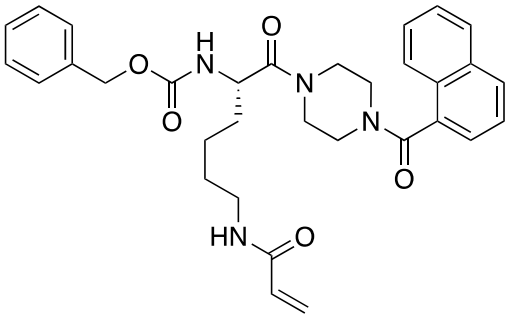

AA9
$k_{inact}/K_I = 244 \times 10^3\ M^{-1}\ min^{-1}$

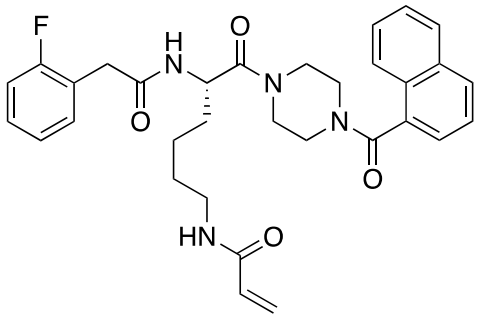

NM72
$k_{inact}/K_I = 443 \times 10^3\ M^{-1}\ min^{-1}$

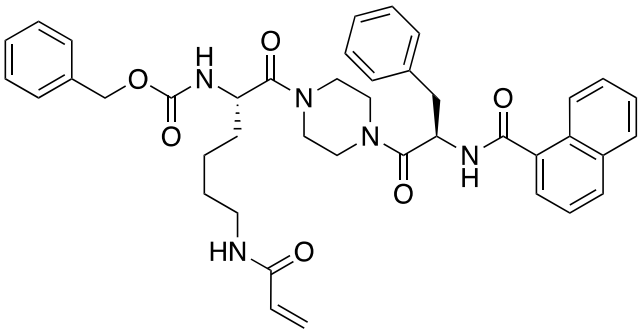

JA38
$k_{inact}/K_I = 760 \times 10^3\ M^{-1}\ min^{-1}$

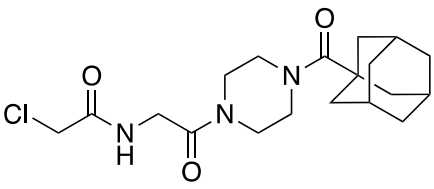

LM-7j
$k_{inact}/K_I = 8047 \times 10^3\ M^{-1}\ min^{-1}$

Figure 1.6. Scaffolds of new era Keillor hTG2 targeted irreversible inhibitors with associated inhibitor efficiency values.[18,69,71]

Much effort has gone into developing assays for hTG2, but those of most relevance to this thesis are the AL5 colorimetric Keillor assay (Figure 1.7) and the fluorogenic A101 isopeptidase pan-TGase assay produced by Zedira GmbH, which will be described in greater detail in Chapter

1.5.2. The AL5 colorimetric assay is based upon a known substrate for hTG2, the Cbz-Gln-Gly motif. Replacing the glutamine with a *p*-nitrophenyl ɣ-substituted glutamic acid, created N-Cbz-L-Glu(ɣ-*p*-nitrophenyl ester)Gly. This substrate enabled a TGase hydrolysis activity assay, initially designed for guinea pig liver transglutaminase but also functional with hTG2, with a recorded K_M = 47.2 ± 4.7 µM.[55,56] In the Keillor Research Group the typical transamidation inhibition assay conditions provide a K_M of approximately 10 µM with negligible background hydrolysis at pH 6.9.[56] A more in-depth discussion of the lack of tools as well as the current standard for hTG2 probes, substrates, and inhibitors will be described in Chapters 3, 4, and 5 of this thesis.

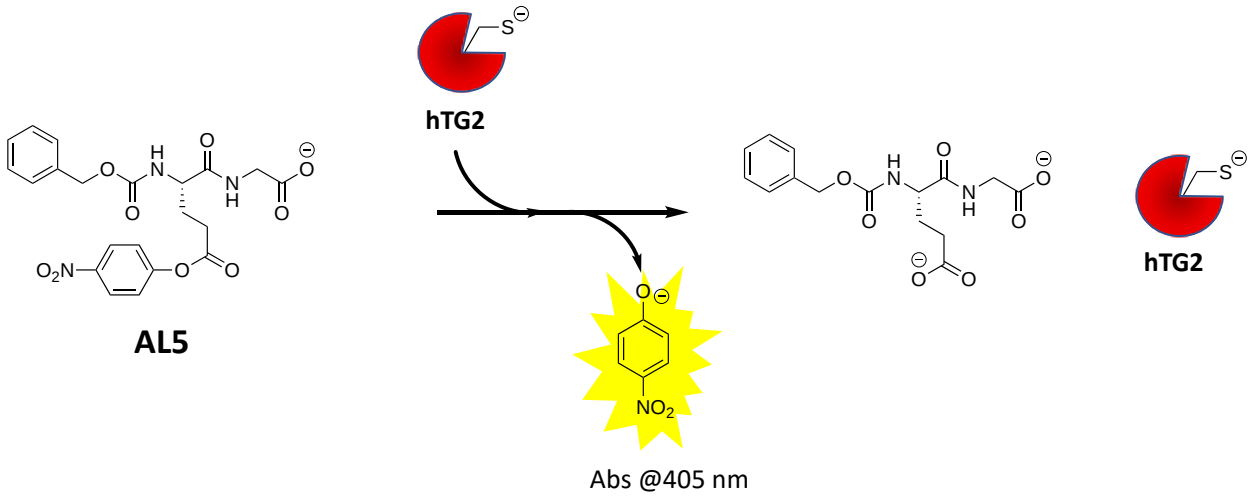

Figure 1.7. A representation of the hydrolysis activity assay substrate N-Cbz-L-Glu(ɣ-p-nitrophenyl ester)Gly (AL5) reacting with hTG2, which leads to the release of p-nitrophenol and can be observed by a spectrophotometer at 405 nm.

1.5. Human Factor XIII

FXIII was the first TGase studied and is the subject of intensive investigation as the mediator of the last step in the blood coagulation cascade, wherein it cross-links fibrin proteins to

form a rigid clot; however, it has also been implicated in extracellular matrix modelling, chondrocyte differentiation, and thrombosis.[40] The enzyme can be found in two distinct forms, a plasma heterodimer isoform and a cellular homodimer isoform. The plasma FXIII consists of two catalytic A subunits and two carrier B subunits. For full activation of the enzyme, the activation peptides need to be cleaved from the two FXIII-A subunits, whose calcium binding sites must be saturated to allow for dissociation from the carrier B subunits. FXIII has 3 calcium binding sites on each A subunit and the first site seems to play an antagonistic role in full activation, but aid in dissociation.[72,73] Although in general, thrombin is required to cleave the activation peptide and low calcium concentrations are required to dissociate the B subunits, activation has also been seen in a variety of circumstances (Figure 1.8).

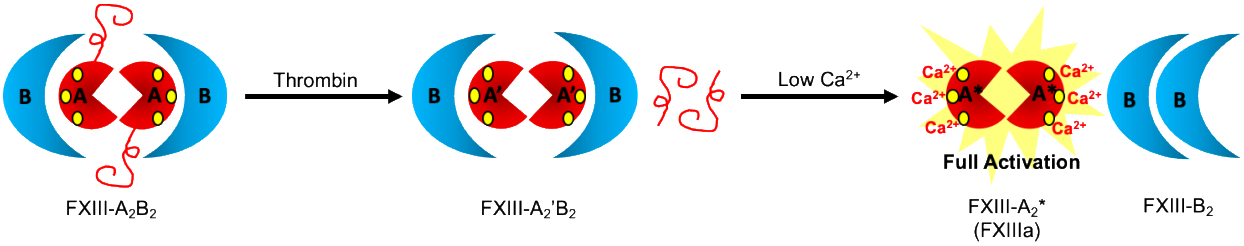

Figure 1.8. Cartoon representation of two step FXIII activation.

1.5.1. Human FXIII: Physiological Roles

Given FXIII's primary localization being in the blood, the physiological roles with which it is commonly associated comprise primarily of circulatory regulation and disorders. Overactivity of FXIIII can lead to venous thrombosis while low activity or decreased presence of FXIII can contribute towards hemophilia. Furthermore, FXIII's plasma soluble functions are attributed to promote clotting, angiogenesis, and wound healing. The intracellular form of FXIII is commonly implicated in osteoblast, macrophage, and monocyte activity. To again highlight the necessity of

designing specific TGase tools, TG2 is implicated to play a role in the stability and repair of vasculature in mice, whereas FXIIIa is hypothesized to play a role in preventing leakage from the vasculature.[74]

1.5.2. Human FXIII: Substrates, Probes, and Inhibitors

The current field of FXIII research has uncovered some specific FXIII substrates, probes, and inhibitors. The Hitomi peptides were based on a phage-display screen and allowed the discovery of various FXIII specific substrate peptides.[75] The optimal recognition sequence is named FK11 and this peptide has since been developed into FXIII probes. In the Keillor group, a truncated version of FK11 was observed to also exhibit FXIII substrate selectivity over TG2. Bearing a DQMMMAF sequence, this peptide mimics the negatively charged N-terminus at physiological pH and hydrophobic C-terminus.[76] The most noteworthy and current industry standard FXIII substrate is A101 (Figure 1.9).[77,78] This assay substrate is composed of a fluorescent anthranilic acid residue which is intramolecularly quenched by a dinitroaniline when not exposed to TGase activity. Upon isopeptidic cleavage of the glutamine-cadaverine bond, the quencher is released, and the assay reporter fluoresces (ex/em 313/418 nm). Given that TGases are more efficient transamidases than hydrolases, when an amine donor such as glycine methyl ester is included in the assay buffer, the TGase can quickly turn over this substrate and maintain its catalytic activity. A101 is classified as a pan-TGase substrate, but it is also the standard FXIII activity assay substrate, with a reported K_M of 9 µM for this isozyme. *In vivo,* however, the substrate would be ineffective at monitoring specifically FXIII activity as the K_M with hTG1, hTG2, hTG3, and hTG6 are 25 µM, 10 µM, 9 µM, and 20 µM respectively. This illustrates the systemic isozyme selectivity obstacle in this field.

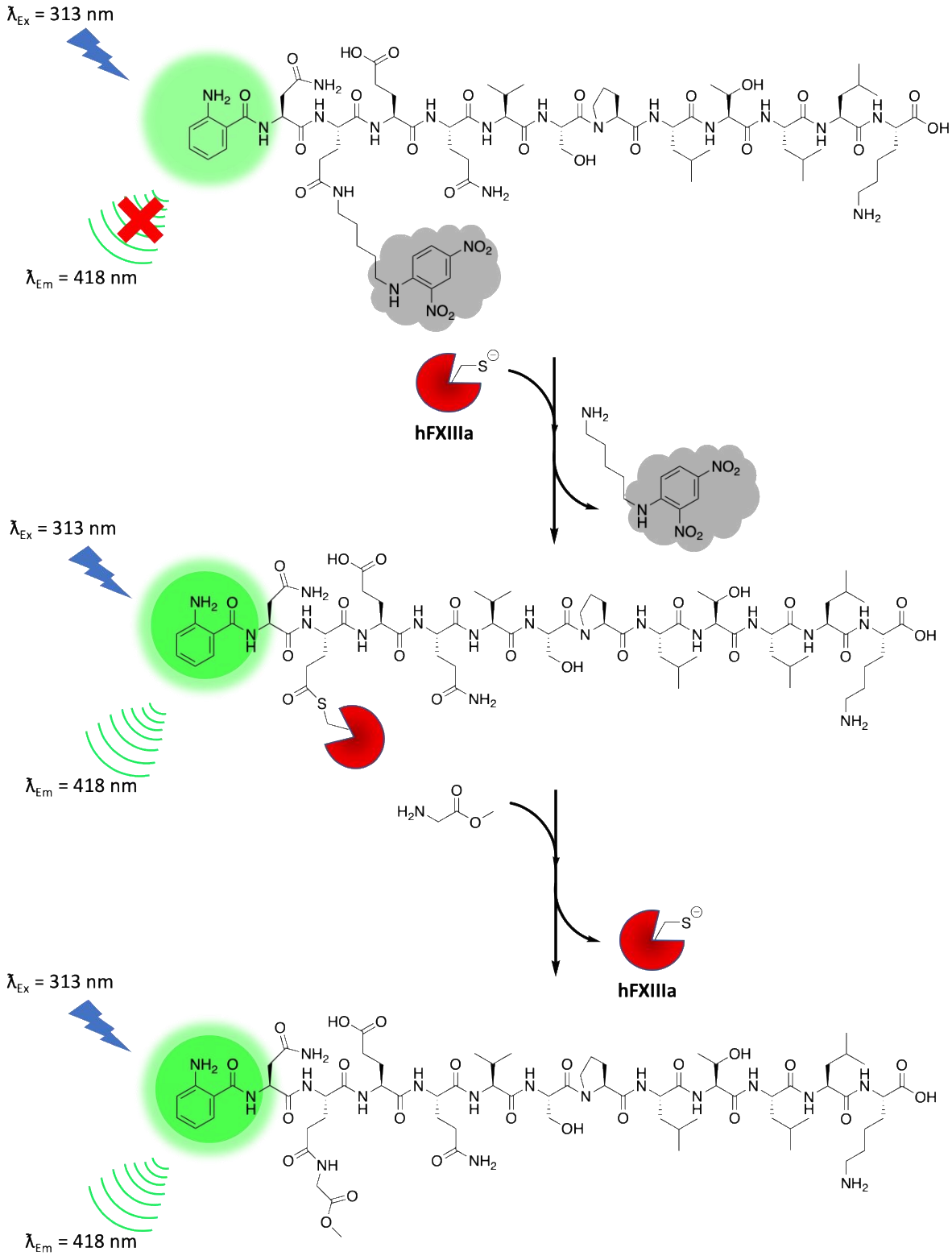

Figure 1.9. Cleavage and mechanism of isopeptidase A101 TGase activity assay.

Probes that are potent and selective for FXIII are few and far between. At this time there are only two known probes capable of monitoring FXIII activity *in vivo*. Either incorporating a Gd-chelating agent or a near-IR fluorophore, both probes are designed to mimic α_2-antiplasmin.[79,80] For such a vital enzyme in blood coagulation, the apparent lack in tools able to label the active form of the enzyme is astonishing and reveals a broad oversight in the toolbox for this isozyme.

There remains a significant lack in FXIII inhibitor research. First pioneered by Merck in the 1990s due to the attractiveness of a potential late acting blood coagulation inhibitor, a series of imidazolium small molecule inhibitors were designed.[81] Unfortunately, Merck's efforts reached a standstill when their scaffolds lacked significant isozyme selectivity. In 2013, Zedira GmbH embarked on a research program which was able to produce effective peptidomimetic inhibitors of FXIII, including ZED1301, which mimics the Hitomi peptides but incorporates a Michael acceptor warhead in place of the glutamine residue.[82] Zedira further optimized the scaffold to produce ZED2360[83] and ZED3197[84], which show increased affinity and more drug-like characteristics. With ZED3197 progressing into *in vivo* rabbit models, it faced an insurmountable hurdle in an extremely short half-life, requiring continuous infusion for a beneficial effect.[84] Further discussion of the inhibitors as well as the probes and substrates for FXIII will be detailed in Chapter 2 of this thesis.

1.6. Enzyme Inhibition

Inhibition is one of the most classic routes to develop therapeutics and research tools for studying the activity of enzymes. By abolishing an enzyme's activity, conclusions can be drawn about said enzyme's roles and impacts from both a fundamental and broader perspective. Common

methods of inhibition include both reversible and irreversible agents, which can either allow the enzyme to regain its catalytic activity or can completely abolish it. These compounds will either be directed towards the active site of the enzyme or an allosteric site which is also able to inhibit the enzymatic activity, or specific protein-protein interactions. Early work focused on reversible binders; however, in recent years, covalent inhibitors have made a dramatic surge in both the literature and as approved therapeutics.[85,86] As it is assumed that once inhibited, the enzyme will eventually be degraded and resynthesized as the activity has been irreversibly inhibited, covalent approaches are becoming more common and not as feared as they once were.

1.7. Proteolysis Targeting Chimeras (PROTACs)

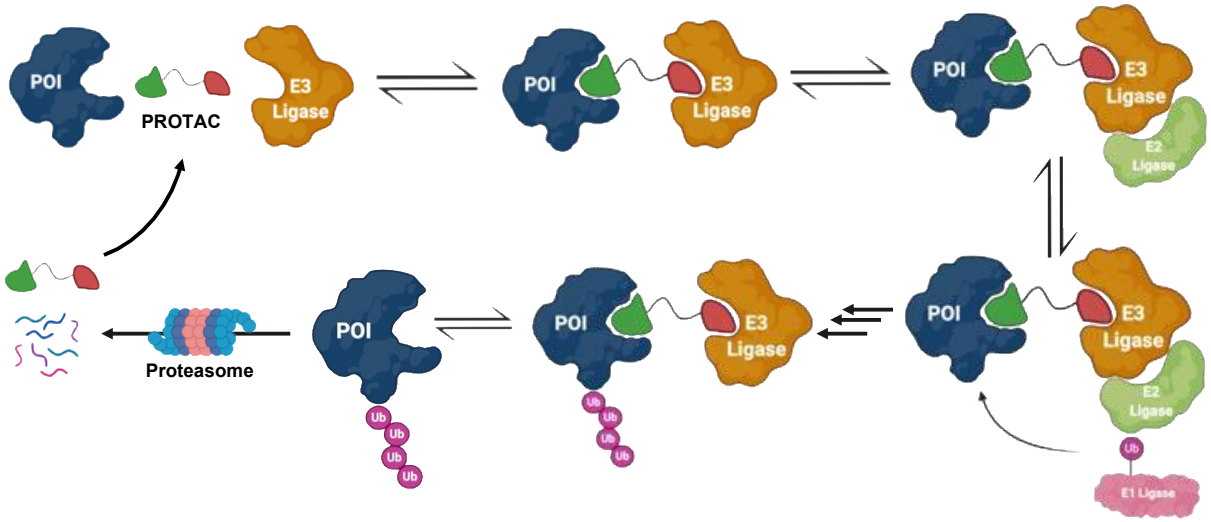

Figure 1.10. General mechanism of proteasomal degradation of a protein of interest by PROTACs.

Proteolysis Targeting Chimaeras are heterobifunctional molecules designed to target a protein of interest for natural proteasomal degradation by polyubiquitylation. Composed of both a protein of interest (POI) ligand, a linker, and an E3 ligase ligand, PROTACs are able to promote the formation of the heterotrimer complex (POI-PROTAC-E3Ligase).[87] The field of E3 ligase

ligands has emerged as a thriving field, conducting SARs on various ligands to identify high affinity binders of these regulatory enzymes.[88] The most common E3 ligases recruited by PROTACs are cereblon (CRBN) and von Hippel-Lindau (VHL). CRBN can be recruited by various versions of the thalidomide including the scaffold itself, pomalidomide, and lenalidomide. VHL is typically recruited by a peptidic VHL ligand. Once the ternary complex is formed and the POI is polyubiquitinated, it will be directed to the proteasome and degraded into fragments (Figure 1.10). In the case of reversible PROTACs, these molecules can dissociate and cause sequential degradation of other target proteins, thereby acting in a sub-stoichiometric manner.[89–91] Similar to traditional inhibitors, PROTACs can be gauged by multiple parameters to rank their effectiveness. The concentration required to reach 50% of the degradation, akin to an IC_{50} value, is termed DC_{50} and the maximum level of degradation possible, as a percentage, is coined D_{max}.[92] A rate of degradation and protein recovery are two further characteristics important in the evaluation of these molecules. Common hurdles PROTACs face are fast resynthesis rates of their targets, thereby making a high D_{max} and low DC_{50} values unachievable, low cellular permeability, and decreased oral bioavailability.[93] High dosing of PROTACs is also not desirable due to the propensity observe the hook effect whereby the POI binding site and E3L binding site are saturated with two individual molecules of PROTAC.

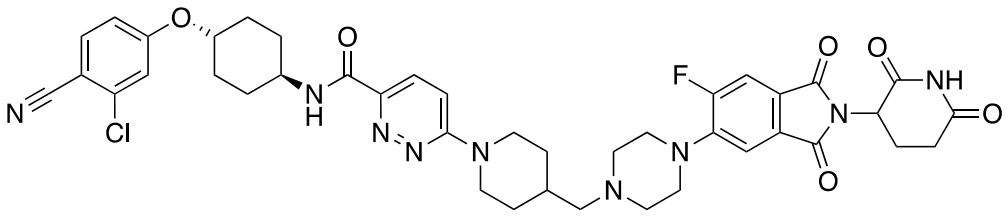

ARV-110
Androgen Receptor PROTAC
Phase II

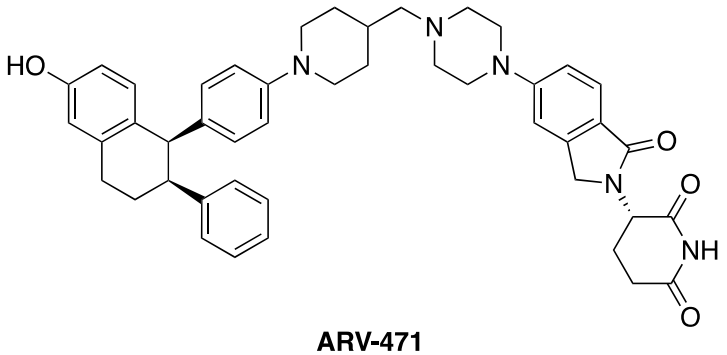

ARV-471
Estrogen Receptor PROTAC
Phase III

Figure 1.11. Structure of two clinical candidate PROTACs pioneered by Arvinas.

The conception of the PROTAC field was pioneered by both the Crews and Deshaies lab in 2001.[94] Initially gaining notoriety for their ability to drug what were considered undruggable targets, and with a lower dosing profile, research in the PROTACs field has primarily resulted in a plethora of research tools; albeit a few noteworthy compounds have progressed into late-stage clinical trials and large pharmaceutical companies have embarked on their own PROTAC research programs.[95] Arvinas, a Connecticut, USA based biotech company is leading the charge in development and optimization of PROTACs for therapeutic applications. Two of the lead candidates ARV-110 (Bavdegalutamide) and ARV-471 (Vepdegestrant, in collaboration with Pfizer) are currently in phase II and phase III clinical trials respectively for the treatment of metastatic prostate and breast cancer (Figure 1.11). Regardless of their progress through the

therapeutic pipeline, this methodology has been revolutionary as novel research tools that are able to chemically knockout a protein without genetic alteration.[96] For multifunctional proteins, these compounds can abrogate all activities of the protein, whereas traditional small molecule inhibitors may only be able to modulate one activity.

1.8. Thesis Overview and Goals

This thesis will be focused on designing, synthesizing, and evaluating chemical research tools for the study of both Factor XIII and transglutaminase 2, with the goal to develop tools that will aid in furthering the understanding of FXIII and TG2 both *in vitro* and *in vivo*. The inhibitors for FXIII will initially be based on known low potency TG2 inhibitors that also showed inhibition of hFXIIIa. The scaffold will then be altered in an SAR approach to fine tune the inhibition parameters and develop the first small molecule FXIII specific inhibitor as well as a fluorescent probe to track the location and activity. In efforts to further advance our understanding of transglutaminase 2, a high affinity activity substrate will be conceptualized from a previous lead inhibitor. Finally, a recent SAR of a peptidic TG2 inhibitor revealed a tailorable site that launched a chemical biology research program aimed at studying the overlapping and conflicting roles of both intracellular and extracellular TG2. Given the broad diversity of cargo incorporated in said chemical biology toolbox, while not sacrificing affinity, efforts were then directed towards targeting TG2 for proteasomal degradation *via* a covalent PROTAC strategy.

The successful molecules synthesized and evaluated in this research study will be passed along to collaborators to evaluate their potential as research tools in the study of both transglutaminase 2 and Factor XIII. With most of these tools already having been applied to preliminary studies within this thesis, the scope of their applications is very broad. Future work

will continue to use these tools in biological settings to aid in our understanding of these multifaceted, vital enzymes.

1.9. Chapter 1 References

(1) Robinson, P. K. Enzymes: Principles and Biotechnological Applications. *Essays Biochem* **2015**, *59*, 1–41. https://doi.org/10.1042/BSE0590001.

(2) Zhang, J.; Yang, P. L.; Gray, N. S. Targeting Cancer with Small Molecule Kinase Inhibitors. *Nature Reviews Cancer*. 2009, pp 28–39. https://doi.org/10.1038/nrc2559.

(3) McKinsey, T. A.; Kass, D. A. Small-Molecule Therapies for Cardiac Hypertrophy: Moving beneath the Cell Surface. *Nature Reviews Drug Discovery*. 2007, pp 617–635. https://doi.org/10.1038/nrd2193.

(4) Ekins, S.; Litterman, N.; Lipinski, C. Small Molecules with Antiviral Activity against the Ebola Virus. *F1000Research*. 2015. https://doi.org/10.12688/f1000research.6120.1.

(5) Gurevich, E. V.; Gurevich, V. V. Therapeutic Potential of Small Molecules and Engineered Proteins. *Handb Exp Pharmacol* **2014**, *219*, 1–12. https://doi.org/10.1007/978-3-642-41199-1_1.

(6) Schreiber, S. L.; Kotz, J. D.; Li, M.; Aubé, J.; Austin, C. P.; Reed, J. C.; Rosen, H.; White, E. L.; Sklar, L. A.; Lindsley, C. W.; Alexander, B. R.; Bittker, J. A.; Clemons, P. A.; De Souza, A.; Foley, M. A.; Palmer, M.; Shamji, A. F.; Wawer, M. J.; McManus, O.; Wu, M.; Zou, B.; Yu, H.; Golden, J. E.; Schoenen, F. J.; Simeonov, A.; Jadhav, A.; Jackson, M. R.; Pinkerton, A. B.; Chung, T. D. Y.; Griffin, P. R.; Cravatt, B. F.; Hodder, P. S.; Roush, W. R.; Roberts, E.; Chung, D. H.; Jonsson, C. B.; Noah, J. W.; Severson, W. E.; Ananthan, S.; Edwards, B.; Oprea, T. I.; Conn, P. J.; Hopkins, C. R.; Wood, M. R.; Stauffer, S. R.; Emmitte, K. A. Advancing Biological Understanding and Therapeutics

Discovery with Small-Molecule Probes. *Cell*. Cell Press 2015, pp 1252–1265. https://doi.org/10.1016/j.cell.2015.05.023.

(7) Nurminskaya, M. V.; Belkin, A. M. Cellular Functions of Tissue Transglutaminase. *Int Rev Cell Mol Biol* **2012**, *294*, 1–97. https://doi.org/10.1016/B978-0-12-394305-7.00001-X.

(8) Eckert, R. L.; Kaartinen, M. T.; Nurminskaya, M.; Belkin, A. M.; Colak, G.; Johnson, G. V. W.; Mehta, K. Transglutaminase Regulation of Cell Function. *Physiol Rev* **2014**, *94* (2), 383–417. https://doi.org/10.1152/physrev.00019.2013.

(9) Wang, Z.; Collighan, R. J.; Pytel, K.; Rathbone, D. L.; Li, X.; Griffin, M. Characterization of Heparin-Binding Site of Tissue Transglutaminase: Its Importance in Cell Surface Targeting, Matrix Deposition, and Cell Signaling. *Journal of Biological Chemistry* **2012**, *287* (16), 13063–13083. https://doi.org/10.1074/jbc.M111.294819.

(10) Sane, D. C.; Kontos, J. L.; Greenberg, C. S. Roles of Transglutaminases in Cardiac and Vascular Diseases. *Frontiers in Bioscience*. NIH Public Access January 1, 2007, pp 2530–2545. https://doi.org/10.2741/2253.

(11) Jiang, W. G.; Ablin, R. J.; Kynaston, H. G.; Mason, M. D. The Prostate Transglutaminase (TGase-4, TGaseP) Regulates the Interaction of Prostate Cancer and Vascular Endothelial Cells, a Potential Role for the ROCK Pathway. *Microvasc Res* **2009**, *77* (2), 150–157. https://doi.org/10.1016/j.mvr.2008.09.010.

(12) Huang, L.; Xu, A. M.; Liu, W. Transglutaminase 2 in Cancer. *Am J Cancer Res* **2015**, *5* (9), 2756–2776.

(13) Wang, Z.; Stuckey, D. J.; Murdoch, C. E.; Camelliti, P.; Lip, G. Y. H.; Griffin, M. Cardiac Fibrosis Can Be Attenuated by Blocking the Activity of Transglutaminase 2 Using a

Selective Small-Molecule Inhibitor. *Cell Death Dis* **2018**, *9* (6). https://doi.org/10.1038/s41419-018-0573-2.

(14) Johnson, T. S.; Fisher, M.; Haylor, J. L.; Hau, Z.; Skill, N. J.; Jones, R.; Saint, R.; Coutts, I.; Vickers, M. E.; El Nahas, A. M.; Griffin, M. Transglutaminase Inhibition Reduces Fibrosis and Preserves Function in Experimental Chronic Kidney Disease. *Journal of the American Society of Nephrology* **2007**, *18* (12), 3078–3088. https://doi.org/10.1681/ASN.2006070690.

(15) Keillor, J. W.; Clouthier, C. M.; Apperley, K. Y. P.; Akbar, A.; Mulani, A. Acyl Transfer Mechanisms of Tissue Transglutaminase. *Bioorg Chem* **2014**, *57*, 186–197. https://doi.org/10.1016/j.bioorg.2014.06.003.

(16) Eckert, R. L.; Sturniolo, M. T.; Broome, A. M.; Ruse, M.; Rorke, E. A. Transglutaminase Function in Epidermis. *Journal of Investigative Dermatology*. Blackwell Publishing Inc. March 1, 2005, pp 481–492. https://doi.org/10.1111/j.0022-202X.2005.23627.x.

(17) Hennies, H. C.; Raghunath, M.; Wiebe, V.; Vogel, M.; Velten, F.; Traupe, H.; Reis, A. Genetic and Immunohistochemical Detection of Mutations Inactivating the Keratinocyte Transglutaminase in Patients with Lamellar Ichthyosis. *Hum Genet* **1998**, *102* (3), 314–318. https://doi.org/10.1007/s004390050697.

(18) McNeil, N. M. R.; Gates, E. W. J.; Firoozi, N.; Cundy, N. J.; Leccese, J.; Eisinga, S.; Tyndall, J. D. A.; Adhikary, G.; Eckert, R. L.; Keillor, J. W. Structure-Activity Relationships of N-Terminal Variants of Peptidomimetic Tissue Transglutaminase Inhibitors. *Eur J Med Chem* **2022**, *232*, 114172. https://doi.org/10.1016/j.ejmech.2022.114172.

(19) Gundemir, S.; Colak, G.; Tucholski, J.; Johnson, G. V. W. Transglutaminase 2: A Molecular Swiss Army Knife. *Biochim Biophys Acta Mol Cell Res* **2012**, *1823* (2), 406–419. https://doi.org/10.1016/j.bbamcr.2011.09.012.

(20) Dolynchuk, K. N. Inhibition of Tissue Transglutaminase and ∈ (γ-Glutamyl) Lysine Cross-Linking in Human Hypertrophic Scar. *Wound Repair and Regeneration* **1996**, *4* (1), 16–20. https://doi.org/10.1046/j.1524-475X.1996.40105.x.

(21) Chhabra, A.; Verma, A.; Mehta, K. Tissue Transglutaminase Promotes or Suppresses Tumors Depending on Cell Context. *Anticancer Research*. June 2009, pp 1909–1919.

(22) Yunes-Medina, L.; Paciorkowski, A.; Nuzbrokh, Y.; Johnson, G. V. W. Depletion of Transglutaminase 2 in Neurons Alters Expression of Extracellular Matrix and Signal Transduction Genes and Compromises Cell Viability. *Molecular and Cellular Neuroscience* **2018**, *86*, 72–80. https://doi.org/10.1016/j.mcn.2017.11.011.

(23) Mehta, K.; Eckert, R. *Transglutaminases: Family of Enzymes with Diverse Functions*; 2005; Vol. 38. https://doi.org/10.1159/000084229.

(24) Ahvazi, B.; Kim, H. C.; Kee, S. H.; Nemes, Z.; Steinert, P. M. Three-Dimensional Structure of the Human Transglutaminase 3 Enzyme: Binding of Calcium Ions Changes Structure for Activation. *EMBO Journal* **2002**, *21* (9), 2055–2067. https://doi.org/10.1093/emboj/21.9.2055.

(25) Klöock, C.; Khosla, C. Regulation of the Activities of the Mammalian Transglutaminase Family of Enzymes. *Protein Science*. Wiley-Blackwell December 2012, pp 1781–1791. https://doi.org/10.1002/pro.2162.

(26) John, S.; Thiebach, L.; Frie, C.; Mokkapati, S.; Bechtel, M.; Nischt, R.; Rosser-Davies, S.; Paulsson, M.; Smyth, N. Epidermal Transglutaminase (TGase 3) Is Required for Proper

Hair Development, but Not the Formation of the Epidermal Barrier. *PLoS One* **2012**, *7* (4), e34252. https://doi.org/10.1371/journal.pone.0034252.

(27) Sárdy, M.; Kárpáti, S.; Merkl, B.; Paulsson, M.; Smyth, N. Epidermal Transglutaminase (TGase 3) Is the Autoantigen of Dermatitis Herpetiformis. *Journal of Experimental Medicine* **2002**, *195* (6), 747–757. https://doi.org/10.1084/jem.20011299.

(28) Savoca, M. P.; Inferrera, A.; Verderio, E. A. M.; Caccamo, D. Search for Novel Diagnostic Biomarkers of Prostate Inflammation-Related Disorders: Role of Transglutaminase Isoforms as Potential Candidates. *Mediators of inflammation*. Hindawi Limited 2019, p 7894017. https://doi.org/10.1155/2019/7894017.

(29) Ablin, R. J.; Owen, S.; Jiang, W. G. Prostate Transglutaminase (TGase-4) Induces Epithelialto-Mesenchymal Transition in Prostate Cancer Cells. *Anticancer Res* **2017**, *37* (2), 481–488. https://doi.org/10.21873/anticanres.11340.

(30) Jiang, W. G.; Ablin, R. J. Prostate Transglutaminase: A Unique Transglutaminase and Its Role in Prostate Cancer. *Biomarkers in Medicine*. Future Medicine Ltd. June 1, 2011, pp 285–291. https://doi.org/10.2217/bmm.11.36.

(31) Jiang, W. G.; Ye, L.; Sanders, A. J.; Ruge, F.; Kynaston, H. G.; Ablin, R. J.; Mason, M. D. Prostate Transglutaminase (TGase-4, TGaseP) Enhances the Adhesion of Prostate Cancer Cells to Extracellular Matrix, the Potential Role of TGase-Core Domain. *J Transl Med* **2013**, *11* (1), 269. https://doi.org/10.1186/1479-5876-11-269.

(32) Cassidy, A. J.; Van Steensel, M. A. M.; Steijlen, P. M.; Van Geel, M.; Van Der Velden, J.; Morley, S. M.; Terrinoni, A.; Melino, G.; Candi, E.; McLean, W. H. I. A Homozygous Missense Mutation in TGM5 Abolishes Epidermal Transglutaminase 5 Activity and

Causes Acral Peeling Skin Syndrome. *Am J Hum Genet* **2005**, *77* (6), 909–917. https://doi.org/10.1086/497707.

(33) Grenard, P.; Bates, M. K.; Aeschlimann, D. Evolution of Transglutaminase Genes: Identification of a Transglutaminase Gene Cluster on Human Chromosome 15q15: Structure of the Gene Encoding Transglutaminase X and a Novel Gene Family Member, Transglutaminase Z. *Journal of Biological Chemistry* **2001**, *276* (35), 33066–33078. https://doi.org/10.1074/jbc.M102553200.

(34) Thomas, H.; Beck, K.; Adamczyk, M.; Aeschlimann, P.; Langley, M.; Oita, R. C.; Thiebach, L.; Hils, M.; Aeschlimann, D. Transglutaminase 6: A Protein Associated with Central Nervous System Development and Motor Function. *Amino Acids* **2013**, *44* (1), 161–177. https://doi.org/10.1007/s00726-011-1091-z.

(35) Lorand, L.; Graham, R. M. Transglutaminases: Crosslinking Enzymes with Pleiotropic Functions. *Nat Rev Mol Cell Biol* **2003**, *4* (2), 140–156. https://doi.org/10.1038/nrm1014.

(36) Muszbek, L.; Bereczky, Z.; Bagoly, Z.; Komáromi, I.; Katona, É. Factor XIII: A Coagulation Factor with Multiple Plasmatic and Cellular Functions. *Physiological Reviews*. 2011, pp 931–972. https://doi.org/10.1152/physrev.00016.2010.

(37) Toye, A. M.; Ghosh, S.; Young, M. T.; Jones, G. K.; Sessions, R. B.; Ramaugé, M.; Leclerc, P.; Basu, J.; Delaunay, J.; Tanner, M. J. A. Protein-4.2 Association with Band 3 (AE1, SLCA4) in Xenopus Oocytes: Effects of Three Natural Protein-4.2 Mutations Associated with Hemolytic Anemia. *Blood* **2005**, *105* (10), 4088–4095. https://doi.org/10.1182/BLOOD-2004-05-1895.

(38) Korsgren, C.; Lawler, J.; Lambert, S.; Speicher, D.; Cohen, C. M. Complete Amino Acid Sequence and Homologies of Human Erythrocyte Membrane Protein Band 4.2. *Proc Natl Acad Sci U S A* **1990**, *87* (2), 613–617. https://doi.org/10.1073/pnas.87.2.613.

(39) Ideguchi, H.; Nishimura, J.; Nawata, H.; Hamasaki, N. A Genetic Defect of Erythrocyte Band 4.2 Protein Associated with Hereditary Spherocytosis. *Br J Haematol* **1990**, *74* (3), 347–353. https://doi.org/10.1111/j.1365-2141.1990.tb02594.x.

(40) Beninati, S.; Bergamini, C. M.; Piacentini, M. An Overview of the First 50 Years of Transglutaminase Research. *Amino Acids* **2009**, *36* (4), 591–598. https://doi.org/10.1007/s00726-008-0211-x.

(41) Jang, T. H.; Lee, D. S.; Choi, K.; Jeong, E. M.; Kim, I. G.; Kim, Y. W.; Chun, J. N.; Jeon, J. H.; Park, H. H. Crystal Structure of Transglutaminase 2 with GTP Complex and Amino Acid Sequence Evidence of Evolution of GTP Binding Site. *PLoS One* **2014**, *9* (9), e107005. https://doi.org/10.1371/journal.pone.0107005.

(42) Ahvazi, B.; Boeshans, K. M.; Idler, W.; Baxa, U.; Steinert, P. M.; Rastinejad, F. Structural Basis for the Coordinated Regulation of Transglutaminase 3 by Guanine Nucleotides and Calcium/Magnesium. *Journal of Biological Chemistry* **2004**, *279* (8), 7180–7192. https://doi.org/10.1074/jbc.M312310200.

(43) Candi, E.; Paradisi, A.; Terrinoni, A.; Pietroni, V.; Oddi, S.; Cadot, B.; Jogini, V.; Meiyappan, M.; Clardy, J.; Finazzi-Agro, A.; Melino, G. Transglutaminase 5 Is Regulated by Guanine–Adenine Nucleotides. *Biochemical Journal* **2004**, *381* (1), 313–319. https://doi.org/10.1042/BJ20031474.

(44) Thomas, H.; Beck, K.; Adamczyk, M.; Aeschlimann, P.; Langley, M.; Oita, R. C.; Thiebach, L.; Hils, M.; Aeschlimann, D. Transglutaminase 6: A Protein Associated with

Central Nervous System Development and Motor Function. *Amino Acids* **2013**, *44* (1), 161–177. https://doi.org/10.1007/S00726-011-1091-Z/FIGURES/4.

(45) Pinkas, D. M.; Strop, P.; Brunger, A. T.; Khosla, C. Transglutaminase 2 Undergoes a Large Conformational Change upon Activation. *PLoS Biol* **2007**, *5* (12), e327. https://doi.org/10.1371/journal.pbio.0050327.

(46) Achyuthan, K. E.; Greenberg, C. S. Identification of a Guanosine Triphosphate-Binding Site on Guinea Pig Liver Transglutaminase. Role of GTP and Calcium Ions in Modulating Activity. *Journal of Biological Chemistry* **1987**, *262* (4), 1901–1906.

(47) Király, R.; Cssz, É.; Kurtán, T.; Antus, S.; Szigeti, K.; Simon-Vecsei, Z.; Korponay-Szabó, I. R.; Keresztessy, Z.; Fésüs, L. Functional Significance of Five Noncanonical Ca2+-Binding Sites of Human Transglutaminase 2 Characterized by Site-Directed Mutagenesis. *FEBS Journal* **2009**, *276* (23), 7083–7096. https://doi.org/10.1111/j.1742-4658.2009.07420.x.

(48) Begg, G. E.; Holman, S. R.; Stokes, P. H.; Matthews, J. M.; Graham, R. M.; Iismaa, S. E. Mutation of a Critical Arginine in the GTP-Binding Site of Transglutaminase 2 Disinhibits Intracellular Cross-Linking Activity. *Journal of Biological Chemistry* **2006**, *281* (18), 12603–12609. https://doi.org/10.1074/jbc.M600146200.

(49) Stamnaes, J.; Pinkas, D. M.; Fleckenstein, B.; Khosla, C.; Sollid, L. M. Redox Regulation of Transglutaminase 2 Activity. *Journal of Biological Chemistry* **2010**, *285* (33), 25402–25409. https://doi.org/10.1074/jbc.M109.097162.

(50) Szondy, Z.; Korponay-Szabó, I.; Király, R.; Sarang, Z.; Tsay, G. J. Transglutaminase 2 in Human Diseases. *BioMedicine (France)* **2017**, *7* (3), 1–13. https://doi.org/10.1051/bmdcn/2017070315.

(51) Leblanc, A.; Day, N.; Ménard, A.; Keillor, J. W. Guinea Pig Liver Transglutaminase: A Modified Purification Procedure Affording Enzyme with Superior Activity in Greater Yield. *Protein Expr Purif* **1999**, *17* (1), 89–95. https://doi.org/10.1006/prep.1999.1107.

(52) Pardin, C.; Pelletier, J. N.; Lubell, W. D.; Keillor, J. W. Cinnamoyl Inhibitors of Tissue Transglutaminase. *Journal of Organic Chemistry* **2008**, *73* (15), 5766–5775. https://doi.org/10.1021/jo8004843.

(53) Pardin, C.; Roy, I.; Chica, R. A.; Bonneil, E.; Thibault, P.; Lubell, W. D.; Pelletier, J. N.; Keillor, J. W. Photolabeling of Tissue Transglutaminase Reveals the Binding Mode of Potent Cinnamoyl Inhibitors †. https://doi.org/10.1021/bi802021c.

(54) Pardin, C.; Gillet, S. M. F. G.; Keillor, J. W. Synthesis and Evaluation of Peptidic Irreversible Inhibitors of Tissue Transglutaminase. *Bioorg Med Chem* **2006**, *14* (24), 8379–8385. https://doi.org/10.1016/j.bmc.2006.09.011.

(55) Leblanc, A.; Gravel, C.; Labelle, J.; Keillor, J. W. Kinetic Studies of Guinea Pig Liver Transglutaminase Reveal a General-Base-Catalyzed Deacylation Mechanism. *Biochemistry* **2001**, *40* (28), 8335–8342. https://doi.org/10.1021/bi0024097.

(56) Akbar, A.; McNeil, N. M. R.; Albert, M. R.; Ta, V.; Adhikary, G.; Bourgeois, K.; Eckert, R. L.; Keillor, J. W. Structure-Activity Relationships of Potent, Targeted Covalent Inhibitors That Abolish Both the Transamidation and GTP Binding Activities of Human Tissue Transglutaminase. *J Med Chem* **2017**, *60* (18), 7910–7927. https://doi.org/10.1021/acs.jmedchem.7b01070.

(57) Keillor, J. W.; Apperley, K. Y. P. Transglutaminase Inhibitors: A Patent Review. *Expert Opin Ther Pat* **2016**, *26* (1), 49–63. https://doi.org/10.1517/13543776.2016.1115836.

(58) De Macédo, P.; Marrano, C.; Keillor, J. W. Synthesis of Dipeptide-Bound Epoxides and α,β-Unsaturated Amides as Potential Irreversible Transglutaminase Inhibitors. *Bioorg Med Chem* **2002**, *10* (2), 355–360. https://doi.org/10.1016/S0968-0896(01)00292-9.

(59) Schuppan, D.; Dieterich, W. A Molecular Warhead and Its Target: Tissue Transglutaminase and Celiac Sprue. *Chemistry and Biology*. Elsevier Ltd March 1, 2003, pp 199–201. https://doi.org/10.1016/S1074-5521(03)00055-3.

(60) Schuppan, D.; Mäki, M.; Lundin, K. E. A.; Isola, J.; Friesing-Sosnik, T.; Taavela, J.; Popp, A.; Koskenpato, J.; Langhorst, J.; Hovde, Ø.; Lähdeaho, M.-L.; Fusco, S.; Schumann, M.; Török, H. P.; Kupcinskas, J.; Zopf, Y.; Lohse, A. W.; Scheinin, M.; Kull, K.; Biedermann, L.; Byrnes, V.; Stallmach, A.; Jahnsen, J.; Zeitz, J.; Mohrbacher, R.; Greinwald, R. A Randomized Trial of a Transglutaminase 2 Inhibitor for Celiac Disease. *New England Journal of Medicine* **2021**, *385* (1), 35–45. https://doi.org/10.1056/NEJMoa2032441.

(61) Büchold, C.; Hils, M.; Gerlach, U.; Weber, J.; Pelzer, C.; Heil, A.; Aeschlimann, D.; Pasternack, R. Features of ZED1227: The First-In-Class Tissue Transglutaminase Inhibitor Undergoing Clinical Evaluation for the Treatment of Celiac Disease. *Cells* **2022**, *11*, 1667. https://doi.org/10.3390/cells11101667.

(62) Badarau, E.; Wang, Z.; Rathbone, D. L.; Costanzi, A.; Thibault, T.; Murdoch, C. E.; El Alaoui, S.; Bartkeviciute, M.; Griffin, M. Development of Potent and Selective Tissue Transglutaminase Inhibitors: Their Effect on TG2 Function and Application in Pathological Conditions. *Chem Biol* **2015**, *22* (10), 1347–1361. https://doi.org/10.1016/j.chembiol.2015.08.013.

(63) Griffin, M.; Rathbone, D.; Badarau, L. E. Acylpiperazines as Inhibitors of Transglutaminase and Their Use in Medicine. WO2014057266A1, 2014.

(64) Wodtke, R.; Hauser, C.; Ruiz-Gómez, G.; Jäckel, E.; Bauer, D.; Lohse, M.; Wong, A.; Pufe, J.; Ludwig, F.-A.; Fischer, S.; Hauser, S.; Greif, D.; Pisabarro, M. T.; Pietzsch, J.; Pietsch, M.; Löser, R. Nε-Acryloyllysine Piperazides as Irreversible Inhibitors of Transglutaminase 2: Synthesis, Structure–Activity Relationships, and Pharmacokinetic Profiling. *J Med Chem* **2018**, *61* (10), 4528–4560. https://doi.org/10.1021/ACS.JMEDCHEM.8B00286.

(65) Wodtke, R.; Wodtke, J.; Hauser, S.; Laube, M.; Bauer, D.; Rothe, R.; Neuber, C.; Pietsch, M.; Kopka, K.; Pietzsch, J.; Löser, R. Development of an 18F-Labeled Irreversible Inhibitor of Transglutaminase 2 as Radiometric Tool for Quantitative Expression Profiling in Cells and Tissues. *J Med Chem* **2021**, *64* (6), 3462–3478. https://doi.org/10.1021/acs.jmedchem.1c00096.

(66) Wityak, J.; Prime, M. E.; Brookfield, F. A.; Courtney, S. M.; Erfan, S.; Johnsen, S.; Johnson, P. D.; Li, M.; Marston, R. W.; Reed, L.; Vaidya, D.; Schaertl, S.; Pedret-Dunn, A.; Beconi, M.; Macdonald, D.; Muñoz-Sanjuan, I.; Dominguez, C. SAR Development of Lysine-Based Inhibitors of Transglutaminase 2 for Huntington's Disease. *ACS Med Chem Lett* **2012**, *3* (12), 1024. https://doi.org/10.1021/ML300241M.

(67) Prime, M. E.; Andersen, O. A.; Barker, J. J.; Brooks, M. A.; Cheng, R. K. Y.; Toogood-Johnson, I.; Courtney, S. M.; Brookfield, F. A.; Yarnold, C. J.; Marston, R. W.; Johnson, P. D.; Johnsen, S. F.; Palfrey, J. J.; Vaidya, D.; Erfan, S.; Ichihara, O.; Felicetti, B.; Palan, S.; Pedret-Dunn, A.; Schaertl, S.; Sternberger, I.; Ebneth, A.; Scheel, A.; Winkler, D.; Toledo-Sherman, L.; Beconi, M.; MacDonald, D.; Muñoz-Sanjuan, I.; Dominguez, C.;

Wityak, J. Discovery and Structure-Activity Relationship of Potent and Selective Covalent Inhibitors of Transglutaminase 2 for Huntington's Disease. *J Med Chem* **2012**, *55* (3), 1021–1046. https://doi.org/10.1021/JM201310Y/SUPPL_FILE/JM201310Y_SI_001.PDF.

(68) Dominguez, C.; Prime, M.; Marston, R.; Brookfield, F. A.; Courtney, S. M.; Macdonald, D.; Wityak, J.; Yarnold, C. J.; Vaidya, D. Transglutaminase TG2 Inhibitors, Pharmaceutical Compositions, and Methods of Use Thereof. WO2014047288A2, 2014.

(69) Cundy, N. J.; Arciszewski, J.; Gates, E. W. J.; Acton, S. L.; Passley, K. D.; Awoonor-Williams, E.; Boyd, E. K.; Xu, N.; Pierson, É.; Fernandez-Ansieta, C.; Albert, M. R.; McNeil, N. M. R.; Adhikary, G.; Eckert, R. L.; Keillor, J. W. Novel Irreversible Peptidic Inhibitors of Transglutaminase 2. *RSC Med Chem* **2023**, *14*, 378–385. https://doi.org/10.1039/D2MD00417H.

(70) Rangaswamy, A. M. M.; Navals, P.; Gates, E. W. J.; Shad, S.; Watt, S. K. I.; Keillor, J. W. Structure-Activity Relationships of Hydrophobic Alkyl Acrylamides as Tissue Transglutaminase Inhibitors. *RSC Med Chem* **2022**, *13*, 413–428. https://doi.org/10.1039/d1md00382h.

(71) Mader, L.; Watt, S. K. I.; Iyer, H. R.; Nguyen, L.; Kaur, H.; Keillor, J. W. The War on HTG2: Warhead Optimization in Small Molecule Human Tissue Transglutaminase Inhibitors. *RSC Med Chem* **2023**, *14*, 277–298. https://doi.org/10.1039/D2MD00378C.

(72) Gupta, S.; Biswas, A.; Akhter, M. S.; Krettler, C.; Reinhart, C.; Dodt, J.; Reuter, A.; Philippou, H.; Ivaskevicius, V.; Oldenburg, J. Revisiting the Mechanism of Coagulation Factor XIII Activation and Regulation from a Structure/Functional Perspective. *Scientific Reports*. Nature Publishing Group July 25, 2016. https://doi.org/10.1038/srep30105.

(73) Singh, S.; Dodt, J.; Volkers, P.; Hethershaw, E.; Philippou, H.; Ivaskevicius, V.; Imhof, D.; Oldenburg, J.; Biswas, A. Structure Functional Insights into Calcium Binding during the Activation of Coagulation Factor XIII A. *Sci Rep* **2019**, *9* (1). https://doi.org/10.1038/s41598-019-47815-z.

(74) Griffin, K. J.; Newell, L. M.; Simpson, K. R.; Beckers, C. M. L.; Drinkhill, M. J.; Standeven, K. F.; Cheah, L. T.; Iismaa, S. E.; Grant, P. J.; Jackson, C. L.; Pease, R. J. Transglutaminase 2 Limits the Extravasation and the Resultant Myocardial Fibrosis Associated with Factor XIII-A Deficiency. *Atherosclerosis* **2020**, *294*, 1–9. https://doi.org/10.1016/j.atherosclerosis.2019.12.013.

(75) Sugimura, Y.; Hosono, M.; Wada, F.; Yoshimura, T.; Maki, M.; Hitomi, K. Screening for the Preferred Substrate Sequence of Transglutaminase Using a Phage-Displayed Peptide Library: Identification of Peptide Substrates for TGase 2 and Factor XIIIa. *Journal of Biological Chemistry* **2006**, *281* (26), 17699–17706. https://doi.org/10.1074/jbc.M513538200.

(76) Mulani, A. SYNTHESIS AND EVALUATION OF PEPTIDIC PROBES FOR TISSUE TRANSGLUTAMINASE AND FACTOR XIIIa. PhD Thesis, University of Ottawa, 2014. https://doi.org/10.20381/ruor-3806.

(77) Oertel, K.; Hunfeld, A.; Specker, E.; Reiff, C.; Seitz, R.; Pasternack, R.; Dodt, J. A Highly Sensitive Fluorometric Assay for Determination of Human Coagulation Factor XIII in Plasma. *Anal Biochem* **2007**, *367* (2), 152–158. https://doi.org/10.1016/j.ab.2007.05.011.

(78) Király, R.; Thangaraju, K.; Nagy, Z.; Collighan, R.; Nemes, Z.; Griffin, M.; Fésüs, L. Isopeptidase Activity of Human Transglutaminase 2: Disconnection from Transamidation

and Characterization by Kinetic Parameters. *Amino Acids* **2016**, *48* (1), 31–40. https://doi.org/10.1007/s00726-015-2063-5.

(79) Tung, C. H.; Ho, N. H.; Zeng, Q.; Tang, Y.; Jaffer, F. A.; Reed, G. L.; Weissleder, R. Novel Factor XIII Probes for Blood Coagulation Imaging. *ChemBioChem* **2003**, *4* (9), 897–899. https://doi.org/10.1002/CBIC.200300602.

(80) Jaffer, F. A.; Tung, C. H.; Wykrzykowska, J. J.; Ho, N. H.; Houng, A. K.; Reed, G. L.; Weissleder, R. Molecular Imaging of Factor XIIIa Activity in Thrombosis Using a Novel, Near-Infrared Fluorescent Contrast Agent That Covalently Links to Thrombi. *Circulation* **2004**, *110* (2), 170–176. https://doi.org/10.1161/01.CIR.0000134484.11052.44.

(81) Freund, K. F.; Doshi, K. P.; Gaul, S. L.; Claremon, D. A.; Remy, D. C.; Baldwin, J. J.; Pitzenberger, S. M.; Stern, A. M. Transglutaminase Inhibition by 2-[(2-Oxopropyl)Thio]Imidazolium Derivatives: Mechanism of Factor Xllla Inactivation. *Biochemistry* **1994**, *33*, 10109–10119.

(82) Stieler, M.; Weber, J.; Hils, M.; Kolb, P.; Heine, A.; Büchold, C.; Pasternack, R.; Klebe, G. Structure of Active Coagulation Factor-Xiii Triggered by Calcium Binding: Basis for the Design of next-Generation Anticoagulants. *Angewandte Chemie - International Edition* **2013**, *52* (45), 11930–11934. https://doi.org/10.1002/anie.201305133.

(83) Stieler, M.; Büchold, C.; Schmitt, M.; Heine, A.; Hils, M.; Pasternack, R.; Klebe, G. Structure-Based Design of FXIIIa-Blockers: Addressing a Transient Hydrophobic Pocket in the Active Site of FXIIIa. *ChemMedChem* **2020**, *15* (10), 900–905. https://doi.org/10.1002/cmdc.202000056.

(84) Pasternack, R.; Büchold, C.; Jähnig, R.; Pelzer, C.; Sommer, M.; Heil, A.; Florian, P.; Nowak, G.; Gerlach, U.; Hils, M. Novel Inhibitor ZED3197 as Potential Drug Candidate

in Anticoagulation Targeting Coagulation FXIIIa (F13a). *Journal of Thrombosis and Haemostasis* **2020**, *18* (1), 191–200. https://doi.org/10.1111/jth.14646.

(85) Boike, L.; Henning, N. J.; Nomura, D. K. Advances in Covalent Drug Discovery. *Nature Reviews Drug Discovery 2022* **2022**, 1–18. https://doi.org/10.1038/s41573-022-00542-z.

(86) Sutanto, F.; Konstantinidou, M.; Dömling, A. Covalent Inhibitors: A Rational Approach to Drug Discovery. *RSC Med Chem* **2020**, *11*, 876–884. https://doi.org/10.1039/D0MD00154F.

(87) Paiva, S. L.; Crews, C. M. Targeted Protein Degradation: Elements of PROTAC Design. *Curr Opin Chem Biol* **2019**, *50*, 111–119. https://doi.org/10.1016/j.cbpa.2019.02.022.

(88) Bricelj, A.; Steinebach, C.; Kuchta, R.; Gütschow, M.; Sosič, I. E3 Ligase Ligands in Successful PROTACs: An Overview of Syntheses and Linker Attachment Points. *Front Chem* **2021**, *9* (707317). https://doi.org/10.3389/FCHEM.2021.707317.

(89) Bondeson, D. P.; Mares, A.; Smith, I. E. D.; Ko, E.; Campos, S.; Miah, A. H.; Mulholland, K. E.; Routly, N.; Buckley, D. L.; Gustafson, J. L.; Zinn, N.; Grandi, P.; Shimamura, S.; Bergamini, G.; Faelth-Savitski, M.; Bantscheff, M.; Cox, C.; Gordon, D. A.; Willard, R. R.; Flanagan, J. J.; Casillas, L. N.; Votta, B. J.; Den Besten, W.; Famm, K.; Kruidenier, L.; Carter, P. S.; Harling, J. D.; Churcher, I.; Crews, C. M. Catalytic in Vivo Protein Knockdown by Small-Molecule PROTACs. *Nat Chem Biol* **2015**, *11* (8), 611–617. https://doi.org/10.1038/NCHEMBIO.1858.

(90) Mares, A.; Miah, A. H.; Smith, I. E. D.; Rackham, M.; Thawani, A. R.; Cryan, J.; Haile, P. A.; Votta, B. J.; Beal, A. M.; Capriotti, C.; Reilly, M. A.; Fisher, D. T.; Zinn, N.; Bantscheff, M.; MacDonald, T. T.; Vossenkamper, A.; Dace, P.; Churcher, I.; Benowitz, A. B.; Watt, G.; Denyer, J.; Scott-Stevens, P.; Harling, J. D. Extended Pharmacodynamic

Responses Observed upon PROTAC-Mediated Degradation of RIPK2. *Commun Biol* **2020**, *3*, 140. https://doi.org/10.1038/s42003-020-0868-6.

(91) Guo, W. H.; Qi, X.; Yu, X.; Liu, Y.; Chung, C. I.; Bai, F.; Lin, X.; Lu, D.; Wang, L.; Chen, J.; Su, L. H.; Nomie, K. J.; Li, F.; Wang, M. C.; Shu, X.; Onuchic, J. N.; Woyach, J. A.; Wang, M. L.; Wang, J. Enhancing Intracellular Accumulation and Target Engagement of PROTACs with Reversible Covalent Chemistry. *Nat Commun* **2020**, *11*, 4268. https://doi.org/10.1038/s41467-020-17997-6.

(92) Riching, K. M.; Caine, E. A.; Urh, M.; Daniels, D. L. The Importance of Cellular Degradation Kinetics for Understanding Mechanisms in Targeted Protein Degradation. *Chem Soc Rev* **2022**, *51*, 6210. https://doi.org/10.1039/d2cs00339b.

(93) Liu, Z.; Hu, M.; Yang, Y.; Du, C.; Zhou, H.; Liu, C.; Chen, Y.; Fan, L.; Ma, H.; Gong, Y.; Xie, Y. An Overview of PROTACs: A Promising Drug Discovery Paradigm. *Molecular Biomedicine* **2022**, *3*, 46. https://doi.org/10.1186/S43556-022-00112-0.

(94) Sakamoto, K. M.; Kim, K. B.; Kumagai, A.; Mercurio, F.; Crews, C. M.; Deshaies, R. J. Protacs: Chimeric Molecules That Target Proteins to the Skp1-Cullin-F Box Complex for Ubiquitination and Degradation. *Proc Natl Acad Sci U S A* **2001**, *98* (15), 8554–8559. https://doi.org/10.1073/PNAS.141230798/ASSET/96E10B62-DC16-4F76-94AF-64F8B7059B8E/ASSETS/GRAPHIC/PQ1412307006.JPEG.

(95) Békés, M.; Langley, D. R.; Crews, C. M. PROTAC Targeted Protein Degraders: The Past Is Prologue. *Nat Rev Drug Discov* **2022**, 1–20. https://doi.org/10.1038/s41573-021-00371-6.

(96) Nalawansha, D. A.; Crews, C. M. PROTACs: An Emerging Therapeutic Modality in Precision Medicine. *Cell Chem Biol* **2020**, *27* (8), 998–1014. https://doi.org/10.1016/j.chembiol.2020.07.020.

Chapter 2: Peptidic Inhibitors and a Fluorescent Probe for the Selective Inhibition and Labelling of Factor XIIIa Transglutaminase

Eric W. J. Gates [1,†], Kian Mansour [1,†], Sahar Ebrahimi Samani [2], Sammir Shad [1], Mari T. Kaartinen [2,3] and Jeffrey W. Keillor [1,*]

[1] Department of Chemistry and Biomolecular Sciences, University of Ottawa, Ottawa, ON K1N 6N5, Canada

[2] Division of Experimental Medicine, Faculty of Medicine, McGill University, Montréal, QC H3A 0C7, Canada

[3] Faculty of Dental Medicine and Oral Health Sciences, McGill University, Montréal, QC H3A 0C7, Canada

* Correspondence: JWK

† These authors contributed equally to this work.

2.1. Introduction to the Research Article Presented Within this Chapter

Early work in the Keillor Research Group had uncovered a potential small molecule scaffold which exhibited FXIIIa selective inhibition activity. Given the window for novel small molecule inhibitors and potential therapeutics targeted against FXIIIa for the treatment of thrombosis, we quickly pursued this initial lead. Through the journey we ultimately conducted another SAR on a peptidic scaffold and optimized it to act as a potent fluorescent probe. The probe was then evaluated *in cellulo* as a fluorescent reporter for active FXIIIa localization.

2.2. Author Contributions

Conceptualization, J.W.K. and E.W.J.G.; formal analysis, K.M., S.S. and E.W.J.G.; investigation, K.M., S.S., E.W.J.G. and S.E.S.; writing—original draft preparation, K.M. and E.W.J.G.; writing—review and editing, E.W.J.G., J.W.K. and M.T.K.; supervision, J.W.K. and M.T.K.; funding acquisition, J.W.K. and M.T.K. All authors have read and agreed to the published version of the manuscript.

2.3. Copyright

2.4. Abstract

Factor XIIIa (FXIIIa) is a transglutaminase of major therapeutic interest for the development of anticoagulants due to its essential role in the blood coagulation cascade. While numerous FXIIIa inhibitors have been reported, they failed to reach clinical evaluation due to their lack of metabolic stability and low selectivity over transglutaminase 2 (TG2). Furthermore, the chemical tools available for the study of FXIIIa activity and localization are extremely limited. To combat these shortcomings, we designed, synthesised, and evaluated a library of 21 novel FXIIIa inhibitors. Electrophilic warheads, linker lengths, and hydrophobic units were varied on small molecule and peptidic scaffolds to optimize isozyme selectivity and potency. A previously

reported FXIIIa inhibitor was then adapted for the design of a probe bearing a rhodamine B moiety, producing the innovative **KM93** as the first known fluorescent probe designed to selectively label active FXIIIa with high efficiency (k_{inact}/K_I = 127,300 M^{-1} min^{-1}) and 6.5-fold selectivity over TG2. The probe **KM93** facilitated fluorescent microscopy studies within bone marrow macrophages, labelling FXIIIa with high efficiency and selectivity in cell culture. The structure–activity trends with these novel inhibitors and probes will help in the future study of the activity, inhibition, and localization of FXIIIa.

2.5. Introduction

The transglutaminase (TGase) family of enzymes is comprised of eight calcium-dependent isozymes and the non-catalytically active erythrocyte membrane protein band 4.2 [1–3]. These enzymes carry out numerous functions in biological settings with a primary role in crosslinking proteins through the formation of N^{ε}(ɣ-glutaminyl)lysine bonds using a Cys-His-Asp catalytic triad [4–6]. Within the TGase family are two isozymes of current therapeutic interest, transglutaminase 2 (TG2) and Factor XIII (FXIII). Human TG2, also referred to as tissue transglutaminase, is ubiquitously expressed throughout virtually all tissues [7,8]. TG2 is noteworthy due to its transamidase activity involved in liver fibrosis, its deamidation role in celiac disease, and its intracellular G-protein activity [9–11] which has been implicated in numerous cancer models including the epithelial-mesenchymal transition of cancer stem cells [12–17]. The major role of FXIII is within the final step of the coagulation cascade, where it mediates the crosslinking of insoluble fibrin monomers to form a rigid 3D blood clot network. This makes it a viable therapeutic target for the development of novel anticoagulant drugs in the treatment of venous thrombosis [18]. Current drugs, including heparins and coumarins, target a multitude of

upstream clotting factors, thus preventing soft clot formation and increasing the risk for severe bleeding [19–21]. Inhibition of the downstream FXIII is believed to provide a milder alternative that would allow for soft clot formation, potentially achieving a blood thinning effect without inducing elevated bleeding risks [22]. Intracellular FXIII is additionally hypothesised to play roles in the activities of osteoblasts, monocytes, and macrophages, making the intracellular isozyme an appealing therapeutic target as well [23].

FXIII is most abundant in the blood and has roles in promoting clotting [24], wound healing [25], and angiogenesis [26]; however, it is also present in the cytosol of cells [27,28]. Plasma-soluble FXIII exists as FXIII-A_2B_2, an inactive hetero-tetramer composed of two catalytic A subunits and two carrier B subunits [29]. The classical activation of FXIII in the blood coagulation cascade begins with thrombin-catalyzed proteolytic cleavage of the N-terminal 37 amino acid activation peptide tethered to each A subunit [30,31]. The interaction of the A and B subunits then weakens and allows for calcium binding to the A subunits. The heterotetramer then dissociates into the A_2 homodimer [32], which finally separates into the enzymatically active monomer of Factor XIIIa (FXIIIa) in the presence of a suitable substrate [33]. It is of note that cellular localised FXIII (FXIII-A) does not exist as a heterotetramer and the intracellular activity can be achieved by calcium binding [34].

Interest in the development of FXIIIa inhibitors has blossomed in recent years due to the potential therapeutic applications highlighted above. Though progress in the FXIII inhibition field has been reviewed elsewhere [35, a general overview of the most relevant details is provided herein. FXIII has historically proven to be incredibly difficult to inhibit in a potent and selective manner. Most reported FXIII inhibitors tend to also inhibit TG2, which is believed to be the most problematic off-target enzyme due to its ubiquitous expression profile [36] and its roles in wound-

healing and angiogenesis, which overlap with those of FXIII [37,38]. In the early 1990s, Merck set out to design imidazolium-based small molecule covalent inhibitors of FXIIIa, but these exhibited low selectivity (Figure 1) [39]. A novel peptidic sequence with a high affinity for FXIIIa was discovered in 2006 through phage-display screening [40]. Replacement of this peptide's glutamine residue with an electrophilic warhead, namely an α,β-unsaturated methyl ester or glutamate-derived Michael acceptor (MA), allowed Zedira to produce irreversible inhibitor ZED1301, which covalently inactivates the catalytic Cys thiolate of FXIIIa. This compound shows relatively high potency (IC_{50} = 110 nM) and moderate selectivity (30-fold) over TG2 [33]. Zedira further optimised ZED1301 into inhibitors such as ZED2360 (IC_{50} = 29 nM) [41] and peptidomimetic ZED3197 (IC_{50} = 16 nM, 19-fold selectivity for FXIIIa over TG2). The latter compound was successfully evaluated in rabbit coagulation models and has shown the most promise of any FXIIIa inhibitor. However, it shows a short half-life of 5–10 min in rabbit models, requiring high doses (6–54 mg/kg ZED3197) administered through intravenous bolus and continuous infusions to maintain adequate plasma levels [22]. There thus remains a need to develop more potent, selective, and drug-like inhibitors of FXIIIa as potential anti-coagulants.

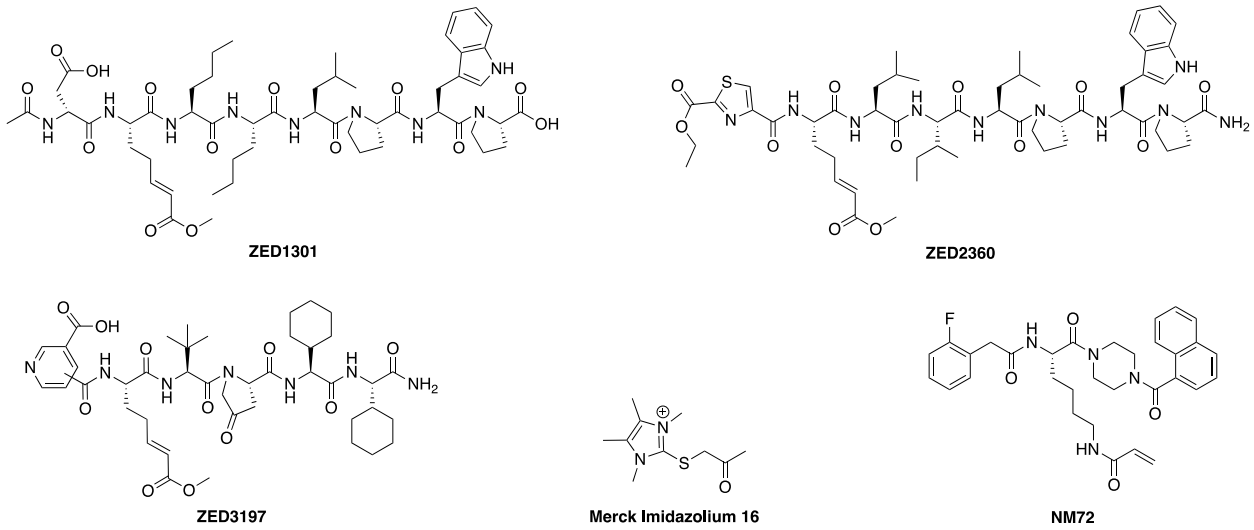

Figure 2.1. Chemical structures of Zedira's ZED1301 [33], ZED2360 [41], ZED3197 [22], Merck's imidazolium inhibitor 16 [39], and Keillor's TG2 targeted small molecule inhibitor NM72 [42].

While Factor XIIIa therapeutics remains an active area of research, the chemical tools currently available for studying this crucial clotting enzyme are comparatively limited. To our knowledge, only two probes for monitoring the activity of FXIIIa in biological systems have been reported to date [43,44]. Both probes serve as α_2-antiplasmin substrate mimics and are tagged with either a near-IR fluorophore or Gd-chelating magnetically resonant contrast moiety. These compounds label blood clots through FXIIIa-mediated incorporation into fibrin, allowing for the indirect deduction of FXIII activity and localization. No known probes have been reported to specifically label the active form of the enzyme itself; the development of such a tool would aid in the study of the localization, migration, and activity of FXIII in cellulo.

In our work on TGases, we developed numerous activity assays, probes, and targeted covalent inhibitors that show high isozyme selectivity, mainly within the context of studying TG2 [42,45–50]. In the current work we design, synthesize, and evaluate inhibitors of FXIIIa, and use the optimised inhibitor design in the production of a fluorescent probe. In order to achieve the

desired isozyme selectivity for FXIII over TG2, we relied upon previous kinetic data and the binding pocket differences between FXIIIa [33,41,51] and TG2 [42,45,46,52] to design several series of peptidic and small molecule inhibitors. More specifically, we explored structure–activity relationships (SAR) with respect to the linker length, electrophilic warhead functionality, hydrophobic moiety, and acidic group, while keeping the scaffold backbone constant. Evaluation of the peptidic and small molecule inhibitor series exposes inconsistent and scaffold-dependent trends, potentially due to conformational dynamism within the active site of the enzyme [41] akin to that observed recently in the TG2 field [45]. We then further modified the most potent scaffold to incorporate a fluorescent moiety, thereby creating a high-affinity fluorescent probe for the specific labelling of FXIIIa within biological settings. The fluorescent probe was assayed in cell culture to display its effectiveness at labelling FXIIIa in cellulo.

2.6. Results and Discussion

2.6.1. Structure Design

2.6.1.1. Design of Peptidic Inhibitors of FXIIIa

Although extensive SAR studies have been performed on the amino acid sequences of the ZED3197 and ZED1301 scaffolds, the crucial warhead residue remains less explored [51,53,54]. With respect to the electrophilic moiety itself, it is noteworthy that the α,β-unsaturated ester warhead is a common feature among Zedira's inhibitors, while other amide-based electrophiles, such as acrylamides and α-chloroacetamide, had not apparently been tested on these peptidic scaffolds. This is surprising as both these amide-based warheads have shown great success in achieving potent transglutaminase inhibition while remaining stable to degradation by glutathione

in the cell [55]. Furthermore, the distance between the scaffold and electrophile, hereinafter referred to as the linker length, was not varied in the Zedira FXIII inhibitor studies available in the literature [51,53,54]. We found that the linker length has a profound impact on peptidomimetic TG2 inhibitor potency, with longer linkers being more efficient than shorter ones [46]. Combined with crystal structure evidence that the active site tunnel leading to the catalytic Cys thiolate is shallower in FXIII than in TG2 [33,52], we hypothesised that the decreasing linker length may be a viable method of increasing potency of FXIIIa inhibition and increasing selectivity over TG2. Thus, a series of peptidic FXIIIa inhibitors with three different electrophilic warheads (α,β-unsaturated ester, acrylamide, and α-chloroacetamide) and four linker lengths (one through four methylene units) was designed in order to investigate the impact of these structural features on the potency of FXIIIa inhibition and selectivity over TG2 (Figure 2). The ZED1301 peptide scaffold was selected for this study due to its known affinity for FXIIIa and ease of synthesis. ZED1301 itself was also independently synthesised and evaluated in order to supplement its original kinetic characterization, a condition-dependent IC_{50} value [33]. Condition-independent k_{inact} and K_I values were acquired for more accurate comparisons with irreversible FXIIIa inhibitors developed herein and in other works.

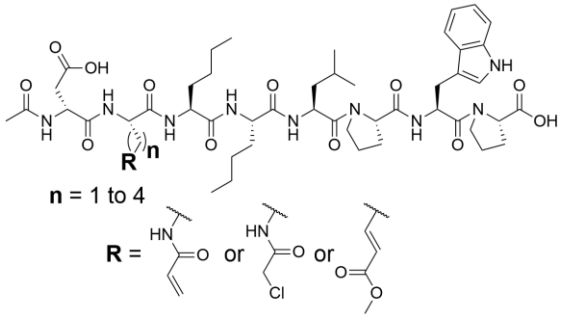

Figure 2.2. Design of the peptidic FXIIIa inhibitor series with various linker lengths and electrophilic warhead functionalities.

2.6.1.2. Design of Small Molecule Inhibitors of FXIIIa

In the hope of developing a FXIII inhibitor with better drug-like properties than the peptide-based inhibitors investigated herein, we also screened a series of small-molecule compounds. Stemming from our extensive research on small-molecule TG2-selective inhibitors, we commenced our search for small-molecule FXIIIa inhibitors by using a previously published scaffold that exhibits low potency against TG2, again noting that the short linker length produces poor TG2 inhibition [46]. Two key elements from the reported high-affinity peptidic sequences [46] for FXIIIa were adapted into the small molecule inhibitor design and retained across our series of compounds, specifically the negatively charged N-terminal moiety and hydrophobic C-terminus. Thus, our SAR work in this small molecule FXIIIa inhibitor investigation encompassed a variety of N-terminal acids and C-terminal hydrophobic units that have shown promise in previous TGase studies (Figure 3) [46]. Small changes in the linker length were also investigated. The distance between the warhead and scaffold was reduced further through incorporation of a D-Dap warhead-bearing residue, allowing the coupling of the acid to the sidechain amine and the warhead to the α-amine. Given the broad scope of the structural features explored in this work, the known reactivity of the acrylamide towards TGases, and its superior presumed stability and selectivity compared to chloroacetamides and esters, the acrylamide warhead was mostly retained throughout the small-molecule FXIIIa SAR. A few derivatives bearing α,β-unsaturated methyl esters, akin to the Zedira peptides, were also synthesised and evaluated in order to provide a preliminary warhead comparison within this small molecule scaffold and between series with the peptidic compounds developed.

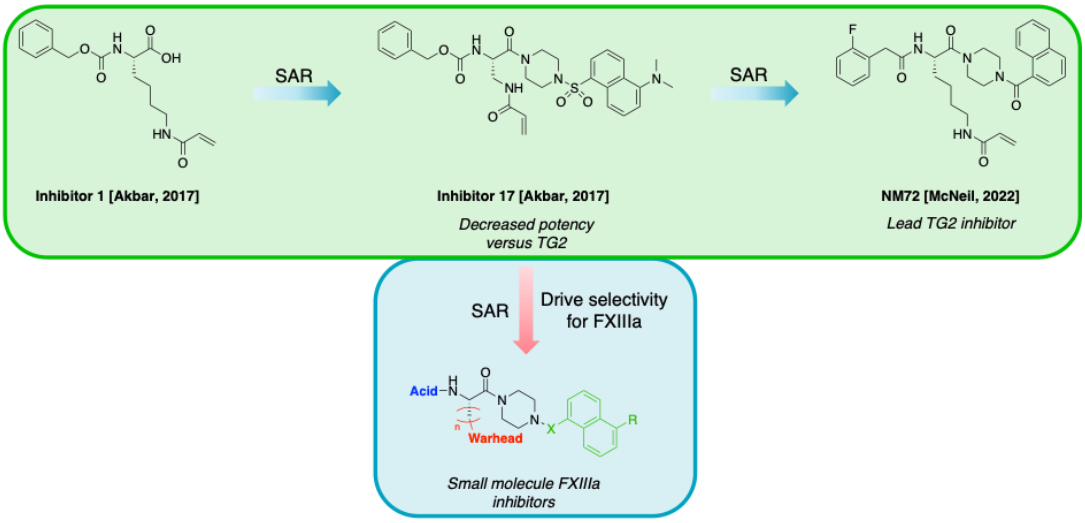

Figure 2.3. Design approach for small-molecule inhibitors of FXIIIa, based on a known low potency TG2 "inhibitor 17" and driving selectivity for FXIIIa with N-terminal acids and C-terminal hydrophobic groups [42,46].

2.6.1.3. Design of Fluorescent Probe of FXIIIa

After completion of the synthesis and evaluation of the peptidic and small-molecule FXIIIa inhibitors, the optimised linker, warhead, and scaffold were used to design a rhodamine B labelled probe for studying FXIIIa. Rhodamine B was attached at the N-terminus through a flexible 6-aminohexanoic acid linker to allow the bulky fluorophore to be held far away from the binding site. The rhodamine B fluorophore was chosen due to its desirable, bright red emission, and minimal overlap with background cellular autofluorescence. It was also linked through a proline residue since the tertiary amide linkage allows the rhodamine to preserve its intrinsic fluorescence (Figure 4).

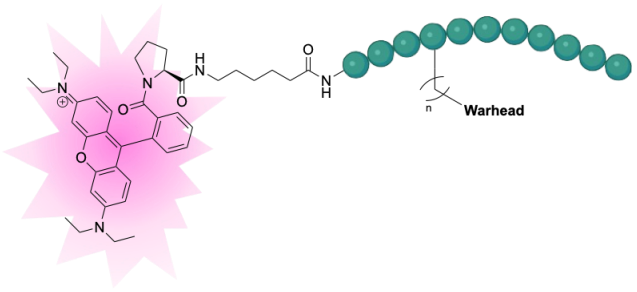

Figure 2.4. Design of fluorescent probe for FXIIIa tethered to the optimised inhibitor structure.

2.6.2. Synthesis

The general synthesis of the inhibitors disclosed herein was achieved through a combination of solid-phase peptide synthesis (SPPS) and in-solution chemistry. For assembly of the peptidic inhibitors bearing amide-based warheads, amino acid monomers with varying linker lengths leading to the appropriate warheads, or precursors thereof, were synthesised and subsequently incorporated into the linear octapeptides. The syntheses of the unsaturated ester-bearing peptides were carried out in a manner similar to that reported by Zedira [51,53]. The small molecule inhibitors were synthesised through careful in-solution manipulations of protecting groups, allowing for the sequential installation of first the various hydrophobic groups and next the electrophilic warhead. These key intermediates with free N-termini were accumulated, allowing for divergent functionalization to final inhibitors bearing different N-terminal acidic moieties. A detailed discussion of the inhibitor syntheses, as well as full experimental procedures and characterization data, is provided in the Supplementary Materials, along with Schemes S1–S21. Between the peptidic and small molecule scaffold series, a total of 22 inhibitors and 1 probe were synthesised and evaluated for inhibition of FXIIIa.

2.6.3. Kinetic Evaluation

All inhibitors synthesised herein were evaluated for inhibition against FXIIIa, using the fluorescence-quenched A101 isopeptidase assay [56,57], and against TG2, using the colorimetric AL5 transamidase assay [46,50]. The assay substrates A101 and AL5 both present labile bonds that are cleaved by the activities of their corresponding transglutaminases, resulting in the release of a fluorophore or chromophore moiety, respectively. The rate of consumption of these assay substrates, indicated by increases in fluorescence or absorbance over time, can be detected for measuring enzyme activity. Assays were run in duplicate at constant reporter substrate concentration with varying concentrations of inhibitor. Representative fluorescence-time plots are shown in Figure 5A,C. The type of inhibition was determined through visual inspection of the fluorescence-time curvature; termination of the enzymatic reaction with the substrate at a plateau lower than the no-inhibitor positive control is indicative of irreversible inhibition. On the other hand, convergence to a common plateau indicates reversible inhibition.

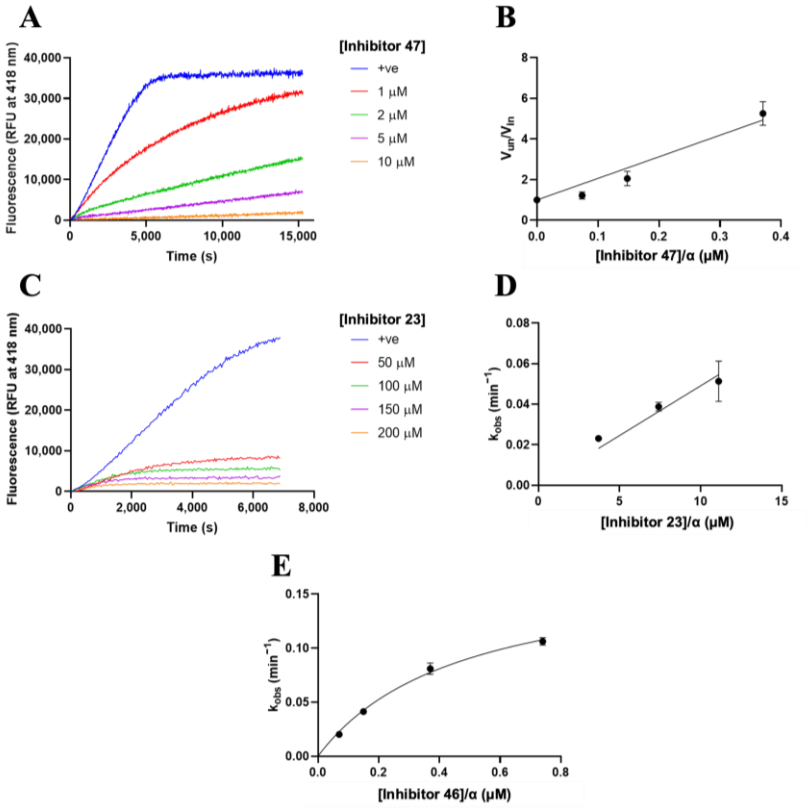

Figure 2.5. Representative kinetic traces and data fitting for TGase inhibition assays. (A) Raw blank-subtracted kinetic traces of FXIIIa activity with substrate A101 and increasing concentrations of reversible inhibitor 47 (0, 1, 2, 5, 10 µM). (B) Dixon plot fitting of initial rates of FXIIIa activity versus inhibitor concentration divided by alpha for inhibitor 47 to obtain K_i. (C) Raw blank subtracted kinetic traces of FXIIIa activity with substrate A101 and increasing concentrations of irreversible inhibitor 23 (0, 50, 100, 150, 200 µM). (D) Linear regression of saturation fitting of k_{obs} versus inhibitor concentration divided by alpha for irreversible inhibitor 23 to obtain a ratio of k_{inact}/K_I. (E) Saturation fitting of k_{obs} versus inhibitor concentration for irreversible inhibitor 46 displaying inhibition saturation kinetics to extract both k_{inact} and K_I parameters.

Irreversibility was tested further through substrate spike experiments. As shown in Supplementary Materials Figures S1–S3, an additional substrate was added to inhibited and uninhibited enzyme reactions after the completion of the positive control reaction. Further

increases in fluorescence upon substrate spike, as in Figure S1, indicate reversibility of inhibition, while the lack of an additional increase, as in Figure S2, suggests that all enzyme has been irreversibly inhibited. Analysis was carried out through corrected Dixon modelling in the case of reversible kinetics, to obtain K_i values (Figure 5B), and hyperbolic saturation modelling was used to obtain k_{inact} and K_I for inhibitors showing irreversibility (Figure 5E) [58,59]. For cases in which the tested inhibitor concentrations were not high enough to reach saturation, a linear regression provided an estimate of the inhibitor's k_{inact}/K_I ratio (Figure 5D). Further details concerning data collection and analysis are provided in the Materials and Methods section.

2.6.3.1. Kinetic Evaluation of Peptidic Inhibitors of FXIIIa

The structures of the 11 peptidic inhibitors synthesised in this work are shown in Table 1. All kinetic data from their evaluation are summarised in Table 2. Several interesting trends can be noted when investigating the impact of the warhead functionality and linker length on the potency of FXIIIa inhibition. While the acrylamide-bearing inhibitors **12–14** show reversible competitive FXIIIa inhibition, the analogous chloroacetamides **21–23** operate in an irreversible manner. Since both warheads are known to be capable of covalent bond formation in the presence of a suitable thiolate, the observed differences in inhibition mode with FXIIIa must be due to geometry rather than intrinsic reactivity. Perhaps binding of the warhead carbonyl into the enzyme's oxyanion pocket places the acrylamide's electrophilic carbon too distant from the thiolate, preventing S-C bond formation, while that of the chloroacetamide, being one position closer to the carbonyl, is just close enough to allow for covalent bond formation. It is also interesting to note that the acrylamide and chloroacetamide series show similar linker length trends. Potency is relatively insensitive to changes in the linker length between 2 through 4 methylene units, as the K_i values

for acrylamides **12–14** are of the same order of magnitude, and the same can be said for the k_{inact}/K_I ratios of chloroacetamides **21–23**. However, in both cases, reducing the linker down to 1 methylene, as in compounds **11** and **20**, results in a complete loss of inhibition. Since the electrophilic carbon placement is different between compounds **11** and **20**, and that of **11** matches **21**, a known inhibitor with an f-position electrophilic carbon, it is clear that the lack of inhibition cannot be explained by improper electrophile placement. Instead, improper carbonyl carbon placement may be responsible for the lack of FXIIIa inhibition in compounds **11** and **20**. Both place the carbonyl carbon at the d-position, which is apparently too close to the scaffold, and may not allow for appropriate binding in the enzyme's active site.

Table 2.1. Structural classification of peptidic FXIIIa inhibitors. The linker length (n methylene units) and warhead are presented along with an alphabetical nomenclature system for noting the distances of the electrophilic carbon (E+ C) and carbonyl carbon (CO C) from the peptide backbone. For example, a designation of d implies that the feature is present at the δ carbon, the 3rd carbon atom away from the backbone's a/α-carbon.

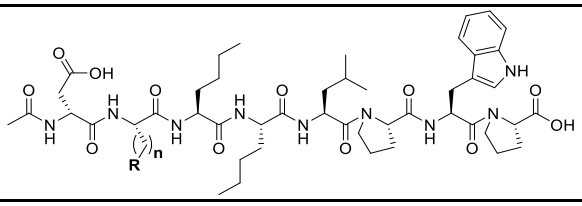

Inh.	R	n	E^+ C Position	CO C Position
11	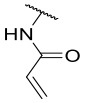	1	f	d
12		2	g	e
13		3	h	f
14		4	i	g
20	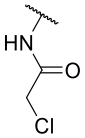	1	e	d
21		2	f	e
22		3	g	f
23		4	h	g
45		1	c	e
46		2	d	f

47	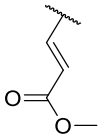	3	e	g

Table 2.2. Kinetic parameters, inhibition modes, and isozyme selectivity of acrylamide-, α-chloroacetamide, and α,β-unsaturated methyl ester-bearing peptidic inhibitors of FXIIIa inhibitors with varying linker lengths. Data were determined using distinct continuous activity assays for FXIIIa and TG2 detailed in the Materials and Methods section.

	FXIIIa				TG2		
Inh.	**Inh. Mode**	**k_{inact} (min^{-1})**	**K_i or K_I (μM)**	**k_{inact}/K_I ($M^{-1}\,min^{-1}$)**	**Inh. Mode**	**k_{inact}/K_I ($M^{-1}\,min^{-1}$)**	**Selectivity**
11	None *	NA	NA	NA	None **	NA	NA
12	Rev	NA	193 ± 20	NA	None **	NA	FXIIIa
13	Rev	NA	135 ± 16	NA	None **	NA	FXIIIa
14	Rev	NA	125 ± 20	NA	None **	NA	FXIIIa
20	None *	NA	NA	NA	Irrev	1962 ± 82	TG2
21	Irrev	-	-	7422 ± 525	None **	NA	FXIIIa
22	Irrev	0.0988 ± 0.0185	7.1 ± 3.1	13,922 ± 6664	Irrev	2922 ± 260	2.6 FXIIIa
23	Irrev	-	-	4907 ± 325	Irrev	3565 ± 229	1.4 FXIIIa
45	Rev	NA	53 ± 12	NA	None **	NA	FXIIIa
46	Irrev	0.1765 ± 0.0160	0.4732 ± 0.0847	372,992 ± 74,839	Irrev	56,520 ± 2044	6.6 FXIIIa
47	Rev	NA	0.0941 ± 0.0105	NA	Irrev	31,780 ± 2218	Irrev TG2

* = no inhibition detected up to 200 Mm; ** = no inhibition detected up to 350 μM.

ZED1301, the lead compound (**46**), was found to be the most potent irreversible inhibitor of the series, with k_{inact}/K_I ratio several orders of magnitude higher than any of the chloroacetamides. The superior potency of ZED1301 (**46**) can be attributed to its unique warhead structure, as the unsaturated ester was the only warhead studied in this work that places the electrophilic carbon closer to the scaffold than the more distal carbonyl. It is believed that this geometric arrangement allows this inhibitor to take full advantage of the non-covalent oxyanion hole interactions and covalent S-C bond formation, as shown in the crystal structure published by Zedira [33], while inhibitors with the acrylamide and chloroacetamide warheads may be unable to form these interactions due to excessive induction of strain required in the enzyme or inhibitor.

This work also represents the first report of condition-independent kinetic parameters, k_{inact} and K_I, for ZED1301 (**46**), which will allow for accurate comparisons with inhibitors developed in this work and other studies. Either decreasing or increasing the linker length from ZED1301 results in a loss of inhibitory potency and changes to inhibition mode. The shorter-linker ester-bearing compound **45** shows weak reversible inhibition similar in potency to that seen with acrylamides **12**–**14**, while the longer-linker ester-bearing inhibitor **47** displays highly potent reversible FXIIIa inhibition. These results further support the strict geometric requirements for binding and covalent bond formation in the active site of FXIIIa. As for the impact of linker and warhead on selectivity over TG2, no clear trends were noted. While none of the acrylamides result in any noticeable TG2 inhibition up to 350 μM, most of the chloroacetamides and ester-bearing inhibitors are irreversible TG2 inhibitors. The lack of inhibition seen with compounds **21** and **45**, as well as the superior potency of the ester warhead, are attributed to geometrical factors governing the enzyme-inhibitor interaction. With the peptidic inhibitors fully evaluated and with ZED1301 (**46**) identified as the most potent of the series, we then evaluated our small molecules as potential selective FXIIIa inhibitors.

2.6.3.2. Kinetic Evaluation of Small Molecule Inhibitors of FXIIIa

Kinetic evaluation of the small molecule inhibitor library began with the dansyl hydrophobic series inhibitors **71**, **73**–**75**, and **79** (Table 3). The dansylated inhibitor scaffold was desirable as it could act in a multi-faceted role as a potent inhibitor scaffold as well as a fluorescent probe which would allow for FXIIIa localization studies. An investigation into the preferences of various alkyl acids revealed that sulfonyl **79** provided the greatest affinity with an apparent K_i of 26.7 ± 1.3 μM (See Supplementary Materials). However, upon analysis of the similarity in the

kinetic results (of both the acid variants and the methyl ester **73)**, some doubts were raised regarding the assay conditions. A substrate spike of the inhibition assays revealed that the FXIIIa was still active, and the inhibitors were not acting in an irreversible manner; potentially implying a reversible mechanism (Supplementary Materials Figure S3). Spiking the **79**-inhibition assay with another dose of inhibitor **79** caused a noticeable decrease in apparent RFU (Supplementary Materials Figure S4). Due to the potential fluorescent quenching of both acrylamide [60] and the fluorescent dansyl moiety of the inhibitor scaffold, they were both evaluated in the inhibition assay. Dansyl amide resulted in nearly identical traces as those obtained using the dansylated inhibitor library (Supplementary Materials Figure S5). A further spectrophotometric analysis of both dansyl and anthranilic acid in the literature revealed that the dansyl absorption peak and anthranilic acid excitation at 313 nm overlap perfectly. Since A101, as well as the similar substrate A138, are the standard continuous assays for FXIIIa activity [56,61] and were found to be incompatible with our fluorescent dansyl inhibitors, the inhibition data for these compounds were set aside, and the scaffold was optimised to eliminate the fluorescence interference effect.

Sulfonyl-naphthalene derivative **76** provided a K_i of 64.3 ± 5.1 μM (Supplementary Materials); however, this scaffold also produced an absorption band that overlaps with the excitation of A101. Further tailoring gave rise to the naphthoyl derivatives **72** and **77** that do not have photochemical properties that interfere with the fluorescent assay. Succinyl derivative **77** was the lead inhibitor from the L-Dap naphthoyl series, with a K_i of 69.0 ± 4.1 μM. An attempt to decrease the linker length to the warhead by one methylene unit, with the incorporation of the D-Dap residue **84**, resulted in the K_i rising to a value of 107.6 ± 19.1 μM. This contradicted our initial intuition that shorter linkers would improve potency against FXIIIa. Since none of the acrylamide-bearing inhibitors in this series led to irreversible inhibition but were clearly binding to the

enzyme's active site, two compounds bearing an unsaturated ester warhead (**87** and **88**) were evaluated. We hoped that the replacement of the acrylamide warhead with the Michael acceptor would result in an irreversible small molecule inhibitor of the enzyme. To our surprise, both the succinic derivative **87** and phthalic acid derivative **88**, with K_i values of 131.1 ± 7.9 μM and 265.0 ± 46.8 μM respectively, had reduced potency versus FXIIIa compared to the acrylamide-bearing compounds. A drastic drop in selectivity was also observed for these scaffolds, such that they were more selective for TG2, with irreversible K_I values of 14.3 ± 7.0 μM and 21.2 ± 9.0 μM, respectively. This unexpected finding hints at some scaffold dependence for the ideal warhead and linker combination for achieving potent, irreversible FXIIIa inhibition. While it was found that a linker length of 1 methylene on the peptidic scaffold and an acrylamide warhead (compound **11**) leads to no inhibition, the analogous small-molecule compound **77** shows reversible inhibition with K_i = 69 μM. Similarly, while **46** (ZED1301) shows the most potent irreversible FXIIIa inhibition in this work, the small molecule with the same two-methylene linker and unsaturated ester warhead in compound **87** shows only weak reversible inhibition with K_i = 131 μM.

Table 2.3. Kinetic parameters and isozyme selectivity of small molecule FXIIIa inhibitors with various N-terminal acidic groups, C-terminal hydrophobic units, and central warhead amino acid residues. Data were determined using distinct continuous activity assays for FXIIIa and TG2 detailed in the Materials and Methods section.

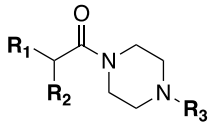

Inh.	R_1	R_2	R_3	FXIIIa K_i (μM)	TG2 K_I (μM)
71	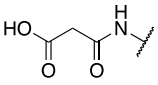	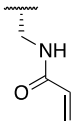	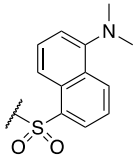	Interference*	>360
79	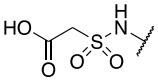	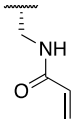	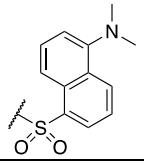	Interference*	>360
75	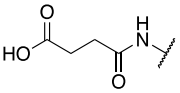	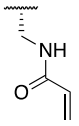	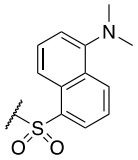	Interference*	>360
74	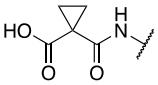	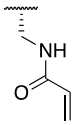	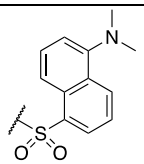	Interference*	>360
73	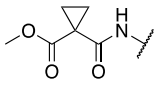	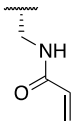	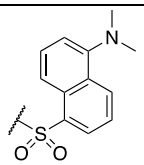	Interference*	>360
76	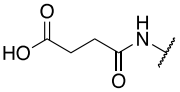	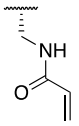	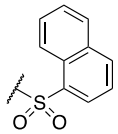	Interference*	>360
72	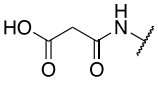	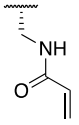	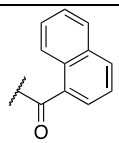	249.1 ± 69.3	>360

77	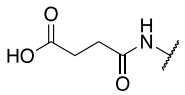	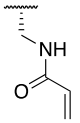	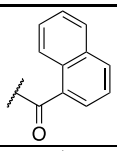	69.0 ± 4.1	>360
84	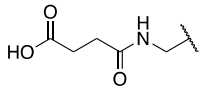	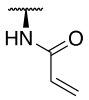	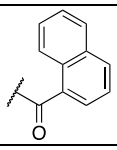	107.6 ± 19.1	>360
87	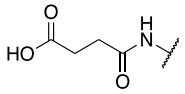	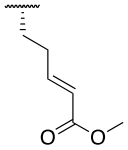	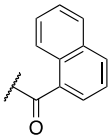	131.1 ± 7.9	14.3 ± 7.0
88	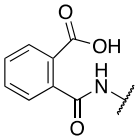	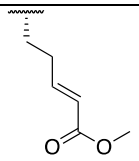	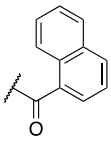	265.0 ± 46.8	21.2 ± 9.0

* Data afflicted by fluorescence interference.

This finding is mirrored perfectly by TG2 investigations in our group, in which we found that longer linkers bearing acrylamides on a peptidomimetic TG2 scaffold led to more potent inhibition than shorter ones [46]. However, more recently we showed that on an abbreviated small-molecule TG2 scaffold, the shortest linker achieves the most potent inhibition [45]. We hypothesize that a significant degree of conformational dynamism exists in the TG2 binding pocket, creating a scaffold dependence for the ideal linker length, based on the enzymatic conformation induced by the binding of different-sized substrates or inhibitors. We believe that a similar phenomenon is at play here with FXIIIa and our inhibitors disclosed herein. It is clear that the two-methylene linker and ester warhead, which are ideal on the peptide, are not as effective on the small molecule scaffold. This notion is further supported by Zedira's recent study revealing a transient hydrophobic pocket in FXIIIa's active site [41]. It appears that trial-and-error may be required to perfectly tailor the linker and warhead for each new scaffold size tested for FXIIIa and that further screening of linkers and warheads on this known binding small molecule scaffold may potentially produce an irreversible, drug-like, small molecule FXIIIa inhibitor.

Since no novel sub-10 μM K_I small molecule inhibitors were developed and **46** (ZED1301) remains the most potent irreversible FXIIIa inhibitor evaluated in this work, we opted to adapt this peptidic scaffold for a potential role as a novel fluorescent probe research tool.

2.6.3.3. Kinetic Evaluation of Fluorescent Rhodamine B FXIIIa Probe

Fluorescent probe **93** (aka **KM93**, Figure 6), whose design incorporates a two-methylene linker, ester warhead, and peptide scaffold from ZED1301, retains irreversible FXIIIa inhibition with acceptable potency for biological applications. The k_{inact}/K_I ratio against FXIIIa (127300 ± 2890 M^{-1} min^{-1}) is approximately three-fold lower for the probe than for the parent ZED1301 (**46**), showing that some potency was lost with the incorporation of the rhodamine B moiety and flexible linker. Fortunately, selectivity was maintained, as the probe remains around 6.5-fold selective for FXIIIa over TG2 (k_{inact}/K_I = 19520 ± 2180 M^{-1} min^{-1}).

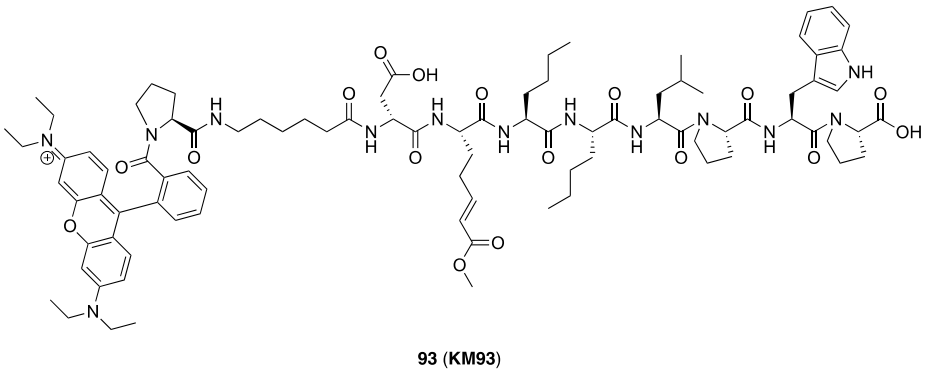

Figure 2.6. Structure of the rhodamine B incorporated FXIIIa probe 93 (aka KM93).

2.6.4. Irreversible Labelling of Purified FXIIIa by SDS-PAGE

Labelling of commercially available FXIIIa with the rhodamine B fluorescent probe **KM93** was then evaluated by SDS-PAGE analysis. FXIIIa was incubated in the presence of 30 μM **KM93** and calcium; SDS-PAGE analysis of the resulting sample revealed a protein band that was red

fluorescent (Figure S6). Coomassie staining then showed that this band corresponds to a molecular weight of ~80 kDa—coinciding with that of the commercially available FXIIIa [30,62]. The appearance of this red fluorescent band, on a gel run under denaturing conditions, allowed us to conclude that **KM93** successfully labelled FXIIIa in a robust, covalent, and irreversible manner.

2.6.5. Labelling of FXIIIa in Bone Marrow Macrophages

Covalent labelling of FXIIIa by **KM93** was tested in cell culture in murine bone marrow macrophages (BMM). BMMs are 'gold standard' expressors of FXIIIa and are responsible for the production of circulating FXIIIa [63]. Labelling of FXIIIa was first performed in cell lysate using 0–20 µM **KM93** and evaluated via SDS-PAGE, using fluoroimaging of the rhodamine B moiety. Supplementary Materials Figure S8A shows detectable, concentration-dependent covalent incorporation of **KM93** to a band at 80 kDa, with strongest labelling at 8-µM and 20-µM concentrations of the probe over both 6-h and 48-h incubations. A background band was detected at ~100 kDa, in the control as well as the test group, but the identity of this protein is unknown. Coomassie staining of the gel confirms equal loading (Figure S8B).

Fluorescent microscopy of the labelling showed rapid clear incorporation of **KM93** into BMM cells at 20 µM concentration after 48-h incubations (Supplementary Materials Figure S9 and Figure 7A). Labelling of Factor XIIIa was deemed to be intracellular (Figure 7A) as confirmed by co-staining with actin (Figure S9) and showed colocalization with an FXIII-A antibody (yellow arrows, Figure 7D). Not all FXIII-A antibody labelling was colocalized with the labelling by **KM93** (white arrows, Figure 7C). Since labelling by **KM93** is based on the enzyme activity of FXIIIa, this result suggests that Factor XIII may be present but not active in these specific macrophages.

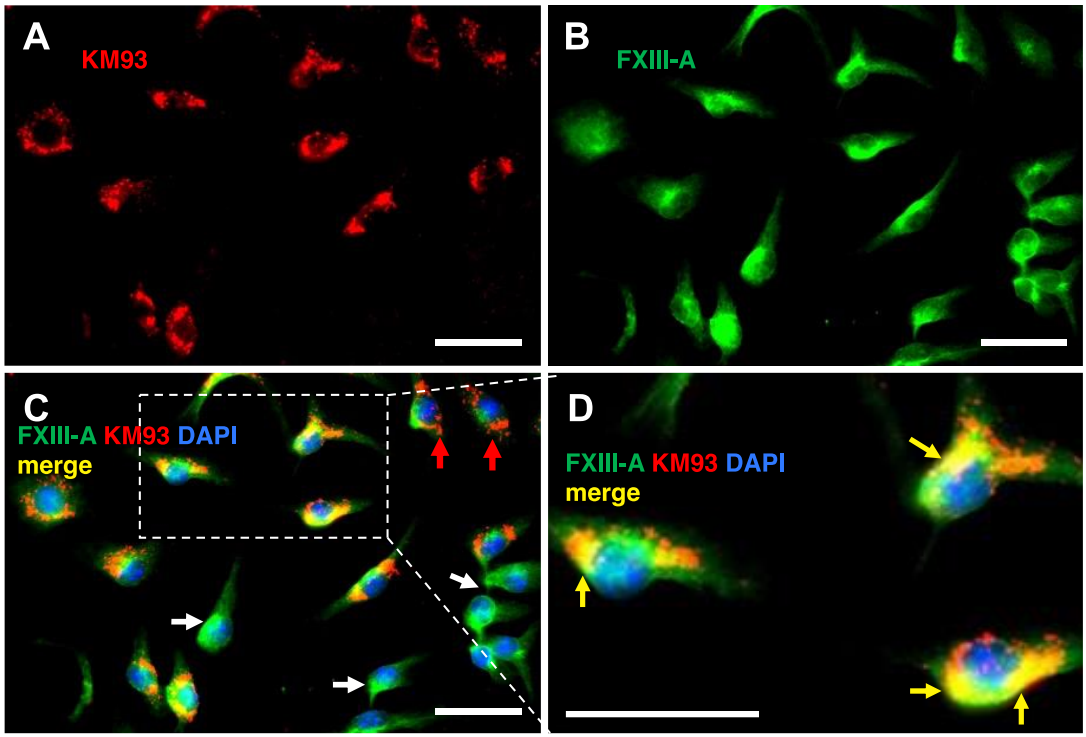

Figure 2.7. Immunofluorescence visualization of the labelling of FXIIIa by KM93 in murine bone marrow macrophages (BMM). Cells were incubated with 20 µM KM93 for 48 h in microscopy chamber slides. At the endpoint, cells were fixed and stained or treated with sheep anti-human FXIII-A antibody, followed by a secondary antibody, donkey anti-sheep AlexaFluor®-488 detection (green, Panel (B)). Nuclei were visualised with DAPI staining (blue). KM93 was visualised at 568 nm (red, Panel (A)). All cells were positive for FXIIIa, incorporation of KM93 into cells was clear and the probe colocalized with FXIII-A (Panel C and yellow arrows, inset Panel (D)). A subset of the macrophages did not incorporate the probe, despite the presence of FXIII-A (white arrows, Panel (C)), indicating that the enzyme may not be active in these specific macrophages. Some cells also showed strong red fluorescence but weak green fluorescence, giving the appearance of little colocalization, despite both probe and enzyme being present at these cellular compartments (red arrows, Panel (C)). White magnification bar represents 20 µm.

An additional experiment was performed in order to confirm the specificity of labelling by **KM93**. Cultured BMM cells were first treated for 2 h with ZED1301 (**46**), a known inhibitor of Factor XIIIa. The cells were then treated with fluorescent probe **KM93** for an additional 4 h, which

was followed by washing and imaging. Negligible fluorescent labelling was observed, relative to cells that were not blocked with ZED1301 prior to being treated similarly with **KM93** (see Supplementary Materials, Figure S10). This strongly suggests that **KM93** only reacts with the same cellular target as ZED1301 and increases our confidence in the specificity of **KM93** for labelling FXIIIa.

2.7. Conclusions

In this work, we set out to explore structure–activity relationships for the linker length and warhead functionality on a peptidic scaffold, as well as for the linker length, hydrophobic group, and acidic group on a small-molecule scaffold. While none of our compounds display improved potency over the lead inhibitor **46** (ZED1301), we showed that the mode and potency of FXIIIa inhibition are highly dependent on both the linker length and warhead functionality and that the optimal combination of these features may be scaffold-dependent due to the conformational dynamism in the enzyme. This work also represents the first report of the condition-independent kinetic parameters for ZED1301 (**46**). These findings set the stage for further developments in FXIIIa inhibitors as potential anticoagulants, as it is believed that the optimization of linkers and warheads on a small-molecule scaffold may be able to provide a drug-like inhibitor. The structure of ZED1301 was also adapted for the design of the rhodamine B-labelled fluorescent probe **93** (aka **KM93**), which was shown to retain irreversible inhibitory activity against the enzyme, to be effective at labelling FXIIIa in cellulo, demonstrating its applicability for localization studies in the further study of the biological roles of FXIIIa.

2.8. Materials and Methods

2.8.1. Kinetic Evaluation of FXIIIa Inhibition

A previously reported fluorescence-quenched isopeptidase assay using the commercially available substrate A101 (Zedira GmbH, Darmstadt, Germany) was employed for the determination of FXIIIa inhibition kinetics [56,57]. All assays were performed at 37 °C on 96-well plates, with fluorescence (excitation at 313 nm, emission at 418 nm) measured continuously using a BioTek Synergy 4 plate reader. For each inhibitor, duplicate trials were run in parallel at 4 inhibitor concentrations, along with duplicate positive controls (no inhibitor) and negative controls (no enzyme and no inhibitor). First, 125 µL of aqueous buffer 1 (111 mM Tris, 16.7 mM $CaCl_2$, 333 mM NaCl, pH 7.5) and 18 µL of aqueous buffer 2 (55.6 mM TCEP, 149 mM H-Gly-OMe, pH 7.5) were added to each well, along with 5 µL of A101 stock solution (4000 µM in DMSO). Next, the appropriate amount of the desired inhibitor, dissolved in DMSO, was added, in addition to the amount of distilled water necessary to reach a total volume of 180 µL in each well. Negative controls were diluted to a final volume of 200 µL. Thrombin-activated human FXIIIa (T070, Zedira GmbH, Darmstadt, Germany), stored at −80 °C in 20-µL aliquots (1 mg/mL enzyme) of storage buffer (50.0 mM Tris, 1.00 mM TCEP, 150 mM NaCl, pH 7.5) was warmed to room temperature and diluted to 0.0741 mg/mL through the addition of 250 µL of storage buffer. The diluted enzyme solution was then aliquoted into 10 separate PCR tubes. The assay plate and enzyme tubes were subsequently incubated at 37 °C for 10 min. After the completion of the incubation period, 20 µL of diluted FXIIIa solution was added from each PCR tube to all wells in the plate excluding the negative controls using a multi-channel pipette. This produced a final volume of 200 µL per well, with final reaction conditions of pH 7.5, 74.4 mM Tris, 10.4 mM

$CaCl_2$, 223 mM NaCl, 5.10 mM TCEP, 13.4 mM H-Gly-OMe, 100 μM A101, and 7.41 μg/mL (94 nM) FXIIIa. The range of inhibitor concentrations tested spanned from 1 to 200 μM, and the final DMSO concentration in the reaction mixture was kept below 10% *v*/*v*. Monitoring of fluorescence emission was commenced after quick stirring by aspiration. Assays were terminated once the fluorescence had plateaued.

2.8.2. Kinetic Evaluation of TG2 Inhibition

A colorimetric transamidase assay using chromogenic substrate AL5 (Cbz-Glu(ɣ-*p*-nitrophenyl ester)Gly-OH) was used to determine TG2 inhibition kinetics as described previously [42,45,46,50]. In brief, assays were conducted at 25 °C in 96-well plates, and absorbance at 405 nm was monitored continuously using a BioTek Synergy 4 plate reader. For each compound, 6 inhibitor concentrations were tested, along with positive (no inhibitor) and negative (no enzyme, no inhibitor) controls. All assays were run in duplicate as separate independent experiments. Human TG2 expressed and purified as described previously [64] and stored in aqueous buffer at −80 °C, was first thawed and diluted to a working concentration of 50 mU/mL in the buffer. The diluted enzyme solution was stored on ice. The appropriate amount of distilled water, 125 μL of aqueous buffer (111 mM MOPS, 15.6 mM $CaCl_2$, pH 6.9), the desired amount of inhibitor (from a DMSO stock solution), and 5.0 μL of AL5 (from a 5.56 mM DMSO solution) were added in that order to 7 Eppendorf tubes to reach final volumes of 250 μL per tube. After mixing thoroughly, 180 μL of the mixture from each tube was transferred to plate wells. To initiate the assay, 20 μL of the diluted TG2 solution was added using a multichannel pipette to each well except the negative control, which was treated with water. The final reaction conditions were pH 6.9, 50.0 mM MOPS, 7.0 mM $CaCl_2$, 100 μM AL5, and 5 mU/mL TG2. The range of inhibitor concentrations tested

spanned from 1 to 350 μM, and levels of DMSO were kept below 10% *v*/*v*. Data collection was then initiated after mixing by quick aspiration, and the assay was allowed to run for 20 min.

2.8.3. Determination of Type of Inhibition

The type of inhibition for both TG2 and FXIIIa was primarily determined by visual inspection of kinetic traces. Inhibitors producing fluorescence-time or absorbance-time kinetic curves that either reached plateaus at the same level as that of the positive control or did not plateau at all throughout the time course of the experiment, even at high inhibitor concentrations, were deemed to be operating through a reversible mechanism. This assumption was tested and validated with inhibitor **47** through an A101 substrate spike experiment. Additional A101 (5 μL of 4000 μM stock in DMSO) was added to enzymatic reactions lacking in inhibitor (positive control) and pre-treated with inhibitor (50, 100, 150, 200 μM) after the initial reactions were complete and fluorescence plateaus had been reached. Data collection at 37 °C was re-commenced immediately after the addition, and fluorescence was monitored over time as previously described. On the other hand, inhibitors producing kinetic curves in which earlier and lower plateaus in fluorescence or absorbance were observed as inhibitor concentration was increased were assumed to be operating through irreversible time-dependent covalent inactivation. This assumption was tested and validated with inhibitor **23** through an A101 substrate spike experiment in which an additional 5 μL of A101 substrate stock solution (4000 μM in DMSO) was added to the positive control and highest inhibitor concentration (200 μM) reaction. In the case of the small molecule inhibitors, an A101 spike experiment was conducted as outlined above, or an inhibitor spike with **79** the substrate spike was replaced with the highest concentration of inhibitor being assayed. Analysis was carried out as described above.

2.8.4. Analysis of In Vitro Kinetic Data

Data analysis for the determination of kinetic inhibition parameters for both FXIIIa and TG2 was performed using Microsoft Excel and GraphPad Prism. Absorbance-time and fluorescence-time plots from all positive controls and inhibitor treatments were corrected for background substrate hydrolysis through subtraction of the negative control and were then set to an initial fluorescence or absorbance of zero through subtraction of y-intercepts at time zero from all points.

For inhibitors displaying reversible competitive kinetics, the first 10% conversion, taken as the time point at which the relative fluorescence or absorbance reached 10% of the maximum at the plateau, was used to obtain the initial rates from linear regressions of fluorescence or absorbance over time. The means and standard deviations from duplicate trials of the ratios of uninhibited (positive control) to inhibited initial rates (v_{un}/v_{in}) were then plotted against the corrected inhibitor concentrations ($[I]/\alpha$), producing a normalised Dixon plot defined by the relationship

$$\frac{v_{un}}{v_{in}} = \frac{1}{K_i}\left(\frac{[I]}{\alpha}\right) + 1 \qquad (1)$$

Inhibitor concentrations were corrected by division with the parameter α, defined as the constant correcting for competition between the substrate and inhibitor for the enzyme's active site. Based on the known K_M of 8 μM for A101 [42,46] and its final concentration of 100 μM under these reaction conditions, α for FXIIIa kinetics was determined to be 13.5 through the equation

$$\alpha = 1 + \frac{[S]}{K_M} \qquad (2)$$

The corresponding α value for TG2 inhibition kinetics was determined to be 11 based on the AL5 K_M of 10 μM [42,46] and 100 μM concentration. Apparent K_i values for inhibitor potency against FXIIIa or TG2 were taken from the reciprocal slopes of linear regressions forced through (0,1) from each normalised Dixon plot and are reported with their graphically determined standard errors.

Inhibitors deemed to be operating irreversibly were evaluated under Kitz & Wilson conditions [58,59]. Observed pseudo-first-order rate constants (k_{obs}) for enzyme inactivation were extracted from the fluorescence-time or absorbance-time data at each inhibitor concentration through non-linear fitting using a mono-exponential decay model as in

$$FA_t = FA_0 + \left(FA_{plateau} - FA_0\right)(1 - e^{-k_{obs}t}) \quad (3)$$

The k_{obs} values from duplicate trials were then averaged and used to determine the first-order half-lives. All fluorescence-time and absorbance-time data sets were treated over 3 half-lives, and the observed rate constants were calculated as described. The mean and standard deviations for the observed rate constants were then plotted against the inhibitor concentrations after correction by division of the appropriate α parameter, producing hyperbolic saturation plots. For inhibitors where a clear plateau in the observed rate constant was observed at high inhibitor concentrations in the saturation plot, non-linear hyperbolic fitting was performed according to Equation (4).

$$k_{obs} = \frac{k_{inact}\frac{[I]}{\alpha}}{K_I + \frac{[I]}{\alpha}} \quad (4)$$

This fitting was used to determine k_{inact} and K_I values, along with their standard errors. These extracted values were then used in the calculation of k_{inact}/K_I, with errors carried forward

appropriately. For inhibitors that did not reach an obvious saturation in the observed rate constant, a linear regression (forced through the origin) was performed on the plots of k_{obs} *vs* [I]/α using the lowest inhibitor concentrations. The ratio of k_{inact}/K_I in these cases was taken from the slope of the linear fit and its corresponding standard error.

2.8.5. Fluorescent Labelling of FXIIIa by SDS-PAGE

To a 1.5-mL Eppendorf was added 10 µg of thrombin-activated FXIIIa (T070 Zedira GmbH, Darmstadt, Germany) as a solution in 10 µL storage buffer (50 mM TRIS, 1 mM TCEP, 150 mM NaCl pH 7.5). A 5-µL aliquot of FXIII kinetic assay buffer (111 mM TRIS, 16 mM $CaCl_2$, 333 mM NaCl pH 7.5) was added to the tube and gently vortexed. The rhodamine B derivatized probe **93** (aka **KM93**), 15 µL of a 60 µM aqueous solution, was subsequently added to the tube, the tube was gently vortexed, and enzyme labelling was allowed to occur for 20 min at room temperature. A 30-µL aliquot of Bio-Rad 2X Laemmli Sample Buffer (5% β-mercaptoethanol) was added to the sample and the solution was boiled for 5 min at 100 °C to ensure denaturation. Once the sample had cooled, 30 µL was loaded into a well of a Bio-Rad Mini-PROTEAN TGX precast 4–20% acrylamide gel. A 10-µL aliquot of Bio-Rad Precision Plus Unstained Protein Standards was loaded and electrophoresis was performed at 120 V for 1 h. The gel was first visualised using a Bio-Rad ChemiDoc MP Imager for fluorescent bands (green epifluorescence illumination 605/50 nm filter). The gel was then stained with Coomassie and visualised again.

2.8.6. Synthesis of Peptidic Inhibitors, Small Molecule Inhibitors, and Fluorescent Probe

Synthetic schemes, experimental procedures, and characterization data for all intermediates and final compounds are provided in the Supplementary Materials.

2.8.7. Cellular Labelling and Microscopy of FXIIIa

2.8.7.1. Reagents and Antibodies

MEM Alpha (αMEM) (12561-056), penicillin-streptomycin, L-glutamine, and sodium pyruvate were from Gibco (Burlington, ON, Canada). Fetal bovine serum was from Hyclone (Waltham, MA, USA). Human M-CSF (macrophage-colony stimulating factor) was from PeproTech (Rocky Hill, NJ, USA). Thiazolyl Blue Tetrazolium Bromide (MTT) was purchased from Sigma. Sheep anti-human Factor XIII-A (SAF13A-AP) was from Affinity Biologicals (Ancaster, ON, Canada). Donkey anti-sheep IgG cross-adsorbed secondary antibody AlexaFluor®-488 (A-11015), AlexaFluor®-488-phalloidin and DAPI (4′, 6- diamidino-2-phenylindole) were from Thermo Fisher Scientific (Rockford, IL).

2.8.7.2. Animals

C57BL/6 mice were purchased from Jackson Laboratory (Bar Harbor, ME, USA). Mice were housed in a pathogen-free environment and maintained under standardised conditions. All experimental protocols were approved by the Animal Care Committee of McGill University.

2.8.7.3. Bone Marrow Macrophage Isolation Culture

Bone marrow cells were extracted from 6- to 10-week-old C57BL/6 mice and cultured for 24 h with 25 ng/mL M-CSF. Non-adherent cells were collected and plated at 5×10^4 cells/cm^2 for another 48 h in the presence of M-CSF. Medium composed of αMEM, 1% penicillin-streptomycin, 1% L-glutamine solution, 1% sodium pyruvate, and 10% FBS was used for the culture. The cells that had adhered to plates were M-CSF-dependent bone marrow-derived macrophages (BMMs).

Probe **93** (aka **KM93**) was diluted in DMSO at stock concentration and added to the cell culture at the indicated concentrations.

2.8.7.4. Protein Extraction and SDS-PAGE

Bone marrow macrophages were cultured in the presence and absence of probe **93** (aka **KM93**) and cells were collected at their experimental endpoints of 6 h and 48 h as follows: cells were washed with PBS and extracted with ice-cold cell lysis buffer containing 50 mM Tris (pH 7.5), 0.5 M NaCl, and 2% Igepal, 1% protease inhibitor cocktail, and 1% phosphatase inhibitor cocktail. Extraction was done with 30 min incubation followed by scraping, 30 s of sonication, and centrifugation at 14,000 g for 15 min at 4 °C. A bicinchoninic acid (BCA) Protein Assay Kit (Thermo Fisher Scientific) was used to measure protein concentration. Twenty (20) µg of proteins were loaded onto 10% SDS-polyacrylamide gels and run in a Bio-Rad electrophoresis system (Bio-Rad, Mississauga, ON, Canada). Protein bands labelled by probe **93** (aka **KM93**) were imaged with a Typhoon 8600 fluoroimager (GE Healthcare) using Ex/Em 532/610 nm and then stained with Coomassie.

2.8.7.5. Immunofluorescence Microscopy

Bone marrow macrophages were plated onto NUNC 8-well cell culture chamber slides (Thermo Scientific) as described above. At the endpoints, cells were fixed with 3.7% formaldehyde for 10 min and then blocked with 2% bovine serum albumin (BSA) for 30 min. Cells were then incubated with probe **93** (**KM93**) for the indicated time and then washed and incubated with primary antibody (Anti-FXIII-A) for 2 h, followed by AlexaFluor® conjugated secondary antibody for 1 h. F-actin was labelled with AlexaFluor® 488-phalloidin and nuclei were stained

with DAPI. Images were taken under 40× objective by using the Zeiss Axioscope 5 microscope (Carl Zeiss, Hamburg, Germany).

2.9. Supplementary Materials

The supporting information containing detailed description of the synthesis [42, 51, 53, 65-77], characterization, and supplementary figures can be downloaded at: www.mdpi.com/xxx/s1, Scheme S1: Synthesis of Fmoc-AA(Acrylamide)-OH monomers 5-8 required for the production of acrylamide-bearing peptidic inhibitors; Scheme S2: Synthesis of Fmoc-D-Asp(OtBu)-OH 9 required for the production of acrylamideand α-chloroacetamide-bearing peptidic inhibitors; Scheme S3: Synthesis of acrylamide-bearing peptidic inhibitors 11-14; Scheme S4: Synthesis of Fmoc-AA(Alloc)-OH monomers 17-19 required for the production of αchloroacetamide-bearing peptidic inhibitors; Scheme S5: Synthesis of α-chloroacetamide-bearing peptidic inhibitors 20-23; Scheme S6: Synthesis of Boc-Glu(MA)-OH 28 required for the production of ZED1301; Scheme S7: Synthesis of Boc-AA(MA)-OH monomers 33 and 37 required for the production of α,β-unsaturated ester-bearing peptidic inhibitors; Scheme S8: Synthesis of Ac-D-Asp(OtBu)-OH 38 required for the production of α,β-unsaturated ester-bearing peptidic inhibitors; Scheme S9: Synthesis of α,β-unsaturated ester-bearing peptidic inhibitors 45-47; Scheme S10: General synthetic scheme to arrive at L-Dap key intermediate for small molecule inhibitors 66-68; Scheme S11: Synthetic scheme to arrive at malonyl inhibitors 71 and 72; Scheme S12: Synthetic scheme to arrive at cyclopropyl inhibitor 74 through the methyl ester 73; Scheme S13: Synthetic scheme to generate succinyl inhibitors 75-77; Scheme S14: Synthetic scheme to synthesize sulfonyl inhibitor 79; Scheme S15: General synthetic scheme to arrive at D-Dap scaffold key intermediate 83; Scheme S16: Synthetic scheme to generate D-Dap succinyl inhibitor 84; Scheme S17: General

synthetic scheme to generate α,β-unsaturated warhead key intermediate 86; Scheme S18: Synthetic scheme to produce α,β-unsaturated succinyl inhibitor 87; Scheme S19: Synthetic scheme to produce α,β-unsaturated phthalyl inhibitor 88; Scheme S20: Synthesis of Rhodamine-B-ZED1301 fluorescent probe 93 (KM93); Scheme S21: Synthesis of Fmoc-6AH-OH 89 required for the production of fluorescent probe 93 (KM93); Figure S1: Fluorescence-time curve of the spike experiment performed with inhibitor 47 to confirm the reversibility of FXIIIa inhibition. Additional A101 substrate was added to the reactions corresponding to the positive control with no inhibitor (+ve), the negative control with no enzyme (-ve), and all 4 inhibitor concentrations (1, 2, 5, and 10 μM) after the initial plateaus in fluorescence had been reached. Fluorescence emission (RFU, relative fluorescence unit emission at 418 nm after excitation at 313 nm) was then monitored over time; Figure S2: Fluorescence-time curve of the spike experiment performed with inhibitor 23 to confirm the irreversibility of FXIIIa inhibition. Additional A101 substrate was added to the reactions corresponding to the positive control with no inhibitor (+ve) and the highest inhibitor concentration (200 μM) after the initial plateaus in fluorescence had been reached. Fluorescence emission (RFU, relative fluorescence unit emission at 418 nm after excitation at 313 nm) was then monitored over time; Figure S3: Substrate spike experiment with small molecule inhibitor 79 and FXIIIa. Upon completion of the activity assay, another 100 μM of A101 was added and the RFU increased, implying FXIIIa was still active (top and bottom left panels); Figure S4: Inhibitor spike experiment with small molecule inhibitor 79. Upon completion of the activity assay another dose of 320 μM 79 was added and the RFU plateau at a lower value (top right panel); Figure S5: Inhibition experiment of FXIIIa with small molecule inhibitor scaffold components dansyl amide and acrylamide assayed at four different concentrations (0, 100, 200, 320 μM); Figure S6: SDS-PAGE of commercially available FXIIIa incubated with 30 μM fluorescent probe 93 (KM93)

visualized first for fluorescence and then using Coomassie Blue staining; Figure S7: Full SDS-PAGE gel of fluorescent labelling of commercially available FXIIIa with 30 µM 93 (KM93). Note the excess labelling agent at the very bottom edge of the gel does not correspond to protein; Figure S8: A) Fluorescent labelling of FXIIIa in murine bone marrow macrophages (BMM). BMMs were incubated with 0-20 µM KM93 for 6 h (top gel) or for 48 h (bottom gel), lysed, and protein extracts were prepared and resolved with denaturing, 10% SDS-PAGE. The gels were visualized using a fluoroimager (Ex/Em 562/610). The gels show a dose dependent labelling of a ~80 kDa band, which corresponds to a molecular weight of FXIIIa, consistent with the red fluorescence of the rhodamine moiety of KM93. The identity of the band at ~100 kDa is unknown but it is also present in the negative control and thus represents background. B) Coomassie Blue stained gels confirm equal loading in each lane; Figure S9: Fluorescence visualization of KM93 in murine bone marrow macrophages (BMM). Cells were incubated with 20 µM KM93 for 48 h in microscopy chamber slides. At end point, cells were fixed, cytoskeletal actin was stained with AlexaFluor®-488-phalloidin (green) and nuclei were stained with DAPI (blue). KM93 was visualized in the 568-nm channel (red). A): Cells that were incubated in the absence of the probe showed no signal in the 568-nm channel (negative control). B): Strong red fluorescence was seen observed after 48 h incubation with 20 µM KM93. The probe was confirmed to be intracellular by actin staining (see inset C). White magnification bar represents 20 µm; Figure S10: FXIIIa inhibitor ZED1301 is able to block labelling by KM93 probe in BMM cells. BMM cells were preincubated in the absence or presence of 20 µM ZED1301 for 2 hours to inhibit FXIIIa, prior to addition of 20 µM KM93 and further incubation for 4 hours. Cells were fixed and washed, nuclei were stained with DAPI (blue) and incorporation of the red probe KM93 was observed by fluorescence microscopy. Negligible

red fluorescence was observed in cells blocked by pre-incubation with ZED1301. Magnification bar equals 40 µm.

2.10. Author Contributions

Conceptualization, J.W.K. and E.W.J.G.; formal analysis, K.M., S.S., and E.W.J.G.; investigation, K.M., S.S., E.W.J.G., and S.E.S.; writing—original draft preparation, K.M. and E.W.J.G.; writing—review and editing, E.W.J.G., J.W.K., and M.T.K.; supervision, J.W.K. and M.T.K.; funding acquisition, J.W.K. and M.T.K. All authors have read and agreed to the published version of the manuscript.

2.11. Funding

This research and the APC were funded by the Natural Sciences and Engineering Research Council of Canada (NSERC), Discovery Grant number RGPIN-2019-05893 (J.W.K.) by the Canadian Institutes of Health Research (CIHR), grant numbers PJT-153089 and PJT-162100 (M.T.K.)

2.12. Institutional Review Board Statement

The animal study protocol was approved by the Animal Care Committee of McGill University (protocol code MCGL-5188, 26 October 2022).

2.13. Informed Consent Statement

Not applicable.

2.14. Data Availability Statement

Data will be provided upon reasonable request.

2.15. Conflicts of Interest

The authors declare no conflict of interest.

2.16. References

1. Lorand, L.; Graham, R.M. Transglutaminases: Crosslinking Enzymes with Pleiotropic Functions. *Nat. Rev. Mol. Cell Biol.* **2003**, *4*, 140–156. https://doi.org/10.1038/nrm1014.
2. Mehta, K.; Eckert, R. *Transglutaminases: Family of Enzymes with Diverse Functions*; Karger: Basel, Switzerland, 2005; Volume 38. ISBN 3805579012.
3. Beninati, S.; Bergamini, C.M.; Piacentini, M. An Overview of the First 50 Years of Transglutaminase Research. *Amino Acids* **2009**, *36*, 591–598. https://doi.org/10.1007/s00726-008-0211-x.
4. Savoca, M.P.; Tonoli, E.; Atobatele, A.G.; Verderio, E.A.M. Biocatalysis by Transglutaminases: A Review of Biotechnological Applications. *Micromachines* **2018**, *9*, 562. https://doi.org/10.3390/MI9110562.
5. Chica, R.A.; Gagnon, P.; Keillor, J.W.; Pelletier, J.N. Tissue Transglutaminase Acylation: Proposed Role of Conserved Active Site Tyr and Trp Residues Revealed by Molecular Modeling of Peptide Substrate Binding. *Protein Sci.* **2004**, *13*, 979. https://doi.org/10.1110/PS.03433304.
6. Keillor, J.W.; Clouthier, C.M.; Apperley, K.Y.P.; Akbar, A.; Mulani, A. Acyl Transfer Mechanisms of Tissue Transglutaminase. *Bioorg. Chem.* **2014**, *57*, 186–197. https://doi.org/10.1016/j.bioorg.2014.06.003.

7. Gundemir, S.; Colak, G.; Tucholski, J.; Johnson, G.V.W. Transglutaminase 2: A Molecular Swiss Army Knife. *Biochim. Biophys. Acta Mol. Cell Res.* **2012**, *1823*, 406–419. https://doi.org/10.1016/j.bbamcr.2011.09.012.
8. Katt, W.P.; Antonyak, M.A.; Cerione, R.A. The Diamond Anniversary of Tissue Transglutaminase: A Protein of Many Talents. *Drug Discov. Today* **2018**, *23*, 575–591. https://doi.org/10.1016/j.drudis.2018.01.037.
9. Szondy, Z.; Korponay-Szabó, I.; Király, R.; Sarang, Z.; Tsay, G.J. Transglutaminase 2 in Human Diseases. *BioMedicine* **2017**, *7*, 15. https://doi.org/10.1051/bmdcn/2017070315.
10. Sane, D.C.; Kontos, J.L.; Greenberg, C.S. Roles of Transglutaminases in Cardiac and Vascular Diseases. *Front. Biosci.* **2007**, *12*, 2530–2545.
11. Dieterich, W.; Ehnis, T.; Bauer, M.; Donner, P.; Volta, U.; Riecken, E.O.; Schuppan, D. Identification of Tissue Transglutaminase as the Autoantigen of Celiac Disease. *Nat. Med.* **1997**, *3*, 797–801. https://doi.org/10.1038/nm0797-797.
12. Huang, L.; Xu, A.M.; Liu, W. Transglutaminase 2 in Cancer. *Am. J. Cancer Res.* **2015**, *5*, 2756–2776.
13. Lee, H.T.; Huang, C.H.; Chen, W.C.; Tsai, C.S.; Chao, Y.L.; Liu, S.H.; Chen, J.H.; Wu, Y.Y.; Lee, Y.J. Transglutaminase 2 Promotes Migration and Invasion of Lung Cancer Cells. *Oncol. Res.* **2018**, *26*, 1175–1182. https://doi.org/10.3727/096504018X15149761920868.
14. Kerr, C.; Szmacinski, H.; Fisher, M.L.; Nance, B.; Lakowicz, J.R.; Akbar, A.; Keillor, J.W.; Lok Wong, T.; Godoy-Ruiz, R.; Toth, E.A.; et al. Transamidase Site-Targeted Agents Alter the Conformation of the Transglutaminase Cancer Stem Cell Survival Protein to Reduce GTP Binding Activity and Cancer Stem Cell Survival. *Oncogene* **2017**, *36*, 2981–2990. https://doi.org/10.1038/onc.2016.452.

15. Tabolacci, C.; de Martino, A.; Mischiati, C.; Feriotto, G.; Beninati, S. The Role of Tissue Transglutaminase in Cancer Cell Initiation, Survival and Progression. *Med. Sci.* **2019**, *7*, 19. https://doi.org/10.3390/medsci7020019.
16. Ayinde, O.; Wang, Z.; Pinton, G.; Moro, L.; Griffin, M. Transglutaminase 2 Maintains a Colorectal Cancer Stem Phenotype by Regulating Epithelial-Mesenchymal Transition. *Oncotarget* **2019**, *10*, 4556–4569. https://doi.org/10.18632/oncotarget.27062.
17. Fisher, M.L.; Keillor, J.W.; Xu, W.; Eckert, R.L.; Kerr, C. Transglutaminase Is Required for Epidermal Squamous Cell Carcinoma Stem Cell Survival. *Mol. Cancer Res.* **2015**, *13*, 1083–1094. https://doi.org/10.1158/1541-7786.MCR-14-0685-T.
18. Wolberg, A.S.; Sang, Y. Fibrinogen and Factor XIII in Venous Thrombosis and Thrombus Stability. *Arterioscler. Thromb. Vasc. Biol.* **2022**, *42*, 931–941. https://doi.org/10.1161/ATVBAHA.122.317164.
19. Steiner, T.; Weitz, J.I.; Veltkamp, R. Anticoagulant-Associated Intracranial Hemorrhage in the Era of Reversal Agents. *Stroke* **2017**, *48*, 1432–1437. https://doi.org/10.1161/STROKEAHA.116.013343.
20. van Es, N.; Coppens, M.; Schulman, S.; Middeldorp, S.; Büller, H.R. Direct Oral Anticoagulants Compared with Vitamin K Antagonists for Acute Venous Thromboembolism: Evidence from Phase 3 Trials. *Blood* **2014**, *124*, 1968–1975. https://doi.org/10.1182/BLOOD-2014-04-571232.
21. Hokusai-VTE Investigators; Büller, H.; Décousus, H.; Grosso, M.; Mercuri, M.; Middeldorp, S.; Prins, M.; Raskob, G.; Schellong, S.; Schwocho, L.; et al. Edoxaban versus Warfarin for the Treatment of Symptomatic Venous Thromboembolism. *N. Engl. J. Med.* **2013**, *369*, 1406–1415. https://doi.org/10.1056/NEJMoa1306638.

22. Pasternack, R.; Büchold, C.; Jähnig, R.; Pelzer, C.; Sommer, M.; Heil, A.; Florian, P.; Nowak, G.; Gerlach, U.; Hils, M. Novel Inhibitor ZED3197 as Potential Drug Candidate in Anticoagulation Targeting Coagulation FXIIIa (F13a). *J. Thromb. Haemost.* **2020**, *18*, 191–200. https://doi.org/10.1111/jth.14646.
23. Cordell, P.A.; Kile, B.T.; Standeven, K.F.; Josefsson, E.C.; Pease, R.J.; Grant, P.J. Association of Coagulation Factor XIII-A with Golgi Proteins within Monocyte-Macrophages: Implications for Subcellular Trafficking and Secretion. *Blood* **2010**, *115*, 2674–2681. https://doi.org/10.1182/BLOOD-2009-08-231316.
24. Duckert, F.; Jung, E.; Shmerling, D.H. A Hitherto Undescribed Congenital Haemorrhagic Diathesis Probably Due to Fibrin Stabilizing Factor Deficiency. *Thromb. Diath. Haemorrh.* **1960**, *5*, 179–186. https://doi.org/10.1055/S-0038-1654918/ID/JR1654918-7.
25. Lauer, P.; Metzner, H.J.; Zettlmeißl, G.; Li, M.; Smith, A.G.; Lathe, R.; Dickneite, G. Targeted Inactivation of the Mouse Locus Encoding Coagulation Factor XIII-A: Hemostatic Abnormalities in Mutant Mice and Characterization of the Coagulation Deficit. *Thromb. Haemost.* **2002**, *88*, 967–974,. https://doi.org/10.1055/s-0037-1613342.
26. Dardik, R.; Solomon, A.; Loscalzo, J.; Eskaraev, R.; Bialik, A.; Goldberg, I.; Schiby, G.; Inbal, A. Novel Proangiogenic Effect of Factor XIII Associated with Suppression of Thrombospondin 1 Expression. *Arterioscler. Thromb. Vasc. Biol.* **2003**, *23*, 1472–1477. https://doi.org/10.1161/01.ATV.0000081636.25235.C6.
27. Muszbek, L.; Bereczky, Z.; Bagoly, Z.; Komáromi, I.; Katona, É. Factor XIII: A Coagulation Factor with Multiple Plasmatic and Cellular Functions. *Physiol. Rev.* **2011**, *91*, 931–972. https://doi.org/10.1152/physrev.00016.2010.

28. Kobbervig, C.; Williams, E. FXIII Polymorphisms, Fibrin Clot Structure and Thrombotic Risk. *Biophys. Chem.* **2004**, *112*, 223–228. https://doi.org/10.1016/j.bpc.2004.07.023.
29. Schroeder, V.; Kohler, H.P. Factor XIII: Structure and Function. *Semin. Thromb. Hemost.* **2016**, *42*, 422–428. https://doi.org/10.1055/S-0036-1571341.
30. Gupta, S.; Biswas, A.; Akhter, M.S.; Krettler, C.; Reinhart, C.; Dodt, J.; Reuter, A.; Philippou, H.; Ivaskevicius, V.; Oldenburg, J. Revisiting the Mechanism of Coagulation Factor XIII Activation and Regulation from a Structure/Functional Perspective. *Sci. Rep.* **2016**, *6*, 30105. https://doi.org/10.1038/srep30105.
31. Handrkova, H.; Schroeder, V.; Kohler, H.P. The Activation Peptide of Coagulation Factor XIII Is Vital for Its Expression and Stability. *J. Thromb. Haemost.* **2015**, *13*, 1449–1458. https://doi.org/10.1111/JTH.13035.
32. Hornyak, T.J.; Shafer, J.A. Role of Calcium Ion in the Generation of Factor XIII Activity. *Biochemistry* **1991**, *30*, 6175–6182. https://doi.org/10.1021/bi00239a014.
33. Stieler, M.; Weber, J.; Hils, M.; Kolb, P.; Heine, A.; Büchold, C.; Pasternack, R.; Klebe, G. Structure of Active Coagulation Factor-Xiii Triggered by Calcium Binding: Basis for the Design of next-Generation Anticoagulants. *Angew. Chem. Int. Ed. Engl.* **2013**, *52*, 11930–11934. https://doi.org/10.1002/anie.201305133.
34. Kristiansen, G.K.; Andersen, M.D. Reversible Activation of Cellular Factor XIII by Calcium. *J. Biol. Chem.* **2011**, *286*, 9833. https://doi.org/10.1074/JBC.M110.174128.
35. Al-Horani, R.A.; Kar, S. Factor XIIIa Inhibitors as Potential Novel Drugs for Venous Thromboembolism. *Eur. J. Med. Chem.* **2020**, *200*, 112442. https://doi.org/10.1016/j.ejmech.2020.112442.

36. Eckert, R.L.; Kaartinen, M.T.; Nurminskaya, M.; Belkin, A.M.; Colak, G.; Johnson, G.V.W.; Mehta, K. Transglutaminase Regulation of Cell Function. *Physiol. Rev.* **2014**, *94*, 383–417. https://doi.org/10.1152/physrev.00019.2013.
37. Haroon, Z.A.; Hettasch, J.M.; Lai, T.; Dewhirst, M.W.; Greenberg, C.S. Tissue Transglutaminase Is Expressed, Active, and Directly Involved in Rat Dermal Wound Healing and Angiogenesis. *FASEB J.* **1999**, *13*, 1787–1795. https://doi.org/10.1096/FASEBJ.13.13.1787.
38. Wang, Z.; Perez, M.; Caja, S.; Melino, G.; Johnson, T.S.; Lindfors, K.; Griffin, M. A Novel Extracellular Role for Tissue Transglutaminase in Matrix-Bound VEGF-Mediated Angiogenesis. *Cell Death Dis.* **2013**, *4*, e808. https://doi.org/10.1038/CDDIS.2013.318.
39. Freund, K.F.; Doshi, K.P.; Gaul, S.L.; Claremon, D.A.; Remy, D.C.; Baldwin, J.J.; Pitzenberger, S.M.; Stern, A.M. Transglutaminase Inhibition by 2-[(2-Oxopropyl)Thio]Imidazolium Derivatives: Mechanism of Factor Xllla Inactivation. *Biochemistry* **1994**, *33*, 10109–10119. https://doi.org/10.1021/bi00199a039.
40. Sugimura, Y.; Hosono, M.; Wada, F.; Yoshimura, T.; Maki, M.; Hitomi, K. Screening for the Preferred Substrate Sequence of Transglutaminase Using a Phage-Displayed Peptide Library: Identification of Peptide Substrates for TGase 2 and Factor XIIIa. *J. Biol. Chem.* **2006**, *281*, 17699–17706. https://doi.org/10.1074/jbc.M513538200.
41. Stieler, M.; Büchold, C.; Schmitt, M.; Heine, A.; Hils, M.; Pasternack, R.; Klebe, G. Structure-Based Design of FXIIIa-Blockers: Addressing a Transient Hydrophobic Pocket in the Active Site of FXIIIa. *ChemMedChem* **2020**, *15*, 900–905. https://doi.org/10.1002/cmdc.202000056.
42. McNeil, N.M.R.; Gates, E.W.J.; Firoozi, N.; Cundy, N.J.; Leccese, J.; Eisinga, S.; Tyndall, J.D.A.; Adhikary, G.; Eckert, R.L.; Keillor, J.W. Structure-Activity Relationships of N-

Terminal Variants of Peptidomimetic Tissue Transglutaminase Inhibitors. *Eur. J. Med. Chem.* **2022**, *232*, 114172. https://doi.org/10.1016/j.ejmech.2022.114172.

43. Tung, C.H.; Ho, N.H.; Zeng, Q.; Tang, Y.; Jaffer, F.A.; Reed, G.L.; Weissleder, R. Novel Factor XIII Probes for Blood Coagulation Imaging. *ChemBioChem* **2003**, *4*, 897–899. https://doi.org/10.1002/CBIC.200300602.
44. Jaffer, F.A.; Tung, C.H.; Wykrzykowska, J.J.; Ho, N.H.; Houng, A.K.; Reed, G.L.; Weissleder, R. Molecular Imaging of Factor XIIIa Activity in Thrombosis Using a Novel, Near-Infrared Fluorescent Contrast Agent That Covalently Links to Thrombi. *Circulation* **2004**, *110*, 170–176. https://doi.org/10.1161/01.CIR.0000134484.11052.44.
45. Rangaswamy, A.M.M.; Navals, P.; Gates, E.W.J.; Shad, S.; Watt, S.K.I.; Keillor, J.W. Structure–Activity Relationships of Hydrophobic Alkyl Acrylamides as Tissue Transglutaminase Inhibitors. *RSC Med. Chem.* **2022**, *13*, 413–428. https://doi.org/10.1039/d1md00382h.
46. Akbar, A.; McNeil, N.M.R.; Albert, M.R.; Ta, V.; Adhikary, G.; Bourgeois, K.; Eckert, R.L.; Keillor, J.W. Structure-Activity Relationships of Potent, Targeted Covalent Inhibitors That Abolish Both the Transamidation and GTP Binding Activities of Human Tissue Transglutaminase. *J. Med. Chem.* **2017**, *60*, 7910–7927. https://doi.org/10.1021/acs.jmedchem.7b01070.
47. Keillor, J.W.; Akbar, A.; Eckert, R.L.; Fisher, M.; Johnson, G.V.W. TG2 Inhibitor Piperazine Compounds and Uses Thereof. WO2017179018A1, 19 October 2017.
48. Chabot, N.; Moreau, S.; Mulani, A.; Moreau, P.; Keillor, J.W. Fluorescent Probes of Tissue Transglutaminase Reveal Its Association with Arterial Stiffening. *Chem. Biol.* **2010**, *17*, 1143–1150. https://doi.org/10.1016/J.CHEMBIOL.2010.06.019.

49. Pardin, C.; Pelletier, J.N.; Lubell, W.D.; Keillor, J.W. Cinnamoyl Inhibitors of Tissue Transglutaminase. *J. Org. Chem.* **2008**, *73*, 5766–5775. https://doi.org/10.1021/jo8004843.
50. Leblanc, A.; Gravel, C.; Labelle, J.; Keillor, J.W. Kinetic Studies of Guinea Pig Liver Transglutaminase Reveal a General-Base-Catalyzed Deacylation Mechanism. *Biochemistry* **2001**, *40*, 8335–8342. https://doi.org/10.1021/bi0024097.
51. Hils, M.; Pasternack, R.; Büchold, C.; Weber, J.; Heine, A.; Klebe, G.; Stieler, M. Crystal Structure of Blood Coagulation Factor XIIIa. WO2014090835A1, 19 June 2014.
52. Pinkas, D.M.; Strop, P.; Brunger, A.T.; Khosla, C. Transglutaminase 2 Undergoes a Large Conformational Change upon Activation. *PLoS Biol.* **2007**, *5*, 327. https://doi.org/10.1371/journal.pbio.0050327.
53. Büchold, C.; Gerlach, U.; Hils, M.; Pasternack, R.; Weber, J. Pyridinone Derivatives as Tissue Transglutaminase Inhibitors. WO2014012858A1, 23 January 2014.
54. Pasternack, R.; Hils, M.; Büchold, C. Inhibitors of Blood Coagulation Factor XIII. WO2019201432A1, 24 October 2019.
55. Pardin, C.; Gillet, S.M.F.G.; Keillor, J.W. Synthesis and Evaluation of Peptidic Irreversible Inhibitors of Tissue Transglutaminase. *Bioorg. Med. Chem.* **2006**, *14*, 8379–8385. https://doi.org/10.1016/j.bmc.2006.09.011.
56. Oertel, K.; Hunfeld, A.; Specker, E.; Reiff, C.; Seitz, R.; Pasternack, R.; Dodt, J. A Highly Sensitive Fluorometric Assay for Determination of Human Coagulation Factor XIII in Plasma. *Anal. Biochem.* **2007**, *367*, 152–158. https://doi.org/10.1016/j.ab.2007.05.011.
57. Király, R.; Thangaraju, K.; Nagy, Z.; Collighan, R.; Nemes, Z.; Griffin, M.; Fésüs, L. Isopeptidase Activity of Human Transglutaminase 2: Disconnection from Transamidation and

Characterization by Kinetic Parameters. *Amino Acids* **2016**, *48*, 31–40. https://doi.org/10.1007/s00726-015-2063-5.

58. Kitz, R.; Wilson, I.B. Esters of Methanesulfonic Acid as Irreversible Inhibitors of Acetylcholinesterase. *J. Biol. Chem.* **1962**, *237*, 3245–3249. https://doi.org/10.1016/s0021-9258(18)50153-8.
59. Stone, S.R.; Hofsteenge, J. Specificity of Activated Human Protein C. *Biochem. J.* **1985**, *230*, 497–502. https://doi.org/10.1042/bj2300497.
60. Ilich, P. Direct Observation of Acrylamide Fluorescence. *Croat. Chem. Acta* **1994**, *67*, 447–453.
61. Leitner, M.; Büchold, C.; Pasternack, R.; Binder, N.B.; Moore, G.W. Clinical Validation of an Automated Fluorogenic Factor XIII Activity Assay Based on Isopeptidase Activity. *Int. J. Mol. Sci.* **2021**, *22*, 1002. https://doi.org/10.3390/ijms22031002.
62. Takahashi, N.; Takahashi, Y.; Putnam, F.W. Primary Structure of Blood Coagulation Factor XIIIa (Fibrinoligase, Transglutaminase) from Human Placenta. *Proc. Natl. Acad. Sci. USA* **1986**, *83*, 8019–8023. https://doi.org/10.1073/pnas.83.21.8019.
63. Ádány, R.; Bárdos, H. Review Factor XIII Subunit A as an Intracellular Transglutaminase. *CMLS Cell. Mol. Life Sci.* **2003**, *60*, 1049–1060. https://doi.org/10.1007/s00018-003-2178-9.
64. Roy, I.; Smith, O.; Clouthier, C.M.; Keillor, J.W. Expression, Purification and Kinetic Characterisation of Human Tissue Transglutaminase. *Protein Expr. Purif.* **2013**, *87*, 41–46. https://doi.org/10.1016/j.pep.2012.10.002.
65. Adamczyk, M.; Johnson, D.D.; Reddy, R.E. Collagen Cross-Links: A Convenient Synthesis of Tert-Butyl-(2S)-2-[(Tert-Butoxycarbonyl)Amino]-4-(2-Oxiranyl)Butanoate. *Tetrahedron Asymmetry* **1999**, *10*, 775–781, doi:10.1016/S0957-4166(99)00055-5.

66. Kokotos, G.; Padrón, J.M.; Martín, T.; Gibbons, W.A.; Martín, V.S. A General Approach to the Asymmetric Synthesis of Unsaturated Lipidic α-Amino Acids. the First Synthesis of α-Aminoarachidonic Acid. *J Org Chem* **1998**, *63*, 3741–3744, doi:10.1021/jo9715128.

67. Olsen, R.K.; Ramasamy, K.; Emery, T. Synthesis of N.alpha.,N.delta.-protected N.delta.-hydroxy-L-ornithine from L-glutamic acid. *J Org Chem* **1984**, *49*, 3527–3534, doi:10.1021/jo00193a016.

68. Goode, D.R.; Sharma, A.K.; Hergenrother, P.J. Using Peptidic Inhibitors to Systematically Probe the S1′ Site of Caspase-3 and Caspase-7. *Org Lett* **2005**, *7*, 3529–3532, doi:10.1021/ol051287d.

69. Fulmer, G.R.; Miller, A.J.M.; Sherden, N.H.; Gottlieb, H.E.; Nudelman, A.; Stoltz, B.M.; Bercaw, J.E.; Goldberg, K.I. NMR Chemical Shifts of Trace Impurities: Common Laboratory Solvents, Organics, and Gases in Deuterated Solvents Relevant to the Organometallic Chemist. *Organometallics* **2010**, *29*, 2176–2179, doi:10.1021/om100106e.

70. Cai, H.; Guengerich, F.P. Mechanism of Aqueous Decomposition of Trichloroethylene Oxide. *J Am Chem Soc* **1999**, *121*, 11656–11663, doi:10.1021/ja9914240.

71. Narita, K.; Matsuhara, K.; Itoh, J.; Akiyama, Y.; Dan, S.; Yamori, T.; Ito, A.; Yoshida, M.; Katoh, T. Synthesis and Biological Evaluation of Novel FK228 Analogues as Potential Isoform Selective HDAC Inhibitors. *Eur J Med Chem* **2016**, *121*, 592–609, doi:10.1016/J.EJMECH.2016.05.031.

72. Eissler, S.; Kley, M.; Bächle, D.; Loidl, G.; Meier, T.; Samson, D. Substitution Determination of Fmoc-Substituted Resins at Different Wavelengths. *J Pept Sci* **2017**, *23*, 757–762, doi:10.1002/PSC.3021.

73. Neises, B.; Steglich, W. Simple Method for the Esterification of Carboxylic Acids. *Angew Chem Int Ed Engl* **1978**, *17*, 522–524, doi:10.1002/ANIE.197805221.
74. Li, X.; Atkinson, R.N.; Bruce King, S. Preparation and Evaluation of New L-Canavanine Derivatives as Nitric Oxide Synthase Inhibitors. *Tetrahedron* **2001**, *57*, 6557–6565, doi:10.1016/S0040-4020(01)00547-6.
75. Zhang, C.; Wu, S.; Xi, Z.; Yi, L. Design and Synthesis of NBD-S-Dye Dyads for Fluorescently Discriminative Detection of Biothiols and Cys/Hcy. *Tetrahedron* **2017**, *73*, 6651–6656, doi:10.1016/j.tet.2017.10.020.
76. Vachal, P.; Fletcher, J.M.; Fong, T.M.; Huang, C.C.R.R.; Lao, J.; Xiao, J.C.; Shen, C.P.; Strack, A.M.; Shearman, L.; Stribling, S.; et al. 1-Sulfonyl-4-Acylpiperazines as Selective Cannabinoid-1 Receptor (CB1R) Inverse Agonists for the Treatment of Obesity. *J Med Chem* **2009**, *52*, 2550–2558, doi:10.1021/jm900063x.
77. Sousbie, M.; Vivancos, M.; Brouillette, R.L.; Besserer-Offroy, É.; Longpré, J.M.; Leduc, R.; Sarret, P.; Marsault, É. Structural Optimization and Characterization of Potent Analgesic Macrocyclic Analogues of Neurotensin (8-13). *J Med Chem* **2018**, *61*, 7103–7115, doi:10.1021/acs.jmedchem.8b00175.

2.17. Disclaimer/Publisher's Note

The statements, opinions and data contained in all publications are solely those of the individual author(s) and contributor(s) and not of MDPI and/or the editor(s). MDPI and/or the editor(s) disclaim responsibility for any injury to people or property resulting from any ideas, methods, instructions or products referred to in the content.

Appendix to Chapter 2

Supplementary Material for:

Peptidic Inhibitors and Fluorescent Probe for the Selective Inhibition and Labelling of Factor XIIIa Transglutaminase

Eric W. J. Gates[†,1], Kian Mansour[†,1], Sahar Ebrahimi Samani[2], Sammir Shad[1], Mari T. Kaartinen[2,3], and Jeffrey W. Keillor[1,]*

[1]Department of Chemistry and Biomolecular Sciences, University of Ottawa, Ottawa, Ontario K1N 6N5, Canada

[2]Faculty of Medicine (Division of Experimental Medicine), McGill University, Montréal, Québec, H3A 0C7, Canada

[3]Faculty of Dental Medicine and Oral Health Sciences, McGill University, Montréal, Québec, H3A 0C7, Canada

*****Correspondence: JWK

[†]These authors contributed equally to this work.

Synthesis of Intermediates and Final Inhibitors

For the synthesis of the acrylamide-bearing inhibitors **11**-**14**, a direct approach involving semi-automated Fmoc-based solid-phase peptide synthesis (SPPS) was envisioned as shown in Scheme S3. Loading 2-chlorotrityl chloride (CTC) resin with Fmoc-Proline to form **10** could be followed by cycles of amide couplings and Fmoc-deprotections to assemble the desired linear octapeptides. The final inhibitors **11**-**14** would then be isolable after N-terminal acetylation, cleavage off resin, and global deprotection of the sidechain protecting groups. In order to carry out this synthesis, unnatural amino acid (AA) monomers bearing acrylamide functionalities on their sidechain amines with different linker lengths were required, and were synthesized accordingly. For ease of introduction into SPPS, the acrylamide-bearing monomers were assembled in the form of Fmoc-AA(Acrylamide)-OH compounds **5**-**8** as shown in Scheme S1. Commercially available Boc-AA-OH compounds were first treated with acryloyl chloride to form Boc-AA(Acrylamide)-OH compounds **1**-**4**. Deprotection of the Boc group with TFA followed by reprotection with Fmoc-chloride prepared the desired monomers **5**-**8** for convenient incorporation into the peptidic inhibitors. The final unnatural amino acid required for SPPS of the acrylamide-bearing inhibitors, namely Fmoc-D-Asp(OtBu)-OH **9**, was prepared from commercially-available H-D-Asp(OtBu)-OH using Fmoc-chloride as shown in Scheme S2. The acrylamide-bearing monomers **5**-**8**, along with the D-Asp derivative **9**, were then carried into the SPPS outlined in Scheme S3, allowing for the production of the desired acrylamide-bearing peptidic inhibitors **11**-**14** in sufficient quantities for characterization and subsequent kinetic evaluation with FXIIIa.

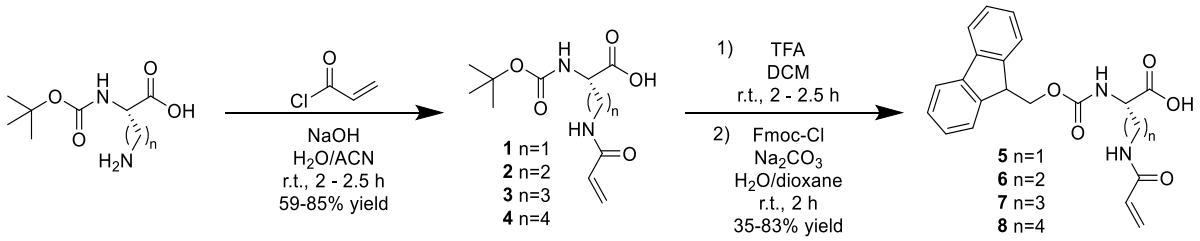

Scheme S1. *Synthesis of Fmoc-AA(Acrylamide)-OH monomers* ***5-8*** *required for the production of acrylamide-bearing peptidic inhibitors.*

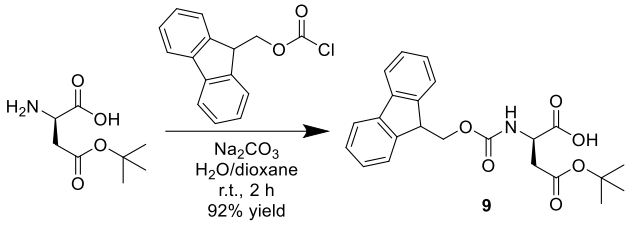

Scheme S2. *Synthesis of Fmoc-*D*-Asp(OtBu)-OH* ***9*** *required for the production of acrylamide- and α-chloroacetamide-bearing peptidic inhibitors.*

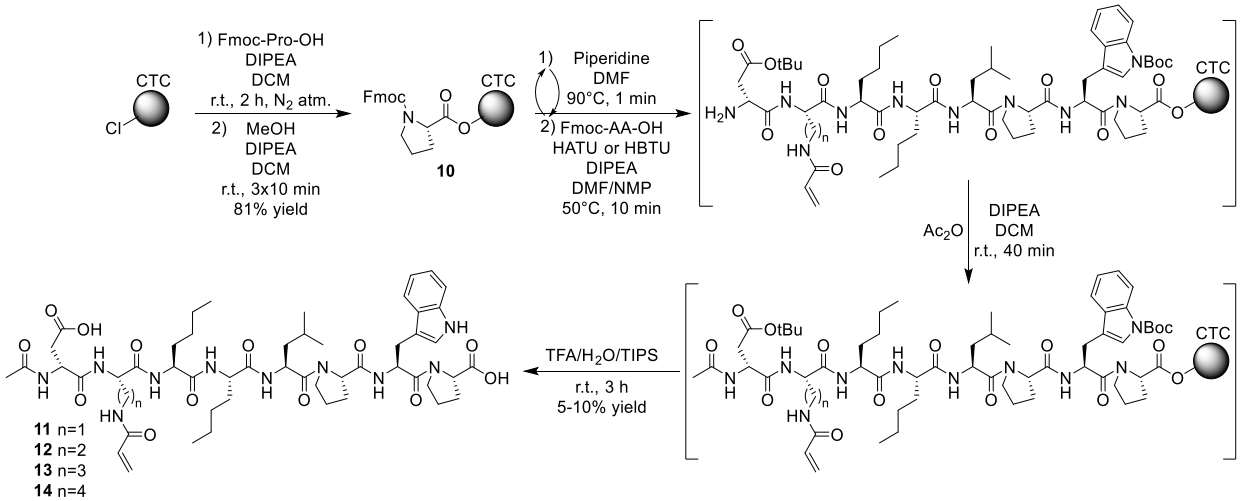

Scheme S3. *Synthesis of acrylamide-bearing peptidic inhibitors* ***11-14****.*

Next, the synthesis of the α-chloroacetamide-bearing inhibitors **20**-**23** was addressed. Due to its high electrophilicity, the α-chloroacetamide functionality was anticipated to be unstable in the presence of high concentrations of piperidine, used in standard SPPS Fmoc deprotections. To avoid this potential issue and prevent exposing the α-chloroacetamide to any piperidine, the warhead would have to be installed onto the peptide after the linear chain had been assembled fully. Rather than introducing the warhead-bearing amino acid as the unnatural monomer already bearing the electrophile, as was performed with the synthesis of the acrylamides in Scheme S1, this residue could be added to the chain while carrying a sidechain amine masked with a protecting group which could later be removed and replaced with the desired α-chloroacetamide moiety. The Alloc protecting group was selected for this purpose due to its orthogonality to the Fmoc, Boc, and *tert*-butyl ester removal conditions. To prepare the required amino acid monomers of the form Fmoc-AA(Alloc)-OH with varying linker lengths, compounds **17**-**19**, standard protecting group manipulations were performed from commercially available starting materials, as shown in Scheme S4. The required amino acid with the longest linker length, namely Fmoc-Lys(Alloc)-OH, was commercially-available. The Alloc-bearing monomers and the D-Asp derivative **9** were carried into the SPPS as described in Scheme S5. Linear chain completion followed by N-terminal acetylation, palladium-catalyzed Alloc-deprotection, warhead attachment with chloroacetic anhydride, and cleavage and global deprotection furnished the α-chloroacetamide-bearing inhibitors **20**-**23** in adequate yield and purity.

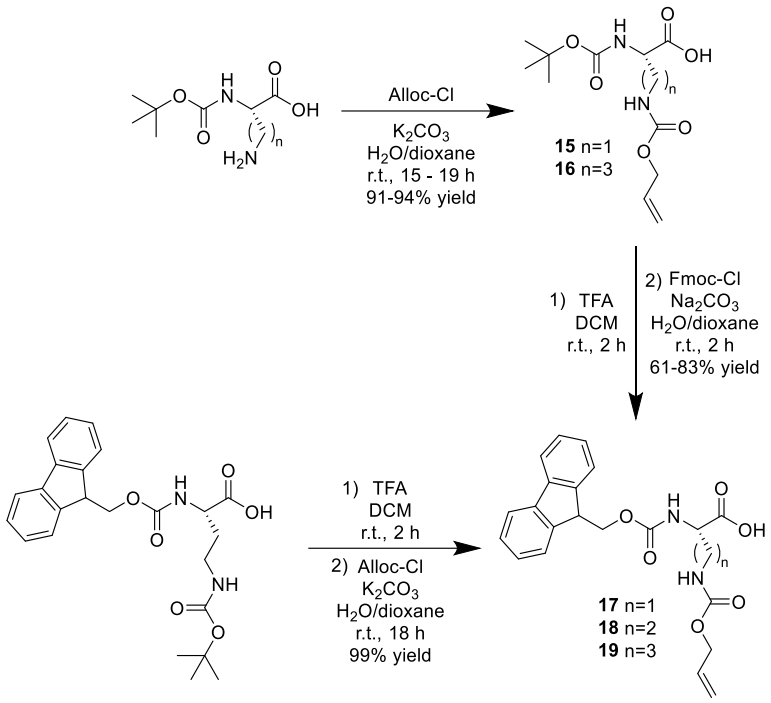

Scheme S4. *Synthesis of Fmoc-AA(Alloc)-OH monomers* ***17-19*** *required for the production of α-chloroacetamide-bearing peptidic inhibitors.*

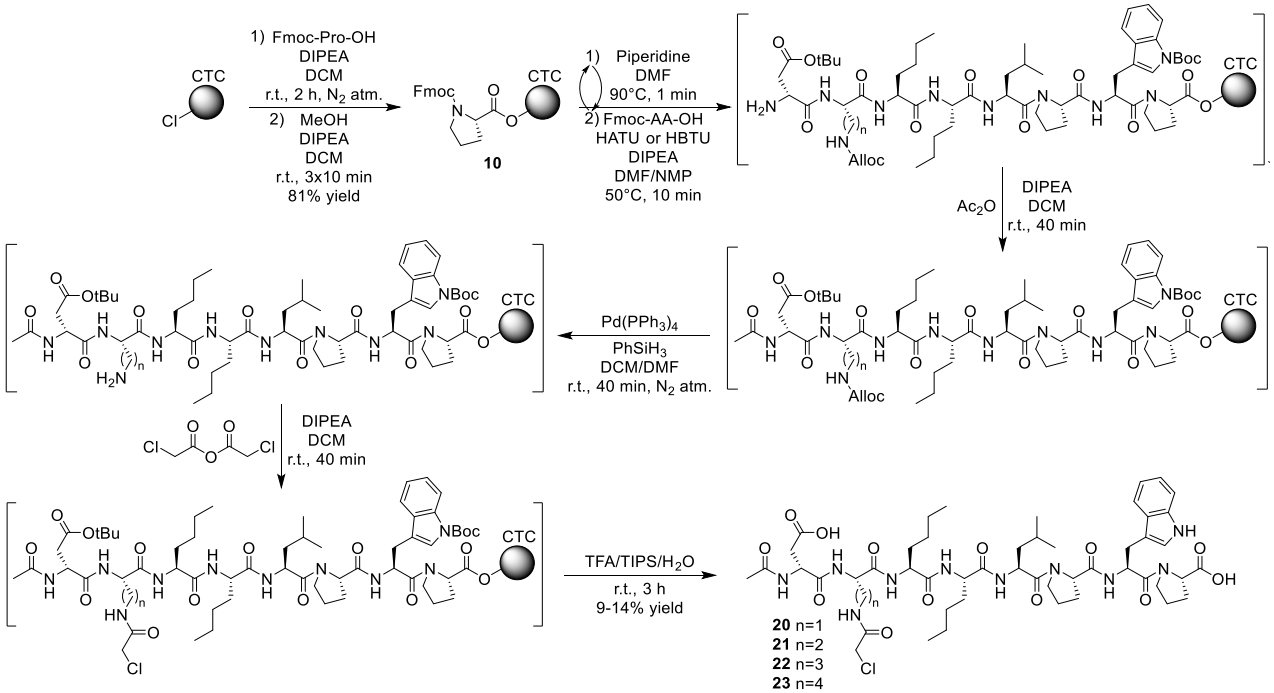

Scheme S5. *Synthesis of α-chloroacetamide-bearing peptidic inhibitors* ***20-23.***

The peptidic inhibitors **45-47**, bearing the unsaturated ester warhead, were synthesized through a route similar to that reported by Zedira in the original ZED1301 synthesis [51,53]. The required amino acids of the form Boc-AA(MA)-OH **28**, **33**, and **37** were prepared as shown in Schemes S6 & S7. For the two-methylene-linker Boc-Glu(MA)-OH **28**, leading to ZED1301, a commercially-available glutamate derivative was first methylated on its sidechain to produce **24** (Scheme S6), and was subsequently di-Boc protected at the α-amine to yield **25**. This di-Boc protection masks the acidic proton which is believed to interfere with the subsequent DIBAL-mediated reduction to aldehyde **26** [65–67], which was subjected to a Wittig reaction to produce the desired unsaturated ester warhead in **27**. Protecting group manipulation then led to the formation of mono-Boc derivative **28**. For longer and shorter linker derivatives of **28**, outlined in Scheme S7, an aspartate derivative was chosen as the starting point. A Steglich esterification of the C-terminus produced compound **29**, which was in perfect shape to proceed through the analogous sequence of protection, DIBAL reduction, Wittig installation of the unsaturated ester, and protecting group manipulation, as described previously, to produce the desired Boc-Asp(MA)-OH compound **33**. To obtain the amino acid with one methylene longer than the glutamate derivative, namely the homoglutamate (Hmg) position unsaturation, the aspartate-derived compound **32** was carried forward, as this already possesses the necessary protecting groups and a carbonyl placed at the ε carbon. Hydrogenation of the unsaturation led to **34**, which after the same sequence of transformations cleanly produced the Boc-Hmg(MA)-OH compound **37**. The final amino acid required for these peptides, Ac-D-Asp(OtBu)-OH **38**, was produced from H-D-Asp(OtBu)-OH through a reported protocol, as shown in Scheme S8 [68]. With all the required amino acids in hand, the peptide synthesis was carried out as shown in Scheme S9, again in a manner similar to that reported for the ZED1301 synthesis by Zedira [51]. Linear chain extension

was terminated after the attachment of the warhead-bearing residue. Deprotection of the N-terminal Boc group with TFA resulted in simultaneous deprotection of the Trp residue's Boc group and cleavage from the resin. The resultant peptides **39**-**41** were subsequently coupled in solution with the final residue **38**, furnishing penultimate intermediates **42**-**44**, which could easily be turned into the desired inhibitors **45**-**47** through *t*-butyl ester deprotection in acid. This synthetic route, developed by Zedira, avoids exposing the electrophilic unsaturated ester moiety to any nucleophilic piperidine.

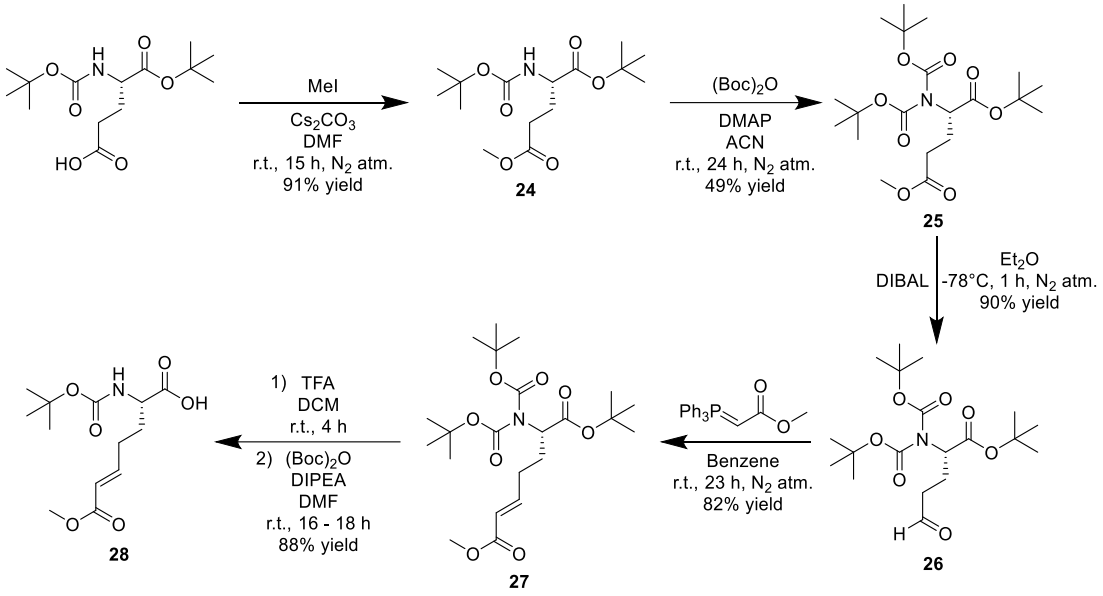

Scheme S6. *Synthesis of Boc-Glu(MA)-OH* ***28*** *required for the production of ZED1301* [53].

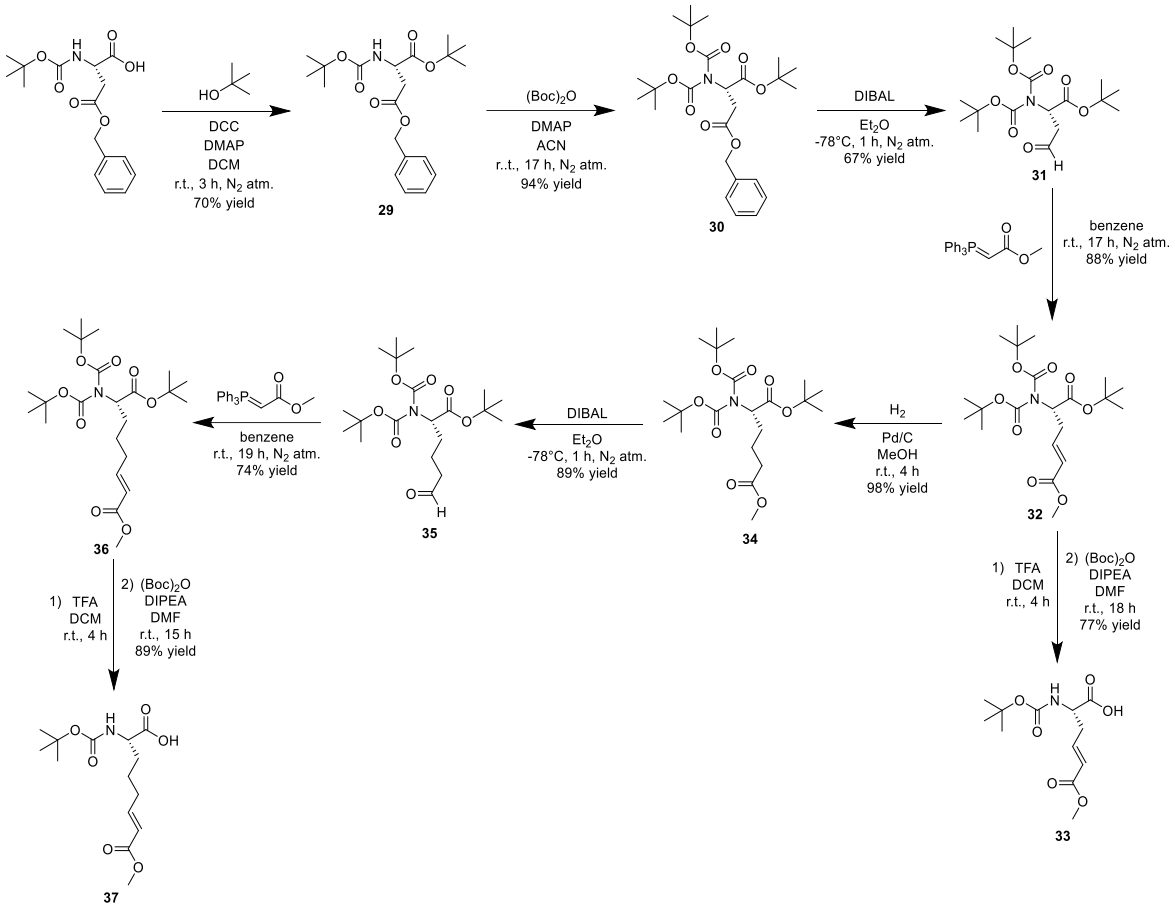

Scheme S7. *Synthesis of Boc-AA(MA)-OH monomers **33** and **37** required for the production of α,β-unsaturated ester-bearing peptidic inhibitors.*

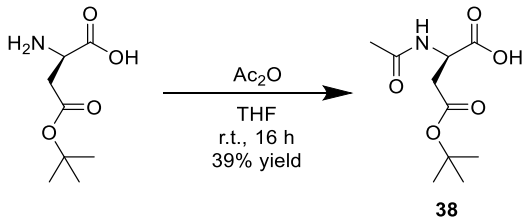

Scheme S8. *Synthesis of Ac-D-Asp(OtBu)-OH **38** required for the production of α,β-unsaturated ester-bearing peptidic inhibitors* [68].

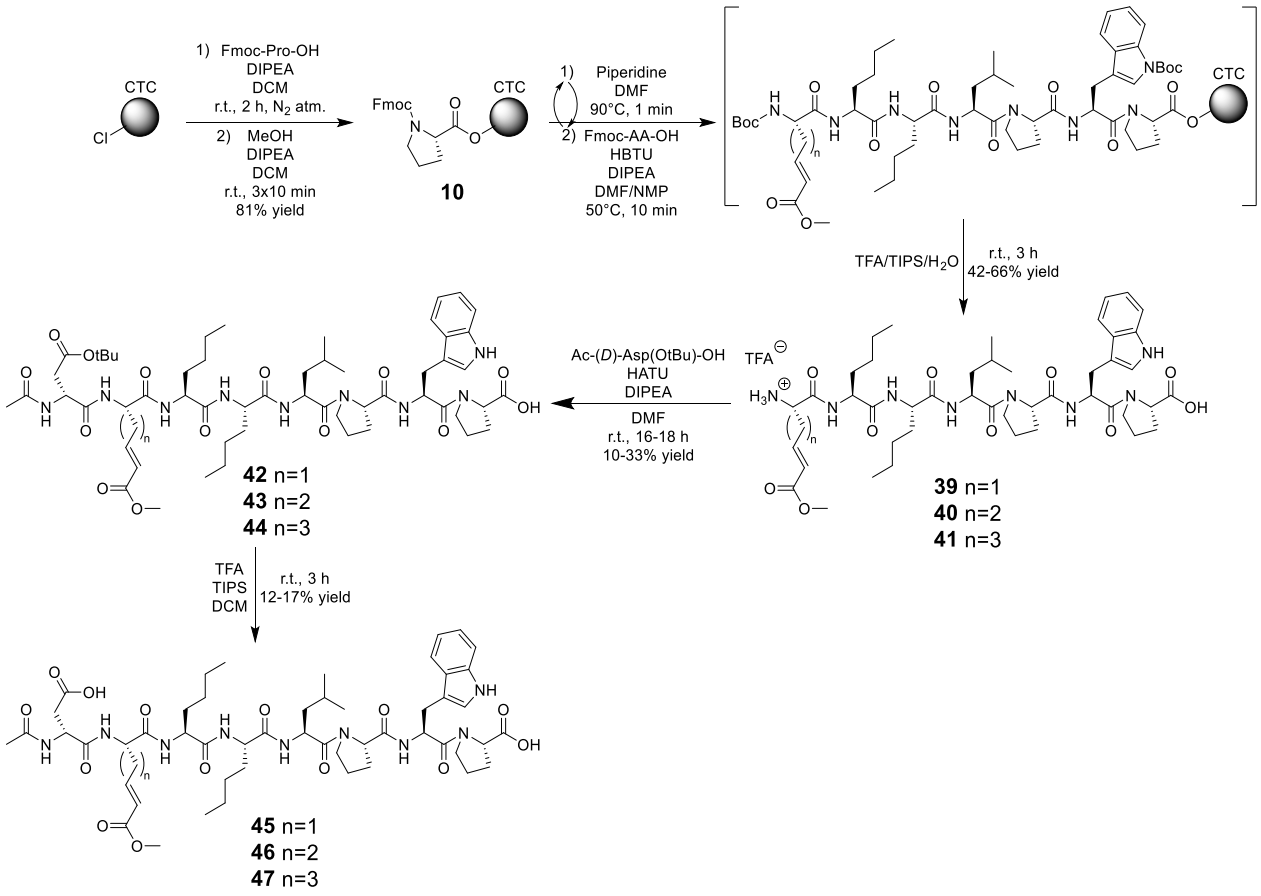

Scheme S9. *Synthesis of α,β-unsaturated ester-bearing peptidic inhibitors* ***45-47*** [51].

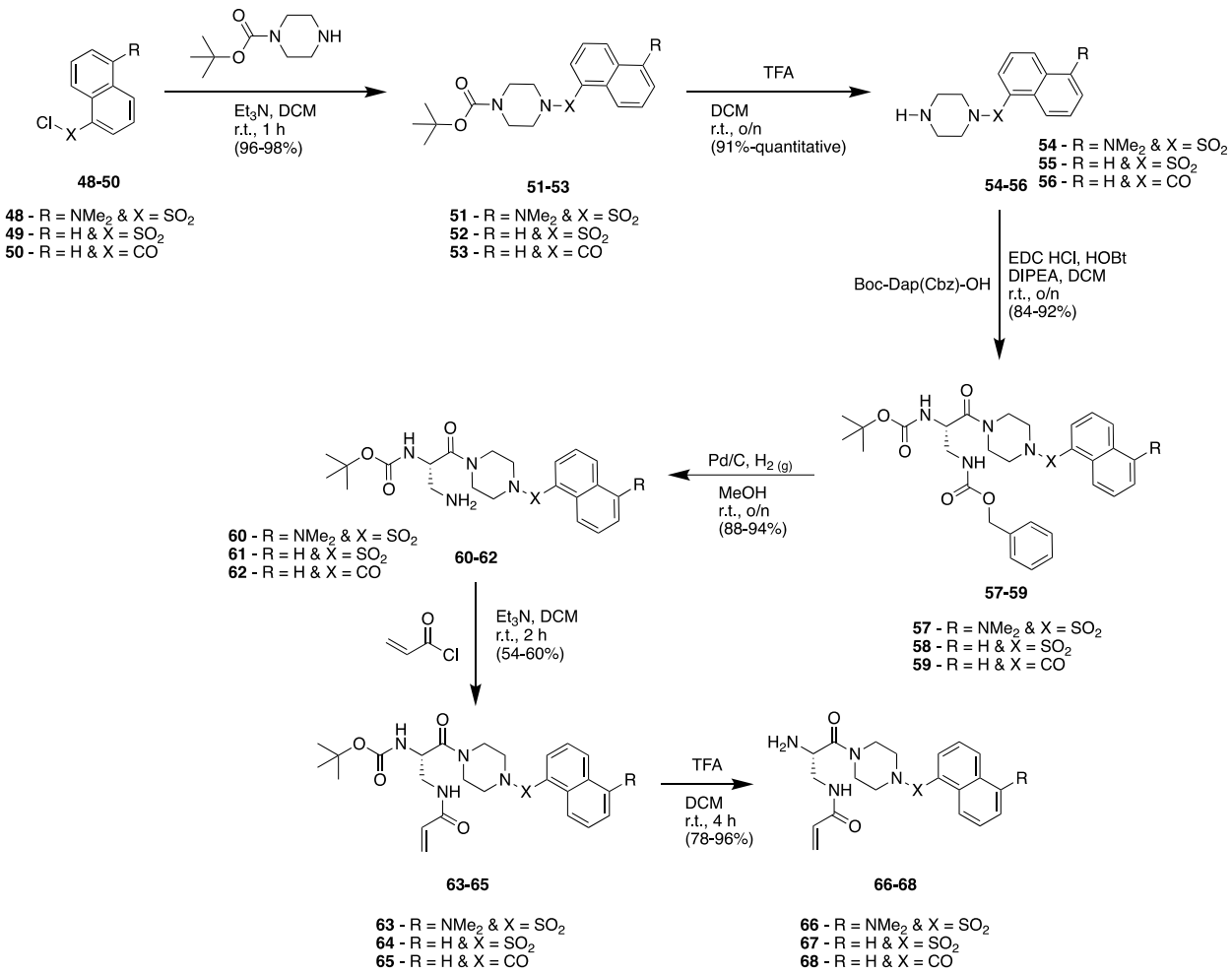

Scheme S10. *General synthetic scheme to arrive at* L*-Dap key intermediate for small molecule inhibitors* ***66-68****.*

The small molecule inhibitors of FXIIIa were synthesized by first generating a key intermediate which would allow for functionalization at the N-terminus with various carboxylic acids (Scheme S10). Starting from commercially available acyl chloride or sulfonyl chlorides **48-50**, an acylation was performed with N-Boc-Piperazine. The Boc group was then cleaved under acidic conditions with TFA to generate the free amines **54-56**. An amide coupling was then performed with EDC, HOBt, and the corresponding Boc-L-Dap(Z)-OH to gain access to the fully

protected **57-59**. Hydrogenolysis with catalytic palladium on carbon liberated the β-amine **60-62**. An acrylation with acryloyl chloride successfully installed the acrylamide warhead to generate the protected key intermediates **63-65**. A final Boc deprotection with TFA yielded the key intermediates **66-68** to allow for functionalization at the N-terminus.

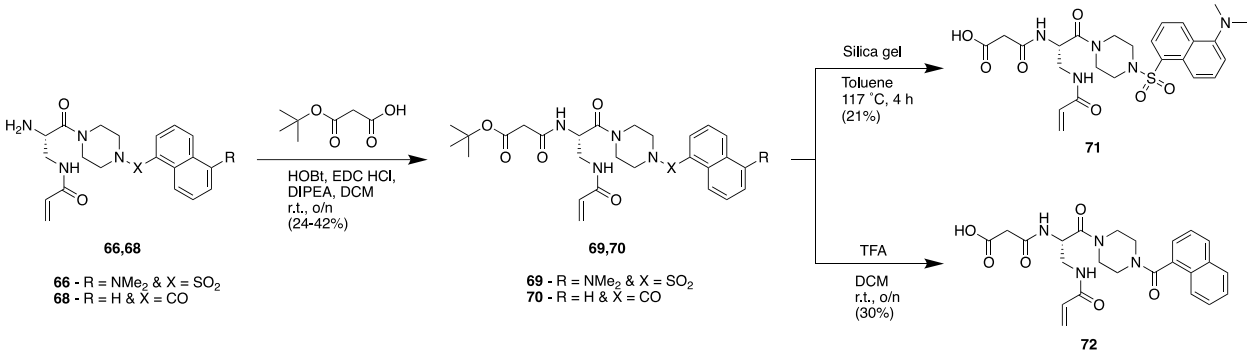

Scheme S11. *Synthetic scheme to arrive at malonyl inhibitors **71** and **72**.*

Malonyl inhibitors **71** and **72** were synthesized by an amide bond coupling with mono-*t*-butyl malonate and subsequent acidic cleavage of the *t*-butyl ester to yield the final inhibitors (Scheme S11).

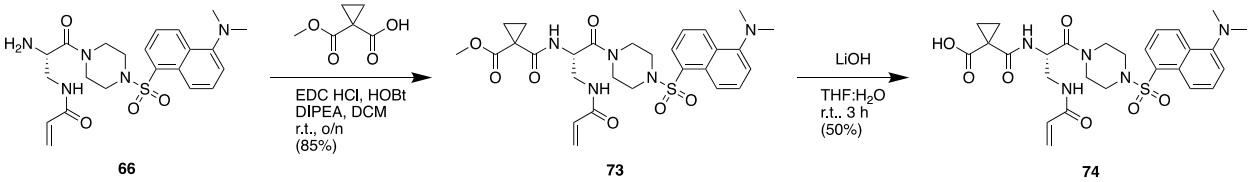

Scheme S12. *Synthetic scheme to arrive at cyclopropyl inhibitor **74** through the methyl ester **73**.*

To generate the cyclopropyl inhibitor **74**, a coupling with the mono-methyl ester protected diacid was accomplished with EDC and HOBt. The ester was then hydrolyzed in aqueous conditions with lithium hydroxide to produce the inhibitor **74** (Scheme S12).

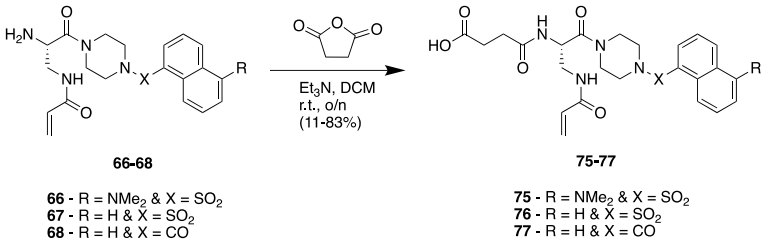

Scheme S13. *Synthetic scheme to generate succinyl inhibitors **75-77**.*

The three succinyl inhibitors were synthesized by a simple anhydride opening with succinic anhydride. Under basic conditions the key intermediates were exposed to succinic anhydride and yielded inhibitors **75-77** (Scheme S13).

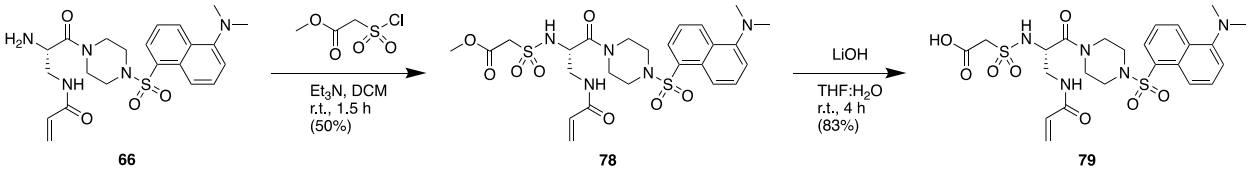

Scheme S14. *Synthetic scheme to synthesize sulfonyl inhibitor **79**.*

The dansyl sulfonamide inhibitor was generated from a sulfonamide coupling with the key intermediate **66** and chlorosulfonyl-acetic acid methyl ester. A methyl ester hydrolysis then deprotected the carboxylate to produce **79** (Scheme S14).

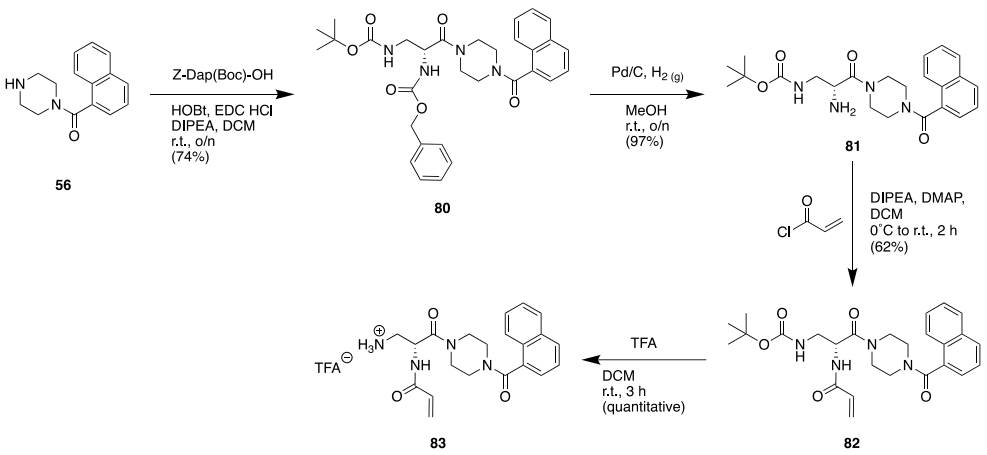

Scheme S15. *General synthetic scheme to arrive at* D*-Dap scaffold key intermediate* ***83****.*

To probe the effect of the decreased linker length to the warhead, a D-Dap scaffold was synthesized through generation of a key intermediate **83**, analogous to the L-Dap scaffold. Starting from the earlier synthesized piperazine-naphthoyl **56**, an amide coupling was performed with Z-D-Dap(Boc)-OH to produce the orthogonally protected **80**. Subsequent hydrogenolysis liberated the free warhead α-amine **81**. An acrylation with acryloyl chloride provided the acrylamide intermediate **82**. A final Boc deprotection with TFA yielded the D-Dap scaffold key intermediate **83** as a TFA salt (Scheme S15).

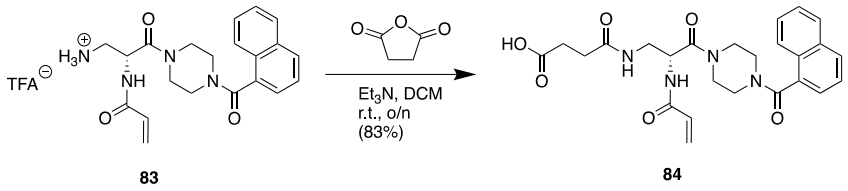

Scheme S16. *Synthetic scheme to generate* D*-Dap succinyl inhibitor* ***84****.*

The D-Dap succinyl inhibitor was synthesized from the TFA salt of key intermediate **83** and succinic anhydride under basic conditions. The carboxylic acid inhibitor **84** was obtained in 83% yield (Scheme S16).

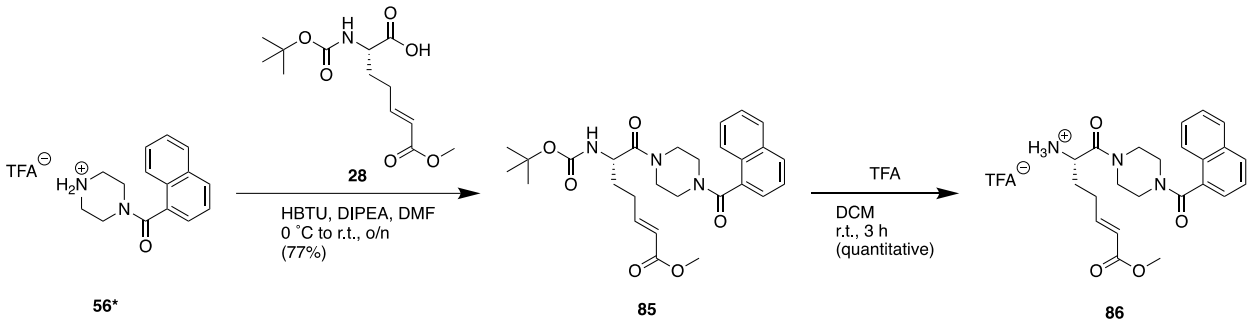

Scheme S17. *General synthetic scheme to generate α,β-unsaturated warhead key intermediate* ***86****.*

Using the α,β-unsaturated ester residue **28** an amide coupling tethered it to the TFA salt of piperazine-naphthoyl **56***. A Boc deprotection of the N-terminal amine formed the α,β-unsaturated warhead key intermediate **86** (Scheme S17).

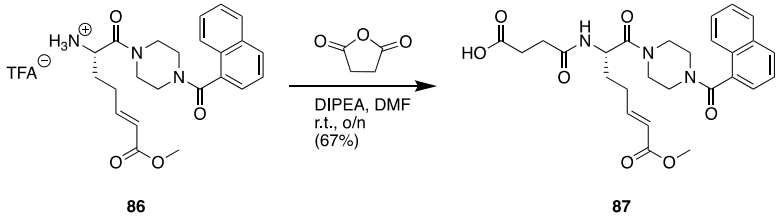

Scheme S18. *Synthetic scheme to produce α,β-unsaturated succinyl inhibitor* ***87****.*

The succinyl derivative of the α,β-unsaturated small molecule library was generated from succinic anhydride under basic conditions. The α,β-unsaturated succinyl inhibitor **87** was obtained in 67% yield (Scheme S18).

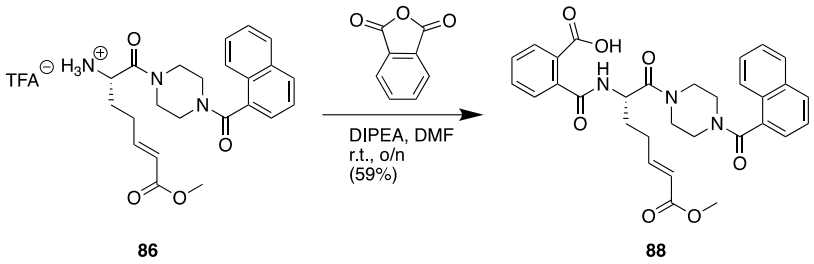

86 88

Scheme S19. *Synthetic scheme to produce α,β-unsaturated phthalyl inhibitor* ***88.***

The α,β-unsaturated phthalyl inhibitor featuring the naphthoyl hydrophobic unit was synthesized using the phthalic anhydride. Under basic conditions, the α,β-unsaturated key intermediate opened the anhydride to yield inhibitor **88** (Scheme S19).

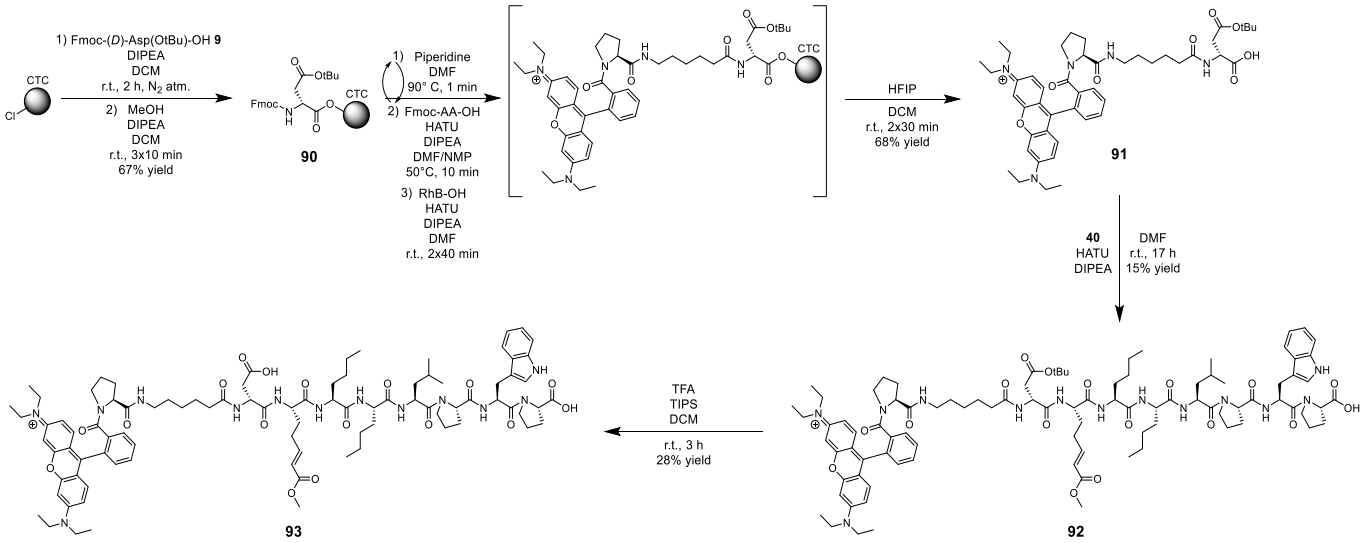

Scheme S20. *Synthesis of Rhodamine-B-ZED1301 fluorescent probe* ***93 (KM93).***

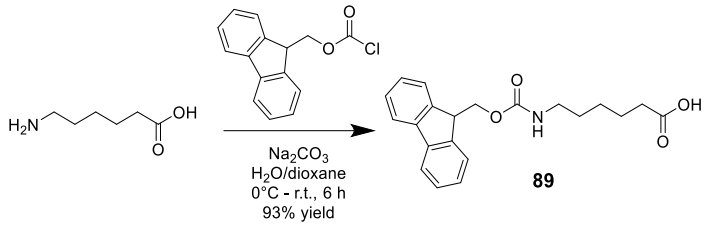

Scheme S21. *Synthesis of Fmoc-6AH-OH* ***89*** *required for the production of fluorescent probe* ***93*** *(**KM93**).*

The Rhodamine-B-tethered ZED1301-derived probe **93** (aka **KM93**) (Scheme S20) was synthesized in a manner similar to ZED1301. The key retrosynthetic bond disconnection made was between the warhead-bearing residue's α-amine and the adjacent D-Asp residue's carbonyl, a bond that is formed through the in-solution coupling in ZED1301 synthesis (Scheme S9). This disconnection leads to two fragments, the first of which is simply compound **40**, prepared previously (Scheme S9) as part of ZED1301. The other fragment is compound **91**, which was synthesized through solid-phase peptide synthesis as shown in Scheme S20. Fmoc-D-Asp(OtBu)-OH **9**, prepared previously in Scheme S2, was first loaded onto chlorotrityl resin, and was subsequently coupled to Fmoc-6-aminohexanoic acid (**89**, prepared in Scheme S21), followed by proline and lastly rhodamine B. Soft cleavage off resin with HFIP produced the peptide **92** in solution while retaining the *tert*-butyl ester protecting group on the aspartate sidechain which was necessary to retain selectivity in the subsequent in-solution coupling with **40** to produce **92**. This was then treated with TFA, yielding the fluorescent probe **93**.

Experimental Data for Intermediates and Final Inhibitors

General Comments

All reagents were obtained from chemical suppliers and used without further purification. All NMR spectra (^{1}H and ^{13}C) were recorded on Bruker 300, 400, or 600 MHz instruments, and chemical shifts are reported in ppm after referencing to the appropriate deuterated solvent peak [69]. High-resolution mass spectra (HRMS) were recorded at the John L. Holmes Mass Spectrometry Facility (University of Ottawa) on a quadrupole time-of-flight (QTOF) analyzer equipped with electrospray ionization (ESI). Automated peptide syntheses were performed on a Liberty Blue™ Automated Microwave Peptide Synthesizer. All solvents, reagents, and starting materials which do not have their synthesis described herein were purchased from commercial suppliers and used without further purification or characterization. Crude peptides were characterized by liquid chromatography mass spectrometry (LC-MS: Shimadzu LC-MS-2020 system; Agilent Eclipse XOB-C18 5.0-µm, 4.6 × 150-mm column or Bischoff Chromatography ProntoSIL 5.0-µm, 4.0 × 125-mm column; ACN/H_2O with 0.05% v/v formic acid, 5-95% gradient, 15 min runs, 1 mL/min; UV detection at 220 and 254 nm; ESI in positive mode, quadrupole mass analysis) for confirmation of their identities. Peptides were purified through semi-preparative high-performance liquid chromatography (HPLC: Gilson HPLC system; Kinetex XB-C18 5.0-µm, 100 Å, 10 × 150-mm column; ACN/H_2O with 0.1% v/v TFA, 10-95% gradient, 45 min runs, 3 mL/min; UV detection at 220 and 254 nm). All final peptidic inhibitors were judged to be at least 95% pure through analytical HPLC (Gilson HPLC system, Kinetex XB-C18 5.0-µm, 100-Å, 4.6 × 150-mm column; ACN/H_2O with 0.1% v/v TFA, 5-95% gradient, 20 min runs, 1 mL/min; UV detection at 220 and 254 nm). Small molecule inhibitors were purified via flash chromatography using either 230-400 mesh silica gel and organic solvent or SiliCycle C_{18} 40-63 µm silica and water/methanol

eluent. Thin layer chromatography (TLC) was performed using SiliCycle aluminum backed TLC plates of 200 µm thickness and F-254 indicator.

General Procedure A: Acryloyl Attachment to Amino Acid Sidechain Amines

This protocol was adapted from that reported by Cai & Guengerich in 1999 [70]. A 1:1 mixture of acetonitrile and 1 M $NaOH_{(aq)}$ was prepared and stirred at room temperature. The appropriate commercially available Boc-AA-OH compound (1.0 eq, [Boc-AA-OH] = 0.2 M) was then added in 1 portion, followed by the dropwise addition of acryloyl chloride (1.2 eq). The reaction was allowed to stir continuously at room temperature until completion by TLC analysis (2 - 2.5 h) before rotary evaporation to remove acetonitrile. The remaining solution was then acidified to pH 1-2 through the addition of 1 M $HCl_{(aq)}$, and was subsequently extracted thrice into EtOAc. The combined organics were dried over $MgSO_4$, filtered, and concentrated by rotary evaporation. Flash column chromatography using 1.5% MeOH, 0.1% AcOH, 98.5% EtOAc as the eluent produced pure products. Residual acetic acid was removed through azeotropic rotary evaporation with toluene and concentration *in vacuo*.

General Procedure B: Deprotection of Boc Group from Sidechain or α-Amines of Amino Acids

The Boc-protected amino acid (1 eq) was dissolved in an appropriate volume of DCM to achieve a concentration of 0.1 M. TFA was then added to reach 20% acid by volume. The resulting mixture was stirred at room temperature until the Boc deprotection reaction was deemed complete by TLC (2 - 2.5 h). DCM was removed by rotary evaporation, and excess TFA was removed through 3 successive co-evaporation with more DCM. The resulting yellow-orange oils or beige solids

containing the TFA salts of the deprotected amino acids were carried forward without further characterization or purification.

General Procedure C: Fmoc-Protection of α-Amines of Amino Acids

This protocol was adapted from that reported by Narita *et al*. in 2016 [71]. The desired amino acid (1 eq), with a free α-amine to be Fmoc-protected, was dissolved in distilled water to produce a concentration of 0.25 M. For cases in which the starting material was carried forward directly from a Boc deprotection in *General Procedure B*, the excess TFA in the acidic aqueous solutions was first neutralized to pH 7 through dropwise addition of concentrated $NaOH_{(aq)}$ at room temperature with vigorous stirring. Next, $Na_2CO_{3(s)}$ (3.8 eq, or 10% w/v) was added to adjust the pH of the solution to roughly 9. Separately, fluorenylmethyloxycarbonyl chloride (1 eq) was dissolved in dioxane (0.25 M), and this was added to the reaction mixture dropwise while stirring at room temperature. After reaction completion (2 - 2.5 h), the crude product was concentrated through rotary evaporation and diluted into distilled water. This was then washed twice with ether before acidification to pH 1-2 by adding 1 M $HCl_{(aq)}$. The acidified aqueous phase was extracted thrice into ethyl acetate, and the combined organics were then washed twice with water, twice with brine, dried over $MgSO_4$, filtered, and concentrated in vacuo to yield pure products.

General Procedure D: Loading of 2-Chlorotrityl Chloride Resin with Fmoc-Protected Amino Acid

Fresh 2-chlorotrityl chloride resin (1 eq) was placed in an oven-dried hand-shaker reaction vessel equipped with a magnetic stir bar. The system was sealed with a septum and a nitrogen atmosphere was prepared with a balloon. Dry DCM (10 mL) was then added, and the resin was stirred to swell it at room temperature for 30 min. After draining the swelling solution, the loading mixture (1.2

eq Fmoc-AA-OH, 4.8 eq DIPEA, 10 mL dry DCM) was added and the reaction was stirred at room temperature under nitrogen for 2 h. After completion, the resin was washed thrice with 5 mL of DCM. The capping solution (30 mL of 17:2:1 DCM/MeOH/DIPEA) was added to the loaded resin in 3 portions of 10 mL, and the resin was stirred at room temperature for 10 min with each portion prior to draining. After capping, the resin was washed thrice with 5 mL DCM, thrice with 5 mL DMF, and thrice more with 5 mL DCM. The resulting capped and loaded resin was air-dried. To test the loading, 1-2 mg of resin was suspended in 3.0 mL of deprotection solution (20% v/v piperidine in DMF). After 1 h of vigorous shaking, 1.0 mL of the solution was diluted to a final volume of 3.0 mL with more deprotection solution and placed in a 1-cm quartz cuvette. Absorbance at 301 nm for this 1/3 dilution was then measured and corrected with a blank. The molar extinction coefficient of 8021 M^{-1} cm^{-1} for the Fmoc-piperidine adduct was used to estimate resin loading [72], while overall loading yields were determined based on the final mass of loaded resin recovered.

General Procedure E: Solid-Phase Peptide Synthesis of Acrylamide-Bearing Inhibitors

Manually-loaded Fmoc-Pro-CTC resin **10** (1 eq) was placed into the automated peptide synthesizer and swelled in 10 mL DMF for 5 min. Deprotections were performed using 3 mL of 20% v/v piperidine in DMF at 90 °C for 1 min. Couplings were done at 50 °C over 10 min with 5 eq of the appropriate Fmoc-AA-OH, 5 eq of HATU or HBTU, and 10 eq of DIPEA in 4.0 mL of a 7:1 DMF/NMP solution. The acrylamide warhead-bearing residues were introduced as the corresponding Fmoc-AA(acrylamide)-OH compounds. After linear chain completion, the resin was removed from the synthesizer and the peptides were manually acetylated at the N-terminus using 5 eq Ac_2O and 10 eq DIPEA in 5 mL DCM for 40 min at room temperature. The resin was

washed 3-9 times with DMF and/or DCM between each step. Cleavage was done with 5 mL of the standard 95:2.5:2.5 TFA/H_2O/TIPS cocktail while stirring at room temperature for 3 h. Elution with DCM, removal of excess liquids through rotary evaporation, precipitation in cold ether, centrifugation, and discarding of the supernatant produced the crude peptides. Peptides were purified through semi-preparative HPLC and were obtained as solids after lyophilization. Purity was assessed through analytical HPLC, while identity was confirmed by HRMS.

General Procedure F: Alloc-Protection of Sidechain Amines of Amino Acids

The appropriate amino acid (1 eq) bearing a free sidechain amine was first dissolved in distilled water to produce a concentration of 0.4 M, then 2.5 eq of $K_2CO_{3(s)}$ was added. For cases in which the starting material was carried forward directly from a Boc deprotection in *General Procedure B*, the excess TFA in the acidic aqueous solutions was neutralized to pH 7 prior to the addition of the carbonate base through dropwise addition of concentrated $NaOH_{(aq)}$ at room temperature with vigorous stirring. Allyl chloroformate (1.2 eq), dissolved in a volume of dioxane equivalent to that of the distilled water, was then added to the reaction dropwise. The reaction was stirred at room temperature overnight. Upon completion, the crude mixture was concentrated by rotary evaporation, then diluted into an appropriate amount of distilled water. This solution was first washed twice with ether, then acidified to pH 1-2 through the addition of 1 M $HCl_{(aq)}$. The acidified aqueous phase was subsequently extracted thrice into ethyl acetate. The combined organics were washed twice with brine, dried over $MgSO_4$, filtered, and concentrated *in vacuo* to produce pure products.

General Procedure G: Solid-Phase Peptide Synthesis of α-Chloroacetamide-Bearing Inhibitors

These syntheses were commenced in a manner identical to that described in *General Procedure E* up until the completion of acetylation. The warhead-bearing amino acid was introduced as Fmoc-AA(Alloc)-OH. For Alloc deprotection, the resin was first suspended in 5 mL DCM and 5 mL DMF, then 15 eq of $PhSiH_3$ was added. The resulting solution was sparged with a nitrogen balloon and septum to prepare an inert atmosphere before the addition of 0.3 eq of $Pd(PPh_3)_4$. The reaction was stirred under nitrogen at room temperature for 40 min. After completion, the resin was washed thrice with 10 mL of 0.02 M sodium diethyldithiocarbamate in DMF while stirring for 5-10 min during each wash. To add on the warhead, 5 mL DCM, 10 eq DIPEA, and 5 eq chloroacetic anhydride were added and the reaction was stirred at room temperature for 40 min. Washes with DCM and DMF were performed between each step. Peptides were then cleaved, precipitated, purified, and characterized as in reported in *General Procedure E*.

General Procedure H: Di-Boc Protection of α-Amines of Amino Acids

Di-Boc protections were performed using a protocol adapted from that reported by Buchold *et al.* in 2016 [53]. The amino acid bearing a singular Boc group on its α-amine (1 eq) was first dissolved in ACN (1.3 M). DMAP (0.2 eq) was added in one portion, and an inert nitrogen atmosphere was prepared using a balloon and septum. Separately, $(Boc)_2O$ (2 eq) was dissolved in ACN (0.8 M), and this solution was then added to the reaction mixture over 5 mins. After allowing the reaction to stir overnight at room temperature under nitrogen, the crude was concentrated through rotary evaporation and purified by flash column chromatography (10% EtOAc in Pet. Ether). Pure products were obtained after concentration in vacuo.

General Procedure I: Reduction of Sidechain Esters to Aldehydes

This protocol was adapted from that reported by Buchold *et al*. in 2016 [53]. The appropriate amino acid bearing a sidechain ester (1 eq) was transferred to a flame-dried or oven-dried round-bottom flask under inert nitrogen atmosphere, and was subsequently dissolved in dry Et_2O (0.16 M). The resulting solution was then cooled to -78 °C in an acetone-dry ice bath, and stirring was commenced. A 1 M solution of DIBAL in hexane (1.1 eq) was then added dropwise (0.1 to 0.2 mL/min) using a syringe pump while continuing to stir and cool at -78 °C under inert atmosphere. After the addition was complete, the reaction was stirred under N_2 for another 1 h, at which point the process was quenched through the dropwise addition of 0.5 to 3.0 mL of MeOH followed by 10 to 50 mL of a saturated aqueous solution of sodium potassium tartrate tetrahydrate. The mixture was allowed to gradually warm to room temperature while stirring under inert atmosphere for 1 to 2 h. The organic phase was then separated, washed 1-3 times with 15 mL of saturated aqueous sodium potassium tartrate tetrahydrate, dried over $MgSO_4$, filtered, and concentrated in-vacuo. Pure aldehydes were obtained at this point in the case of methyl ester reduction, so these products were carried forward without further purification. For the reduction of benzyl esters, the crude aldehydes were purified by flash column chromatography (12% EtOAc in Pet. Ether) to obtain pure products.

General Procedure J: Installation of α,β-Unsaturated Methyl Ester on Sidechain Aldehydes

This protocol was adapted from that reported by Buchold *et al*. in 2016 [53].The corresponding aldehyde (1 eq) was dissolved in benzene (1.6 M) under a nitrogen balloon atmosphere, and the solution was stirred at room temperature. Next, methyl (triphenylphosphoranylidene)acetate (1 eq) was added in 1 portion, along with the minimal amount of benzene needed to dissolve the reagent.

The reaction was stirred overnight at room temperature under N_2. Upon completion, excess solvent was removed through rotary evaporation, and the crude was purified by flash column chromatography (10% EtOAc in Pet. Ether) before concentration *in vacuo* to produce pure product.

General Procedure K: Di-Boc and Tert-Butyl Ester Deprotection Followed by Mono-Boc Reprotection

This protocol was adapted from that reported by Buchold *et al*. in 2016 [53]. The appropriate amino acid bearing a di-Boc-protected amine and *tert*-butyl ester (1 eq) was dissolved in a 1:1.75 DCM/TFA mixture (0.14 M) and stirred at room temperature for 4 h. Upon completion, the resulting mixture was concentrated through rotary evaporation. Excess TFA was removed through 3 successive co-evaporations with more DCM. The deprotected intermediate was used in the subsequent reaction without further purification or characterization. An excess of DIPEA, around 6 mL, was then added to the crude intermediate to neutralize excess TFA and produce a pH 9 environment. The resulting oil was dissolved in DMF (0.32 M) and another 2 eq of DIPEA was added. Next, 1.2 eq of $(Boc)_2O$ was added in one portion, and the reaction was stirred at room temperature overnight. Upon completion, solvents were removed through rotary evaporation. The crude residue was dissolved in a 5% aqueous $KHSO_4$ solution, and this was extracted thrice into equal volumes of EtOAc. The combined organics were washed twice with equal volumes of brine before drying over $MgSO_4$, filtration, and concentration in-vacuo. The crude product was then purified by flash column chromatography (65:35 toluene/EtOAc + 0.5% AcOH), producing the desired compounds in high purity.

General Procedure L: Solid-Phase Peptide Synthesis of α,β-Unsaturated Ester-Bearing Inhibitors

Manually-loaded Fmoc-Pro CTC resin **10** (1 eq) was placed into the automated peptide synthesizer and swelled in 20 mL DMF for 5 min. Deprotections were performed using 10 mL of 20% v/v piperidine in DMF at 90 °C for 1 min. Couplings were done at 50 °C over 10 min with 4 eq of the appropriate Fmoc-AA-OH, 4 eq of HBTU, and 8 eq of DIPEA in 16 mL of a 7:1 DMF/NMP solution. The warhead-bearing amino acid was introduced as Boc-AA(MA)-OH (2 eq). The resin was washed 3 times with 7-10 mL of DMF between each step. After linear chain completion, the resin was removed from the synthesizer and the peptide was manually cleaved by stirring for 3 h at room temperature in a 95:2.5:2.5 TFA/TIPS/H_2O solution. Elution with DCM, removal of excess liquids through rotary evaporation, precipitation in cold ether, centrifugation, and discarding of the supernatant produced the crude peptide. This was subsequently dissolved in DMF and concentrated further through rotary evaporation. The TFA salts of the desired peptides were obtained after extensive drying in vacuo, and their identities were confirmed through LC-MS analysis. Crude peptides were carried forward without further purification.

General Procedure M: In-Solution Coupling of N-Terminal Residue of α,β-Unsaturated Ester-Bearing Inhibitors

The TFA salts of the peptide fragments, assembled in *General Procedure L*, leading to the desired ester-bearing inhibitors, were coupled in-solution to the final N-terminal residue through a reported protocol [51]. The peptide of the form TFA.H-AA(MA)-Nle-Nle-Leu-Pro-Trp-Pro-OH (1 eq) was dissolved in DMF (0.12 M) and stirred at room temperature. Separately, the appropriate N-terminal fragment bearing a free acid, namely either Ac-D-Asp(OtBu)-OH **38** or RhB-Pro-6AH-D-Asp(OtBu)-OH **91** (1 eq), was dissolved in DMF (0.12 M) and stirred in an ice-water bath. HATU

(1.0 eq) and DIPEA (3.0 eq) were then added to the cooled amino acid solution, and this was stirred at 0 °C for 30 min. Next, the activated amino acid solution was added dropwise to the peptide solution, and the resulting mixture was set to pH 8 through the addition of more DIPEA. The reaction was left to stir overnight, and solvents were removed through rotary evaporation upon completion. Approximately one-third of the crude residue was then purified by semi-preparative HPLC, while the remaining two-thirds were stored for later use. After concentration in vacuo, peptide identity was confirmed through LC-MS, and products were carried forward without further characterization.

General Procedure N: In-Solution Final Deprotection of t-Bu Ester Group of α,β-Unsaturated Ester-Bearing Inhibitors

The final ester-bearing peptidic inhibitors were obtained following *t*-Bu ester deprotection of peptides produced in *General Procedure M* through a reported method [51]. Peptides of the form Ac-D-Asp(OtBu)-AA(MA)-Nle-Nle-Leu-Pro-Trp-Pro-OH or RhB-Pro-6AH-D-Asp(OtBu)-Glu(MA)-Nle-Nle-Leu-Pro-Trp-Pro-OH (1 eq) were dissolved in DCM (0.0064 M), then TIPS was added (7.3 eq). Next, TFA (volume half of DCM) was added, and the reaction was stirred at room temperature for 3 h. Upon completion, excess liquids were removed through rotary evaporation, and the product was purified by semi-preparative HPLC. Solid products were obtained after lyophilization. Purity was assessed through analytical HPLC, while identity was confirmed by HRMS.

General Procedure O: Acylation or Sulfonylation of N-Boc-Piperazine

To a round bottom flask was added N-Boc-Piperazine (1.1 eq) solubilized in a mixture of dichloromethane and triethylamine (1.1 eq). The corresponding acid chloride or sulfonyl chloride **48-50** (1 eq) was subsequently added portion wise, and the solution was stirred at room temperature overnight. Upon completion, the solution was washed three times with 1 M HCl, water, a saturated solution of sodium bicarbonate, and brine. In the synthesis of compound **1** the acid and water washes were excluded. The organic phase was dried with $MgSO_4$, filtered, and concentrated under reduced pressure. The crude oil was purified via flash chromatography to yield the product.

General Procedure P: Boc Deprotection of Small Molecule Intermediates

To a round bottom flask, the Boc-protected amine (1 eq) was dissolved in dichloromethane. Trifluoroacetic acid (10 % v/v) was added to the solution. The reaction mixture was stirred at room temperature overnight. Upon completion, a saturated solution of $NaHCO_3$ was added to the reaction flask and allowed to stir for half an hour. The solution was then washed with $NaHCO_3$ five more times and extracted with dichloromethane. The organic phase was dried with $MgSO_4$, filtered, and concentrated under reduced pressure. The resulting amine was carried forward without further purification.

General Procedure Q: Amide Coupling

To a round bottom flask was added the acid (1 eq), EDC HCl (1.2 eq), HOBt (1.2 eq), and DIPEA (3.0 eq) solubilized in dichloromethane and stirred for half an hour. The amine (1.2 eq) was then added, and the solution was stirred at room temperature overnight. Upon completion, the reaction mixture was washed three times with 1 M HCl, water, a saturated solution of $NaHCO_3$, and brine.

In the synthesis of compound **57** the acid and water washes were excluded. The organic phase was dried with $MgSO_4$, filtered, and concentrated under reduced pressure. The crude oil was purified via flash chromatography to yield the product.

General Procedure R: Hydrogenolysis of Small Molecule Intermediates

The Cbz-protected starting material (1 eq) was dissolved in dry methanol under nitrogen gas in a round bottom flask. Palladium on carbon (20 mol%) was added and the flask was evacuated under vacuum and backfilled three times with nitrogen gas. The flask was then evacuated under vacuum and backfilled three times with hydrogen gas and equipped with a balloon of hydrogen gas. The solution was stirred overnight at room temperature. Upon completion, the hydrogen gas was removed, the reaction mixture was filtered over celite, and concentrated under reduced pressure. The resulting product was carried forward without further purification.

General Procedure S: Acrylation of Small Molecule Intermediates

To a round bottom flask was added the free amine starting material (1 eq) solubilized in dichloromethane. To the flask was subsequently added triethylamine (2.4 eq) and acryloyl chloride (2.4 eq) dropwise. The reaction was stirred for 2 h. Upon completion the reaction mixture was washed three times with water and a saturated solution of $NaHCO_3$. The aqueous phase was re extracted with DCM and the organic layers were combined, dried with $MgSO_4$, filtered, and concentrated under reduced pressure. The resulting crude oil was purified via flash chromatography to yield the product.

General Procedure T: Methyl Ester Hydrolysis

To a round bottom flask was added the methyl ester starting material (1 eq) solubilized in a 1:1 mixture of THF:H_2O. To the flask was subsequently added LiOH H_2O (2 eq) and the reaction mixture was stirred for 4 h. Upon completion, the volatiles were removed under reduced pressure and the crude oil was purified via flash chromatography to yield the product.

General Procedure U: Anhydride Coupling

To a round bottom flask was added the starting free amine (1 eq) along with triethylamine (1 eq) solubilized in DCM. To the flask was subsequently added the corresponding anhydride (1.2 eq) and triethylamine (1.5 eq). The reaction mixture was then stirred overnight at room temperature. Upon completion, the reaction mixture was concentrated under reduced pressure and the resulting crude oil was purified via flash chromatography to yield the product.

*Boc-Dap(Acrylamide)-OH (**1**).* Compound **1** was prepared from commercially available Boc-Dap-OH (500 mg, 2.45 mmol) through *General Procedure A*, and was obtained as a clear, colourless oil (375 mg, 1.45 mmol, 59% yield). ^{1}H NMR (400 MHz, CD_3OD) δ 6.28 – 6.15 (m, 2H), 5.65 (dd, J = 7.9, 4.1 Hz, 1H), 4.32 (dd, J = 7.7, 4.6 Hz, 1H), 3.71 (dd, J = 13.8, 4.7 Hz, 1H), 3.59 (dd, J = 13.9, 7.6 Hz, 1H), 1.42 (s, 9H); ^{13}C NMR (101 MHz, CD_3OD) δ 173.66, 168.61, 157.68, 131.64, 127.16, 80.65, 54.97, 41.67, 28.65; HRMS (ESI-QTOF) *m/z* $[M + Na]^+$ calcd for $C_{11}H_{18}N_2O_5Na$ 281.1113; found 281.1102.

*Boc-Dab(Acrylamide)-OH (**2**).* Compound **2** was prepared from commercially available Boc-Dab-OH (481 mg, 2.20 mmol) through *General Procedure A*, and was obtained as a clear, colourless

oil (487 mg, 1.79 mmol, 81% yield). ^{1}H NMR (400 MHz, CD_3OD) δ 6.26 – 6.17 (m, 2H), 5.65 (dd, J = 7.6, 4.4 Hz, 1H), 4.14 (dd, J = 9.4, 4.7 Hz, 1H), 3.48 – 3.35 (m, 1H), 3.33 – 3.21 (m, 1H), 2.06 (1, 1H), 1.91 – 1.79 (m, 1H), 1.49 – 1.38 (s, 9H); ^{13}C NMR (101 MHz, CD_3OD) δ 175.66, 168.25, 158.15, 131.96, 126.70, 80.60, 52.72, 41.75, 32.27, 28.70; HRMS (ESI-QTOF) *m/z* [M + Na]$^{+}$ calcd for $C_{12}H_{20}N_2O_5Na$ 295.1270; found 295.1275.

*Boc-Orn(Acrylamide)-OH (**3**).* Compound **3** was prepared from commercially available Boc-Orn-OH (500 mg, 2.15 mmol) through *General Procedure A*, and was obtained as a white solid (447 mg, 1.56 mmol, 72% yield). ^{1}H NMR (400 MHz, CD_3OD) δ 6.23 – 6.13 (m, 2H), 5.61 (dd, J = 8.4, 3.6 Hz, 1H), 4.13 – 4.02 (m, 1H), 3.25 (t, J = 6.5 Hz, 2H), 1.89 – 1.75 (m, 1H), 1.72 – 1.52 (m, 3H), 1.40 (s, 9H); ^{13}C NMR (101 MHz, CD_3OD) δ 175.79, 167.98, 157.86, 131.92, 126.63, 80.38, 54.51, 39.88, 30.16, 28.72, 26.76; HRMS (ESI-QTOF) *m/z* [M + Na]$^{+}$ calcd for $C_{13}H_{22}N_2O_5Na$ 309.1426; found 309.1411.

*Boc-Lys(Acrylamide)-OH (**4**).* Compound **4** was prepared from commercially available Boc-Lys-OH (500 mg, 2.03 mmol) through *General Procedure A*, and was obtained as a clear, colourless oil (516 mg, 1.72 mmol, 85% yield). ^{1}H NMR (400 MHz, CD_3OD) δ 6.25 – 6.19 (m, 2H), 5.63 (dd, J = 7.9, 4.2 Hz, 1H), 4.14 – 4.04 (m, 1H), 3.26 (t, J = 6.9 Hz, 2H), 1.89 – 1.76 (m, 1H), 1.73 – 1.61 (m, 1H), 1.61 – 1.51 (m, 2H), 1.48 – 1.41 (m, 11H); ^{13}C NMR (101 MHz, CD_3OD) δ 176.17, 168.08, 158.10, 132.05, 126.51, 80.43, 54.76, 40.09, 32.41, 29.88, 28.72, 24.27; HRMS (ESI-QTOF) *m/z* [M + Na]$^{+}$ calcd for $C_{14}H_{24}N_2O_5Na$ 323.1583; found 323.1589.

*Fmoc-Dap(Acrylamide)-OH (**5**).* Compound **5** was prepared from Boc-Dap(Acrylamide)-OH **1** (375 mg, 1.45 mmol) through *General Procedure B* followed by *General Procedure C*, and was obtained as a white solid (342 mg, 0.90 mmol, 62% yield). ^{1}H NMR (400 MHz, CD_3OD) δ 7.68 (d, J = 7.5 Hz, 2H), 7.55 (dd, J = 7.1, 4.6 Hz, 2H), 7.30 (t, J = 7.5 Hz, 2H), 7.23 (td, J = 7.5, 1.2 Hz, 2H), 6.26 – 6.20 (m, 2H), 5.66 – 5.59 (m, 1H), 4.43 (dd, J = 7.8, 4.7 Hz, 1H), 4.32 – 4.20 (m, 2H), 4.10 (t, J = 7.0 Hz, 1H), 3.78 (dd, J = 13.9, 4.7 Hz, 1H), 3.64 (dd, J = 13.9, 7.8 Hz, 1H); ^{13}C NMR (101 MHz, CD_3OD) δ 173.41, 168.68, 158.34, 145.03, 144.97, 142.34, 131.55, 128.65, 128.03, 127.30, 126.11, 120.81, 68.08, 55.33, 48.10, 41.53; HRMS (ESI-QTOF) *m/z* $[M + Na]^+$ calcd for $C_{21}H_{20}N_2O_5Na$ 403.1270; found 403.1273.

*Fmoc-Dab(Acrylamide)-OH (**6**).* Compound **6** was prepared from Boc-Dab(Acrylamide)-OH **2** (487 mg, 1.79 mmol) through *General Procedure B* followed by *General Procedure C*, and was obtained as a white solid (502 mg, 1.27 mmol, 71% yield). ^{1}H NMR (400 MHz, CD_3OD) δ 7.70 (d, J = 7.6 Hz, 2H), 7.65 – 7.56 (m, 2H), 7.36 – 7.29 (m, 2H), 7.29 – 7.22 (m, 2H), 6.28 – 6.21 (m, 2H), 5.67 – 5.59 (m, 1H), 4.40 – 4.23 (m, 3H), 4.18 – 4.09 (m, 1H), 3.54 – 3.40 (m, 1H), 3.38 – 3.24 (m, 1H), 2.22 – 2.11 (m, 1H), 1.96 – 1.88 (m, 1H); ^{13}C NMR (101 MHz, CD_3OD) δ 175.35, 168.24, 158.54, 145.10, 144.95, 142.37, 142.33, 131.76, 128.65, 128.03, 126.89, 126.10, 120.82, 67.92, 53.07, 48.18, 37.19, 32.06; HRMS (ESI-QTOF) *m/z* $[M + Na]^+$ calcd for $C_{22}H_{22}N_2O_5Na$ 417.1426; found 417.1412.

*Fmoc-Orn(Acrylamide)-OH (**7**).* Compound **7** was prepared from Boc-Orn(Acrylamide)-OH **3** (447 mg, 1.56 mmol) through *General Procedure B* followed by *General Procedure C*, and was obtained as a white solid (225 mg, 0.55 mmol, 35% yield). ^{1}H NMR (400 MHz, CD_3OD) δ 7.72

(d, J = 7.4 Hz, 2H), 7.61 (t, J = 8.2 Hz, 2H), 7.33 (t, J = 7.4 Hz, 2H), 7.25 (td, J = 7.5, 0.9 Hz, 2H), 6.29 – 6.14 (m, 2H), 5.62 (dd, J = 6.8, 5.2 Hz, 1H), 4.30 (dd, J = 7.0, 4.9 Hz, 2H), 4.23 – 4.11 (m, 2H), 3.27 (t, J = 6.8 Hz, 2H), 1.96 – 1.82 (m, 1H), 1.78 – 1.52 (m, 3H); ^{13}C NMR (101 MHz, CD_3OD) δ 175.64, 168.11, 158.55, 145.21, 145.01, 142.44, 131.93, 128.69, 128.08, 126.65, 126.17, 126.14, 120.85, 67.86, 55.04, 48.27, 39.90, 30.07, 26.87; HRMS (ESI-QTOF) *m/z* [M + Na]$^+$ calcd for $C_{23}H_{24}N_2O_5Na$ 431.1583; found 431.1569.

*Fmoc-Lys(Acrylamide)-OH (**8**).* Compound **8** was prepared from Boc-Lys(Acrylamide)-OH **4** (516 mg, 1.72 mmol) through *General Procedure B* followed by *General Procedure C*, and was obtained as a white solid (599 mg, 1.42 mmol, 83% yield). ^{1}H NMR (400 MHz, CD_3OD) δ 7.68 (d, J = 7.6 Hz, 2H), 7.58 (t, J = 8.4 Hz, 2H), 7.30 (t, J = 7.5 Hz, 2H), 7.23 (td, J = 7.4, 1.1 Hz, 2H), 6.27 – 6.13 (m, 2H), 5.58 (t, J = 6.0 Hz, 1H), 4.29 (dd, J = 7.1, 3.2 Hz, 1H), 4.17 (dd, J = 9.1, 4.7 Hz, 1H), 4.11 (t, J = 7.0 Hz, 2H), 3.22 (t, J = 6.9 Hz, 2H), 1.91 – 1.78 (m, 1H), 1.76 – 1.62 (m, 1H), 1.60 – 1.47 (m, 2H), 1.47 – 1.35 (m, 2H); ^{13}C NMR (101 MHz, CD_3OD) δ 175.84, 168.07, 158.50, 145.14, 144.94, 142.38, 131.86, 128.67, 128.05, 128.03, 126.68, 126.13, 126.09, 120.84, 67.83, 55.11, 48.21, 40.09, 32.21, 29.71, 24.17; HRMS (ESI-QTOF) *m/z* [M + Na]$^+$ calcd for $C_{24}H_{26}N_2O_5Na$ 445.1739; found 445.1728.

Fmoc-D-*Asp(OtBu)-OH (**9**).* Compound **9** was prepared from commercially-available H-D-Asp(OtBu)-OH (2.00 g, 10.6 mmol) through *General Procedure C*, and was obtained as a white solid (3.99 g, 9.70 mmol, 92% yield). ^{1}H NMR (400 MHz, CD_3OD) δ 7.79 (d, *J* = 7.5 Hz, 2H), 7.70 – 7.62 (m, 2H), 7.41 – 7.36 (m, 2H), 7.34 – 7.26 (m, 2H), 4.60 – 4.50 (m, 1H), 4.34 (d, *J* = 7.5 Hz, 2H), 4.23 (t, *J* = 7.1 Hz, 1H), 2.81 (dd, *J* = 16.0, 5.3 Hz, 1H), 2.68 (dd, *J* = 16.1, 7.9 Hz,

1H), 1.44 (s, 9H); ^{13}C NMR (101 MHz, CD_3OD) δ 174.30, 171.38, 158.35, 145.27, 145.17, 142.57, 128.78, 128.16, 126.27, 120.91, 82.44, 68.14, 52.08, 48.32, 38.74, 28.28; HRMS (ESI-QTOF) *m/z* $[M + Na]^+$ calcd for $C_{23}H_{25}NO_6Na$ 434.1580; found 434.1584.

*Fmoc-Pro-CTC (**10**)*. Compound **10** was prepared from fresh 2-chlorotrityl chloride resin (100-200 mesh, 1.00 g, 1.06 mmol, 1 eq) and commercially available Fmoc-Pro-OH (1.2 eq) through *General Procedure D*. The resin loading was estimated as 0.664 mmol/g, and 1.29 g of loaded resin was recovered (0.853 mmol, 81% yield).

*Ac-*D*-Asp-Dap(Acrylamide)-Nle-Nle-Leu-Pro-Trp-Pro-OH (**11**)*. Compound **11** was prepared through *General Procedure E* using commercially available amino acids in addition to Fmoc-Pro-CTC resin **10** (0.1 mmol, 1 eq), Fmoc-D-Asp(OtBu)-OH **9** (0.5 mmol, 5 eq), and Fmoc-Dap(Acrylamide)-OH **5** (0.5 mmol, 5 eq) prepared herein. The desired peptide was obtained as a beige-white solid (10.0 mg, 0.0097 mmol, 10% yield). HRMS (ESI-QTOF) *m/z* $[M + Na]^+$ calcd for $C_{51}H_{74}N_{10}O_{13}Na$ 1057.5335; found 1057.5308.

*Ac-*D*-Asp-Dab(Acrylamide)-Nle-Nle-Leu-Pro-Trp-Pro-OH (**12**)*. Compound **12** was prepared through *General Procedure E* using commercially available amino acids in addition to Fmoc-Pro-CTC resin **10** (0.1 mmol, 1 eq), Fmoc-D-Asp(OtBu)-OH **9** (0.5 mmol, 5 eq), and Fmoc-Dab(Acrylamide)-OH **6** (0.5 mmol, 5 eq) prepared herein. The desired peptide was obtained as a white solid (8.6 mg, 0.0082 mmol, 8% yield). HRMS (ESI-QTOF) *m/z* $[M + Na]^+$ calcd for $C_{52}H_{76}N_{10}O_{13}Na$ 1071.5491; found 1071.5516.

*Ac-*D*-Asp-Orn(Acrylamide)-Nle-Nle-Leu-Pro-Trp-Pro-OH (**13**)*. Compound **13** was prepared through *General Procedure E* using commercially available amino acids in addition to Fmoc-Pro-CTC resin **10** (0.1 mmol, 1 eq), Fmoc-D-Asp(OtBu)-OH **9** (0.5 mmol, 5 eq), and Fmoc-Orn(Acrylamide)-OH **7** (0.5 mmol, 5 eq) prepared herein. The desired peptide was obtained as a white solid (5.0 mg, 0.0047 mmol, 5% yield). HRMS (ESI-QTOF) *m/z* $[M + Na]^+$ calcd for $C_{53}H_{78}N_{10}O_{13}Na$ 1085.5648; found 1085.5608.

*Ac-*D*-Asp-Lys(Acrylamide)-Nle-Nle-Leu-Pro-Trp-Pro-OH (**14**)*. Compound **14** was prepared through *General Procedure E* using commercially available amino acids in addition to Fmoc-Pro-CTC resin **10** (0.1 mmol, 1 eq), Fmoc-D-Asp(OtBu)-OH **9** (0.5 mmol, 5 eq), and Fmoc-Lys(Acrylamide)-OH **8** (0.5 mmol, 5 eq) prepared herein. The desired peptide was obtained as a white solid (6.7 mg, 0.0062 mmol, 6% yield). HRMS (ESI-QTOF) *m/z* $[M + Na]^+$ calcd for $C_{54}H_{80}N_{10}O_{13}Na$ 1099.5804; found 1099.5751.

*Boc-Dap(Alloc)-OH (**15**).* Compound **15** was prepared from commercially available Boc-Dap-OH (500 mg, 2.45 mmol) through *General Procedure F*, and was obtained as a white solid (643 mg, 2.23 mmol, 91% yield). ^{1}H NMR (400 MHz, CD_3OD) δ 5.91 (ddt, *J* = 17.3, 10.6, 5.4 Hz, 1H), 5.28 (dd, *J* = 17.3, 1.7 Hz, 1H), 5.16 (dd, *J* = 10.5, 1.6 Hz, 1H), 4.52 (d, *J* = 5.4 Hz, 2H), 4.28 (dd, *J* = 7.4, 4.6 Hz, 1H), 3.62 – 3.51 (m, 1H), 3.49 – 3.38 (m, 1H), 1.43 (s, 9H); ^{13}C NMR (101 MHz, CD_3OD) δ 173.73, 158.66, 157.56, 134.10, 117.54, 80.56, 66.41, 55.08, 43.00, 28.67; HRMS (ESI-QTOF) *m/z* $[M + Na]^+$ calcd for $C_{12}H_{20}N_2O_6Na$ 311.1219; found 311.1214.

*Boc-Orn(Alloc)-OH (**16**).* Compound **16** was prepared from commercially available Boc-Orn-OH (500 mg, 2.15 mmol) through *General Procedure F*, and was obtained as a clear, colourless oil (642 mg, 2.03 mmol, 94% yield). ^{1}H NMR (300 MHz, CD_3OD) δ 5.92 (ddt, *J* = 17.2, 10.6, 5.4 Hz, 1H), 5.28 (dd, *J* = 17.4, 1.7 Hz, 1H), 5.16 (dd, *J* = 10.5, 1.5 Hz, 1H), 4.51 (dt, *J* = 5.4, 1.6 Hz, 2H), 4.16 – 4.03 (m, 1H), 3.13 (t, *J* = 6.5 Hz, 2H), 1.94 – 1.74 (m, 1H), 1.74 – 1.51 (m, 3H), 1.44 (s, 9H); ^{13}C NMR (75 MHz, CD_3OD) δ 175.88, 158.58, 157.87, 134.39, 117.41, 80.37, 66.17, 54.51, 41.20, 30.01, 28.72, 27.27; HRMS (ESI-QTOF) *m/z* $[M + Na]^+$ calcd for $C_{14}H_{24}N_2O_6Na$ 339.1532; found 339.1534.

*Fmoc-Dap(Alloc)-OH (**17**).* Compound **17** was prepared from Boc-Dap(Alloc)-OH **15** (643 mg, 2.23 mmol), through *General Procedure B* followed by *General Procedure C*, and was obtained as a white solid (756 mg, 1.84 mmol, 83% yield). ^{1}H NMR (400 MHz, CD_3OD) δ 7.83 – 7.73 (m, 2H), 7.71 – 7.61 (m, 2H), 7.43 – 7.35 (m, 2H), 7.34 – 7.27 (m, 2H), 5.91 (ddt, *J* = 17.2, 10.7, 5.4 Hz, 1H), 5.28 (dd, *J* = 17.1, 1.7 Hz, 1H), 5.15 (dd, *J* = 10.6, 1.7 Hz, 1H), 4.59 – 4.49 (m, 2H), 4.38 – 4.30 (m, 3H), 4.23 (t, *J* = 7.0 Hz, 1H), 3.61 (dd, *J* = 14.1, 4.7 Hz, 1H), 3.45 (dd, *J* = 14.0, 7.7 Hz, 1H); ^{13}C NMR (101 MHz, CD_3OD) δ 173.60, 158.97, 158.54, 145.26, 145.24, 142.56, 134.32, 128.78, 128.17, 126.30, 120.91, 117.51, 68.19, 66.56, 55.70, 48.33, 42.98; HRMS (ESI-QTOF) *m/z* $[M + Na]^+$ calcd for $C_{22}H_{22}N_2O_6Na$ 433.1376; found 433.1378.

*Fmoc-Dab(Alloc)-OH (**18**).* Compound **18** was prepared from commercially-available Fmoc-Dab(Boc)-OH (500 mg, 1.14 mmol) through *General Procedure B* followed by *General Procedure F*, and was obtained as a white solid (477 mg, 1.12 mmol, 99% yield). ^{1}H NMR (400 MHz, CD_3OD) δ 7.70 (d, *J* = 7.5 Hz, 2H), 7.62 (t, *J* = 7.4 Hz, 2H), 7.33 (t, *J* = 7.5 Hz, 2H), 7.26

(tt, *J* = 7.5, 1.5 Hz, 2H), 5.89 (ddt, *J* = 17.2, 10.6, 5.4 Hz, 1H), 5.27 (dq, *J* = 17.2, 1.7 Hz, 1H), 5.15 (d, *J* = 10.0 Hz, 1H), 4.58 – 4.44 (m, 2H), 4.38 – 4.25 (m, 3H), 4.14 (t, *J* = 7.0 Hz, 1H), 3.37 – 3.26 (m, 1H), 3.26 – 3.13 (m, 1H), 2.20 – 2.08 (m, 1H), 1.95 – 1.79 (m, 1H); ^{13}C NMR (101 MHz, CD_3OD) δ 175.47, 158.48, 145.07, 144.93, 142.32, 134.19, 128.62, 128.01, 126.11, 120.80, 117.54, 67.88, 66.33, 52.84, 48.13, 38.40, 32.62; HRMS (ESI-QTOF) *m/z* $[M + Na]^+$ calcd for $C_{23}H_{24}N_2O_6Na$ 447.1532; found 447.1545.

*Fmoc-Orn(Alloc)-OH (**19**).* Compound **19** was prepared from Boc-Orn(Alloc)-OH **16** (642 mg, 2.03 mmol) through *General Procedure B* followed by *General Procedure C,* and was obtained as a white solid (540 mg, 1.23 mmol, 61% yield). ^{1}H NMR (400 MHz, CD_3OD) δ 7.79 (d, *J* = 7.6 Hz, 2H), 7.70 – 7.63 (m, 2H), 7.38 (d, *J* = 7.6 Hz, 2H), 7.30 (td, *J* = 7.5, 1.2 Hz, 2H), 5.92 (ddt, *J* = 17.1, 10.7, 5.4 Hz, 1H), 5.29 (dq, *J* = 17.2, 1.7 Hz, 1H), 5.17 (dq, *J* = 10.5, 1.5 Hz, 1H), 4.57 – 4.46 (m, 2H), 4.43 – 4.29 (m, 2H), 4.22 (t, *J* = 7.0 Hz, 1H), 4.15 (dd, *J* = 9.0, 4.7 Hz, 1H), 3.13 (t, *J* = 6.8 Hz, 2H), 1.95 – 1.82 (m, 1H), 1.76 – 1.50 (m, 3H); ^{13}C NMR (101 MHz, CD_3OD) δ 175.77, 158.82, 158.69, 145.35, 145.17, 142.58, 134.54, 128.77, 128.17, 128.15, 126.29, 126.27, 120.90, 117.38, 67.94, 66.28, 55.12, 48.41, 41.25, 29.93, 27.49; HRMS (ESI-QTOF) *m/z* $[M + Na]^+$ calcd for $C_{24}H_{26}N_2O_6Na$ 461.1689; found 461.1671.

*Ac-*D*-Asp-Dap(α-Chloroacetamide)-Nle-Nle-Leu-Pro-Trp-Pro-OH (**20**).* Compound **20** was prepared through *General Procedure G* using commercially available amino acids in addition to Fmoc-Pro-CTC resin **10** (0.1 mmol, 1 eq), Fmoc-D-Asp(OtBu)-OH **9** (0.5 mmol, 5 eq), and Fmoc-Dap(Alloc)-OH **17** (0.5 mmol, 5 eq) prepared herein. The desired peptide was obtained as a white

solid (9.6 mg, 0.0091 mmol, 9% yield). HRMS (ESI-QTOF) *m/z* [M + Na]$^+$ calcd for $C_{50}H_{73}ClN_{10}O_{13}Na$ 1079.4945; found 1079.4952.

*Ac-*D*-Asp-Dab(α-Chloroacetamide)-Nle-Nle-Leu-Pro-Trp-Pro-OH (**21**)*. Compound **21** was prepared through *General Procedure G* using commercially available amino acids in addition to Fmoc-Pro-CTC resin **10** (0.1 mmol, 1 eq), Fmoc-D-Asp(OtBu)-OH **9** (0.5 mmol, 5 eq), and Fmoc-Dab(Alloc)-OH **18** (0.5 mmol, 5 eq) prepared herein. The desired peptide was obtained as a white solid (11.4 mg, 0.0106 mmol, 11% yield). HRMS (ESI-QTOF) *m/z* [M + Na]$^+$ calcd for $C_{51}H_{75}ClN_{10}O_{13}Na$ 1093.5101; found 1093.5128.

*Ac-*D*-Asp-Orn(α-Chloroacetamide)-Nle-Nle-Leu-Pro-Trp-Pro-OH (**22**)*. Compound **22** was prepared through *General Procedure G* using commercially available amino acids in addition to Fmoc-Pro-CTC resin **10** (0.1 mmol, 1 eq), Fmoc-D-Asp(OtBu)-OH **9** (0.5 mmol, 5 eq), and Fmoc-Orn(Alloc)-OH **19** (0.5 mmol, 5 eq) prepared herein. The desired peptide was obtained as a white solid (11.6 mg, 0.0107 mmol, 11% yield). HRMS (ESI-QTOF) *m/z* [M + Na]$^+$ calcd for $C_{52}H_{77}ClN_{10}O_{13}Na$ 1107.5258; found 1107.5211.

*Ac-*D*-Asp-Lys(α-Chloroacetamide)-Nle-Nle-Leu-Pro-Trp-Pro-OH (**23**)*. Compound **23** was prepared through *General Procedure G* using commercially available amino acids, including Fmoc-Lys(Alloc)-OH, in addition to Fmoc-Pro-CTC resin **10** (0.1 mmol, 1 eq) and Fmoc-D-Asp(OtBu)-OH **9** (0.5 mmol, 5 eq) prepared herein. The desired peptide was obtained as a beige solid (15.5 mg, 0.014 mmol, 14% yield). HRMS (ESI-QTOF) *m/z* [M + Na]$^+$ calcd for $C_{53}H_{79}ClN_{10}O_{13}Na$ 1121.5414; found 1121.5399.

*Boc-Glu(OMe)-OtBu (**24**).* Compound **24** was prepared from commercially available Boc-Glu-OtBu as previously reported by Buchold *et al*. in 2016. Boc-Glu-OtBu (4.55 g, 15.0 mmol, 1 eq) was dissolved in 75 mL of DMF to produce a concentration of 0.2 M. An inert nitrogen atmosphere was prepared by flushing the reaction flask with a balloon. Cs_2CO_3 (0.55 eq) was then added in 1 portion, and the mixture was stirred under inert atmosphere at room temperature for 1 h. Next, MeI (1 eq) was added dropwise over 5 min, and the reaction was stirred under inert atmosphere at room temperature overnight. Upon reaction completion, the crude mixture was concentrated by rotary evaporation to remove DMF. The resulting crude residue was dissolved in 150 mL of EtOAc, and excess undissolved Cs_2CO_3 was removed by filtration. The filtrate was washed thrice with 30 mL of 10% citric acid, thrice with 30 mL of 10% $NaHCO_3$, and thrice with 30 mL of brine. The resulting organic phase was dried over $MgSO_4$, filtered, and concentrated in vacuo. Pure product was obtained as 4.33 g (13.6 mmol, 91% yield) of yellow-white solid. ^{1}H NMR (400 MHz, $CDCl_3$) δ 5.14 – 4.99 (m, 1H), 4.27 – 4.14 (m, 1H), 3.67 (s, 3H), 2.49 – 2.27 (m, 2H), 2.22 – 2.06 (m, 1H), 1.99 – 1.82 (m, 1H), 1.45 (s, 9H), 1.43 (s, 9H). Characterization matches previous reports [53].

*Boc_2-Glu(OMe)-OtBu (**25**).* Compound **25** was prepared from Boc-Glu(OMe)-OtBu **24** (4.33 g, 13.6 mmol, 1 eq) through *General Procedure H*. The title compound was obtained as a colourless oil (2.79 g, 6.68 mmol, 49% yield). ^{1}H NMR (400 MHz, $CDCl_3$) δ 4.82 – 4.72 (m, 1H), 3.65 (s, 3H), 2.48 – 2.31 (m, 3H), 2.20 – 2.09 (m, 1H), 1.48 (s, 18H), 1.42 (s, 9H). Characterization matches previous reports [53].

*Boc_2-Glu(H)-OtBu (**26**)*. Compound **26** was prepared from Boc_2-Glu(OMe)-OtBu **25** (2.79 g, 6.68 mmol, 1 eq) through *General Procedure I*, furnishing pure product as a colourless oil (2.33 g, 6.01 mmol, 90% yield). ^{1}H NMR (400 MHz, $CDCl_3$) δ 9.74 (t, J = 1.2 Hz, 1H), 4.71 (dd, J = 9.4, 5.3 Hz, 1H), 2.63 – 2.31 (m, 3H), 2.20 – 2.03 (m, 1H), 1.48 (s, 18H), 1.42 (s, 9H). Characterization matches previous reports [53].

*Boc_2-Glu(MA)-OtBu (**27**).* Compound **27** was prepared from Boc_2-Glu(H)-OtBu **26** (2.33 g, 6.01 mmol, 1 eq) through *General Procedure J*. The title compound was obtained as a colourless oil (2.18 g, 4.92 mmol, 82% yield). ^{1}H NMR (400 MHz, $CDCl_3$) δ 6.93 (dt, J = 15.7, 6.7 Hz, 1H), 5.83 (dt, J = 15.6, 1.4 Hz, 1H), 4.69 (dd, J = 9.6, 4.7 Hz, 1H), 3.70 (s, 3H), 2.32 – 2.13 (m, 3H), 2.07 – 1.95 (m, 1H), 1.48 (s, 18H), 1.42 (s, 9H). Characterization matches previous reports [53].

*Boc-Glu(MA)-OH (**28**)*. Compound **28** was prepared from Boc_2-Glu(MA)-OtBu **27** (1.90 g, 4.28 mmol, 1 eq) through *General Procedure K*. The title compound was obtained as a yellow oil (1.08 g, 3.75 mmol, 88% yield). ^{1}H NMR (400 MHz, CD_3OD) δ 6.97 (dt, J = 15.6, 7.0 Hz, 1H), 5.88 (dt, J = 15.6, 1.5 Hz, 1H), 4.15 – 4.05 (m, 1H), 3.71 (s, 3H), 2.39 – 2.25 (m, 2H), 2.06 – 1.90 (m, 1H), 1.86 – 1.72 (m, 1H), 1.44 (s, 9H). Characterization matches previous reports [53].

*Boc-Asp(OBzl)-OtBu (**29**).* Compound **29** was prepared through a Steglich esterification reported previously [73,74]. Around 4.85 g of commercially available Boc-Asp(OBzl)-OH (15 mmol, 1 eq) was added to an oven-dried round bottom flask equipped with a stir bar. This was then dissolved in 9.7 mL of dry DCM (1.6 M) under inert atmosphere (N_2 balloon). Stirring was then commenced at room temperature. Next, DMAP was added in 1 portion (0.1 eq), followed by *t*-BuOH (1.2 eq),

and DCC (1.2 eq). The reaction was then stirred for 3 h at room temperature under inert atmosphere. Upon completion, the crude mixture was filtered to remove the precipitated urea of DCC, and the filtrate was concentrated through rotary evaporation. The crude residue was subsequently purified by column chromatography (10% EtOAc in hexanes), yielding 3.96 g of pure product as a colourless oil (10.4 mmol, 70% yield). ^{1}H NMR (400 MHz, $CDCl_3$) δ 7.41 – 7.27 (m, 5H), 5.49 – 5.41 (m, 1H), 5.15 (d, J = 12.3 Hz, 1H), 5.10 (d, J = 12.3 Hz, 1H), 4.50 – 4.41 (m, 1H), 2.99 (dd, J = 16.8, 4.6 Hz, 1H), 2.82 (dd, J = 16.8, 4.8 Hz, 1H), 1.44 (s, 9H), 1.41 (s, 9H); ^{13}C NMR (101 MHz, $CDCl_3$) δ 171.01, 170.07, 155.56, 135.68, 128.72, 128.49, 128.44, 82.47, 79.99, 66.78, 50.67, 37.21, 28.45, 27.96; HRMS (ESI-QTOF) *m/z* $[M + Na]^+$ calcd for $C_{20}H_{29}NO_6Na$ 402.1893; found 402.1902.

*Boc_2-Asp(OBzl)-OtBu (**30**).* Compound **30** was prepared from Boc-Asp(OBzl)-OtBu **29** (4.36 g, 11.5 mmol) through *General Procedure H*, and was obtained as a colourless oil (5.20 g, 10.8 mmol, 94% yield). ^{1}H NMR (400 MHz, $CDCl_3$) δ 7.37 – 7.29 (m, 5H), 5.36 (dd, J = 7.2, 6.5 Hz, 1H), 5.18 (d, J = 12.4 Hz, 1H), 5.09 (d, J = 12.3 Hz, 1H), 3.27 (dd, J = 16.4, 7.2 Hz, 1H), 2.73 (dd, J = 16.4, 6.5 Hz, 1H), 1.49 (s, 18H), 1.43 (s, 9H); ^{13}C NMR (101 MHz, $CDCl_3$) δ 170.89, 168.75, 152.10, 135.92, 128.63, 128.34, 128.30, 83.28, 82.05, 66.67, 55.69, 35.76, 28.13, 27.99; HRMS (ESI-QTOF) *m/z* $[M + Na]^+$ calcd for $C_{25}H_{37}NO_8Na$ 502.2417; found 502.2425.

*Boc_2-Asp(H)-OtBu (**31**).* Compound **31** was prepared from Boc_2-Asp(OBzl)-OtBu **30** (4.23 g, 8.82 mmol) through *General Procedure I*, and was obtained as a colourless oil (2.22 g, 5.94 mmol, 67% yield). ^{1}H NMR (400 MHz, $CDCl_3$) δ 9.77 (t, J = 1.4 Hz, 1H), 5.40 (dd, J = 6.9, 6.0 Hz, 1H), 3.35 (ddd, J = 17.7, 7.0, 1.6 Hz, 1H), 2.75 (ddd, J = 17.7, 6.0, 1.3 Hz, 1H), 1.50 (s, 18H), 1.43 (s, 9H);

^{13}C NMR (101 MHz, $CDCl_3$) δ 199.01, 168.79, 152.24, 83.49, 82.32, 53.88, 44.74, 28.15, 28.00; HRMS (ESI-QTOF) *m/z* $[M + Na]^+$ calcd for $C_{18}H_{31}NO_7Na$ 396.1998; found 396.2008.

*Boc_2-Asp(MA)-OtBu (**32**).* Compound **32** was prepared from Boc_2-Asp(H)-OtBu **31** (2.73 g, 7.32 mmol) through *General Procedure J*, and was obtained as a colourless oil (2.78 g, 6.47 mmol, 88% yield). ^{1}H NMR (400 MHz, $CDCl_3$) δ 6.90 (ddd, J = 15.3, 8.6, 6.4 Hz, 1H), 5.85 (dt, J = 15.6, 1.5 Hz, 1H), 4.89 (dd, J = 9.8, 5.2 Hz, 1H), 3.70 (s, 3H), 3.01 – 2.89 (m, 1H), 2.86 – 2.73 (m, 1H), 1.49 (s, 18H), 1.44 (s, 9H); ^{13}C NMR (101 MHz, $CDCl_3$) δ 168.86, 166.66, 152.31, 145.12, 123.57, 83.26, 81.98, 57.77, 51.54, 32.76, 28.12, 28.04; HRMS (ESI-QTOF) *m/z* $[M + Na]^+$ calcd for $C_{21}H_{35}NO_8Na$ 452.2260; found 452.2267.

*Boc-Asp(MA)-OH (**33**).* Compound **33** was prepared from Boc_2-Asp(MA)-OtBu **32** (1.25 g, 2.90 mmol) through *General Procedure K*, and was obtained as a faint yellow oil (608 mg, 2.22 mmol, 77% yield). ^{1}H NMR (400 MHz, CD_3OD) δ 6.91 (dt, J = 15.0, 7.3 Hz, 1H), 5.94 (dt, J = 15.5, 1.4 Hz, 1H), 4.25 (dd, J = 8.9, 4.9 Hz, 1H), 3.71 (s, 3H), 2.81 – 2.69 (m, 1H), 2.63 – 2.50 (m, 1H), 1.44 (s, 9H); ^{13}C NMR (101 MHz, CD_3OD) δ 174.65, 168.16, 157.89, 145.63, 124.64, 80.65, 53.89, 52.01, 35.48, 28.66; HRMS (ESI-QTOF) *m/z* $[M + Na]^+$ calcd for $C_{12}H_{19}NO_6Na$ 296.1110; found 296.1114.

*Boc_2-Hmg(OMe)-OtBu (**34**).* Approximately 1.21 g of Boc_2-Asp(MA)-OtBu **32** (1.21 g, 2.82 mmol, 1 eq) was dissolved in MeOH (0.1 M) under inert nitrogen balloon atmosphere. Next, 10 wt. % loaded Pd/C was added in one portion (0.1 eq), and the nitrogen atmosphere was re-prepared prior to replacement with hydrogen gas. The reaction was stirred for 4 h at room temperature under

hydrogen, at which point nitrogen was pumped back in and the transformation was deemed complete by TLC analysis. The mixture was then filtered over Celite and washed through with excess methanol prior to concentration in-vacuo. Pure product was obtained as 1.19 g of colourless oil (2.76 mmol, 98% yield). ^{1}H NMR (400 MHz, $CDCl_3$) δ 4.71 (dd, J = 9.7, 5.1 Hz, 1H), 3.65 (s, 3H), 2.43 – 2.24 (m, 2H), 2.12 – 1.99 (m, 1H), 1.96 – 1.82 (m, 1H), 1.74 – 1.61 (m, 2H), 1.50 (s, 18H), 1.43 (s, 9H); ^{13}C NMR (101 MHz, $CDCl_3$) δ 173.84, 169.81, 152.58, 82.95, 81.38, 58.64, 51.64, 33.77, 28.78, 28.15, 28.07, 21.96; HRMS (ESI-QTOF) *m/z* $[M + Na]^+$ calcd for $C_{21}H_{37}NO_8Na$ 454.2417; found 454.2428.

*Boc_2-Hmg(H)-OtBu (**35**)*. Compound **35** was prepared from Boc_2-Hmg(OMe)-OtBu **34** (1.50 g, 3.47 mmol) through *General Procedure I*, and was obtained as a colourless oil (1.24 g, 3.09 mmol, 89% yield). ^{1}H NMR (400 MHz, $CDCl_3$) δ 9.75 (t, J = 1.6 Hz, 1H), 4.71 (dd, J = 9.5, 5.2 Hz, 1H), 2.57 – 2.36 (m, 2H), 2.13 – 1.99 (m, 1H), 1.97 – 1.83 (m, 1H), 1.73 – 1.61 (m, 2H), 1.50 (s, 18H), 1.43 (s, 9H); ^{13}C NMR (101 MHz, $CDCl_3$) δ 202.16, 169.74, 152.64, 83.03, 81.46, 58.62, 43.53, 28.80, 28.16, 28.06, 19.14; HRMS (ESI-QTOF) *m/z* $[M + Na]^+$ calcd for $C_{20}H_{35}NO_7Na$ 424.2311; found 424.2306.

*Boc_2-Hmg(MA)-OtBu (**36**)*. Compound **36** was prepared from Boc_2-Hmg(H)-OtBu **35** (1.24 g, 3.09 mmol) through *General Procedure J*, and was obtained as a colourless oil (1.04 g, 2.28 mmol, 74% yield). ^{1}H NMR (400 MHz, $CDCl_3$) δ 6.94 (dt, J = 15.6, 6.9 Hz, 1H), 5.82 (dt, J = 15.6, 1.6 Hz, 1H), 4.70 (dd, J = 9.6, 5.2 Hz, 1H), 3.71 (s, 3H), 2.34 – 2.12 (m, 2H), 2.12 – 1.99 (m, 1H), 1.94 – 1.80 (m, 1H), 1.55 – 1.46 (m, 20H), 1.44 (s, 9H); ^{13}C NMR (101 MHz, $CDCl_3$) δ 169.87,

167.16, 152.64, 149.03, 121.43, 82.97, 81.39, 58.65, 51.52, 31.88, 28.82, 28.17, 28.08, 25.04; HRMS (ESI-QTOF) *m/z* $[M + Na]^+$ calcd for $C_{23}H_{39}NO_8Na$ 480.2573; found 480.2566.

*Boc-Hmg(MA)-OH (**37**).* Compound **37** was prepared from Boc_2-Hmg(MA)-OtBu **36** (1.04 g, 2.28 mmol) through *General Procedure K*, and was obtained as a faint yellow oil (614 mg, 2.04 mmol, 89% yield). ^{1}H NMR (400 MHz, CD_3OD) δ 6.96 (dt, J = 15.6, 7.0 Hz, 1H), 5.87 (dt, J = 15.6, 1.6 Hz, 1H), 4.17 – 4.02 (m, 1H), 3.71 (s, 3H), 2.30 – 2.20 (m, 2H), 1.89 – 1.76 (m, 1H), 1.72 – 1.53 (m, 3H), 1.44 (s, 9H); ^{13}C NMR (101 MHz, CD_3OD) δ 176.03, 168.66, 158.15, 150.39, 122.23, 80.48, 54.53, 51.93, 32.50, 32.25, 28.71, 25.42; HRMS (ESI-QTOF) *m/z* $[M + Na]^+$ calcd for $C_{14}H_{23}NO_6Na$ 324.1423; found 324.1437.

*Ac-*D*-Asp(OtBu)-OH (**38**)*. Compound **38** was produced from commercially available H-D-Asp(OtBu)-OH through a previously-reported method. The amino acid starting material (1.135 g, 6.00 mmol, 1.0 eq) was dissolved in dry THF (0.5 M) under inert (N_2 balloon) atmosphere in an oven-dried round-bottom flask equipped with a stir bar. While stirring at room temperature, excess Ac_2O (3.0 eq) was then added, and the reaction was allowed to stir at room temperature overnight. The reaction was then acidified to pH 2 through the addition of a minimal amount of 1 M $HCl_{(aq)}$ (approximately 2 mL), and excess solvents were subsequently removed through rotary evaporation. The water bath temperature was kept at or below 35 °C to prevent the deprotection of the *tert*-butyl ester. Excess water was removed through azeotropic evaporation with toluene, producing a white solid. The solid obtained was then cleaned through vacuum filtration while rinsing with EtOAc, yielding the desired compound as a white solid in 39% yield (540 mg, 2.33 mmol). ^{1}H NMR (400 MHz, CD_3OD) δ 4.73 (dd, J = 7.4, 5.4 Hz, 1H), 2.78 (dd, J = 16.1, 5.4 Hz,

1H), 2.67 (dd, J = 16.2, 7.4 Hz, 1H), 1.98 (s, 3H), 1.45 (s, 9H). Characterization matches previous reports [68].

*TFA.H-Asp(MA)-Nle-Nle-Leu-Pro-Trp-Pro-OH (**39**)*. Compound **39** was prepared through *General Procedure L* using commercially available amino acids in addition to Fmoc-Pro-CTC resin **10** (0.5 mmol, 1 eq) and Boc-Asp(MA)-OH **33** (1.0 mmol, 2 eq) prepared herein. The desired peptide was obtained as a brown oil (336 mg, 0.33 mmol, 66% yield). LC-MS *m/z* 894 for $[M + H]^+$.

*TFA.H-Glu(MA)-Nle-Nle-Leu-Pro-Trp-Pro-OH (**40**)*. Compound **40** was prepared through *General Procedure L* using commercially available amino acids in addition to Fmoc-Pro-CTC resin **10** (0.5 mmol, 1 eq) and Boc-Glu(MA)-OH **28** (1.0 mmol, 2 eq) prepared herein. The desired peptide was obtained as a beige solid (326 mg, 0.320 mmol, 64% yield). LC-MS *m/z* 908 for $[M + H]^+$.

*TFA.H-Hmg(MA)-Nle-Nle-Leu-Pro-Trp-Pro-OH (**41**)*. Compound **41** was prepared through *General Procedure L* using commercially available amino acids in addition to Fmoc-Pro-CTC resin **10** (0.5 mmol, 1 eq) and Boc-Hmg(MA)-OH **37** (1.0 mmol, 2 eq) prepared herein. The desired peptide was obtained as a beige solid (220 mg, 0.21 mmol, 42% yield). LC-MS *m/z* 922 for $[M + H]^+$.

Ac-D-*Asp(OtBu)-Asp(MA)-Nle-Nle-Leu-Pro-Trp-Pro-OH* (**42**). Compound **42** was prepared through *General Procedure M* using TFA.H-Asp(MA)-Nle-Nle-Leu-Pro-Trp-Pro-OH **39** (336 mg,

0.33 mmol, 1 eq) and Ac-D-Asp(OtBu)-OH **38** (0.33 mmol, 1 eq), both prepared herein. The desired peptide was obtained as a beige solid (57.3 mg, 0.052 mmol, 16% yield). LC-MS *m/z* 1107 for $[M + H]^+$.

Ac-D-Asp(OtBu)-Glu(MA)-Nle-Nle-Leu-Pro-Trp-Pro-OH (**43**). Compound **43** was prepared through *General Procedure M* using TFA.H-Glu(MA)-Nle-Nle-Leu-Pro-Trp-Pro-OH **40** (326 mg, 0.32 mmol, 1 eq) and Ac-D-Asp(OtBu)-OH **38** (0.32 mmol, 1 eq), both prepared herein. The desired peptide was obtained as a yellow solid (36.0 mg, 0.032 mmol, 10% yield). LC-MS *m/z* 1121 for $[M + H]^+$.

Ac-D-Asp(OtBu)-Hmg(MA)-Nle-Nle-Leu-Pro-Trp-Pro-OH (**44**). Compound **44** was prepared through *General Procedure M* using TFA.H-Hmg(MA)-Nle-Nle-Leu-Pro-Trp-Pro-OH **41** (220 mg, 0.21 mmol, 1 eq) and Ac-D-Asp(OtBu)-OH **38** (0.21 mmol, 1 eq), both prepared herein. The desired peptide was obtained as a white solid (79.8 mg, 0.070 mmol, 33% yield). LC-MS *m/z* 1135 for $[M + H]^+$.

Ac-D-Asp-Asp(MA)-Nle-Nle-Leu-Pro-Trp-Pro-OH (**45**). Compound **45** was prepared through *General Procedure N* from Ac-D-Asp(OtBu)-Asp(MA)-Nle-Nle-Leu-Pro-Trp-Pro-OH **42** (57.3 mg, 0.052 mmol, 1.0 eq). The desired peptide was obtained as a white solid (7.8 mg, 0.0074 mmol, 14% yield). HRMS (ESI-QTOF) *m/z* $[M + Na]^+$ calcd for $C_{52}H_{75}N_9O_{14}Na$ 1072.5331; found 1072.5323.

Ac-D-*Asp-Glu(MA)-Nle-Nle-Leu-Pro-Trp-Pro-OH* (**46,** ZED1301). Compound **46** was prepared through *General Procedure N* from Ac-D-Asp(OtBu)-Glu(MA)-Nle-Nle-Leu-Pro-Trp-Pro-OH **43** (36.0 mg, 0.032 mmol, 1.0 eq). The desired peptide was obtained as a white solid (5.7 mg, 0.0054 mmol, 17% yield). HRMS (ESI-QTOF) *m/z* $[M + Na]^+$ calcd for $C_{53}H_{77}N_9O_{14}Na$ 1086.5488; found 1086.5507.

Ac-D-*Asp-Hmg(MA)-Nle-Nle-Leu-Pro-Trp-Pro-OH* (**47**). Compound **47** was prepared through *General Procedure N* from Ac-D-Asp(OtBu)-Hmg(MA)-Nle-Nle-Leu-Pro-Trp-Pro-OH **44** (79.8 mg, 0.070 mmol, 1.0 eq). The desired peptide was obtained as a white solid (9.3 mg, 0.0086 mmol, 12% yield). HRMS (ESI-QTOF) *m/z* $[M + Na]^+$ calcd for $C_{54}H_{79}N_9O_{14}Na$ 1100.5644; found 1100.5662.

N-Boc-Piperazine-Dansyl (**51**). Compound **51** was synthesized using a sulfonylation reaction detailed in *General Procedure O* (yield 96%). Characterization consistent with data from literature [75].

N-Boc-Piperazine-Sulfonyl-Naphthalene (**52**). Compound **52** was synthesized via an a sulfonylation reaction detailed in *General Procedure O* (yield 96%). Characterization consistent with data from literature [76].

N-Boc-Piperazine-Naphthoyl (**53**). Compound **53** was synthesized using the acylation reaction outlined in *General Procedure O* (yield 98%). Characterization consistent with data from literature [42].

*H-Piperazine-Dansyl (***54**). Compound **54** was synthesized according to the acid catalyzed Boc deprotection detailed in *General Procedure P*. The product was carried forward without further purification or characterization.

H-Piperazine-Sulfonyl-Naphthalene (**55**). Compound **55** was synthesized according to the acid catalyzed Boc deprotection detailed in *General Procedure P*. The product was carried forward without further purification or characterization.

H-Piperazine-Naphthoyl (**56**). Compound **56** was synthesized according to the acid catalyzed Boc deprotection detailed in *General Procedure P*. The product was carried forward without further purification or characterization.

Boc-L-*Dap(Cbz)-Piperazine-Dansyl* (**57**). Compound **57** was synthesized using an amide bond coupling outlined in *General Procedure Q* (yield 92%). ^{1}H NMR (400 MHz, $CDCl_3$) δ 8.57 (d, *J* = 8.5 Hz, 1H), 8.34 (d, *J* = 8.7 Hz, 1H), 8.19 (dd, *J* = 7.3, 1.3 Hz, 1H), 7.54 (ddt, *J* = 9.4, 7.3, 4.2 Hz, 2H), 7.35 – 7.22 (m, 5H), 7.17 (d, *J* = 7.5 Hz, 1H), 5.50 (d, *J* = 8.3 Hz, 1H), 5.37 (s, 1H), 5.01 (s, 2H), 4.66 (s, 1H), 3.73 – 3.02 (m, 10H), 2.87 (s, 6H), 1.35 (s, 9H). ^{13}C NMR (101 MHz, $CDCl_3$) δ 168.60, 156.64, 155.41, 151.93, 136.39, 132.40, 131.12, 130.82, 130.33, 130.14, 128.54, 128.37, 128.20, 128.08, 125.10, 123.23, 120.23, 119.36, 115.44, 80.20, 66.85, 50.18, 45.62, 45.47, 45.18, 43.74, 41.78, 28.30. HRMS (ESI-QTOF) m/z [M + Na]+ calcd for $C_{32}H_{41}N_5O_7SNa$ 662.2624; found 662.2599.

Boc-L-*Dap(Cbz)-Piperazine-Sulfonyl-Naphthalene* (**58**). Compound **58** was synthesized using an amide bond coupling outlined in *General Procedure Q* (yield 85%). ^{1}H NMR (400 MHz, $CDCl_3$) δ 8.72 (d, *J* = 8.6 Hz, 1H), 8.21 (d, *J* = 7.4 Hz, 1H), 8.10 (d, *J* = 8.2 Hz, 1H), 7.94 (d, *J* = 8.0 Hz, 1H), 7.70 – 7.54 (m, 3H), 7.37 – 7.27 (m, 5H), 5.38 (d, *J* = 8.2 Hz, 1H), 5.20 (t, *J* = 6.2 Hz, 1H), 5.02 (s, 2H), 4.65 (s, 1H), 3.79 – 3.02 (m, 10H), 1.37 (s, 9H). ^{13}C NMR (101 MHz, $CDCl_3$) δ 168.42, 156.31, 155.35, 134.90, 134.42, 132.13, 130.79, 129.08, 128.87, 128.51, 128.40, 128.18, 128.03, 127.05, 124.88, 124.19, 80.29, 66.87, 50.15, 45.60, 45.18, 43.82, 41.72, 28.23. HRMS (ESI-QTOF) m/z [M + Na]+ calcd for $C_{30}H_{36}N_4O_7SNa$ 619.2202; found 619.2208.

Boc-L-*Dap(Cbz)-Piperazine-Naphthoyl* (**59**). Compound **59** was synthesized using an amide bond coupling outlined in *General Procedure Q* (yield 84%). ^{1}H NMR (400 MHz, $CDCl_3$) δ 7.91 (d, *J* = 8.3 Hz, 2H), 7.81 (s, 1H), 7.57 – 7.39 (m, 4H), 7.32 (d, *J* = 14.2 Hz, 5H), 5.51 (d, *J* = 8.1 Hz, 1H), 5.27 (s, 1H), 5.15 – 4.99 (m, 2H), 4.84 – 4.60 (m, 1H), 4.05 – 3.15 (m, 10H), 1.47 – 1.36 (m, 9H). ^{13}C NMR (101 MHz, $CDCl_3$) δ 169.75, 156.77, 155.52, 133.66, 129.75, 128.65, 128.30, 127.41, 126.79, 125.32, 80.41, 67.05, 50.64, 46.69, 42.81, 41.64, 28.44. HRMS (ESI-QTOF) m/z [M + Na]+ calcd for $C_{31}H_{36}N_4O_6Na$ 583.2533; found 583.2544.

Boc-L-*Dap-Piperazine-Dansyl* (**60**). Compound **60** was synthesized according to the hydrogenolysis reaction detailed in *General Procedure R*. The product was carried forward without further purification or characterization.

Boc-L-*Dap-Piperazine-Sulfonyl-Naphthalene* (**61**). Compound **61** was synthesized according to the hydrogenolysis reaction detailed in *General Procedure R*. The product was carried forward without further purification or characterization.

Boc-L-*Dap-Piperazine-Naphthoyl* (**62**). Compound **62** was synthesized according to the hydrogenolysis reaction detailed in *General Procedure R*. The product was carried forward without further purification or characterization.

Boc-L-*Dap(Acryl)-Piperazine-Dansyl* (**63**). Compound **63** was synthesized according to the acrylation reaction provided in *General Procedure S* (yield 60%). ^{1}H NMR (400 MHz, $CDCl_3$) δ 8.59 (dt, *J* = 8.6, 1.1 Hz, 1H), 8.37 (dt, *J* = 8.7, 0.9 Hz, 1H), 8.21 (dd, *J* = 7.3, 1.3 Hz, 1H), 7.55 (ddd, *J* = 8.5, 7.5, 1.0 Hz, 2H), 7.21 (dd, *J* = 7.6, 0.9 Hz, 1H), 6.36 (s, 1H), 6.24 – 6.15 (m, 1H), 6.02 (dd, *J* = 17.0, 10.3 Hz, 1H), 5.61 (dd, *J* = 10.3, 1.4 Hz, 1H), 5.53 (d, *J* = 7.9 Hz, 1H), 4.66 (td, *J* = 7.8, 3.7 Hz, 1H), 3.83 – 3.50 (m, 4H), 3.37 – 3.11 (m, 1H), 2.91 (s, 6H), 1.37 (s, 9H). ^{13}C NMR (101 MHz, $CDCl_3$) δ 168.51, 166.28, 151.51, 132.50, 131.09, 131.00, 130.51, 130.41, 130.11, 128.43, 127.05, 123.48, 119.77, 115.67, 80.55, 50.29, 45.73, 45.60, 45.35, 45.26, 42.92, 41.97, 28.35. HRMS (ESI-QTOF) m/z [M + Na]+ calcd for $C_{27}H_{37}N_5O_6SNa$ 582.2362; found 582.2332.

Boc-L-*Dap(Acryl)-Piperazine-Sulfonyl-Naphthalene* (**64**). Compound **64** was synthesized according to the acrylation reaction provided in *General Procedure S* (yield 56%). ^{1}H NMR (600 MHz, $CDCl_3$) δ 8.69 (dd, *J* = 8.7, 1.1 Hz, 1H), 8.20 (dd, *J* = 7.4, 1.2 Hz, 1H), 8.08 (dt, *J* = 8.4, 1.1 Hz, 1H), 7.93 (dd, *J* = 8.2, 1.5 Hz, 1H), 7.70 – 7.52 (m, 3H), 6.48 – 6.36 (m, 1H), 6.17 (d, *J* = 17.0 Hz, 1H), 6.00 (dd, *J* = 17.0, 10.3 Hz, 1H), 5.62 – 5.55 (m, 2H), 4.65 (td, *J* = 7.9, 4.0 Hz, 1H), 3.73

– 3.48 (m, 5H), 3.35 – 3.09 (m, 5H), 1.34 (s, 9H). ^{13}C NMR (151 MHz, $CDCl_3$) δ 168.62, 166.22, 155.73, 135.02, 134.49, 132.13, 130.91, 130.47, 129.17, 128.90, 128.50, 127.14, 126.98, 124.91, 124.29, 80.43, 50.17, 45.70, 45.28, 42.63, 41.87, 28.30. HRMS (ESI-QTOF) m/z [M + Na]+ calcd for $C_{25}H_{32}N_4O_6SNa$ 539.1940; found 539.1948.

Boc-L-*Dap(Acryl)-Piperazne-Naphthoyl* (**65**). Compound **65** was synthesized according to the acrylation reaction provided in *General Procedure S* (yield 54%). ^{1}H NMR (600 MHz, $CDCl_3$) δ 7.92 – 7.76 (m, 3H), 7.59 – 7.37 (m, 4H), 6.49 (s, 1H), 6.27 – 6.14 (m, 1H), 6.10 – 5.96 (m, 1H), 5.73 – 5.55 (m, 2H), 4.81 – 4.60 (m, 1H), 4.06 – 3.13 (m, 10H), 1.48 – 1.31 (m, 9H). ^{13}C NMR (151 MHz, $CDCl_3$) δ 169.73, 168.68, 166.27, 155.81, 133.59, 133.41, 130.62, 130.44, 129.73, 129.53, 128.73, 127.34, 126.95, 126.76, 125.30, 124.45, 124.10, 80.51, 50.51, 47.19, 46.68, 46.06, 45.61, 42.81, 42.35, 41.80, 41.48, 28.40. HRMS (ESI-QTOF) m/z [M + Na]+ calcd for $C_{26}H_{32}N_4O_5Na$ 503.2270; found 503.2266.

H-L-*Dap(Acryl)-Piperazine-Dansyl* (**66**). Compound **66** was synthesized according to the acid catalyzed Boc deprotection detailed in *General Procedure P*. The product was carried forward without further purification or characterization.

H-L-*Dap(Acryl)-Piperazine-Sulfonyl-Naphthalene* (**67**). Compound **67** was synthesized according to the acid catalyzed Boc deprotection detailed in *General Procedure P*. The product was carried forward without further purification or characterization.

H-L-*Dap(Acryl)-Piperazine-Naphthoyl* (**68**). Compound **68** was synthesized according to the acid catalyzed Boc deprotection detailed in *General Procedure P*. The product was carried forward without further purification or characterization.

t-Butyl-Malonyl-L-*Dap(Acryl)-Piperazine-Dansyl* (**69**). Compound **69** was synthesized according to amide bond coupling reaction outlined in *General Procedure Q* (yield 24%). ^{1}H NMR (400 MHz, $CDCl_3$) δ 8.58 (dt, *J* = 8.6, 1.1 Hz, 1H), 8.33 (dt, *J* = 8.7, 0.9 Hz, 1H), 8.21 (dd, *J* = 7.4, 1.3 Hz, 1H), 7.62 (d, *J* = 7.6 Hz, 1H), 7.54 (ddd, *J* = 8.5, 7.4, 3.5 Hz, 2H), 7.19 (dd, *J* = 7.6, 0.9 Hz, 1H), 6.60 (t, *J* = 5.9 Hz, 1H), 6.19 (dd, *J* = 17.1, 1.4 Hz, 1H), 6.02 (dd, *J* = 17.1, 10.3 Hz, 1H), 5.60 (dd, *J* = 10.3, 1.4 Hz, 1H), 4.96 (td, *J* = 7.4, 3.4 Hz, 1H), 3.79 – 3.57 (m, 5H), 3.39 – 3.04 (m, 7H), 2.88 (s, 6H), 1.44 (s, 9H). ^{13}C NMR (101 MHz, $CDCl_3$) δ 168.21, 167.72, 166.29, 166.11, 152.02, 131.25, 130.95, 130.61, 130.24, 128.49, 126.87, 123.31, 119.40, 115.54, 83.06, 49.67, 45.65, 45.56, 45.33, 42.97, 42.55, 42.03, 28.11. HRMS (ESI-QTOF) m/z [M + Na]+ calcd for $C_{29}H_{39}N_5O_7SNa$ 624.2468; found 624.2469.

t-Butyl-Malonyl-L-*Dap(Acryl)-Piperazine-Naphthoyl* (**70**). Compound **70** was synthesized according to amide bond coupling reaction outlined in *General Procedure Q* (yield 42%). ^{1}H NMR (400 MHz, $CDCl_3$) δ 7.94 – 7.70 (m, 4H), 7.67 – 7.39 (m, 4H), 6.66 (s, 1H), 6.30 – 6.14 (m, 1H), 6.13 – 5.97 (m, 1H), 5.62 (dd, *J* = 15.4, 10.3 Hz, 1H), 5.12 – 4.91 (m, 1H), 4.28 – 3.17 (m, 12H), 1.47 (s, 9H). ^{13}C NMR (101 MHz, $CDCl_3$) δ 169.76, 168.30, 167.85, 166.41, 166.11, 133.64, 133.40, 130.71, 130.53, 129.78, 129.59, 128.77, 127.50, 126.90, 126.77, 125.30, 124.48, 124.16, 83.11, 50.03, 47.15, 46.64, 46.13, 45.63, 43.12, 42.45, 41.71, 41.44, 28.12. HRMS (ESI-QTOF) m/z [M + Na]+ calcd for $C_{28}H_{34}N_4O_6Na$ 545.2376; found 545.2351.

Malonyl-L-*Dap(Acryl)-Piperazine-Dansyl* (**71**). To a round bottom flask was added 0.028 g of the starting **69** (0.047 mmol, 1 eq) suspended in 2 mL toluene. To the flask was then added 0.284 g silica gel (10 × mass) and the reaction mixture was heated to 117 ˚C and stirred for 4 h. Upon completion the reaction mixture was diluted with 10% methanol in DCM and filtered through a pad a celite. The solution was then concentrated under reduced pressure and the resulting crude oil was purified via flash chromatography to yield 0.006 g (21%) of the product as a white yellow solid ^{1}H NMR (600 MHz, MeOD) δ 8.65 – 8.53 (m, 1H), 8.39 (dt, *J* = 8.7, 0.9 Hz, 1H), 8.21 (dd, *J* = 7.3, 1.3 Hz, 1H), 7.61 (ddd, *J* = 16.2, 8.6, 7.4 Hz, 2H), 7.29 (dd, *J* = 7.6, 0.9 Hz, 1H), 6.25 – 6.04 (m, 2H), 5.57 (dd, *J* = 9.5, 2.5 Hz, 1H), 4.99 (dd, *J* = 7.9, 4.5 Hz, 1H), 3.72 – 3.51 (m, 5H), 3.30 – 3.10 (m, 5H), 2.88 (s, 6H), 2.66 (s, 2H). ^{13}C NMR (151 MHz, MeOD) δ 174.89, 171.62, 169.87, 168.63, 153.26, 134.03, 132.02, 131.88, 131.82, 131.56, 131.43, 129.33, 126.86, 124.40, 120.75, 116.65, 107.10, 50.20, 49.57, 46.85, 46.41, 45.78, 42.88, 42.14, 40.41. HRMS (ESI-QTOF) m/z [M + Na]+ calcd for $C_{25}H_{31}N_5O_7SNa$ 568.1842; found 568.1822.

Malonyl-L-*Dap(Acryl)-Piperazine-Naphthoyl* (**72**). Compound **72** was synthesized according to *General Procedure P* and purified via flash chromatography (yield 30%). ^{1}H NMR (400 MHz, MeOD) δ 8.01 – 7.89 (m, 2H), 7.83 (t, *J* = 8.8 Hz, 1H), 7.64 – 7.45 (m, 4H), 6.26 – 6.12 (m, 2H), 5.71 – 5.58 (m, 1H), 5.22 – 4.99 (m, 1H), 4.21 – 3.04 (m, 12H). ^{13}C NMR (101 MHz, MeOD) δ 171.78, 171.66, 169.91, 168.97, 168.72, 134.96, 134.56, 131.78, 131.67, 130.77, 130.69, 129.70, 128.47, 128.44, 127.80, 127.18, 126.36, 125.47, 125.23, 50.44, 47.82, 46.93, 46.39, 43.59, 43.06, 43.01, 42.56, 41.98. HRMS (ESI-QTOF) m/z [M + Na]+ calcd for $C_{24}H_{26}N_4O_6Na$ 489.1750; found 489.1767.

Methyl-Ester-Cyclopropyl-L-*Dap(Acryl)-Piperazine-Dansyl* (**73**). Compound **73** was synthesized according to the amide bond coupling reaction detailed in *General Procedure Q* (yield 85%). ^{1}H NMR (400 MHz, $CDCl_3$) δ 9.52 (d, *J* = 7.4 Hz, 1H), 8.58 (d, *J* = 8.5 Hz, 1H), 8.34 (d, *J* = 8.7 Hz, 1H), 8.24 – 8.13 (m, 1H), 7.62 – 7.45 (m, 2H), 7.19 (d, *J* = 7.6 Hz, 1H), 6.53 (t, *J* = 5.8 Hz, 1H), 6.18 (dd, *J* = 17.0, 1.5 Hz, 1H), 6.02 (dd, *J* = 17.0, 10.2 Hz, 1H), 5.58 (dd, *J* = 10.2, 1.5 Hz, 1H), 4.95 (td, *J* = 7.2, 3.7 Hz, 1H), 3.85 – 3.51 (m, 8H), 3.40 – 3.08 (m, 6H), 2.89 (s, 6H), 1.55 (tdd, *J* = 18.8, 9.3, 5.5 Hz, 4H). ^{13}C NMR (101 MHz, $CDCl_3$) δ 173.34, 169.41, 168.24, 166.10, 132.51, 131.05, 130.69, 130.39, 128.38, 126.84, 123.56, 115.77, 52.58, 49.79, 45.70, 45.36, 45.28, 42.78, 41.97, 26.34, 20.51, 20.37. HRMS (ESI-QTOF) m/z [M + Na]+ calcd for $C_{28}H_{35}N_5O_7SNa$ 608.2155; found 608.2166.

Acid-Cyclopropyl-L-*Dap(Acryl)-Piperazine-Dansyl* (**74**). Compound **74** was synthesized according to the hydrolysis reaction in *General Procedure T* (yield 50%). ^{1}H NMR (600 MHz, MeOD) δ 8.62 (dt, *J* = 8.6, 1.1 Hz, 1H), 8.39 (dt, *J* = 8.7, 0.9 Hz, 1H), 8.20 (dd, *J* = 7.3, 1.3 Hz, 1H), 7.60 (ddd, *J* = 17.4, 8.6, 7.5 Hz, 2H), 7.28 (dd, *J* = 7.6, 0.9 Hz, 1H), 6.17 – 6.04 (m, 2H), 5.56 (dd, *J* = 7.0, 5.0 Hz, 1H), 5.01 (dd, *J* = 7.5, 5.1 Hz, 1H), 3.74 – 3.60 (m, 3H), 3.58 – 3.50 (m, 2H), 3.35 (dd, *J* = 13.7, 7.5 Hz, 1H), 3.30 – 3.12 (m, 4H), 2.88 (s, 6H), 1.33 – 1.26 (m, 2H), 1.23 – 1.19 (m, 1H), 1.16 – 1.11 (m, 1H). ^{13}C NMR (151 MHz, MeOD) δ 178.43, 175.05, 170.39, 168.58, 153.26, 134.02, 132.02, 131.77, 131.70, 131.56, 131.42, 129.34, 127.00, 124.41, 120.71, 116.64, 50.16, 46.89, 46.53, 46.48, 45.78, 42.92, 42.28, 28.42, 19.18, 18.99. HRMS (ESI-QTOF) m/z [M + Na]+ calcd for $C_{27}H_{32}N_5O_7SNa_2$ 616.1818; found 616.1846.

Succinyl-L-*Dap(Acryl)-Piperazine-Dansyl* (**75**). Compound **75** was synthesized according to *General Procedure U* with succinic anhydride (yield 83%). ^{1}H NMR (400 MHz, MeOD) δ 8.65 – 8.58 (m, 1H), 8.39 (d, *J* = 8.7 Hz, 1H), 8.20 (dd, *J* = 7.4, 1.3 Hz, 1H), 7.60 (ddd, *J* = 10.9, 8.6, 7.4 Hz, 2H), 7.27 (d, *J* = 7.5 Hz, 1H), 6.12 (d, *J* = 6.0 Hz, 2H), 5.56 (t, *J* = 6.0 Hz, 1H), 4.96 (dd, *J* = 7.5, 5.1 Hz, 1H), 3.71 – 3.49 (m, 5H), 3.35 (d, *J* = 2.7 Hz, 1H), 3.30 – 3.07 (m, 4H), 2.87 (s, 6H), 2.55 – 2.32 (m, 4H). ^{13}C NMR (101 MHz, MeOD) δ 174.41, 170.08, 168.57, 153.24, 133.93, 132.02, 131.85, 131.70, 131.56, 131.39, 129.32, 127.05, 124.40, 120.73, 116.62, 49.97, 46.95, 46.47, 46.43, 45.77, 42.91, 41.92, 31.65, 30.71. HRMS (ESI-QTOF) m/z [M + Na]+ calcd for $C_{26}H_{33}N_5O_7SNa$ 582.1998; found 582.1996.

Succinyl-L-*Dap(Acryl)-Piperazine-Sulfonyl-Naphthalene* (**76**). Compound **76** was synthesized according to *General Procedure U* with succinic anhydride (yield 24%). ^{1}H NMR (600 MHz, MeOD) δ 8.74 (dq, *J* = 8.7, 0.9 Hz, 1H), 8.20 (td, *J* = 7.4, 1.1 Hz, 2H), 8.02 (ddt, *J* = 8.1, 1.3, 0.6 Hz, 1H), 7.69 (ddd, *J* = 8.6, 6.9, 1.4 Hz, 1H), 7.66 (s, 2H), 6.15 – 6.05 (m, 2H), 5.60 – 5.53 (m, 1H), 4.96 (dd, *J* = 7.5, 5.2 Hz, 1H), 3.70 – 3.57 (m, 3H), 3.57 – 3.47 (m, 2H), 3.33 (d, *J* = 7.5 Hz, 1H), 3.29 – 3.07 (m, 4H), 2.55 – 2.50 (m, 2H), 2.46 – 2.32 (m, 2H). ^{13}C NMR (151 MHz, MeOD) δ 176.37, 174.21, 170.08, 168.55, 136.03, 135.94, 133.56, 131.92, 131.64, 130.22, 130.09, 129.30, 128.13, 127.11, 126.10, 125.44, 49.92, 46.98, 46.50, 46.41, 42.88, 41.89, 31.29, 30.11. HRMS (ESI-QTOF) m/z [M + Na]+ calcd for $C_{24}H_{28}N_4O_7SNa$ 539.1576; found 539.1563.

Succinyl-L-*Dap(Acryl)-Piperazine-Naphthoyl* (**77**). Compound **77** was synthesized according to *General Procedure U* with succinic anhydride (yield 11%). ^{1}H NMR (600 MHz, MeOD) δ 8.01 – 7.90 (m, 2H), 7.83 (t, *J* = 8.0 Hz, 1H), 7.63 – 7.47 (m, 4H), 6.30 – 6.10 (m, 2H), 5.72 – 5.58 (m,

1H), 5.17 – 4.95 (m, 1H), 4.16 – 3.36 (m, 9H), 3.28 – 3.15 (m, 1H), 2.63 – 2.38 (m, 4H). ^{13}C NMR (151 MHz, MeOD) δ 177.07, 174.59, 171.81, 170.23, 168.67, 134.98, 134.58, 131.82, 131.70, 130.77, 130.71, 129.70, 129.55, 128.43, 127.80, 127.13, 126.36, 125.49, 125.21, 125.10, 50.32, 48.39, 47.87, 46.93, 46.37, 43.59, 43.09, 43.00, 42.59, 41.99, 31.77, 30.84. HRMS (ESI-QTOF) m/z [M + Na]+ calcd for $C_{25}H_{28}N_4O_6Na$ 503.1907; found 503.1898.

*Methyl-Ester-Sulfonyl-*L*-Dap(Acryl)-Piperazine-Dansyl* (**78**). Compound **78** was synthesized via a sulfonylation reaction. To a round bottom flask was added 0.091 g of the free amine starting material **66** (0.198 mmol, 1 eq) along with 0.030 mL triethylamine (0.218 mmol, 1.1 eq) solubilized in 2 mL DCM. To the flask was subsequently added 0.037 g methyl (chlorosulfonyl)acetate (0.218 mmol, 1.1 eq) and the reaction mixture was stirred at room temperature for 1.5 h. Upon completion the reaction mixture was washed three times with a saturated solution of $NaHCO_3$ and brine. The organic layer was dried over $MgSO_4$, filtered, and concentrated under reduced pressure. The resulting crude oil was purified via flash chromatography to obtain 0.059 g (50%) of product **78** and carried forward to the hydrolysis reaction without further characterization.

*Acid-Sulfonyl-*L*-Dap(Acryl)-Piperazine-Dansyl* (**79**). Compound **79** was synthesized according to *General Procedure T* (yield 83%). ^{1}H NMR (400 MHz, MeOD) δ 8.61 (dt, *J* = 8.6, 1.1 Hz, 1H), 8.37 (d, *J* = 8.7 Hz, 1H), 8.20 (dd, *J* = 7.4, 1.3 Hz, 1H), 7.60 (ddd, *J* = 9.9, 8.7, 7.5 Hz, 2H), 7.27 (dd, *J* = 7.6, 0.9 Hz, 1H), 6.23 – 6.07 (m, 2H), 5.57 (dd, *J* = 8.9, 3.0 Hz, 1H), 4.69 (dd, *J* = 7.8, 4.8 Hz, 1H), 3.83 (s, 2H), 3.72 (t, *J* = 5.2 Hz, 2H), 3.60 (t, *J* = 5.2 Hz, 2H), 3.50 (dd, *J* = 13.7, 4.7 Hz, 1H), 3.35 (s, 1H), 3.31 – 3.15 (m, 4H), 2.87 (s, 6H). ^{13}C NMR (101 MHz, MeOD) δ 170.46, 169.38,

168.57, 153.19, 134.05, 131.99, 131.71, 131.62, 131.45, 131.34, 129.34, 127.23, 124.39, 120.63, 116.61, 53.90, 46.74, 46.58, 46.30, 45.77, 43.13. HRMS (ESI-QTOF) m/z [M + Na]+ calcd for $C_{24}H_{30}N_5O_8S_2Na_2$ 626.1331; found 626.1343.

Cbz-D-*Dap(Boc)-Piperazine-Naphthoyl* (**80**). Compound **80** was synthesized according to the amide bond coupling reaction outlined in *General Procedure Q* (yield 74%). ^{1}H NMR (400 MHz, $CDCl_3$) δ 7.96 – 7.76 (m, 3H), 7.57 – 7.38 (m, 4H), 7.37 – 7.26 (m, 5H), 6.06 – 5.85 (m, 1H), 5.14 – 4.97 (m, 3H), 4.89 – 4.63 (m, 1H), 4.20 – 3.12 (m, 10H), 1.47 – 1.30 (m, 9H). ^{13}C NMR (101 MHz, $CDCl_3$) δ 169.72, 168.56, 156.14, 156.07, 136.25, 133.62, 129.70, 128.73, 128.65, 128.36, 128.25, 128.19, 127.37, 126.76, 125.30, 124.56, 124.08, 79.95, 67.15, 51.30, 47.14, 46.59, 46.05, 45.59, 43.09, 42.79, 42.34, 41.76, 41.41, 28.40. HRMS (ESI-QTOF) m/z [M + Na]+ calcd for $C_{31}H_{36}N_4O_6Na$ 583.2533; found 583.2540.

H-D-*Dap(Boc)-Piperazine-Naphthoyl* **(81**). Compound **81** was synthesized according to the hydrogenolysis reaction detailed in *General Procedure R*. The product was carried forward without further purification or characterization.

Acryl-D-*Dap(Boc)-Piperazine-Naphthoyl* (**82**). To a round bottom flask was added 2.49 g of the starting amine **81** (5.842 mmol, 1 eq), 2.035 mL DIPEA (11.684 mmol, 2 eq), and 0.071 g DMAP (0.584 mmol, 0.1 eq) solubilized in 60 mL DCM at 0 ˚C. To the flask was then added 0.563 mL acryloyl chloride (7.010 mmol, 1.2 eq) dropwise. The reaction was allowed to warm to room temperature and stirred for 2 h. Upon completion, the reaction mixture was washed with water, and three times with a saturated solution of $NaHCO_3$. The organic phase was dried with $MgSO_4$,

filtered, and concentrated under reduced pressure. The resulting crude oil was purified via flash chromatography to yield 1.730 g (62%) of the product **82** as a white solid. ^{1}H NMR (400 MHz, $CDCl_3$) δ 7.96 – 7.76 (m, 3H), 7.59 – 7.38 (m, 4H), 6.92 (s, 1H), 6.38 – 6.05 (m, 2H), 5.71 – 5.61 (m, 1H), 5.16 – 4.92 (m, 2H), 4.28 – 3.65 (m, 4H), 3.62 – 3.13 (m, 6H), 1.48 – 1.34 (m, 9H). ^{13}C NMR (101 MHz, $CDCl_3$) δ 169.76, 168.47, 165.36, 156.21, 133.63, 133.48, 130.37, 129.75, 129.64, 128.74, 127.53, 127.41, 126.77, 125.31, 124.59, 124.10, 80.03, 50.21, 47.08, 46.57, 46.10, 45.63, 42.87, 42.42, 41.71, 41.36, 28.42. HRMS (ESI-QTOF) m/z [M + Na]+ calcd for $C_{26}H_{32}N_4O_5Na$ 503.2270; found 503.2256.

TFA.Acryl-D-*Dap-Piperazine-Naphthoyl* (**83**). Compound **83** was synthesized according to the Boc deprotection reaction outlined in *General Procedure P*, excluding the $NaHCO_3$ washes and carried forward as the TFA salt in quantitate yield after concentrating the reaction mixture.

Acryl-D-*Dap(Succinyl)-Piperazine-Naphthoyl* (**84**). Compound **84** was synthesized according to *General Procedure U* with succinic anhydride (yield 83%). ^{1}H NMR (400 MHz, MeOD) δ 8.03 – 7.77 (m, 3H), 7.62 – 7.45 (m, 4H), 6.39 – 6.13 (m, 2H), 5.75 – 5.62 (m, 1H), 5.24 – 4.98 (m, 1H), 4.14 – 3.34 (m, 9H), 3.29 – 3.12 (m, 1H), 2.58 – 2.37 (m, 4H). ^{13}C NMR (101 MHz, MeOD) δ 177.25, 175.64, 171.80, 170.32, 167.72, 134.95, 134.59, 131.57, 130.77, 130.70, 129.70, 128.46, 127.80, 127.62, 126.37, 125.50, 125.23, 52.13, 50.45, 47.85, 46.99, 46.45, 43.64, 43.04, 42.59, 41.88, 31.99, 31.92, 31.07, 30.65, 30.23. HRMS (ESI-QTOF) m/z [M + Na]+ calcd for $C_{25}H_{28}N_4O_6Na$ 503.1907; found 503.1897.

Boc-Glu(MA)-Piperazine-Naphthoyl (**85**). Compound **85** was synthesized via an amide bond coupling reaction. To a round bottom flask was added 0.737 g of compound **28** (2.567 mmol, 1

eq) with 1.168 g HBTU (3.080 mmol, 1.2 eq) and 1.733 mL DIPEA (10.267 mmol, 4 eq) solubilized in 7 DMF at 0 ˚C. The activation of the acid was allowed to occur for 0.5 h upon which 1.091 g of the corresponding TFA salt **56*** (3.080 mmol, 1.2 eq) was added as a solution in 2 mL DMF with 0.433 mL DIPEA (2.567 mmol, 1 eq). The reaction was allowed to stir overnight at room temperature. Upon completion, the reaction mixture was diluted with ethyl acetate and washed with 1 M HCl, water, a saturated solution of $NaHCO_3$, and brine. The organic layer was dried over $MgSO_4$, filtered, and concentrated under reduced pressure. The resulting crude oil was purified via flash chromatography to yield 1.000 g (77%) of the product as a white solid. ^{1}H NMR (400 MHz, $CDCl_3$) δ 8.00 – 7.72 (m, 3H), 7.64 – 7.35 (m, 4H), 7.01 – 6.79 (m, 1H), 5.91 – 5.75 (m, 1H), 5.35 (d, *J* = 8.6 Hz, 1H), 4.79 – 4.38 (m, 1H), 4.20 – 3.11 (m, 11H), 2.39 – 2.14 (m, 2H), 1.93 – 1.56 (m, 2H), 1.53 – 1.32 (m, 9H). ^{13}C NMR (101 MHz, $CDCl_3$) δ 170.59, 169.74, 166.81, 155.46, 147.49, 133.62, 133.40, 129.74, 128.74, 127.40, 126.76, 125.29, 124.52, 124.08, 122.06, 80.18, 51.61, 49.56, 47.32, 46.89, 45.81, 45.62, 42.72, 42.26, 42.02, 41.64, 31.89, 28.42, 28.00. HRMS (ESI-QTOF) m/z [M + Na]+ calcd for $C_{28}H_{35}N_3O_6Na$ 532.2424; found 532.2449.

TFA.H-Glu(MA)-Piperazine-Naphthoyl (**86**). Compound **86** was synthesized according to *General Procedure P*, excluding the $NaHCO_3$ washes and carried forward as the TFA salt in quantitate yield after concentrating the reaction mixture.

Succinyl-Glu(MA)-Piperazine-Naphthoyl (**87**). Compound **87** was synthesized according to *General Procedure U* with succinic anhydride, DIPEA as the base, and DMF as the solvent (yield 67%). ^{1}H NMR (400 MHz, MeOD) δ 8.01 – 7.77 (m, 3H), 7.63 – 7.46 (m, 4H), 7.03 – 6.84 (m, 1H), 5.95 – 5.80 (m, 1H), 4.72 (dd, *J* = 8.6, 5.3 Hz, 1H), 4.17 – 3.43 (m, 9H), 3.30 – 3.20 (m, 2H),

2.65 – 2.60 (m, 1H), 2.57 – 2.43 (m, 3H), 2.34 – 2.18 (m, 2H), 1.97 – 1.72 (m, 2H). ^{13}C NMR (101 MHz, MeOD) δ 176.07, 174.15, 172.06, 171.74, 168.52, 149.58, 134.94, 134.58, 130.75, 129.69, 128.44, 127.78, 126.35, 125.49, 125.22, 122.62, 52.18, 51.95, 49.85, 47.91, 46.97, 46.39, 43.58, 43.14, 42.99, 42.66, 31.41, 31.23, 30.04, 29.79, 29.25. HRMS (ESI-QTOF) m/z [M + Na]+ calcd for $C_{27}H_{31}N_3O_7Na$ 532.2060; found 532.2076.

Phthalyl-Glu(MA)-Piperazine-Naphthoyl (**88**). Compound **88** was synthesized according to *General Procedure U* with phthalic anhydride, DIPEA as the base, and DMF as the solvent (yield 59%). ^{1}H NMR (400 MHz, MeOD) δ 8.04 – 7.92 (m, 2H), 7.91 – 7.76 (m, 2H), 7.65 – 7.33 (m, 6H), 7.24 – 7.09 (m, 1H), 7.05 – 6.88 (m, 1H), 5.99 – 5.83 (m, 1H), 5.08 (s, 1H), 4.27 – 3.33 (m, 8H), 3.36 – 3.08 (m, 3H), 2.32 (s, 2H), 2.04 – 1.78 (m, 2H). ^{13}C NMR (101 MHz, MeOD) δ 175.26, 171.74, 168.56, 168.53, 164.82, 149.66, 138.89, 138.51, 134.96, 134.60, 132.24, 130.93, 130.76, 129.91, 129.70, 129.20, 128.93, 128.45, 127.79, 126.36, 126.29, 125.50, 125.23, 122.71, 122.66, 51.97, 50.36, 47.92, 46.63, 43.77, 43.14, 42.68, 36.93, 31.64, 31.18, 30.90, 29.43. HRMS (ESI-QTOF) m/z [M + Na]+ calcd for $C_{31}H_{31}N_3O_7Na$ 580.2060; found 580.2090.

*Fmoc-6AH-OH **89***. Commercially available 6-aminohexanoic acid (1.000 g, 7.62 mmol, 1 eq) and $Na_2CO_{3(s)}$ (3 eq) were added to a round-bottom flask and dissolved in a 1:1 mixture of H_2O/dioxane (0.1 M). The flask was cooled to 0 °C, stirring was commenced, and fluorenylmethyloxycarbonyl chloride (1 eq) was added in 1 portion. The reaction mixture was stirred at 0 °C for 10 min, and was then allowed to warm to room temperature where it was stirred for another 6 h. Upon completion, dioxane was removed through rotary evaporation and the resulting aqueous solution was washed with Et_2O. The recovered aqueous layer was subsequently acidified to around pH 2

through the addition of 1 M $HCl_{(aq)}$ and extracted thrice into EtOAc. The combined organics were dried over $MgSO_4$, filtered, and concentrated under reduced pressure to yield the desired product as a white solid (2.500 g, 7.09 mmol, 93% yield). Characterization matches previous reports [77].

Fmoc-D-*Asp(OtBu)-CTC* ***90***. Compound **90** was prepared from fresh 2-chlorotrityl chloride resin (100-200 mesh, 1.00 g, 0.75 mmol, 1 eq) and Fmoc-D-Asp(OtBu)-OH **9** (1.2 eq) through *General Procedure D*. The resin loading was estimated as 0.500 mmol/g, and 1.00 g of loaded resin was recovered (0.50 mmol, 67% yield).

RhB-Pro-6AH-D-*Asp(OtBu)-OH* ***91***. Manually-loaded Fmoc-D-Asp(OtBu)-CTC resin **90** (0.5 mmol, 1 eq) was placed into the automated peptide synthesizer and swelled in 20 mL DMF for 5 min. Fmoc-6AH-OH **89** (4 eq) and Fmoc-Pro-OH (4 eq) were then coupled through cycles of standard deprotections (10 mL of 20% v/v piperidine in DMF at 90 °C for 1 min) and couplings (4 eq HATU, 8 eq DIPEA in 16 mL 7:1 DMF/NMP solution at 50 °C over 10 min). The resin was washed 3 times with 7-10 mL of DMF between each step. After deprotection of the Pro residue's Fmoc group, the resin was removed from the instrument. Rhodamine B was double-coupled manually (5 eq rhodamine B, 5 eq HATU, 10 eq DIPEA, 10 mL DMF, two cycles of 40 min each at room temperature). The resin was then washed with DMF and DCM. The peptide was cleaved from the resin through two 30 min treatments with 20% HFIP in DCM. The crude mixture was concentrated through rotary evaporation, precipitated in cold ether, and pelleted through centrifugation. Discarding of the supernatant and extensive drying under vacuum produced the desired peptide as a red solid (282 mg, 0.34 mmol, 68% yield), which was carried forward without further purification. LC-MS *m/z* 825 for $[M]^+$.

*RhB-Pro-6AH-*D*-Asp(OtBu)-Glu(MA)-Nle-Nle-Leu-Pro-Trp-Pro-OH (**51**).* Compound **92** was prepared through *General Procedure M* using TFA.H-Glu(MA)-Nle-Nle-Leu-Pro-Trp-Pro-OH **40** (347 mg, 0.34 mmol, 1 eq) and RhB-Pro-6AH-D-Asp(OtBu)-OH **91** (282 mg, 0.34 mmol, 1 eq), both prepared herein. The reaction flask was covered with aluminum foil to prevent degradation of the fluorophore from exposure to light. The desired peptide was obtained as a deep purple solid (85.7 mg, 0.050 mmol, 15% yield). LC-MS *m/z* 1714 for $[M]^+$.

*RhB-Pro-6AH-*D*-Asp-Glu(MA)-Nle-Nle-Leu-Pro-Trp-Pro-OH (**93, KM93**).* Compound **93** (**KM93**) was prepared through *General Procedure N* from RhB-Pro-6AH-D-Asp(OtBu)-Glu(MA)-Nle-Nle-Leu-Pro-Trp-Pro-OH **92** (85.7 mg, 0.050 mmol, 1 eq). The reaction flask was covered with aluminum foil to prevent degradation of the fluorophore from exposure to light. The desired peptide was obtained as a bright magenta solid (23.6 mg, 0.014 mmol, 28% yield). HRMS (ESI-QTOF) *m/z* $[M]^+$ calcd for $C_{90}H_{122}N_{13}O_{17}$ 1656.9082; found 1656.9102.

Supplementary Kinetic Traces and Inhibition Experiments

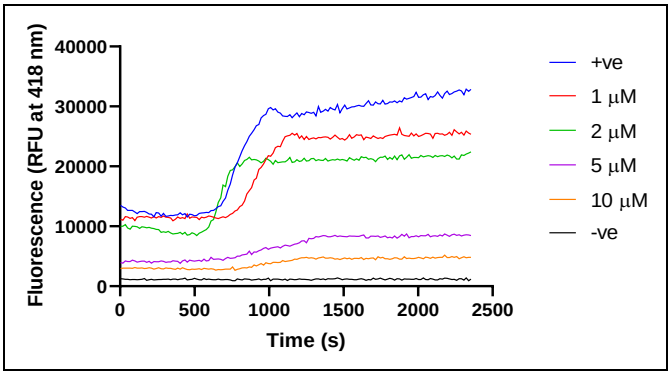

Figure S1. *Fluorescence-time curve of the spike experiment performed with inhibitor* ***47*** *to confirm the reversibility of FXIIIa inhibition. Additional A101 substrate was added to the reactions corresponding to the positive control with no inhibitor (+ve), the negative control with no enzyme (-ve), and all 4 inhibitor concentrations (1, 2, 5, and 10 µM) after the initial plateaus in fluorescence had been reached. Fluorescence emission (RFU, relative fluorescence unit emission at 418 nm after excitation at 313 nm) was then monitored over time.*

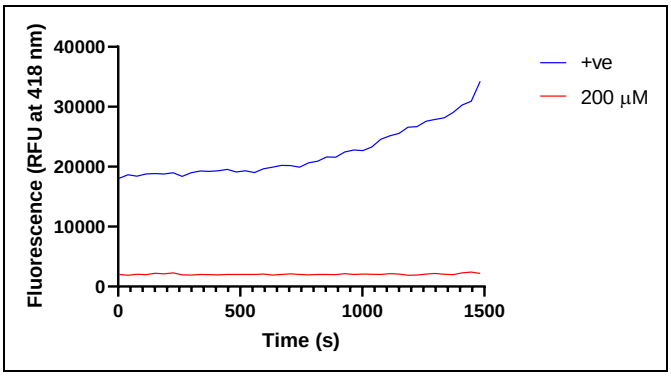

Figure S2. *Fluorescence-time curve of the spike experiment performed with inhibitor* ***23*** *to confirm the irreversibility of FXIIIa inhibition. Additional A101 substrate was added to the reactions corresponding to the positive control with no inhibitor (+ve) and the highest inhibitor concentration (200 µM) after the initial plateaus in fluorescence had been reached.*

Fluorescence emission (RFU, relative fluorescence unit emission at 418 nm after excitation at 313 nm) was then monitored over time.

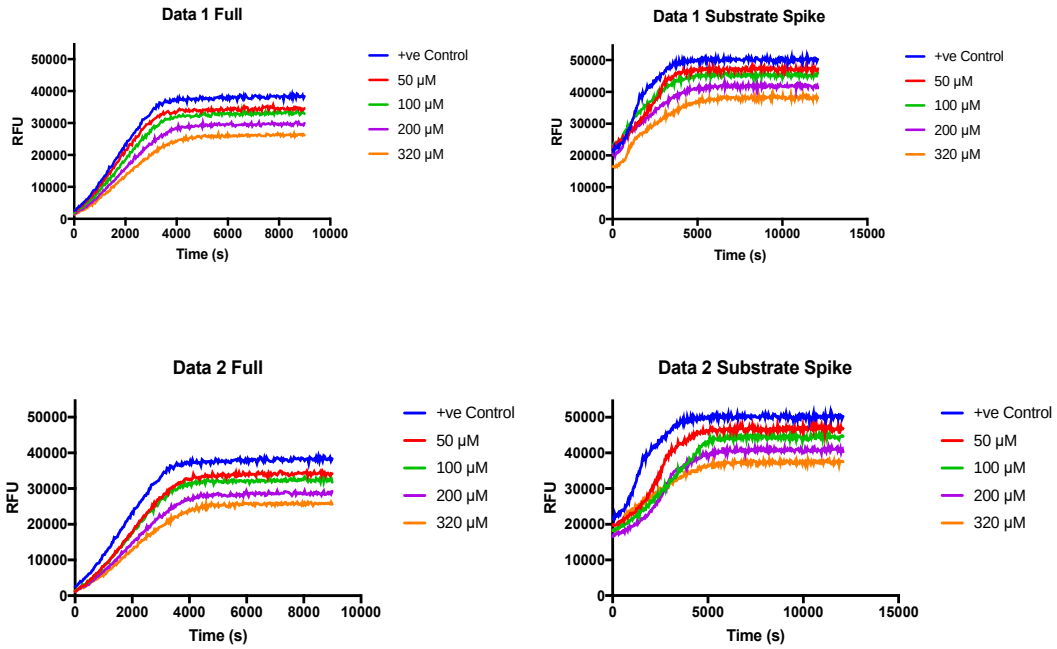

Figure S3. *Substrate spike experiment with small molecule inhibitor* ***79*** *and FXIIIa. Upon completion of the activity assay, another 100 µM of A101 was added and the RFU increased, implying FXIIIa was still active (top and bottom left panels).*

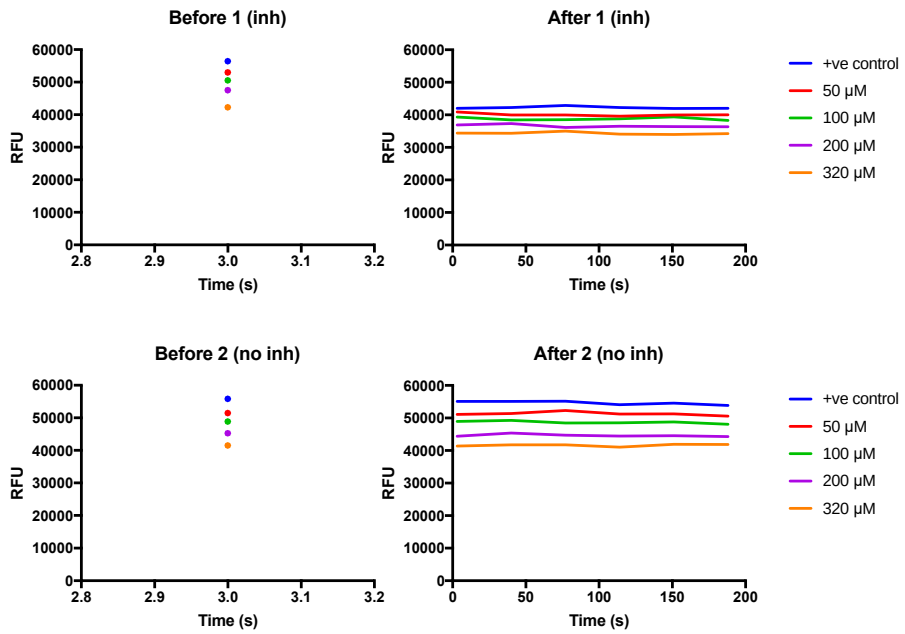

Figure S4. *Inhibitor spike experiment with small molecule inhibitor* ***79****. Upon completion of the activity assay another dose of 320 µM* ***79*** *was added and the RFU plateau at a lower value (top right panel).*

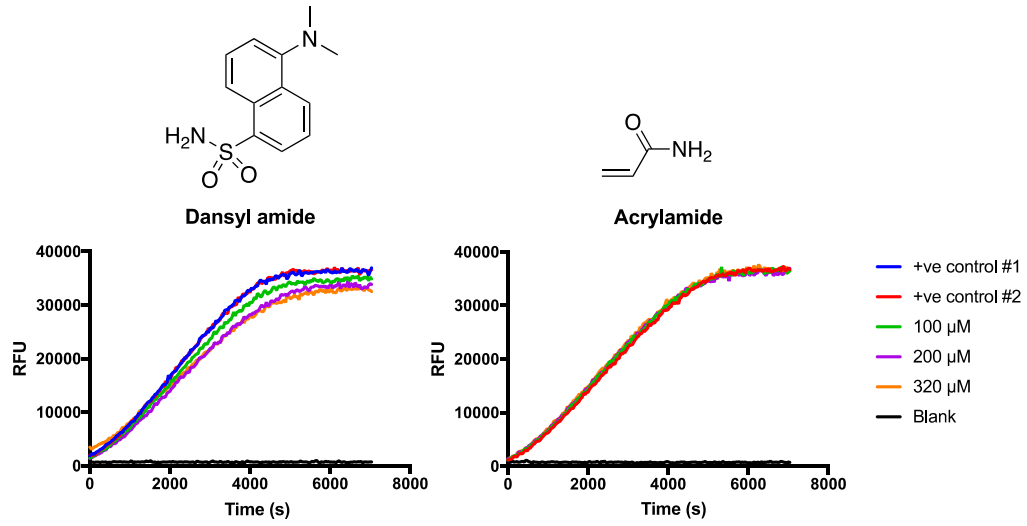

Figure S5. *Inhibition experiment of FXIIIa with small molecule inhibitor scaffold components dansyl amide and acrylamide assayed at four different concentrations (0, 100, 200, 320 µM).*

SDS-PAGE of Fluorescent Labelling Experiment

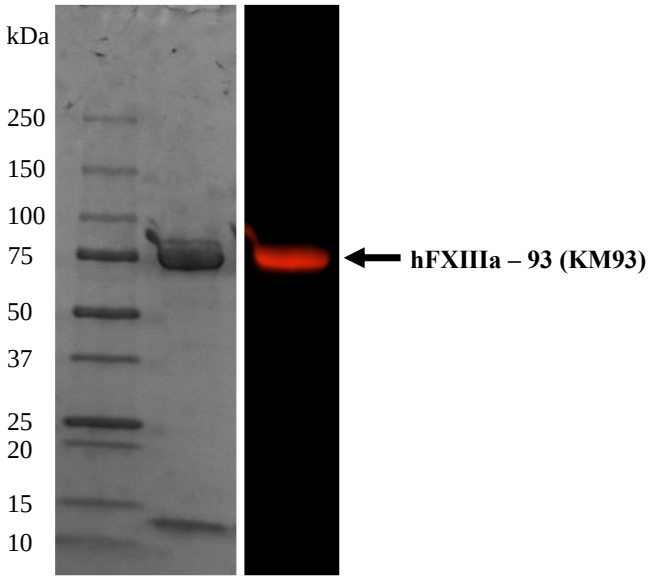

Figure S6. *SDS-PAGE of commercially available FXIIIa incubated with 30 µM fluorescent probe* ***93 (KM93)*** *visualized first for fluorescence and then using Coomassie Blue staining.*

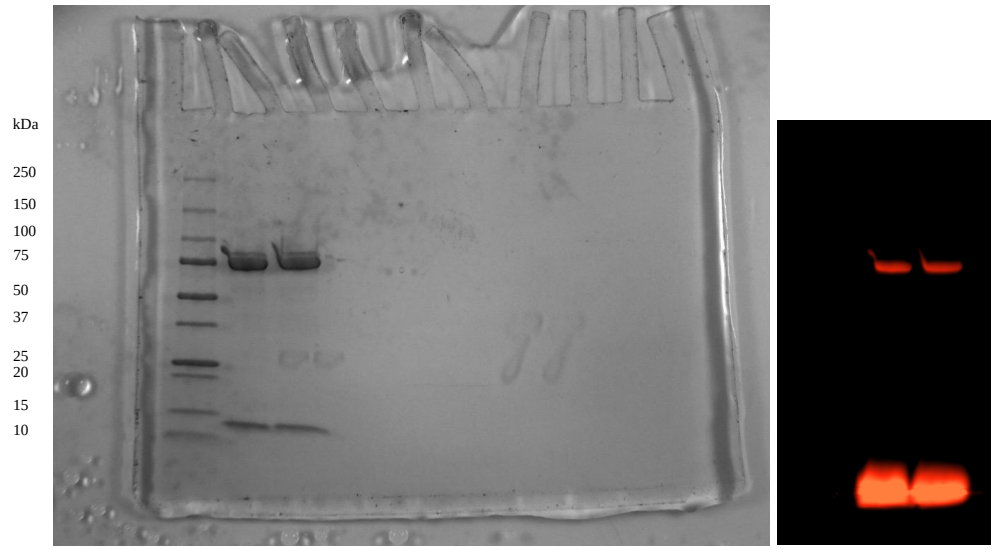

Figure S7. *Full SDS-PAGE gel of fluorescent labelling of commercially available FXIIIa with 30 µM* ***93 (KM93)****. Note the excess labelling agent at the very bottom edge of the gel does not correspond to protein.*

Supplementary Cellular Labelling Figures

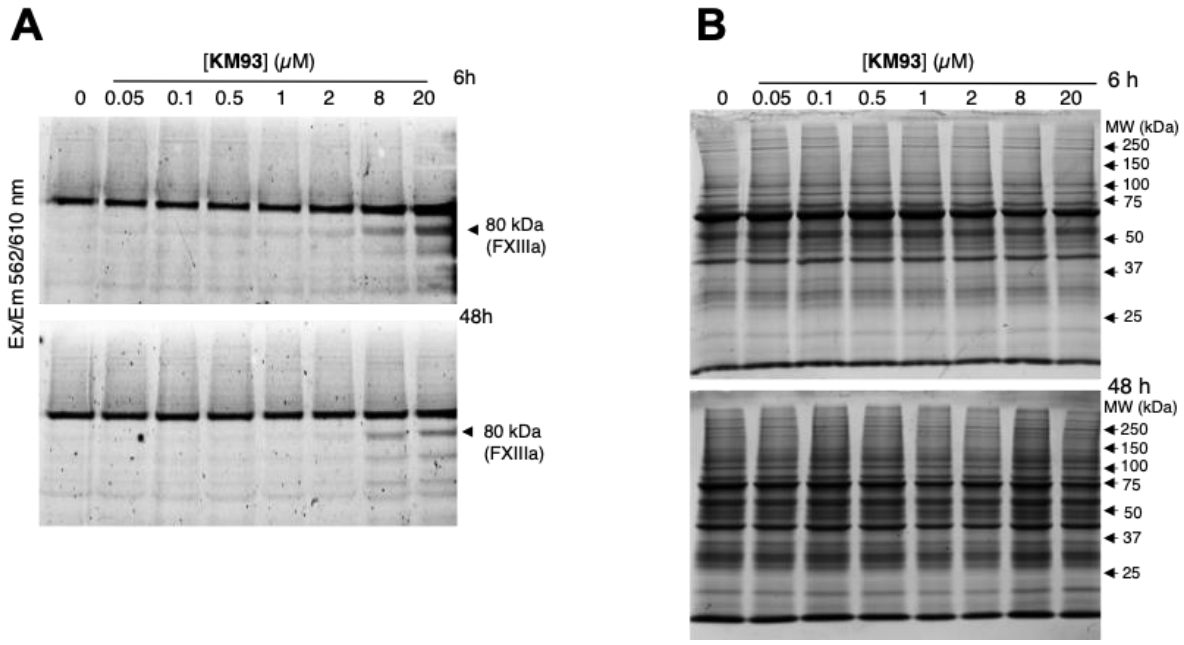

Figure S8. A) Fluorescent labelling of FXIIIa in murine bone marrow macrophages (BMM). BMMs were incubated with 0-20 µM **KM93** for 6 h (top gel) or for 48 h (bottom gel), lysed, and protein extracts were prepared and resolved with denaturing, 10% SDS-PAGE. The gels were visualized using a fluoroimager (Ex/Em 562/610). The gels show a dose dependent labelling of a ~80 kDa band, which corresponds to a molecular weight of FXIIIa, consistent with the red fluorescence of the rhodamine moiety of **KM93**. The identity of the band at ~100 kDa is unknown but it is also present in the negative control and thus represents background. **B)** Coomassie Blue stained gels confirm equal loading in each lane.

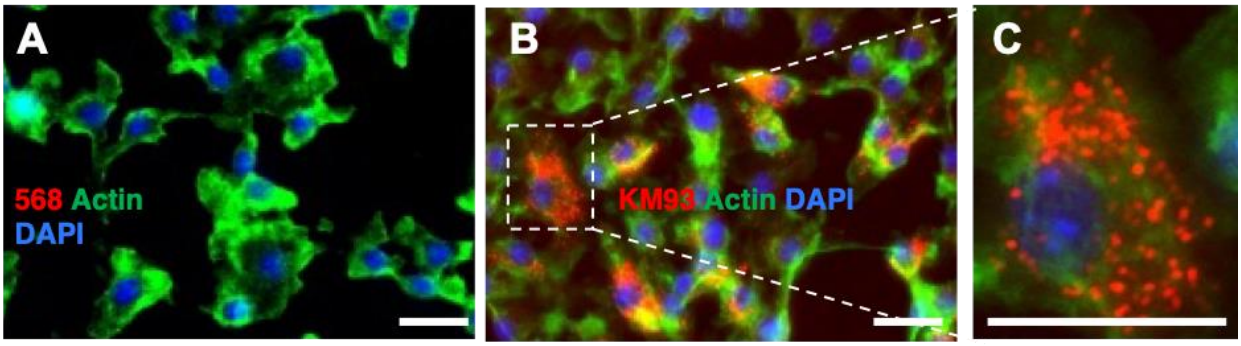

Figure S9. Fluorescence visualization of **KM93** in murine bone marrow macrophages (BMM). Cells were incubated with 20 µM **KM93** for 48 h in microscopy chamber slides. At end point, cells were fixed, cytoskeletal actin was stained with AlexaFluor®-488-phalloidin (green) and nuclei were stained with DAPI (blue). **KM93** was visualized in the 568-nm channel (red). **A)**: Cells that were incubated in the absence of the probe showed no signal in the 568-nm channel (negative control). **B)**: Strong red fluorescence was seen observed after 48 h incubation with 20 µM **KM93**. The probe was confirmed to be intracellular by actin staining (see inset **C**). White magnification bar represents 20 µm.

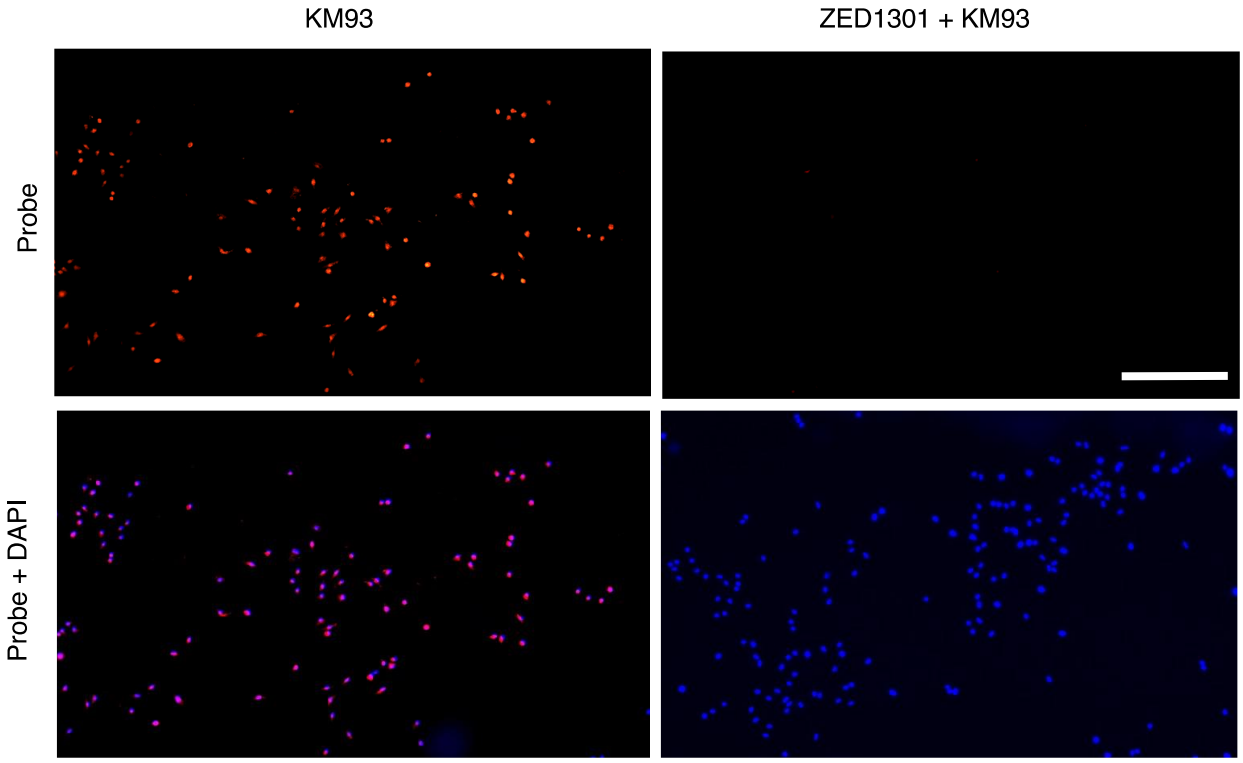

Figure S10. FXIIIa inhibitor ZED1301 is able to block labelling by KM93 probe in BMM cells. BMM cells were preincubated in the absence or presence of 20 µM ZED1301 for 2 hours to inhibit FXIIIa, prior to addition of 20 µM **KM93** and further incubation for 4 hours. Cells were fixed and washed, nuclei were stained with DAPI (blue) and incorporation of the red probe **KM93** was observed by fluorescence microscopy. Negligible red fluorescence was observed in cells blocked by pre-incubation with ZED1301. Magnification bar equals 40 µm.

Kinetic Fitting for Inhibitors

Inhibitor	FXIIIa	TG2
11	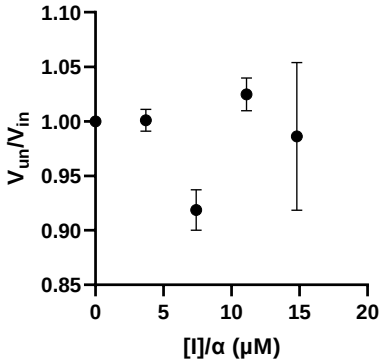 No inhibition	No inhibition
12	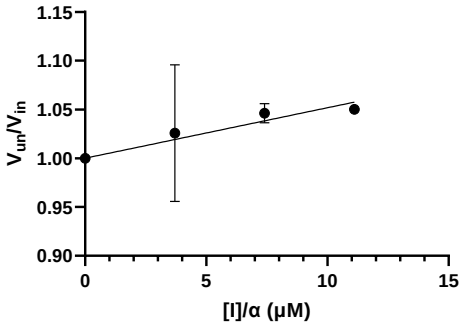 K_i = 193 ± 20 μM	No inhibition
13	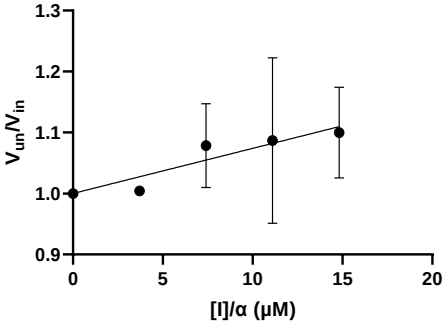 K_i = 135 ± 16 μM	No inhibition

14	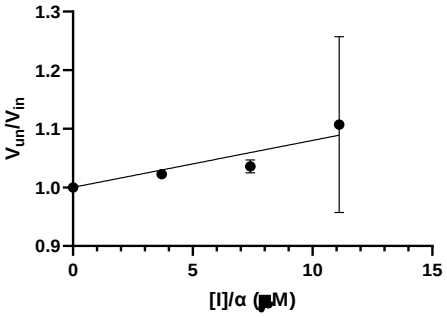 K_i = 125 ± 20 μM	No inhibition
20	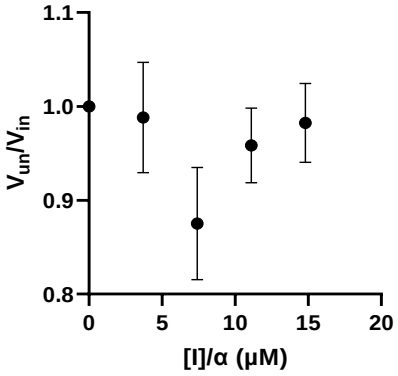 No inhibition	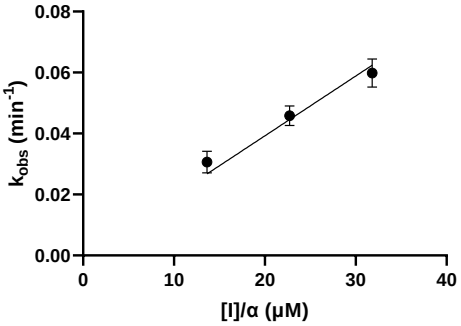 k_{inact}/K_I = 7422 ± 525 M^{-1} min^{-1}
21	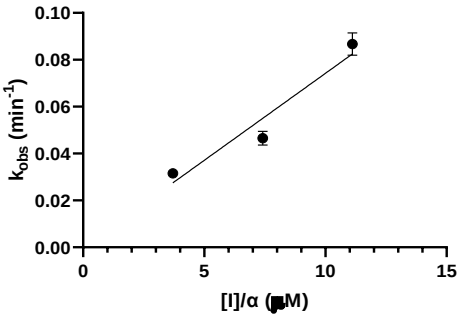 k_{inact}/K_I = 7422 ± 525 M^{-1} min^{-1}	No inhibition

22	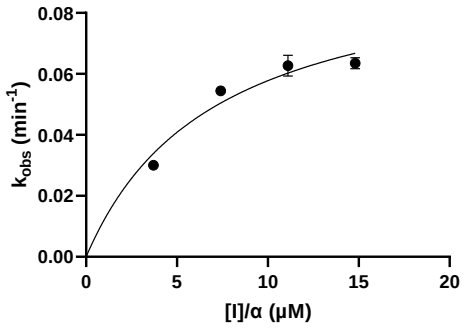 k_{inact}/K_I = 13922 ± 6664 M^{-1} min^{-1} k_{inact} = 0.0988 ± 0.0185 min^{-1} K_I = 7.1 ± 3.1 μM	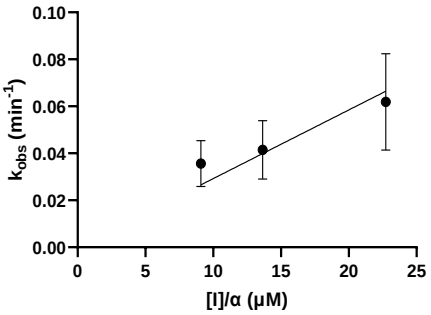 k_{inact}/K_I = 2922 ± 260 M^{-1} min^{-1}
23	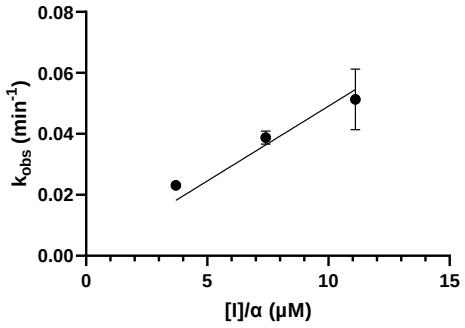 k_{inact}/K_I = 4907 ± 325 M^{-1} min^{-1}	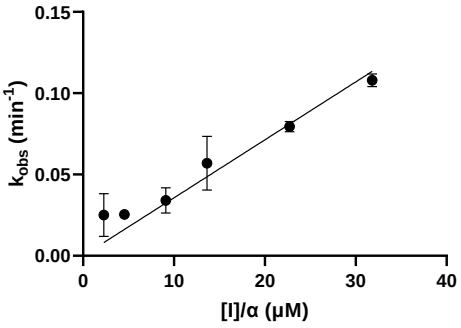 k_{inact}/K_I = 3565 ± 229 M^{-1} min^{-1}
45	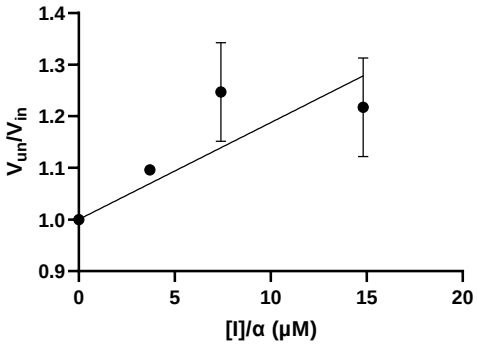 K_i = 53 ± 12 μM	No inhibition

46	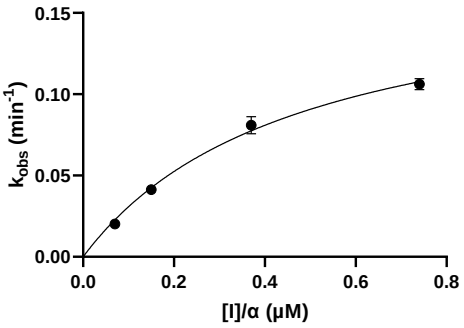 k_{inact}/K_I = 372992 ± 74839 M^{-1} min^{-1} k_{inact} = 0.1765 ± 0.0160 min^{-1} K_I = 0.4732 ± 0.0847 μM	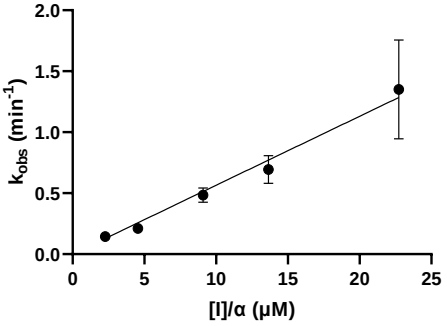 k_{inact}/K_I = 56520 ± 2044 M^{-1} min^{-1}
47	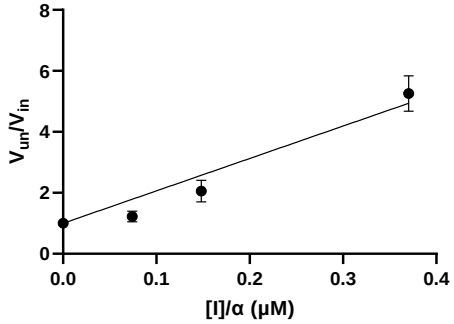 K_i = 0.0941 ± 0.0105 μM	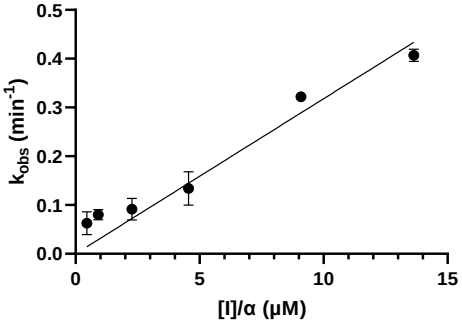 k_{inact}/K_I = 31780 ± 2218 M^{-1} min^{-1}

71	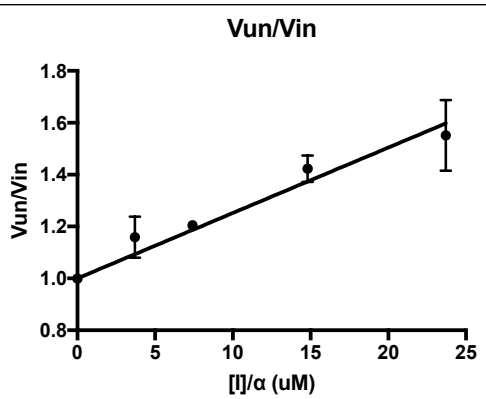 Slope = 0.02521 ± 0.001641 K_i = 39.7 ± 2.6 µM (*interference*)	No inhibition up to 360 µM
79	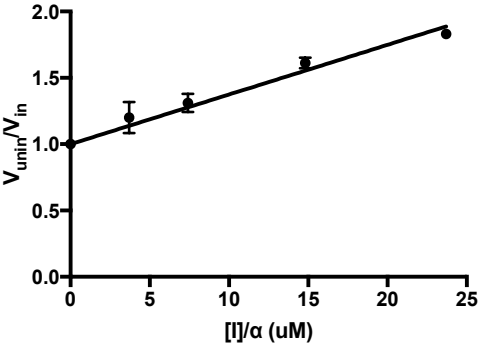 Slope = 0.03745 ± 0.001839 K_i = 26.7 ± 1.3 µM (*interference*)	No inhibition up to 360 µM

75	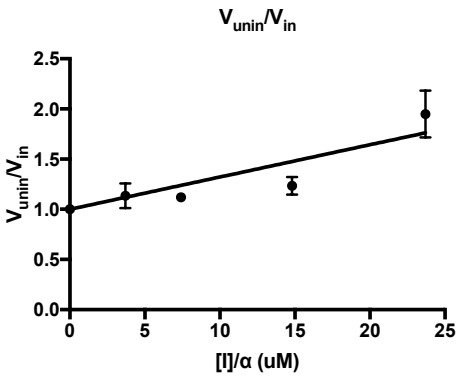 Slope = 0.03216 ± 0.00562 K_i = 31.1 ± 5.4 µM (*interference*)	No inhibition up to 360 µM
74	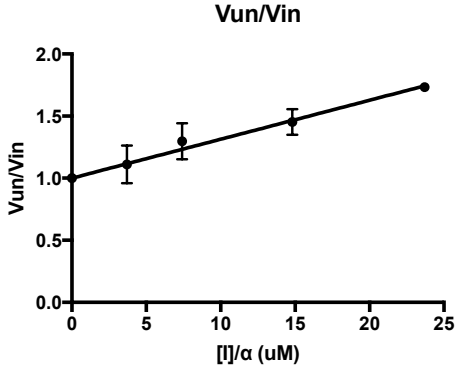 Slope = 0.03137 ± 0.001151 K_i = 31.9 ± 1.2 µM (*interference*)	No inhibition up to 360 µM

73	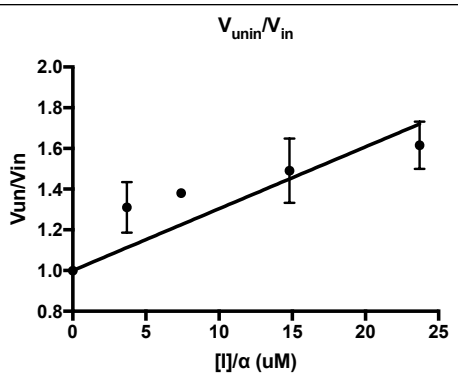 Slope = 0.03038 ± 0.004724 K_i = 32.9 ± 5.1 µM (*interference*)	No inhibition up to 360 µM
76	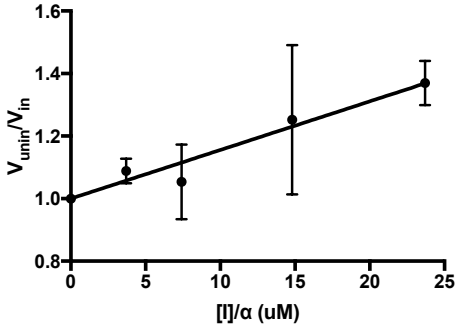 Slope = 0.01556 ± 0.001242 K_i = 64.3 ± 5.1 µM (*interference*)	No inhibition up to 360 µM
72	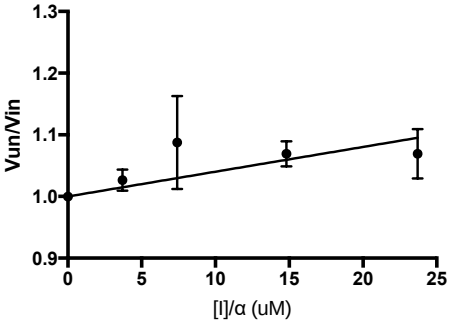 Slope = 0.004014 ± 0.001116 K_i = 249.1 ± 69.3 µM	No inhibition up to 360 µM

77	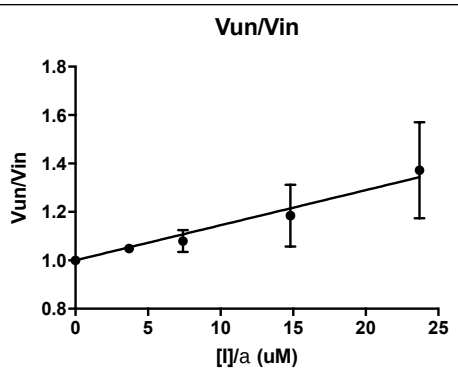 Slope = 0.01449 ± 0.0008536 K_i = 69.0 ± 4.1 µM	No inhibition up to 360 µM
84	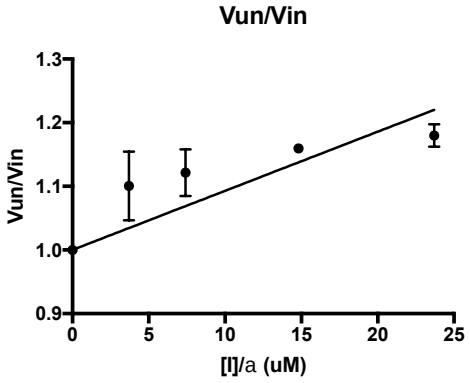 Slope = 0.009292 ± 0.00165 K_i = 107.6 ± 19.1 µM	No inhibition up to 360 µM

87	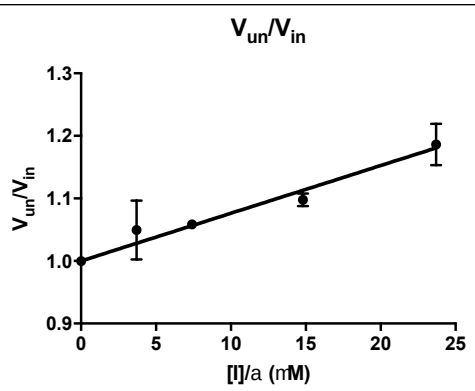 Slope = 0.007625 ± 0.0004603 K_i = 131.1 ± 7.9 µM	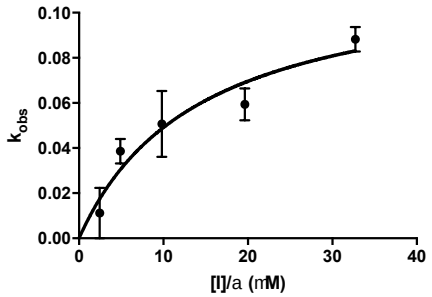 k_{inact}/K_I = 8350 ± 4488 M^{-1} min^{-1} k_{inact} = 0.1194 ± 0.0262 min^{-1} K_I = 14.3 ± 7.0 µM
88	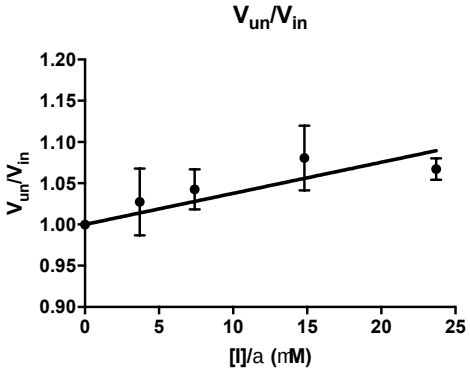 Slope = 0.003773 ± 0.0006661 K_i = 265.0 ± 46.8 µM	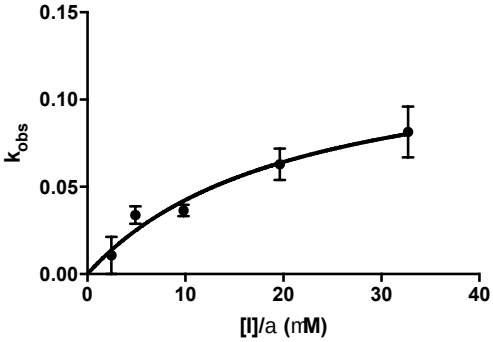 k_{inact}/K_I = 6245 ± 2973 M^{-1} min^{-1} k_{inact} = 0.1322 ± 0.0288 min^{-1} K_I = 21.17 ± 8.96 µM
93 (**KM93**)	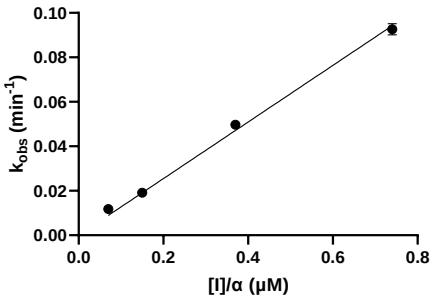 k_{inact}/K_I = 127300 ± 2890 M^{-1} min^{-1}	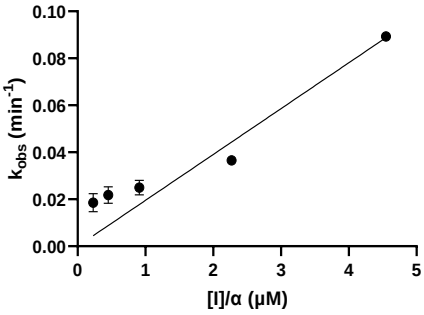 k_{inact}/K_I = 19520 ± 2108 M^{-1} min^{-1}

HPLC Traces of Peptidic Inhibitors

Compound 11. Ac-D-Asp-Dap(Acrylamide)-Nle-Nle-Leu-Pro-Trp-Pro-OH.

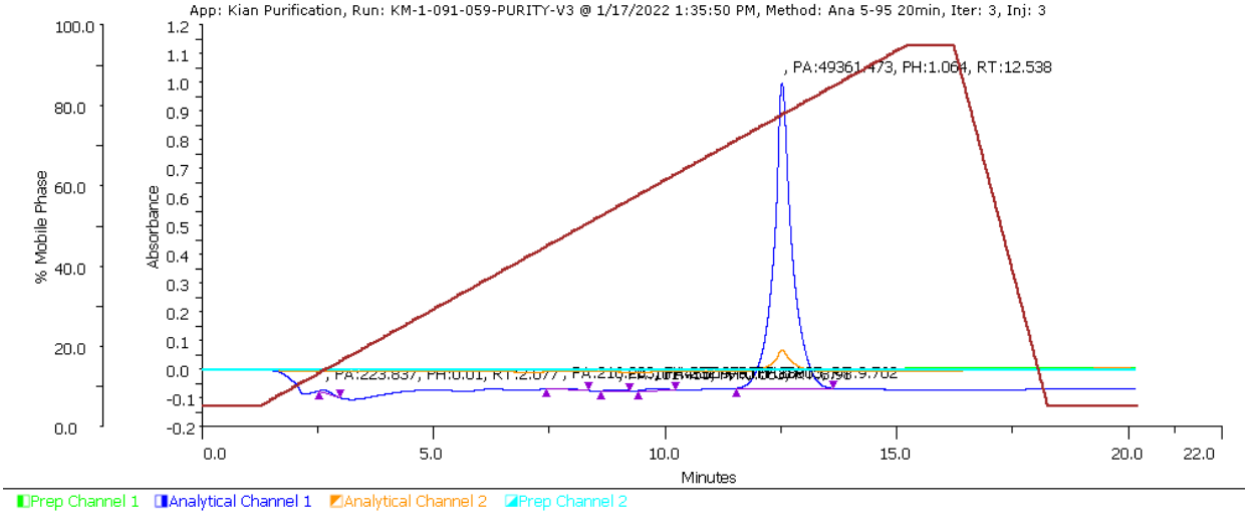

Sample Table

Injection Number	Peak Name	Retention Time (min)	Area (mAUmin x100)	Height (AU)	Sample Name	Sample Location	Fraction Site(s)	Area %
3	1	2.677	223.8372	0.01	KM-1-091redo	Sample Zone->163		0.446
3	2	12.538	49361.4728	1.064	KM-1-091redo	Sample Zone->163		98.416
3	3	9.762	252.9785	0.005	KM-1-091redo	Sample Zone->163		0.504
3	4	8.98	101.4551	0.003	KM-1-091redo	Sample Zone->163		0.202
3	5	7.888	216.2027	0.004	KM-1-091redo	Sample Zone->163		0.431

Compound 12. Ac-D-Asp-Dab(Acrylamide)-Nle-Nle-Leu-Pro-Trp-Pro-OH.

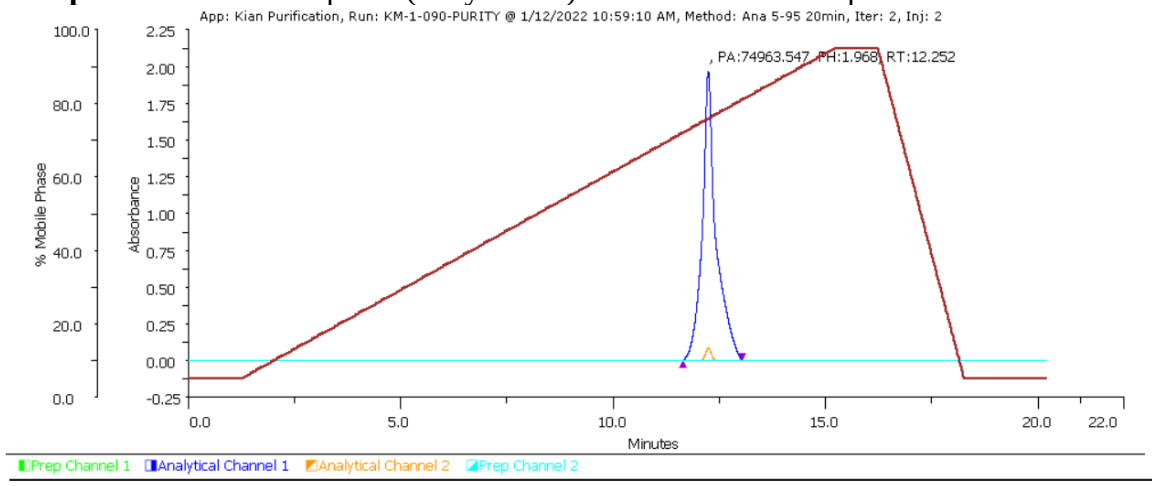

Sample Table

Injection Number	Peak Name	Retention Time (min)	Area (mAUmin x100)	Height (AU)	Sample Name	Sample Location	Fraction Site(s)	Area %
2	1	12.252	74963.5466	1.968	KM-1-090-PURITY	Sample Zone->162		100

Compound 13. Ac-D-Asp-Orn(Acrylamide)-Nle-Nle-Leu-Pro-Trp-Pro-OH.

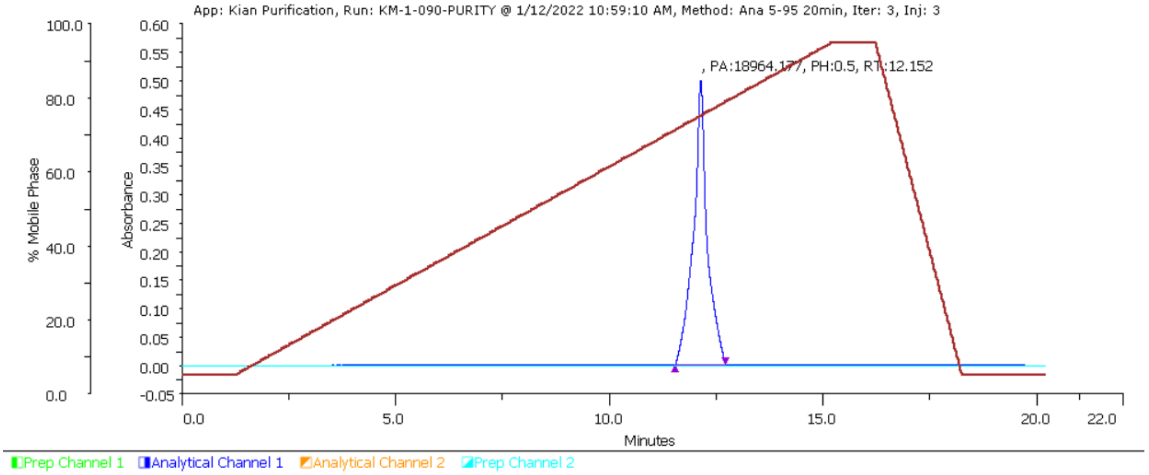

Sample Table

Injection Number	Peak Name	Retention Time (min)	Area (mAUmin x100)	Height (AU)	Sample Name	Sample Location	Fraction Site(s)	Area %
3	1	12.152	18964.1767	0.5	KM-1-043-PURITY	Sample Zone->162		100

Compound 14. Ac-D-Asp-Lys(Acrylamide)-Nle-Nle-Leu-Pro-Trp-Pro-OH.

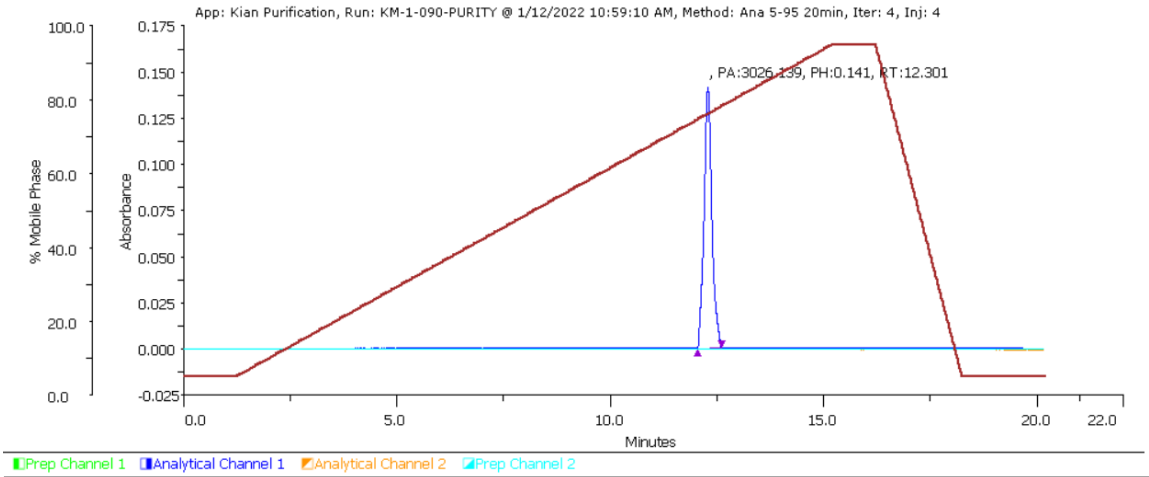

Sample Table

Injection Number	Peak Name	Retention Time (min)	Area (mAUmin x100)	Height (AU)	Sample Name	Sample Location	Fraction Site(s)	Area %
4	1	12.301	3026.1386	0.141	KM-1-042-PURITY	Sample Zone->162		100

Compound 20. Ac-D-Asp-Dap(α-chloroacetamide)-Nle-Nle-Leu-Pro-Trp-Pro-OH.

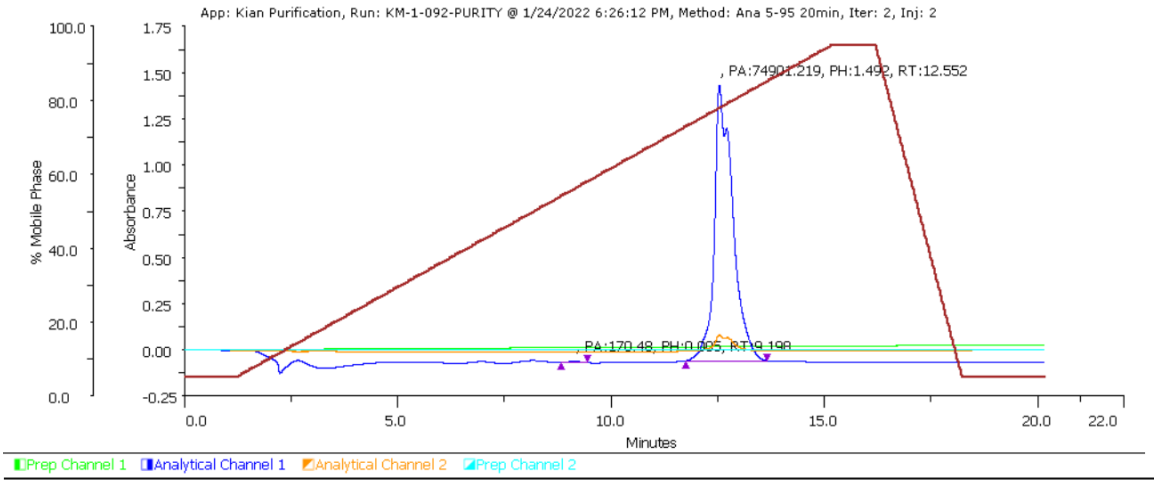

Sample Table

Injection Number	Peak Name	Retention Time (min)	Area (mAUmin x100)	Height (AU)	Sample Name	Sample Location	Fraction Site(s)	Area %
2	1	12.552	74901.2188	1.492	KM-1-092-PURITY	Sample Zone->163		99.773
2	2	9.198	170.4799	0.005	KM-1-092-PURITY	Sample Zone->163		0.227

Compound 21. Ac-D-Asp-Dab(α-chloroacetamide)-Nle-Nle-Leu-Pro-Trp-Pro-OH.

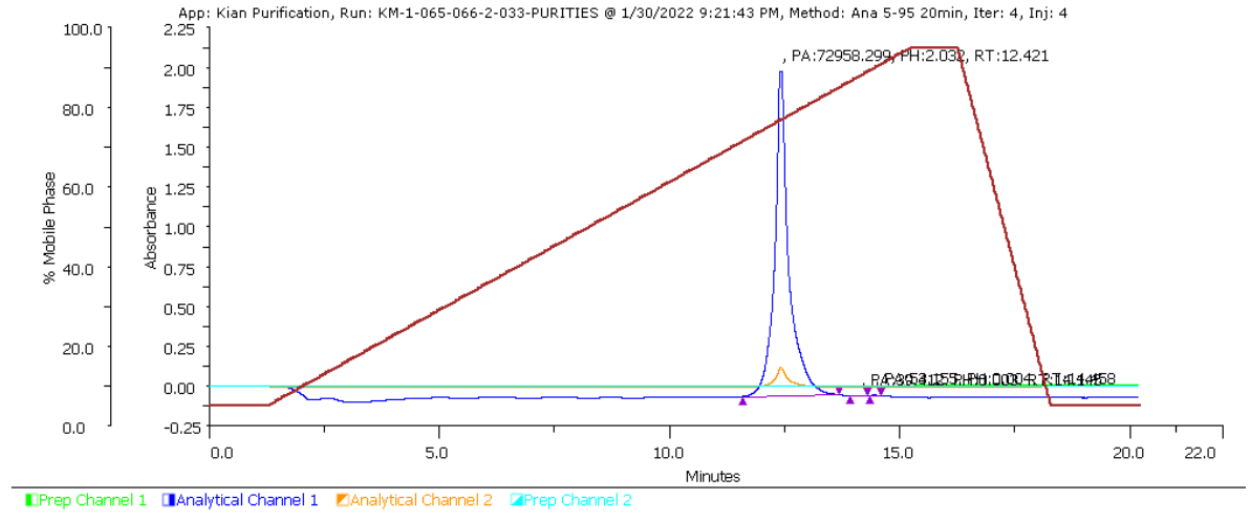

Sample Table

Injection Number	Peak Name	Retention Time (min)	Area (mAUmin x100)	Height (AU)	Sample Name	Sample Location	Fraction Site(s)	Area %
4	1	12.421	72958.2993	2.032	KM-1-065	Sample Zone->150		99.873
4	2	14.458	53.1548	0.004	KM-1-065	Sample Zone->150		0.073
4	3	14.145	39.4118	0.003	KM-1-065	Sample Zone->150		0.054

Compound 22. Ac-D-Asp-Orn(α-chloroacetamide)-Nle-Nle-Leu-Pro-Trp-Pro-OH.

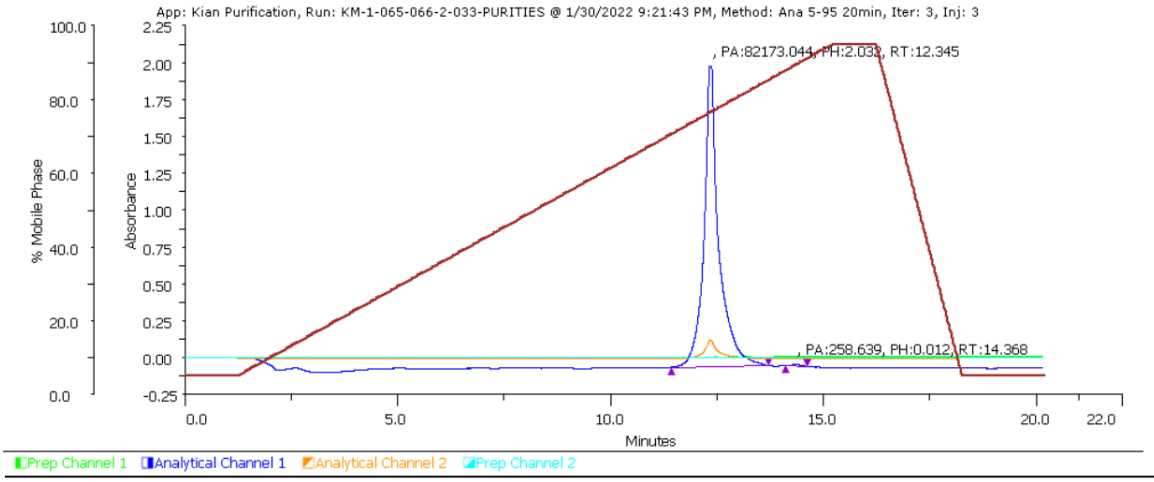

Sample Table

Injection Number	Peak Name	Retention Time (min)	Area (mAUmin x100)	Height (AU)	Sample Name	Sample Location	Fraction Site(s)	Area %
3	1	12.345	82173.0436	2.032	KM-1-066	Sample Zone->149		99.686
3	2	14.368	258.6394	0.012	KM-1-066	Sample Zone->149		0.314

Compound 23. Ac-D-Asp-Lys(α-chloroacetamide)-Nle-Nle-Leu-Pro-Trp-Pro-OH.

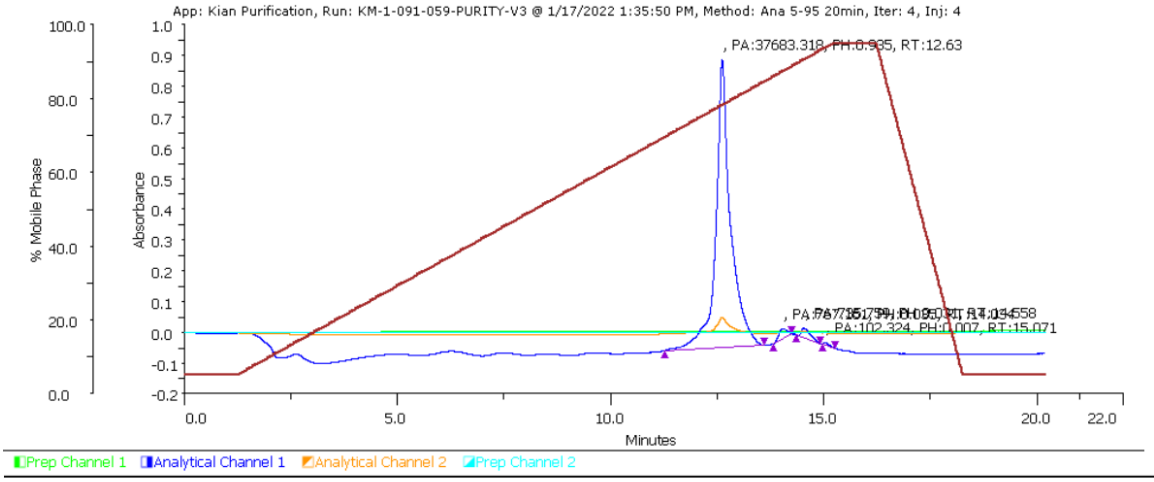

Sample Table

Injection Number	Peak Name	Retention Time (min)	Area (mAUmin x100)	Height (AU)	Sample Name	Sample Location	Fraction Site(s)	Area %
4	1	12.63	37683.3183	0.935	KM-1-059	Sample Zone->163		95.914
4	2	14.034	767.1615	0.035	KM-1-059	Sample Zone->163		1.953
4	3	14.558	735.7587	0.031	KM-1-059	Sample Zone->163		1.873
4	4	15.071	102.3235	0.007	KM-1-059	Sample Zone->163		0.26

Compound 45. Ac-D-Asp-Asp(MA)-Nle-Nle-Leu-Pro-Trp-Pro-OH.

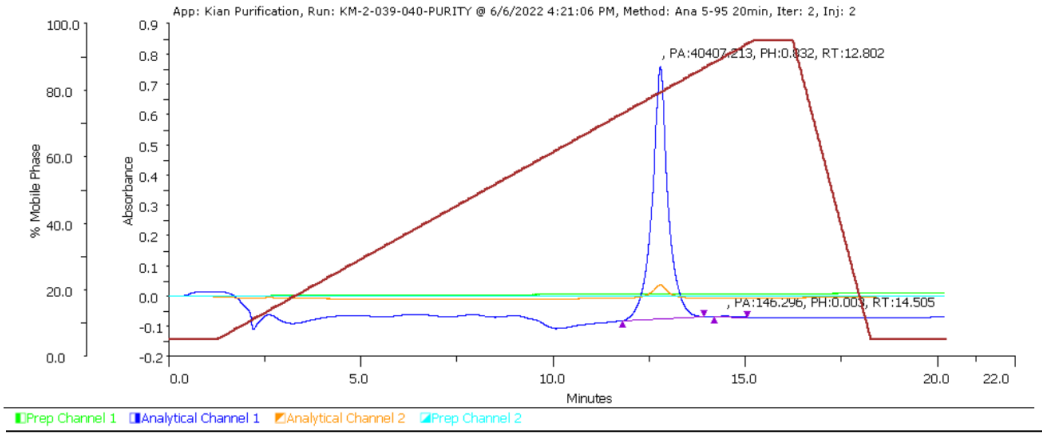

Sample Table

Injection Number	Peak Name	Retention Time (min)	Area (mAUmin x100)	Height (AU)	Sample Name	Sample Location	Fraction Site(s)	Area %	
2	1	12.802	40407.2126	0.832	KM-2-039-PURITY	Sample Zone->160		99.639	
2	2	14.505	146.2959	0.003	KM-2-039-PURITY	Sample Zone->160		0.361	

Compound 46 (ZED1301). Ac-D-Asp-Glu(MA)-Nle-Nle-Leu-Pro-Trp-Pro-OH.

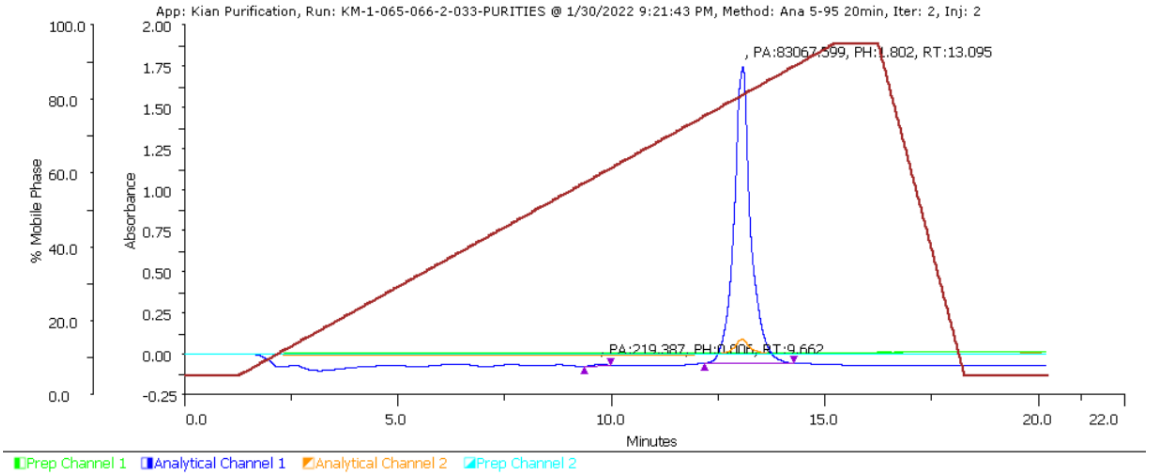

Sample Table

Injection Number	Peak Name	Retention Time (min)	Area (mAUmin x100)	Height (AU)	Sample Name	Sample Location	Fraction Site(s)	Area %
2	1	13.095	83067.5993	1.802	KM-2-033	Sample Zone->148		99.737
2	2	9.662	219.3874	0.006	KM-2-033	Sample Zone->148		0.263

Compound 47. Ac-D-Asp-Hmg(MA)-Nle-Nle-Leu-Pro-Trp-Pro-OH.

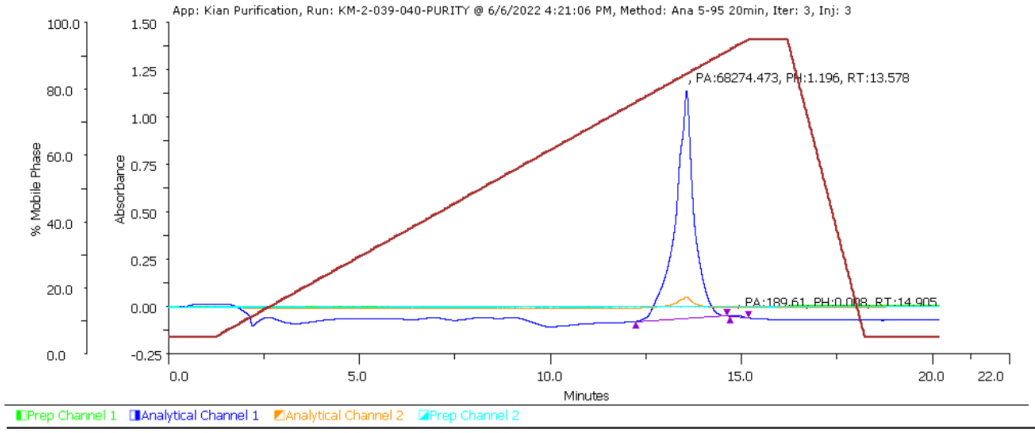

Sample Table

Injection Number	Peak Name	Retention Time (min)	Area (mAUmin x100)	Height (AU)	Sample Name	Sample Location	Fraction Site(s)	Area %	
3	1	13.578	68274.4729	1.196	KM-2-040-PURITY	Sample Zone->161		99.723	
3	2	14.905	189.6096	0.008	KM-2-040-PURITY	Sample Zone->161		0.277	

Compound 93 (**KM93**)**.** RhB-Pro-6AH-D-Asp-Glu(MA)-Nle-Nle-Leu-Pro-Trp-Pro-OH.

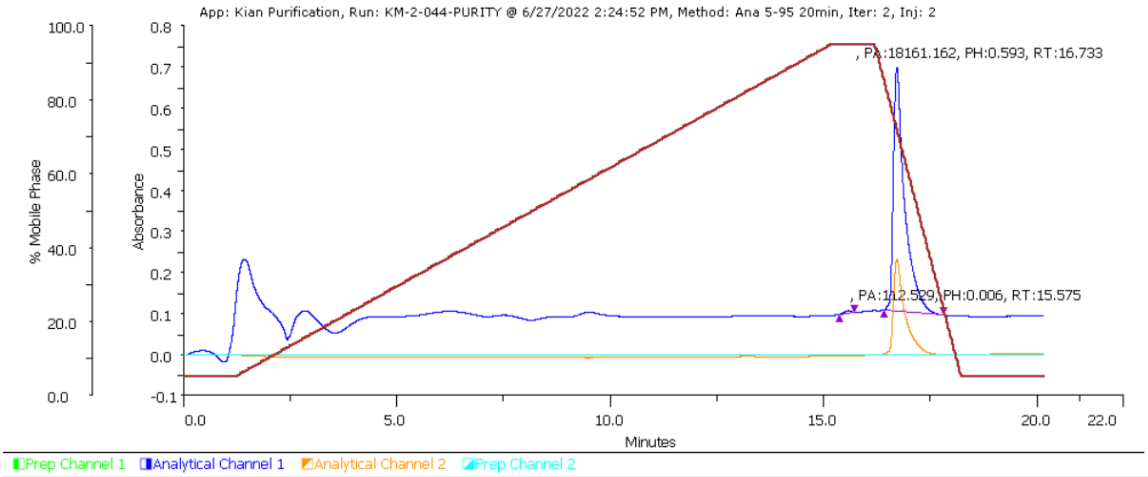

Sample Table

Injection Number	Peak Name	Retention Time (min)	Area (mAUmin x100)	Height (AU)	Sample Name	Sample Location	Fraction Site(s)	Area %
2	1	15.575	112.5295	0.006	KM-2-044-PURITY	Sample Zone->163		0.616
2	2	16.733	18161.1618	0.593	KM-2-044-PURITY	Sample Zone->163		99.384

Chapter 3: Cell Impermeable Inhibitors Confirm That Intracellular Human Transglutaminase 2 Is Responsible for the Transglutaminase-Associated Cancer Phenotype

Eric W. J. Gates [1], Nicholas D. Calvert [1], Nicholas J. Cundy [1], Federica Brugnoli [2], Pauline Navals [1], Alexia Kirby [1], Nicoletta Bianchi [2], Gautam Adhikary [3], Adam J. Shuhendler [1], Richard L. Eckert [3] and Jeffrey W. Keillor [1]*

[1] Department of Chemistry and Biomolecular Sciences, University of Ottawa, Ottawa, Ontario, K1N 6N5, Canada

[2] Department of Translational Medicine, University of Ferrara, Ferrara, 44021, Italy

[3] Department of Biochemistry and Molecular Biology, University of Maryland School of Medicine, Baltimore, MD, 21201, USA

* Correspondence: JWK

3.1. Introduction to the Research Article Presented Within this Chapter

This research project follows from a recent structure activity relationship (SAR) study conducted in the Keillor Research Group on a peptidic inhibitor scaffold for TG2. During that investigation, various hydrophobic amino acids were incorporated to increase the linker space between the lysine(acrylamide) and naphthoyl moieties. A dramatic increase in potency was observed when the spacer residue was placed between the piperazine and naphthoyl moieties. Given the widespread increase in inhibitor efficiency, we proposed that a residue that allowed for functionalization on the side chain would increase the chemical biology scope of these inhibitors by allowing attachment of various cargos.

Although human transglutaminase 2 is the most well studied isozyme of the TGase family, conflicting and overlapping biological activities have been assigned. One of the most prevalent misconceptions is the role of intracellular *versus* extracellular TG2 – especially in the field of oncology. Our goal within this project is to start to rule out these convoluted roles by designing, synthesizing, and evaluating cell impermeable inhibitors, cell permeable fluorescent probes, and biorthogonal compatible labels. These tools were then applied to preliminary cancer biology studies in multiple cancer cell lines to determine which localization of TG2 is responsible for the TG2-associated cancer phenotype. Given that the conclusions drawn from this chapter hinge heavily on the proteome-wide selectivity of the tools evaluated in this work, a preliminary investigation of the selectivity was also conducted post-submission of the manuscript. The data that demonstrate the high selectivity of the NCEG-RHB probe in SH-SY5Y cell lysate can be found in the final section of the Appendix to Chapter 3 (Figure 3.5). This additional result reinforces the confidence of using NCEG-RHB and our conclusions drawn about the role of intracellular *versus* extracellular TG2 in cancer cell biology.

3.2. Author Contributions

Conceptualization, J.W.K., E.W.J.G. and N.J.C.; formal analysis, E.W.J.G. and N.D.C.; investigation, E.W.J.G., N.D.C., N.J.C., F.B., P.N., A.K., N.B. and G.A.; writing—original draft preparation, E.W.J.G.; writing—review and editing, E.W.J.G., J.W.K., A.J.S. and R.L.E.; visualization, E.W.J.G., N.D.C., F.B., P.N., N.B. and G.A.; supervision, N.B., A.J.S. and J.W.K.; project administration, J.W.K.; funding acquisition, J.W.K. All authors have read and agreed to the published version of the manuscript.

3.3. Copyright

Gates, E.W.J.; Calvert, N.D.; Cundy, N.J.; Brugnoli, F.; Navals, P.; Kirby, A.; Bianchi, N.; Adhikary, G.; Shuhendler, A.J.; Eckert, R.; Keillor, J.W. Cell Impermeable Inhibitors Confirm That Intracellular Human Transglutaminase 2 is Responsible for the Transglutaminase-Associated Cancer Phenotype. *Int. J. Mol. Sci.* **2023**, *24*(16), 12546. https://doi.org/10.3390/ijms241612546

3.4. Abstract

Transglutaminase 2 (TG2) is a multifunctional enzyme primarily responsible for crosslinking proteins. Ubiquitously expressed in humans, TG2 can act either as a transamidase by crosslinking two substrates through formation of an N^{ε}(ɣ-glutaminyl)lysine bond or as an intracellular G-protein. These discrete roles are tightly regulated by both allosteric and environmental stimuli and are associated with dramatic changes in the conformation of the enzyme. The pleiotropic nature of TG2 and multi-faceted activities have resulted in TG2 being implicated in numerous disease pathologies including celiac disease, fibrosis, and cancer. Targeted TG2 therapies have not been selective for subcellular localization, such that currently no tools exist to selectively target extracellular over intracellular TG2. Herein, we have designed novel TG2-selective inhibitors that are not only highly potent and irreversible, but also cell impermeable, targeting only extracellular TG2. We have also further derivatized the scaffold to develop probes that are intrinsically fluorescent or bear an alkyne handle, which target both intra- and extracellular TG2, in order to facilitate cellular labelling and pull-down assays. The fluorescent probes were

internalized and imaged in cellulo, and provide the first implicit experimental evidence that by comparison with their cell-impermeable analogues, it is specifically *intracellular* TG2, and presumably its G-protein activity, that contributes to transglutaminase-associated cancer progression.

3.5. Introduction

The transglutaminases (TGases) are a family of multi-functional enzymes primarily responsible for cross-linking proteins [1–3]. The family is composed of eight calcium-dependent isozymes that can be found throughout the human body. These enzymes mediate the formation of a covalent link between two substrate proteins through the formation of an N^{ε}(ɣ-glutaminyl)lysine bond, through a transamidation reaction involving a catalytic cysteine residue [4]. Transglutaminase 2 (TG2), or tissue transglutaminase, is of specific interest not only for its ubiquitous expression and cross-linking activity, but also for its ability to act as a G-protein [5]. TG2 can adopt two dramatically different conformations that are exclusively associated with its two distinct activities [6]. When acting as a G-protein, the four sub-domains of TG2 are folded in on themselves in a compact 'closed' conformation, obscuring the cross-linking active site and forming a GTP binding site on the medial *C*-terminal β-barrel [7]. However, when TG2 adopts its cross-linking enzymatic form, the two *C*-terminal β-barrels are extended away from the catalytic core in an 'open' linear conformation, exposing substrate protein binding sites, while dismantling the GTP binding site [8]. Present in both extracellular and intracellular locations [9–13], TG2 has been implicated in numerous pathologies ranging from the survival and epithelial-mesenchymal transition of cancer stem cells to fibrosis to celiac disease [14–21]. Targeted TG2 therapies in the treatment of celiac disease and liver fibrosis have recently been progressed to Phase 2b clinical

trials [22,23]; however, there remains a need to further investigate the roles of TG2 in other biological contexts. One of the areas that remains to be thoroughly investigated is the effect of targeting extracellular versus intracellular TG2. Given that the protein is present both inside and outside the cell, extracellular-selective inhibition may allow the unambiguous assignment of various roles of extracellular TG2, without convoluting this interpretation through the simultaneous inhibition of intracellular TG2. The lack of precise chemical tools has also hindered investigation into which TG2 activities are associated with which sub-cellular environments. The role of TG2 in the proliferation and migration of cancer cells has been ascribed to both intracellular (G-protein) [14,24–28] and extracellular (crosslinking) [29–31] activities, suggesting that the specific localization of the enzyme associated with a phenotype (and cell type) has yet to be assigned. This ambiguity can be viewed as incomplete target validation that hinders the development of potential therapeutic agents.

Herein, we disclose several novel chemical probes built on a peptidomimetic scaffold designed to be selective for TG2 over other isozymes. The probes include functional groups that decrease cell permeability, are fluorescent, or provide sites for bioorthogonal reactivity. Herein, we show that the first-in-class cell-impermeable irreversible inhibitors are highly potent but fail to alter cancer stem cell progression and invasion. In contrast, the fluorescent version of the probe is both cell permeable and halts cancer cell invasion, providing direct evidence that inhibition of intracellular TG2 (and presumably its G-protein activity) is necessary to generate the anti-cancer phenotype.

3.6. Results

3.6.1. Design

Our previous study of structure–activity relationships in irreversible inhibitors of TG2 revealed a dramatic increase in efficiency when the original lead compound (AA9) [26] was modified to incorporate an additional amino acid spacer residue in its peptidomimetic backbone (Figure 1) [32]. This extension of the peptidomimetic scaffold led to inhibitors that were selective for TG2 over the other isozymes in the TGase family. They were also shown to abolish GTP binding, presumably by locking TG2 in its open conformation [33–36]. To expressly design first-in-class cell-impermeable inhibitors of TG2, we introduced a bulky negatively charged moiety on the amino acid spacer of the scaffold. This was achieved through solid-phase peptide synthesis (SPPS) of a tri-Asp sequence, connected to the rest of the scaffold through an alkyl or peptidic linker. The extended scaffold was also modified at the same site by incorporating bright fluorophores, producing novel TG2 fluorescent probes. Finally, the same site was modified to add an alkyne group, to allow subsequent copper-assisted azide alkyne cycloaddition (CuAAC) reactions for attaching alternative cargo.

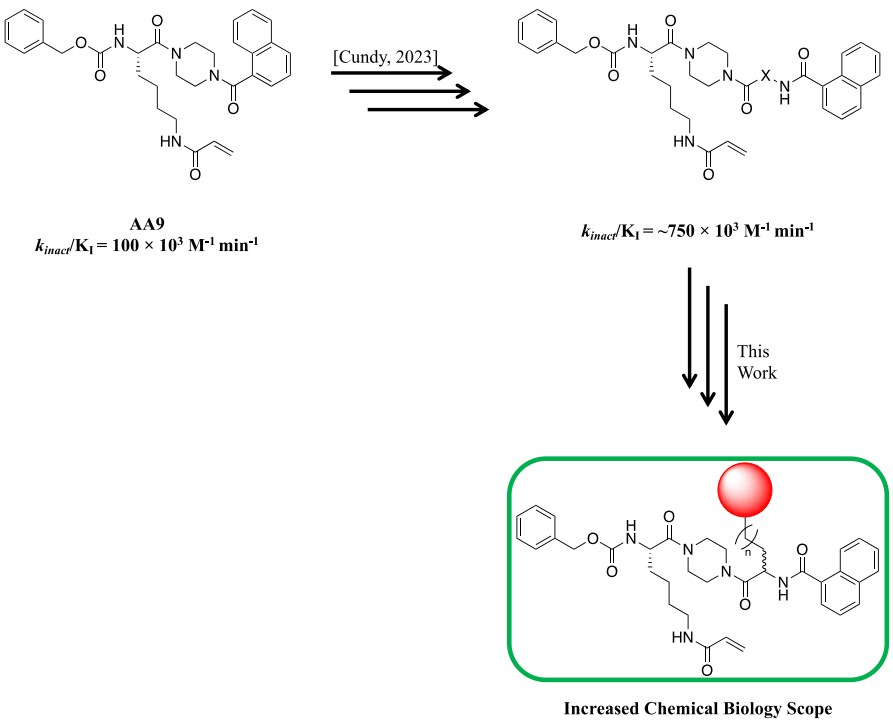

Figure 3.1. Previous libraries of inhibitors giving rise to the scaffold disclosed in this work [32].

3.6.2. Synthesis

To generate these various chemical tools, a linear synthetic scheme was designed, featuring the formation of the naphthoyl-glutamate moiety **6** (Scheme 1) and a common stable key intermediate **16**. Derivatization of the glutamate residue in the peptidomimetic scaffold of the key intermediate **16** then allowed various chemical tools to be obtained by late-stage diversification.

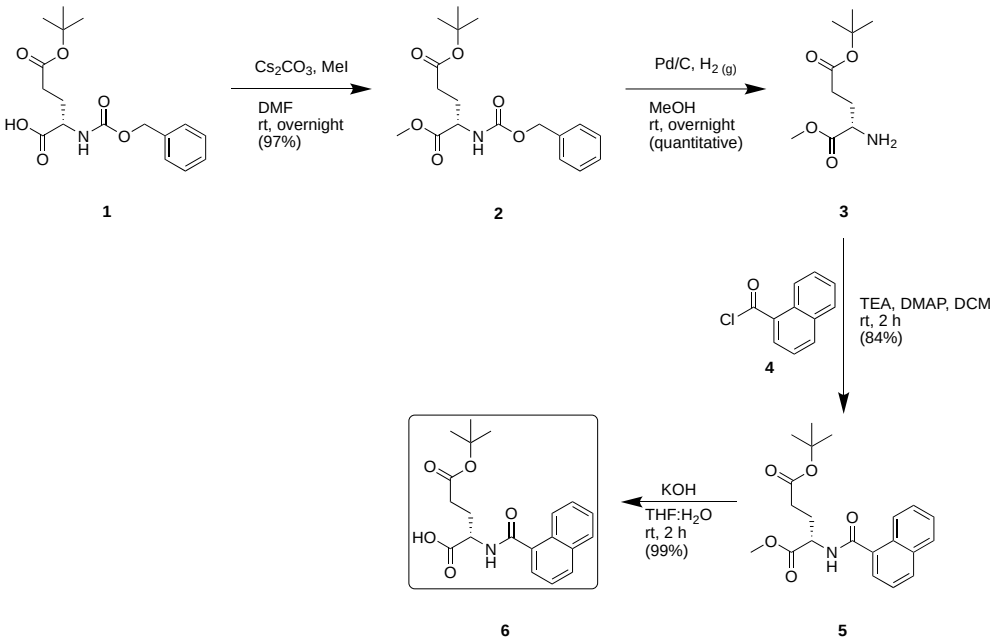

Scheme 3.1. Synthetic scheme to generate naphthoyl-glutamate moiety.

Starting from commercially available Z-Glu(OtBu)-OH (**1**), a methylation was performed to generate the corresponding methyl ester **2** (Scheme 1). The Cbz protecting group was then removed by palladium catalyzed hydrogenolysis to liberate the *N*-terminus on glutamate **3**. Acylation with 1-naphthoyl chloride **4** was then performed under basic conditions with triethylamine to generate the protected intermediate **5**. Finally, hydrolysis of the *C*-terminal ester generated the naphthoyl-glutamate intermediate **6** to be used in the convergent synthesis described below (Scheme 2).

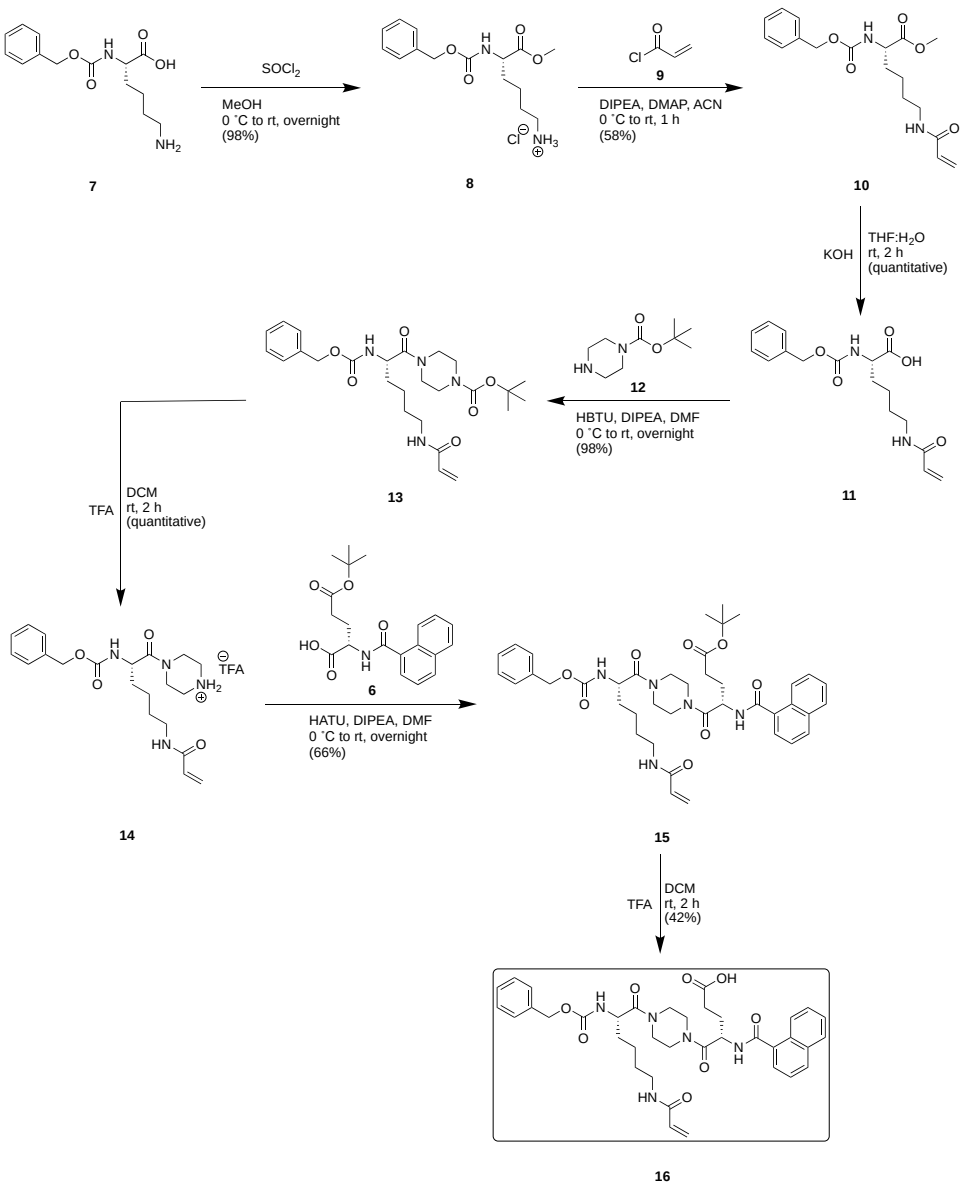

Scheme 3.2. Synthetic scheme to generate key intermediate, allowing for subsequent functionalization of the glutamate sidechain.

Commercially available Z-Lys-OH (**7**) was subjected to methyl esterification using thionyl chloride and methanol to protect the *C*-terminus and generate **8** (Scheme 2). The addition of the acrylamide warhead was achieved by reaction with acryloyl chloride **9** and Hünig's base to yield the acrylated lysine **10**. The *C*-terminal ester of **10** was then hydrolyzed to produce **11**, which was

subsequently coupled to *N*-Boc-piperazine **12**, using HATU, to gain access to the Boc-protected amine **13**. Removal of the Boc group with TFA delivered intermediate amine **14** as its TFA salt. Coupling **14** with the glutamate intermediate **6** produced the *t*-butyl ester **15**. A final hydrolysis of this ester using TFA exposed the ɣ-carboxylate of the glutamate and provided key intermediate **16**.

Once key intermediate **16** was acquired, cell-impermeable inhibitors were generated by SPPS, allowing all inhibitors to be prepared on-resin in an automated peptide synthesizer (Scheme 3). Starting from manually pre-loaded Fmoc-Asp(OtBu)-Wang resin, two sequential cycles of coupling with Fmoc-Asp and Fmoc deprotection were performed. The resulting tri-Asp peptide was then further derivatized to either incorporate an aminohexanoic acid linker or a tri-Gly linker by further cycles of SPPS. A final coupling with key intermediate **16** executed by the peptide synthesizer produced the protected precursors bound to Wang resin. The resin was subsequently cleaved, and the remaining protecting groups were removed using TFA to yield the cell-impermeable inhibitors **17** and **18**, which were purified by semi-preparative reverse phase HPLC.

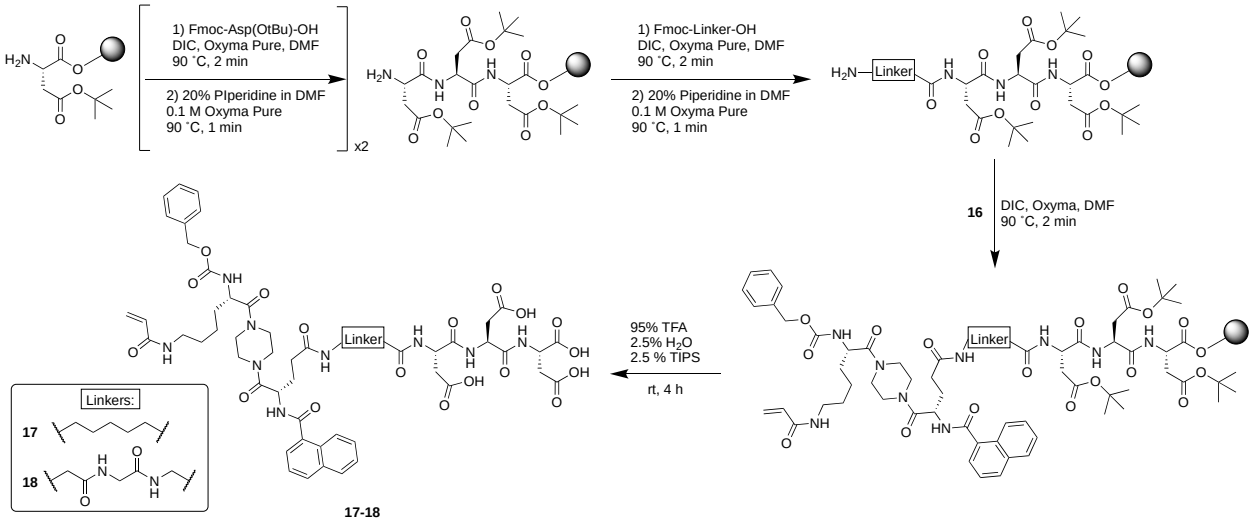

Scheme 3.3. Synthetic scheme from key intermediate to generate cell-impermeable inhibitors 17 and 18.

To make fluorescent probes starting from key intermediate **16**, fluorescein, coumarin, and rhodamine B fluorophores were linked to the scaffold through a cadaverine spacer (Scheme 4). Compound **16** was subjected to amide coupling with HATU to attach *N*-Boc-Cadaverine to the glutamate residue. The intermediate amine **19** was then deprotected using 4 M HCl in dioxane and free amine **20** was coupled to the diethylamino coumarin probe **21**. This yielded the coumarin fluorescent probe compound **22** in 59% yield. The addition of FITC to cadaverine intermediate **20** generated fluorescein probe **23** (Scheme S1 in Supplementary Materials).

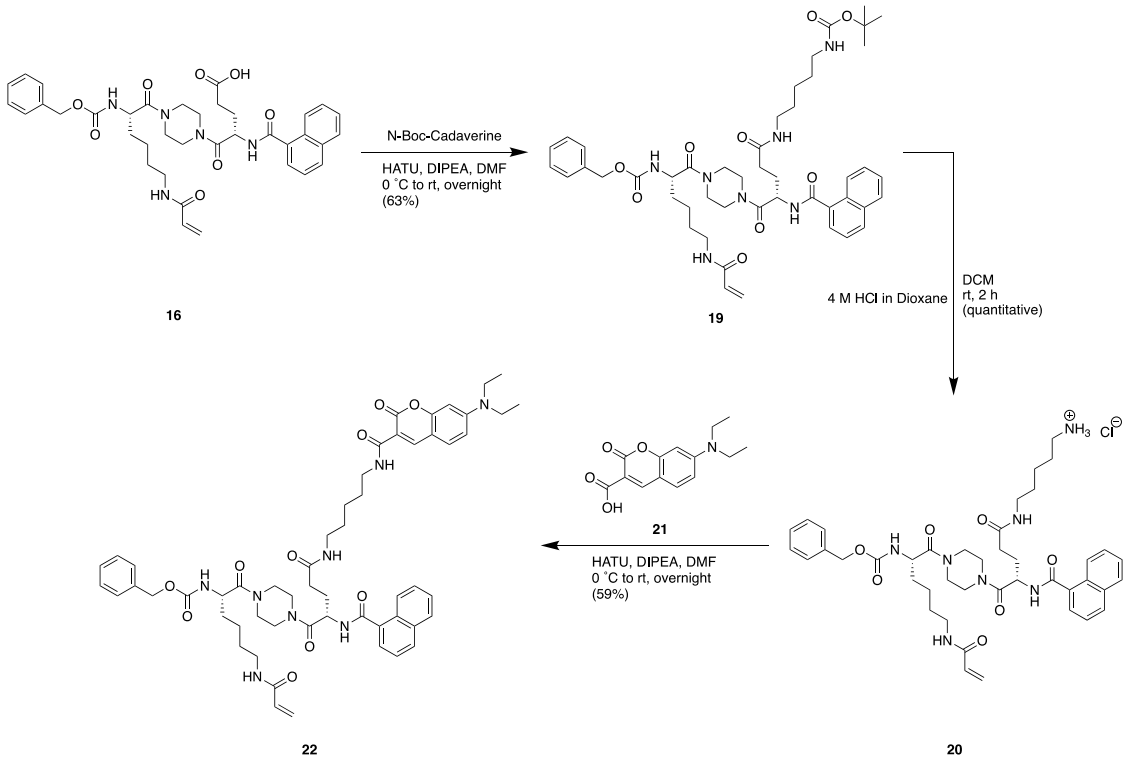

Scheme 3.4. Synthetic scheme from key intermediate to generate fluorescent coumarin probe 22.

The preparation of a rhodamine B probe required a different synthetic route relative to the other probes. Starting from commercially available Z-Pro-OH **24**, an amide coupling using HATU was preformed to attach *N*-Boc-cadaverine and generate **25** (Scheme S2 in Supplementary Materials). Palladium-catalyzed hydrogenolysis then deprotected the *N*-terminus of the proline and

yielded intermediate **26**. Rhodamine B was then linked to the proline using HATU-mediated amide coupling, providing tertiary amide **27**. The Boc protecting group on the cadaverine linker was then removed using 4 M HCl in dioxane to generate amine **28**. A final amide coupling with HATU and key intermediate **16** provided the rhodamine B probe **29**.

Finally, to generate a 'clickable' TG2 labelling agent, the key intermediate **16** was coupled to propargylamine **30** by HATU to generate the propargyl derivative **31** presenting a free alkyne handle (Scheme S3 in Supplementary Materials). To validate that CuAAC was possible on the propargyl scaffold, **31** was exposed to desthiobiotin-PEG3-azide **32**, copper (II) sulfate, and sodium ascorbate (Scheme S4 in Supplementary Materials). The desthiobiotin handle was efficiently installed to give probe **33** in 90% yield.

3.6.3. Kinetics

Relative to the original scaffold, we expected the potency of these novel chemical biology tools to decrease slightly, due to the additional bulk incorporated on the glutamate sidechain. Although we expected the sidechain moiety to be directed into bulk solvent, we were concerned that its mass and charge would disfavor the binding interaction. Therefore, we kinetically characterized these probes as rigorously as possible, in order to determine their relative affinity and reactivity. For most inhibitors we have made, including the parent inhibitor AA9 (Figure 1), we have been able to measure kinetic parameters under Kitz and Wilson conditions [37]. This experimental approach is based on the use of a continuous activity assay [38] and the measurement of first-order rate constants for the time-dependent inactivation of enzyme (see Figure 2A and Figures S1–S5 in Supplementary Materials). The dependence of these observed rate constants (k_{obs}) on the inhibitor concentration divided by alpha ([I]/α) can then be fitted to a hyperbolic

saturation model where the upper plateau represents the rate constant of inactivation (k_{inact}), and the concentration providing half the rate constant of inactivation represents K_I (Figure 2B) [26,27,39]. Aside from inhibitor **22**, the inhibitors disclosed herein exhibited excellent rates of inactivation; however, this assay was unable to provide reliable values for the observed rate constants (k_{obs}) at high concentrations and, thus, was a poor saturation fitting. To compensate for this, the overall efficiency of the inhibitor (k_{inact}/K_I) can be derived from the slope of the linear region of the saturation plot (Figure 2C). To gauge the individual parameters, a double reciprocal fitting was also employed where K_I can be calculated from the x-axis intercept and k_{inact} can be calculated from the y-axis intercept (Figure 2D).

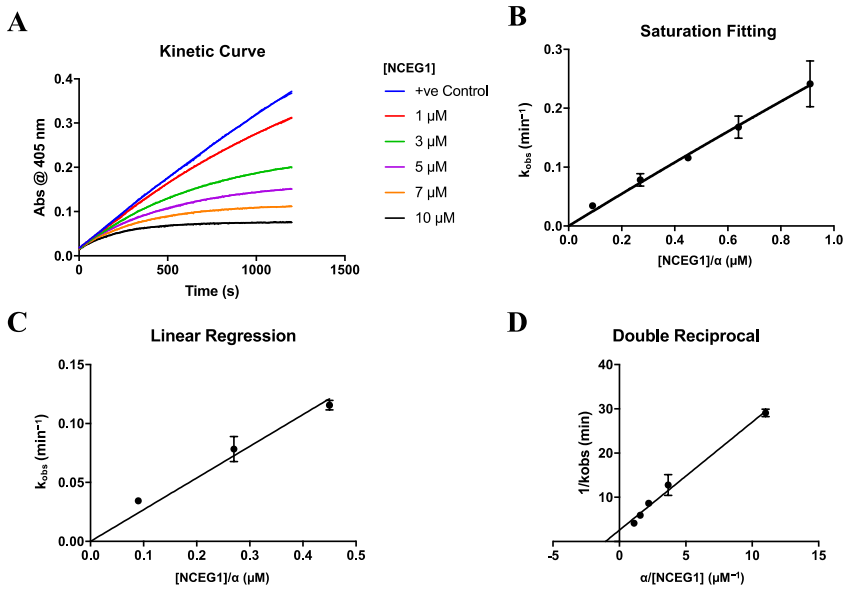

Figure 3.2. Representative kinetic data for inhibitors. Data shown for compound 17 with (A) time-dependent inactivation of TG2 (blank subtracted), (B) fitting of observed first-order rate constants to a hyperbolic model for saturation kinetics, (C) linear regression of lowest concentration rate constants, and (D) double reciprocal fitting of the data shown in B.

Despite our concerns, we were pleased to see that nearly all of our derivatives maintained excellent potency in their inhibition of TG2. In fact, the cell-impermeable inhibitors **17** and **18** were nearly threefold more potent than our original lead compound (AA9) (Table 1) [26]. We ascribe the increased affinity of these new inhibitors to the amino acid residue added to the peptidomimetic backbone, as recently described elsewhere [32]. The fluorescent probes also showed potent inhibition of TG2; with a k_{inact}/K_I value of 1186×10^3 $M^{-1}min^{-1}$, FITC derivative **23** is one of the most efficient TG2 inhibitors known. The coumarin probe **22** showed only modestly efficient inhibition of TG2, with a k_{inact}/K_I value of 188×10^3 $M^{-1}min^{-1}$, although it should be noted that this derivative displayed decreased solubility in aqueous solutions above 25 μM. The propargyl derivative **31** exhibited highly efficient inhibition of TG2 similar to the cell-impermeable inhibitors, with a k_{inact}/K_I value of 497×10^3 $M^{-1}min^{-1}$. The diversity of the cargo that can be attached at the glutamate residue, without abrogation of inhibitory efficiency, implies that this site can be broadly varied for numerous applications. Considering the putative binding mode [27] for these peptidomimetic inhibitors featured the naphthoyl moiety bound in the large hydrophobic binding pocket of TG2, it seems reasonable to hypothesize that the glutamate sidechain cargo must be directed out into solvent, where it has little effect on binding affinity. Molecular docking confirmed this hypothesis, with key intermediate **16**, cell-impermeable **18 (NCGE2)**, and fluorescent probe **29 (NCEG-RHB)** all having their sidechain and cargo directed away from the enzyme (Figure S6 in Supplementary Materials).

Table 3.1. Kinetic data for cell impermeable inhibitors, fluorescent probes, and propargyl inhibitor.

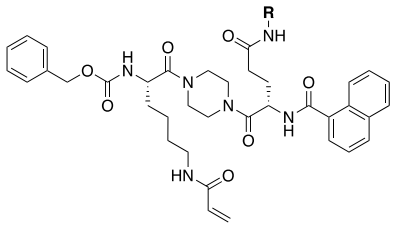

Compound	R	K_I (μM)	k_{inact} (min^{-1})	k_{inact}/K_I ($\times 10^3$ M^{-1} min^{-1})
17 *	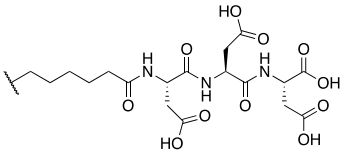	1.0 ± 0.3	0.39 ± 0.10	409 ± 22
18 (**NCEG2**) *	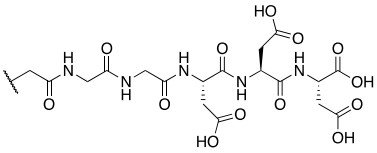	4.1 ± 2.1	2.33 ± 1.12	563 ± 13
22	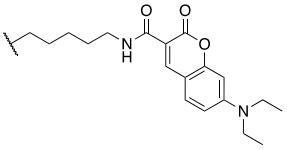	1.3 ± 1.1	0.24 ± 0.07	188 ± 167
23	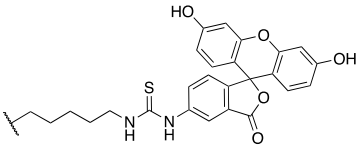	n.d.	n.d.	1186 ± 91 **
29 (**NCEG-RHB**)	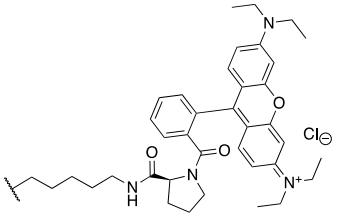	n.d.	n.d.	223 ± 3 **
31 *		0.9 ± 0.5	0.46 ± 0.26	497 ± 33

* Kinetic data fitted to a double reciprocal model; ** Kinetic data from lowest concentrations of saturation plot fitted to a linear model.

3.6.4. Isozyme Selectivity

In the development of probes for TGases, isozyme selectivity is always a significant challenge. Since the catalytic machinery of the active sites of all TGases features a conserved Gly-Gln-Cys-Trp-Val sequence, selectivity for one isozyme over the others requires exploitation of slight differences in the protein substrate binding sites [40,41]. In order to assess the isozyme selectivity of our cell-impermeable inhibitors, TG2 and four other therapeutically relevant TGases (Factor XIII, TG1, TG3, and TG6) were exposed to a concentration of inhibitor representing the same apparent competition with respect to the assay substrate (AL5 [38] or A101 [42,43]). In other words, both the substrate and inhibitor concentrations were varied so that the [I]/α values were identical [27]. Under these conditions, both **17** and **18** displayed excellent selectivity by irreversibly inactivating TG2 with no detectable inhibition of the other isozymes (see Figures S7 and S8 in Supplementary Materials). This provides confidence that in further applications, these cell-impermeable inhibitors will selectively target TG2 over other transglutaminases.

3.6.5. Pharmacokinetic Properties

The cell-impermeable inhibitors **17** and **18** were designed to violate virtually all of the rules for cellular permeability described by Lipinski and Veber [44,45]. They were also empirically evaluated with respect to their pharmacokinetic properties, in particular to determine their cell permeability. In a PAMPA test, the −Log Pe values were very high (Table 2). The measured values of >9.02 and >8.79 are much higher than the traditionally accepted upper limit of 6, suggesting these derivatives would show low permeability. Indeed, neither compound was even detected in the receptor compartment for the PAMPA, resulting in the lower limit of detection being reported as an approximate value. This suggests that cell permeability is negligible. In cultured MDCK cell

permeability assays, both of these compounds exhibited very low permeability again, independent of the Pgp-mediated efflux pathway.

Table 3.2. Representative pharmacokinetic properties for cell impermeable inhibitors 17 and 18.

Compound	17	18 (NCEG2)
cLog P *	0.94	−1.19
Log D	<−2.73	<−2.63
−Log P_e	>9.02	>8.79
$P_{app(A-B)}$ (10^{-6}, cm/s)	0.31	0.47
$P_{app(B-A)}$ (10^{-6}, cm/s)	0.42	0.56
Efflux Ratio	1.39	1.18
$P_{app(A-B)}$ (10^{-6}, cm/s) + Pgp Inh.	0.33	0.57
$P_{app(B-A)}$ (10^{-6}, cm/s) + Pgp Inh.	0.35	0.36
Efflux Ratio + Pgp Inh.	1.04	0.66

* cLog P was calculated using SwissADME online web tool [46].

3.6.6. Fluorescent Labelling

To validate that the novel fluorescent probes were indeed labelling TG2 irreversibly, recombinantly expressed and purified human TG2 [47] was exposed to 30 μM of each probe for 25 min at room temperature. The samples were then analyzed by SDS-PAGE, revealing a fluorescent band at 78 kDa in each sample corresponding to full-length TG2. Upon irradiation at the relevant excitation wavelength, the fluorescent emission of each probe confirmed that TG2 was covalently labelled by each fluorescent probe (see Figure S9 in Supplementary Materials for full gel images). Given the high isozyme selectivity of the cell-impermeable inhibitors **17** and **18**,

it is reasonable to assume the fluorescent probe versions would display similar selectivity and prove to be very useful for fluorescence microscopy.

We elected to use the rhodamine B-labelled **29** (**NCEG-RHB**) in subsequent fluorescence microscopy studies in SH-SY5Y cells due to its high solubility and desirable photochemical properties. SH-SY5Y cells can be differentiated upon the addition of retinoic acid, which induces overexpression of TG2 [48–50]. As shown in (Figure 3A), compound **29** (aka **NCEG-RHB**) is cell permeant and clearly visible in the cytoplasm, but not in the nucleus. A noticeable increase in red fluorescence is observed in cells pre-treated with retinoic acid treatment, suggestive of an increased expression and labelling of intracellular TG2 (Figure 3B).

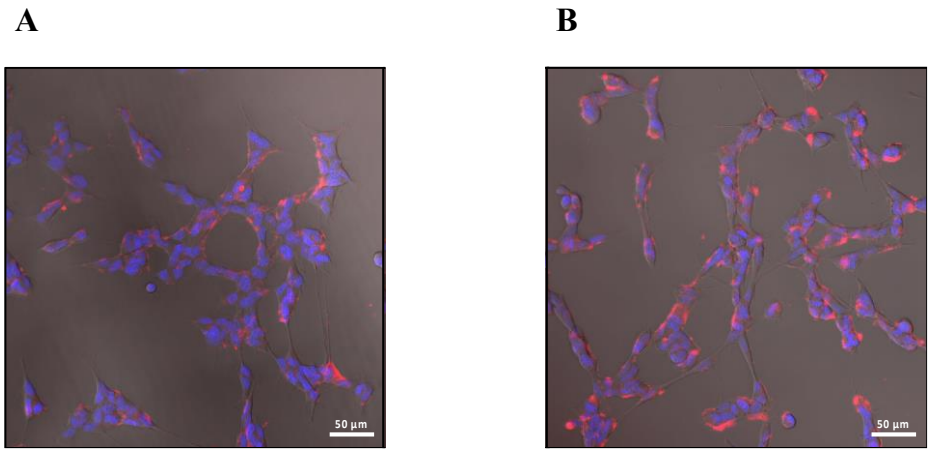

Figure 3.3. (A) Cell microscopy of SH-SY5Y cells incubated with 30 µM 29 (NCEG-RHB) (red) for 30 min and nucleus stained with Hoechst (blue). (B) Cell microscopy of SH-SY5Y cells differentiated with 20 µM retinoic acid for 4 days, incubated with 30 µM 29 (NCEG-RHB) (red) for 30 min and nucleus stained with Hoechst (blue).

3.6.7. Evaluation of Cancer Cell Proliferation and Migration

The library of research tools disclosed herein are all potent irreversible inhibitors of TG2, as measured in our biochemical activity assay (see above). However, these molecular tools differ

markedly in their cell permeability, allowing us to apply these contrasting agents to determine whether the role of TG2 in the proliferation and migration of cancer cells is due to its intracellular or extracellular activity. The unique properties of our cell-impermeable inhibitors make them powerful tools to answer this longstanding question. Remarkably, cell-impermeable inhibitor **18** (**NCEG2**) did not have any effect on cell proliferation of MDA-MB-231, MDA-MB-436, MDA-MB-468, HaCaT, or SCC-13 cell lines at concentrations up to 100 μM (Figure 4 and Supplementary Materials Figure S10). In further support, **18** (**NCEG2**) failed to suppress migration of MDA-MB-436 and MDA-MB-231, a trait commonly associated with TG2 activity in cancer cells (Figure S11) [51]. The rhodamine B-labelled probe **29** (**NCEG-RHB**) was first validated as being cell permeable in SH-SY5Y, HaCat, and SCC-13 cells through fluorescence microscopy (see Figures 3 and 4A). It was then tested in a similar manner to **18**, in SCC-13, MDA-MB-436, and MDA-MB-231 cells. Notably, in three different cancer cell lines, the fluorescent probe **29** (**NCEG-RHB**) also suppressed migration and proliferation significantly—even more so than previous lead inhibitors AA9 and NC9 (Figures 4B,D and S10). In this regard, probe **29** (**NCEG-RHB**) enables both diagnostic and pharmacological applications [52]. In light of the markedly different effects observed for the cell-*permeable* inhibitor **29** compared to the cell-*impermeable* inhibitor **18**, we conclude that targeting the cancer-associated roles of TG2 requires the inhibition of *intracellular* TG2. Further, it is presumably the *intracellular G-protein activity* of TG2 that contributes to cancer progression, since these chemical tools were designed to irreversibly inactivate the transamidase active site, but also to block GTP binding by locking TG2 in its open conformation [26,27].

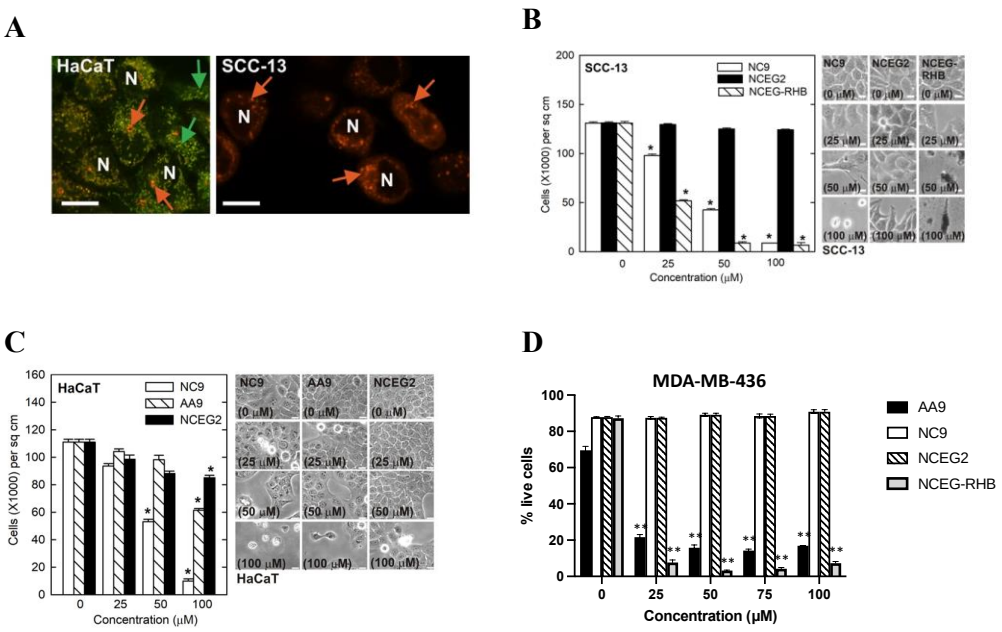

Figure 3.4. Treatment of cancer cells with cell-permeable and cell-impermeable inhibitors. (A) HaCaT and SCC-13 are epidermis-derived cutaneous squamous cell carcinoma cells that were treated for 10 h with NCEG-RHB prior to imaging using a spinning disc confocal microscope. NCEG-RHB localization is detected adjacent to the nuclei (N) in both cell types and is indicated by red arrows. The HaCaT cell cultures were also stained for 15 min with MitoTracker Green before imaging. MitoTracker Green detects mitochondria membrane proteins inside the cell and the labelling is indicated by green arrows. White scale bars = 100 µm. (B) SCC-13 cells treated with cell-impermeable inhibitor 18 (NCEG2) and cell-permeable inhibitors NC9, AA9, and NCEG-RHB. Scale bars represent 50 µm; (*) *p* value < 0.001 (C) HaCaT cells treated with cell-impermeable inhibitor 18 (NCEG2) and cell-permeable inhibitors NC9 and AA9. Scale bars represent 50 µm; (*) *p* value < 0.001. (D) MDA-MB-436 cells treated with cell-impermeable 18 (NCEG2) and with cell-permeable inhibitors NC9, AA9 and NCEG-RHB. Experiments were carried out in triplicate and are represented as average ± SD of the percentage of living cells; (**) *p* value < 0.01.

3.6.8. Pull-Down of TG2 from *E. coli* Lysate

While this manuscript was in preparation, Hauser et al. published a novel biotinylated TG2 inhibitor (Figure S12) that is highly efficient, exhibiting a k_{inact}/K_I value of 7260 $M^{-1}s^{-1}$ (or 435,600

M^{-1} min^{-1}) [53]. It is noteworthy that this inhibitor exploits the same binding pocket as our inhibitors disclosed herein, implying that this site of similar inhibitor scaffolds is broadly tailorable, with minimal impact on binding affinity. Our propargylated inhibitor **31** shows comparable efficiency to Hauser's (see Table 1). Further, TG2 that has been labelled with inhibitor **31** should be amenable to incorporation of a wide variety of azide-functionalized cargo, including desthiobiotin, which would allow pull-down with streptavidin resin and subsequent elution under milder conditions than its biotinylated counterpart. More specifically, incorporating desthiobiotin instead of biotin allows for elution from streptavidin resin using low millimolar concentrations of biotin for competitive displacement from the streptavidin binding site instead of the harsh denaturing conditions required for typical biotinylated chemical tools [54]. Inhibitor **31** may, therefore, allow for more protein–protein interactions to be retained during the elution process in the discovery of novel TG2 interactions.

As a proof of concept, previously described BL21 *E. coli* cells were transformed with a plasmid (pGST-PSP-rhTG2) to induce overexpression of recombinant human TG2 (rhTG2) as a GST fusion protein [47]. The bacterial cells were then lysed and exposed to the propargylated inhibitor **31** to allow for labelling. A subsequent CuAAC reaction was then performed in the same cell lysate to incorporate the desthiobitoin-PEG3-azide into labelled TG2. The lysate was then passed over streptavidin resin to isolate all proteins that had reacted with inhibitor **31**. These proteins were then eluted from the resin using a solution of 4 mM biotin, and the eluant was analyzed by SDS-PAGE. As can be seen in Figure S13 in the Supplementary Materials, the only protein efficiently isolated in this experiment corresponds to the GST-TG2 fusion protein (MW = 25 kDa + 78 kDa). This validates not only the TG2-selectivity of probe **31**, but also the efficiency

of the click reaction of the GST-TG2-**31** adduct, allowing for the isolation of TG2 from cell lysate in a very mild manner.

3.7. Materials and Methods

3.7.1. Chemical Synthesis

All details and experimental procedures for the chemical synthesis executed within this study along with characterization data can be found in the Supplementary Materials [55,56].

3.7.2. Molecular Docking of Compounds 16, 18, and 29 into TG2 Active Site

The "compute" tool from MOE was used to perform docking analysis of each ligand with TG2 (PDB: 2Q3Z) one by one, following a non-covalent approach where ligand placement was achieved using the Triangle Matcher protocol (London dG) to produce 30 poses. In addition, a rigid receptor refinement protocol was performed (GBVI/WSA dG) and a total of 5 final poses were obtained. Finally, using the builder tool from MOE, the covalent bonds between residue CYS277 and the acrylamide warhead of the bound inhibitors were manually created, prior to minimization of the system (to 0.001 kcal mol^{-1} $Å^2$).

3.7.3. rhTG2 Inhibition Assay

Recombinant human TG2 was expressed and purified using previously published protocols [47]. The inhibition was monitored using a continuous chromogenic substrate AL5 [38] under Kitz and Wilson conditions [37,57]. In brief, 125 µL of assay buffer composed of 111.11 mM MOPS, 15.56 $CaCl_2$ pH 6.9 was added to a 1.5 mL Eppendorf tube to achieve final assay concentrations of 50 mM MOPS and 7.5 mM $CaCl_2$. To the tube was then added the respective concentration of inhibitor from an aqueous working stock (<5% DMSO final conditions). Various volumes of water

were then added to ensure the final volumes were equal. The AL5 substrate was added to the Eppendorf tube as a 5 µL 5.56 mM solution in DMSO to obtain a final assay concentration of 100 µM. A 96-well polystyrene microplate then had 180 µL of the assay mixture added to it. The enzymatic reaction was finally initiated by addition of 20 µL 5 mU prediluted TG2 in assay buffer using a multichannel pipette. The reaction was monitored at 405 nm using a BioTek Synergy 4 plate reader for 20 min at 25 °C. A positive control with no inhibitor and a blank with no enzyme nor inhibitor were also included. The blank subtracted kinetic curves were then analyzed. The observed first-order rate constants of inactivation were gathered through a one-phase association model using the GraphPad software package. The rate constants were then fit to various models to elucidate the inhibition parameters. If saturation was achieved, they were fit to a saturation model versus the inhibitor concentration divided by alpha (where $\alpha = 1 + \frac{[Substrate]}{Km}$). A linear regression of the linear region of this saturation fitting was calculated to obtain a ratio of k_{inact}/K_I. A further double reciprocal model was used if saturation could not be observed due to the limitations in sensitivity of the assay or if solubility issues were present.

3.7.4. TGase Isozyme Selectivity

The selectivity of the cell-impermeable inhibitors was evaluated against four other therapeutically relevant TGases (TG1, TG3a, TG6, and FXIIIa, all purchased from Zedira GmbH (Darmstadt, Germany). By varying both the inhibitor and assay substrate concentrations with each isozyme, we ensured that the [I]/α values remained constant as each isozyme had a different K_m for its respective substrate. In order to obey Kitz and Wilson conditions, the substrate concentrations were varied, and the inhibitor concentrations were adjusted to account for this change in affinity. TG1, TG6, and TG2 were all monitored using the aforementioned rhTG2

inhibition assay procedure. The AL5 substrate concentrations for TG1 and TG6 were 112 µM and 435 µM, respectively, with 0.1 µM TG1 or 0.32 µM TG6. To monitor the activity of TG3a and TG6, a FRET-quenched substrate A101 (Zedira Gmbh) was used [42,43]. In brief, 125 µL assay buffer #1 (containing TRIS, $CaCl_2$, and NaCl pH 7.5), 18 µL assay buffer #2 (containing TCEP and acceptor substrate H-Gly-OMe pH 7.5), and a respective concentration of inhibitor aqueous working stock balanced with various volumes of water were combined in a 96-well black plate with clear bottom/top. The enzymatic reactions were then initiated by addition of 20 µL of prediluted enzyme with a microchannel pipette to provide 0.11 µM FXIIIa or 0.17 µM TG3a. The isopeptidase activity of the respective TGase was then monitored at Ex/Em = 313/418 nm with a BioTek Synergy 4 plate reader at 25 °C. The final assay conditions contained a final volume of 200 µL 69 mM TRIS, 10 mM $CaCl_2$, 208 mM NaCl, 5 mM TCEP, and 13 mM H-Gly-OMe pH 7.5. A positive control with no inhibitor and a blank with no enzyme nor inhibitor were included. The kinetic curves then had the blank subtracted and were compared versus the other isozymes.

3.7.5. Fluorescent Labelling of Purified rhTG2

Recombinant human TG2 was expressed and purified from *E. coli* using a previously in-house-developed method [47]. The purified TG2 was stored in cleavage buffer (20 mM TRIS, 150 mM NaCl, 1 mM EDTA, 1 mM TCEP, 15% glycerol, pH 7.2) at −80 °C. The concentration obtained was 1.166 mg/mL (~15 µM TG2) by a Bradford assay. Totals of 10 µL of this stock, 5 µL of a 20 mM TRIS buffered solution of 50 mM $CaCl_2$ (pH 7.2), and 10 µL of a 75 µM stock of the respective fluorescent probe (2.5% DMSO in mQ H_2O) were added to a 1.5 mL Eppendorf tube and then vortexed. The labelling was allowed to occur for 25 min at room temperature. A total of 25 µL of a 2× Laemelli buffer with 5% BME was added to the Eppendorf tube, and the

tube was heated to 100 °C for 5 min to ensure denaturation. The solutions were then allowed to cool and 20 µL was loaded onto a BioRad Mini-PROTEAN TGX 4–20% polyacrylamide precast SDS-PAGE gel along with 10 µL BioRad Precision Plus Protein Unstained Standards. Electrophoresis (120 V) was then performed for 1 h in 25 mM TRIS, 192 mM glycine, 0.1% SDS buffer. The gel was first visualized using a BioRad ChemiDoc MP Imager exciting at each specific wavelength (**23** blue epi illumination 530/28 nm filter, **22** UV trans illumination 530/28 nm filter, and **29 (NCEG-RHB)** green epi illumination 605/50 nm filter) to observe the fluorescent bands, and then the gel was stained with Coomassie Blue and visualized again.

3.7.6. SH-SY5Y Fluorescent Microscopy

SH-SY5Y cells (CRL-2266, ATCC) were thawed and grown under cell culture conditions (5% CO_2, 37 °C, humidified) to 80% confluency in Dulbecco's Modified Eagle Medium (DMEM) supplemented with penicillin/streptomycin (P/S, 100 U/mL/100 µg/mL) and heat-inactivated fetal bovine serum (FBS, 10%). Cells were passaged three times before being seeded into 12-well glass-bottom imaging plates. Cells were either grown to confluency using the previously mentioned methods or differentiated using an adapted protocol from Singh et al. [50]. Briefly, cells to be differentiated were seeded at 20% confluency and grown in DMEM supplemented with 3% heat inactivated FBS, P/S, and 20 µM trans-retinoic acid (RA). The medium was changed daily for 4 days, at which point cells were 80% confluent and used for experimentation.

Triplicate wells of both differentiated and undifferentiated cells, once 80% confluent, were treated with or without 20 µM of probe in their respective medium containing 0.1% DMSO and incubated under cell culture conditions for 2 h. Following incubation, cells were washed three times with 37 °C, sterile Dulbecco's phosphate-buffered saline (PBS) and incubated for 20 min in

phenol red-free medium with 1 µg/mL Hoechst 33342 under cell culture conditions. Each well was imaged on a Zeiss LSM 880 confocal microscope with both 20× and 63× objectives, simultaneously collecting both brightfield, nuclear fluorescence (Hoechst 33342, ex/em 405/461 nm) and any fluorescence associated with the remaining intracellular probe (ex/em 514/600 nm).

3.7.7. Cell Proliferation Assay

MDA-MB-468 cells were cultured in Dulbecco's Modified Eagle Medium (DMEM)/F-12 DMEM, Gibco Laboratories, New York, NY, USA), 10% FBS (Gibco Laboratories, New York, NY, USA), 50 U/mL penicillin, and 50 µg/mL streptomycin (Gibco Laboratories, New York, NY, USA), while MDA-MB-231 and MDA-MB-436 cells were cultured in DMEM High Glucose with/stable L-Glutamine (EuroClone, Pero, MI, Italy), 10% FBS, and antibiotics, all grown at 37 °C and in 5% CO_2 humidified atmosphere.

The compounds were added to the cultures at the concentrations of 25, 50, 75, and 100 µM and 0.1% DMSO represented the negative control. After 48 h, the cells were trypsinized for 2 min at 37 °C, trypsin was inactivated using 1 mL of the recovered supernatants (containing 10% FBS), centrifuged at room temperature 5 min at 1200 rpm, washed with PBS and resuspended in complete medium. Finally, 50 µL of cells were diluted in 500 µL of Count & Viability Reagent (Luminex, Prodotti Gianni, Milan, Italy) and analyzed by MUSE®.

The experiments were carried out in triplicate and the average ± SD of the percentage of living cells was reported. Statistical analysis was performed calculating *p* value by a Student's *t*-test, two-tailed, with homovariance and significance expressed by (*) p value < 0.05.

3.7.8. Real-Time Cell Migration Assay

We assayed the motility of MDA-MB-436 cells in the presence of vehicle or TG2 inhibitors **18 (NCEG2)**, **19 (NCEG-RHB)**, and NC9 at 25 μM concentration with the xCELLigence RTCA system (Real-Time Cell Analyzer System, Acea Biosciences Inc., San Diego, CA, USA) [58]. About 3×10^5 cells/wells were put into the top chambers of CIM-16 plates and the bottom chambers were filled with medium containing 5% FBS (Gibco Laboratories, New York, NY, USA) as a chemoattractant. Signal detection was done every 15 min for 24 h and each determination was performed in triplicate. Impedance values were expressed as a dimensionless parameter (Cell Index, CI), and values greater than 0.1 were considered positive. The rate of cell migration was also quantified by calculating the steepness, inclination, gradient, and changing rate of the CI curves over time (Slope).

3.7.9. HaCaT and SCC-13 Cell Staining

SCC-13 and HaCaT cells (0.1×10^6) were plated in 35 mm Mat Tek glass bottom cell culture dishes. After 24 h, the cells were treated with 25 μM **18** (**NCEG-RHB**), a rhodamine-B-labelled cell-permeable TG2 inhibitor, for 18 h. The cells were washed three times with phosphate-buffered saline prior to spinning disc confocal microscopy. In addition, the HaCaT cells were treated with 50 nM MitoTracker GreenFM (#M7514) dye, obtained from Invitrogen (Waltham, MA, USA). The cells were then washed three times with PBS before live cell imaging using a Nikon spinning disc confocal microscope. HaCaT and SCC-13 are epidermis-derived cutaneous squamous cell carcinoma cells [59,60]. **NCEG-RHB** (**18**) is detected adjacent to the nuclei (**N**) in both cell types and is indicated by red arrows. MitoTracker GreenFM stains mitochondria

membrane proteins inside the cell, which is indicated by the green arrows. The sizing bar in the images represents 100 microns.

3.7.10. Pull-Down of rhTG2 from *E. coli* Lysate

A total of 400 µL of the aforementioned *E. coli* cell lysate combined with 133 µL of a solution of 75 µM **31** was added to a 1.5 mL Eppendorf tube. The labelling was allowed to occur for 25 min. Totals of 25 µL of a solution of 500 µM azide-PEG3-desthiobiotin **32** and 500 µM cupric sulfate in 20 mM HEPES at pH 8.0 were added to the tube. To initiate the click reaction, 100 µL of 150 µM sodium ascorbate solution in mQ H_2O was added and gently rocked for 2.5 h at room temperature. Using 100 µL slurry of equilibrated (washed 3× with PBS) streptavidin agarose resin in PBS (pH 7.4), 200 µL of the click reaction mixture was combined in an Eppendorf tube. The tube was gently mixed, and binding was allowed to occur for 0.5 h at room temperature with gentle rocking. The tube was then centrifuged (500× *g* (3000 rpm) for 1 min) to pellet the resin and the supernatant was removed and saved for the gel (FT1). An additional 100 µL of PBS buffer (pH 7.4) was added and the tube was gently mixed, and the resin was pelleted again. The supernatant was removed and saved for the gel (FT2). The wash with PBS buffer was then repeated once more (FT3). To elute the protein from the resin, 50 µL of elution buffer containing 4 mM biotin in PBS (pH 7.4) was added. The tube was gently mixed and allowed to gently shake at 37 °C for 10 min. To resin was pelleted and the supernatant was removed and saved for the gel (EL1). The elution step was then repeated two more times (EL2 and EL3).

For SDS-PAGE analysis of the elution, 15 µL of each fraction (or 15 µL of raw cell lysate) was combined with 15 µL 2× Laemelli buffer (5% BME) and boiled at 100 °C for 5 min for denaturation. The wells of a BioRad Mini-PROTEAN TGX Stain-Free 4–15% polyacrylamide

precast SDS-PAGE gel were then loaded with 20 µL of the corresponding sample along with 10 µL of BioRad Precision Plus Protein Unstained Standards. Electrophoresis (120 V) was performed for 50 min and the gel was visualized by Coomassie staining.

3.8. Conclusions

In this work, we have disclosed novel chemical tools designed to selectively label tissue transglutaminase (TG2). The cell-impermeable inhibitors described herein are first-in-class inhibitors that display excellent potency and efficiency of TG2 inhibition in addition to confirmed cellular impermeability. As such, they should prove to be powerful tools for the selective inhibition of the extracellular activities of TG2. Fluorescent probes were also prepared and shown to be highly efficient at labelling TG2, and to be cell permeable. A propargylated inhibitor was also designed and used to irreversibly inactivate TG2, which was then modified by a subsequent click reaction, incorporating desthiobitoin and allowing TG2 to be pulled down from cell lysate.

These probes should all prove to be of broad utility for investigations of the biological roles of TG2. However, the most important conclusion from this work may be from our interrogation of the relative importance of extracellular and intracellular TG2 activity in the propagation and invasion of certain cancer cells. Direct comparison of the results obtained with cell-impermeable inhibitor **18** (**NCEG2**) with those of cell-permeable inhibitor **29** (**NCEG-RHB**) provides the first concrete evidence that *intracellular* TG2 activity contributes to the cancer-associated phenotype, at least in the cell lines studied herein. This validates the rationale for specifically targeting intracellular TG2 when trying to alter cancer progression and advances our understanding of the importance of the sub-cellular context. The future application of these chemical tools should allow further discovery of the sub-cellular roles of TG2 and lead to other therapeutic applications.

3.9. Supplementary Materials

The following supporting information can be downloaded at: https://www.mdpi.com/article/10.3390/ijms241612546/s1.

3.10. Author Contributions

Conceptualization, J.W.K., E.W.J.G. and N.J.C.; formal analysis, E.W.J.G. and N.D.C.; investigation, E.W.J.G., N.D.C., N.J.C., F.B., P.N., A.K., N.B. and G.A.; writing—original draft preparation, E.W.J.G.; writing—review and editing, E.W.J.G., J.W.K., A.J.S. and R.L.E.; visualization, E.W.J.G., N.D.C., F.B., P.N., N.B. and G.A.; supervision, N.B., A.J.S. and J.W.K.; project administration, J.W.K.; funding acquisition, J.W.K. All authors have read and agreed to the published version of the manuscript.

3.11. Funding

This research was funded by the Natural Sciences and Engineering Research Council of Canada, grant number RGPIN-2019-05893 (J.W.K.), and the Canada Research Chair Program, grant number 950-230735 (A.J.S.).

3.12. Institutional Review Board Statement

Not applicable.

3.13. Acknowledgments

We thank Co.Pe.Go. (Soc. Coop. O. P.) for generous voluntary contribution to the research team of N. Bianchi.

3.14. Informed Consent Statement

Not applicable.

3.15. Data Availability Statement

Data will be provided upon reasonable request.

3.16. Conflicts of Interest

The authors declare no conflict of interest.

3.17. References

1. Lorand, L.; Graham, R.M. Transglutaminases: Crosslinking Enzymes with Pleiotropic Functions. *Nat. Rev. Mol. Cell Biol.* **2003**, *4*, 140–156. https://doi.org/10.1038/nrm1014.
2. Gundemir, S.; Colak, G.; Tucholski, J.; Johnson, G.V.W. Transglutaminase 2: A Molecular Swiss Army Knife. *Biochim. Biophys. Acta Mol. Cell Res.* **2012**, *1823*, 406–419. https://doi.org/10.1016/j.bbamcr.2011.09.012.
3. Beninati, S.; Bergamini, C.M.; Piacentini, M. An Overview of the First 50 Years of Transglutaminase Research. *Amino Acids* **2009**, *36*, 591–598. https://doi.org/10.1007/s00726-008-0211-x.
4. Keillor, J.W.; Clouthier, C.M.; Apperley, K.Y.P.; Akbar, A.; Mulani, A. Acyl Transfer Mechanisms of Tissue Transglutaminase. *Bioorg. Chem.* **2014**, *57*, 186–197. https://doi.org/10.1016/j.bioorg.2014.06.003.
5. Begg, G.E.; Holman, S.R.; Stokes, P.H.; Matthews, J.M.; Graham, R.M.; Iismaa, S.E. Mutation of a Critical Arginine in the GTP-Binding Site of Transglutaminase 2 Disinhibits

Intracellular Cross-Linking Activity. *J. Biol. Chem.* **2006**, *281*, 12603–12609. https://doi.org/10.1074/jbc.M600146200.

6. Pinkas, D.M.; Strop, P.; Brunger, A.T.; Khosla, C. Transglutaminase 2 Undergoes a Large Conformational Change upon Activation. *PLoS Biol.* **2007**, *5*, e327. https://doi.org/10.1371/journal.pbio.0050327.
7. Jang, T.H.; Lee, D.S.; Choi, K.; Jeong, E.M.; Kim, I.G.; Kim, Y.W.; Chun, J.N.; Jeon, J.H.; Park, H.H. Crystal Structure of Transglutaminase 2 with GTP Complex and Amino Acid Sequence Evidence of Evolution of GTP Binding Site. *PLoS ONE* **2014**, *9*, e107005. https://doi.org/10.1371/journal.pone.0107005.
8. Keillor, J.W.; Johnson, G.V.W. Transglutaminase 2 as a Therapeutic Target for Neurological Conditions. *Expert. Opin. Ther. Targets* **2021**, *25*, 721–731. https://doi.org/10.1080/14728222.2021.1989410.
9. Siegel, M.; Strnad, P.; Watts, R.E.; Choi, K.; Jabri, B.; Omary, M.B.; Khosla, C. Extracellular Transglutaminase 2 Is Catalytically Inactive, but Is Transiently Activated upon Tissue Injury. *PLoS ONE* **2008**, *3*, e1861. https://doi.org/10.1371/JOURNAL.PONE.0001861.
10. Tatsukawa, H.; Furutani, Y.; Hitomi, K.; Kojima, S. Transglutaminase 2 Has Opposing Roles in the Regulation of Cellular Functions as Well as Cell Growth and Death. *Cell Death Dis.* **2016**, *7*, e2244. https://doi.org/10.1038/cddis.2016.150.
11. Nadalutti, C.; Viiri, K.M.; Kaukinen, K.; Mäki, M.; Lindfors, K. Extracellular Transglutaminase 2 Has a Role in Cell Adhesion, Whereas Intracellular Transglutaminase 2 Is Involved in Regulation of Endothelial Cell Proliferation and Apoptosis. *Cell Prolif.* **2011**, *44*, 49–58. https://doi.org/10.1111/J.1365-2184.2010.00716.X.

12. Piacentini, M.; D'Eletto, M.; Farrace, M.G.; Rodolfo, C.; Del Nonno, F.; Ippolito, G.; Falasca, L. Characterization of Distinct Sub-Cellular Location of Transglutaminase Type II: Changes in Intracellular Distribution in Physiological and Pathological States. *Cell Tissue Res* **2014**, *358*, 793–805. https://doi.org/10.1007/s00441-014-1990-x.
13. Upchurch, H.F.; Conway, E.; Patterson, M.K.; Maxwell, M.D. Localization of Cellular Transglutaminase on the Extracellular Matrix after Wounding: Characteristics of the Matrix Bound Enzyme. *J. Cell. Physiol.* **1991**, *149*, 375–382. https://doi.org/10.1002/JCP.1041490304.
14. Fisher, M.L.; Keillor, J.W.; Xu, W.; Eckert, R.L.; Kerr, C. Transglutaminase Is Required for Epidermal Squamous Cell Carcinoma Stem Cell Survival. *Mol. Cancer Res.* **2015**, *13*, 1083–1094. https://doi.org/10.1158/1541-7786.MCR-14-0685-T.
15. Olsen, K.C.; Sapinoro, R.E.; Kottmann, R.M.; Kulkarni, A.A.; Iismaa, S.E.; Johnson, G.V.W.; Thatcher, T.H.; Phipps, R.P.; Sime, P.J. Transglutaminase 2 and Its Role in Pulmonary Fibrosis. *Am. J. Respir. Crit. Care Med.* **2011**, *184*, 699–707. https://doi.org/10.1164/rccm.201101-0013OC.
16. Benn, M.C.; Weber, W.; Klotzsch, E.; Vogel, V.; Pot, S.A. Tissue Transglutaminase in Fibrosis—More than an Extracellular Matrix Cross-Linker. *Curr. Opin. Biomed. Eng.* **2019**, *10*, 156–164. https://doi.org/10.1016/j.cobme.2019.06.003.
17. Dieterich, W.; Ehnis, T.; Bauer, M.; Donner, P.; Volta, U.; Riecken, E.O.; Schuppan, D. Identification of Tissue Transglutaminase as the Autoantigen of Celiac Disease. *Nat. Med.* **1997**, *3*, 797–801. https://doi.org/10.1038/nm0797-797.
18. Huang, L.; Xu, A.M.; Liu, W. Transglutaminase 2 in Cancer. *Am. J. Cancer Res.* **2015**, *5*, 2756–2776.

19. Tabolacci, C.; de Martino, A.; Mischiati, C.; Feriotto, G.; Beninati, S. The Role of Tissue Transglutaminase in Cancer Cell Initiation, Survival and Progression. *Med. Sci.* **2019**, *7*, 19–38. https://doi.org/10.3390/medsci7020019.

20. Shweke, N.; Boulos, N.; Jouanneau, C.; Vandermeersch, S.; Melino, G.; Dussaule, J.C.; Chatziantoniou, C.; Ronco, P.; Boffa, J.J. Tissue Transglutaminase Contributes to Interstitial Renal Fibrosis by Favoring Accumulation of Fibrillar Collagen through TGF-β Activation and Cell Infiltration. *Am. J. Pathol.* **2008**, *173*, 631–642. https://doi.org/10.2353/ajpath.2008.080025.

21. Daneshpour, N.; Griffin, M.; Collighan, R.; Perrie, Y. Targeted Delivery of a Novel Group of Site-Directed Transglutaminase Inhibitors to the Liver Using Liposomes: A New Approach for the Potential Treatment of Liver Fibrosis. *J. Drug Target.* **2011**, *19*, 624–631. https://doi.org/10.3109/1061186X.2010.531731.

22. Schuppan, D.; Mäki, M.; Lundin, K.E.A.; Isola, J.; Friesing-Sosnik, T.; Taavela, J.; Popp, A.; Koskenpato, J.; Langhorst, J.; Hovde, Ø.; et al. A Randomized Trial of a Transglutaminase 2 Inhibitor for Celiac Disease. *N. Engl. J. Med.* **2021**, *385*, 35–45. https://doi.org/10.1056/NEJMoa2032441.

23. Büchold, C.; Hils, M.; Gerlach, U.; Weber, J.; Pelzer, C.; Heil, A.; Aeschlimann, D.; Pasternack, R. Features of ZED1227: The First-In-Class Tissue Transglutaminase Inhibitor Undergoing Clinical Evaluation for the Treatment of Celiac Disease. *Cells* **2022**, *11*, 1667–1687. https://doi.org/10.3390/cells11101667.

24. Fisher, M.L.; Kerr, C.; Adhikary, G.; Grun, D.; Xu, W.; Keillor, J.W.; Eckert, R.L. Transglutaminase Interaction with A6/B4-Integrin Stimulates YAP1-Dependent ΔNp63α

Stabilization and Leads to Enhanced Cancer Stem Cell Survival and Tumor Formation. *Cancer Res.* **2016**, *76*, 7265–7276. https://doi.org/10.1158/0008-5472.CAN-16-2032.

25. Fisher, M.L.; Adhikary, G.; Xu, W.; Kerr, C.; Keillor, J.W.; Eckert, R.L. Type II Transglutaminase Stimulates Epidermal Cancer Stem Cell Epithelial-Mesenchymal Transition. *Oncotarget* **2015**, *6*, 20525–20539. https://doi.org/10.18632/ONCOTARGET.3890.
26. Akbar, A.; McNeil, N.M.R.; Albert, M.R.; Ta, V.; Adhikary, G.; Bourgeois, K.; Eckert, R.L.; Keillor, J.W. Structure-Activity Relationships of Potent, Targeted Covalent Inhibitors That Abolish Both the Transamidation and GTP Binding Activities of Human Tissue Transglutaminase. *J. Med. Chem.* **2017**, *60*, 7910–7927. https://doi.org/10.1021/acs.jmedchem.7b01070.
27. McNeil, N.M.R.; Gates, E.W.J.; Firoozi, N.; Cundy, N.J.; Leccese, J.; Eisinga, S.; Tyndall, J.D.A.; Adhikary, G.; Eckert, R.L.; Keillor, J.W. Structure-Activity Relationships of N-Terminal Variants of Peptidomimetic Tissue Transglutaminase Inhibitors. *Eur. J. Med. Chem.* **2022**, *232*, 114172–114196. https://doi.org/10.1016/j.ejmech.2022.114172.
28. Rorke, E.A.; Adhikary, G.; Szmacinski, H.; Lakowicz, J.R.; Weber, D.J.; Godoy-Ruiz, R.; Puranik, P.; Keillor, J.W.; Gates, E.W.J.; Eckert, R.L. Sulforaphane Covalently Interacts with the Transglutaminase 2 Cancer Maintenance Protein to Alter Its Structure and Suppress Its Activity. *Mol. Carcinog.* **2022**, *61*, 19–32. https://doi.org/10.1002/mc.23356.
29. Sima, L.E.; Matei, D.; Condello, S. The Outside-In Journey of Tissue Transglutaminase in Cancer. *Cells* **2022**, *11*, 1779–1802. https://doi.org/10.3390/CELLS11111779.

30. Yakubov, B.; Chelladurai, B.; Schmitt, J.; Emerson, R.; Turchi, J.J.; Matei, D. Extracellular Tissue Transglutaminase Activates Noncanonical NF-KB Signaling and Promotes Metastasis in Ovarian Cancer. *Neoplasia* **2013**, *15*, 609–619. https://doi.org/10.1593/NEO.121878.
31. Belkin, A.M. Extracellular TG2: Emerging Functions and Regulation. *FEBS J.* **2011**, *278*, 4704–4716. https://doi.org/10.1111/J.1742-4658.2011.08346.X.
32. Cundy, N.J.; Arciszewski, J.; Gates, E.W.J.; Acton, S.L.; Passley, K.D.; Awoonor-Williams, E.; Boyd, E.K.; Xu, N.; Pierson, É.; Fernandez-Ansieta, C.; et al. Novel Irreversible Peptidic Inhibitors of Transglutaminase 2. *RSC Med. Chem.* **2023**, *14*, 378–385. https://doi.org/10.1039/D2MD00417H.
33. Kerr, C.; Szmacinski, H.; Fisher, M.L.; Nance, B.; Lakowicz, J.R.; Akbar, A.; Keillor, J.W.; Lok Wong, T.; Godoy-Ruiz, R.; Toth, E.A.; et al. Transamidase Site-Targeted Agents Alter the Conformation of the Transglutaminase Cancer Stem Cell Survival Protein to Reduce GTP Binding Activity and Cancer Stem Cell Survival. *Oncogene* **2017**, *36*, 2981–2990. https://doi.org/10.1038/onc.2016.452.
34. Caron, N.S.; Munsie, L.N.; Keillor, J.W.; Truant, R. Using FLIM-FRET to Measure Conformational Changes of Transglutaminase Type 2 in Live Cells. *PLoS ONE* **2012**, *7*, e44159. https://doi.org/10.1371/journal.pone.0044159.
35. Clouthier, C.M.; Mironov, G.G.; Okhonin, V.; Berezovski, M.V.; Keillor, J.W. Real-Time Monitoring of Protein Conformational Dynamics in Solution Using Kinetic Capillary Electrophoresis. *Angew. Chem. Int. Ed.* **2012**, *51*, 12464–12468. https://doi.org/10.1002/anie.201205575.

36. Mironov, G.G.; Clouthier, C.M.; Akbar, A.; Keillor, J.W.; Berezovski, M.V. Simultaneous Analysis of Enzyme Structure and Activity by Kinetic Capillary Electrophoresis-MS. *Nat. Chem. Biol.* **2016**, *12*, 918–922. https://doi.org/10.1038/nchembio.2170.

37. Kitz, R.; Wilson, I.B. Esters of Methanesulfonic Acid as Irreversible Inhibitors of Acetylcholinesterase. *J. Biol. Chem.* **1962**, *237*, 3245–3249. https://doi.org/10.1016/s0021-9258(18)50153-8.

38. Leblanc, A.; Gravel, C.; Labelle, J.; Keillor, J.W. Kinetic Studies of Guinea Pig Liver Transglutaminase Reveal a General-Base-Catalyzed Deacylation Mechanism. *Biochemistry* **2001**, *40*, 8335–8342. https://doi.org/10.1021/bi0024097.

39. Rangaswamy, A.M.M.; Navals, P.; Gates, E.W.J.; Shad, S.; Watt, S.K.I.; Keillor, J.W. Structure–Activity Relationships of Hydrophobic Alkyl Acrylamides as Tissue Transglutaminase Inhibitors. *RSC Med. Chem.* **2022**, *13*, 413–428. https://doi.org/10.1039/d1md00382h.

40. Keillor, J.W.; Apperley, K.Y.P. Transglutaminase Inhibitors: A Patent Review. *Expert. Opin. Ther. Pat.* **2016**, *26*, 49–63. https://doi.org/10.1517/13543776.2016.1115836.

41. Song, M.; Hwang, H.; Im, C.Y.; Kim, S.-Y. Recent Progress in the Development of Transglutaminase 2 (TGase2) Inhibitors. *J. Med. Chem.* **2016**, *60*, 554–567. https://doi.org/10.1021/ACS.JMEDCHEM.6B01036.

42. Oertel, K.; Hunfeld, A.; Specker, E.; Reiff, C.; Seitz, R.; Pasternack, R.; Dodt, J. A Highly Sensitive Fluorometric Assay for Determination of Human Coagulation Factor XIII in Plasma. *Anal. Biochem.* **2007**, *367*, 152–158. https://doi.org/10.1016/j.ab.2007.05.011.

43. Király, R.; Thangaraju, K.; Nagy, Z.; Collighan, R.; Nemes, Z.; Griffin, M.; Fésüs, L. Isopeptidase Activity of Human Transglutaminase 2: Disconnection from Transamidation and

Characterization by Kinetic Parameters. *Amino Acids* **2016**, *48*, 31–40. https://doi.org/10.1007/s00726-015-2063-5.

44. Lipinski, C.A. Drug-like Properties and the Causes of Poor Solubility and Poor Permeability. *J. Pharmacol. Toxicol. Methods* **2000**, *44*, 235–249. https://doi.org/10.1016/S1056-8719(00)00107-6.
45. Veber, D.F.; Johnson, S.R.; Cheng, H.Y.; Smith, B.R.; Ward, K.W.; Kopple, K.D. Molecular Properties That Influence the Oral Bioavailability of Drug Candidates. *J. Med. Chem.* **2002**, *45*, 2615–2623. https://doi.org/10.1021/jm020017n.
46. Daina, A.; Michielin, O.; Zoete, V. SwissADME: A Free Web Tool to Evaluate Pharmacokinetics, Drug-Likeness and Medicinal Chemistry Friendliness of Small Molecules. *Sci. Rep.* **2017**, *7*, 42717. https://doi.org/10.1038/srep42717.
47. Roy, I.; Smith, O.; Clouthier, C.M.; Keillor, J.W. Expression, Purification and Kinetic Characterisation of Human Tissue Transglutaminase. *Protein Expr. Purif.* **2013**, *87*, 41–46. https://doi.org/10.1016/j.pep.2012.10.002.
48. Zhang, J.; Lesort, M.; Guttmann, R.P.; Johnson, G.V.W. Modulation of the in Situ Activity of Tissue Transglutaminase by Calcium and GTP. *J. Biol. Chem.* **1998**, *273*, 2288–2295. https://doi.org/10.1074/JBC.273.4.2288.
49. Tucholski, J.; Lesort, M.; Johnson, G.V.W. Tissue Transglutaminase Is Essential for Neurite Outgrowth in Human Neuroblastoma SH-SY5Y Cells. *Neuroscience* **2001**, *102*, 481–491. https://doi.org/10.1016/S0306-4522(00)00482-6.
50. Singh, U.S.; Pan, J.; Kao, Y.L.; Joshi, S.; Young, K.L.; Baker, K.M. Tissue Transglutaminase Mediates Activation of RhoA and MAP Kinase Pathways during Retinoic Acid-Induced

Neuronal Differentiation of SH-SY5Y Cells. *J. Biol. Chem.* **2003**, *278*, 391–399. https://doi.org/10.1074/JBC.M206361200.

51. Lee, H.T.; Huang, C.H.; Chen, W.C.; Tsai, C.S.; Chao, Y.L.; Liu, S.H.; Chen, J.H.; Wu, Y.Y.; Lee, Y.J. Transglutaminase 2 Promotes Migration and Invasion of Lung Cancer Cells. *Oncol. Res.* **2018**, *26*, 1175–1182. https://doi.org/10.3727/096504018X15149761920868.
52. Sotiropoulou, G.; Zingkou, E.; Bisyris, E.; Pampalakis, G. Activity-Based Probes for Proteases Pave the Way to Theranostic Applications. *Pharmaceutics* **2022**, *14*, 977. https://doi.org/10.3390/PHARMACEUTICS14050977.
53. Hauser, S.; Sommerfeld, P.; Wodtke, J.; Hauser, C.; Schlitterlau, P.; Pietzsch, J.; Löser, R.; Pietsch, M.; Wodtke, R. Application of a Fluorescence Anisotropy-Based Assay to Quantify Transglutaminase 2 Activity in Cell Lysates. *Int. J. Mol. Sci.* **2022**, *23*, 4475–4507. https://doi.org/10.3390/ijms23094475.
54. Hirsch, J.D.; Eslamizar, L.; Filanoski, B.J.; Malekzadeh, N.; Haugland, R.P.; Beechem, J.M.; Haugland, R.P. Easily Reversible Desthiobiotin Binding to Streptavidin, Avidin, and Other Biotin-Binding Proteins: Uses for Protein Labeling, Detection, and Isolation. *Anal. Biochem.* **2002**, *308*, 343–357. https://doi.org/10.1016/S0003-2697(02)00201-4.
55. Atherton, E.; Logan, C.J.; Sheppard, R.C. Peptide Synthesis. Part 2. Procedures for Solid-Phase Synthesis Using Nα-Fluorenylmethoxycarbonylamino-Acids on Polyamide Supports. Synthesis of Substance P and of Acyl Carrier Protein 65-74 Decapeptide. *J. Chem. Soc. Perkin Trans. 1* **1981**, *12*, 538–546. https://doi.org/10.1039/P19810000538.
56. Gude, M.; Ryf, J.; White, P.D. An Accurate Method for the Quantitation of Fmoc-Derivatized Solid Phase Supports. *Lett. Pept. Sci.* **2002**, *9*, 203–206. https://doi.org/10.1007/BF02538384.

57. Stone, S.R.; Hofsteenge, J. Specificity of Activated Human Protein C. *Biochem. J.* **1985**, *230*, 497–502. https://doi.org/10.1042/bj2300497.
58. Bianchi, N.; Brugnoli, F.; Grassilli, S.; Bourgeois, K.; Keillor, J.W.; Bergamini, C.M.; Aguiari, G.; Volinia, S.; Bertagnolo, V. The Motility and Mesenchymal Features of Breast Cancer Cells Correlate with the Levels and Intracellular Localization of Transglutaminase Type 2. *Cells* **2021**, *10*, 3059–3078. https://doi.org/10.3390/cells10113059.
59. Rheinwald, J.G.; Beckett, M.A. Tumorigenic Keratinocyte Lines Requiring Anchorage and Fibroblast Support Cultured from Human Squamous Cell Carcinomas. *Cancer Res.* **1981**, *41*, 1657–1663.
60. Boukamp, P.; Petrussevska, R.T.; Breitkreutz, D.; Hornung, J.; Markham, A.; Fusenig, N.E. Normal Keratinization in a Spontaneously Immortalized Aneuploid Human Keratinocyte Cell Line. *J. Cell Biol.* **1988**, *106*, 761–771. https://doi.org/10.1083/jcb.106.3.761.

3.18. Disclaimer/Publisher's Note

The statements, opinions and data contained in all publications are solely those of the individual author(s) and contributor(s) and not of MDPI and/or the editor(s). MDPI and/or the editor(s) disclaim responsibility for any injury to people or property resulting from any ideas, methods, instructions or products referred to in the content.

Appendix to Chapter 3

Supporting Information

for

Cell-Impermeable Inhibitors Confirm that Intracellular Human Transglutaminase 2 is Responsible for the Transglutaminase-Associated Cancer Phenotype

*Eric W. J. Gates[1], Nicholas D. Calvert[1], Nicholas J. Cundy[1], Federica Brugnoli[2], Pauline Navals[1], Alexia Kirby[1], Nicoletta Bianchi[2], Gautam Adhikary[3], Adam J. Shuhendler[1], Richard L. Eckert[3], Jeffrey W. Keillor[1]**

[1]Department of Chemistry and Biomolecular Sciences, University of Ottawa, Ottawa, Ontario K1N 6N5, Canada

[2]Department of Translational Medicine, University of Ferrara, Ferrara, 44121, Italy

[3]Department of Biochemistry and Molecular Biology, University of Maryland School of Medicine, Baltimore, Maryland 21201, United States

Supplementary synthetic schemes

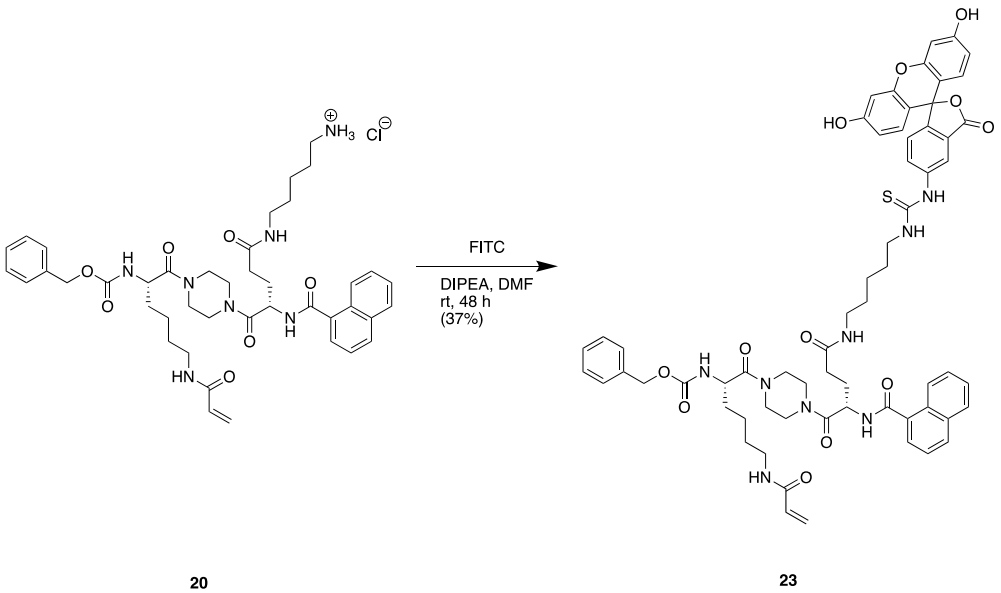

Scheme S1. Synthetic scheme from key intermediate to generate fluorescent FITC probe **23**.

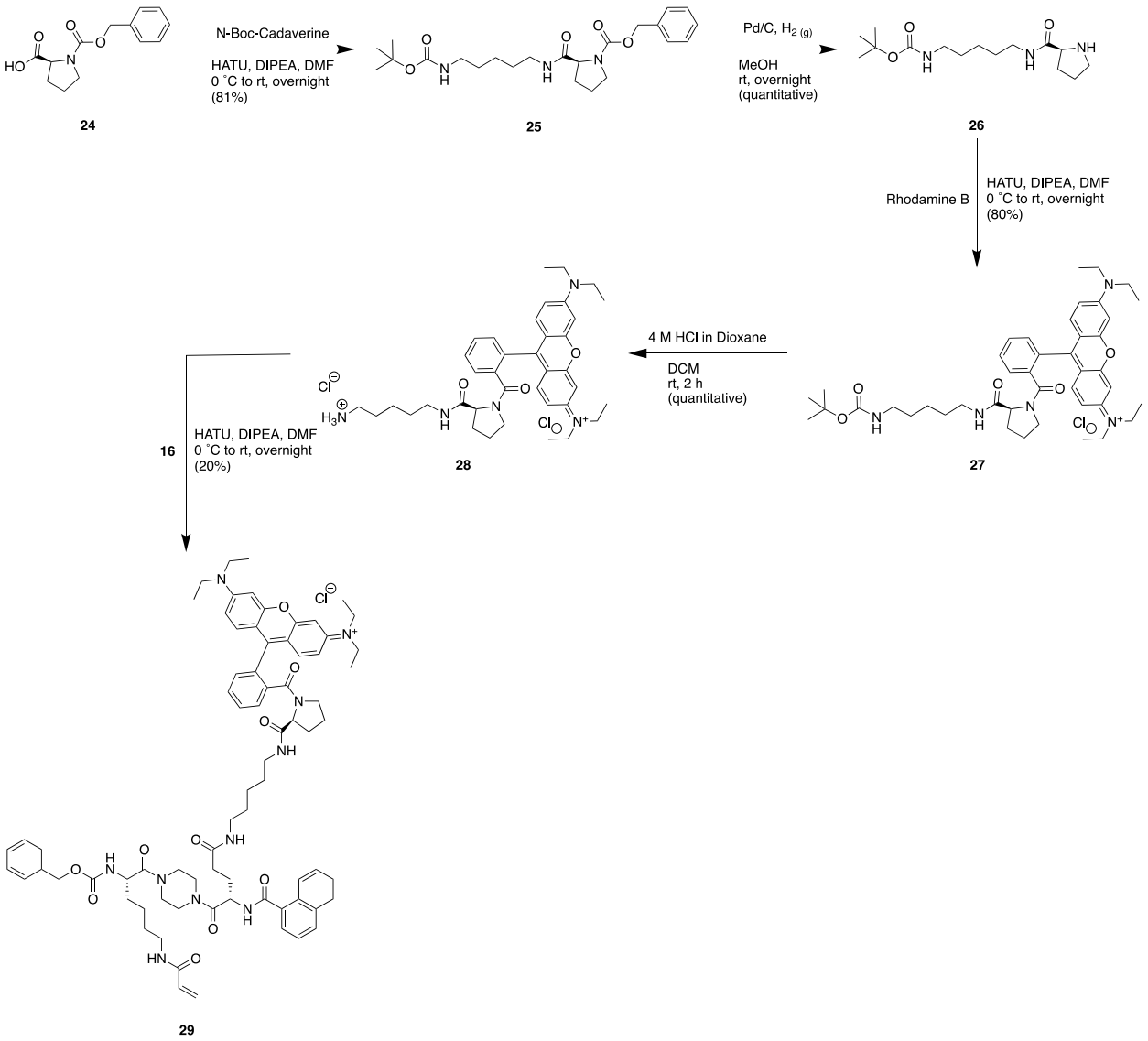

Scheme S2. Synthetic scheme from key intermediate **16** to generate fluorescent rhodamine B probe **29**.

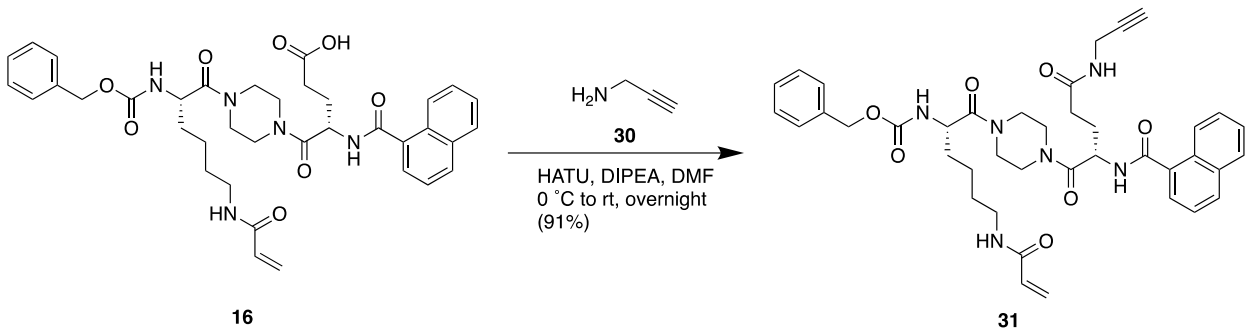

Scheme S3. Synthetic scheme from key intermediate **16** to generate propargyl derivative **31**, appropriate for subsequent 'click' modification.

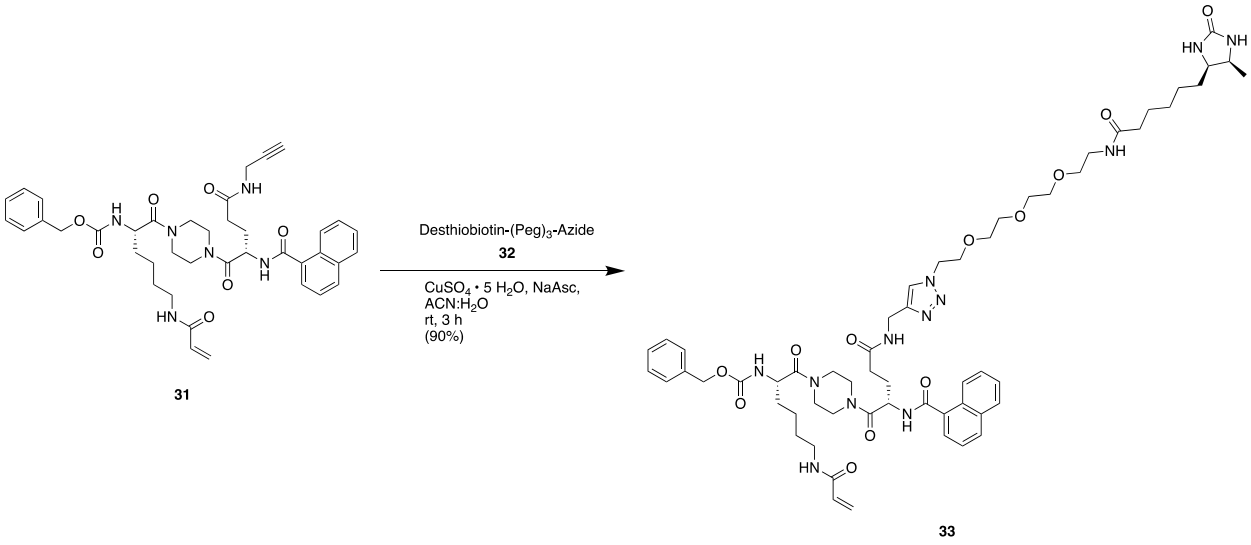

Scheme S4. CuAAC 'click' reaction to generate the desthiobiotin derivative **33** used in the pull-down assay.

Supplementary kinetic traces and fitting

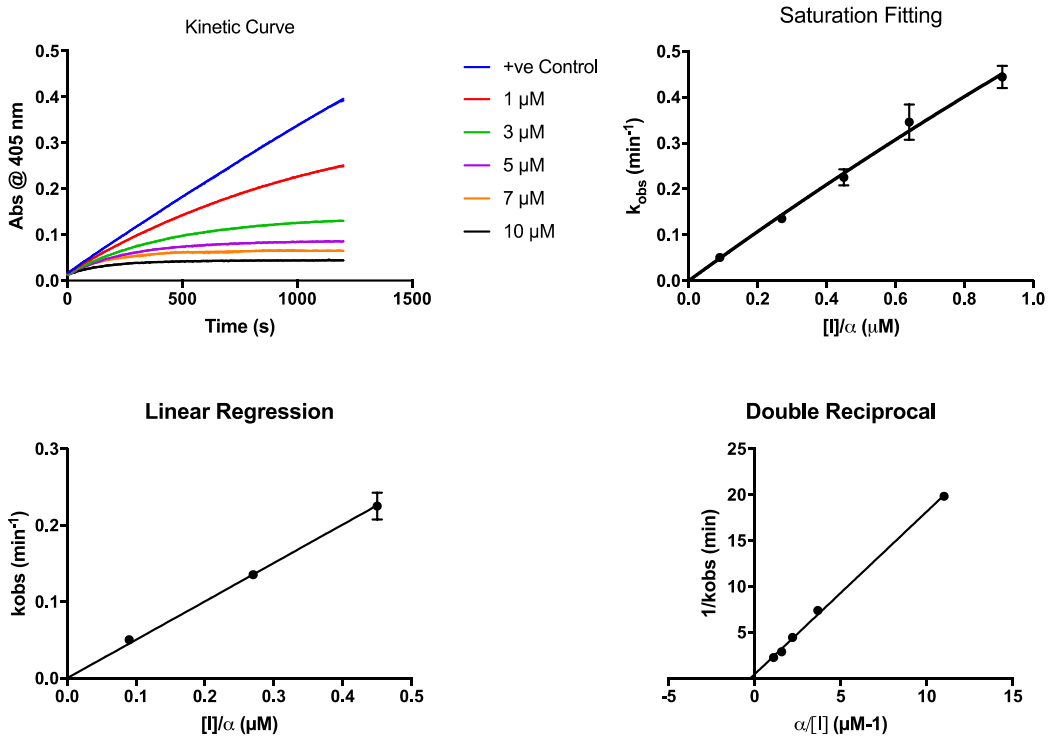

Figure S1. Kinetic traces and fitting of **18 (NCEG2)**.

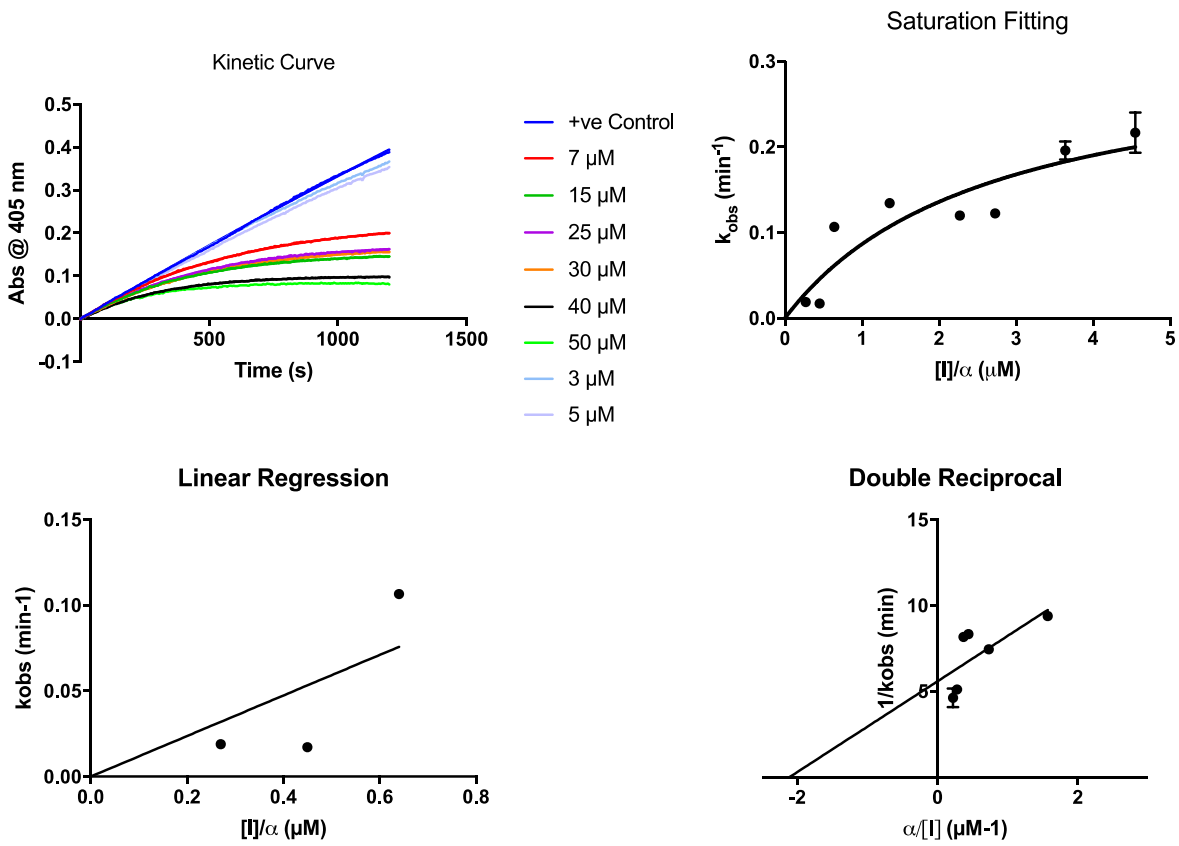

Figure S2. Kinetic traces and fitting for **22**.

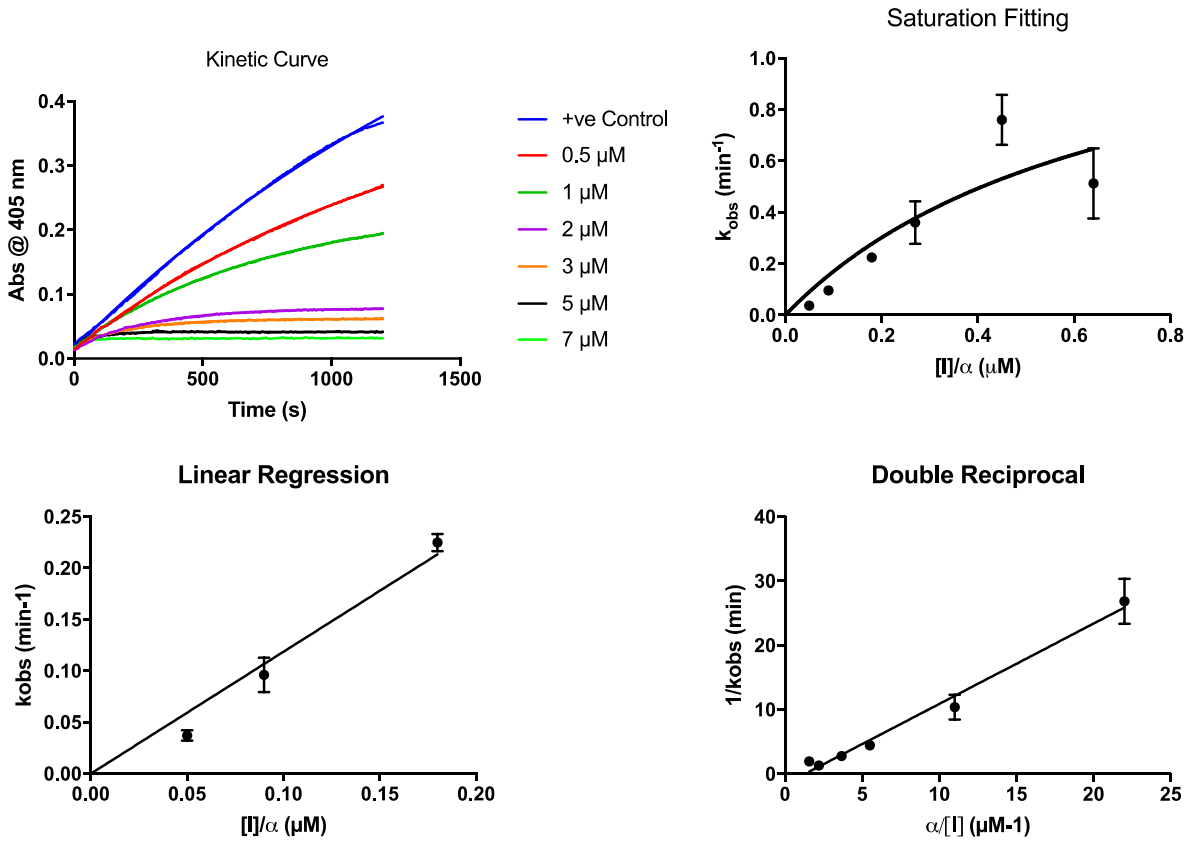

Figure S3. Kinetic traces and fitting for **23**.

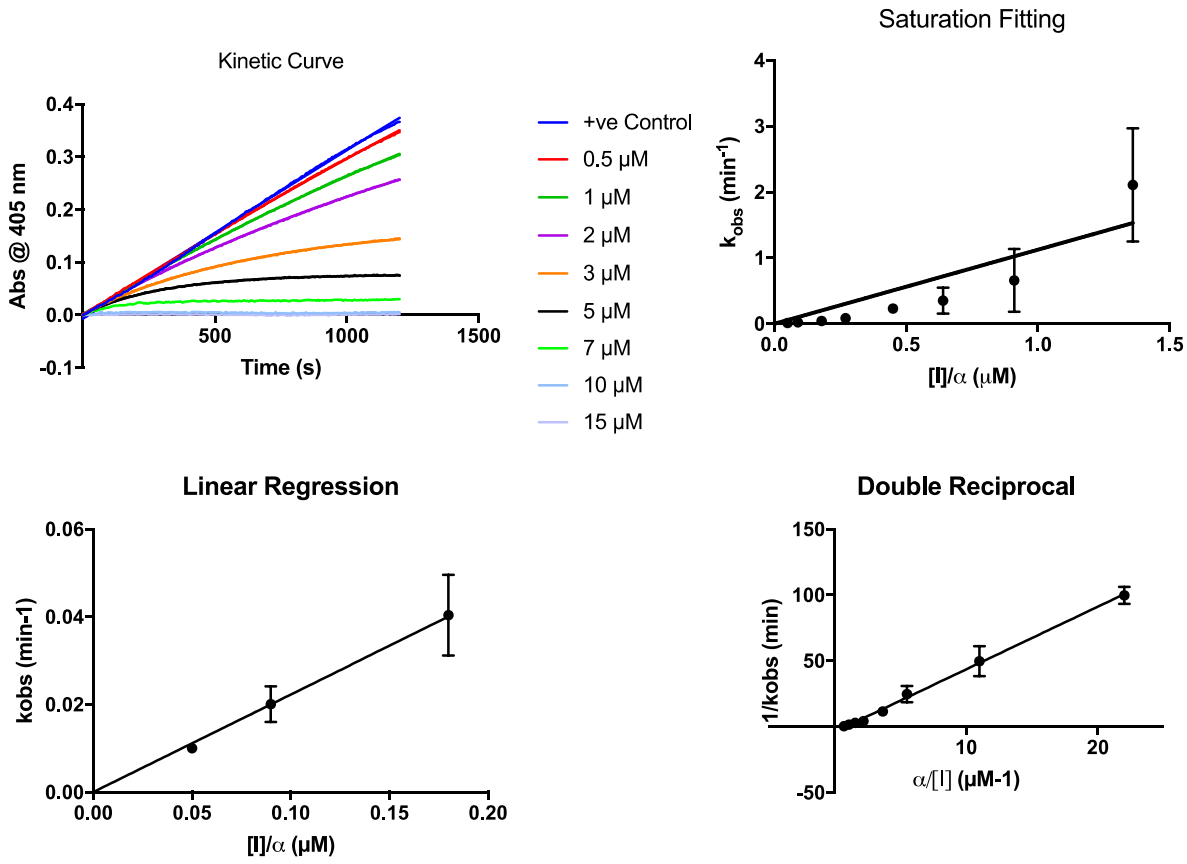

Figure S4. Kinetic traces and fitting for **29 (NCEG-RHB)**.

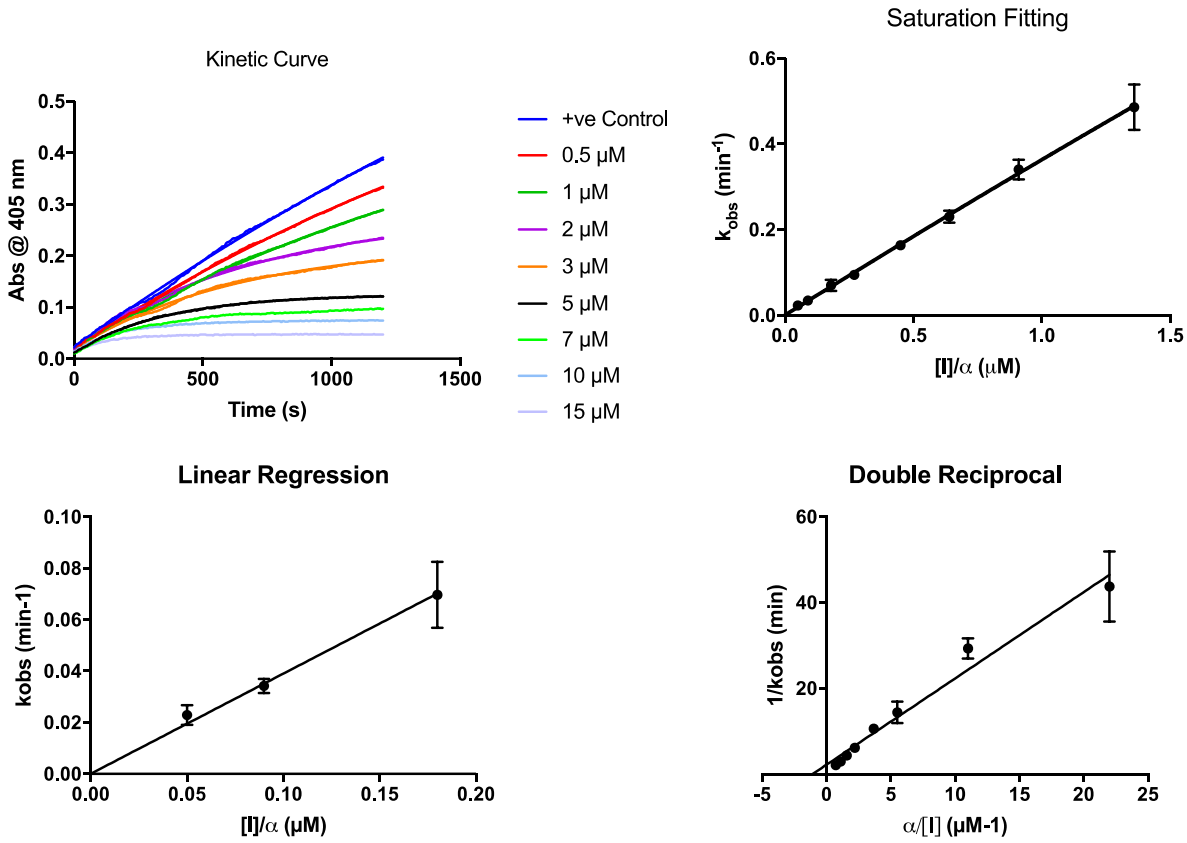

Figure S5. Kinetic traces and fitting for **31**.

Molecular docking of compounds in TG2 active site

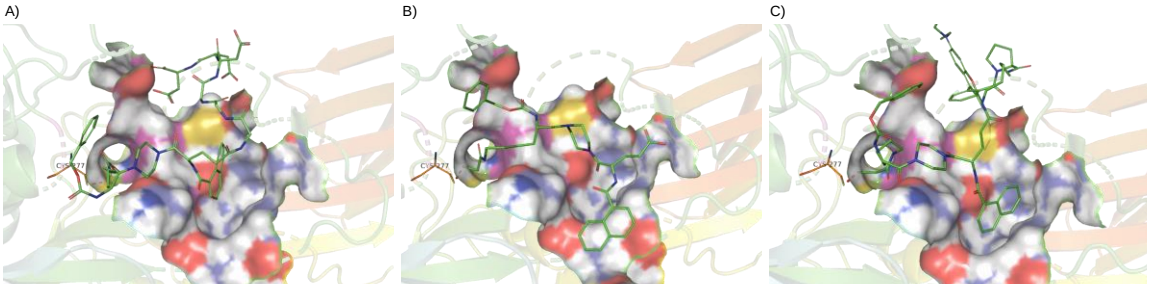

Figure S6. **Structural representation of inhibitors 16, 18 (NCEG2), and 29 (NCEG-RHB) covalently bound to the catalytic pocket of TG2 (PDB: 2Q3Z) via CYS277 (orange residue). A) inhibitor 18, S score = -9.63. B) inhibitor 16, S score -9.92. C) inhibitor 29, S score -10.93.**

Isozyme selectivity

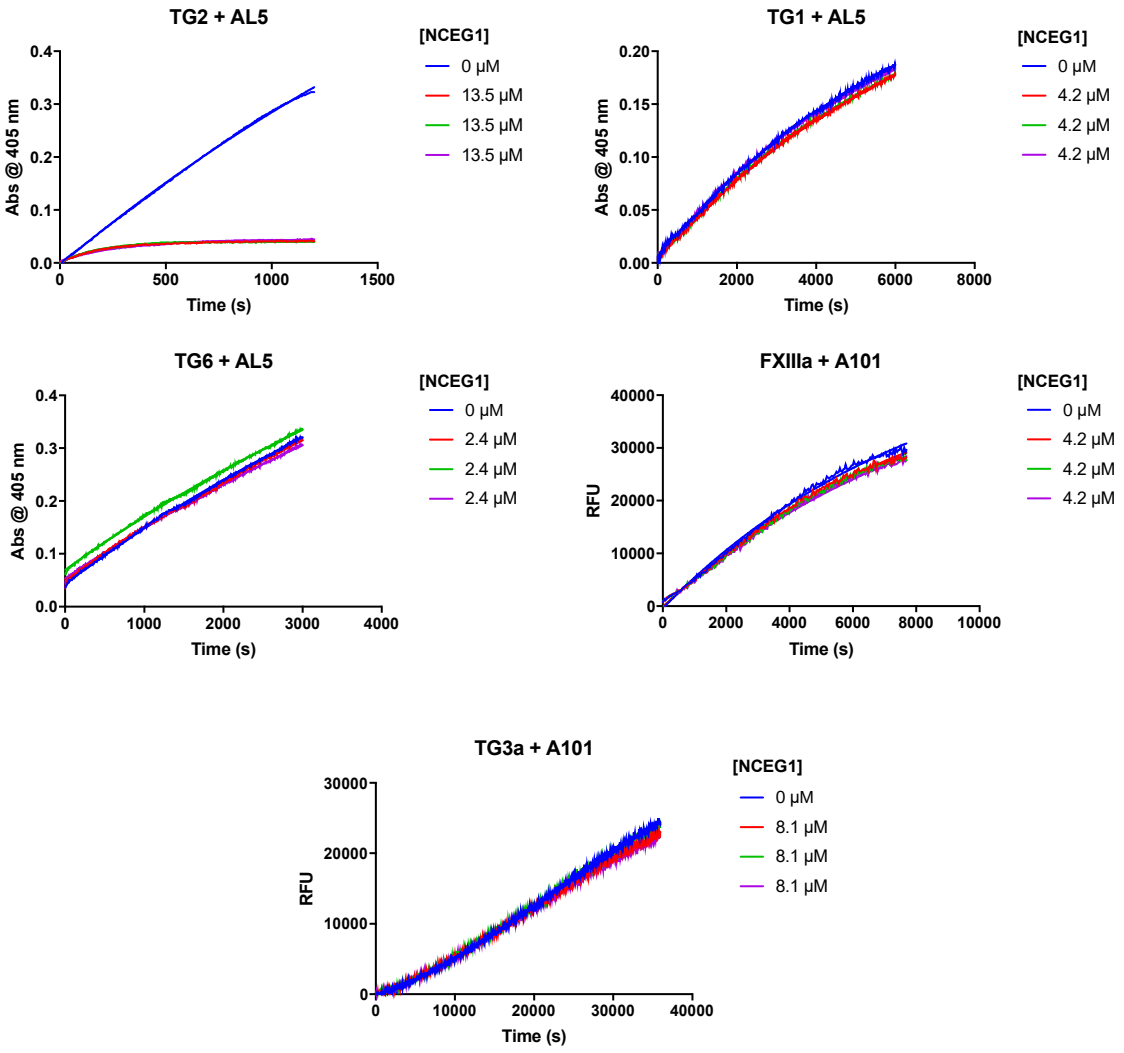

Figure S7. Isozyme selectivity of **17** with respect to therapeutically relevant human transglutaminases TG2, TG1, TG6, FXIIIa, and TG3a, using either chromogenic substrate AL5 or fluorescently quenched isopeptidase substrate A101.

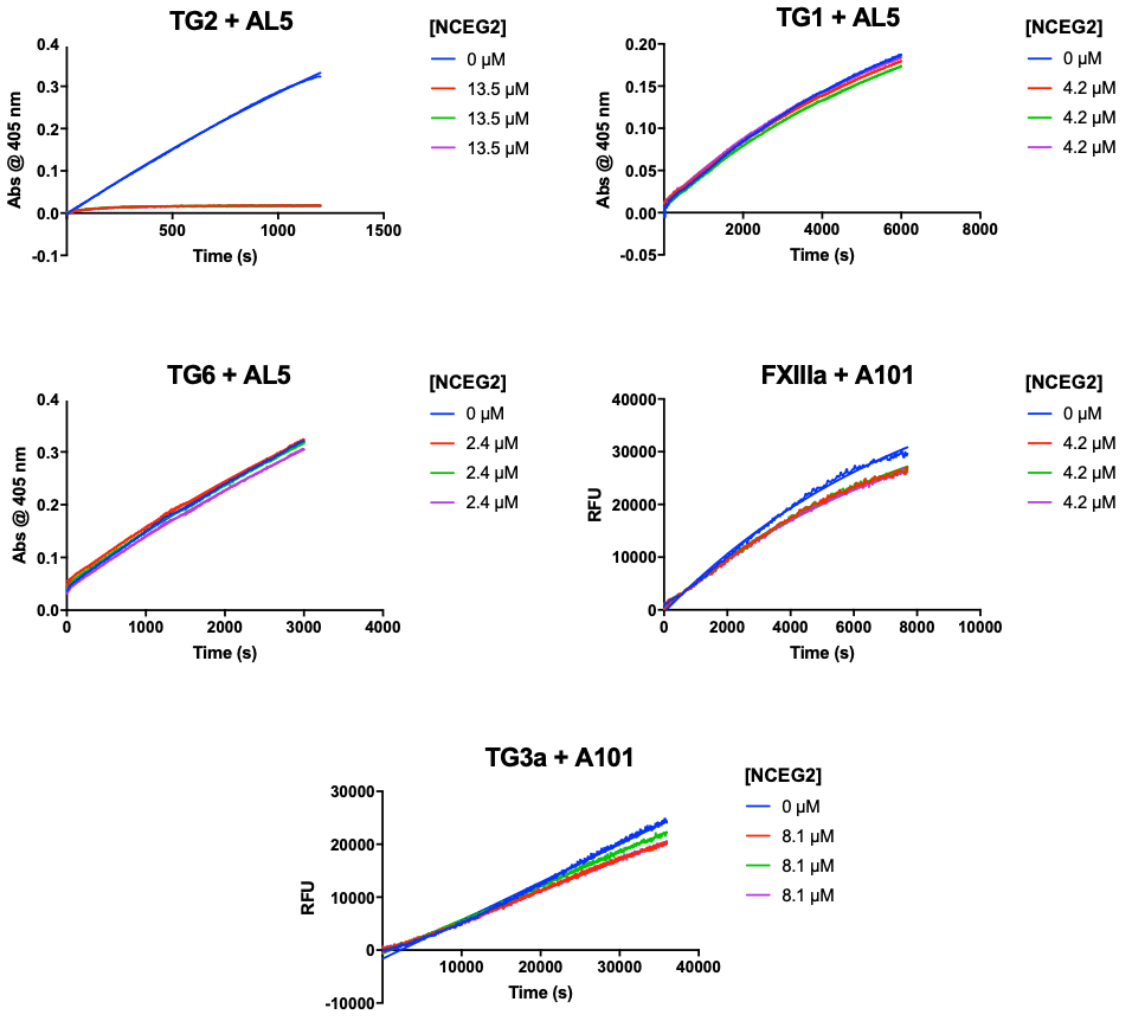

Figure S8. Isozyme selectivity of **18** (**NCEG2**) with respect to therapeutically relevant human transglutaminases TG2, TG1, TG6, FXIIIa, and TG3a, using either chromogenic substrate AL5 or fluorescently quenched isopeptidase substrate A101.

Supplementary fluorescent labelling images

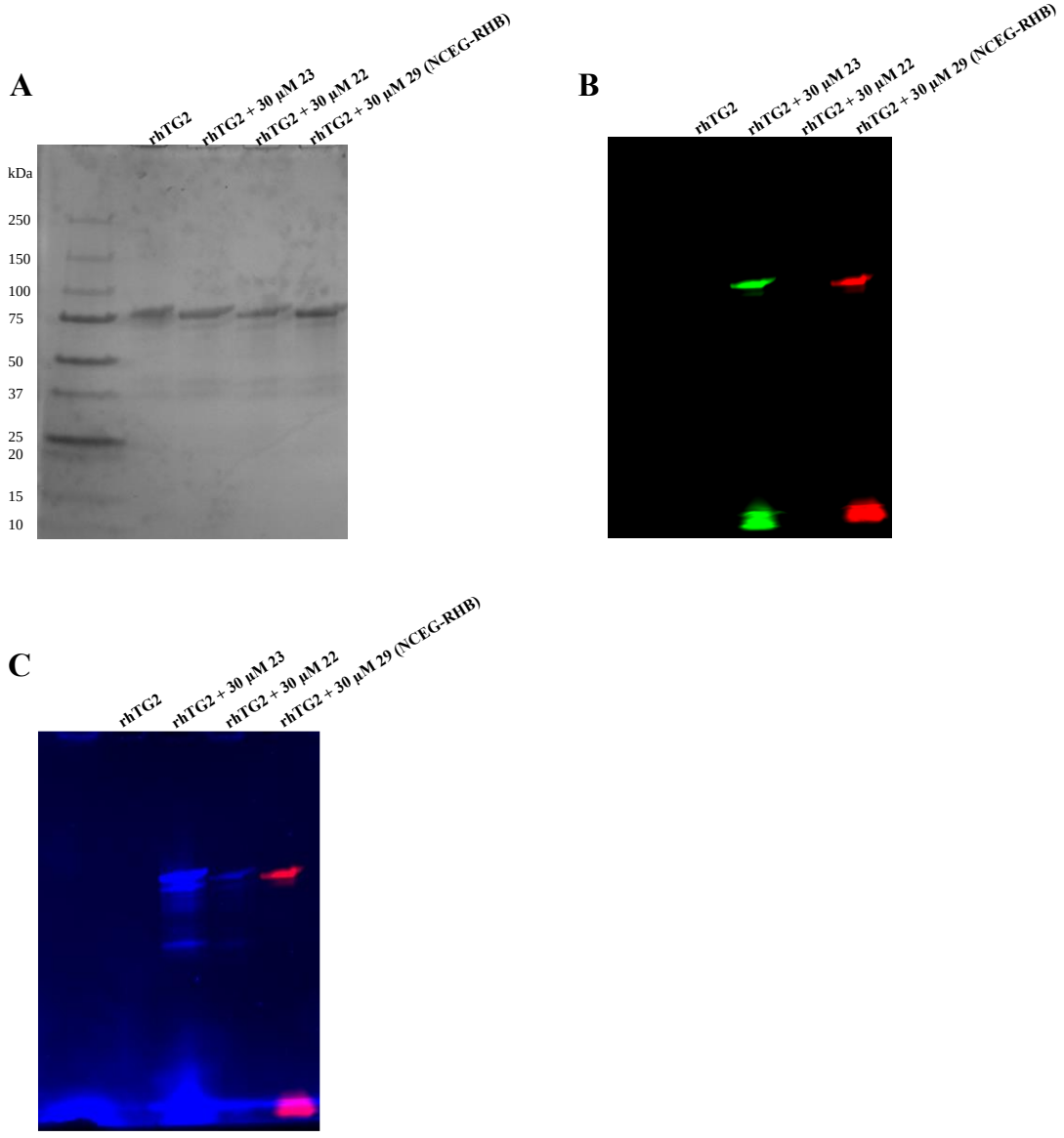

Figure S9. **A)** Coomassie stain of full SDS-PAGE used for fluorescent labelling of purified rhTG2. **B)** Multi-channel blue epi illumination with 530/28 nm filter (green band colour) and green epi illumination with 605/50 nm filter (red band colour) of full SDS-PAGE used for fluorescent labelling of purified rhTG2. **C)** Multi-channel UV

trans illumination with 530/28 nm filter (blue band colour) and green epi illumination with 605/50 nm filter (red band colour) of full SDS-PAGE used for fluorescent labelling of purified rhTG2.

Supplementary cellular evaluation figures

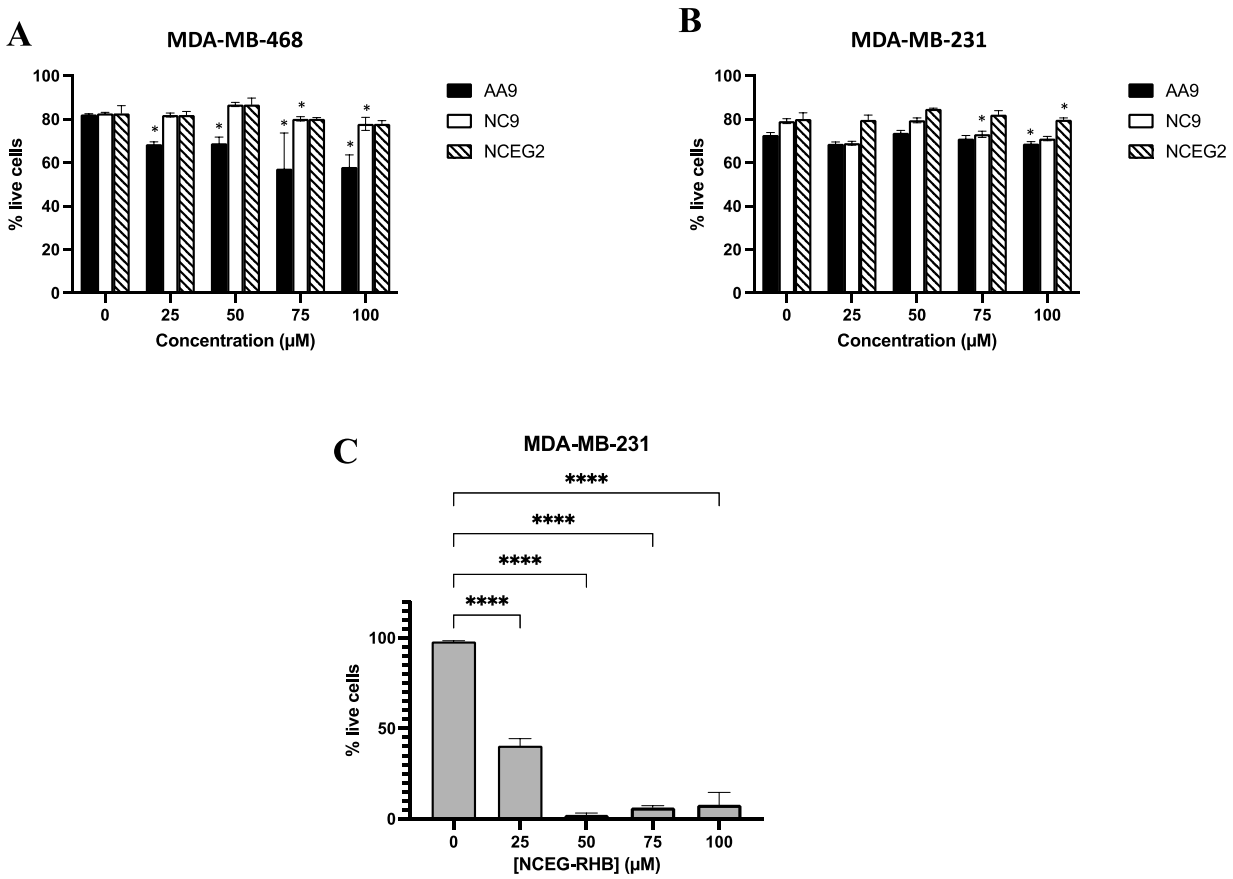

Figure S10. Viability assay: Treatment of (**A**) MDA-MB-468 breast cancer cell line with cell impermeable inhibitor **18 (NCEG2)** and cell permeable inhibitors NC9 and AA9, employed at the indicated concentrations and (**B)** MDA-MB-231 breast cancer cell line with cell impermeable inhibitor **18 (NCEG2)** and cell permeable inhibitors NC9, AA9, and **(C) NCEG-RHB** employed at the indicated concentrations. Experiments were carried out in triplicate and are represented as average ± SD of the percentage of living cells; (*) *P* value < 0.05; (****) *P* value < 0.0001.

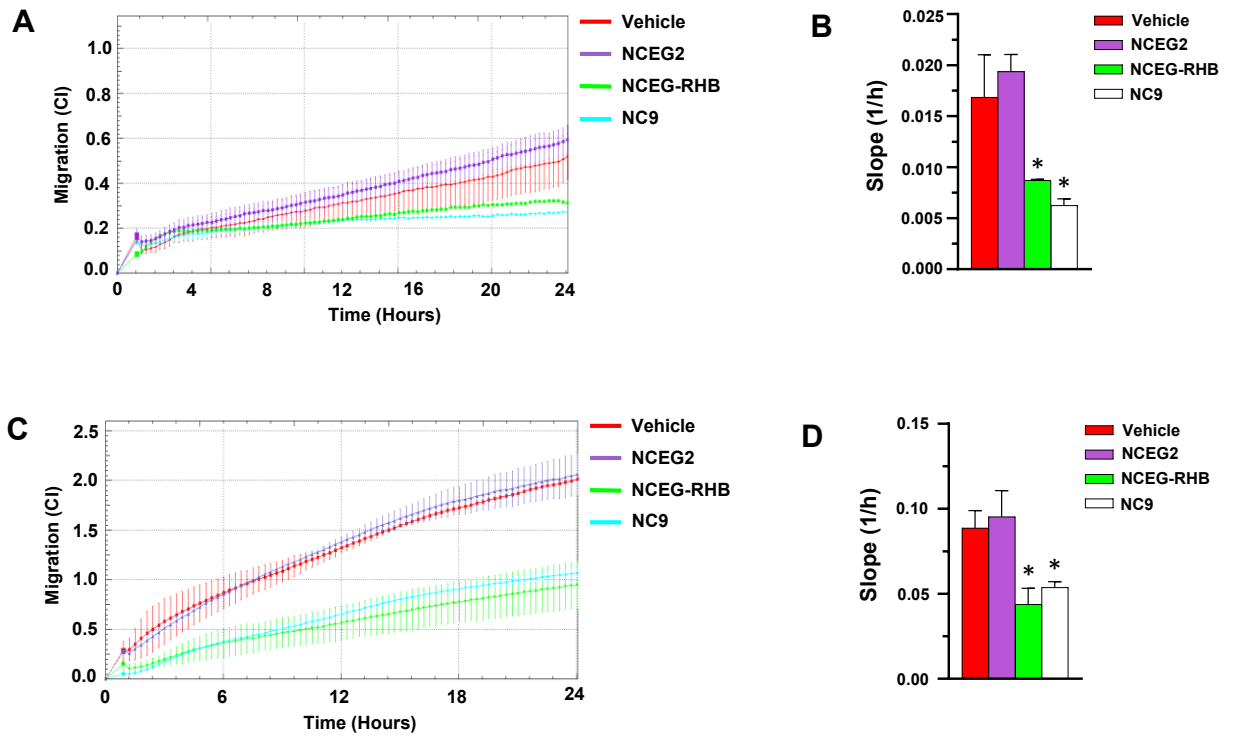

Figure S11. Migration assay: **A)** Dynamic monitoring of the migration of MDA-MB-436 cells. We recorded for 24 hours the migration of the cells in the presence only of the vehicle or of the indicated TG2 inhibitors, used at 25 µM concentrations. Data are reported as Cell Index (CI) values ± SD. **B)** Slope analysis shown at 24 h comprising the steepness, inclination, gradient, and changing rate of the CI curves of MDA-MB-436 cells over the time. * $P < 0.05$ *versus* vehicle. **C)** Dynamic monitoring of the migration of MDA-MB-231 cells. We recorded for 24 hours the migration of the cells in the presence only of the vehicle or of the indicated TG2 inhibitors, used at 25 µM concentrations. Data are reported as Cell Index (CI) values ± SD. **D)** Slope analysis shown at 24 h comprising the steepness, inclination, gradient, and changing rate of the CI curves of MDA-MB-231 cells over the time. * $P < 0.05$ *versus* vehicle.

Biotinylated inhibitor published by Hauser *et al.*

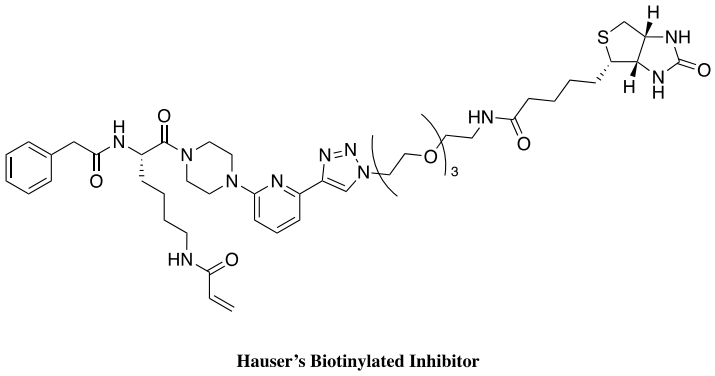

Figure S12. Structure of biotinylated TG2 inhibitor recently published by Hauser *et al.* [53].

SDS-PAGE of pull-down from *E. coli*

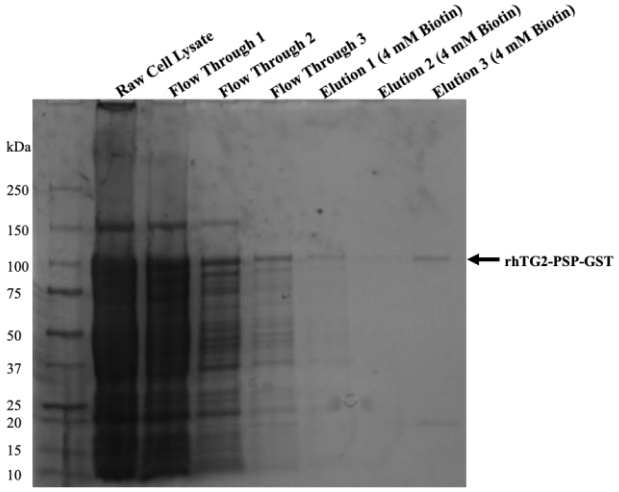

Figure S13. SDS-PAGE of pull-down experiment of recombinant human TG2 from *E. coli* cell lysate visualized with Coomassie staining.

Synthesis and characterization of intermediates and final compounds

Experimental Section

Where available, commercially available reagents and solvents were purchased from suppliers including Sigma-Aldrich, Oakwood Products, Combi-Blocks, and Fisher Scientific and used without further purification. Solid phase peptide synthesis resin was purchased from MilliporeSigma. Thin layer chromatography (TLC) was performed using SiliCycle aluminium backed TLC plates 200-µm thickness with F-254 indicator and visualized using short wave UV light. Preparatory-TLC was executed on SiliCycle SiliaPlate glass backed TLC with extra hard layer 60Å 250 µm thickness plates and F-254 indicator. Flash chromatography purification was performed using 230-400 mesh silica gel. All ^{1}H- and ^{13}C-NMR spectra were referenced to the indicated deuterated solvent and acquired using a Bruker 400-MHz or 600-MHz instrument to report the peaks in ppm. The high-resolution mass spectra were obtained using an electrospray ionization source (ESI) and quadrupole time-of-flight (QTOF) analyser. All final compounds were further evaluated for purity by HPLC where indicated.

General synthetic procedure A

To a round bottom flask equipped with magnetic stir bar was added the acid (1 eq) solubilized in a 1:1 mixture of THF:H_2O (0.1 M). To the flask was added finely ground potassium hydroxide (4 eq). The reaction mixture was then stirred for 2 h. Upon completion, the reaction mixture was diluted with H_2O and washed once with ether. The aqueous phase was then acidified to pH 2 with 1 M HCl. The aqueous layer was then extracted three times with ethyl acetate. The organic layers were combined, washed once with brine, dried over $MgSO_4$, filtered, and concentrated under reduced pressure to yield the product without further purification.

General synthetic procedure B

To a round bottom flask equipped with magnetic stir bar was added the acid (1.5 eq), HATU (1.5 eq), and DIPEA (3 eq) solubilized in DMF (0.5 M) at 0 ˚C. After 0.5 h, the amine (1 eq) was added dropwise as a solution in DMF (0.5 M) with DIPEA (1 eq). The ice bath was removed, and the reaction was allowed to stir overnight at room temperature. Upon completion, the reaction mixture was quenched with H_2O and extracted once with ethyl acetate. The organic layer was then washed with 1 M HCl, H_2O, sat. $NaHCO_3$ solution, and brine. The organic phase was then dried over $MgSO_4$, filtered, and concentrated under reduced pressure. The resulting crude oil was then purified *via* flash chromatography to obtain the product.

SPPS Wang resin loading procedure

To pre-load the first residue onto Wang resin, a procedure using a symmetrical anhydride was adapted from Atherton *et al.* [55]. To a dry SPPS reaction vessel was added 1 gram of Wang resin. The resin was suspended in 15 mL dry DMF under inert atmosphere and allowed to swell for 30 min. To form the corresponding anhydride to load onto the resin, 4.937 g Fmoc-Asp(OtBu)-OH (12 mmol, 10 eq) was solubilized in 120 mL dry DCM in a flame-dried round-bottom flask equipped with magnetic stir bar under inert atmosphere. To the flask was added 0.929 mL DIC (6 mmol, 5 eq) and the solution was stirred for 20 min at 0 ˚C. The volatiles were then removed from the round bottom flask under reduced pressure the residue was re-solubilized in a minimum amount of DMF. The solution was then added along with 0.015 g DMAP (1.2 mmol, 0.1 eq) to the SPPS reaction vessel, which was subsequently sealed and occasionally stirred for 1 h. Upon completion, the resin was washed with DMF and DCM. The resin was then dried under reduced

pressure and the loading was quantified according to the procedure published by Gude *et al*. [56]. The resin was finally capped using 0.319 mL acetic anhydride (6 mmol, 5 eq), 1.176 mL DIPEA (12 mmol, 10 eq) in 15 mL DCM for 15 min. The resin was once again washed and dried under reduced pressure.

General synthetic procedure C

Wang resin was preloaded with Fmoc-Asp(OtBu)-OH offline using the resin loading protocol described above. Resin was loaded into a CEM Liberty Blue Peptide Synthesizer, and the cell impermeable inhibitors were generated using 2 min couplings at 90 ˚C (0.2 M amino acid (5 eq) in DMF, 1.0 M DIC (10 eq) in DMF, and 1.0 M Oxyma Pure (5 eq) in DMF and 1 min Fmoc deprotections at 90˚C. The deprotection solution contained 20% Piperidine in DMF with 0.1 M Oxyma Pure to prevent aspartimide formation. Upon completion, the peptidic inhibitors were cleaved from resin using a cleavage cocktail of 95% TFA, 2.5% H_2O, and 2.5% TIPS for 4 h. The crude peptide was precipitated using cold ether, collected by centrifugation, and purified by semi-preparative HPLC.

Synthesis of compound 2

To a round bottom flask equipped with magnetic stir bar was added 5.000 g of commercially available Z-Glu(OtBu)-OH **1** (14.821 mmol, 1 eq) solubilized in 30 mL DMF with 2.656 g cesium carbonate (8.151 mmol, 0.55 eq) and stirred for 1 h. After which 0.923 mL iodomethane (14.821 mmol, 1 eq) was added and the reaction mixture was stirred overnight. Upon completion, the

reaction mixture was diluted with ethyl acetate and washed sequentially with 1 M HCl, H_2O, sat. $NaHCO_3$ solution, and brine. The organic layer was dried over $MgSO_4$, filtered, and concentrated under reduced pressure to yield 5.04 g (97%) of the product as a white solid.

^{1}H NMR (400 MHz, $CDCl_3$) δ 7.39 – 7.28 (m, 5H), 5.46 (d, *J* = 8.2 Hz, 1H), 5.09 (s, 2H), 4.38 (td, *J* = 8.3, 5.0 Hz, 1H), 3.73 (s, 3H), 2.40 – 2.21 (m, 2H), 2.20 – 2.07 (m, 1H), 2.00 – 1.86 (m, 1H), 1.42 (s, 9H).

^{13}C NMR (101 MHz, $CDCl_3$) δ 172.55, 172.02, 156.02, 136.33, 128.59, 128.24, 128.17, 80.87, 67.08, 53.54, 52.53, 31.47, 28.13, 27.67.

HRMS (ESI-QTOF) m/z [M + Na]+ calcd for $C_{18}H_{25}NO_6Na$ 374.1580; found 374.1583.

Synthesis of compound 3

To a round bottom flask under inert atmosphere was added 5.04 g compound **2** (14.451 mmol, 1 eq) solubilized in 143 mL methanol. Palladium on carbon (0.305 g, 2.869 mmol, 20 mol%) was then added to the flask which was subsequently evacuated and backfilled three times with $N_{2\,(g)}$. The flask was then evacuated and backfilled three times with $H_{2\,(g)}$ and stirred overnight. Upon completion, the mixture was evacuated and backfilled three times with $N_{2\,(g)}$ and filtered over a pad a celite. The filtrate was then concentrated under reduced pressure to yield the product as a clear oil in quantitative yield (3.057 g) and carried forward without further purification.

^{1}H NMR (400 MHz, MeOD) δ 3.79 (s, 3H), 2.50 – 2.30 (m, 2H), 2.13 – 1.90 (m, 2H), 1.45 (s, 9H).

^{13}C NMR (101 MHz, MeOD) δ 173.71, 173.44, 81.97, 53.85, 53.12, 31.98, 28.77, 28.32.

HRMS (ESI-QTOF) m/z [M + Na]+ calcd for $C_{10}H_{19}NO_4Na$ 240.1212; found 240.1216.

Synthesis of compound 5

To a round bottom flask equipped with magnetic stir bar was added 3.057 g compound **3** (14.343 mmol, 1 eq) solubilized in 143 mL DCM with 2.199 mL triethylamine (15.778 mmol, 1.2 eq). To the flask was added 2.734 g 1-naphthoyl chloride **4** (14.343 mmol, 1.1 eq) dropwise and the reaction was stirred. After five minutes 0.175 g DMAP (1.434 mmol, 10 mol%) was added and the reaction mixture was stirred for 2 h. Upon completion the reaction mixture was washed sequentially with 1 M HCl, H_2O, sat. $NaHCO_3$ solution, and brine. The organic layer was then dried over $MgSO_4$, filtered, and concentrated under reduced pressure. The resulting crude oil was purified *via* flash chromatography to yield 4.47 g (84%) of the product as a white solid.

^{1}H NMR (400 MHz, $CDCl_3$) δ 8.41 – 8.33 (m, 1H), 7.92 (dt, *J* = 8.3, 1.2 Hz, 1H), 7.88 – 7.84 (m, 1H), 7.67 (dd, *J* = 7.1, 1.2 Hz, 1H), 7.59 – 7.49 (m, 2H), 7.45 (dd, *J* = 8.3, 7.0 Hz, 1H), 6.78 (d, *J* = 7.9 Hz, 1H), 3.81 (s, 3H), 2.54 – 2.24 (m, 3H), 2.18 – 2.01 (m, 1H), 1.41 (s, 9H).

^{13}C NMR (101 MHz, $CDCl_3$) δ 172.56, 172.28, 169.46, 133.80, 133.71, 131.09, 130.31, 128.39, 127.36, 126.57, 125.55, 125.39, 124.76, 81.13, 52.74, 52.36, 31.71, 28.14, 27.39.

HRMS (ESI-QTOF) m/z [M + Na]+ calcd for $C_{21}H_{25}NO_5Na$ 394.1630; found 394.1641.

Synthesis of compound 6

Compound **6** was synthesized according to general synthetic procedure A. The product was obtained as a white solid (4.30 g, 99%).

^{1}H NMR (400 MHz, $CDCl_3$) δ 8.39 – 8.29 (m, 1H), 7.89 (dt, *J* = 8.2, 1.0 Hz, 1H), 7.86 – 7.80 (m, 1H), 7.63 (dd, *J* = 7.1, 1.3 Hz, 1H), 7.57 – 7.46 (m, 2H), 7.40 (dd, *J* = 8.3, 7.0 Hz, 1H), 7.09 (d, *J* = 7.4 Hz, 1H), 4.85 (td, *J* = 7.8, 5.0 Hz, 1H), 2.57 – 2.25 (m, 3H), 2.18 – 2.06 (m, 1H), 1.40 (s, 9H).

^{13}C NMR (101 MHz, $CDCl_3$) δ 175.21, 173.05, 170.30, 133.74, 133.16, 131.26, 130.24, 128.39, 127.42, 126.59, 125.62, 125.46, 124.71, 81.56, 52.64, 31.89, 28.10, 26.93.

HRMS (ESI-QTOF) m/z [M + Na]+ calcd for $C_{20}H_{23}NO_5Na$ 380.1474; found 380.1468.

Synthesis of compound 8

To a round bottom flask equipped with magnetic stir bar was added 2.000 g of commercially available Z-Lys-OH **7** (7.13 mmol, 1 eq) suspended in 50 mL MeOH under nitrogen atmosphere. The suspension was cooled to 0 ˚C and 0.78 mL thionyl chloride (10.7 mmol, 1.5 eq) was added

dropwise. The reaction mixture was allowed to warm to room temperature and was stirred overnight. Upon completion, the volatiles were removed under reduced pressure to yield the product in quantitative yield (2.35 g) as a white solid and was carried forward without further purification or characterization.

Synthesis of compound 10

To a round bottom flask equipped with magnetic stir bar was added 4.348 g compound **8** (13.144 mmol, 1 eq) solubilized in 40 mL ACN with 6.868 mL DIPEA (39.431 mmol, 3 eq) and 0.161 g DMAP (1.314 mmol, 10 mol%) at 0 ˚C. Acryloyl chloride **9** (1.267 mL, 15.772 mmol, 1.2 eq) was solubilized in 12 mL ACN and added dropwise to the reaction mixture *via* dropping funnel. The reaction was stirred for 1 h after which the reaction mixture was concentrated under reduced pressure and the resulting oil was taken up in ethyl acetate. The organic mixture was washed once with 1 M HCl, H_2O, sat. $NaHCO_3$ solution, and brine. The organic layer was then dried over $MgSO_4$, filtered, and concentrated under reduced pressure. The resulting crude oil was purified *via* flash chromatography to yield 2.65 g of the product (58%) as a white solid.

^{1}H NMR (400 MHz, $CDCl_3$) δ 7.29 (d, *J* = 5.0 Hz, 5H), 6.58 – 6.47 (m, 1H), 6.20 (dd, *J* = 17.0, 1.8 Hz, 1H), 6.07 (dd, *J* = 17.0, 10.1 Hz, 1H), 5.75 (d, *J* = 8.1 Hz, 1H), 5.51 (dd, *J* = 10.0, 1.8 Hz, 1H), 5.04 (s, 2H), 4.26 (td, *J* = 8.2, 4.7 Hz, 1H), 3.66 (s, 3H), 3.23 (qt, *J* = 10.6, 5.6 Hz, 2H), 1.84 – 1.58 (m, 2H), 1.57 – 1.40 (m, 2H), 1.40 – 1.25 (m, 2H).

^{13}C NMR (101 MHz, $CDCl_3$) δ 172.91, 165.85, 156.18, 136.18, 130.89, 128.44, 128.10, 127.95, 126.08, 66.84, 53.66, 52.30, 38.84, 31.79, 28.73, 22.44.

Synthesis of compound 11

Compound **11** was synthesized according to general synthetic procedure A. The product was obtained as a white solid (7.807 g, quantitative yield).

^{1}H NMR (400 MHz, $CDCl_3$) δ 7.36 – 7.27 (m, 5H), 6.30 – 6.19 (m, 2H), 6.08 (dd, *J* = 17.0, 10.3 Hz, 1H), 5.75 (d, *J* = 8.0 Hz, 1H), 5.60 (dd, *J* = 10.3, 1.4 Hz, 1H), 5.08 (d, *J* = 1.8 Hz, 2H), 4.35 (q, *J* = 7.3 Hz, 1H), 3.29 (d, *J* = 2.9 Hz, 2H), 1.95 – 1.67 (m, 2H), 1.60 – 1.30 (m, 4H).

^{13}C NMR (101 MHz, $CDCl_3$) δ 174.91, 166.49, 156.40, 136.18, 130.43, 128.54, 128.21, 128.06, 127.11, 67.06, 53.52, 39.22, 31.79, 28.73, 22.22.

HRMS (ESI-QTOF) m/z [M + Na]+ calcd for $C_{17}H_{22}N_2O_5Na$ 357.1426; found 357.1446.

Synthesis of compound 13

Compound **13** was synthesized according to general synthetic procedure B. The product was obtained after flash chromatography as a white solid (1.816 g, 98%).

^{1}H NMR (400 MHz, $CDCl_3$) δ 7.34 – 7.27 (m, 5H), 6.29 (t, *J* = 5.7 Hz, 1H), 6.21 (dd, *J* = 17.0, 1.7 Hz, 1H), 6.06 (dd, *J* = 17.0, 10.2 Hz, 1H), 5.95 (d, *J* = 8.3 Hz, 1H), 5.54 (dd, *J* = 10.1, 1.7 Hz, 1H), 5.04 (s, 2H), 4.59 (td, *J* = 8.2, 4.4 Hz, 1H), 3.66 – 3.21 (m, 10H), 1.70 – 1.61 (m, 1H), 1.60 – 1.46 (m, 3H), 1.43 (s, 9H), 1.40 – 1.30 (m, 2H).

^{13}C NMR (101 MHz, $CDCl_3$) δ 170.47, 165.76, 156.23, 154.42, 136.24, 130.93, 128.52, 128.18, 127.99, 126.15, 80.42, 66.91, 50.33, 45.36, 41.96, 38.96, 32.75, 28.80, 28.35, 22.26.

HRMS (ESI-QTOF) m/z [M + Na]+ calcd for $C_{26}H_{38}N_4O_6Na$ 525.2689; found 525.2674.

Synthesis of compound 14

To a round bottom flask equipped with magnetic stir bar was added 1.816 g compound **13** (3.613 mmol, 1 eq) solubilized in 36 mL of a 20% v/v TFA in DCM solution. The reaction mixture was stirred for 2 h upon which the solvent was removed under reduced pressure. The resulting oil was co-evaporated 3 times with DCM under reduced pressure to yield the product in quantitate yield (1.866 g) as a brown oil. The product was carried forward as the TFA salt without further purification or characterization.

Synthesis of compound 15

Compound **15** was synthesized according to general synthetic procedure B. The product was obtained after flash chromatography as a white solid (1.778 g, 66%)

^{1}H NMR (400 MHz, $CDCl_3$) δ 8.32 (d, *J* = 7.9 Hz, 1H), 7.88 (d, *J* = 8.3 Hz, 1H), 7.83 (dd, *J* = 7.6, 1.8 Hz, 1H), 7.63 (ddd, *J* = 7.1, 3.0, 1.2 Hz, 1H), 7.55 – 7.46 (m, 2H), 7.41 (dd, *J* = 8.3, 7.0 Hz, 1H), 7.31 (d, *J* = 3.4 Hz, 5H), 7.25 – 7.18 (m, 1H), 6.31 – 6.27 (m, 1H), 6.26 – 6.15 (m, 1H), 6.12 – 5.98 (m, 2H), 5.57 – 5.50 (m, 1H), 5.32 – 5.26 (m, 1H), 5.05 (s, 2H), 4.64 – 4.57 (m, 1H), 3.94 – 3.11 (m, 11H), 2.54 – 2.30 (m, 2H), 2.18 – 2.06 (m, 1H), 1.87 – 1.76 (m, 1H), 1.66 – 1.28 (m, 15H).

^{13}C NMR (101 MHz, $CDCl_3$) δ 172.08, 170.60, 170.24, 169.20, 165.63, 156.20, 136.26, 133.64, 130.90, 130.14, 128.51, 128.32, 128.18, 128.00, 127.17, 126.41, 126.08, 125.28, 124.65, 80.89, 66.89, 50.31, 48.40, 45.04, 42.10, 38.85, 32.54, 30.56, 28.84, 28.09, 27.87, 22.24. (Rotamers of piperazine observed at 45.04 ppm and 42.10 ppm)

HRMS (ESI-QTOF) m/z [M + Na]+ calcd for $C_{41}H_{51}N_5O_8Na$ 764.3635; found 764.3645.

Synthesis of compound 16

To a round bottom flask equipped with magnetic stir bar was added 0.100 g compound **15** (0.135 mmol, 1 eq) solubilized in 1.5 mL of a 20% v/v TFA in DCM solution. The reaction mixture was stirred for 4 h upon which the solvent was removed under reduced pressure. The resulting brown oil was then precipitated using cold ether. The crude solid was further purified by flash chromatography to yield 0.039 g (42%) of product as a white solid.

^{1}H NMR (600 MHz, $CDCl_3$) δ 8.31 – 8.24 (m, 1H), 7.88 (t, *J* = 8.1 Hz, 1H), 7.85 – 7.80 (m, 1H), 7.66 – 7.61 (m, 1H), 7.57 – 7.45 (m, 2H), 7.43 – 7.27 (m, 7H), 6.34 – 6.19 (m, 2H), 6.13 – 5.96 (m, 2H), 5.61 – 5.51 (m, 1H), 5.40 – 5.30 (m, 1H), 5.10 – 5.02 (m, 2H), 4.71 – 4.60 (m, 1H), 3.93 – 3.15 (m, 11H), 2.66 – 2.55 (m, 1H), 2.53 – 2.43 (m, 1H), 2.22 – 2.08 (m, 1H), 2.00 – 1.80 (m, 1H), 1.72 – 1.42 (m, 4H), 1.40 – 1.28 (m, 2H).

^{13}C NMR (151 MHz, $CDCl_3$) δ 175.18, 170.62, 169.64, 166.38, 166.11, 156.40, 136.30, 133.75, 133.34, 133.31, 131.22, 130.67, 130.18, 128.66, 128.48, 128.33, 128.14, 128.12, 127.40, 126.60, 125.64, 125.34, 124.78, 67.16, 67.15, 67.12, 67.10, 50.50, 48.82, 48.77, 48.60, 45.57, 42.15, 39.13, 32.64, 29.51, 28.83, 22.33.

HRMS (ESI-QTOF) m/z [M + Na]+ calcd for $C_{37}H_{43}N_5O_8Na$ 708.3009; found 708.2991.

Synthesis of compound 17

Compound **17** was synthesized according to general synthetic procedure C using Fmoc-Aminohexanoic acid-OH as linker on 0.1 mmol scale (3.4 mg isolated).

HRMS (ESI-QTOF) m/z $[M - H]^-$ calcd for $C_{55}H_{68}N_9O_{18}$ 1142.4682; found 1442.4698.

Purity: 95.5%

Synthesis of compound 18 (NCEG2)

Compound **18** was synthesized according to general synthetic procedure C using three glycine residues (iterative couplings and deprotections) as linker on 0.1 mmol scale (7.4 mg isolated).

HRMS (ESI-QTOF) m/z $[M - H]^-$ calcd for $C_{55}H_{66}N_{11}O_{20}$ 1200.4486; found 1200.4473.

Purity: 96.4%

Synthesis of compound 19

Compound **19** was synthesized according to general synthetic procedure B. The product was obtained after flash chromatography as a white solid (0.098 g, 63%).

HRMS (ESI-QTOF) m/z [M + Na]+ calcd for $C_{47}H_{63}N_7O_9Na$ 892.4585; found 892.4579.

Synthesis of compound 20

To a round bottom flask equipped with magnetic stir bar was added 0.319 g **19** (0.367 mmol, 1 eq) solubilized in 2 mL of a 1:1 mixture of 4 M HCl in dioxane and DCM. The reaction was stirred for 2 h after which the solvents were removed under reduced pressure. The product was carried forward as the HCl salt in quantitative yield (0.296 g) and without further purification or characterization.

Synthesis of compound 22

Compound **22** was synthesized according to general synthetic procedure B. The product was obtained after flash chromatography as a vibrant yellow solid (0.073 g, 59%).

HRMS (ESI-QTOF) m/z [M + Na]+ calcd for $C_{56}H_{68}N_8O_{10}Na$ 1035.4956; found 1035.4944.

Purity: 85.3%

Synthesis of compound 23

To a round bottom flask equipped with magnetic stir bar was added 0.099 g compound **20** (0.123 mmol, 1 eq) solubilized in 2 mL DMF with 0.021 mL DIPEA (0.123 mmol, 1 eq). To the flask was added 0.053 g fluorescein isothiocyanate isomer I (0.135 mmol, 1.1 eq) and 0.043 mL DIPEA (0.246 mmol, 2 eq). The reaction mixture was stirred for 48 h at room temperature. The volatiles were then evaporated by a stream of compressed air overnight. The resulting crude oil was purified *via* flash chromatography twice to yield 0.052 g (37%) of the product as a yellow solid.

HRMS (ESI-QTOF) m/z [M + Na]+ calcd for $C_{63}H_{66}N_8O_{12}SNa$ 1181.4419; found 1181.4425.

Purity: 89.9%

Synthesis of compound 25

Compound **25** was synthesized according to general synthetic procedure B. The product was obtained after flash chromatography as a colourless oil (0.470 g, 81%).

^{1}H NMR (400 MHz, $CDCl_3$) δ 7.31 – 7.21 (m, 5H), 5.14 – 4.94 (m, 2H), 4.26 – 4.19 (m, 1H), 3.56 – 3.31 (m, 2H), 3.19 – 2.90 (m, 4H), 2.25 – 2.01 (m, 1H), 1.94 – 1.72 (m, 3H), 1.45 – 1.16 (m, 15H).

^{13}C NMR (101 MHz, $CDCl_3$) δ 172.05, 155.98, 136.29, 128.39, 127.98, 127.69, 78.74, 67.08, 60.50, 46.92, 40.20, 39.02, 29.36, 28.98, 28.32, 23.73.

HRMS (ESI-QTOF) m/z [M + Na]+ calcd for $C_{23}H_{35}N_3O_5Na$ 456.2474; found 256.2462.

Synthesis of compound 26

To a round bottom flask under inert atmosphere was added 0.470 g compound **25** (1.084 mmol, 1 eq) solubilized in 11 mL methanol. Palladium on carbon (0.023 g, 0.217 mmol, 20 mol%) was then added to the flask which was subsequently evacuated and backfilled three times with $N_{2\,(g)}$. The flask was then evacuated and backfilled three times with $H_{2\,(g)}$ and stirred overnight. Upon completion, the mixture was evacuated and backfilled three times with $N_{2\,(g)}$ and filtered over a

pad a celite. The filtrate was then concentrated under reduced pressure to yield the product as a clear oil in quantitative yield (0.325 g) and carried forward without further purification or characterization.

Synthesis of compound 27

Compound **27** was synthesized according to general synthetic procedure B excluding the 1 M HCl washes. The product was obtained after flash chromatography as a purple solid (0.663 g, 80%).

^{1}H NMR (400 MHz, $CDCl_3$) δ 7.77 – 7.48 (m, 3H), 7.35 – 7.27 (m, 2H), 7.24 – 7.14 (m, 1H), 6.93 – 6.85 (m, 1H), 6.82 – 6.74 (m, 2H), 6.67 (dd, *J* = 3.5, 2.4 Hz, 1H), 4.19 (dd, *J* = 7.7, 5.3 Hz, 1H), 3.65 – 3.46 (m, 10H), 3.32 – 2.87 (m, 5H), 2.11 – 1.14 (m, 31H).

^{13}C NMR (101 MHz, $CDCl_3$) δ 172.43, 170.79, 167.88, 167.48, 157.94, 155.64, 136.96, 136.48, 133.35, 132.37, 131.44, 130.61, 130.49, 130.29, 130.23, 130.16, 129.87, 129.80, 129.41, 127.92, 127.34, 115.78, 114.61, 114.13, 114.06, 113.89, 113.61, 113.35, 62.54, 60.17, 50.49, 46.16, 39.25, 32.51, 29.57, 29.05, 28.97, 28.55, 28.53, 28.28, 25.45, 24.02, 23.96, 22.19, 12.66.

HRMS (ESI-QTOF) m/z [M]+ calcd for $C_{43}H_{58}N_5O_5$ 724.4438; found 724.4414.

Synthesis of compound 28

To a round bottom flask equipped with magnetic stir bar was added 0.103 g **27** (0.135 mmol, 1 eq) solubilized in 1 mL of a 1:1 mixture of 4 M HCl in dioxane and DCM. The reaction was stirred for 2.5 h after which the solvents were removed under reduced pressure. The product was co-evaporated twice with DCM and then carried forward as the HCl salt in quantitative yield (0.094 g) and without further purification or characterization.

Synthesis of compound 29

Compound **29** was synthesized according to general synthetic procedure B excluding the 1 M HCl washes. The product was obtained after flash chromatography as a purple solid (0.035 g, 20%).

HRMS (ESI-QTOF) m/z [M]+ calcd for $C_{75}H_{91}N_{10}O_{10}$ 1291.6920; found 1291.6892.

Purity: 91.9%

Synthesis of compound 31

Compound **31** was synthesized according to general synthetic procedure B. The product was obtained after flash chromatography as a white solid (0.103 g, 91%).

^{1}H NMR (600 MHz, $CDCl_3$) δ 8.35 – 8.28 (m, 1H), 7.95 – 7.90 (m, 1H), 7.86 (d, *J* = 8.1 Hz, 1H), 7.68 – 7.63 (m, 1H), 7.58 – 7.49 (m, 2H), 7.45 – 7.30 (m, 6H), 6.27 – 6.17 (m, 1H), 6.16 – 6.01 (m, 2H), 5.95 – 5.81 (m, 1H), 5.61 – 5.53 (m, 1H), 5.23 – 5.13 (m, 1H), 5.09 – 5.02 (m,

2H), 4.66 – 4.57 (m, 1H), 4.17 – 4.06 (m, 1H), 4.06 – 3.94 (m, 1H), 3.87 – 3.12 (m, 10H), 2.54 – 2.43 (m, 1H), 2.42 – 2.34 (m, 1H), 2.25 – 2.14 (m, 2H), 1.97 – 1.86 (m, 1H), 1.72 – 1.44 (m, 4H), 1.42 – 1.31 (m, 2H).

^{13}C NMR (151 MHz, $CDCl_3$) δ 172.00, 170.67, 170.00, 169.90, 165.78, 156.25, 136.31, 136.29, 133.80, 133.79, 131.38, 130.94, 130.15, 130.13, 128.74, 128.63, 128.55, 128.31, 128.29, 128.14, 128.11, 128.09, 127.46, 127.44, 127.41, 126.62, 126.41, 126.40, 125.68, 125.65, 125.22, 125.20, 124.76, 80.05, 71.30, 67.06, 50.36, 50.34, 50.25, 49.03, 49.01, 48.99, 48.94, 45.60, 45.54, 45.16, 45.11, 42.05, 41.79, 41.73, 39.04, 39.00, 38.97, 32.74, 32.72, 32.68, 32.65, 32.03, 32.01, 29.29, 29.27, 29.24, 29.19, 29.18, 29.00, 28.93, 28.90, 22.38, 22.29, 22.27.

HRMS (ESI-QTOF) m/z [M + Na]+ calcd for $C_{40}H_{46}N_6O_7Na$ 745.3326; found 745.3307.

Purity: 94.7%

Synthesis of compound 32

Compound **32** was synthesized according to general synthetic procedure B using commercially available desthiobiotin and amine-peg3-azide. The product was obtained after flash chromatography as an orange oil (0.320 g, >99%).

^{1}H NMR (400 MHz, $CDCl_3$) δ 6.62 (t, *J* = 5.6 Hz, 1H), 5.91 (s, 1H), 5.16 (s, 1H), 3.86 – 3.75 (m, 1H), 3.73 – 3.57 (m, 11H), 3.54 (dd, *J* = 5.6, 4.6 Hz, 2H), 3.45 – 3.33 (m, 4H), 2.17 (t, *J* = 7.4 Hz, 2H), 1.63 (p, *J* = 7.1 Hz, 2H), 1.53 – 1.19 (m, 8H), 1.09 (d, *J* = 6.5 Hz, 3H).

^{13}C NMR (101 MHz, $CDCl_3$) δ 173.33, 164.08, 70.73, 70.58, 70.22, 70.11, 70.01, 56.19, 51.54, 50.73, 39.23, 35.97, 29.51, 28.63, 25.92, 25.26, 15.80.

HRMS (ESI-QTOF) m/z [M + Na]+ calcd for $C_{18}H_{34}N_6O_5Na$ 437.2488; found 437.2462.

Synthesis of compound 33

To a round bottom flask equipped with magnetic stir bar was added a slurry of 0.038 g alkyne **31** (0.053 mmol, 1 eq), desthiobiotin-peg3-azide **32** (0.053 mmol, 1 eq), and copper (II) sulfate pentahydrate (0.053 mmol, 1 eq) in 1 mL 1:1 ACN:H_2O. To the flask was then added 0.010 g sodium ascorbate (0.053 mmol, 1 eq) and the reaction was stirred at room temperature for 3 h. Upon completion the reaction mixture was filtered and subsequently concentrated under reduced pressure. The resulting crude oil was purified *via* preparatory-TLC to obtain the product as a clear oil (0.054 g, 90%)

HRMS (ESI-QTOF) m/z [M + Na]+ calcd for $C_{58}H_{80}N_{12}O_{12}Na$ 1159.5916; found 1159.5928.

Purity: 92.4%

NMR spectra of intermediates and final compounds

Compound 2

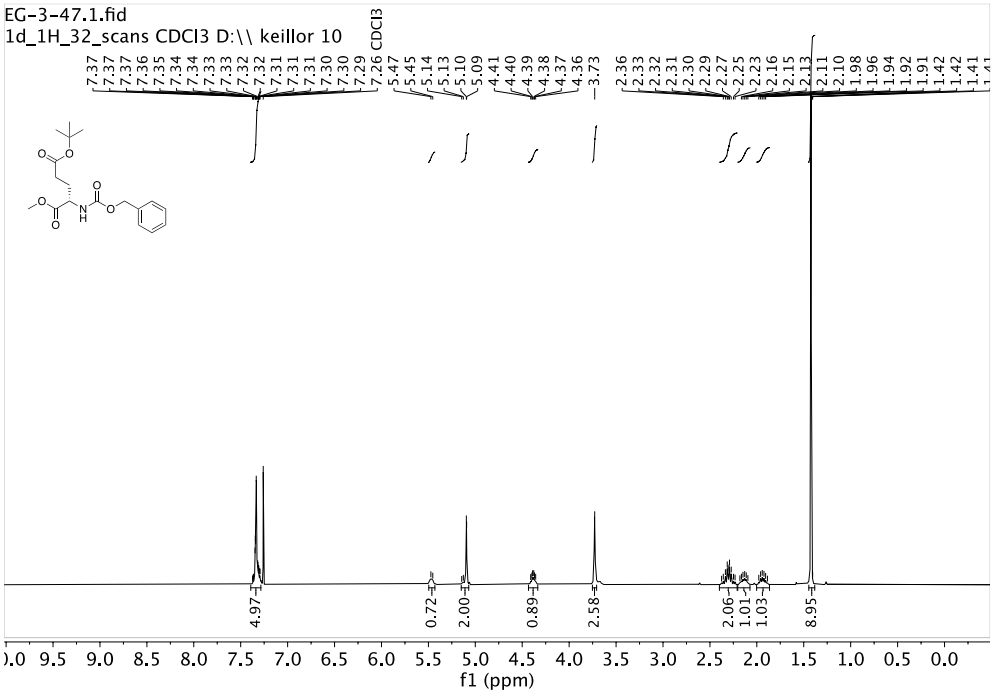

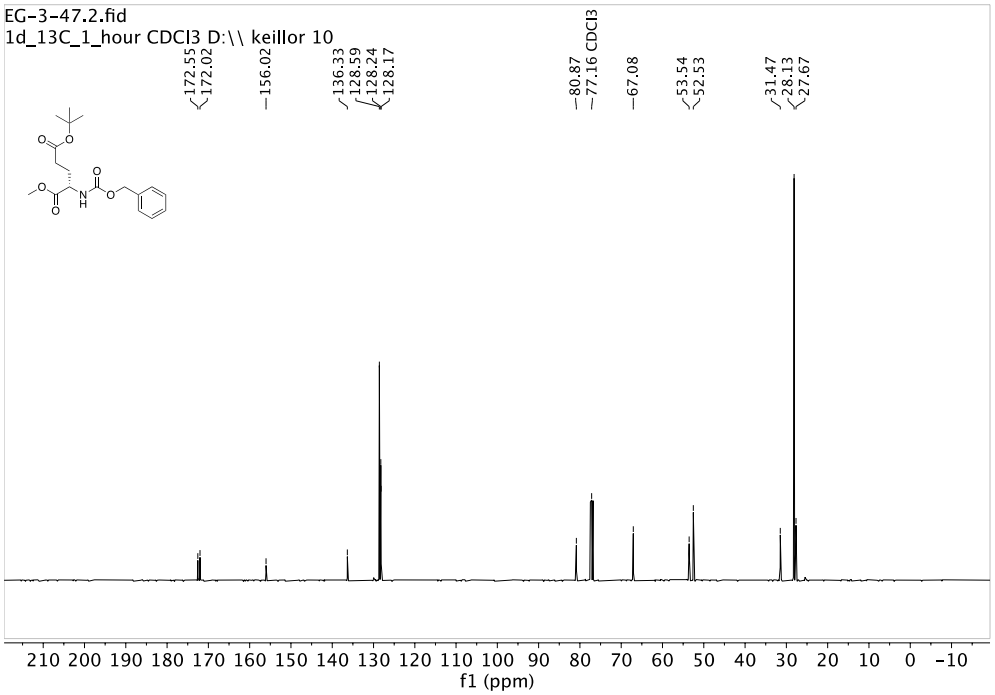

Compound 3

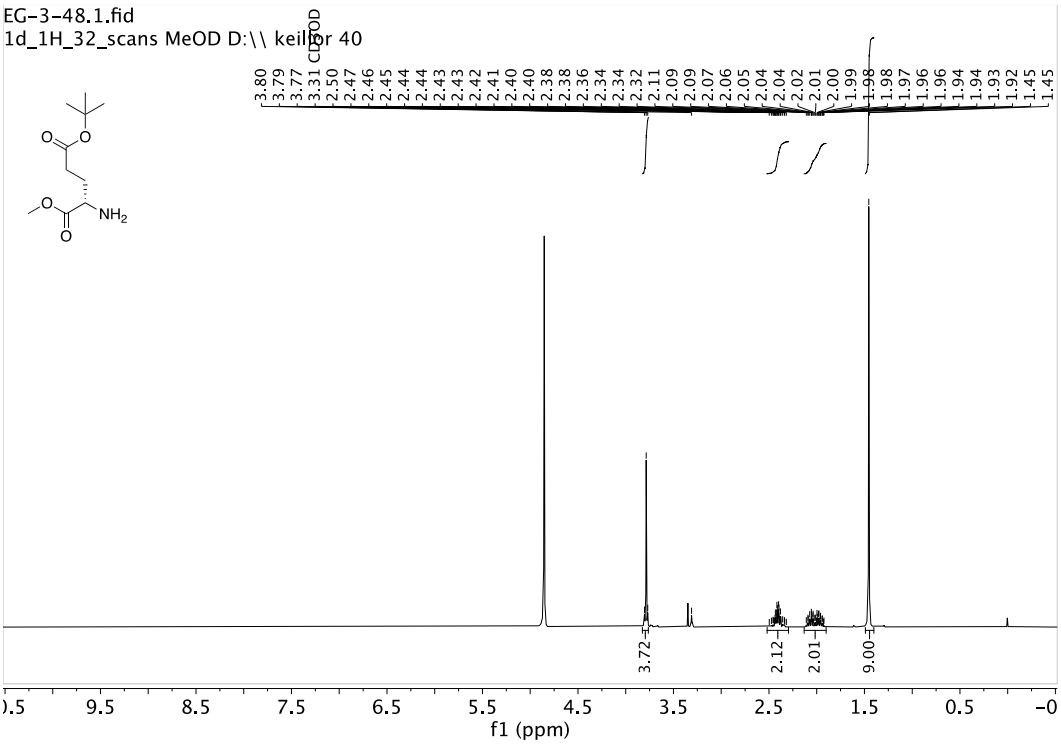
EG-3-48.1.fid
1d_1H_32_scans MeOD D:\\ keillor 40
CD3OD
3.72
2.12
2.01
9.00
f1 (ppm)

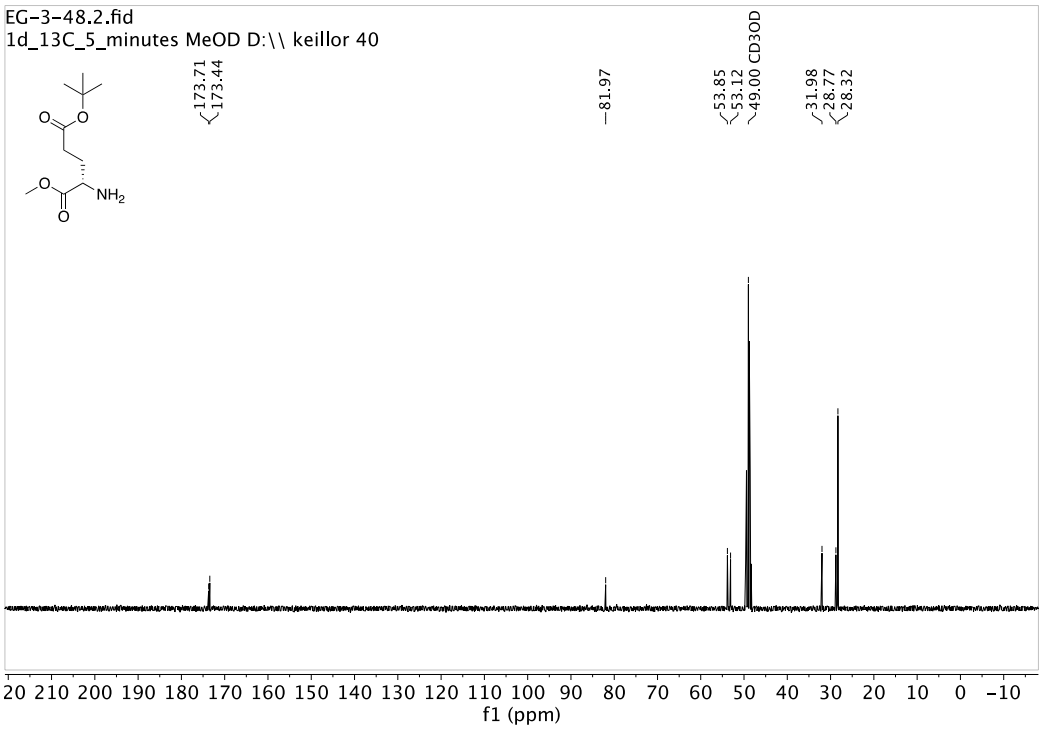
EG-3-48.2.fid
1d_13C_5_minutes MeOD D:\\ keillor 40
173.71
173.44
81.97
53.85
53.12
49.00 CD3OD
31.98
28.77
28.32
f1 (ppm)

Compound 5

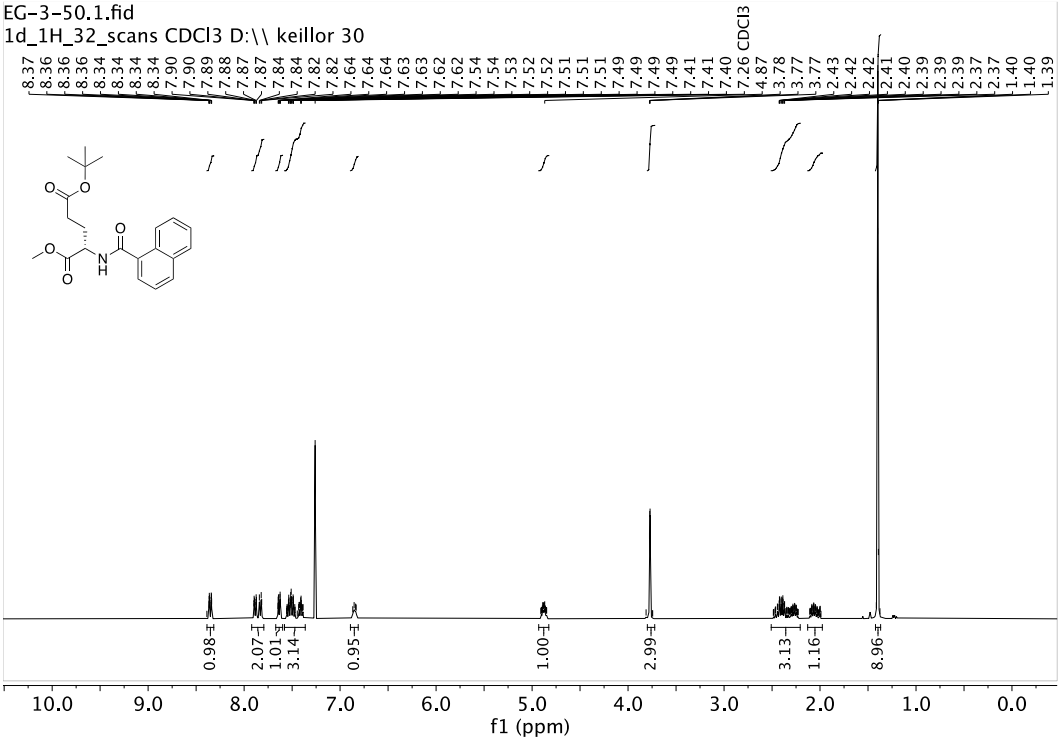
EG-3-50.1.fid
1d_1H_32_scans CDCl3 D:\\ keillor 30
f1 (ppm)

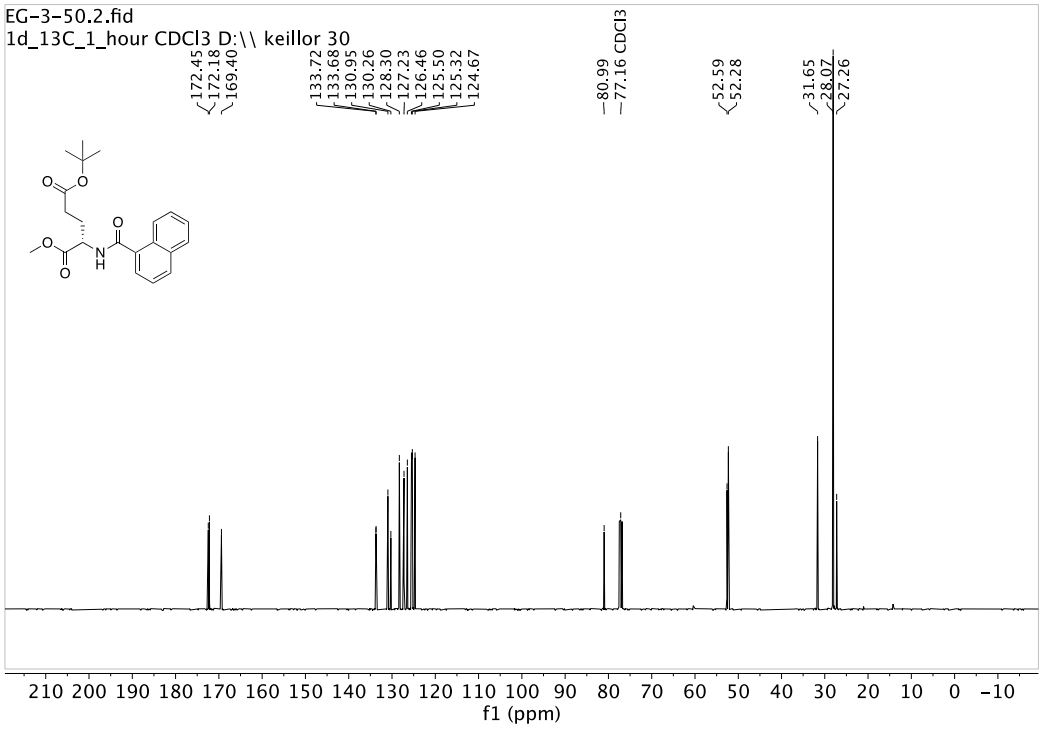
EG-3-50.2.fid
1d_13C_1_hour CDCl3 D:\\ keillor 30
f1 (ppm)

Compound 6

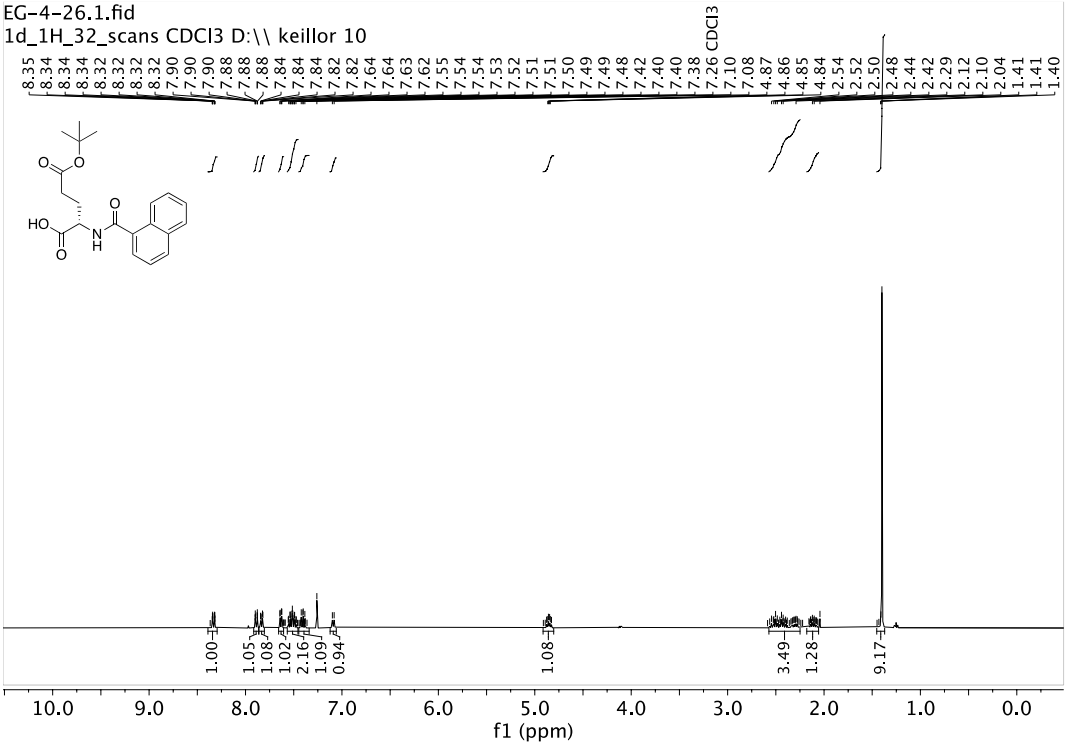
EG-4-26.1.fid
1d_1H_32_scans CDCl3 D:\\ keillor 10
CDCl3
1.00
1.05
1.08
1.02
2.16
1.09
0.94
1.08
3.49
1.28
9.17
f1 (ppm)

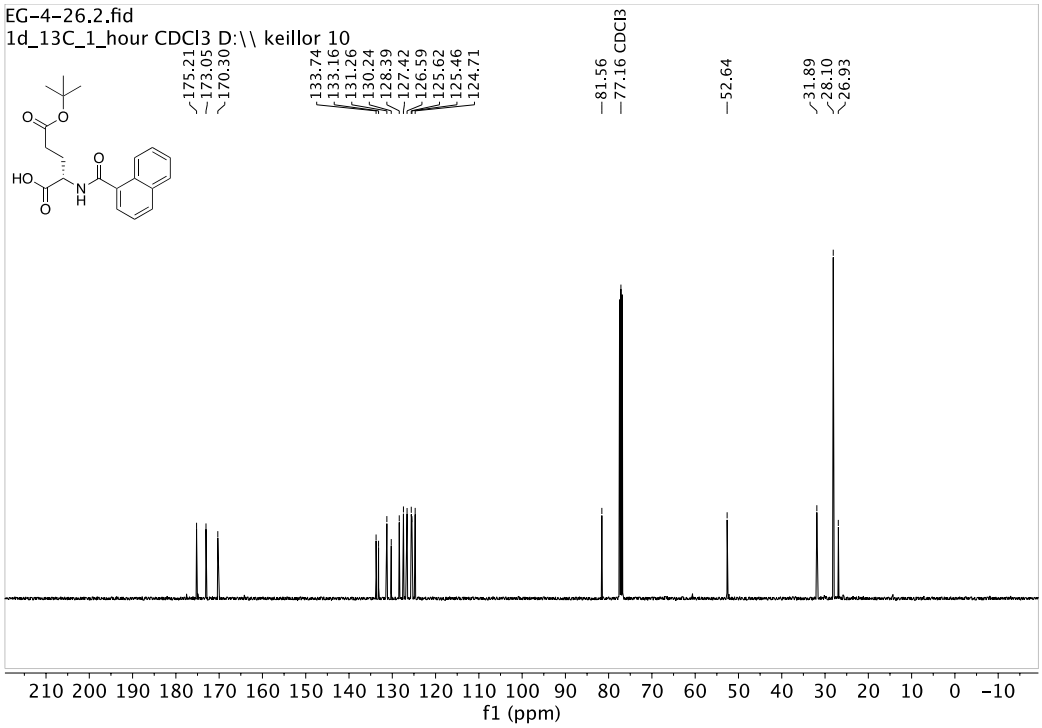
EG-4-26.2.fid
1d_13C_1_hour CDCl3 D:\\ keillor 10
175.21
173.05
170.30
133.74
133.16
131.26
130.24
128.39
127.42
126.59
125.62
125.46
124.71
81.56
77.16 CDCl3
52.64
31.89
28.10
26.93
f1 (ppm)

Compound 10

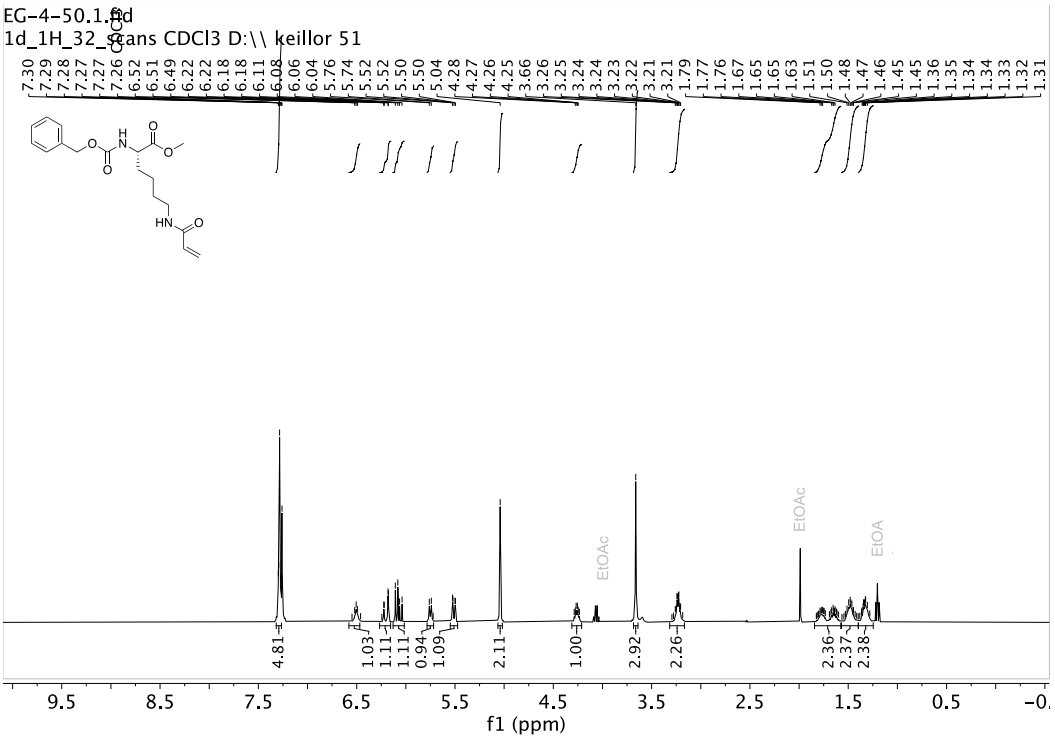
EG-4-50.1.fid
1d_1H_32_scans CDCl3 D:\\ keillor 51
7.30 7.29 7.28 7.27 7.27 7.26 CDCl3 6.52 6.51 6.49 6.22 6.22 6.18 6.18 6.11 6.08 6.06 6.04 5.76 5.74 5.52 5.52 5.50 5.50 5.04 4.28 4.27 4.26 4.25 3.66 3.26 3.25 3.24 3.24 3.23 3.22 3.21 3.21 1.79 1.77 1.76 1.67 1.65 1.65 1.63 1.51 1.50 1.48 1.47 1.46 1.45 1.45 1.36 1.35 1.34 1.34 1.33 1.32 1.31
EtOAc
EtOAc
EtOA
4.81 1.03 1.11 1.11 0.94 1.09 2.11 1.00 2.92 2.26 2.36 2.37 2.38
9.5 8.5 7.5 6.5 5.5 4.5 3.5 2.5 1.5 0.5
f1 (ppm)

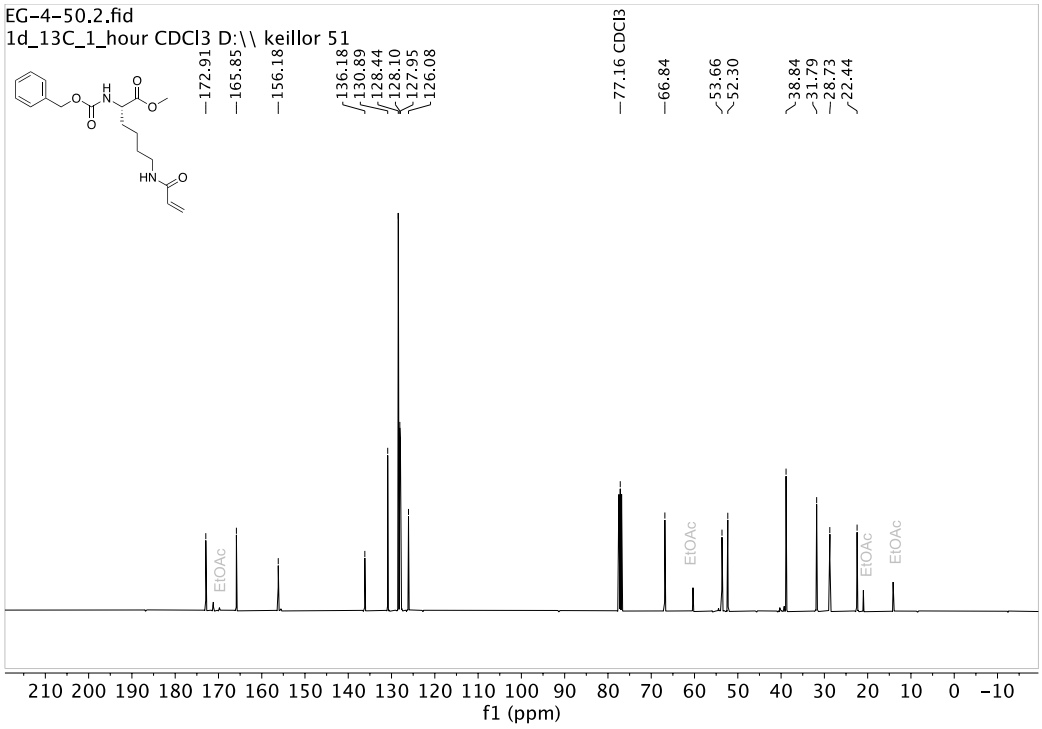
EG-4-50.2.fid
1d_13C_1_hour CDCl3 D:\\ keillor 51
172.91 165.85 156.18 136.18 130.89 128.44 128.10 127.95 126.08 77.16 CDCl3 66.84 53.66 52.30 38.84 31.79 28.73 22.44
EtOAc
EtOAc
EtOAc
EtOAc
210 200 190 180 170 160 150 140 130 120 110 100 90 80 70 60 50 40 30 20 10 0 -10
f1 (ppm)

Compound 11

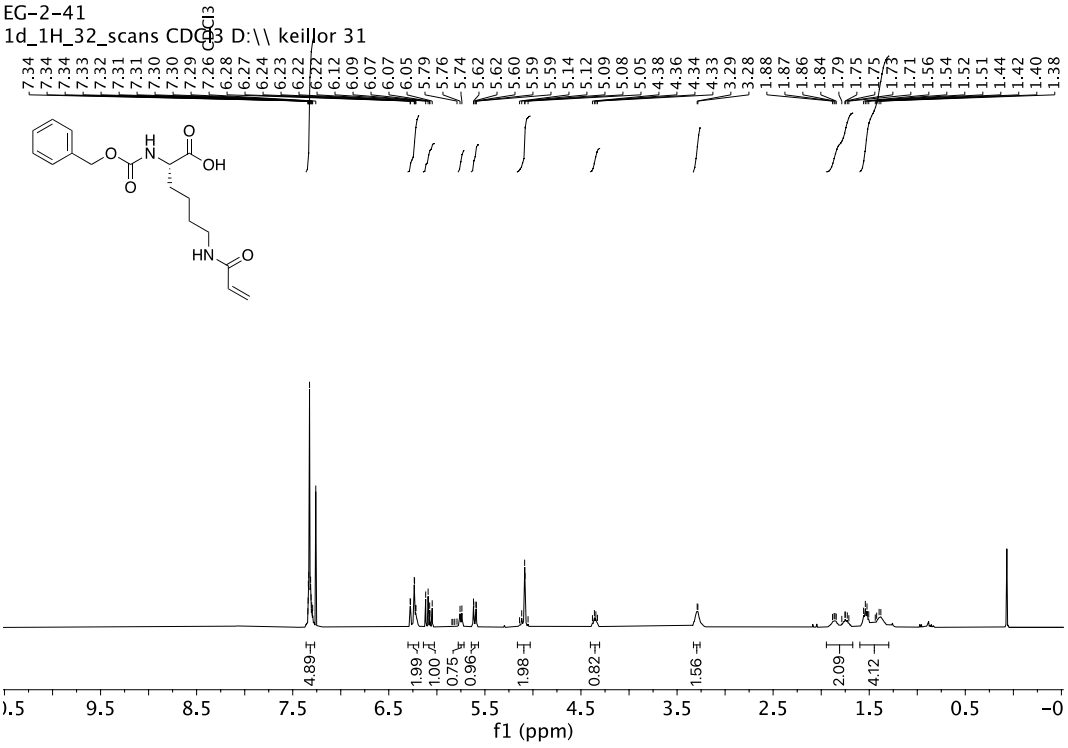
EG-2-41
1d_1H_32_scans CDCl3 D:\\ keillor 31
CDCl3
7.34 7.34 7.34 7.33 7.32 7.31 7.31 7.30 7.30 7.29 7.26 6.28 6.27 6.24 6.23 6.22 6.22 6.12 6.09 6.07 6.07 6.05 5.79 5.76 5.74 5.62 5.62 5.60 5.59 5.59 5.14 5.12 5.09 5.08 5.05 4.38 4.36 4.34 4.33 3.29 3.28 1.88 1.87 1.86 1.84 1.79 1.75 1.75 1.73 1.71 1.56 1.54 1.52 1.51 1.44 1.42 1.40 1.38
4.89 1.99 1.00 0.75 0.96 1.98 0.82 1.56 2.09 4.12
9.5 8.5 7.5 6.5 5.5 4.5 3.5 2.5 1.5 0.5 -0
f1 (ppm)

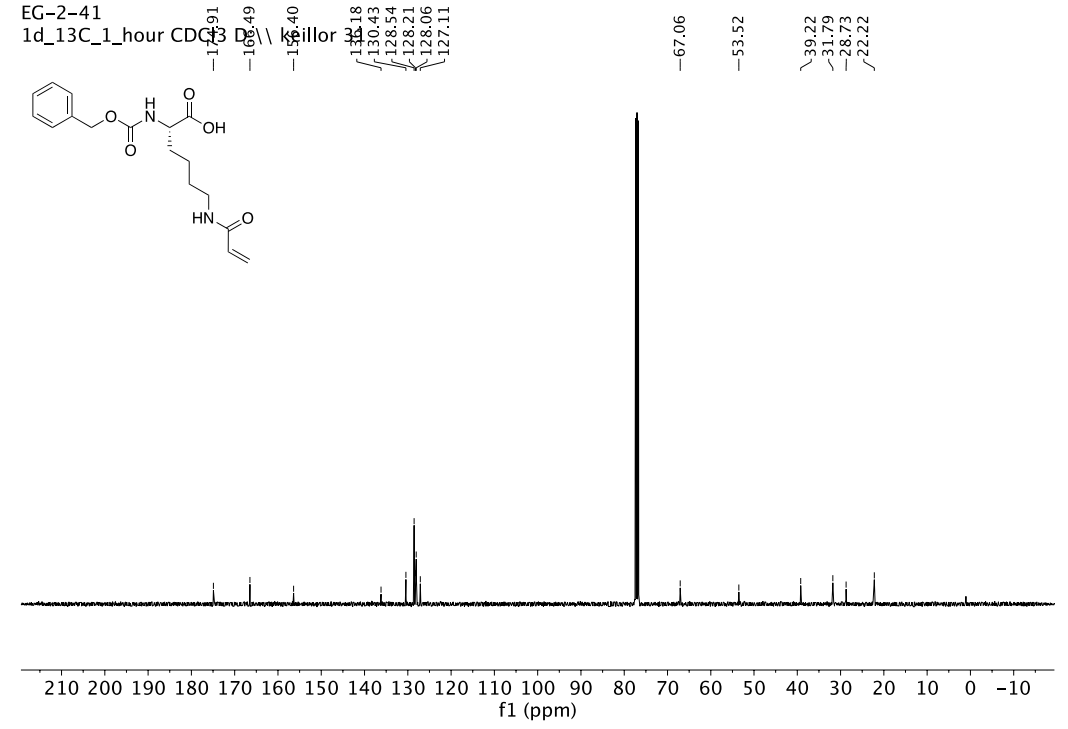
EG-2-41
1d_13C_1_hour CDCl3 D:\\ keillor 31
171.91 160.49 156.40 136.18 130.43 128.54 128.21 128.06 127.11 67.06 53.52 39.22 31.79 28.73 22.22
210 200 190 180 170 160 150 140 130 120 110 100 90 80 70 60 50 40 30 20 10 0 -10
f1 (ppm)

Compound 13

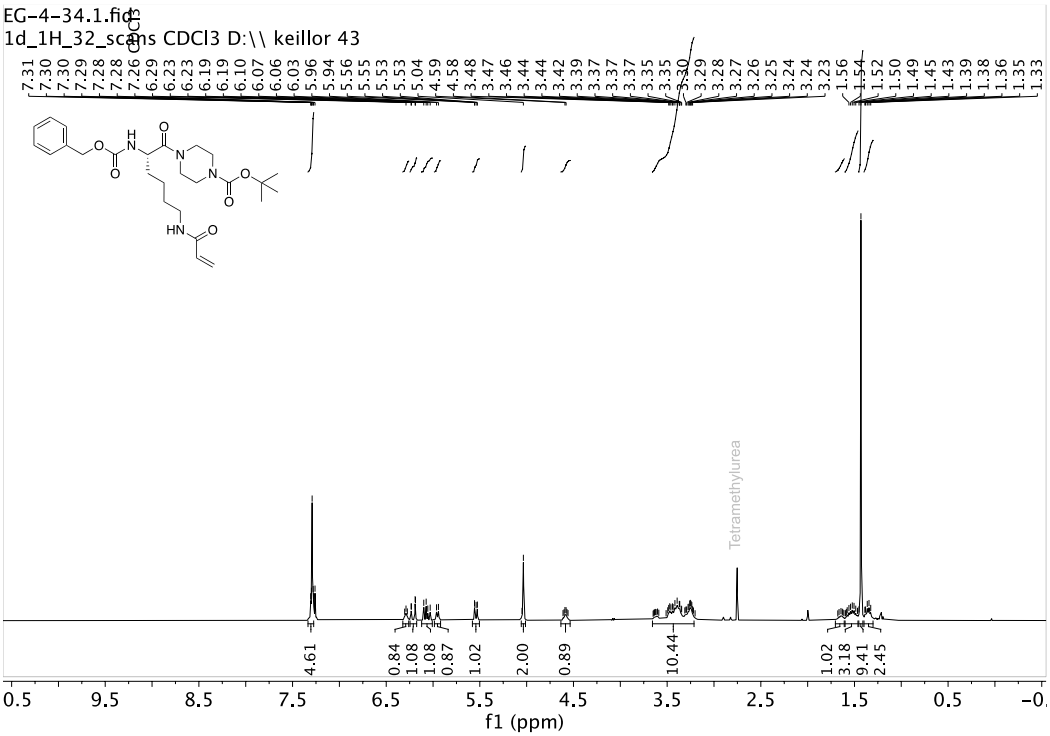
EG-4-34.1.fid
1d_1H_32_scans CDCl3 D:\\ keillor 43
CDCl3
Tetramethylurea
4.61
0.84
1.08
1.08
0.87
1.02
2.00
0.89
10.44
1.02
3.18
9.41
2.45
f1 (ppm)

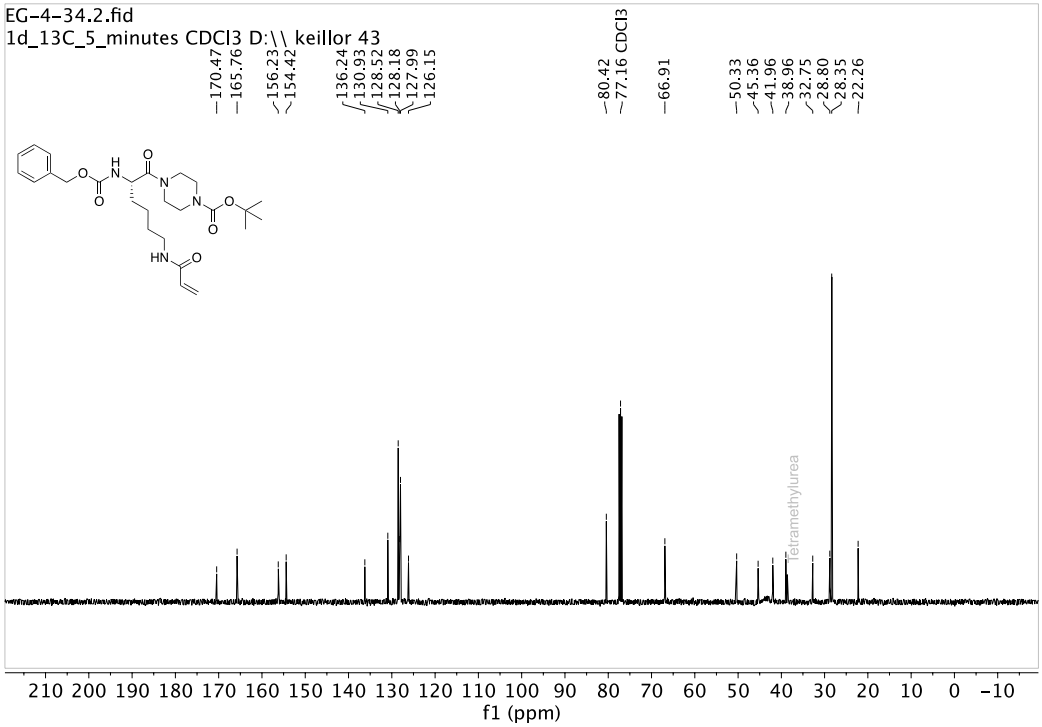
EG-4-34.2.fid
1d_13C_5_minutes CDCl3 D:\\ keillor 43
170.47
165.76
156.23
154.42
136.24
130.93
128.52
128.18
127.99
126.15
80.42
77.16 CDCl3
66.91
50.33
45.36
41.96
38.96
32.75
28.80
28.35
22.26
Tetramethylurea
f1 (ppm)

Compound 15

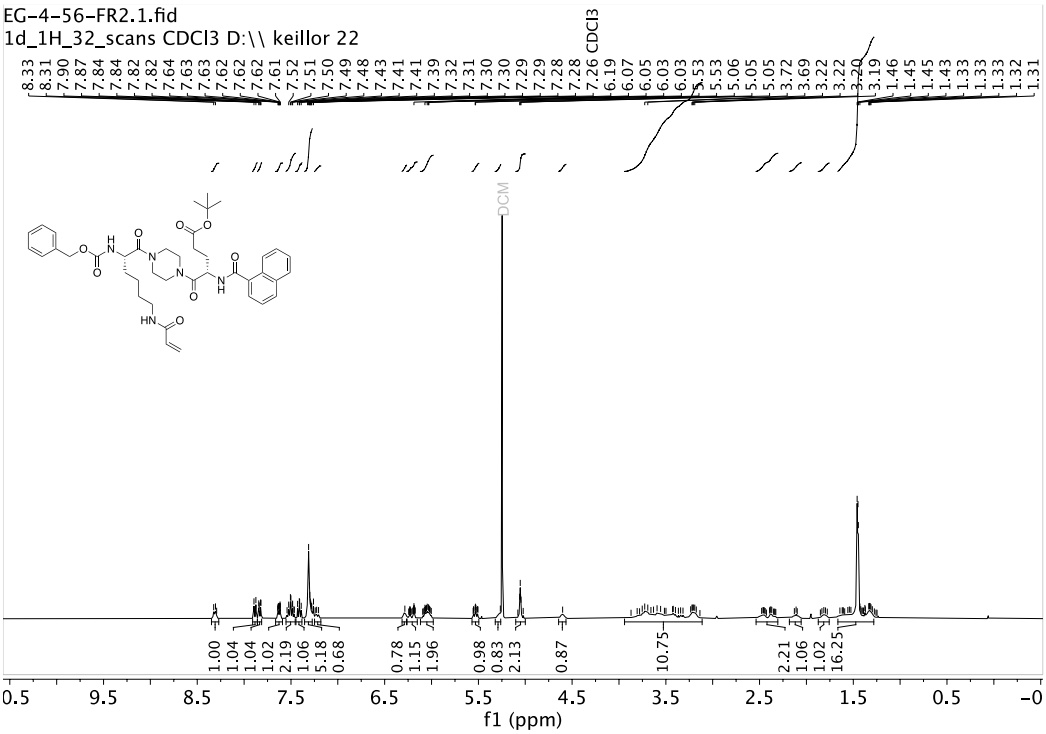
EG-4-56-FR2.1.fid
1d_1H_32_scans CDCl3 D:\\ keillor 22
f1 (ppm)

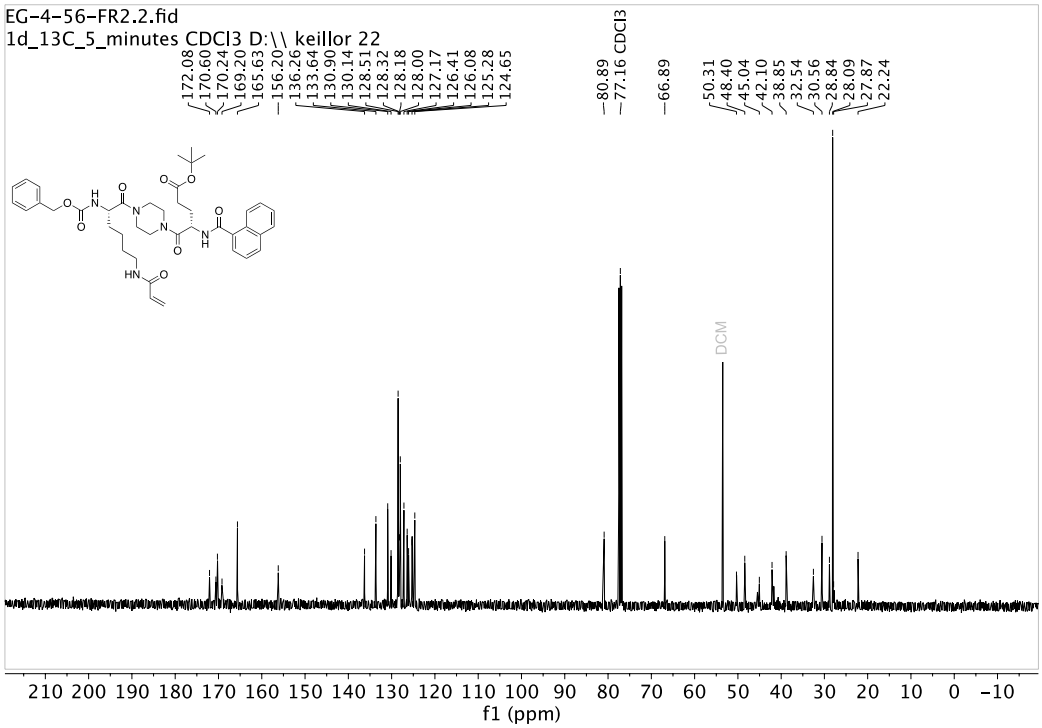
EG-4-56-FR2.2.fid
1d_13C_5_minutes CDCl3 D:\\ keillor 22
f1 (ppm)

Compound 16

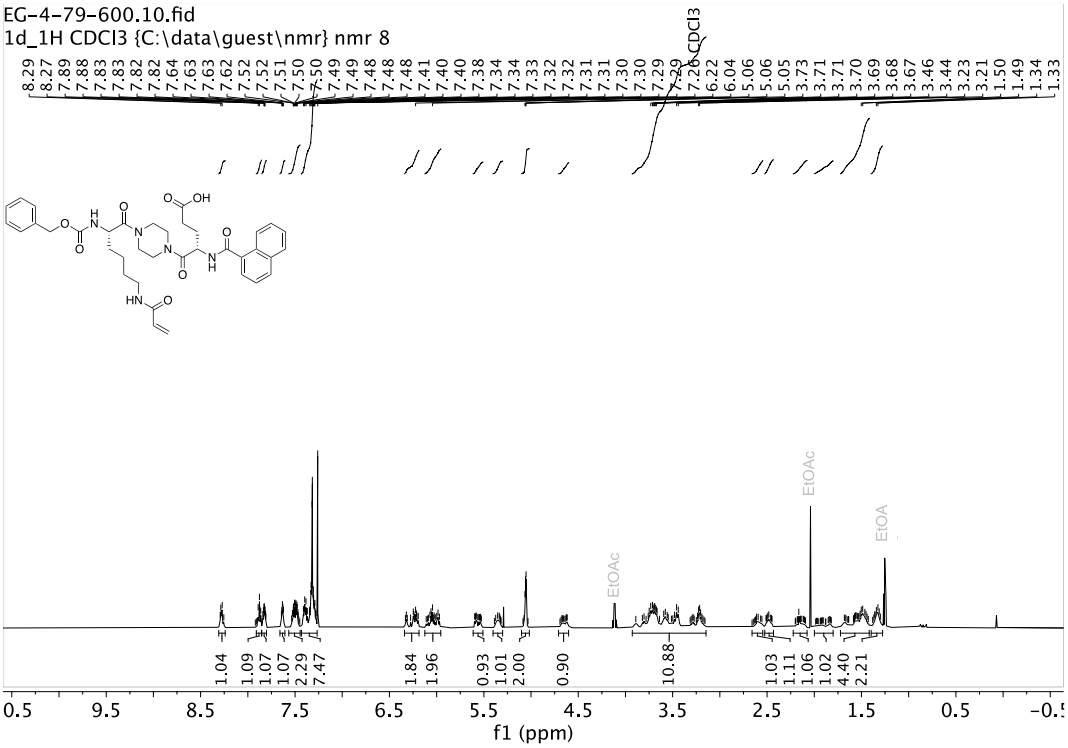
EG-4-79-600.10.fid
1d_1H CDCl3 {C:\data\guest\nmr} nmr 8
f1 (ppm)

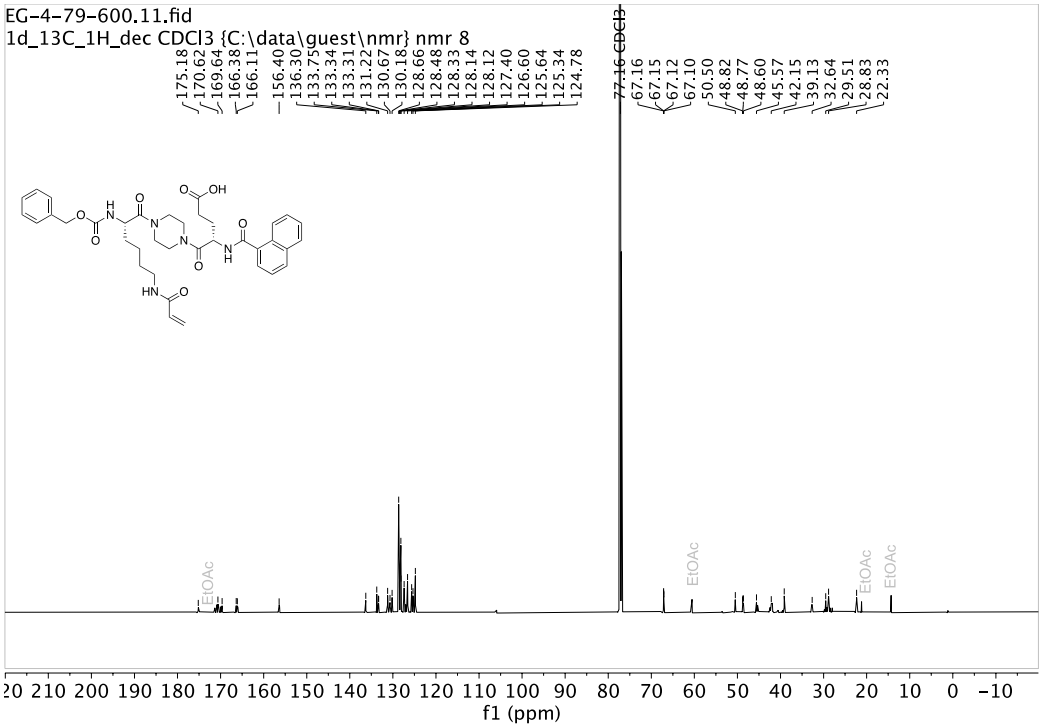
EG-4-79-600.11.fid
1d_13C_1H_dec CDCl3 {C:\data\guest\nmr} nmr 8
f1 (ppm)

Compound 25

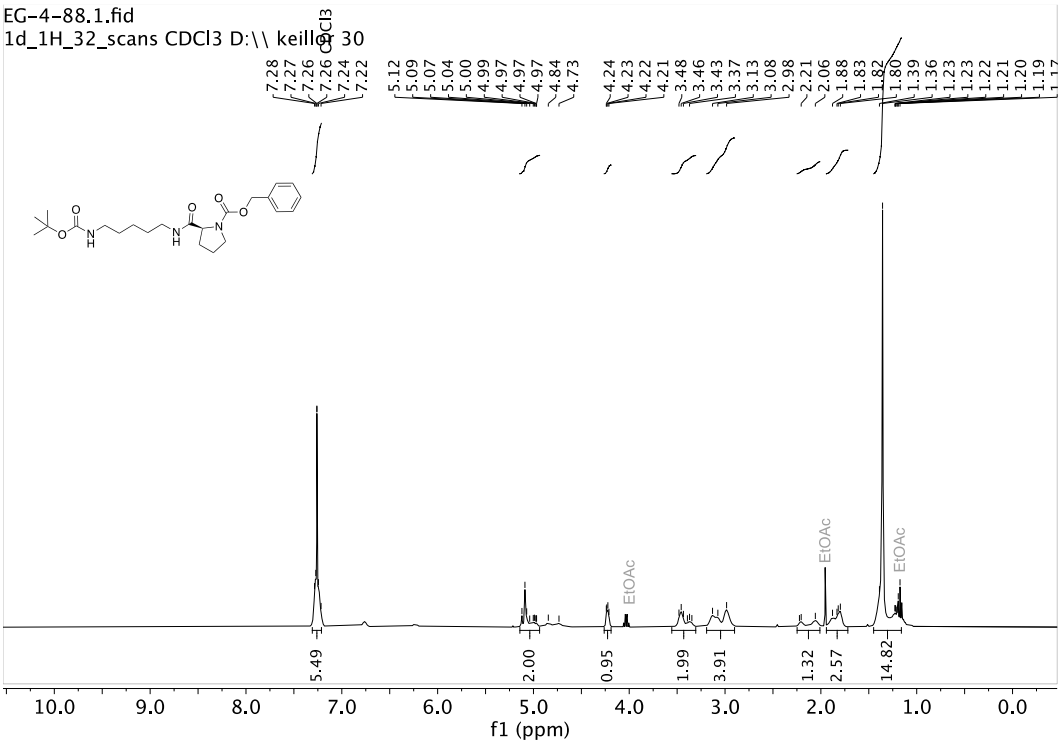
EG-4-88.1.fid
1d_1H_32_scans CDCl3 D:\\ keillor 30
CDCl3
EtOAc
EtOAc
EtOAc
5.49
2.00
0.95
1.99
3.91
1.32
2.57
14.82
f1 (ppm)

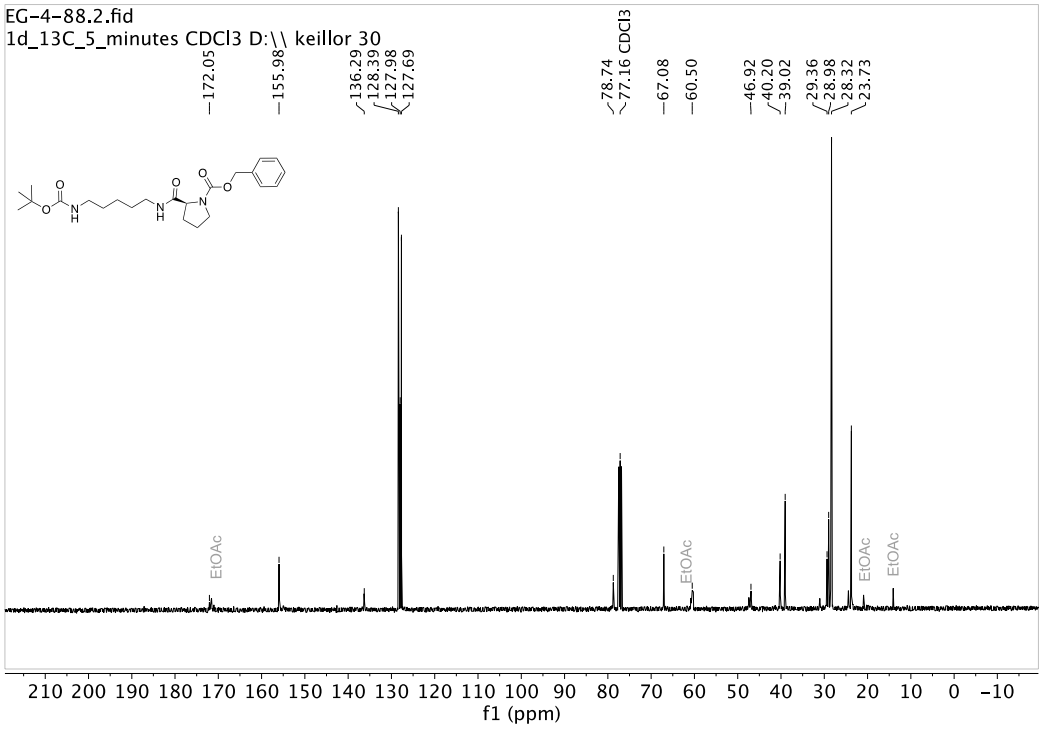
EG-4-88.2.fid
1d_13C_5_minutes CDCl3 D:\\ keillor 30
CDCl3
EtOAc
EtOAc
EtOAc
EtOAc
f1 (ppm)

Compound 27

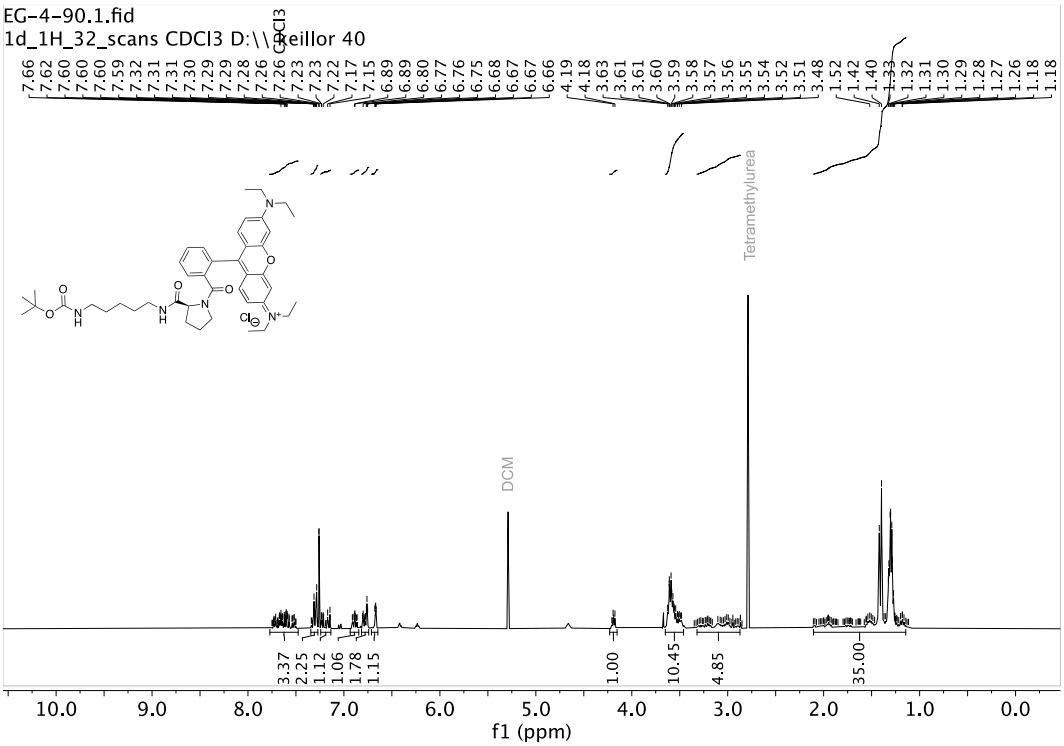
EG-4-90.1.fid
1d_1H_32_scans CDCl3 D:\\ keillor 40
CDCl3
Tetramethylurea
DCM
3.37
2.25
1.12
1.06
1.78
1.15
1.00
10.45
4.85
35.00
f1 (ppm)

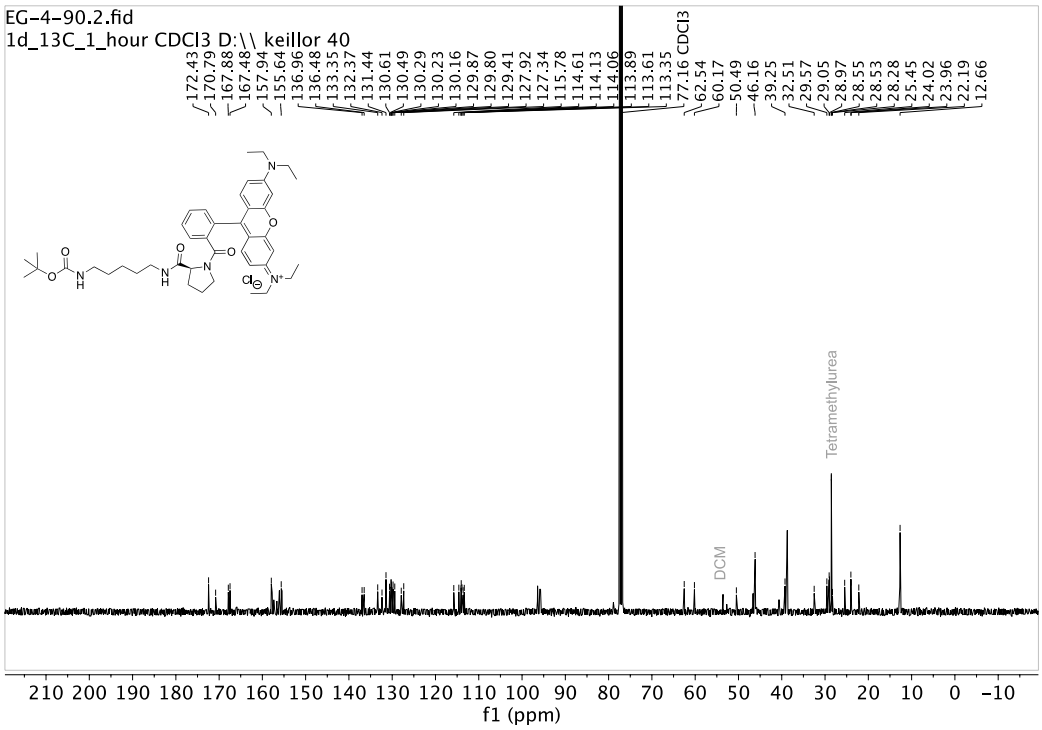
EG-4-90.2.fid
1d_13C_1_hour CDCl3 D:\\ keillor 40
CDCl3
Tetramethylurea
DCM
f1 (ppm)

Compound 31

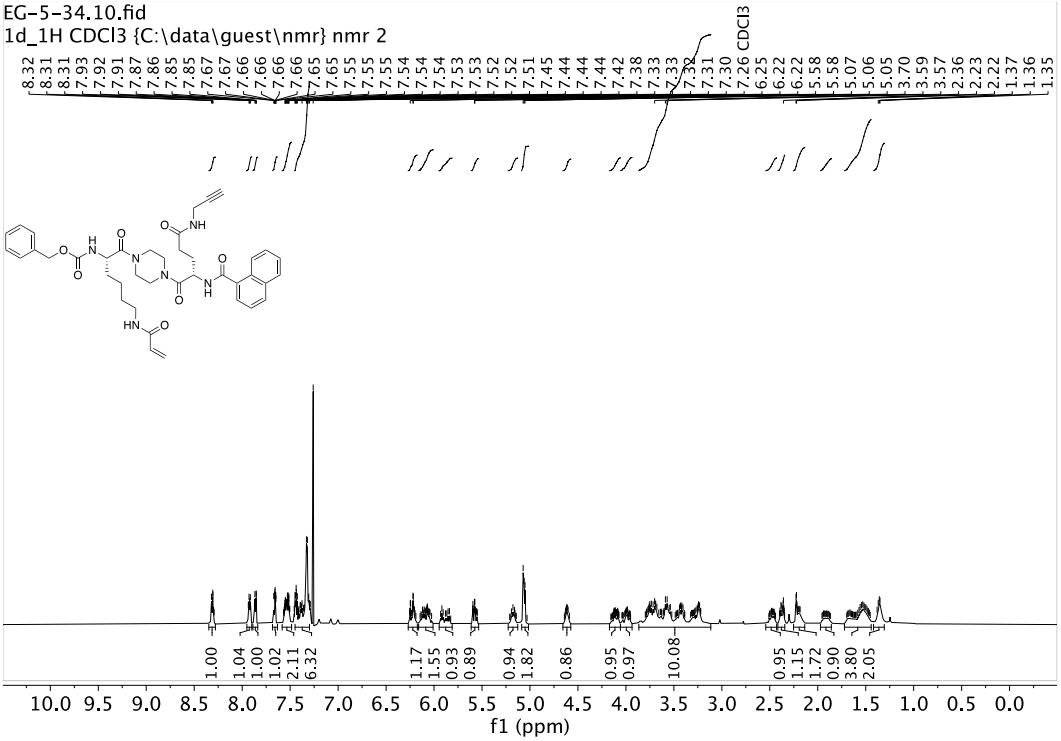
EG-5-34.10.fid
1d_1H CDCl3 {C:\data\guest\nmr} nmr 2
f1 (ppm)

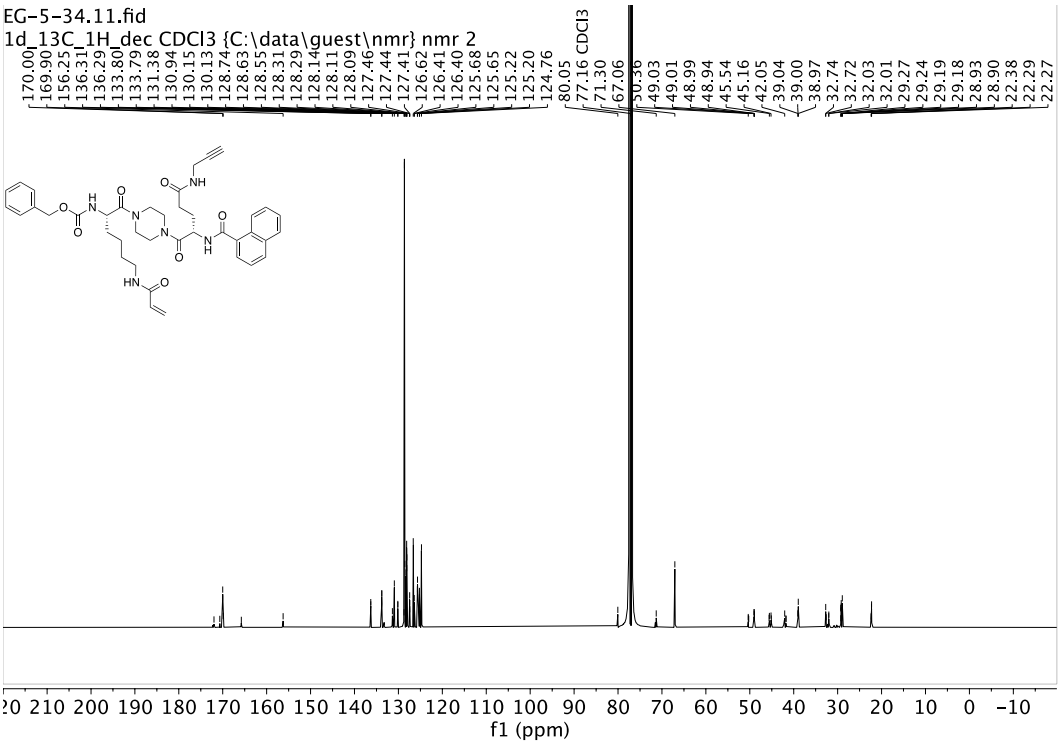
EG-5-34.11.fid
1d_13C_1H_dec CDCl3 {C:\data\guest\nmr} nmr 2
f1 (ppm)

Compound 32

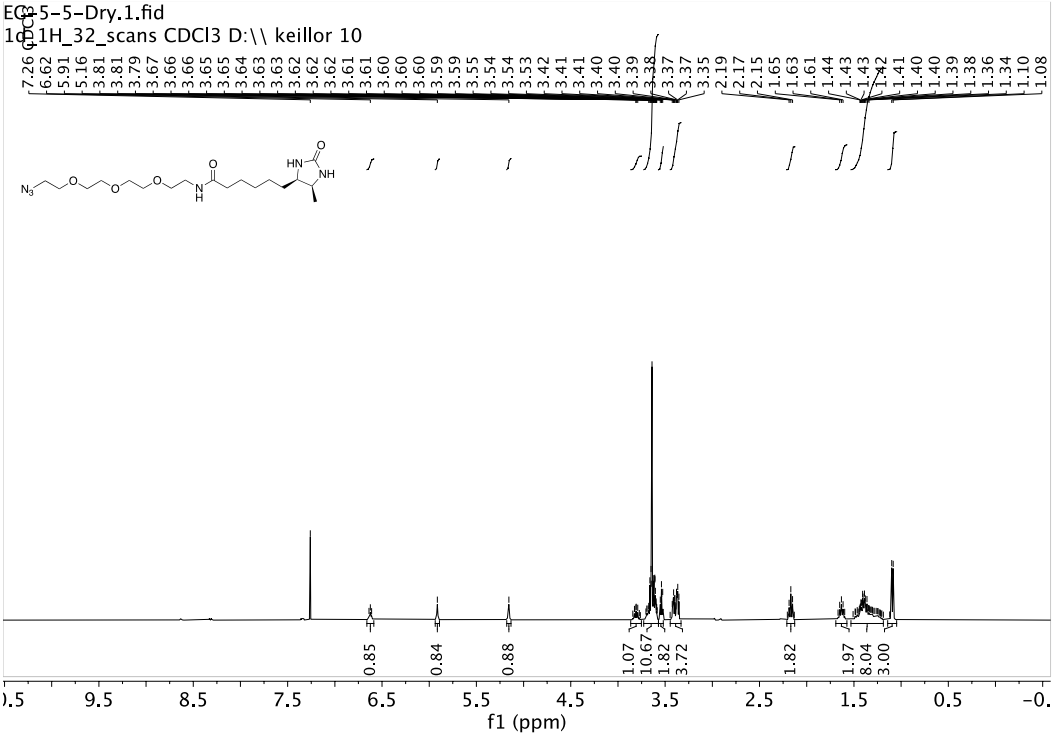
EG-5-5-Dry.1.fid
1d_1H_32_scans CDCl3 D:\\ keillor 10
0.85
0.84
0.88
1.07
10.67
1.82
3.72
1.82
1.97
8.04
3.00
f1 (ppm)

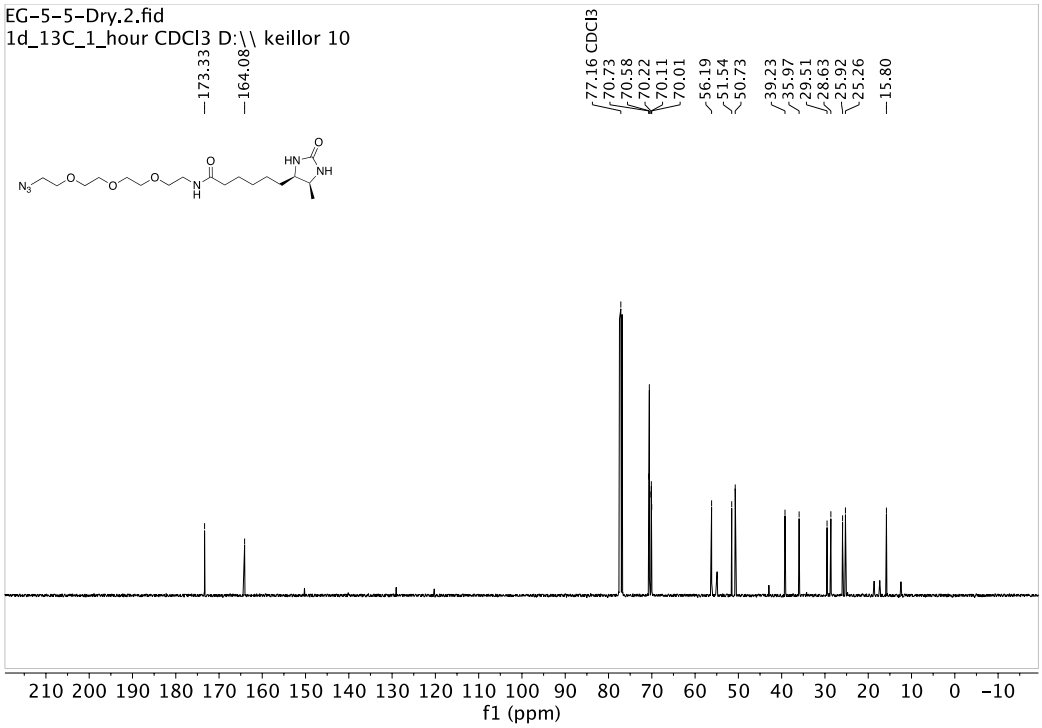
EG-5-5-Dry.2.fid
1d_13C_1_hour CDCl3 D:\\ keillor 10
f1 (ppm)

HPLC traces of final compounds

Compound 17:

<Sample Information>

Sample Name	: EG-4-29		
Sample ID	: EG-4-29		
Data Filename	: EG-4-29		
Method Filename	: 5-95% Method.lcm		
Batch Filename	: EG-4-29		
Vial #	: 1-19	Sample Type	: Unknown
Injection Volume	: 30 uL		
Date Acquired	: 12/15/2021 11:59:11 AM	Acquired by	: Eric Gates
Date Processed	: 12/15/2021 12:14:15 PM	Processed by	: Eric Gates

<Chromatogram>

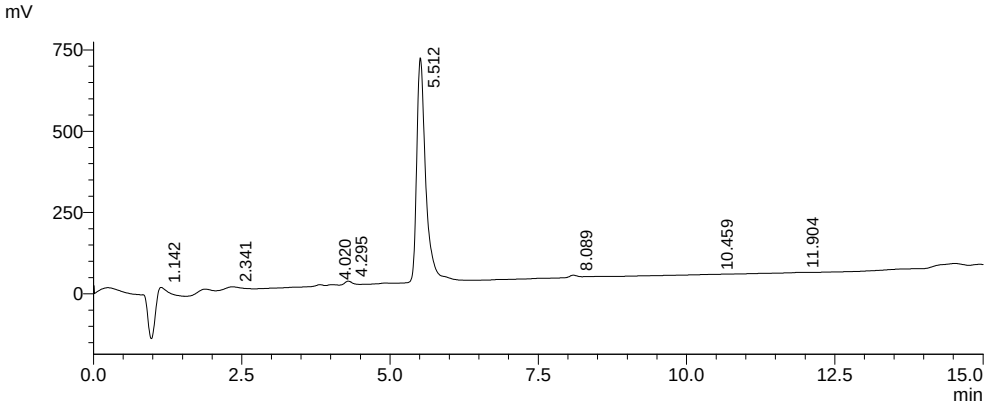

Peak Table

Detector A Channel 1 220nm

Peak#	Ret. Time	Area%
1	1.142	0.805
2	2.341	1.503
3	4.020	0.498
4	4.295	1.070
5	5.512	95.488
6	8.089	0.572
7	10.459	0.023
8	11.904	0.041
Total		100.000

Compound 18 (NCEG2):

<Sample Information>

Sample Name	: EG-5-11-Purity		
Sample ID	: EG-5-11-Purity		
Data Filename	: EG-5-11-Purity.lcd		
Method Filename	: 5-95% Method.lcm		
Batch Filename	:		
Vial #	: 0-2	Sample Type	: Unknown
Injection Volume	: 10 uL		
Date Acquired	: 9/1/2022 11:01:55 AM	Acquired by	: Boddy lab
Date Processed	: 9/1/2022 11:21:26 AM	Processed by	: Boddy lab

<Chromatogram>

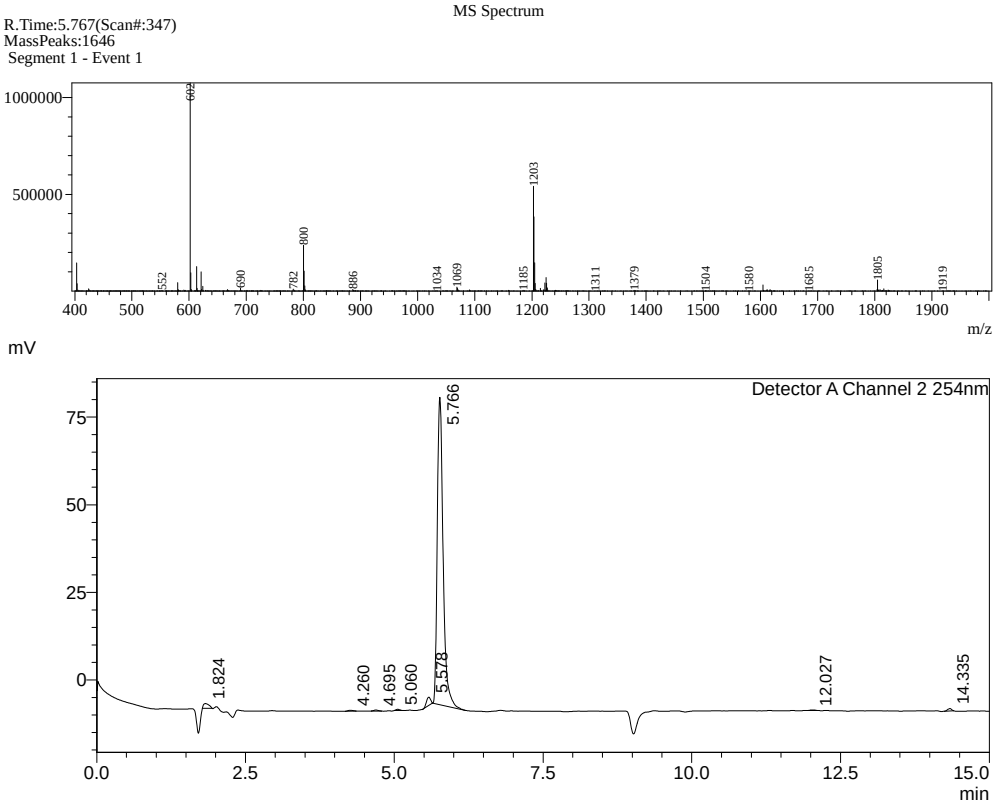

Peak Table
Detector A Channel 2 254nm

Peak#	Ret. Time	Area%
1	1.824	1.438
2	4.260	0.222
3	4.695	0.219
4	5.060	0.272
5	5.578	1.827
6	5.766	95.387
7	12.027	0.144
8	14.335	0.492
Total		100.000

Compound 22:

<Sample Information>

Sample Name	: EG-4-65		
Sample ID	: EG-4-65		
Data Filename	: EG-4-65_002.lcd		
Method Filename	: 5-95% Method.lcm		
Batch Filename	: EG-4-64-65-87-Purity.lcb		
Vial #	: 0-5	Sample Type	: Unknown
Injection Volume	: 10 uL		
Date Acquired	: 4/29/2022 10:20:06 AM	Acquired by	: Boddy lab
Date Processed	: 4/29/2022 10:35:07 AM	Processed by	: Boddy lab

<Chromatogram>

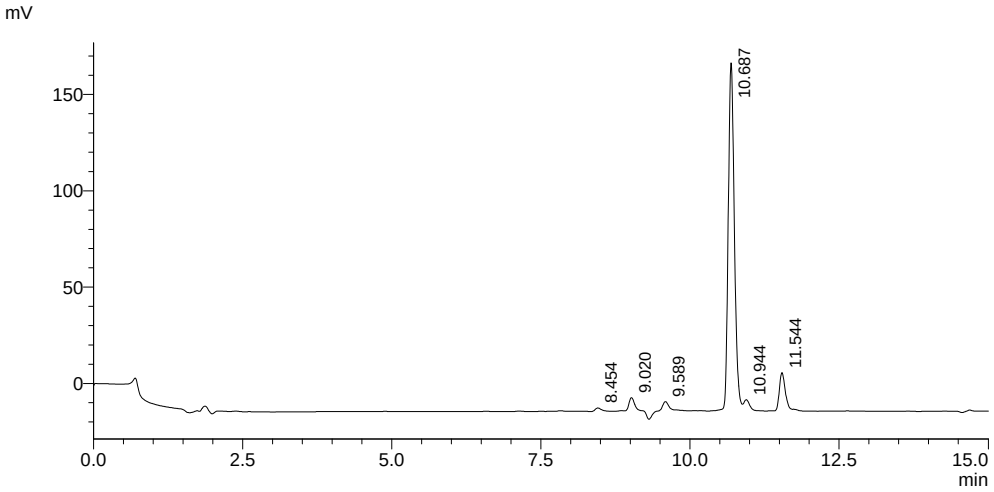

Peak Table
Detector A Channel 2 254nm

Ret. Time	Area%
8.454	0.580
9.020	2.489
9.589	1.625
10.687	85.300
10.944	1.605
11.544	8.401
	100.000

MS Spectrum

R.Time:10.683(Scan#:642)
MassPeaks:1273
Segment 1 - Event 1

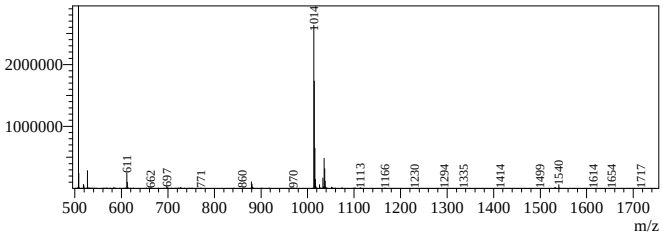

Compound 23:

<Sample Information>

Sample Name	: EG-4-64		
Sample ID	: EG-4-64		
Data Filename	: EG-4-64_001.lcd		
Method Filename	: 5-95% Method.lcm		
Batch Filename	: EG-4-64-65-87-Purity.lcb		
Vial #	: 0-4	Sample Type	: Unknown
Injection Volume	: 10 uL		
Date Acquired	: 4/29/2022 10:04:34 AM	Acquired by	: Eric Gates
Date Processed	: 4/29/2022 10:19:36 AM	Processed by	: Eric Gates

<Chromatogram>

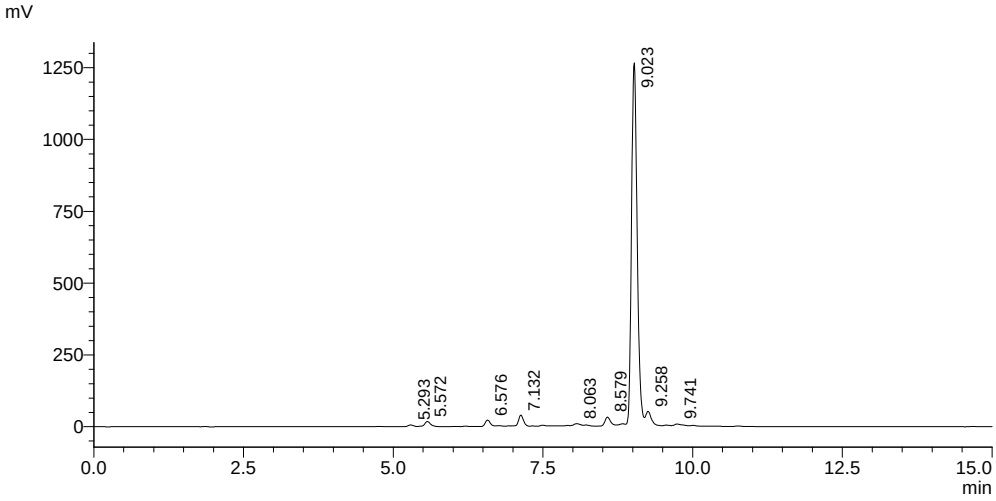

Peak Table
Detector A Channel 2 254nm

Ret. Time	Area%
5.293	0.255
5.572	0.943
6.576	1.268
7.132	2.143
8.063	0.425
8.579	1.827
9.023	89.915
9.258	3.059
9.741	0.166
	100.000

MS Spectrum
R.Time:9.017(Scan#:542)
MassPeaks:1293
Segment 1 - Event 1

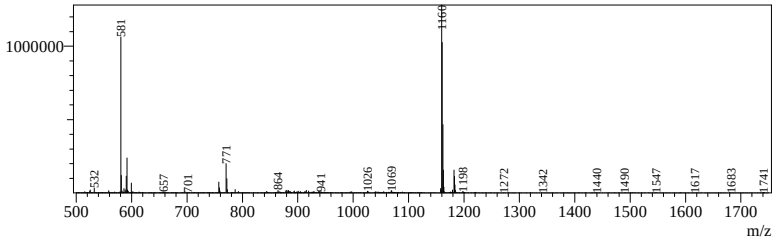

Compound 29 (NCEG-RHB):

<Sample Information>

Sample Name	: EG-5-2-Purity		
Sample ID	: EG-5-2-Purity		
Data Filename	: EG-5-2-Purity_002.lcd		
Method Filename	: 5-95% Method.lcm		
Batch Filename	: EG-4-77-EG-5-2-6-Purity.lcb		
Vial #	: 0-3	Sample Type	: Unknown
Injection Volume	: 10 uL		
Date Acquired	: 9/19/2022 11:35:22 AM	Acquired by	: Boddy lab
Date Processed	: 9/19/2022 11:50:24 AM	Processed by	: Boddy lab

<Chromatogram>

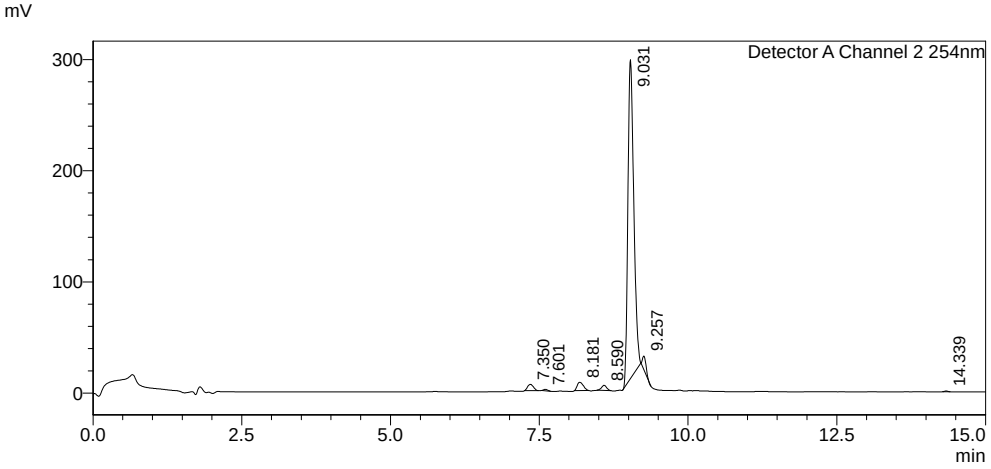

Peak Table
Detector A Channel 2 254nm

Peak#	Ret. Time	Area%
1	7.350	1.839
2	7.601	0.242
3	8.181	2.447
4	8.590	1.270
5	9.031	91.881
6	9.257	2.184
7	14.339	0.137
Total		100.000

Compound 31:

<Sample Information>

Sample Name	: EG-4-77-Purity		
Sample ID	: EG-4-77-Purity		
Data Filename	: EG-4-77-Purity_001.lcd		
Method Filename	: 5-95% Method.lcm		
Batch Filename	: EG-4-77-EG-5-2-6-Purity.lcb		
Vial #	: 0-2	Sample Type	: Unknown
Injection Volume	: 10 uL		
Date Acquired	: 9/19/2022 11:19:51 AM	Acquired by	: Boddy lab
Date Processed	: 9/19/2022 11:49:31 AM	Processed by	: Boddy lab

<Chromatogram>

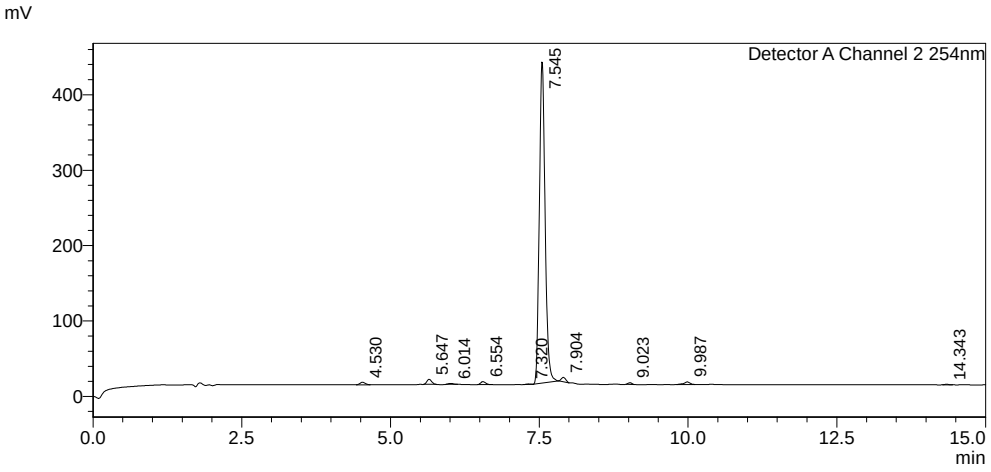

Peak Table
Detector A Channel 2 254nm

Peak#	Ret. Time	Area%
1	4.530	0.673
2	5.647	1.273
3	6.014	0.224
4	6.554	0.787
5	7.320	0.115
6	7.545	94.734
7	7.904	0.937
8	9.023	0.317
9	9.987	0.825
10	14.343	0.116
Total		100.000

Compound 33:

<Sample Information>

Sample Name	: EG-5-6-Purity		
Sample ID	: EG-5-6-Purity		
Data Filename	: EG-5-6-Purity_003.lcd		
Method Filename	: 5-95% Method.lcm		
Batch Filename	: EG-4-77-EG-5-2-6-Purity.lcb		
Vial #	: 0-4	Sample Type	: Unknown
Injection Volume	: 10 uL		
Date Acquired	: 9/19/2022 11:50:54 AM	Acquired by	: Boddy lab
Date Processed	: 9/19/2022 12:05:56 PM	Processed by	: Boddy lab

<Chromatogram>

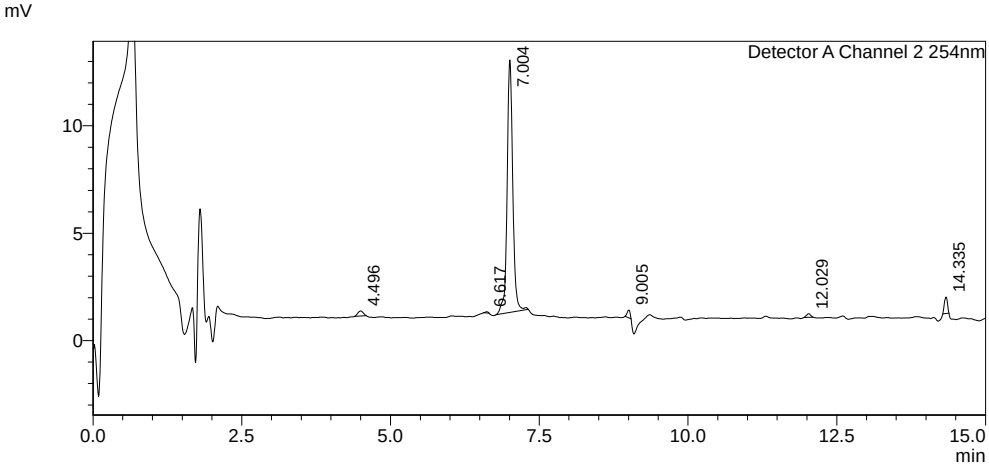

Peak Table
Detector A Channel 2 254nm

Peak#	Ret. Time	Area%
1	4.496	1.831
2	6.617	0.238
3	7.004	92.413
4	9.005	1.459
5	12.029	0.916
6	14.335	3.142
Total		100.000

This break indicates the end of the supporting information section for the research article presented within this chapter. The section presented below was conducted post-submission of the manuscript to IJMS and was thus not published with article.

Selectivity of NCEG-RHB in SH-SY5Y Lysate

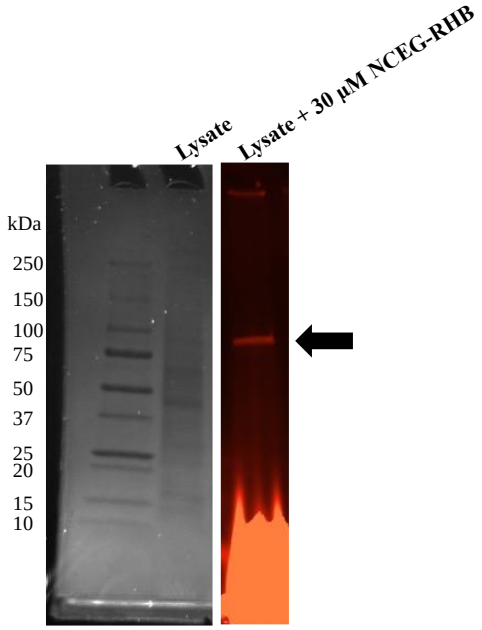

Figure 3.5. SDS-PAGE analysis of SH-SY5Y cell lysate. Left panel, Coomassie stain of protein standards and raw lysate. Right panel, fluorescence visualization of lysate and 30 µM NCEG-RHB.

In order to confirm the selectivity of the cell permeant rhodamine B fluorescent probe, **NCEG-RHB**, SH-SY5Y cells were grown and differentiated using the aforementioned procedure within this chapter. The cells were lysed and 30 µM **NCEG-RHB** was added along with 10 mM $CaCl_2$ to ensure TG2 remained catalytically active. Upon SDS-PAGE analysis of the labelled lysate, one red fluorescent band was identified, corresponding to ~78 kDa (Figure 3.5). Given the molecular weight of TG2 is approximately 78 kDa, we are confident this band does indeed correspond to TG2 that has been covalently labelled by **NCEG-RHB**. Furthermore, as there are no other protein bands which are also red fluorescent, this confirms that **NCEG-RHB** does exhibit a high degree of selectivity within mammalian cell lysate and reinforces that inhibition of intracellular TG2 is the mechanism of action by which our inhibitors exert their anti-cancer

activity. Future efforts will be directed to quantifying the degree of selectivity of these tools *via* western blot and proteomics.

Materials and Methods for the Selectivity of NCEG-RHB in SH-SY5Y Lysate

SH-SY5Y (CRL-2266, ATCC) cells were grown under cell culture conditions (5% CO_2, 37 ˚C, humidified) to 80% confluency in Dulbecco's Modified Eagle Medium (DMEM) supplemented with penicillin/streptomycin (P/S, 100 U/mL / 100 µg/mL) and heat-inactivated fetal bovine serum (FBS, 10%). Cells were passaged three times before being seeded into a T175 cell culture flask. Cells were grown to 70% confluency using an adapted protocol from Singh *et al.* [50]. Briefly, cells were differentiated and grown in DMEM supplemented with 3% heat inactivated FBS, P/S, and 20 µM *trans*-retinoic acid (RA). Medium was changed daily for 7 days at which point cells were 70% confluent and used for the lysate experiment. Lysis was performed with RIPA lysis buffer lacking protease inhibitors at 4 ˚C with gentle shaking for 30 min and subsequently scraped with a rubber policeman. The lysate was centrifuged at 17000 × g for 10 min at 4 ˚C and the supernatant was retained. To six 1.5-mL Eppendorf tubes were added 50 µL of this raw lysate. Three of these tubes then acted as lysate controls and received 5 µL of milliQ H_2O and 5 µL of a 120 mM $CaCl_2$ solution to provide a final $CaCl_2$ concentration of 10 mM. The other three tubes acted as labelling treatment replicates and had 5 µL of the 120 mM $CaCl_2$ solution along with 5 µL of an aqueous solution of 360 µM **NCEG-RHB** (12% v/v DMSO) to provide a final probe concentration of 30 µM. All tubes were then gently vortexed and incubated at room temperature for 25 min. Upon completion, 30 µL of the samples were removed and placed into six new 1.5-mL Eppendorf tubes, which then had 30 µL of 2X Laemmli Buffer (5% BME) added to them. The samples were boiled at 100 ˚C for 5 min to ensure denaturation, and then cooled. The

wells of a BioRad Mini-PROTEAN TGX 4-20% polyacrylamide precast SDS-PAGE were then loaded with 40 µL of the corresponding sample and 10 µL of BioRad Precision Plus Protein Unstained Standards. Electrophoresis was then executed at 120 V for 1 h using 25 mM TRIS, 192 mM glycine, and 0.1% SDS running buffer. Once complete, the gel was first visualized *via* a BioRad ChemiDoc MP Imager with green epi illumination and 605/50 nm filter to generate the fluorescent image, and then Coomassie stained to visualize the protein standards and total loading.

Supporting Information for the Selectivity of NCEG-RHB in SH-SY5Y Lysate

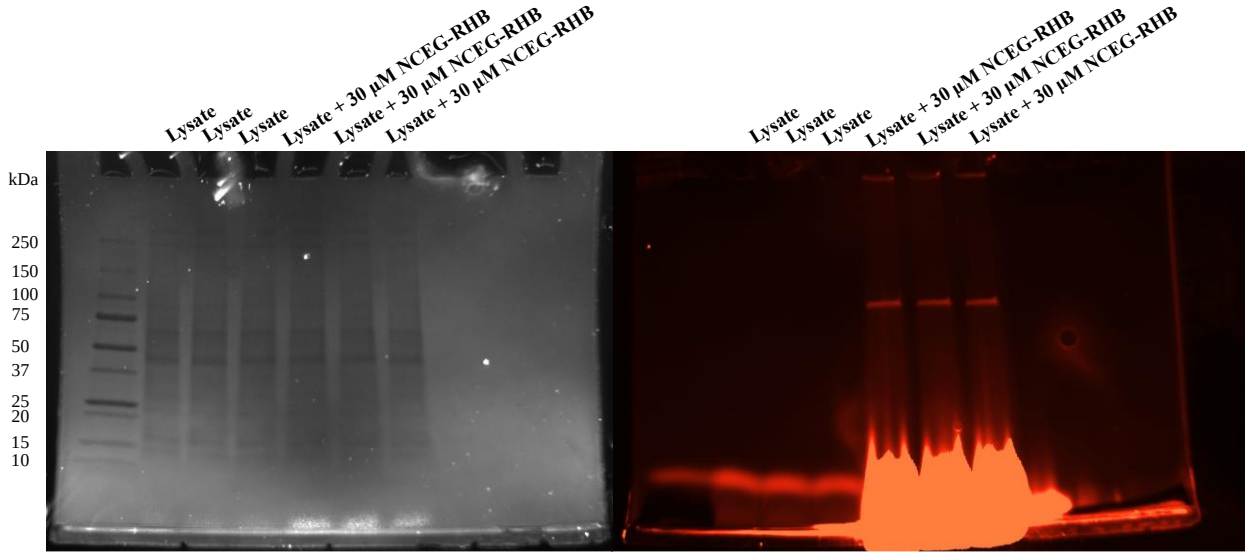

Figure S14. Full SDS-PAGE images of the gel analyzed within this section.

Chapter 4: High Affinity Fluorogenic Substrate for Tissue Transglutaminase Reveals Enzymatic Hysteresis

Eric W. J. Gates[1], Adrien Prince-Hallée[1], Yasaman Heidari[2], Abootaleb Sedighi[2], and Jeffrey W. Keillor[1,*]

[1] Department of Chemistry and Biomolecular Sciences, University of Ottawa, Ottawa, Ontario, K1N 6N5, Canada

[2] Dalriada Drug Discovery, Mississauga, Ontario L5N 8G4, Canada.

* Corresponding author: JWK

4.1. Introduction to the Research Article Presented Within this Chapter

The work presented within this chapter derived from our wish to initially design an in-house fluorogenic activity assay for Factor XIII. Due to the fluorescence interreference hurdle we experienced in our investigation of small molecule FXIII inhibitors in Chapter 2, we believed that there would be room in the FXIII field for a fluorogenic substrate with more desirable photochemical properties than the traditional A101 substrate. We designed the scaffold based on a lead compound from the TG2 SAR studies, namely AA9, and replaced the lysine(acrylamide) residue with a glutamyl(umbelliferone) ester. Although this scaffold is TG2 selective, we hypothesized that we could exploit a minimal amount of reactivity with FXIII to still observe a signal. Through TGase catalyzed hydrolysis of the ester linkage, the fluorescent reporter would be released and could be monitored.

Upon initial investigation of the novel substrate, we observed a high degree of affinity and reactivity for TG2, but minimal for FXIII. We elected to continue our studies of this substrate with TG2 as it represents the most potent synthetic substrate for TG2 to date. Our further investigation with this substrate then uncovered an unknown mechanistic phenomenon within this class of enzymes and has resulted in a greater understanding for how pliable and impressionable TG2's catalytic activity is. Utilizing RapidFire Mass Spectrometry, an emerging technique in medicinal chemistry, inhibition constants were gathered in the absence of a continuous activity assay substrate. RapidFire MS allows the determination of the covalent incorporation of an inhibitor to an enzyme of interest through the change in molecular weight. Utilizing a robotic sampler, inhibitor can be added to a solution of enzyme and immediately analyzed *via* MS, the observed rate constants can then be analyzed using an analogous method to activity assays. Taken together, the work in this chapter represents an interesting journey through the development of a leading high affinity activity substrate for TG2 and the discovery of a new aspect of its enzymatic activity.

4.2. Author Contributions

Conceptualization, J.W.K. and E.W.J.G.; formal analysis, E.W.J.G., A.P.H., and Y.H.; investigation, E.W.J.G., A.P.H., Y.H., and A.S.; writing—original draft preparation, E.W.J.G., A.P.H., and J.W.K.; writing—review and editing, E.W.J.G. and J.W.K.; visualization, E.W.J.G. and J.W.K.; supervision, J.W.K.; project administration, J.W.K.; funding acquisition, J.W.K. All authors have read and agreed to the published version of the manuscript.

4.3. Copyright

Reprinted (adapted) with permission from Gates, E. W. J. et al. High-Affinity Fluorogenic Substrate for Tissue Transglutaminase Reveals Enzymatic Hysteresis. *Biochemistry* **2023**. Copyright 2023 American Chemical Society.

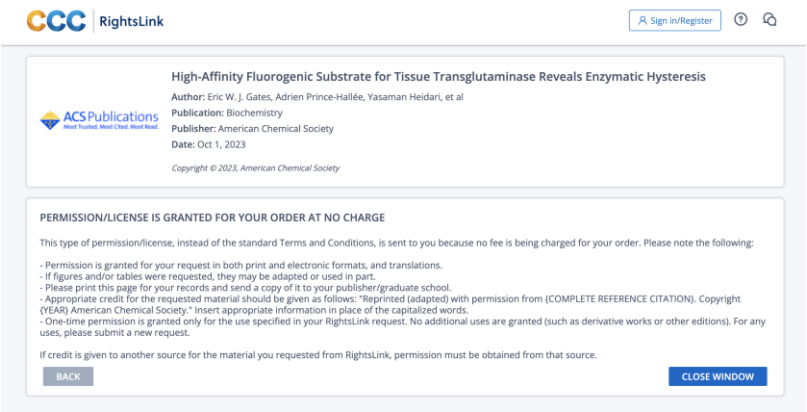

4.4. Abstract

Transglutaminases (TGases) are a family of calcium-dependent enzymes primarily known for their ability to cross- link proteins. Transglutaminase 2 (TG2) is one isozyme in this family whose role is multifaceted. TG2 can act not only as a typical transamidase through its catalytic core but also as a G-protein via its GTP binding site. These two discrete activities are tightly regulated by both environmental stimuli and redox reactions. Ubiquitously expressed in humans, TG2 has been implicated in numerous disease pathologies that require extensive investigation. The catalytic activity of TG2 can be monitored through various mechanisms, including hydrolysis, transamidation, or cleavage of isopeptide bonds. Activity assays are required to monitor the activity of this isozyme not only for studying its transamidation reaction but also for validation of therapeutics designed to abolish this activity. Herein, we present the design, synthesis, and evaluation of a new TG2 activity substrate based on a previously optimized inhibitor scaffold. The

substrate **APH7** exhibits excellent affinity, selectivity, and reactivity with TG2 (*K*M = 3.0 μM). Furthermore, its application also allowed the discovery of unique hysteresis at play within the catalytic activity and inhibition reactivity of TG2.

4.5. Introduction

The transglutaminase (TGase) family is made up of nine distinct calcium-dependent isozymes with the primary function of performing various post-translational protein modifications.[1,2] TGases cross-link specific protein substrates by introduction of an N^{ϵ}(γ-glutaminyl)lysine bond.[3] One isozyme of particular interest is transglutaminase 2 (TG2, UniProt: P21980) or tissue transglutaminase. TG2 is the most well studied of the TGase family and is a 78 kDa enzyme composed of four domains: an N- terminal β-sandwich, an α/β-catalytic core, and two C-terminal β-barrels.[4,5] Being ubiquitously expressed in humans, TG2 has two main biologically relevant activities. First, TG2 can act in a typical TGase fashion to catalyze transamidation, mediating cross-linking between protein-bound glutamine and lysine substrates. However, TG2 distinguishes itself from most of the other TGases by also acting as a G-protein important to cell signaling, by virtue of its GTP binding domain. These two discrete activities are associated with two discrete conformations. In the extracellular matrix, an open and linear conformation of TG2 is stabilized by calcium binding, allowing easy access to the catalytic active site and facilitating enzymatic cross-linking. When TG2 is localized intracellularly, it predominantly adopts a closed and compact conformation, which allows formation of its GTP binding site on the first β- barrel located proximally to the catalytic core.[6–8] Due to its multiple activities and ubiquitous expression, TG2 has been implicated in numerous physiological roles and disease states including cancer, celiac disease, and fibrosis.[9–17]

Chemical tools are required to specifically evaluate the activity of TG2 in vitro to help elucidate the vast array of TG2's roles as well as to assess potential inhibitors to be used as therapeutics. Some of the current assays developed to monitor the activity of TG2 lack selectivity for one isozyme in the TGase family, which reduces their applicability to measuring isozyme activity in in cellulo and in vivo models. The chromogenic substrate Cbz- Glu(p-NP)-Gly-OH (AL5) is suitable to monitor the hydrolysis activity of TG2 but also TG1 and TG6; this illustrates the hurdle to isozyme selectivity. Recently, we have also confronted the limits of the AL5 assay when testing highly potent inhibitors.[18–20] The Löser group improved upon this assay by replacing the nitrophenol leaving group with an umbelliferyl leaving group, thereby resulting in a sensitive fluorescent signal when cleaved.[21] Our fluorogenic assay substrate ZFBC is also suitable for monitoring the activity of TGases through release of the umbelliferone.[22] Zedira Gmbh has also generated alternative isopeptidase assays, including one based on the use of fluorogenic peptide A101 (Figure S1); however, this substrate is most useful as a pan-TGase assay and not necessarily for its selectivity for TG2.[23,24] Other assays typically involve coupled enzyme reactions, such as the GDH-TGase coupled assay[25] or end-point assays where an amine or glutamine donor is incorporated into a complementary substrate.[26]

TGases catalyze a number of acyl transfer reactions. They are named for their catalysis of glutamine transamidation reactions; however, they can also mediate the reverse isopeptidase reaction, resulting in the cleavage of a secondary amide bond as well as the hydrolysis of activated esters. The assay described herein exploits the hydrolytic activity of TG2 to generate a "turn on" fluorescence response, reporting the activity of TG2 with great sensitivity. This new assay substrate was based on the optimized scaffold of an inhibitor that we previously reported,[20] and it exhibits excellent affinity, stability, and selectivity for TG2. Furthermore, the novel structure of

the substrate and the sensitivity of the assay method allowed us to discover a pattern of enzymatic hysteresis related to the structure of the assay substrate employed, illustrating the effect of subtle conformational changes on the catalytic activity.

4.6. Materials and Methods

4.6.1. Synthesis

Commercially available reagents and solvents were used without further purification. ^{1}H and ^{13}C NMR spectra were recorded on a Bruker 400 or 600 MHz instrument, and chemical shifts were reported in parts per million referenced to the deuterated solvent peak. High-resolution mass spectra were obtained with a quadrupole time-of-flight (QTOF) analyzer and electrospray ionization (ESI) source by the John L. Holmes Mass Spectrometry Facility at the University of Ottawa. Purification of intermediates and final compounds was executed using flash chromatography with 230−400 mesh silica gel. Thin layer chromatography with SiliCycle 200 μm thickness F-254 indicator aluminum-backed plates was utilized for reaction monitoring by short-wave UV visualization. The final compound was also evaluated for purity via HPLC using a Shimadzu LC- MS-2020 and Agilent Eclipse XOB-C18 5.0 μm, 4.6 × 150 mm column, ACN/H_2O with 0.05% v/v formic acid, 5−95% elution gradient, 15 min total runtime, 1 mL/min flow rate, and UV detection at 254 nm instrument parameters.

*Procedure for the Synthesis of **3** (Boc-piperazine-naphthoyl).* The commercially available naphthoic acid 1 (8.712 mmol, 1 equiv) was dissolved in EDC·HCl (10.454 mmol, 1.2 equiv), HOBt (10.454 mmol, 1.2 equiv), DIPEA (26.136 mmol, 3 equiv), and 87 mL of DCM (0.1 M) and stirred at room temperature for 30 min. Boc-piperazine 2 (10.454 mmol, 1.2 equiv) was added, and the reaction was stirred at room temperature overnight. The solution was concentrated under reduced pressure and the residue was dissolved in DCM. The solution was washed with water, saturated $NaHCO_3$ solution, and brine, dried with $MgSO_4$, filtered, and concentrated under reduced pressure to provide clear, colorless oils. The crude product was purified by flash chromatography

over silica gel (elution with a gradient of 2.5−5% MeOH in DCM) to provide the pure product as a white solid. Yield: 2.966 g (95%). Spectral data matched those from previously reported synthesis.[20] ^{1}H NMR (400 MHz, $CDCl_3$): δ 7.53 (dd, J = 27.3, 8.0 Hz, 3H), 7.20−7.03 (m, 4H), 3.89−3.44 (m, 2H), 3.29 (d, J = 6.1 Hz, 2H), 2.88 (d, J = 62.2 Hz, 4H), 1.16 (d, J = 10.2 Hz, 9H).

*Procedure for the Synthesis of **4** (Piperazine-naphthoyl TFA Salt).* Boc-piperazine-naphthoyl 3 (8.276 mmol, 1 equiv) was dissolved in 83 mL of DCM (0.1 M) with 8.3 mL of TFA (10% v/v) and stirred at room temperature overnight. The solution was washed three times with $NaHCO_3$, dried with $MgSO_4$, filtered, and evaporated under reduced pressure to provide the desired product as a clear, colorless oil. Yield: 1.989 g (quantitative).

*Procedure for the Synthesis of **5** [Z-Glu(OtBu)-piperazine-naphthoyl]*. The commercially available Z-Glu(OtBu)-OH (6.897 mmol, 1 equiv) was dissolved in EDC·HCl (8.277 mmol, 1.2 equiv), HOBt (8.277 mmol, 1.2 equiv), DIPEA (20.691 mmol, 3 equiv), and 69 mL of ACN (0.1 M) and stirred at room temperature for 30 min. Piperazine-naphthoyl 4 (8.277 mmol, 1.2 equiv) was added and the reaction was stirred at room temperature overnight. The solution was concentrated under reduced pressure and the residue was dissolved in DCM. The solution was washed with water, saturated $NaHCO_3$ solution and brine, dried with $MgSO_4$, filtered, and concentrated under reduced pressure to provide clear, colorless oils. The crude product was purified by flash chromatography over silica gel (elution with 7.5% MeOH in DCM) to provide the pure product as a white solid. Yield: 3.354 g (87%). ^{1}H NMR (400 MHz, $CDCl_3$): δ 7.96−7.86 (m, 2H), 7.83 (d, J = 6.6 Hz, 1H), 7.60− 7.47 (m, 3H), 7.43 (t, J = 4.3 Hz, 1H), 7.34 (q, J = 4.2 Hz, 5H), 5.66 (d, J = 8.3 Hz, 1H), 5.17−4.99 (m, 2H), 4.86−4.56 (m, 1H), 4.18−3.10 (m, 8H), 2.47−2.17 (m, 2H), 2.10−1.80 (m, 2H), 1.46 (s, 5H), 1.38 (d, J = 4.0 Hz, 4H). ^{13}C NMR (101 MHz, $CDCl_3$) δ: 172.10, 170.45, 169.62, 156.15, 136.27, 133.46, 129.60, 128.29−127.85 (m), 127.30,

126.65, 125.20, 124.47, 123.96, 80.87, 66.96, 49.95, 47.18, 46.74, 45.44, 42.60, 42.17, 41.88, 41.50, 34.68, 31.60, 30.29 (d, J = 17.2 Hz), 28.44−27.88 (m), 25.29, 14.14. HRMS (ESI-QTOF) m/z: $[M + Na]^+$ calcd for $C_{32}H_{37}N_3O_6Na$, 582.2580; found, 582.2598.

*Procedure for the Synthesis of **6** (Z-Glu-piperazine-naphthoyl).* Z-Glu(OtBu)-piperazine-naphthoyl 5 (5.064 mmol, 1 equiv) was dissolved in 51 mL of DCM (0.1 M) with 5.1 mL of TFA (10% v/v) and stirred at room temperature overnight. The solution was washed three times with 0.01 M HCl, dried with $MgSO_4$, filtered, and evaporated under reduced pressure to provide the desired product as a clear, colorless oil. Yield: 1.896 g (74%). ^{1}H NMR (400 MHz, $CDCl_3$): δ 7.94− 7.85 (m, 2H), 7.79 (t, J = 9.1 Hz, 1H), 7.59−7.45 (m, 3H), 7.41 (t,J=6.1Hz,1H),7.31(q,J=5.2,4.5Hz,5H),5.93(d,J=10.4 Hz, 1H), 5.06 (d, J = 18.5 Hz, 2H), 4.92−4.60 (m, 1H), 4.18− 2.99 (m, 8H), 2.62−2.27 (m, 2H), 1.95 (d, J = 51.9 Hz, 2H). ^{13}C NMR (101 MHz, $CDCl_3$) δ: 175.97, 170.60, 169.84, 156.55, 136.07, 133.49, 129.67, 129.48, 128.58 (d, J = 8.5 Hz), 128.23, 128.03 (d, J = 7.0 Hz), 127.33, 126.67, 125.18, 124.43, 124.02, 67.19, 65.87, 49.90, 47.20, 46.78, 45.42, 42.66, 42.08, 41.50, 28.91, 28.38, 15.25. HRMS (ESI-QTOF) m/z: $[M + Na]^+$ calcd for $C_{28}H_{29}N_3O_6Na$, 526.1954; found, 526.1943.

*Procedure for the Synthesis of **7** (**APH7**).* Z-Glu-piperazine-naphthoyl 6 (0.118 mmol, 1 equiv), HATU (0.153 mmol, 1.3 equiv), and DIPEA (0.306 mmol, 2.6 equiv) were dissolved in 1.2 mL of DCM (0.1 M) and stirred for 30 min. Umbelliferone (0.153 mmol, 1.3 equiv) was added, and the reaction was stirred at room temperature for 2.75 h. The solution was concentrated under reduced pressure and purified via flash chromatography over silica gel (elution with 5% MeOH in DCM) to provide the pure product as a green-yellow solid. Yield: 42.80 mg (56%). ^{1}H NMR (600 MHz, DMSO-d_6): δ 8.07 (dd, J = 17.7, 9.7 Hz, 1H), 8.03−7.99 (m, 2H), 7.83−7.70 (m, 2H), 7.69−7.64 (m, 1H), 7.62−7.53 (m, 3H), 7.48 (d, J = 6.9 Hz, 1H), 7.40−7.09 (m, 7H), 6.53−6.43

(m, 1H), 5.12−4.94 (m, 2H), 4.71−4.38 (m, 1H), 3.94−3.34 (m, 6H), 3.18−2.96 (m, 2H), 2.79−2.58 (m, 2H), 2.08−1.77 (m, 2H). ^{13}C NMR (151 MHz, DMSO-d_6) δ: 171.60, 170.24, 168.59, 160.20, 156.57, 154.55, 153.27, 144.33, 137.46, 134.41, 133.48, 129.82, 129.44, 128.93, 128.87, 128.37, 128.28, 128.15, 127.64, 127.05, 125.91, 125.18, 124.38, 119.08, 117.22, 116.08, 110.55, 66.16, 50.18, 47.22, 46.80, 45.59, 45.12, 42.50, 41.96, 41.53, 40.57, 30.28, 26.93. (Note: rotamers of piperazine were observed) HRMS (ESI-QTOF) *m*/*z*: $[M + Na]^+$ calcd for $C_{37}H_{33}N_3O_8Na$, 670.2165; found, 670.2170. Purity via HPLC = 85.0%.

4.6.2. Standard Curve Protocol

The assay was conducted at 25 °C in 50 mM MOPS buffer (pH 6.9) containing 7 mM CaCl2. Stock solutions of 7-HC (umbelliferone) were prepared in DMSO such that its final concentrations ranged from 8 to 32 μM while the concentration of DMSO was always 2.5% v/v. The fluorescence emission was measured (Ex 365 nm/Em 465 nm) in a polystyrene 96-well microplate using a BioTek Synergy 4 plate reader. The experiment was performed in triplicate. A negative control was made of the same solution as the experimental conditions but no 7-HC (umbelliferone).

4.6.3. Kinetic Assay Protocol

Activity Assay with hTG2. The affinity of **APH7** with hTG2 (UniProt: P21980) was measured via an activity assay in which the reaction between substrate and enzyme was monitored by the release of umbelliferone from the hydrolysis of the **APH7**. The assay was conducted at 25 °C in 50 mM MOPS buffer (pH 6.9) containing 7 mM $CaCl_2$. Stock solutions of **APH7** were prepared in DMSO such that its final concentrations ranged from 5 to 100 μM while the concentration of DMSO was always 2.5% v/v. The reaction was initiated with the addition of 0.005

U/mL of hTG2 (final concentration 250 nM) to provide a final assay volume of 200 μL. Product formation was monitored by the fluorescence emission (Ex 365 nm/Em 465 nm) in a polystyrene 96-well microplate using a BioTek Synergy 4 plate reader. The experiment was performed in triplicate. A negative control was made of the same solution as the experimental conditions: 5 μM **APH7** and no enzyme. Initial rates of hydrolysis were determined from linear regression fit of the observed fluorescence of the enzymatic hydrolysis product, umbelliferone. The initial rates were plotted versus the concentration of **APH7**, giving a Michaelis−Menten plot from which the K_M and V_{max} were provided. All data analysis was done using GraphPad Prism.

4.6.4. Michaelis-Menten Fitting

Initial rates of hydrolysis were determined from linear regression fit of the observed fluorescence of the enzymatic hydrolysis product, umbelliferone. The initial rates were divided by the slope of the standard curve to provide conc/min and then plotted versus the concentration of **APH7**, giving a Michaelis−Menten plot from which the K_M and V_{max} were fitted. All data analysis was done using GraphPad Prism.

4.6.5. Isozyme Selectivity Protocol

The hydrolysis of **APH7** was tested in the presence of TG1 (UniProt: P22735, T009 Zedira Gmbh), TG2, dispase activated TG3 (TG3a, UniProt: Q08188, T013 Zedira Gmbh), TG6 (UniProt: O95932, T021 Zedira Gmbh), and thrombin-activated FXIIIA (FXIIIa, UniProt: P00488, T070 Zedira Gmbh) to assess selectivity. For TG1, TG2, and TG6, a solution of 50 mM MOPS buffer (pH 6.9) containing 7 mM $CaCl_2$ was used, while for TG3 and FXIIIa, it was a solution of 98 mM Tris (pH 7.5) containing 291 mM NaCl, 14 mM $CaCl_2$, and 7 mM TCEP. A stock solution of **APH7** was prepared in DMSO such that its final concentration was 10 μM in each solution while

the concentration of DMSO was 2.5% v/v. Each reaction was initiated with the addition of enzyme to a final concentration of 10 μg/mL. Product formation was monitored by the fluorescence emission (Ex 365 nm/Em 465 nm) in a polystyrene 96-well microplate using a BioTek Synergy 4 plate reader. Each kinetic experiment was performed in triplicate. Negative controls were performed, consisting of identical solutions but without enzymes.

4.6.6. Enzymatic Inhibition Assay

Irreversible inhibition assay. The activity of hTG2 was measured via a colorimetric assay using the chromogenic substrate AL5 or fluorometric assays using fluorogenic **APH7**, ZFBC, or A101. The assays were conducted at 25 °C in 69.44 mM MOPS buffer (pH 6.9) containing 10.41 mM $CaCl_2$. For the A101 assay, the buffer also included 18.05 mM glycine methyl ester. Enzymatic inhibition assays were conducted under continuous assay "Kitz and Wilson" conditions[27] using either 100 μM AL5, 50 μM **APH7**, 100 μM A101, or 91 μM ZFBC. Stock solutions of the substrates and inhibitors were prepared in DMSO such that the final concentration of this cosolvent remained below 5% v/v. The reaction was initiated with the addition of 0.005 U/mL of hTG2. Product formation was monitored with absorption at 405 nm (AL5), with fluorescence (Ex 365 nm/Em 465 nm for **APH7** and ZFBC) or with fluorescence at 313 and 418 nm (A101) in a polystyrene 96-well microplate using a BioTek Synergy 4 plate reader. The experiment was completed in triplicate. A negative control was made of the same solution as the experimental conditions, with water in place of the enzyme and inhibitor. A positive control was made of the same solution as the experimental conditions, with water in place of the inhibitor. Monoexponential time-dependent inactivation was observed. First-order rate constants of inactivation (k_{obs}) were determined from nonlinear regression fit to a monoexponential model (eq

1.1 for AL5, eq 1.2 for A101, eq 1.3 for **APH7** and ZFBC) of the observed absorbance or fluorescence of the enzymatic hydrolysis product, *p*-nitrophenolate for AL5, umbelliferone for **APH7** and ZFBC, or Abz-NEEQVSPLTLLK-OH (Abz) for A101. The k_{obs} did not typically demonstrate saturation at high inhibitor concentrations for any of the three assays, so a double reciprocal plot of eq 2 was applied to provide a k_{inact}/K_I value. This method does not provide the two kinetic parameters separately. All data analysis was done using GraphPad Prism.

.

$$f(\mathrm{pNP}) = [\mathrm{pNP}]_0 + (\mathrm{plateau} - [\mathrm{pNP}]_0)(1 - \mathrm{e}^{(k_{obs}t)}) \qquad \textit{eq. 1.1}$$

$$f(\mathrm{Abz}) = [\mathrm{Abz}]_0 + (\mathrm{plateau} - [\mathrm{Abz}]_0)(1 - \mathrm{e}^{(k_{obs}t)}) \qquad \textit{eq. 1.2}$$

$$f(\mathrm{7HC}) = [\mathrm{7HC}]_0 + (\mathrm{plateau} - [\mathrm{7HC}]_0)(1 - \mathrm{e}^{(k_{obs}t)}) \qquad \textit{eq. 1.3}$$

$$k_{obs} = \frac{k_{inact}[\mathrm{I}]}{[\mathrm{I}] + K_I(1 + \frac{[\mathrm{S}]}{K_M})} \qquad \textit{eq. 2}$$

4.6.7. Fluorescence Quenching Assay

The fluorescence of 10 μM umbelliferone was measured at 25 °C in 69.44 mM MOPS buffer (pH 6.9) containing 10.41 mM $CaCl_2$. A stock solution of hydrolysis product **6** was prepared in DMSO such that its final concentration was 10 μM while the concentration of DMSO was 2.5% v/v. The fluorescence emission was measured (Ex 365 nm/ Em 465 nm) in a polystyrene 96-well microplate using a BioTek Synergy 4 plate reader. The experiment was performed in triplicate. A negative control was made of the same solution as the experimental conditions but no umbelliferone. A positive control was made of the same solution as the experimental conditions but without hydrolysis product **6**. An average of all the RFU data was calculated.

4.6.8. Covalent Binding Kinetics Characterization by RapidFire-MS

Preparation of Reaction Mixtures. The reaction mixture (30 μL) was prepared in a 96-well plate format. It consisted of the protein at a concentration of 250 nM, and the inhibitor concentration ranged from 0.78 to 50 μM. The reaction was carried out in 50 mM MOPS buffer (pH 6.95), 7.5 mM $CaCl_2$, and 3% DMSO. The protein and inhibitor were incubated for a period ranging from 0.7 to 120.7 min. The reactions were automated in a 96-well plate format using the FAST SN 41, Formulatrix liquid handler, to ensure consistent reaction initiation and quenching. To initiate the reaction, the compound solution was carefully transferred onto a plate containing the protein and mixed thoroughly. At specific intervals, the reaction was quenched by the addition of formic acid to the mixture, followed by mixing.

RapidFire-Intact Mass Analysis. The Agilent RapidFire- TOF system was utilized to determine the covalent modification or occupancy of TG2 by AA9 and inhibitor **8**. The system included a RapidFire-400 and a 6230 nm TOF mass spectrometer with a MassHunter workstation. The plates containing quenched samples were submitted to RapidFire TOF mass spectrometry. A volume of 10 μL was loaded onto an SPE cartridge (PLRP-S, 30 μm, 1000 Å material) by loading buffer [water: acetonitrile (9:1, v/v), 0.1% FA, 0.6 mL/min]. After desalting, the sample was eluted into the TOF-MS using the elution buffer consisting of acetonitrile: water: [(65:35, v/v), 0.1% FA, 0.5 mL/min]. MassHunter software was used for data acquisition, while BioConfirm software was used for deconvolution.

Data Analysis. The intensities of unmodified and modified proteins resulting from BioConfirm were processed using a script written in “R”. To obtain percentage occupancies, the following eq 3 was used:

$$\% \text{ Occupancy} = \frac{Imod}{Imod + Iunmod} \times 100 \quad \textbf{\textit{eq. 3}}$$

where I_{unmod} and I_{mod} are the signal intensities of the unmodified and covalently modified proteins. Prism 9 (GraphPad Software) was used for kinetic data analysis. The time- and concentration-dependent % occupancy data were fit to an exponential eq (eq 4) to generate k_{obs} for each inhibitor concentration. Then, k_{obs} as a function of the compound concentration was fit to a hyperbolic saturation kinetic eq (eq 5) to provide the k_{inact} and K_I values.

$$Y = Y0 + (\text{Plateau} - Y0) \times (1 - e^{(-kobs \times X)}) \quad \textbf{\textit{eq. 4}}$$

$$kobs = \frac{kinact \times [I]}{KI + [I]} \qquad \textbf{\textit{eq.5}}$$

4.7. Results and Discussion

4.7.1. Design

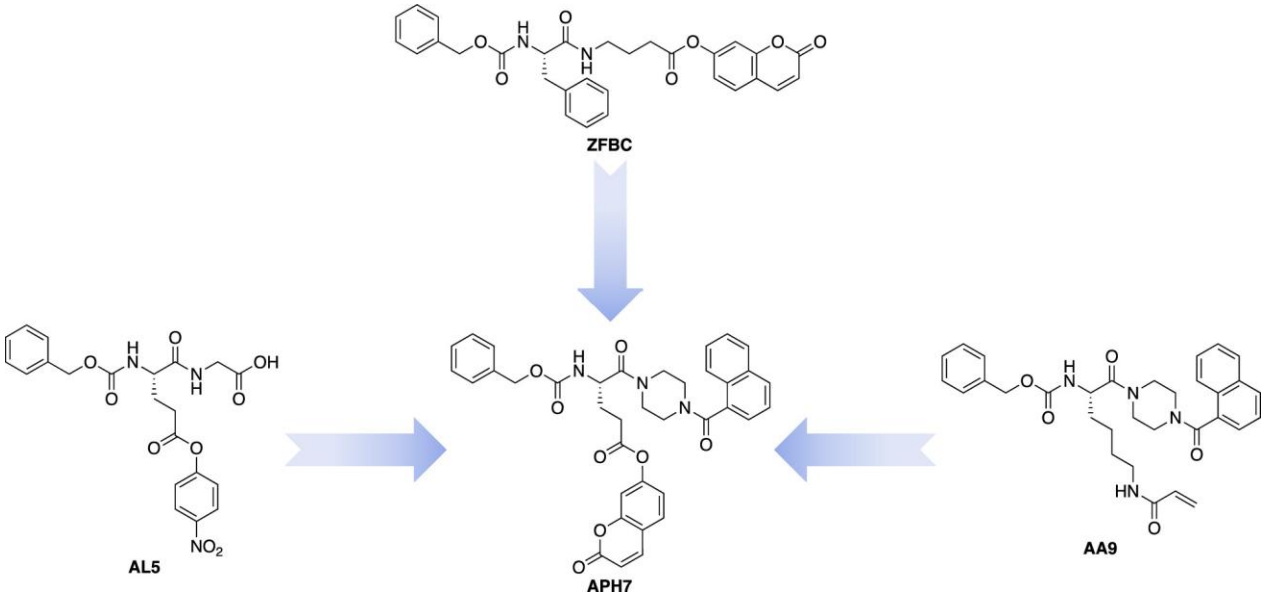

Figure 4.1. Rational design incorporating the key elements of the lead inhibitor scaffold (AA9) and the previous activity substrates for TG2.

The design for this substrate initially stemmed from one of the lead compounds optimized in our medicinal chemistry efforts to target TG2 (Figure 1). Irreversible inhibitor AA9 displays excellent potency and selectivity for TG2, due in part to its naphthoyl group which presumably occupies the large hydrophobic binding pocket in the substrate binding site of TG2.[6,19,20] From this scaffold, we hypothesized that we could replace the acrylamide warhead of the irreversible inhibitor with an ester capable of being cleaved by TG2-mediated hydrolysis. Improving upon both of our previously published substrates AL5 and ZFBC, we replaced the central lysine of AA9 with a glutamate residue and linked an umbelliferyl group to the γ- carboxylate. The synthetic route to this scaffold was planned in a direct linear manner, manipulating orthogonal protecting groups to allow for the final derivatization of the γ-carboxylate.

4.7.2. Synthesis

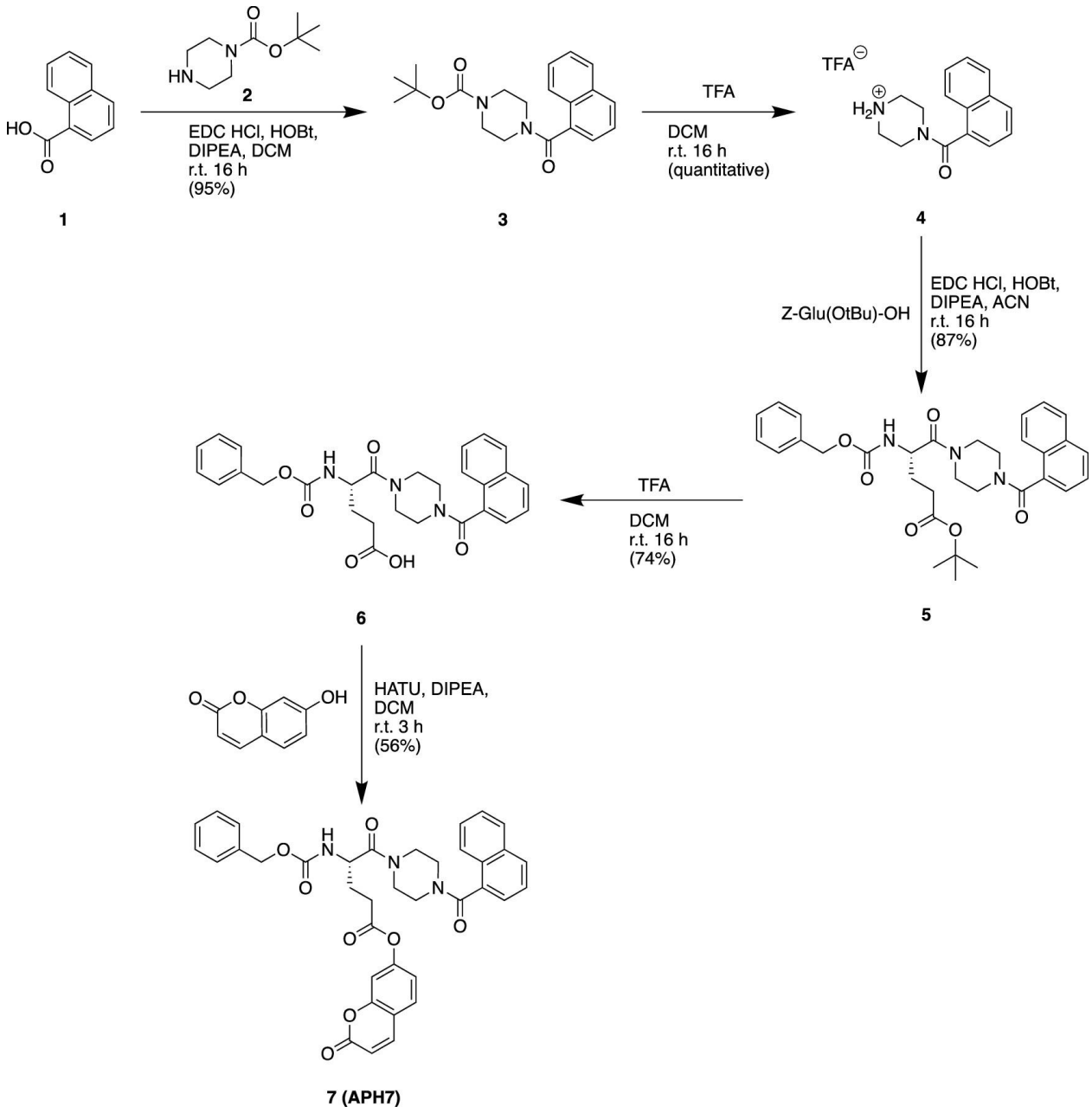

Scheme 4.1. Synthetic scheme to generate fluorescent activity substrate 7 (APH7).

As shown in Scheme 1, starting from commercially available *N*-Boc-piperazine **2**, an amide coupling with 1-naphthoic acid **1** was performed to generate the protected piperazine-naphthoyl moiety **3**. The Boc group was then cleaved with TFA to produce the resulting TFA salt of amine

4. Commercially available Cbz-Glu(OtBu)-OH was then coupled via HATU-mediated amide coupling to yield protected scaffold **5**. From here, the γ-carboxylate of the glutamate residue was deprotected under acidic conditions to yield free acid **6**. Finally, the reporter umbelliferyl ester was synthesized through HATU-mediated esterification using umbelliferone (7-hydroxycoumarin, 7-HC) to generate ester **7** (**APH7**).

4.7.3. Kinetics

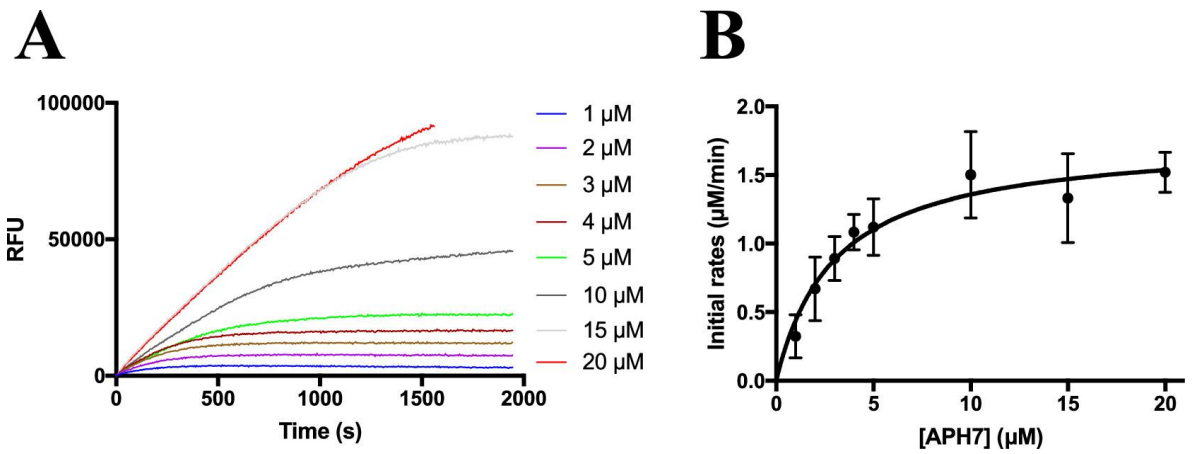

Figure 4.2. Kinetic traces and fittings for APH7 with TGases. (A) Raw kinetic traces of the reaction of APH7 with TG2. (B) Saturation fitting of initial rates versus [APH7].

Table 4.1. Relative comparison of the k_{cat}, K_M, and k_{bkg} (background hydrolysis rate constant) for three TG2 activity substrates (50 mM MOPS, 7 mM $CaCl_2$, 25 °C, pH 6.9).

Substrate	k_{cat} (min^{-1})	K_M (μM)	k_{cat}/K_M (μM^{-1} min^{-1})	k_{bkg} ($\times 10^{-4}$ min^{-1})
AL5	10.3 ± 0.8	12.0 ± 2.8	0.86	15.8 ± 0.1
ZFBC	7.4 ± 0.6	9.1 ± 2.4	0.81	1.1 ± 0.4
APH7	7.1 ± 0.5	3.0 ± 0.6	2.4	5.9 ± 0.1

To validate that **APH7** could serve as a new substrate for TG2, we measured its Michaelis−Menten kinetic parameters as indicators of binding affinity and hydrolytic reactivity. The TG2-mediated hydrolysis of **APH7** is shown in Figure 2A, where the released product umbelliferone generates an intense fluorescence signal. A standard curve correlating the fluorescence intensity of the umbelliferone product to its molar concentration was measured under the assay conditions, providing a linear response (see Figure S2) that allowed us to convert the relative rates to molar rates shown in Figure 2B. From this saturation kinetics curve, it is evident that **APH7** exhibits excellent affinity for TG2, with a K_M as low as 3.0 ± 0.6 μM and a k_{cat} value of 7.1 ± 0.5 min^{-1}. From this kinetic characterization, it is clear that the high-affinity scaffold of AA9 was effectively translated to a high-affinity activity substrate. **APH7** represents an improved substrate relative to our previous activity assay substrates AL5 and ZFBC, which show K_M values of 12 and 9 μM, respectively, in these assay conditions (Table 1).[18,22] Furthermore, the rate of background hydrolysis of **APH7**, in the absence of TG2, was very low, with a pseudo-first order rate constant of (5.9 ± 0.1) × 10^{-4} min^{-1} estimated by the initial rates method, approximately 2.7-fold lower than that of AL5 under these assay conditions. In order to explore the selectivity of **APH7**, we also tested it against thrombin-activated factor XIIIA (FXIIIa, UniProt: P00488), another therapeutically relevant TGase. No enzymatic activity was detected over background hydrolysis at concentrations up to 50 μM, suggesting **APH7** may be useful as a TG2-selective activity substrate (Figure S3). Furthermore, we also tested **APH7** against commercial TG1 (UniProt: P22735), TG3 (UniProt: Q08188), and TG6 (UniProt: O95932), but observed no activity, confirming the selectivity of **APH7** for TG2, in vitro.

4.7.4. Application to Irreversible Inhibition

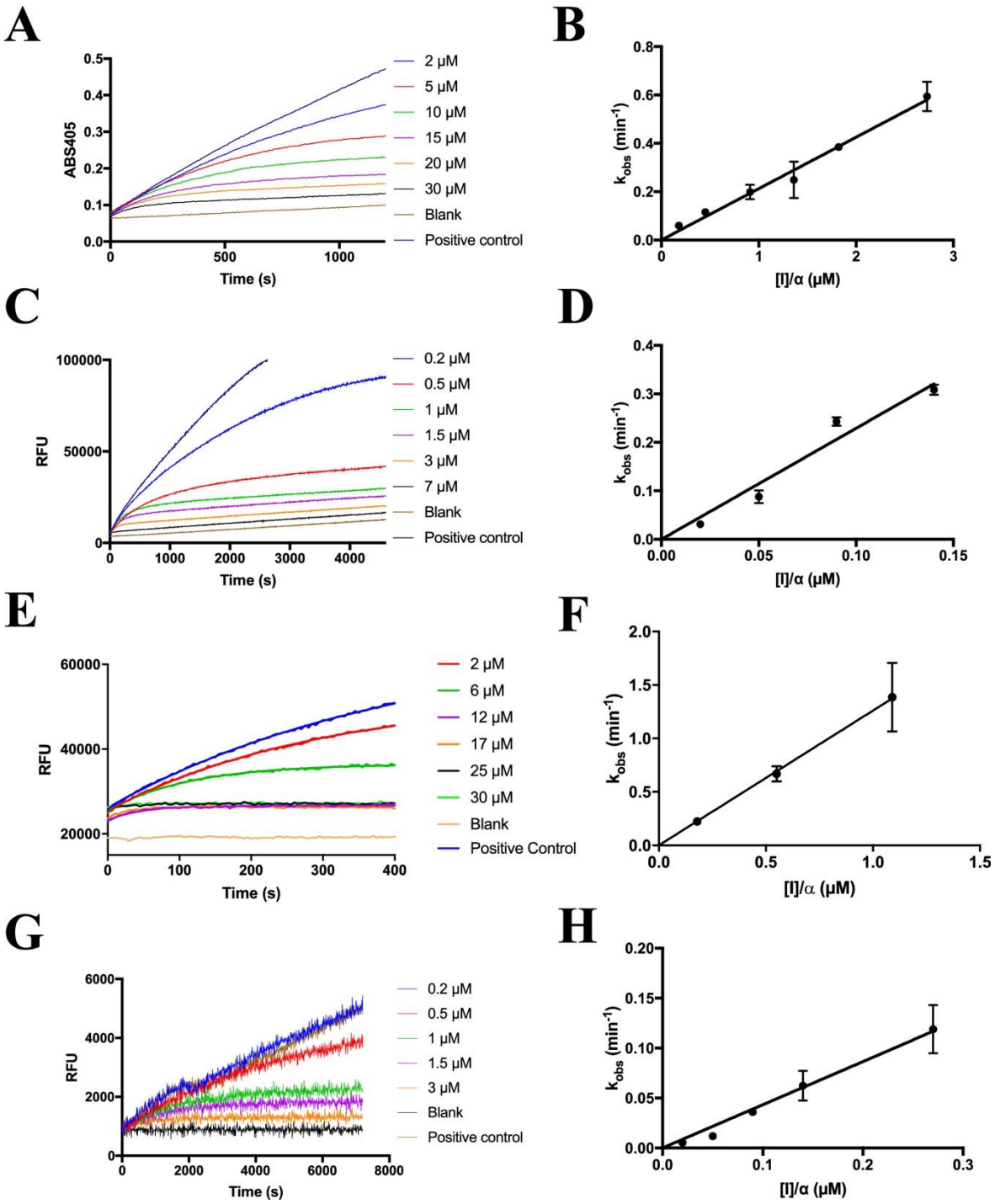

Figure 4.3. Inhibition of TG2 with the irreversible inhibitor AA9. (A) Raw kinetic traces obtained using chromogenic substrate AL5. (B) Linear region of saturation plot of observed rate constants obtained with

AL5 vs [AA9]. (C) Raw kinetic traces were obtained using fluorogenic substrate APH7. (D) Linear region of saturation plot of observed rate constants obtained with APH7 vs [AA9]. (E) Raw kinetic traces using fluorogenic substrate ZFBC. (F) Linear region of saturation plot of observed rate constants obtained with ZFBC vs [AA9]. (G) Raw kinetic traces using fluorescently quenched substrate A101. (H) Linear region of saturation plot of observed rate constants obtained with A101 vs [AA9].

After observing the high efficiency of **APH7** as a TG2 substrate, we turned to the application of this new substrate for evaluating the irreversible inhibition of TG2. We first set out to determine the inhibition parameters of our lead inhibitor AA9 using so-called "Kitz and Wilson conditions", as we have described previously.[20,27,28] In brief, under these conditions, whereby the time-dependent inactivation of an enzyme is measured in the presence of a competitive substrate, over the course of a continuous activity assay, k_{inact} and K_I values may be measured directly, using very little material. Astonishingly, the inhibition observed in the presence of **APH7** was nearly an order of magnitude more efficient than the inhibition observed for the same inhibitor with the original substrate AL5. When **APH7** was used as the reporter substrate, a value of (2292 ± 163) × 10^3 M^{-1} min^{-1} was obtained, whereas AL5 provided a k_{inact}/K_I value of (213 ± 6) × 10^3 M^{-1} min^{-1} (Figure 3A−D). This discrepancy inspired us to investigate this inhibition more closely.

First, we selected additional substrates to use in different continuous activity assays in order to repeat the measurement of irreversible inhibition parameters under the same continuous assay conditions. ZFBC[22] (Figure 1) is a coumarin ester, like **APH7**, but its simple peptidomimetic scaffold resembles that of AL5.[22] When this substrate was used to measure inhibitor efficiency for AA9, a k_{inact}/K_I value of (1260 ± 149) × 10^3 M^{-1} min^{-1} was obtained (Figure 3E,F). A101 is a large quenched- fluorophore peptide, whose cleavage provides direct fluorescent visualization of TGase isopeptidase activity.[23,24] The use of this distinctly different substrate provided a k_{inact}/K_I ratio of

(433 ± 17) × 10^3 M^{-1} min^{-1} (Figure 3G,H). Notably, the use of four different substrates based on four different structural scaffolds provided four different values for these inhibition "constants".

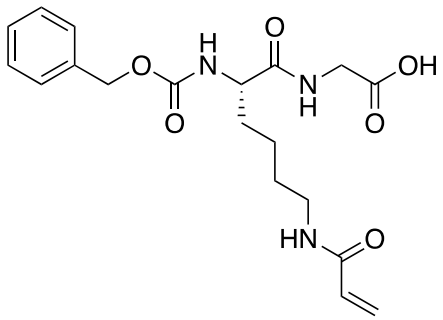

8
(Z-Lys(Acryl)-Gly-OH)

Figure 4.4. Structure of AL5 structural mimic inhibitor 8 [Z-Lys(Acryl)-Gly-OH].

At this point, it was obvious that the substrate used in the activity assay clearly influenced the susceptibility of the enzyme to react with irreversible inhibitor AA9. We noted that the most potent inhibition by AA9 was observed in the presence of a substrate that resembles it most strongly, namely, our new substrate **APH7**. Therefore, we continued our investigation by testing a structurally distinct inhibitor, Z-Lys(Acryl)-Gly-OH **8** (Figure 4). Using AL5, we measured a k_{inact}/K_I ratio of (28 ± 2) × 10^3 M^{-1} min^{-1} for this inhibitor, which is consistent with the previously reported data.[20] However, when **APH7** was used as the reporter substrate, the measured k_{inact}/K_I ratio increased to (310 ± 4) × 10^3 M^{-1} min^{-1} for the same inhibitor (Figures S4 and S5 in Supporting Information). In summary, we observed an order-of-magnitude increase in inhibition efficiency for a second inhibitor after changing the assay substrate from AL5 to **APH7**.

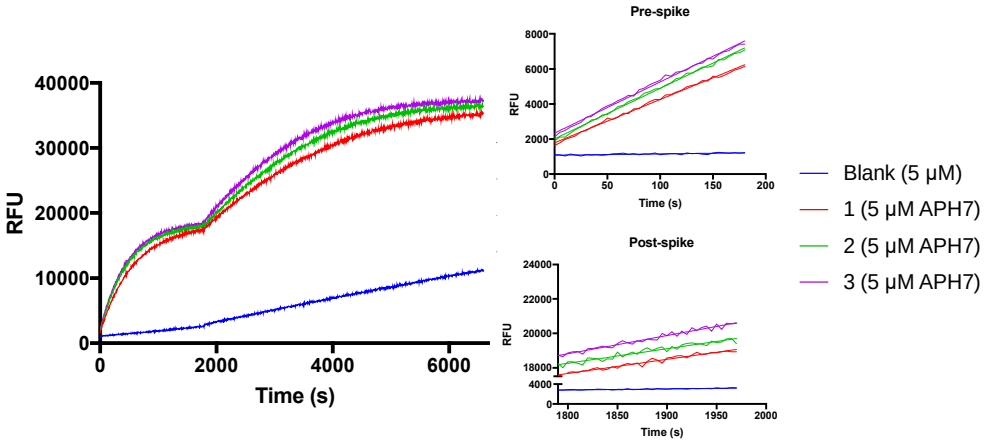

Figure 4.5. TG2 activity measured by 5 µM fluorescent substrate APH7 pre- and post-spiking with a further 5 µM APH7. Initial rates were calculated by linear regression of the first 200s.

One possible explanation for an apparent increase in inhibitor potency while the substrate is varied is product inhibition. We first attempted to refute the hypothesis by conducting a substrate spike experiment. TG2 was incubated with 5 μM **APH7**, and the time-dependent increase of fluorescence was monitored. When a plateau was attained, indicating that all of the substrates had been consumed, an additional 5 μM **APH7** was added to the reaction mixture. If no product inhibition was at play, the initial rates of pre- and postspike should be identical. We observed slopes that were not identical but similar (see Figure 5), especially considering that after 30 min incubation at room temperature, TG2 is known to lose some activity. We also tested the hypothesis of product inhibition by evaluating the reaction of TG2 with **APH7** in the presence of increasing concentrations of synthetic intermediate **6**, which is one of the products of the TG2-mediated hydrolysis of **APH7** (Figure S6A). Similarly, we evaluated the rate of TG2-mediated hydrolysis of AL5, in the presence of increasing concentrations of umbelliferone, the other hydrolysis product from the reaction of TG2 with **APH7** (Figure S6B). Neither of these reaction products had any

significant effect on the TG2 activity, effectively refuting the hypothesis that product inhibition in the **APH7** assay was responsible for the enhanced inhibition by AA9 and **8**.

Another possible explanation for enhanced apparent inhibition is that the hydrolysis products may partially quench the fluorescence signal of product umbelliferone, thereby decreasing fluorescence and accentuating the curvature of the time-dependent plots shown in Figure 3C. However, the presence of hydrolysis product **6** had a negligible effect on the fluorescence intensity of umbelliferone, confirming that fluorescence quenching was not at play (Figure S7).

4.7.5. TG2 Exhibits Enzymatic Hysteresis

Further reflection on the effect of reporter substrate on inhibitor binding led us to consider possible conformational effects since TG2 is known to undergo slow, but dramatic, conformational changes, between states that are catalytically active and inactive.[6–8] More specifically, we hypothesized that ligand-binding events may affect conformational equilibria and therefore the overall activity of the enzyme. Careful inspection of the Michaelis−Menten curve for **APH7** (Figure 2B) shows that at the lowest concentrations of **APH7**, the mean observed rates fall slightly below the curve fitted to a simple isotherm binding model, which would be consistent with ligand binding-induced hysteresis.[6,8,29] [Although the error bars on these points make it impossible to claim that these mean values are statistically significantly different than those described by the simple Michaelis−Menten equation, the fitting to a hysteresis model (see Figure S8) provides higher correlation]. We propose that the binding of **APH7** may alter a *slow* conformational equilibrium of the uninhibited enzyme, such that at higher concentrations of **APH7**, a larger proportion of the free enzyme would exist in a more catalytically active form (see form *E**, Scheme

S1). If this form also shows more affinity for inhibitor AA9 (which closely resembles **APH7**), higher concentrations of **APH7** would also render TG2 more susceptible to inhibition after accounting for the competitive binding between substrate and inhibitor. For example, after TG2 reacts with **APH7**, the side chain of Trp332 or the Gly239-Asn243 flap, both of which form the "tunnel" to the active site Cys277, may be displaced into a conformation that shows higher affinity for AA9 than the conformation these residues would adopt after reaction with the smaller AL5 substrate.[6]

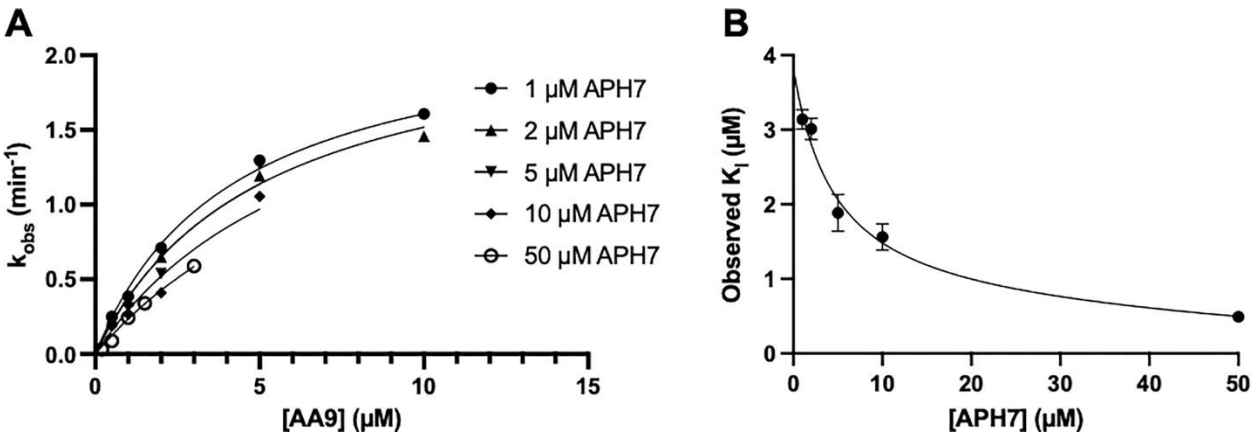

Figure 4.6. (A) Irreversible inhibition of TG2 by AA9 in the presence of varied concentrations of reporter substrate APH7. Fitting was simplified by using the fixed value of k_{inact} = 2.28 min^{-1}, measured for the data set showing the highest degree of saturation (at 1.0 μM APH7). (B) Graphical representation of the effect of [APH7] on the observed K_I values measured in panel A. The line fitted through the data points represents a binding isotherm, reflecting saturation of the conformational effect of APH7.

According to this model, higher concentrations of **APH7** would shift the conformational equilibrium of TG2 to a higher proportion of the form that shows a higher affinity for AA9. We tested this hypothetical concentration dependence by repeating the continuous assay inhibition experiment over a range of concentrations of **APH7**, from 1 to 50 μM (see Figure 6A). As shown in Table S1, the K_I values measured in this way were indeed inversely dependent on the

concentration of **APH7** used in the experiment. Furthermore, since the concentration of **APH7** is proposed to exert a conformational effect related to a binding event, one might expect to see a binding isotherm relation between the observed value of K_I and the concentration of the substrate at which it was measured. As shown in Figure 6B, from the fitting of the observed K_I versus [**APH7**] data to a binding model, K_I is predicted to decrease from a theoretical maximum of 3.8 μM, in the absence of any conformational effect of **APH7**, toward an asymptotic value of 0.46 μM, which would be realized when the enzyme existed fully in the state showing the highest affinity for the inhibitor (K_I* in Scheme S1). The $K_{0.5}$ value for the hyperbolic concentration dependence of this putative conformational effect was determined to be 4.6 μM.

4.7.6. Substrate-Free Inhibition Profile

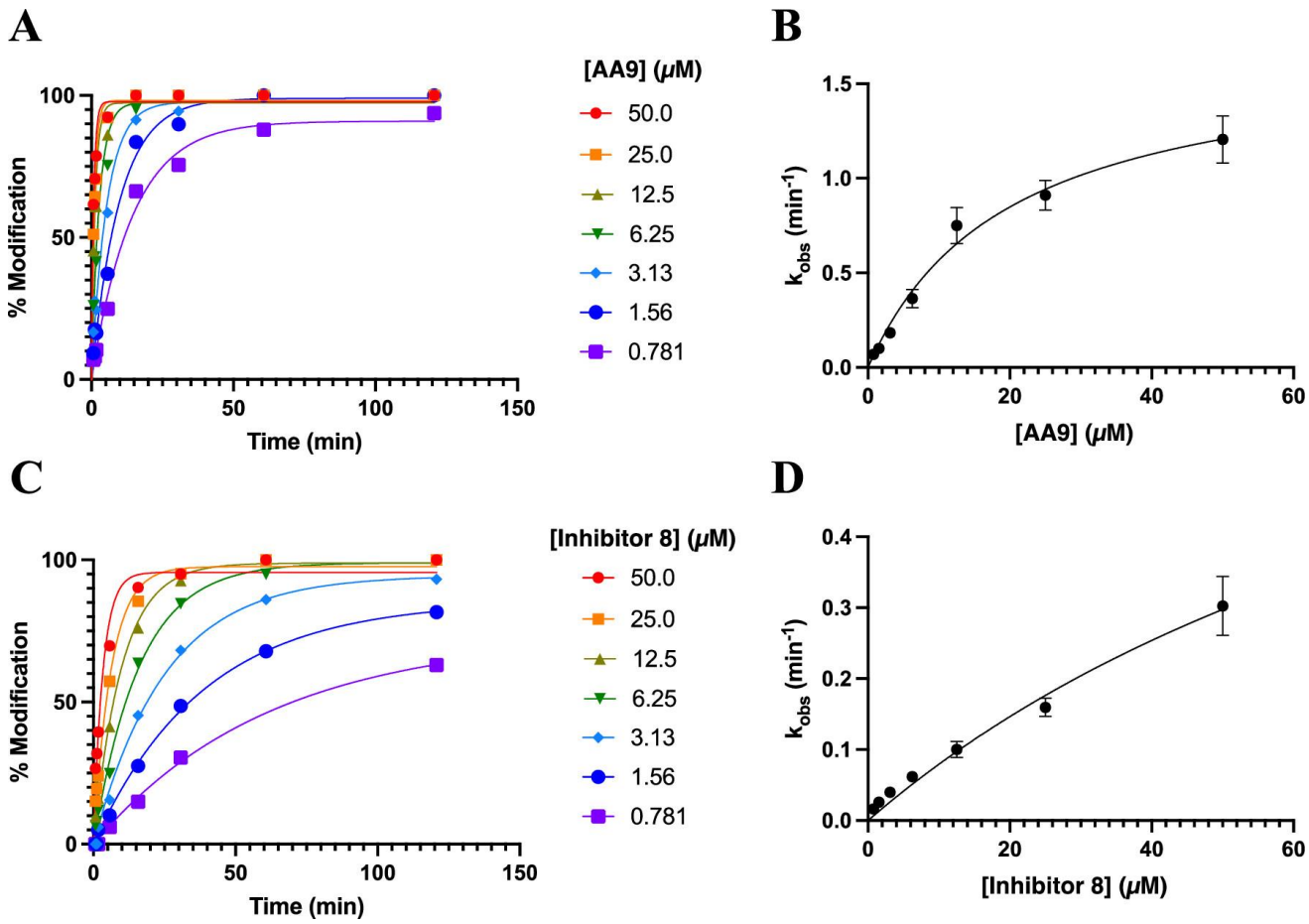

Figure 4.7. (A) Time-dependent covalent modification of TG2 by AA9, in the absence of reporter substrate. (B) Saturation kinetic analysis of the associated rate constants of inactivation by AA9. (C) Time-dependent covalent modification of TG2 by inhibitor 8, in the absence of reporter substrate. (D) Saturation kinetic analysis of the associated rate constants of inactivation by inhibitor 8.

Table 4.2. Inhibitor efficiency values determined for AA9 and 8 when using various activity substrates under continuous assay experimental conditions.[a]

Substrate	experimentally measured k_{inact}/K_I ($\times 10^3$ M^{-1} min^{-1})	
	AA9	Inhibitor **8**
AL5	213 ± 6	28 ± 2
APH7	2290 ± 160	310 ± 4
ZFBC	1260 ± 149	n.d.
A101	433 ± 17	n.d.

[a]n.d. = Not determined

Finally, in order to confirm the effect of assay substrate on observed inhibition behavior, we elected to analyze the inhibition by both AA9 and inhibitor **8** via RapidFire mass spectrometry. This method is based on the rapid, temporal sampling of a reaction mixture of enzyme and irreversible inhibitor in the absence of any reporter substrate. Intact mass analysis of the protein mixture reveals the proportion of enzyme that has been covalently modified, at each time point (see Figure S10 for representative spectral data). As shown in Figure 7A, this allows substrate-free quantification of the time-dependent covalent modification of TG2 due to the reaction with AA9. Evaluation of the rate constants for these modification reactions according to a saturation kinetics model (Figure 7B) provided kinetic parameters of k_{inact} = 1.68 ± 0.15 min^{-1}, K_I = 19.6 ± 3.8 μM, and k_{inact}/K_I = (85.7 ± 18.3) × 10^3 M^{-1} min^{-1}. Treatment of inhibitor **8** in the same manner (see Figure 7C,D) provided kinetic parameters of k_{inact} = 0.95 ± 0.33 min^{-1}, K_I = 110 ± 51 μM, and k_{inact}/K_I = (8.65 ± 4.99) × 10^3 M^{-1} min^{-1}. Comparison of these values to those reported in Table 2 shows that both inhibitors have the lowest apparent potency when tested in the absence of substrate, slightly

higher efficiency when evaluated in the presence of the small assay substrate AL5, and the greatest efficiency when evaluated in the presence of the high-affinity substrate **APH7**.

It is also interesting to note that the value measured for k_{inact} does not vary significantly as a function of the substrate concentration. For example, in the absence of a substrate, as measured by mass spectrometry, the k_{inact} value for AA9 was determined to be 1.68 ± 0.15 min^{-1} (above). In the presence of 1 μM **APH7**, a value of 2.28 ± 0.14 min^{-1} was measured (Figure 6A). When inhibition kinetics were performed in the presence of 50 μM **APH7**, the k_{inact} value deriving from the saturation fitting was 1.39 ± 0.22 min^{-1} (Figure S9). (Incidentally, these values are also similar to those we have reported recently for a wide variety of other optimized acrylamide inhibitors of TG2, from our recent publications,[19,30] in the range of 0.5−2.3 min^{-1}.) The similarity of the k_{inact} values measured in this work suggests that the order of magnitude increase in k_{inact}/K_I observed with **APH7** (see Table 2) is largely due to a decrease in K_I, which is consistent with our suggestion that the binding and reaction with **APH7** lead to an activated form of the enzyme having a greater affinity for AA9 (see above).

Taken together, these lines of evidence support the proposal that assay substrates can promote a concentration-dependent conformational change in TG2 that renders the enzyme more susceptible to inhibition and that this effect appears to depend at least partly on the structure of the substrate. This finding represents an important previously unreported phenomenon for TG2 that should be considered in future inhibitor screening campaigns.

4.8. Conclusions

The work described herein reveals interesting biochemical behavior that was discovered during the development of a new fluorogenic substrate for TG2. The substrate **APH7** that was

designed, synthesized, and evaluated in this study revealed excellent affinity, sensitivity, and reactivity with TG2. Upon further investigation of this substrate for applications in inhibition assays, a previously unreported phenomenon was observed with TG2. The acyltransferase activity of TG2 may be susceptible to ligand binding-induced hysteresis, and we propose that small conformational changes induced by substrate binding may significantly affect the activity of TG2 and its susceptibility to inhibition by structurally similar inhibitors. These findings should be investigated further to determine how broadly this phenomenon is manifested for TG2 and for other isozymes in the TGase family. Apart from this biochemical mechanistic information, this work presents **APH7** as one of the most efficient synthetic TG2 substrates known to date, allowing for future studies involving the acyltransferase activity of TG2. Its low background rate of hydrolysis, the sensitivity of detection of its intensely fluorescent umbelliferone product, and its high affinity scaffold are all characteristics that should allow **APH7** to overcome the limitations shown by AL5 and other previous TGase assay substrates.

4.9. Supporting Information

The Supporting Information is available free of charge at https://pubs.acs.org/doi/10.1021/acs.biochem.3c00337.

Additional figures, schemes and tables; structure of A101; standard fluorescence curve of 7-HC (umbelliferone); kinetic data fittings; product inhibition experiment; fluorescence quenching experiment; fitting of saturation kinetics data to a hysteresis model; inhibition of TG2 with AA9 at high [**APH7**]; observed KI of AA9 with various [**APH7**]; RapidFire-MS supplementary figure; proposed ligand-induced conformational equilibria; scaled NMR spectra of **APH7**; NMR spectra of **APH7**; and HPLC traces of **APH7** (PDF)

4.10. Accession Codes

Human transglutaminase 2 (TG2, UniProt: P21980); human Factor XIIIA (FXIIIA, UniProt: P00488); human transglutaminase 1 (TG1, UniProt: P22735); human transglutaminase 3 (TG3, UniProt: Q08188); human transglutaminase 6 (TG6, UniProt: O95932)

4.11. Funding

This work was funded by the Natural Sciences and Engineering Research Council of Canada (NSERC) in the form of a Discovery Grant to J.W.K. E.W.J.G. is also grateful to NSERC for a doctoral scholarship.

4.12. Notes

The authors declare no competing financial interest.

4.13. References

(1) Lorand, L., and Graham, R. M. (2003) Transglutaminases: Crosslinking enzymes with pleiotropic functions. *Nat Rev Mol Cell Biol 4*, 140–156.

(2) Mehta, K., and Eckert, R. (2005) Mammalian Transglutaminases: A Family Portrait. *Prog Exp Tumor Res 38*, 1–254.

(3) Keillor, J. W., Clouthier, C. M., Apperley, K. Y. P., Akbar, A., and Mulani, A. (2014) Acyl transfer mechanisms of tissue transglutaminase. *Bioorg Chem 57*, 186–197.

(4) Liu, S., Cerione, R. A., and Clardy, J. (2002) Structural basis for the guanine nucleotide-binding activity of tissue transglutaminase and its regulation of transamidation activity. *Proc Natl Acad Sci U S A 99*, 2743–2747.

(5) Gundemir, S., Colak, G., Tucholski, J., and Johnson, G. V. W. (2012) Transglutaminase 2: A molecular Swiss army knife. *Biochim Biophys Acta Mol Cell Res 1823*, 406–419.

(6) Pinkas, D. M., Strop, P., Brunger, A. T., and Khosla, C. (2007) Transglutaminase 2 undergoes a large conformational change upon activation. *PLoS Biol 5*, 327.

(7) Clouthier, C. M., Mironov, G. G., Okhonin, V., Berezovski, M. V., and Keillor, J. W. (2012) Real-time monitoring of protein conformational dynamics in solution using kinetic capillary electrophoresis. *Angew Chem Int Ed 51*, 12464–12468.

(8) Caron, N. S., Munsie, L. N., Keillor, J. W., and Truant, R. (2012) Using FLIM-FRET to Measure Conformational Changes of Transglutaminase Type 2 in Live Cells. *PLoS One 7*, e44159.

(9) Huang, L., Xu, A. M., and Liu, W. (2015) Transglutaminase 2 in cancer. *Am J Cancer Res 5*, 2756–2776.

(10) Lee, H. T., Huang, C. H., Chen, W. C., Tsai, C. S., Chao, Y. L., Liu, S. H., Chen, J. H., Wu, Y. Y., and Lee, Y. J. (2018) Transglutaminase 2 promotes migration and invasion of lung cancer cells. *Oncol Res 26*, 1175–1182.

(11) Kerr, C., Szmacinski, H., Fisher, M. L., Nance, B., Lakowicz, J. R., Akbar, A., Keillor, J. W., Lok Wong, T., Godoy-Ruiz, R., Toth, E. A., Weber, D. J., and Eckert, R. L. (2017) Transamidase site-targeted agents alter the conformation of the transglutaminase cancer stem cell survival protein to reduce GTP binding activity and cancer stem cell survival. *Oncogene 36*, 2981–2990.

(12) Dieterich, W., Ehnis, T., Bauer, M., Donner, P., Volta, U., Riecken, E. O., and Schuppan, D. (1997) Identification of tissue transglutaminase as the autoantigen of celiac disease. *Nat Med 3*, 797–801.

(13) Schuppan, D., Mäki, M., Lundin, K. E. A., Isola, J., Friesing-Sosnik, T., Taavela, J., Popp, A., Koskenpato, J., Langhorst, J., Hovde, Ø., Lähdeaho, M.-L., Fusco, S., Schumann, M., Török, H. P., Kupcinskas, J., Zopf, Y., Lohse, A. W., Scheinin, M., Kull, K., Biedermann, L., Byrnes, V., Stallmach, A., Jahnsen, J., Zeitz, J., Mohrbacher, R., and Greinwald, R. (2021) A Randomized Trial of a Transglutaminase 2 Inhibitor for Celiac Disease. *N Engl J Med 385*, 35–45.

(14) Büchold, C., Hils, M., Gerlach, U., Weber, J., Pelzer, C., Heil, A., Aeschlimann, D., and Pasternack, R. (2022) Features of ZED1227: The First-In-Class Tissue Transglutaminase Inhibitor Undergoing Clinical Evaluation for the Treatment of Celiac Disease. *Cells 11*, 1667.

(15) Benn, M. C., Weber, W., Klotzsch, E., Vogel, V., and Pot, S. A. (2019) Tissue transglutaminase in fibrosis — more than an extracellular matrix cross-linker. *Curr Opin Biomed Eng 10*, 156–164.

(16) Shweke, N., Boulos, N., Jouanneau, C., Vandermeersch, S., Melino, G., Dussaule, J. C., Chatziantoniou, C., Ronco, P., and Boffa, J. J. (2008) Tissue transglutaminase contributes to interstitial renal fibrosis by favoring accumulation of fibrillar collagen through TGF-β activation and cell infiltration. *Am J Pathol 173*, 631–642.

(17) Szondy, Z., Korponay-Szabó, I., Király, R., Sarang, Z., and Tsay, G. J. (2017) Transglutaminase 2 in human diseases. *BioMedicine 7*, 15.

(18) Leblanc, A., Gravel, C., Labelle, J., and Keillor, J. W. (2001) Kinetic studies of guinea pig liver transglutaminase reveal a general-base-catalyzed deacylation mechanism. *Biochemistry 40*, 8335–8342.

(19) McNeil, N. M. R., Gates, E. W. J., Firoozi, N., Cundy, N. J., Leccese, J., Eisinga, S., Tyndall, J. D. A., Adhikary, G., Eckert, R. L., and Keillor, J. W. (2022) Structure-activity relationships of N-terminal variants of peptidomimetic tissue transglutaminase inhibitors. *Eur J Med Chem 232*, 114172.

(20) Akbar, A., McNeil, N. M. R., Albert, M. R., Ta, V., Adhikary, G., Bourgeois, K., Eckert, R. L., and Keillor, J. W. (2017) Structure-Activity Relationships of Potent, Targeted Covalent Inhibitors That Abolish Both the Transamidation and GTP Binding Activities of Human Tissue Transglutaminase. *J Med Chem 60*, 7910–7927.

(21) Wodtke, R., Schramm, G., Pietzsch, J., Pietsch, M., and Löser, R. (2016) Synthesis and Kinetic Characterisation of Water-Soluble Fluorogenic Acyl Donors for Transglutaminase 2. *ChemBioChem* 1263–1281.

(22) Gillet, S. M. F. G., Pelletier, J. N., and Keillor, J. W. (2005) A direct fluorometric assay for tissue transglutaminase. *Anal Biochem 347*, 221–226.

(23) Oertel, K., Hunfeld, A., Specker, E., Reiff, C., Seitz, R., Pasternack, R., and Dodt, J. (2007) A highly sensitive fluorometric assay for determination of human coagulation factor XIII in plasma. *Anal Biochem 367*, 152–158.

(24) Király, R., Thangaraju, K., Nagy, Z., Collighan, R., Nemes, Z., Griffin, M., and Fésüs, L. (2016) Isopeptidase activity of human transglutaminase 2: Disconnection from transamidation and characterization by kinetic parameters. *Amino Acids 48*, 31–40.

(25) Day, N., and Keillor, J. W. (1999) A continuous spectrophotometric linked enzyme assay for transglutaminase activity. *Anal Biochem 274*, 141–144.

(26) Case, A., and Stein, R. L. (2003) Kinetic Analysis of the Action of Tissue Transglutaminase on Peptide and Protein Substrates. *Biochemistry 42*, 9466–9481.

(27) Kitz, R., and Wilson, I. B. (1962) Esters of methanesulfonic acid as irreversible inhibitors of acetylcholinesterase. *J Biol Chem 237*, 3245–3249.

(28) Stone, S. R., and Hofsteenge, J. (1985) Specificity of activated human Protein C. *Biochem J 230*, 497–502.

(29) Jiang, Y., Li, X., Morrow, B. R., Pothukuchy, A., Gollihar, J., Novak, R., Reilly, C. B., Ellington, A. D., and Walt, D. R. (2019) Single-Molecule Mechanistic Study of Enzyme Hysteresis. *ACS Cent Sci 5*, 1691–1698.

(30) Rangaswamy, A. M. M., Navals, P., Gates, E. W. J., Shad, S., Watt, S. K. I., and Keillor, J. W. (2022) Structure-activity relationships of hydrophobic alkyl acrylamides as tissue transglutaminase inhibitors. *RSC Med Chem 13*, 413–428.

Appendix to Chapter 4

Supporting Information

for

High Affinity Fluorogenic Substrate for Tissue Transglutaminase Reveals Enzymatic Hysteresis

Eric W. J. Gates[1], Adrien Prince-Hallée[1], Yasaman Heidari[2],

Abootaleb Sedighi[2], and Jeffrey W. Keillor[1,]*

[1]Department of Chemistry and Biomolecular Sciences, University of Ottawa, Ottawa, Ontario, K1N 6N5, Canada.

[2] Dalriada Drug Discovery, Mississauga, Ontario L5N 8G4, Canada.

* Corresponding author: JWK

Supplementary Figures/Table/Scheme

Structure of A101

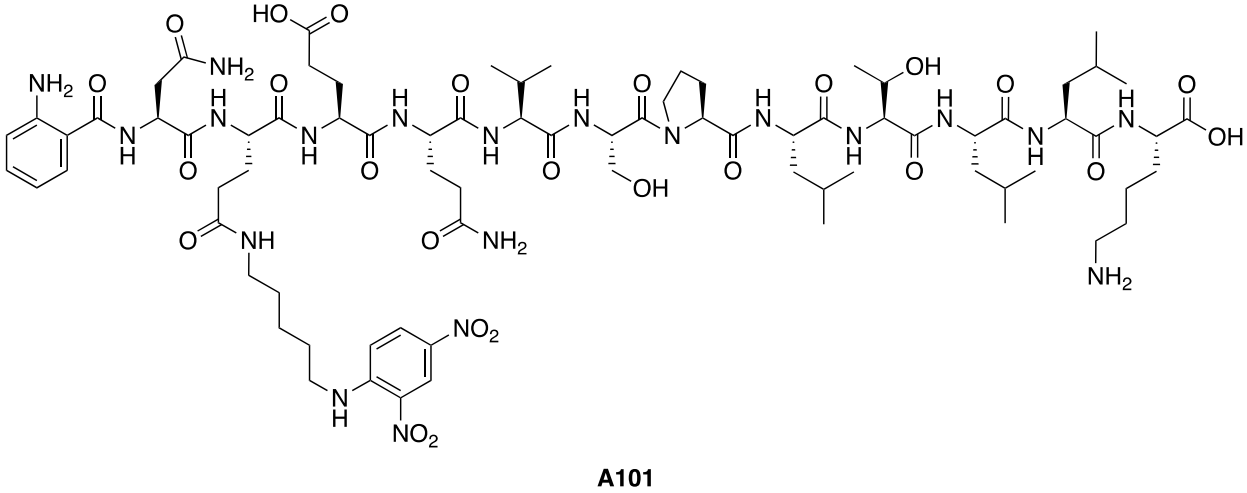

Figure S1. Structure of pan-TGase activity assay substrate A101.

Standard Fluorescence Curve of 7-HC (Umbelliferone)

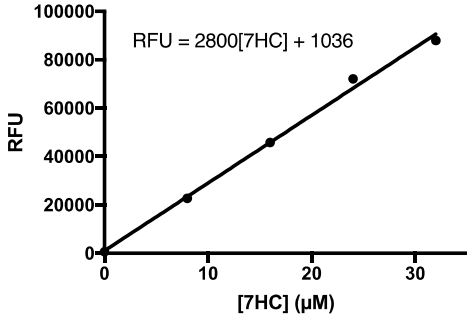

Figure S2. Fluorescence intensity of 7-HC (umbelliferone) *versus* concentration. Slope used to convert raw rate data into molar initial rates.

Supplementary Kinetic Data Fittings

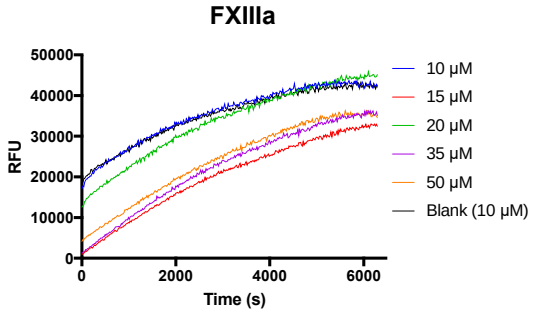

Figure S3. Raw kinetic traces of **APH7** displaying negligible reactivity with FXIIIa.

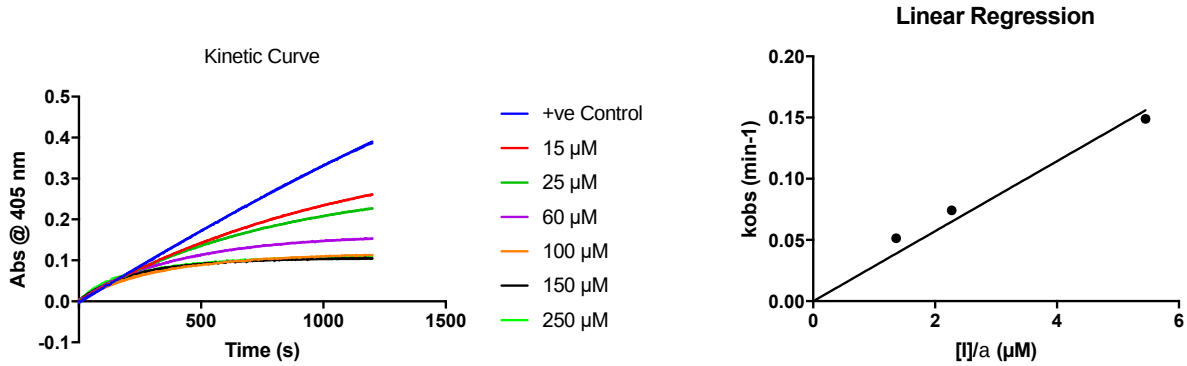

Figure S4. Kinetic data and fitting for the inhibition of TG2 with AL5 as substrate and Z-Lys(Acryl)-Gly-OH **8** as inhibitor.

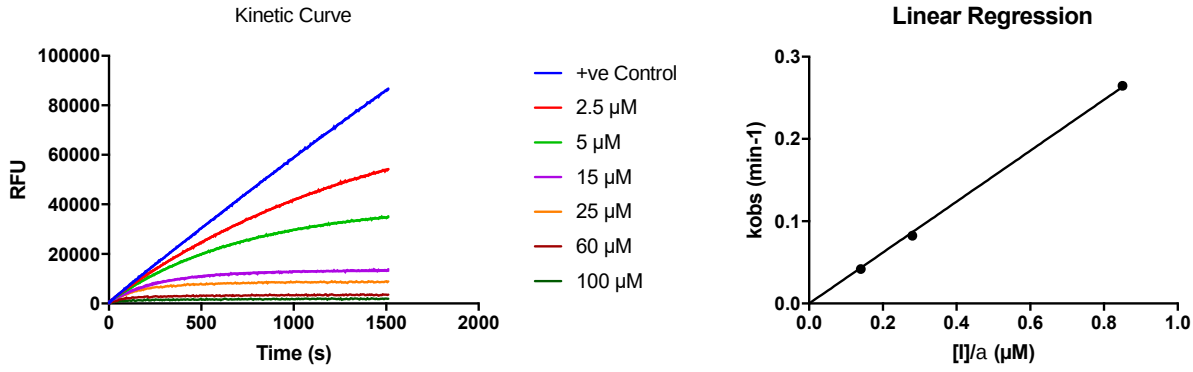

Figure S5. Kinetic data and fitting for the inhibition of TG2 with **APH7** as substrate and Z-Lys(Acryl)-Gly-OH **8** as inhibitor.

Product Inhibition Experiment

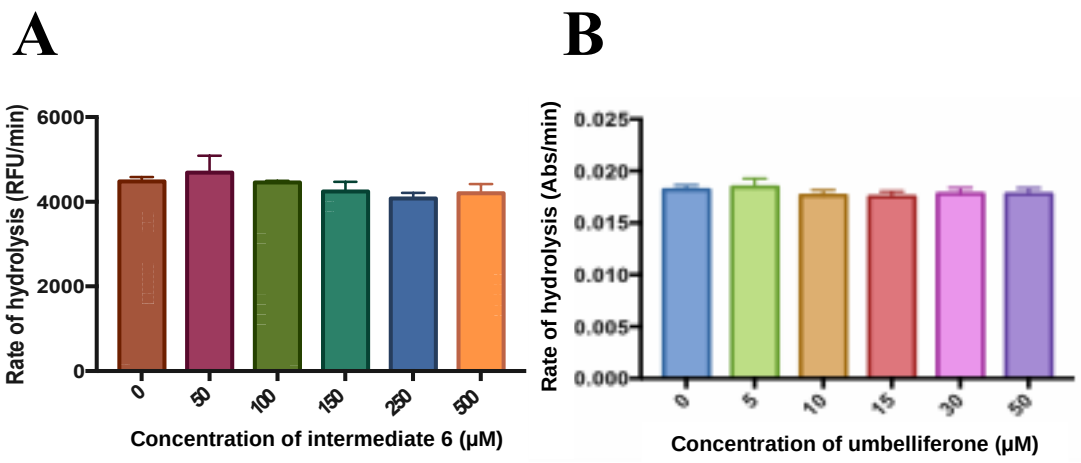

Figure S6. Product inhibition experiments. **A)** Rate of TG2-catalyzed hydrolysis of 50 µM **APH7** in the presence of increasing concentration of the hydrolysis product **6**. **B)** Rate of TG2-catalyzed hydrolysis of 100 µM chromogenic substrate AL5, in the presence of increasing concentration of hydrolysis product umbelliferone.

Fluorescence Quenching Experiment

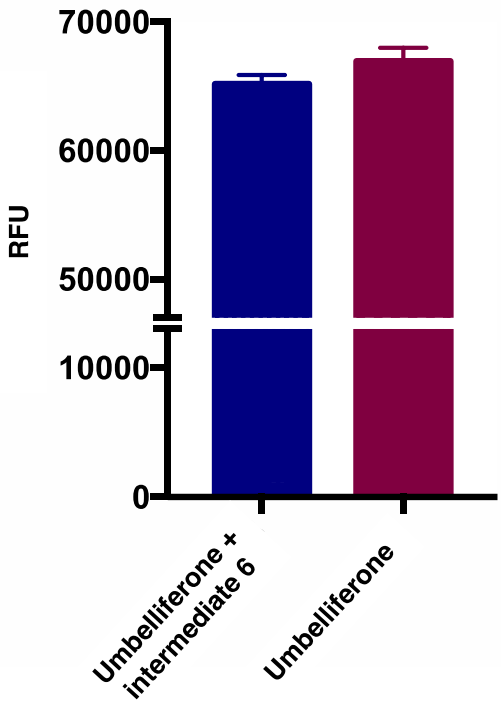

Figure S7. Fluorescent quenching experiment of 10 µM of fluorescent hydrolysis product umbelliferone in the absence and presence of 10 µM hydrolysis product product **6**.

Fitting of Saturation Kinetics Data to a Hysteresis Model

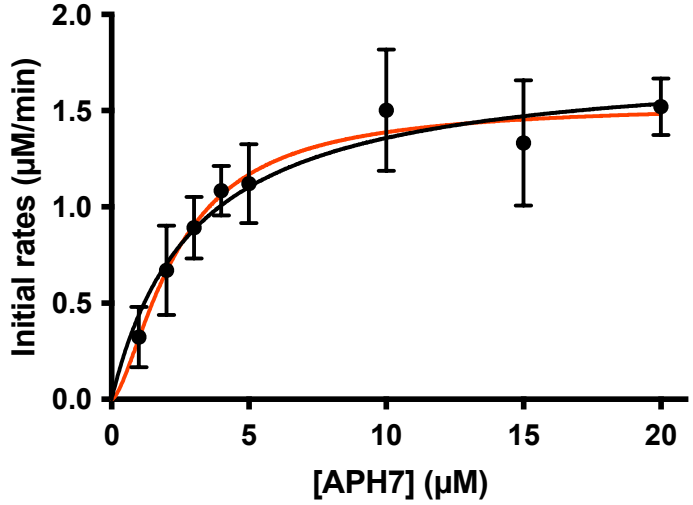

Figure S8. Fitting of the kinetic data from Figure 2B to a hysteresis model (red line) provides V^{max} = 1.54 µM/min, $K_{0.5}$ = 2.38 µM, a Hill parameter of h = 1.55, and a correlation of R^2 = 0.9733. The black line, shown for comparison, derives from the fitting to a non-allosteric Michaelis-Menten model and provided a correlation of R^2 = 0.9493.

Inhibition of TG2 with AA9 at high [APH7]

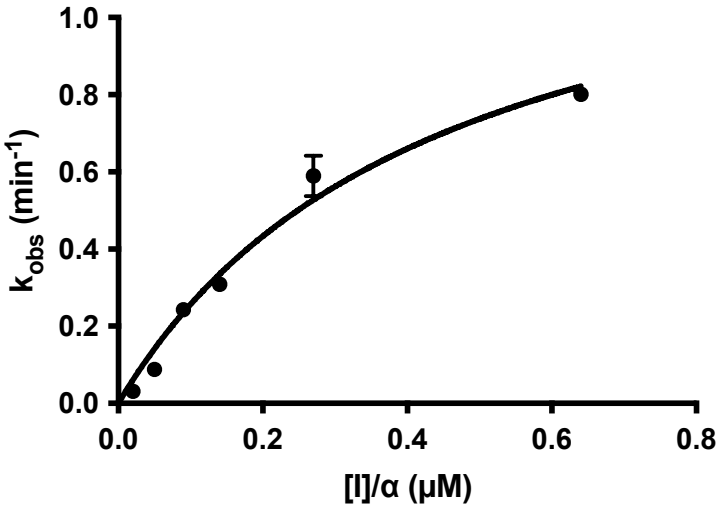

Figure S9. Irreversible inhibition of TG2 by AA9, under Kitz & Wilson conditions in the presence of 50 μM of reporter substrate **APH7**. This fitting provided a k_{inact} value of 1.39 ± 0.22 min^{-1} and a K_I value of 0.44 ± 0.13 μM.

Observed K_I of AA9 with Various [APH7]

Table S1. Observed K_I *versus* [APH7]. Observed K_I values were measured from saturation fitting as described in Figure 6A.

[APH7] (μM)	Observed K_I (μM)
1.0	3.14 ± 0.13
2.0	3.01 ± 0.14
5.0	1.88 ± 0.25
10	1.56 ± 0.18
50	0.49 ± 0.02

RapidFire MS Supplementary Figure

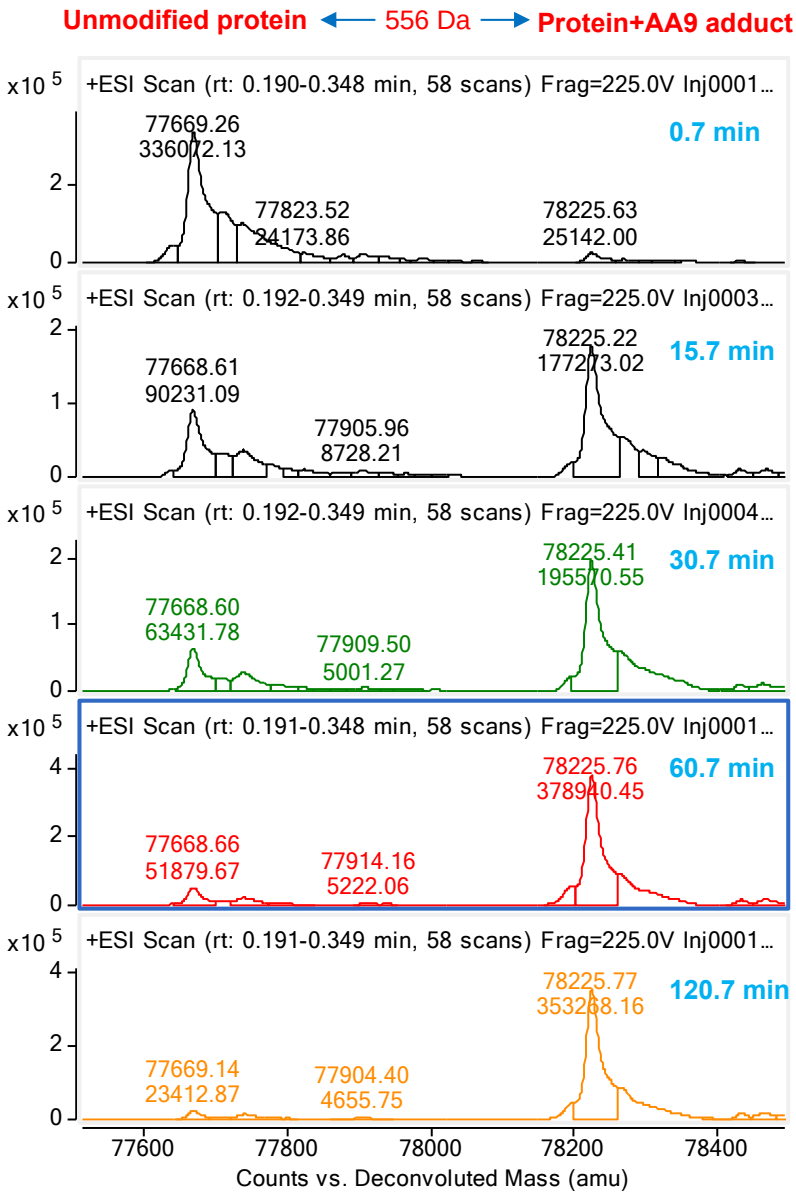

Figure S10. Representative RapidFire mass spectra. Time dependent covalent modification of TG2 by inhibitor AA9 in the absence of reporter substrate.

Proposed Ligand-Induced Conformational Equilibria

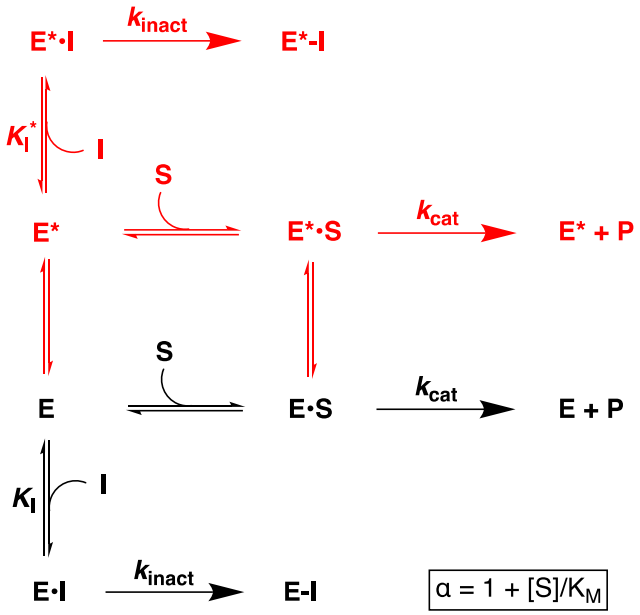

Scheme S1: Shown in black is the typical kinetic scheme for irreversible inactivation of enzyme E with irreversible inhibitor I, in the presence of continuous assay substrate S, under so-called "Kitz and Wilson" conditions. E*, shown in red, represents a different conformation of active enzyme that is favoured by binding substrate, and shows higher susceptibility for inhibition, due to K_I* being lower than K_I.

NMR Spectra of 7 (APH7)

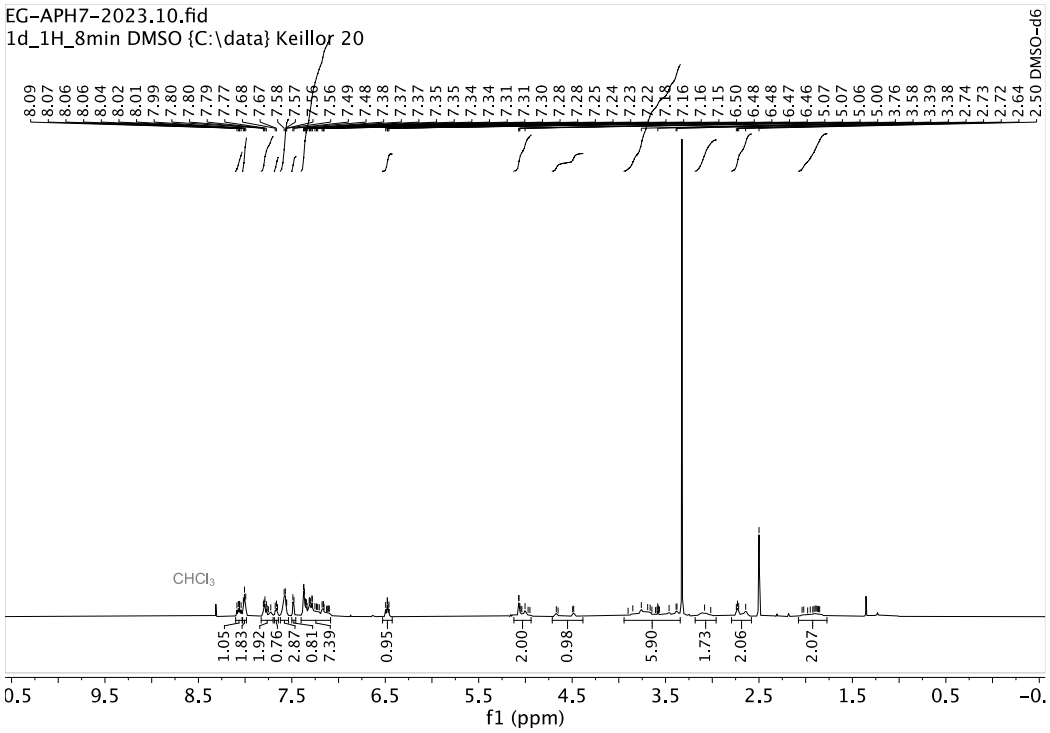

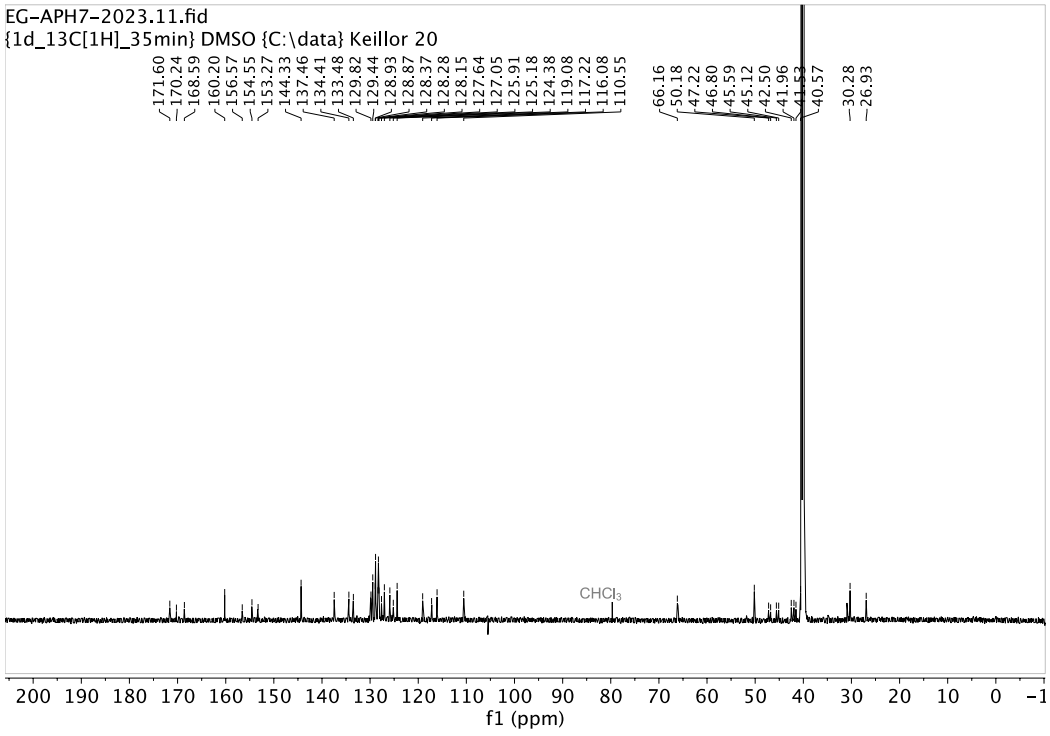

Scaled NMR Spectra of 7 APH7

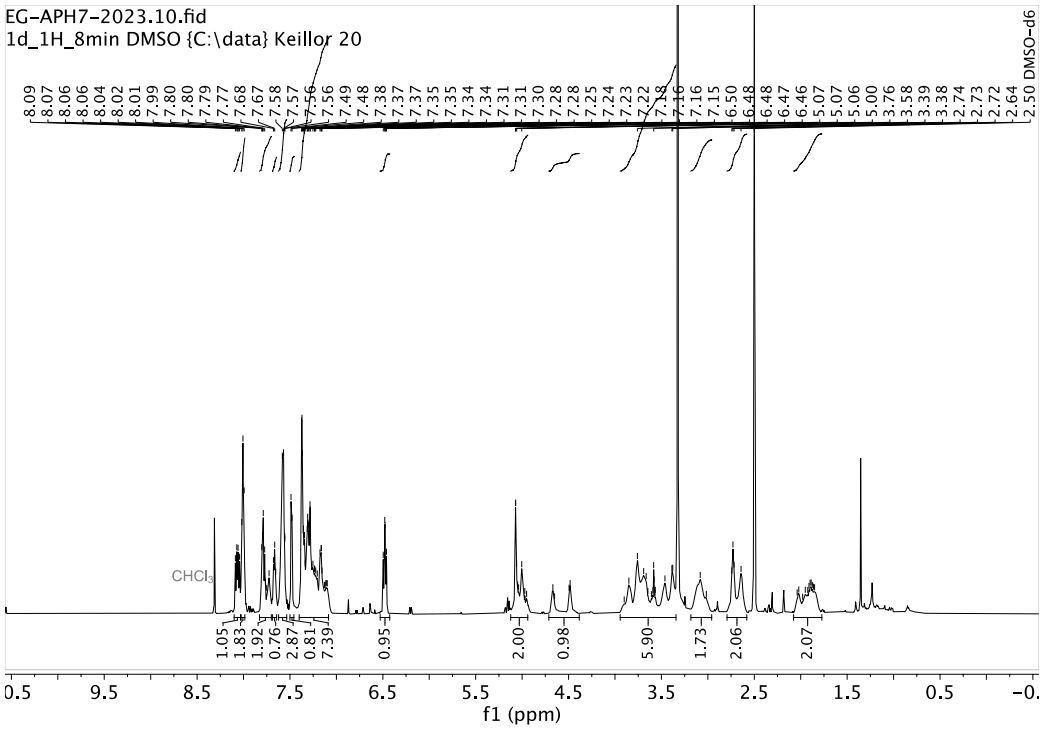

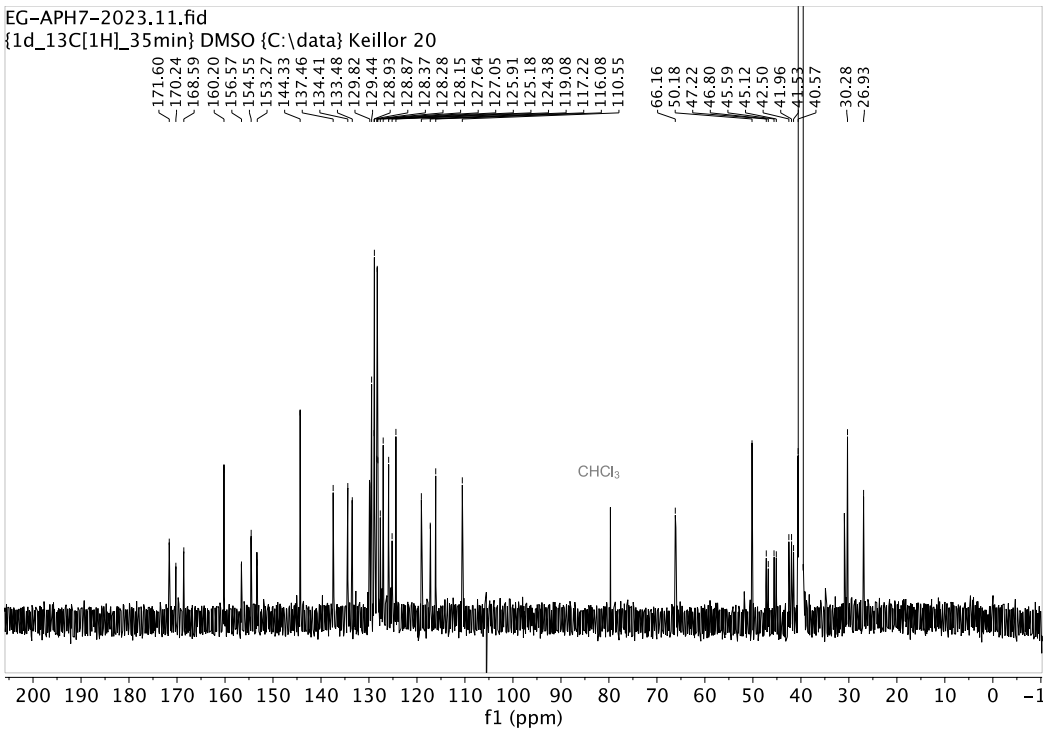

HPLC Trace/LCMS of 7 (APH7)

<Sample Information>

Sample Name	: EG-APH7-Purity		
Sample ID	: EG-APH7-Purity		
Data Filename	: EG-APH7-Purity_002.lcd		
Method Filename	: 5-95% Method.lcm		
Batch Filename	: EG-APH7-Purity.lcb		
Vial #	: 0-3	Sample Type	: Unknown
Injection Volume	: 10 uL		
Date Acquired	: 6/20/2023 11:53:49 AM	Acquired by	: Boddy lab
Date Processed	: 6/20/2023 12:08:51 PM	Processed by	: Boddy lab

<Chromatogram>

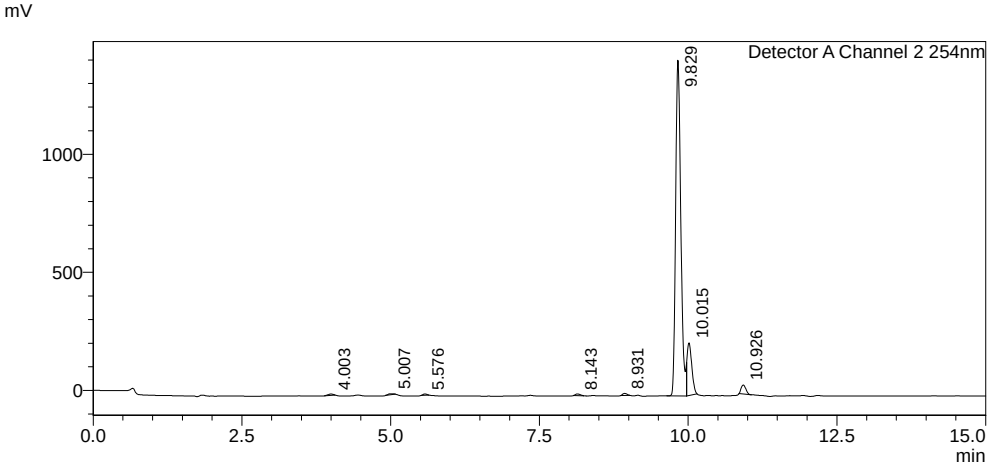

Peak Table

Detector A Channel 2 254nm

Peak#	Ret. Time	Area%
1	4.003	0.322
2	5.007	0.254
3	5.576	0.220
4	8.143	0.367
5	8.931	0.426
6	9.829	85.024
7	10.015	11.429
8	10.926	1.957
Total		100.000

MS Spectrum

R.Time:9.833(Scan#:591)
MassPeaks:1618
Segment 1 - Event 1

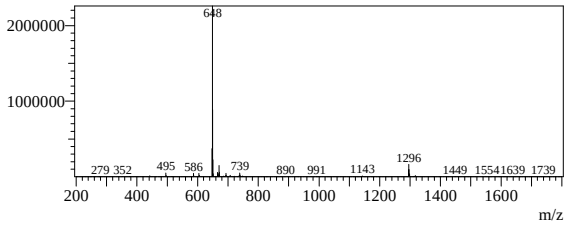

Chapter 5: Towards TG2 Active Site Directed PROTACs

5.1. Introduction

Transglutaminase 2 has been an enzyme targeted by multiple medicinal chemistry efforts in recent years.[1–8] These studies are mostly directed toward active site inhibitors, although there has also been some investigation into *N*-terminal binders designed to disrupt the TG2-fibronectin interaction.[9,10] Numerous research groups have disclosed novel TG2 inhibitors albeit few have been able to progress into clinical trials. The only noteworthy candidates are those which are being used in the treatment of Celiac disease and liver fibrosis developed by Zedira GmbH – no inhibitors to date have been effective enough as a cancer therapeutic despite TG2's direct correlation. Future efforts should be directed toward developing specific therapeutic strategies to target TG2's oncogenic role. Given that the oncogenic characteristic of TG2 is most likely linked to its G-protein activity as well as its intracellular scaffolding role, methods that abolish all of TG2's activities are of immediate interest.

As a multifunctional protein, namely both a transamidase as well as a G-protein, TG2 plays roles that are mutually exclusive and seem to be both inhibited by many active site targeted small molecule inhibitors.[3,11–13] An activity that is still being uncovered to date is that related to the protein-protein interactions formed by TG2. Interactions of TG2 with many oncoproteins including fibronectin, PLCδ1, PTEN, and NF-κB have already been established,[9,10,14–16] but more are being uncovered as chemical biology techniques are applied, including isothermal titration calorimetry, co-immunoprecipiation, and intact MS.[17] Although small molecule inhibitors can target the G-protein and transamidase activity, these classical inhibitors have not been designed to target the protein-protein interactions or scaffolding capabilities of TG2. Some TG2-FN inhibitors

have been reported in the literature but remain to be optimized into high affinity scaffolds. With the chemical knockout induced by PROTACs, or at least knockdown (if a high D_{max} is not achieved), , this methodology represents a novel tool to potentially perturb and disrupt all of TG2's activities *in cellulo*.

Traditionally, PROTACs have been based on reversible ligands that show high affinity for their protein of interest. Due to a desire to target proteins that were considered to be undruggable, covalent PROTACs have just recently emerged as an appealing avenue.[18,19] Irreversible PROTACs are of interest for TG2 due to their ability to bind covalently and lock TG2 in its open conformation. A hurdle in TG2 therapeutics is that most are designed to target the catalytic active site, a region that is only accessible, and more so only formed, for a fraction of the time within cells as TG2 preferentially adopts its closed G-protein conformation in the intracellular environment. In the case of intracellular TG2, the formation of the transamidase binding site is not favoured, requiring active site inhibitors to compete with this equilibrium. To combat this equilibrium, an irreversible PROTAC could aid in ensuring degradation is observed, as a reversible binder could easily dissociate before ubiquitinylation occurs, and would then have to wait again for the equilibrium to form the transamidase site.

5.2. Results and Discussion

5.2.1. Design

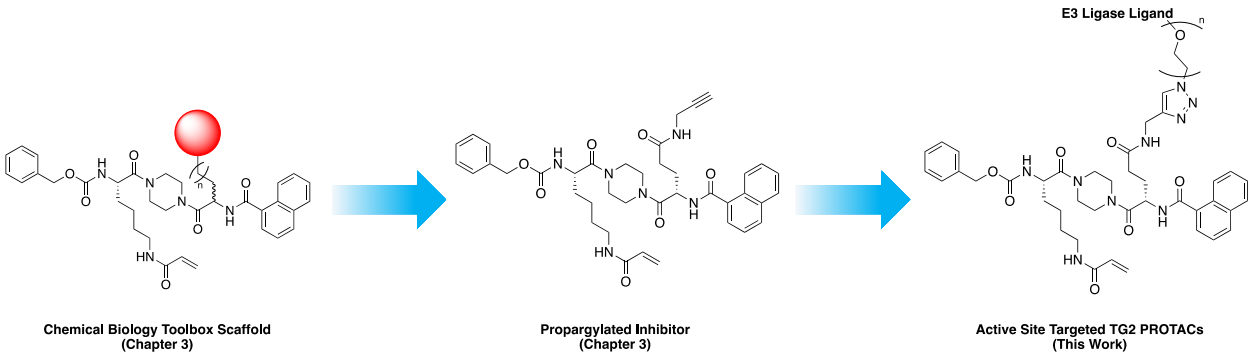

Figure 5.1. Design strategy for the active site targeted TG2 PROTACs, stemming from previous work on chemical biology research tools.

The scaffold design of these molecules stems from our recent work in the chemical biology space, detailed in Chapter 3 of this thesis. Having a broad diversity of cargo incorporated at the side chain of the glutamate residue of a peptidomimetic scaffold, while not sacrificing any apparent affinity for the enzyme, we believed that we could further exploit this position (Figure 5.1). By installing E3 ligase ligands at this site, we proposed to create a small library of potential TG2 active site targeted PROTACs, an avenue of research which has yet to be explored in the literature. As a primary screen, the linkers to these E3L ligands will be based on varying lengths of PEG to allow reasonable flexibility, various distances, and moderate hydrophilicity. Incorporating three E3L ligands will also increase the propensity for degradation by having attempting to recruit three distinct E3 ligases.[20,21] To create a convergent synthetic strategy, utilizing a propargyl peptidomimetic inhibitor (see Chapter 3) would then allow for a simple copper-catalysed azide-alkyne cycloaddition (CuAAC) reaction to install the corresponding azide-linker-E3L ligand and generate the full irreversible TG2 PROTAC.

5.2.2. Synthesis

The synthetic route derived for these molecules mirrors that of the chemical biology project outlined in Chapter 3. Once the propargyl inhibitor had been generated in the same fashion as previously disclosed, CuAAC reactions could be executed with a corresponding azide. A parallel synthetic route was derived to link PEG units one through four to the three E3L ligands, lenalidomide, VHL ligand, and IAP ligand.

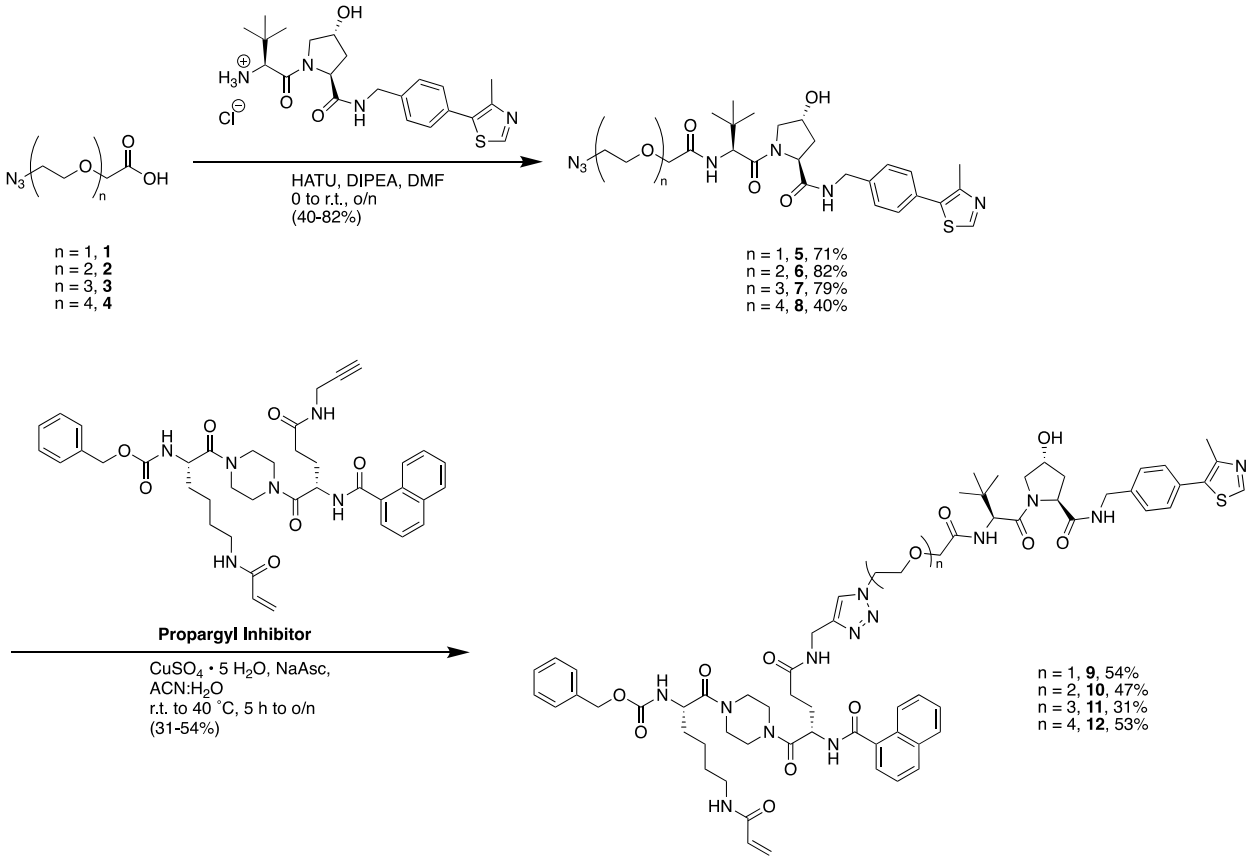

Figure 5.2. Synthetic scheme to generate VHL TG2 PROTACs 9-12.

Starting from the commercially available azide-PEG_n-acetic acids **1-4** a HATU-mediated coupling was executed to link the VHL ligand and produce intermediates **5-8** (Figure 5.2). A subsequent CuAAC reaction was then used with copper (II) sulfate and sodium ascorbate to click

the main propargyl inhibitor scaffold to the linkers. Upon purification, the potential VHL PROTACs **9-12** were obtained in 31-54% yield.

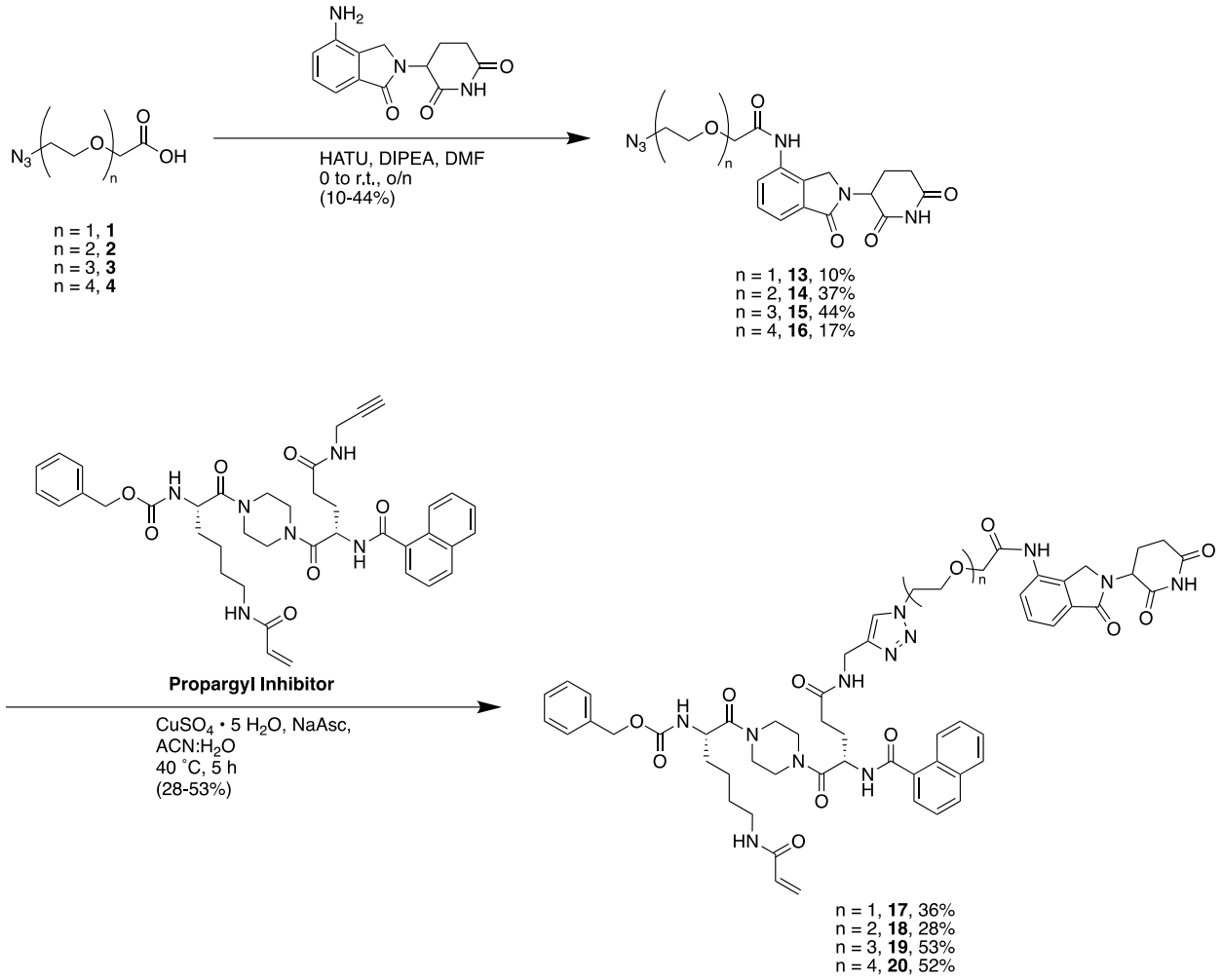

Figure 5.3. Synthetic scheme to generate lenalidomide TG2 PROTACs 17-20.

To synthesize the lenalidomide PROTACs, a similar synthetic scheme was employed starting again from the azide-PEG$_n$-acetic acids (Figure 5.3). A first step amide bond coupling with HATU was utilized to couple the linkers to the lenalidomide scaffold and yield intermediates **13-16**. Once coupled the intermediates **13-16** could then be clicked to the propargyl inhibitor scaffold again *via* a CuAAC reaction to access lenalidomide PROTACs **17-20** in 28-53% yield.

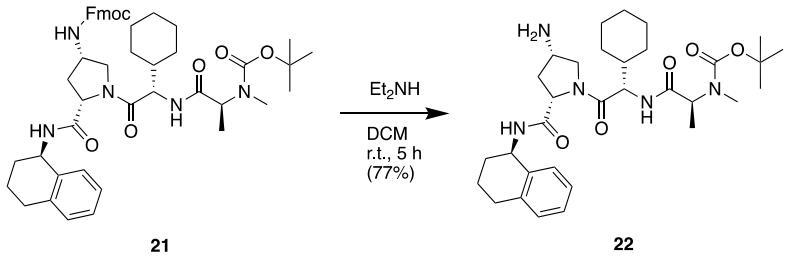

Figure 5.4. Synthetic scheme for the Fmoc deprotection of the IAP ligand to yield free amine 22.

The IAP PROTACs first needed to go through an Fmoc deprotection of the amino proline residue to gain access to the amine handle (Figure 5.4). Using diethylamine in DCM, the deprotected **22** was generated in 77% yield.

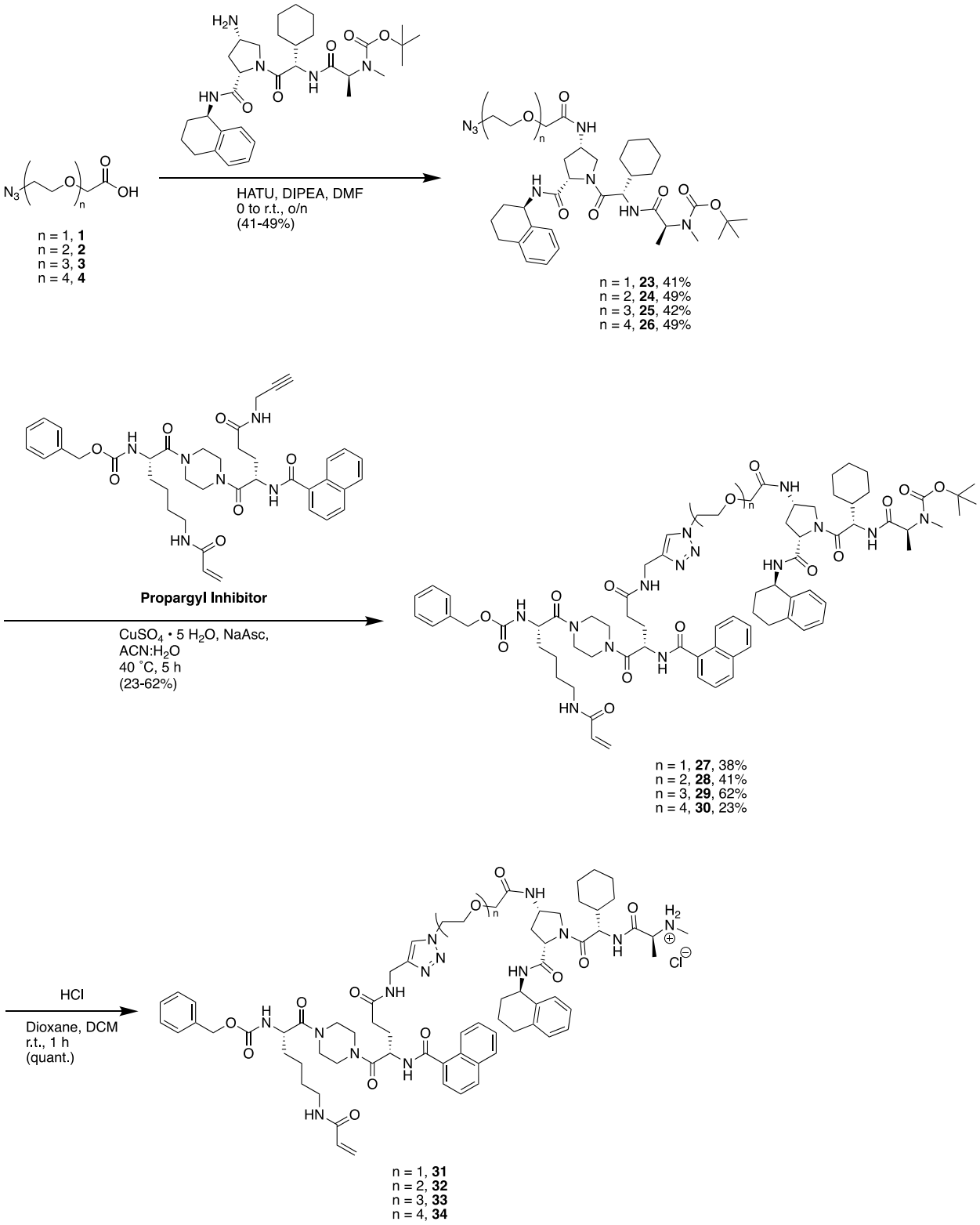

Figure 5.5. Synthetic scheme to generate IAP TG2 PROTACs 31-34.

Once the free amine **22** had been accessed, the IAP TG2 PROTACs could be accessed through a route akin to the others in the library (Figure 5.5). A first step amide bond coupling with HATU, the azide-PEG_n-acetic acids and the amine **22** produced intermediates **23-26** in 41-49% yield. These intermediates were then subjected to a subsequent click reaction with the propargyl inhibitor to produce the Boc-protected IAP PROTACs **27-30**. A final Boc deprotection with hydrogen chloride in dioxane and DCM was employed to generate the final IAP PROTACs **31-34** in quantitative yield.

5.2.3. Kinetic Evaluation

In order to ensure these potential PROTACs do indeed bind to the catalytic active site of TG2, we employed our in-house colorimetric assay[22] as we traditionally use for the small molecule inhibitors.[3–7,23] In contrast to obtaining full binding kinetics and inhibition parameters, we elected to test one low concentration, such that the inhibitor concentration is much greater than the estimated K_I. This simplification allowed us to obtain an approximate value for k_{inact}/K_I by dividing the k_{obs} by the inhibitor concentration tested, and multiplying by the value of α (Figure 5.6). Given that binding affinity does not always correlate with the extent of protein degradation by PROTACs, this allowed us to rank the PROTACs by a relative hierarchy in affinity. A further qualitative confirmation of their reactivity was conducted to ensure that they showed fast inhibition of TG2 at 10 μM, with complete knockout of enzymatic activity in less than 100 s (data shown in Appendix to Chapter 5). The ultimate criteria to rank these molecules will be those parameters that relate directly to the degradation of TG2, including D_{max} and DC_{50}.

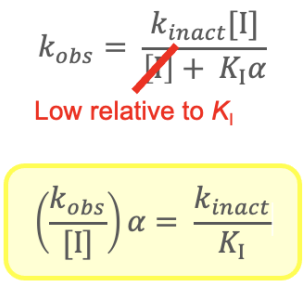

Figure 5.6. Simplification of inhibition saturation equation to estimate k_{inact}/K_I.

Through the evaluation of these derivatives, a trend became apparent in terms of the E3L ligands incorporated (Table 5.1). Each family of E3L ligand PROTACs provided excellent inhibitory efficiency values above 222 × 10^3 M^{-1} min^{-1}, which are on par or greater than the efficiency of the original parent compound AA9.[3,5] It also appears that there is a preference for the less sterically bulky lenalidomide PROTACs **17-20** compared to the other E3L ligands, with the lead compound **19** reaching an efficiency ratio of k_{inact}/K_I = 431 × 10^3 M^{-1} min^{-1}.

Table 5.1. Approximate TG2 inhibition efficiency values of active site targeted PROTACs.

	Compound	Estimated k_{inact}/K_I ± SD ($\times 10^3$ M^{-1} min^{-1})
VHL PROTACs	**9**	231 ± 35
	10	228 ± 71
	11	222 ± 32
	12	226 ± 51
Lenalidomide PROTACs	**17**	380 ± 14
	18	300 ± 27
	19	431 ± 115
	20	397 ± 9
IAP PROTACs	**31**	325 ± 14
	32	313 ± 21
	33	339 ± 19
	34	257 ± 33

5.3. Conclusions and Future Work

This chapter reports preliminary results towards our objectives to design, synthesize, and evaluate PROTACs to target TG2 for proteasomal degradation. Given the difficulties in the small molecule inhibitor medicinal chemistry efforts, including selectivity, reactivity, and desirable PK properties; the PROTAC therapeutic methodology is an appealing avenue of research.

The potential degraders were designed based on the scaffold utilized in our chemical biology efforts detailed in Chapter 3. They were synthesized using a convergent strategy to allow final functionalization with CuAAC reactions and created a library of twelve PROTACs. The library was then screened against recombinant human TG2 for their ability to inhibit the transamidase activity and ensure they bind to the active site. Although no significant trends can be

observed from the kinetic data, it does appear that there may be a slight preference for the smaller lenalidomide ligand, followed by the IAP ligand, and then finally VHL. Affinity for the protein of interest does not always correlate with degradation but does provide us insight towards which will be most efficient at forming the heterodimer TG2-PROTAC complex.

The potential active site targeted TG2 PROTACs have currently been fully characterized synthetically and *in vitro* for their ability to bind and inhibit the transamidase activity of TG2. The future of this project involves the evaluation of their ability to degrade TG2 *in cellulo* which will be examined initially by ELISA, through our existing collaboration with Prof. Nicoletta Bianchi at the University of Ferrara, in Italy. If this library contains an efficient degrader of TG2, the scaffold can then be further tailored to optimize both the PK and PD properties. As a mitigation strategy, should there be no molecules that induce the degradation of TG2 *in cellulo*, the field of E3L ligands is quickly expanding to reveal new binders as well as covalent ligands.[24–27] Having a dual covalent PROTAC, which binds irreversibly to both the protein of interest and to E3 ligase could also be an appealing avenue of research in the search for an agent that abolishes all of TG2's activities *via* degradation, but exploits the irreversible inhibition kinetics to its full potential.

5.4. Chapter 5 References

(1) Prime, M. E.; Andersen, O. A.; Barker, J. J.; Brooks, M. A.; Cheng, R. K. Y.; Toogood-Johnson, I.; Courtney, S. M.; Brookfield, F. A.; Yarnold, C. J.; Marston, R. W.; Johnson, P. D.; Johnsen, S. F.; Palfrey, J. J.; Vaidya, D.; Erfan, S.; Ichihara, O.; Felicetti, B.; Palan, S.; Pedret-Dunn, A.; Schaertl, S.; Sternberger, I.; Ebneth, A.; Scheel, A.; Winkler, D.; Toledo-Sherman, L.; Beconi, M.; MacDonald, D.; Muñoz-Sanjuan, I.; Dominguez, C.; Wityak, J. Discovery and Structure-Activity Relationship of Potent and Selective Covalent Inhibitors of Transglutaminase 2 for Huntington's Disease. *J Med Chem* **2012**, *55* (3), 1021–1046. https://doi.org/10.1021/JM201310Y/SUPPL_FILE/JM201310Y_SI_001.PDF.

(2) Badarau, E.; Wang, Z.; Rathbone, D. L.; Costanzi, A.; Thibault, T.; Murdoch, C. E.; El Alaoui, S.; Bartkeviciute, M.; Griffin, M. Development of Potent and Selective Tissue Transglutaminase Inhibitors: Their Effect on TG2 Function and Application in Pathological Conditions. *Chem Biol* **2015**, *22* (10), 1347–1361. https://doi.org/10.1016/j.chembiol.2015.08.013.

(3) Akbar, A.; McNeil, N. M. R.; Albert, M. R.; Ta, V.; Adhikary, G.; Bourgeois, K.; Eckert, R. L.; Keillor, J. W. Structure-Activity Relationships of Potent, Targeted Covalent Inhibitors That Abolish Both the Transamidation and GTP Binding Activities of Human Tissue Transglutaminase. *J Med Chem* **2017**, *60* (18), 7910–7927. https://doi.org/10.1021/acs.jmedchem.7b01070.

(4) Rangaswamy, A. M. M.; Navals, P.; Gates, E. W. J.; Shad, S.; Watt, S. K. I.; Keillor, J. W. Structure-Activity Relationships of Hydrophobic Alkyl Acrylamides as Tissue

Transglutaminase Inhibitors. *RSC Med Chem* **2022**, *13*, 413–428. https://doi.org/10.1039/d1md00382h.

(5) McNeil, N. M. R.; Gates, E. W. J.; Firoozi, N.; Cundy, N. J.; Leccese, J.; Eisinga, S.; Tyndall, J. D. A.; Adhikary, G.; Eckert, R. L.; Keillor, J. W. Structure-Activity Relationships of N-Terminal Variants of Peptidomimetic Tissue Transglutaminase Inhibitors. *Eur J Med Chem* **2022**, *232*, 114172. https://doi.org/10.1016/j.ejmech.2022.114172.

(6) Cundy, N. J.; Arciszewski, J.; Gates, E. W. J.; Acton, S. L.; Passley, K. D.; Awoonor-Williams, E.; Boyd, E. K.; Xu, N.; Pierson, É.; Fernandez-Ansieta, C.; Albert, M. R.; McNeil, N. M. R.; Adhikary, G.; Eckert, R. L.; Keillor, J. W. Novel Irreversible Peptidic Inhibitors of Transglutaminase 2. *RSC Med Chem* **2023**, *14*, 378–385. https://doi.org/10.1039/D2MD00417H.

(7) Mader, L.; Watt, S. K. I.; Iyer, H. R.; Nguyen, L.; Kaur, H.; Keillor, J. W. The War on HTG2: Warhead Optimization in Small Molecule Human Tissue Transglutaminase Inhibitors. *RSC Med Chem* **2023**, *14*, 277–298. https://doi.org/10.1039/D2MD00378C.

(8) Wodtke, R.; Hauser, C.; Ruiz-Gómez, G.; Jäckel, E.; Bauer, D.; Lohse, M.; Wong, A.; Pufe, J.; Ludwig, F.-A.; Fischer, S.; Hauser, S.; Greif, D.; Pisabarro, M. T.; Pietzsch, J.; Pietsch, M.; Löser, R. Nε-Acryloyllysine Piperazides as Irreversible Inhibitors of Transglutaminase 2: Synthesis, Structure–Activity Relationships, and Pharmacokinetic Profiling. *J Med Chem* **2018**, *61* (10), 4528–4560. https://doi.org/10.1021/ACS.JMEDCHEM.8B00286.

(9) Sima, L. E.; Yakubov, B.; Zhang, S.; Condello, S.; Grigorescu, A. A.; Nwani, N. G.; Chen, L.; Schiltz, G. E.; Arvanitis, C.; Zhang, Z. Y.; Matei, D. Small Molecules Target

the Interaction between Tissue Transglutaminase and Fibronectin. *Mol Cancer Ther* **2019**, *18* (6), 1057–1068. https://doi.org/10.1158/1535-7163.MCT-18-1148.

(10) Stamnaes, J.; Cardoso, I.; Iversen, R.; Sollid, L. M. Transglutaminase 2 Strongly Binds to an Extracellular Matrix Component Other than Fibronectin via Its Second C-Terminal Beta-Barrel Domain. *FEBS J* **2016**, *283* (21), 3994–4010. https://doi.org/10.1111/FEBS.13907.

(11) Keillor, J. W.; Johnson, G. V. W. Transglutaminase 2 as a Therapeutic Target for Neurological Conditions. *Expert Opin Ther Targets* **2021**, *25*, 721–731. https://doi.org/10.1080/14728222.2021.1989410.

(12) Kerr, C.; Szmacinski, H.; Fisher, M. L.; Nance, B.; Lakowicz, J. R.; Akbar, A.; Keillor, J. W.; Lok Wong, T.; Godoy-Ruiz, R.; Toth, E. A.; Weber, D. J.; Eckert, R. L. Transamidase Site-Targeted Agents Alter the Conformation of the Transglutaminase Cancer Stem Cell Survival Protein to Reduce GTP Binding Activity and Cancer Stem Cell Survival. *Oncogene* **2017**, *36* (21), 2981–2990. https://doi.org/10.1038/onc.2016.452.

(13) Rorke, E. A.; Adhikary, G.; Szmacinski, H.; Lakowicz, J. R.; Weber, D. J.; Godoy-Ruiz, R.; Puranik, P.; Keillor, J. W.; Gates, E. W. J.; Eckert, R. L. Sulforaphane Covalently Interacts with the Transglutaminase 2 Cancer Maintenance Protein to Alter Its Structure and Suppress Its Activity. *Mol Carcinog* **2022**, *61* (1), 19–32. https://doi.org/10.1002/mc.23356.

(14) Wang, Y.; Ande, S. R.; Mishra, S. Phosphorylation of Transglutaminase 2 (TG2) at Serine-216 Has a Role in TG2 Mediated Activation of Nuclear Factor-Kappa B and in the

Downregulation of PTEN. *BMC Cancer* **2012**, *12* (1), 1–12. https://doi.org/10.1186/1471-2407-12-277/FIGURES/7.

(15) Cardoso, I.; Stamnaes, J.; Andersen, J. T.; Melino, G.; Iversen, R.; Sollid, L. M. Transglutaminase 2 Interactions with Extracellular Matrix Proteins as Probed with Celiac Disease Autoantibodies. *FEBS J* **2015**, *282* (11), 2063–2075. https://doi.org/10.1111/FEBS.13276.

(16) Nurminskaya, M. V.; Belkin, A. M. Cellular Functions of Tissue Transglutaminase. *Int Rev Cell Mol Biol* **2012**, *294*, 1–97. https://doi.org/10.1016/B978-0-12-394305-7.00001-X.

(17) Walport, L. J.; Low, J. K. K.; Matthews, J. M.; MacKay, J. P. The Characterization of Protein Interactions – What, How and How Much? *Chem Soc Rev* **2021**, *50* (22), 12292–12307. https://doi.org/10.1039/D1CS00548K.

(18) Yan, J.; Li, T.; Miao, Z.; Wang, P.; Sheng, C.; Zhuang, C. Homobivalent, Trivalent, and Covalent PROTACs: Emerging Strategies for Protein Degradation. *J Med Chem* **2022**. https://doi.org/10.1021/ACS.JMEDCHEM.2C00728.

(19) Guo, W. H.; Qi, X.; Yu, X.; Liu, Y.; Chung, C. I.; Bai, F.; Lin, X.; Lu, D.; Wang, L.; Chen, J.; Su, L. H.; Nomie, K. J.; Li, F.; Wang, M. C.; Shu, X.; Onuchic, J. N.; Woyach, J. A.; Wang, M. L.; Wang, J. Enhancing Intracellular Accumulation and Target Engagement of PROTACs with Reversible Covalent Chemistry. *Nat Commun* **2020**, *11*, 4268. https://doi.org/10.1038/s41467-020-17997-6.

(20) Sosič, I.; Bricelj, A.; Steinebach, C. E3 Ligase Ligand Chemistries: From Building Blocks to Protein Degraders. *Chem Soc Rev* **2022**, *51* (9), 3487–3534. https://doi.org/10.1039/D2CS00148A.

(21) Bricelj, A.; Steinebach, C.; Kuchta, R.; Gütschow, M.; Sosič, I. E3 Ligase Ligands in Successful PROTACs: An Overview of Syntheses and Linker Attachment Points. *Front Chem* **2021**, *9* (707317). https://doi.org/10.3389/FCHEM.2021.707317.

(22) Leblanc, A.; Gravel, C.; Labelle, J.; Keillor, J. W. Kinetic Studies of Guinea Pig Liver Transglutaminase Reveal a General-Base-Catalyzed Deacylation Mechanism. *Biochemistry* **2001**, *40* (28), 8335–8342. https://doi.org/10.1021/bi0024097.

(23) Gates, E. W. J.; Mansour, K.; Ebrahimi Samani, S.; Shad, S.; Kaartinen, M. T.; Keillor, J. W. Peptidic Inhibitors and a Fluorescent Probe for the Selective Inhibition and Labelling of Factor XIIIa Transglutaminase. *Molecules* **2023**, *28*, 1634. https://doi.org/10.3390/molecules28041634.

(24) Zheng, S.; Crews, C. M. Electrophilic Screening Platforms for Identifying Novel Covalent Ligands for E3 Ligases. *Biochemistry* **2021**, *60* (31), 2367–2370. https://doi.org/10.1021/ACS.BIOCHEM.1C00301/ASSET/IMAGES/LARGE/BI1C00301_0004.JPEG.

(25) Yuan, M.; Chu, Y.; Duan, Y. Reversible Covalent PROTACs: Novel and Efficient Targeted Degradation Strategy. *Front Chem* **2021**, *9*, 691093. https://doi.org/10.3389/FCHEM.2021.691093/BIBTEX.

(26) Gabizon, R.; London, N. The Rise of Covalent Proteolysis Targeting Chimeras. *Curr Opin Chem Biol* **2021**, *62*, 24–33. https://doi.org/10.1016/J.CBPA.2020.12.003.

(27) Kiely-Collins, H.; Winter, G. E.; Bernardes, G. J. L. The Role of Reversible and Irreversible Covalent Chemistry in Targeted Protein Degradation. *Cell Chem Biol* **2021**, *28* (7), 952–968. https://doi.org/10.1016/J.CHEMBIOL.2021.03.005.

(28) Roy, I.; Smith, O.; Clouthier, C. M.; Keillor, J. W. Expression, Purification and Kinetic Characterisation of Human Tissue Transglutaminase. *Protein Expr Purif* **2013**, *87* (1), 41–46. https://doi.org/10.1016/j.pep.2012.10.002.

(29) Stone, S. R.; Hofsteenge, J. Specificity of Activated Human Protein C. *Biochemical Journal* **1985**, *230* (2), 497–502. https://doi.org/10.1042/bj2300497.

(30) Kitz, R.; Wilson, I. B. Esters of Methanesulfonic Acid as Irreversible Inhibitors of Acetylcholinesterase. *J Biol Chem* **1962**, *237* (10), 3245–3249. https://doi.org/10.1016/s0021-9258(18)50153-8.

Appendix to Chapter 5

General Synthesis Remarks:

When available, commercially available starting materials, reagents, and solvents were purchase from various suppliers including Sigma-Aldrich, Oakwood Products, Combi-Blocks, Fisher Scientific, AA Blocks, and Aaron Chemicals and were used without further purification. To monitor reaction progress, thin layer chromatography (TLC) was employed with SiliCycle 200-µm thickness F-254 indicator aluminum backed TLC plates and were visualized using short wave UV light. Flash chromatography was utilized to purify intermediates as well as final products with 230-400 mesh silica gel and was either conducted manually or automatically *via* a Biotage Selekt system. All ^{1}H- and ^{13}C-NMR spectra were first referenced to the specified deuterated solvent and obtained using a Bruker 400-MHz or 600-MHz instrument to report the peaks in ppm. The high-resolution mass spectra (HRMS) for characterization were obtained *via* an electrospray ionization source (ESI) in positive mode and a quadrupole time-of-flight (QTOF) analyser by the John L. Holmes Mass Spectrometry Facility at the University of Ottawa. All final compounds were also evaluated for purity via HPLC using a Shimadzu LC-MS-2020 and Agilent Eclipse XOB-C18 5.0-µm, 4.6 ×150-mm column or Bischoff Chromatography ProntoSIL 5.0-µm, 4.0 ×125-mm column; ACN/H2O with 0.05% v/v formic acid, 5-95% gradient, 15 min runtime, 1 mL/min flowrate; UV detection at 220 and 254 nm instrument parameters.

***In Vitro* Kinetic Evaluation of PROTACs Against hTG2:**

To evaluate the extent of transamidase inhibition of recombinant hTG2[28] induced by the proposed PROTACs, an in-house developed colorimetric assay was employed under Kitz and Wilson conditions with hTG2 as published previously.[3,29,30] In brief, a master mix buffer solution containing 111 mM MOPS, 15 mM $CaCl_2$ in water was brought to pH 6.9. Stock solutions of the

chromogenic substrate AL5[22] (40 mM) and respective PROTAC (3 mM) were prepared in DMSO. Two aqueous working stocks (25 µM and 200 µM) of the PROTAC were then prepared from the DMSO stock to ensure the percent DMSO remained below 5% in the final assay conditions. To a 1.5 mL Eppendorf tube was added 125 µL master mix and the corresponding amount of water and inhibitor working stock, such that the final concentration of inhibitor would be 1 µM or 10 µM in the plate. To the tube was finally added 5 µL of AL5 stock and the mixture was vortexed. A 180 µL aliquot was then removed and placed in a well of a 96-well polystyrene microplate. A 20 µL aliquot of pre-dilute recombinant human TG2 in master mix was added to the well and was aspirated to initiate the reaction and obtain a final activity of 5 mU TG2 in the well. Each well was monitored for absorbance at 405 nm using a BioTek Synergy plate reader and had final concentrations of 50 mM MOPS, 7 mM $CaCl_2$, 5 mU TG2, 100 µM AL5, and 1 µM or 10 µM PROTAC. A positive control which did not contain any inhibitor as well as a blank which did not receive enzyme and had water in place of those components were also included and the experiment was performed in triplicate. The raw data obtained was then blank subtracted to correct for the background rate of hydrolysis of the substrate.

In order to estimate the inhibition parameters, observed first order rate constants were extracted by fitting the 1 µM data to a one phase association model. Utilizing Graphpad Prism, the observed rate constants were then divided by the inhibitor concentration (1 µM) and multiplied by 11 (the value of α). The error in each value was estimated using the standard deviation from the three replicates.

General Procedure A: (Azide PEG linker coupling to VHL ligand)

To a round bottom flask was added 1.5 eq of the corresponding carboxylic acid, 1.5 eq HATU, and 3 eq DIPEA solubilized in DMF at 0 ˚C. The pre-activation was stirred for 0.5 h, upon which

1 eq of the corresponding amine was added as a solution in DMF with 1 eq DIPEA. The ice bath was removed, and the reaction mixture was allowed to warm to room temperature and stirred overnight. Upon completion, the reaction mixture was diluted with ethyl acetate and washed twice with brine, once with water, and then again twice with brine. The organic layer was dried over $MgSO_4$, filtered, and concentrated under reduced pressure. The resulting crude oil was purified *via* flash chromatography to yield the product.

General Procedure B: (Azide PEG linker coupling to IAP ligand)

To a round bottom flask was added 1.5 eq of the corresponding carboxylic acid, 1.5 eq HATU, and 3 eq DIPEA solubilized in DMF at 0 ˚C. The pre-activation was stirred for 0.5 h, upon which 1 eq of the corresponding amine was added as a solution in DMF. The ice bath was removed, and the reaction mixture was allowed to warm to room temperature and stirred overnight. Upon completion, the reaction mixture was diluted with ethyl acetate and washed twice with brine, once with 1 M HCl, brine, sat. $NaHCO_3$, and then again twice with brine. The organic layer was dried over $MgSO_4$, filtered, and concentrated under reduced pressure. The resulting crude oil was purified *via* flash chromatography to yield the product.

General Procedure C: (Azide PEG linker coupling to lenalidomide)

To a round bottom flask was added 1.5 eq of the corresponding carboxylic acid, 1.5 eq HATU, and 4 eq DIPEA solubilized in DMF at 0 ˚C. The pre-activation was stirred for 0.5 h, upon which 1 eq of lenalidomide was added to the flask. The ice bath was removed, and the reaction mixture was allowed to warm to room temperature and stirred overnight. Upon completion the reaction mixture was diluted with EtOAc and washed twice with brine. The organic layer was then washed

with 1 M HCl, brine, sat. $NaHCO_3$, and brine again. The organic layer was subsequently dried over $MgSO_4$, filtered, and concentrated under reduced pressure. The resulting crude oil was purified *via* flash chromatography to yield the product.

General Procedure D: (CuAAC reaction with propargylated scaffold and azides)

To a vial was added 1 eq of the corresponding azide, 1 eq of the propargylated scaffold, and 1 eq of copper (II) sulfate pentahydrate solubilized in a 1:1 mixture of ACN:H_2O. The mixture was stirred at 40 ˚C for 5 h upon which the volatiles were removed under reduced pressure. The resulting crude residue was then purified *via* flash chromatography or preparative thin layer chromatography to yield the product. The product was then subjected to one final step of purification by filtering through a 1 g SiliCycle SiliaPrep SPE cartridge functionalized with imidazole to scavenge any remaining copper.

General Procedure E: (Boc deprotection to yield IAP PROTACs)

To a vial was added 1 eq of the Boc-protected starting materials solubilized in a 1:1 mixture of 4 M HCl in dioxane and DCM. The reaction mixture was stirred for 1 h upon which the volatiles were removed under reduced pressure. The residue was co-evaporated with DCM to yield the product as a hydrochloride salt without any further purification.

Fmoc Deprotection of IAP Ligand **(Compound 22, EG-5-28)*:***

To a round bottom flask was added 1 eq of Fmoc- and Boc-protected IAP ligand solubilized in a solution of 40% diethylamine in DCM [0.25 M]. The reaction mixture was stirred for 5 h upon which the volatiles were removed under reduced pressure. The resulting crude oil was then

resolubilized in DCM and co-evaporated three times. The crude solid was then triturated with hexanes to yield the Fmoc deprotected product without any further purification as a white solid (309 mg, 77%).

^{1}H NMR (600 MHz, $CDCl_3$) δ 7.25 (dd, *J* = 7.4, 1.7 Hz, 1H), 7.15 – 7.08 (m, 2H), 7.05 (dd, *J* = 7.4, 1.7 Hz, 1H), 5.13 – 5.08 (m, 1H), 4.53 (dd, *J* = 9.2, 3.4 Hz, 1H), 4.46 (t, *J* = 7.9 Hz, 1H), 3.99 (dd, *J* = 10.6, 5.8 Hz, 1H), 3.74 – 3.67 (m, 1H), 3.43 (dd, *J* = 10.5, 3.4 Hz, 1H), 2.82 – 2.69 (m, 6H), 2.30 – 2.20 (m, 4H), 1.91 – 1.75 (m, 4H), 1.64 – 1.59 (m, 6H), 1.46 (s, 9H), 1.16 – 0.96 (m, 6H). ^{13}C NMR (151 MHz, $CDCl_3$) δ 171.97, 171.58, 170.82, 137.42, 136.57, 129.19, 128.76, 127.28, 126.27, 80.70, 60.46, 56.67, 55.25, 51.32, 47.76, 40.87, 35.97, 34.78, 30.10, 29.78, 29.33, 29.17, 28.46, 26.12, 26.00, 25.85, 25.39, 20.11. HRMS (ESI-QTOF) m/z [M + Na]+ calcd for $C_{32}H_{49}N_5O_5Na$ 606.3631; found 606.3616.

Propargylated Inhibitor **(EG-5-34)**

Synthesised using previously published procedure (white solid, 549 mg, 85%) (See Chapter 3). *The following NMR spectral data are the same as those reported in that manuscript (Chapter 3):*

"^{1}H NMR (600 MHz, $CDCl_3$) δ 8.35 – 8.28 (m, 1H), 7.95 – 7.90 (m, 1H), 7.86 (d, J = 8.1 Hz, 1H), 7.68 – 7.63 (m, 1H), 7.58 – 7.49 (m, 2H), 7.45 – 7.30 (m, 6H), 6.27 – 6.17 (m, 1H), 6.16 – 6.01 (m, 2H), 5.95 – 5.81 (m, 1H), 5.61 – 5.53 (m, 1H), 5.23 – 5.13 (m, 1H), 5.09 – 5.02 (m, 2H), 4.66 – 4.57 (m, 1H), 4.17 – 4.06 (m, 1H), 4.06 – 3.94 (m, 1H), 3.87 – 3.12 (m, 10H), 2.54 – 2.43 (m, 1H), 2.42 – 2.34 (m, 1H), 2.25 – 2.14 (m, 2H), 1.97 – 1.86 (m, 1H), 1.72 – 1.44 (m, 4H), 1.42 – 1.31 (m, 2H). ^{13}C NMR (151 MHz, $CDCl_3$) δ 172.00, 170.67, 170.00, 169.90, 165.78, 156.25, 136.31, 136.29, 133.80, 133.79, 131.38, 130.94, 130.15, 130.13, 128.74, 128.63, 128.55, 128.31,

128.29, 128.14, 128.11, 128.09, 127.46, 127.44, 127.41, 126.62, 126.41, 126.40, 125.68, 125.65, 125.22, 125.20, 124.76, 80.05, 71.30, 67.06, 50.36, 50.34, 50.25, 49.03, 49.01, 48.99, 48.94, 45.60, 45.54, 45.16, 45.11, 42.05, 41.79, 41.73, 39.04, 39.00, 38.97, 32.74, 32.72, 32.68, 32.65, 32.03, 32.01, 29.29, 29.27, 29.24, 29.19, 29.18, 29.00, 28.93, 28.90, 22.38, 22.29, 22.27."

Azide-PEG1-VHL (Compound 5, EG-5-17)

Synthesised using *General Procedure A* (colourless oil, 85 mg, 71%)

^{1}H NMR (600 MHz, $CDCl_3$) δ 8.66 (s, 1H), 7.47 (t, *J* = 5.9 Hz, 1H), 7.36 – 7.28 (m, 4H), 7.20 (d, *J* = 8.6 Hz, 1H), 4.70 (t, *J* = 7.9 Hz, 1H), 4.55 – 4.46 (m, 3H), 4.30 (dd, *J* = 15.1, 5.3 Hz, 1H), 4.04 – 3.92 (m, 3H), 3.71 – 3.60 (m, 3H), 3.50 – 3.37 (m, 2H), 2.49 (s, 3H), 2.48 – 2.43 (m, 1H), 2.12 – 2.05 (m, 1H), 0.95 (s, 9H). ^{13}C NMR (151 MHz, $CDCl_3$) δ 171.25, 170.99, 169.74, 150.43, 148.52, 138.21, 131.71, 130.95, 129.55, 128.12, 70.62, 70.31, 70.20, 58.73, 57.36, 56.80, 50.76, 43.26, 36.22, 35.18, 26.44, 16.13. HRMS (ESI-QTOF) m/z [M + Na]+ calcd for $C_{26}H_{35}N_7O_5Sna$ 580.2318; found 580.2297.

Azide-PEG2-VHL (Compound 6, EG-5-18)

Synthesised using *General Procedure A* (colourless oil, 106 mg, 82%)

^{1}H NMR (600 MHz, $CDCl_3$) δ 8.61 (s, 1H), 7.41 (t, *J* = 6.0 Hz, 1H), 7.29 – 7.25 (m, 4H), 7.22 – 7.20 (m, 1H), 4.64 (t, *J* = 7.8 Hz, 1H), 4.49 – 4.43 (m, 3H), 4.26 (dd, *J* = 15.0, 5.4 Hz, 1H), 3.95 – 3.87 (m, 3H), 3.62 – 3.56 (m, 7H), 3.35 – 3.26 (m, 2H), 2.43 (s, 3H), 2.42 – 2.36 (m, 1H), 2.06 – 2.00 (m, 1H), 0.89 (s, 9H). ^{13}C NMR (151 MHz, $CDCl_3$) δ 171.20, 171.03, 170.23, 150.43, 148.47, 138.24, 131.68, 130.91, 129.52, 128.12, 71.15, 70.44, 70.41, 70.14, 70.09, 58.74, 57.04,

56.77, 50.59, 43.22, 36.20, 35.35, 26.43, 16.11. HRMS (ESI-QTOF) m/z [M + Na]+ calcd for $C_{28}H_{39}N_7O_6SNa$ 624.2580; found 624.2584.

Azide-PEG3-VHL (Compound 7, EG-5-19)

Synthesised using *General Procedure A* (colourless oil, 109 mg, 79%)

^{1}H NMR (600 MHz, $CDCl_3$) δ 8.61 (s, 1H), 7.43 (t, *J* = 6.0 Hz, 1H), 7.30 – 7.24 (m, 4H), 7.23 (d, *J* = 8.6 Hz, 1H), 4.63 (t, *J* = 7.8 Hz, 1H), 4.49 – 4.42 (m, 3H), 4.27 (dd, *J* = 15.1, 5.5 Hz, 1H), 3.96 – 3.86 (m, 3H), 3.61 – 3.56 (m, 11H), 3.28 (dd, *J* = 5.6, 4.5 Hz, 2H), 2.43 (s, 3H), 2.40 – 2.33 (m, 1H), 2.07 – 2.00 (m, 1H), 0.89 (s, 9H). ^{13}C NMR (151 MHz, $CDCl_3$) δ 171.15, 171.07, 170.30, 150.39, 148.43, 138.24, 131.66, 130.84, 129.47, 128.04, 71.18, 70.71, 70.70, 70.51, 70.32, 70.07, 70.04, 58.74, 57.03, 56.73, 50.67, 43.16, 36.27, 35.29, 26.41, 16.08. HRMS (ESI-QTOF) m/z [M + Na]+ calcd for $C_{30}H_{43}N_7O_7SNa$ 668.2842; found 668.2832.

Azide-PEG4-VHL (Compound 8, EG-5-20)

Synthesised using *General Procedure A* (colourless oil, 59 mg, 40%)

^{1}H NMR (600 MHz, $CDCl_3$) δ 8.66 (s, 1H), 7.44 (t, *J* = 5.8 Hz, 1H), 7.35 – 7.29 (m, 4H), 7.25 (d, *J* = 8.6 Hz, 1H), 4.71 – 4.66 (m, 1H), 4.53 – 4.47 (m, 3H), 4.32 (dd, *J* = 15.1, 1.6 Hz, 1H), 4.01 – 3.91 (m, 3H), 3.66 – 3.60 (m, 15H), 3.38 – 3.34 (m, 2H), 2.50 – 2.47 (m, 3H), 2.46 – 2.40 (m, 1H), 2.12 – 2.05 (m, 1H), 0.94 (s, 9H). ^{13}C NMR (151 MHz, $CDCl_3$) δ 171.30, 171.29, 171.27, 171.26, 171.04, 171.03, 171.01, 171.00, 170.46, 170.46, 170.44, 150.41, 148.49, 148.48, 138.26, 131.69, 130.92, 130.91, 129.53, 128.11, 128.10, 71.16, 70.68, 70.66, 70.61, 70.60, 70.43, 70.32, 70.13, 70.08, 58.72, 58.70, 58.69, 57.18, 56.75, 50.70, 43.22, 36.24, 36.21, 36.19, 35.25,

35.24, 35.22, 35.20, 26.45, 16.12. HRMS (ESI-QTOF) m/z [M + Na]+ calcd for $C_{32}H_{47}N_7O_8SNa$ 712.3105; found 712.3099.

Azide-PEG1-IAP (Compound 23, EG-5-29)

Synthesized using *General Procedure B* (colourless oil, 39 mg, 41%)

^{1}H NMR (600 MHz, $CDCl_3$) δ 7.12 (t, *J* = 7.6 Hz, 2H), 7.05 (t, *J* = 7.6 Hz, 2H), 5.15 – 5.10 (m, 1H), 4.73 (d, *J* = 8.9 Hz, 1H), 4.69 – 4.64 (m, 1H), 4.35 – 4.30 (m, 1H), 4.11 – 4.03 (m, 3H), 3.73 (dt, *J* = 10.0, 5.0 Hz, 1H), 3.68 (dt, *J* = 10.1, 5.0 Hz, 1H), 3.61 (d, *J* = 10.8 Hz, 1H), 3.49 (t, *J* = 5.1 Hz, 2H), 2.84 – 2.71 (m, 5H), 2.44 (d, *J* = 13.8 Hz, 1H), 2.24 – 2.16 (m, 1H), 2.05 – 1.97 (m, 1H), 1.87 – 1.79 (m, 3H), 1.66 – 1.52 (m, 5H), 1.44 (s, 9H), 1.27 (d, *J* = 7.1 Hz, 4H), 1.04 (d, *J* = 10.3 Hz, 3H), 0.92 – 0.82 (m, 2H). ^{13}C NMR (151 MHz, $CDCl_3$) δ 172.85, 171.57, 170.68, 169.49, 137.37, 136.30, 129.28, 128.33, 127.38, 126.12, 80.67, 70.78, 70.70, 60.27, 55.70, 55.30, 50.65, 48.94, 47.91, 40.46, 31.32, 30.05, 29.50, 29.25, 28.43, 26.03, 26.01, 25.83, 20.13. HRMS (ESI-QTOF) m/z [M + Na]+ calcd for $C_{36}H_{54}N_8O_7Na$ 733.4013; found 733.4021.

Azide-PEG2-IAP (Compound 24, EG-5-30)

Synthesized using *General Procedure B* (white solid, 49 mg, 49%)

^{1}H NMR (600 MHz, $CDCl_3$) δ 7.14 – 7.09 (m, 2H), 7.04 (d, *J* = 7.5 Hz, 2H), 5.13 – 5.07 (m, 1H), 4.72 (d, *J* = 8.8 Hz, 1H), 4.62 (q, *J* = 6.4 Hz, 1H), 4.32 (t, *J* = 7.5 Hz, 1H), 4.09 – 3.99 (m, 3H), 3.76 – 3.68 (m, 5H), 3.67 – 3.62 (m, 2H), 3.61 – 3.57 (m, 1H), 3.35 – 3.27 (m, 2H), 2.84 – 2.68 (m, 5H), 2.46 (d, *J* = 13.7 Hz, 1H), 2.19 (ddd, *J* = 13.7, 8.9, 6.6 Hz, 1H), 2.04 – 1.96 (m, 1H), 1.88 – 1.75 (m, 3H), 1.63 – 1.49 (m, 5H), 1.44 (s, 9H), 1.28 – 1.16 (m, 4H), 1.08 – 0.97 (m, 3H), 0.94 – 0.79 (m, 2H). ^{13}C NMR (151 MHz, $CDCl_3$) δ 172.86, 171.51, 170.64, 170.10,

137.25, 136.38, 129.24, 128.28, 127.34, 126.15, 80.62, 71.44, 70.96, 70.54, 70.22, 60.19, 55.52, 55.26, 50.66, 48.95, 47.78, 40.49, 31.15, 30.06, 29.42, 29.22, 28.41, 25.98, 25.81, 20.19. HRMS (ESI-QTOF) m/z [M + Na]+ calcd for $C_{38}H_{58}N_8O_8Na$ 777.4275; found 777.4298.

Azide-PEG3-IAP (Compound 25, EG-5-31)

Synthesized using *General Procedure B* (colourless oil, 44 mg, 42%)

^{1}H NMR (600 MHz, $CDCl_3$) δ 7.15 – 7.08 (m, 2H), 7.04 (d, *J* = 7.3 Hz, 2H), 5.13 – 5.07 (m, 1H), 4.71 (d, *J* = 8.8 Hz, 1H), 4.65 – 4.58 (m, 1H), 4.32 (t, *J* = 7.9 Hz, 1H), 4.10 – 4.03 (m, 3H), 3.78 – 3.54 (m, 12H), 3.32 (t, *J* = 5.1 Hz, 2H), 2.83 – 2.68 (m, 5H), 2.45 (d, *J* = 13.8 Hz, 1H), 2.20 (ddd, *J* = 13.7, 8.9, 6.7 Hz, 1H), 2.04 – 1.98 (m, 1H), 1.87 – 1.76 (m, 3H), 1.65 – 1.48 (m, 5H), 1.44 (s, 9H), 1.29 – 1.21 (m, 4H), 1.09 – 0.98 (m, 3H), 0.93 – 0.80 (m, 2H). ^{13}C NMR (151 MHz, $CDCl_3$) δ 172.83, 171.53, 170.58, 170.26, 137.25, 136.39, 129.23, 128.36, 127.33, 126.16, 80.66, 71.38, 70.92, 70.79, 70.75, 70.69, 70.66, 70.07, 60.18, 55.49, 55.27, 50.70, 48.93, 47.76, 40.50, 31.21, 30.05, 29.42, 29.23, 28.41, 26.00, 25.98, 25.81, 20.15. HRMS (ESI-QTOF) m/z [M + Na]+ calcd for $C_{40}H_{62}N_8O_9Na$ 821.4537; found 821.4508.

Azide-PEG4-IAP (Compound 26, <u>EG-5-26</u>/EG-5-32)

Synthesized using *General Procedure B* (colourless oil, 71 mg, 49%)

^{1}H NMR (600 MHz, $CDCl_3$) δ 7.14 – 7.06 (m, 2H), 7.03 (d, *J* = 7.0 Hz, 2H), 5.09 (dd, *J* = 8.6, 5.9 Hz, 1H), 4.70 (d, *J* = 8.8 Hz, 1H), 4.65 – 4.56 (m, 1H), 4.31 (t, *J* = 7.8 Hz, 1H), 4.10 – 4.00 (m, 3H), 3.90 – 3.42 (m, 16H), 3.38 – 3.30 (m, 2H), 2.79 – 2.70 (m, 5H), 2.44 (dd, *J* = 14.0, 1.7 Hz, 1H), 2.18 (ddd, *J* = 13.6, 8.9, 6.6 Hz, 1H), 2.02 – 1.93 (m, 1H), 1.86 – 1.74 (m, 3H), 1.65 – 1.46 (m, 5H), 1.42 (s, 9H), 1.27 – 1.12 (m, 4H), 1.07 – 0.96 (m, 3H), 0.92 – 0.78 (m, 2H). ^{13}C

NMR (151 MHz, $CDCl_3$) δ 172.74, 171.45, 170.52, 170.21, 137.17, 136.35, 129.17, 128.33, 127.27, 126.11, 80.57, 71.32, 70.88, 70.71, 70.67, 70.64, 70.62, 70.54, 70.04, 60.12, 55.45, 55.19, 50.68, 48.87, 47.68, 40.47, 31.16, 30.00, 29.37, 29.18, 28.36, 25.95, 25.93, 25.77, 20.09. HRMS (ESI-QTOF) m/z [M + Na]+ calcd for $C_{42}H_{66}N_8O_{10}Na$ 865.4800; found 865.4814.

Azide-PEG1-Lenalidomide (Compound 13, EG-5-39)

Synthesized using *General Procedure C* (white solid, 23 mg, 10%)

^1H NMR (600 MHz, $CDCl_3$) δ 8.37 (d, *J* = 12.3 Hz, 1H), 7.90 – 7.84 (m, 1H), 7.74 (d, *J* = 7.5 Hz, 1H), 7.50 (t, *J* = 7.8 Hz, 1H), 5.21 (dd, *J* = 13.4, 5.2 Hz, 1H), 4.43 (q, *J* = 16.3 Hz, 2H), 4.17 (s, 2H), 3.79 (t, *J* = 4.8 Hz, 2H), 3.55 (q, *J* = 4.6 Hz, 2H), 2.91 – 2.75 (m, 2H), 2.33 (qd, *J* = 13.2, 4.9 Hz, 1H), 2.19 (dtd, *J* = 12.9, 5.2, 2.5 Hz, 1H). ^{13}C NMR (151 MHz, $CDCl_3$) δ 171.26, 169.68, 168.95, 167.19, 133.37, 132.87, 131.83, 129.49, 125.48, 121.48, 121.46, 70.71, 70.56, 51.89, 50.89, 46.15, 31.61, 23.47. HRMS (ESI-QTOF) m/z [M + Na]+ calcd for $C_{17}H_{18}N_6O_5Na$ 409.1236; found 409.1242.

Azide-PEG2-Lenalidomide (Compound 14, EG-5-40)

Synthesized using *General Procedure C* (white solid, 93 mg, 37%)

^1H NMR (600 MHz, $CDCl_3$) δ 8.73 (s, 1H), 8.69 (s, 1H), 7.73 (dd, *J* = 7.6, 1.0 Hz, 1H), 7.65 (dd, *J* = 8.0, 1.0 Hz, 1H), 7.47 (t, *J* = 7.7 Hz, 1H), 5.18 (dd, *J* = 13.3, 5.1 Hz, 1H), 4.41 (d, *J* = 2.1 Hz, 2H), 4.16 (d, *J* = 1.2 Hz, 2H), 3.81 – 3.77 (m, 2H), 3.75 – 3.66 (m, 4H), 3.38 – 3.33 (m, 2H), 2.84 – 2.74 (m, 2H), 2.32 (qd, *J* = 13.0, 5.3 Hz, 1H), 2.15 (dtd, *J* = 12.9, 5.2, 2.6 Hz, 1H). ^{13}C NMR (151 MHz, $CDCl_3$) δ 171.65, 169.97, 168.91, 168.28, 134.78, 132.99, 131.88, 129.21,

126.43, 121.66, 71.20, 70.52, 70.18, 70.16, 51.89, 50.52, 46.58, 31.58, 23.39. HRMS (ESI-QTOF) m/z [M + Na]+ calcd for $C_{19}H_{22}N_6O_6Na$ 453.1499; found 453.1490.

Azide-PEG3-Lenalidomide (Compound 15, EG-5-41)

Synthesized using *General Procedure C* (white solid, 120 mg, 44%)

^{1}H NMR (600 MHz, $CDCl_3$) δ 8.92 (s, 1H), 8.90 (s, 1H), 7.71 (dd, *J* = 7.5, 1.0 Hz, 1H), 7.63 (dd, *J* = 8.0, 0.9 Hz, 1H), 7.45 (t, *J* = 7.7 Hz, 1H), 5.16 (dd, *J* = 13.4, 5.1 Hz, 1H), 4.41 (s, 2H), 4.19 – 4.08 (m, 2H), 3.77 (ddd, *J* = 6.0, 2.8, 1.8 Hz, 2H), 3.74 – 3.70 (m, 2H), 3.69 – 3.65 (m, 2H), 3.58 – 3.54 (m, 2H), 3.46 (ddd, *J* = 5.6, 4.5, 1.3 Hz, 2H), 3.20 (ddd, *J* = 6.5, 5.4, 4.4 Hz, 2H), 2.77 (s, 2H), 2.36 – 2.23 (m, 1H), 2.13 (dtd, *J* = 12.9, 5.1, 2.8 Hz, 1H). ^{13}C NMR (151 MHz, $CDCl_3$) δ 171.72, 169.95, 168.86, 168.67, 134.96, 132.96, 132.05, 129.06, 126.53, 121.56, 71.38, 70.66, 70.45, 70.36, 70.26, 69.94, 51.86, 50.53, 46.65, 31.54, 23.33. HRMS (ESI-QTOF) m/z [M + Na]+ calcd for $C_{21}H_{26}N_6O_7Na$ 497.1761; found 497.1772.

Azide-PEG4-Lenalidomide (Compound 16, EG-5-42)

Synthesized using *General Procedure C* (white solid, 51 mg, 17%)

^{1}H NMR (600 MHz, $CDCl_3$) δ 8.97 (s, 1H), 8.67 (s, 1H), 7.73 (dd, *J* = 7.5, 1.0 Hz, 1H), 7.68 (dd, *J* = 7.9, 1.0 Hz, 1H), 7.47 (t, *J* = 7.7 Hz, 1H), 5.19 (dd, *J* = 13.4, 5.1 Hz, 1H), 4.48 – 4.38 (m, 2H), 4.19 – 4.09 (m, 2H), 3.80 – 3.76 (m, 2H), 3.74 – 3.70 (m, 2H), 3.69 – 3.66 (m, 2H), 3.61 – 3.54 (m, 4H), 3.51 – 3.47 (m, 4H), 3.32 – 3.29 (m, 2H), 2.87 – 2.73 (m, 2H), 2.34 (qd, *J* = 13.1, 5.1 Hz, 1H), 2.17 (dtd, *J* = 13.0, 5.2, 2.6 Hz, 1H). ^{13}C NMR (151 MHz, $CDCl_3$) δ 171.55, 169.81, 168.93, 168.68, 134.82, 132.94, 132.16, 129.13, 126.49, 121.56, 71.45, 70.70, 70.60,

70.47, 70.40, 70.38, 70.14, 70.02, 51.90, 50.67, 46.64, 31.61, 23.43. HRMS (ESI-QTOF) m/z [M + Na]+ calcd for $C_{23}H_{30}N_6O_8Na$ 541.2023; found 541.2008.

Boc-IAP-PEG1-TG2Ligand (Compound 27, EG-5-43-2)

Synthesized using *General Procedure D* (white solid, 30 mg, 38%)

^{1}H NMR (600 MHz, MeOD) δ 8.28 – 8.21 (m, 1H), 8.11 – 8.04 (m, 1H), 7.97 (d, *J* = 8.3 Hz, 1H), 7.94 – 7.89 (m, 1H), 7.69 (t, *J* = 6.3 Hz, 1H), 7.52 (ddd, *J* = 15.3, 7.2, 4.7 Hz, 3H), 7.40 – 7.25 (m, 6H), 7.16 – 7.09 (m, 2H), 7.08 – 7.01 (m, 1H), 6.23 – 6.15 (m, 2H), 5.65 – 5.58 (m, 1H), 5.23 – 5.12 (m, 1H), 5.10 – 5.05 (m, 2H), 5.05 – 4.99 (m, 1H), 4.72 – 4.35 (m, 10H), 4.06 (dd, *J* = 10.8, 5.8 Hz, 1H), 3.96 – 3.40 (m, 14H), 3.28 – 3.19 (m, 2H), 2.90 – 2.66 (m, 5H), 2.50 – 2.37 (m, 3H), 2.24 – 2.13 (m, 1H), 2.02 – 1.81 (m, 6H), 1.80 – 1.62 (m, 8H), 1.59 – 1.51 (m, 2H), 1.48 – 1.44 (m, 9H), 1.32 – 1.26 (m, 3H), 1.25 – 0.98 (m, 5H). HRMS (ESI-QTOF) m/z [M + Na]+ calcd for $C_{76}H_{100}N_{14}O_{14}Na$ 1455.7441; found 1455.7455.

Boc-IAP-PEG2-TG2Ligand (Compound 28, EG-5-44-2)

Synthesized using *General Procedure D* (white solid, 39 mg, 41%)

^{1}H NMR (600 MHz, MeOD) δ 8.27 – 8.22 (m, 1H), 8.00 – 7.88 (m, 3H), 7.72 – 7.67 (m, 1H), 7.57 – 7.47 (m, 3H), 7.39 – 7.26 (m, 6H), 7.14 – 7.09 (m, 2H), 7.08 – 7.03 (m, 1H), 6.24 – 6.16 (m, 2H), 5.67 – 5.57 (m, 1H), 5.22 – 5.14 (m, 1H), 5.08 (dd, *J* = 11.7, 3.1 Hz, 2H), 5.05 – 4.98 (m, 1H), 4.67 – 4.34 (m, 10H), 4.11 – 4.03 (m, 1H), 3.90 – 3.42 (m, 18H), 3.27 – 3.19 (m, 2H), 2.84 – 2.70 (m, 5H), 2.56 – 2.38 (m, 3H), 2.24 – 2.16 (m, 1H), 2.05 – 1.81 (m, 6H), 1.78 – 1.62 (m, 8H), 1.59 – 1.52 (m, 2H), 1.46 (s, 9H), 1.34 – 1.27 (m, 3H), 1.24 – 0.97 (m, 5H). HRMS (ESI-QTOF) m/z [M + Na]+ calcd for $C_{78}H_{104}N_{14}O_{15}Na$ 1499.7703; found 1499.7689.

Boc-IAP-PEG3-TG2Ligand (Compound 29, EG-5-45-2)

Synthesized using *General Procedure D* (white solid, 52 mg, 62%)

^{1}H NMR (600 MHz, MeOD) δ 8.28 – 8.21 (m, 1H), 8.04 – 7.88 (m, 3H), 7.69 (d, *J* = 7.0 Hz, 1H), 7.59 – 7.48 (m, 3H), 7.38 – 7.27 (m, 6H), 7.17 – 7.10 (m, 2H), 7.09 – 7.01 (m, 1H), 6.25 – 6.15 (m, 2H), 5.65 – 5.57 (m, 1H), 5.21 – 5.13 (m, 1H), 5.11 – 5.05 (m, 2H), 5.03 (t, *J* = 6.4 Hz, 1H), 4.72 – 4.36 (m, 10H), 4.14 (dd, *J* = 10.5, 6.4 Hz, 1H), 3.99 – 3.42 (m, 22H), 3.28 – 3.18 (m, 2H), 2.88 – 2.69 (m, 5H), 2.53 – 2.40 (m, 3H), 2.25 – 2.16 (m, 1H), 2.06 – 1.80 (m, 6H), 1.79 – 1.62 (m, 8H), 1.59 – 1.52 (m, 2H), 1.48 – 1.44 (m, 9H), 1.33 – 1.28 (m, 3H), 1.25 – 0.99 (m, 5H). HRMS (ESI-QTOF) m/z [M + Na]+ calcd for $C_{80}H_{108}N_{14}O_{16}Na$ 1543.7965; found 1543.7966.

Boc-IAP-PEG4-TG2Ligand (Compound 30, EG-5-46-2)

Synthesized using *General Procedure D* (white solid, 36 mg, 23%)

^{1}H NMR (600 MHz, MeOD) δ 8.29 – 8.21 (m, 1H), 8.02 – 7.88 (m, 3H), 7.76 – 7.67 (m, 1H), 7.59 – 7.46 (m, 3H), 7.41 – 7.25 (m, 6H), 7.19 – 7.11 (m, 2H), 7.09 – 7.04 (m, 1H), 6.24 – 6.16 (m, 2H), 5.69 – 5.55 (m, 1H), 5.22 – 5.13 (m, 1H), 5.12 – 5.06 (m, 2H), 5.04 (t, *J* = 6.2 Hz, 1H), 4.67 – 4.36 (m, 10H), 4.14 (dd, *J* = 10.5, 6.3 Hz, 1H), 3.98 – 3.49 (m, 26H), 3.28 – 3.20 (m, 2H), 2.87 – 2.68 (m, 5H), 2.53 – 2.39 (m, 3H), 2.25 – 2.15 (m, 1H), 2.06 – 1.81 (m, 6H), 1.80 – 1.62 (m, 8H), 1.60 – 1.53 (m, 2H), 1.46 (s, 9H), 1.32 – 1.28 (m, 3H), 1.25 – 1.01 (m, 5H). HRMS (ESI-QTOF) m/z [M + Na]+ calcd for $C_{82}H_{112}N_{14}O_{17}Na$ 1587.8228; found 1587.8235.

VHL-PROTAC-1 (Compound 9, EG-5-35)

To a vial was added 1 eq of the corresponding azide, 1 eq of the propargylated scaffold, and 1 eq of copper (II) sulfate pentahydrate solubilized in a 1:1 mixture of ACN:H_2O. The mixture was stirred at room temperature overnight upon which the volatiles were removed under reduced pressure. The resulting crude residue was resolubilized in DCM and washed with water. The organic layer was then purified *via* flash chromatography to yield the product. The product was then subjected to one final step of purification by filtering through a 1 g SiliCycle SiliaPrep SPE cartridge functionalized with imidazole to scavenge any remaining copper.

(white solid, 105 mg, 54%)

^{1}H NMR (600 MHz, MeOD) δ 8.89 (s, 1H), 8.25 (d, *J* = 4.2 Hz, 1H), 8.04 – 7.92 (m, 2H), 7.91 – 7.86 (m, 1H), 7.72 – 7.65 (m, 1H), 7.54 – 7.45 (m, 3H), 7.44 – 7.23 (m, 9H), 6.24 – 6.15 (m, 2H), 5.63 – 5.56 (m, 1H), 5.20 – 5.15 (m, 1H), 5.10 – 5.04 (m, 2H), 4.67 – 4.53 (m, 5H), 4.52 – 4.43 (m, 3H), 4.41 – 4.32 (m, 2H), 4.00 – 3.42 (m, 14H), 3.26 – 3.17 (m, 2H), 2.50 – 2.39 (m, 4H), 2.26 – 2.12 (m, 2H), 2.02 – 1.93 (m, 3H), 1.72 – 1.28 (m, 6H), 0.99 – 0.92 (m, 9H). HRMS (ESI-QTOF) m/z [M + Na]+ calcd for $C_{66}H_{81}N_{13}O_{12}SNa$ 1302.5746; found 1302.5713. Purity *via* HPLC = 84.4%.

VHL-PROTAC-2 (Compound 10, EG-5-36)

Synthesized using *General Procedure D* (white solid, 109 mg, 47%)

^{1}H NMR (600 MHz, MeOD) δ 8.66 (s, 1H), 8.33 – 8.23 (m, 1H), 7.96 (d, *J* = 8.1 Hz, 2H), 7.90 (d, *J* = 7.3 Hz, 1H), 7.74 – 7.67 (m, 1H), 7.60 – 7.50 (m, 3H), 7.42 – 7.28 (m, 9H), 6.23 – 6.16 (m, 2H), 5.64 – 5.57 (m, 1H), 5.29 – 5.14 (m, 1H), 5.13 – 5.04 (m, 2H), 4.76 – 4.22 (m, 10H), 3.96 – 3.47 (m, 18H), 3.26 – 3.18 (m, 2H), 2.76 – 1.85 (m, 9H), 1.69 – 1.27 (m, 6H), 0.99 (s,

9H). HRMS (ESI-QTOF) m/z [M + Na]+ calcd for $C_{68}H_{85}N_{13}O_{13}SNa$ 1346.6008; found 1346.5962. Purity *via* HPLC = 84.3%.

VHL-PROTAC-3 (Compound 11, EG-5-37)

Synthesized using *General Procedure D* (white solid, 72 mg, 31%)

^{1}H NMR (600 MHz, MeOD) δ 8.70 (s, 1H), 8.30 – 8.21 (m, 1H), 8.14 – 7.95 (m, 2H), 7.90 (d, *J* = 7.4 Hz, 1H), 7.70 (t, *J* = 6.6 Hz, 1H), 7.56 – 7.48 (m, 3H), 7.44 – 7.24 (m, 9H), 6.27 – 6.13 (m, 2H), 5.67 – 5.57 (m, 1H), 5.18 (s, 1H), 5.12 – 5.04 (m, 2H), 4.72 – 4.30 (m, 10H), 4.03 – 3.52 (m, 22H), 3.26 – 3.19 (m, 2H), 2.62 – 2.32 (m, 5H), 2.25 – 2.15 (m, 2H), 2.11 – 1.99 (m, 2H), 1.71 – 1.30 (m, 6H), 1.02 (s, 9H). HRMS (ESI-QTOF) m/z [M + Na]+ calcd for $C_{70}H_{89}N_{13}O_{14}SNa$ 1390.6270; found 1390.6266. Purity *via* HPLC = 84.9%.

VHL-PROTAC-4 (Compound 12, EG-5-38)

Synthesized using *General Procedure D* (white solid, 64 mg, 53%)

^{1}H NMR (600 MHz, MeOD) δ 8.83 (s, 1H), 8.29 – 8.22 (m, 1H), 8.15 – 7.94 (m, 2H), 7.90 (d, *J* = 7.3 Hz, 1H), 7.70 (t, *J* = 6.3 Hz, 1H), 7.58 – 7.47 (m, 3H), 7.46 – 7.24 (m, 9H), 6.25 – 6.14 (m, 2H), 5.64 – 5.57 (m, 1H), 5.23 – 5.15 (m, 1H), 5.09 – 5.03 (m, 2H), 4.70 – 4.29 (m, 10H), 4.06 – 3.44 (m, 26H), 3.27 – 3.18 (m, 2H), 2.61 – 2.35 (m, 5H), 2.25 – 2.18 (m, 2H), 2.10 – 1.97 (m, 2H), 1.73 – 1.27 (m, 6H), 1.02 (s, 9H). HRMS (ESI-QTOF) m/z [M + Na]+ calcd for $C_{72}H_{93}N_{13}O_{15}SNa$ 1434.6533; found 1434.6508. Purity *via* HPLC = 85.7%.

IAP-PROTAC-1 (Compound 31, EG-5-58-2)

Synthesized using *General Procedure E* (white solid, mg, %)

^{1}H NMR (600 MHz, d_6-DMSO) δ 9.65 – 9.57 (m, 1H), 8.93 – 8.87 (m, 1H), 8.81 (d, *J* = 8.1 Hz, 2H), 8.53 (d, *J* = 8.7 Hz, 1H), 8.47 – 8.41 (m, 2H), 8.26 – 8.21 (m, 1H), 8.19 – 8.13 (m, 1H), 8.05 – 7.95 (m, 3H), 7.64 (d, *J* = 6.9 Hz, 1H), 7.59 – 7.51 (m, 4H), 7.40 – 7.26 (m, 6H), 7.18 – 7.11 (m, 1H), 7.11 – 7.04 (m, 2H), 6.28 – 6.16 (m, 1H), 6.13 – 6.02 (m, 1H), 5.59 – 5.50 (m, 1H), 5.10 – 4.90 (m, 4H), 4.62 – 4.52 (m, 2H), 4.48 – 4.29 (m, 6H), 4.07 – 3.98 (m, 1H), 3.89 – 3.79 (m, 6H), 3.67 – 3.41 (m, 10H), 3.14 – 3.06 (m, 2H), 2.77 – 2.64 (m, 2H), 2.44 (t, *J* = 5.4 Hz, 3H), 2.41 – 2.27 (m, 3H), 2.06 – 1.95 (m, 1H), 1.92 – 1.76 (m, 6H), 1.73 – 1.53 (m, 8H), 1.41 – 1.29 (m, 6H), 1.17 – 1.11 (m, 2H), 1.06 – 0.99 (m, 2H). HRMS (ESI-QTOF) m/z [M + Na]+ calcd for $C_{71}H_{92}N_{14}O_{12}Na$ 1355.6917; found 1355.6942. Purity *via* HPLC = 86.2%.

IAP-PROTAC-2 (Compound 32, EG-5-59-2)

Synthesized using *General Procedure E* (white solid, mg, %)

^{1}H NMR (600 MHz, d_6-DMSO) δ 9.73 – 9.65 (m, 1H), 8.94 – 8.89 (m, 1H), 8.81 (d, *J* = 7.8 Hz, 2H), 8.54 – 8.44 (m, 2H), 8.38 (d, *J* = 8.4 Hz, 1H), 8.27 – 8.14 (m, 2H), 8.01 (d, *J* = 8.3 Hz, 1H), 7.99 – 7.94 (m, 1H), 7.93 – 7.88 (m, 1H), 7.64 (d, *J* = 7.0 Hz, 1H), 7.58 – 7.50 (m, 4H), 7.40 – 7.26 (m, 6H), 7.18 – 7.02 (m, 3H), 6.31 – 6.16 (m, 1H), 6.13 – 6.00 (m, 1H), 5.59 – 5.50 (m, 1H), 5.11 – 4.86 (m, 4H), 4.49 – 4.39 (m, 4H), 4.39 – 4.29 (m, 4H), 4.01 (dd, *J* = 10.1, 6.4 Hz, 1H), 3.85 – 3.76 (m, 6H), 3.72 – 3.47 (m, 14H), 3.13 – 3.07 (m, 2H), 2.79 – 2.64 (m, 2H), 2.43 (t, *J* = 5.4 Hz, 3H), 2.41 – 2.25 (m, 3H), 2.06 – 1.98 (m, 1H), 1.92 – 1.76 (m, 6H), 1.73 – 1.52 (m, 8H), 1.43 – 1.29 (m, 6H), 1.18 – 1.10 (m, 2H), 1.07 – 0.98 (m, 2H). HRMS (ESI-QTOF) m/z [M + H]+ calcd for $C_{73}H_{97}N_{14}O_{13}$ 1377.7360; found 1377.7354. Purity *via* HPLC = 86.3%.

IAP-PROTAC-3 (Compound 33, EG-5-60-2)

Synthesized using *General Procedure E* (white solid, mg, %)

^{1}H NMR (600 MHz, d_6-DMSO) δ 9.80 – 9.72 (m, 1H), 8.97 – 8.91 (m, 1H), 8.85 – 8.78 (m, 2H), 8.53 – 8.46 (m, 2H), 8.37 (d, *J* = 8.4 Hz, 1H), 8.27 – 8.16 (m, 2H), 8.01 (d, *J* = 8.3 Hz, 1H), 7.98 – 7.94 (m, 1H), 7.94 – 7.89 (m, 1H), 7.65 (d, *J* = 6.9 Hz, 1H), 7.60 – 7.48 (m, 4H), 7.42 – 7.25 (m, 6H), 7.18 – 7.03 (m, 3H), 6.28 – 6.18 (m, 1H), 6.08 – 6.03 (m, 1H), 5.57 – 5.50 (m, 1H), 5.08 – 4.90 (m, 4H), 4.51 – 4.41 (m, 4H), 4.38 – 4.29 (m, 4H), 4.06 – 4.00 (m, 1H), 3.92 – 3.39 (m, 24H), 3.18 – 3.04 (m, 2H), 2.79 – 2.64 (m, 2H), 2.43 (t, *J* = 5.4 Hz, 3H), 2.40 – 2.26 (m, 3H), 2.07 – 1.97 (m, 1H), 1.94 – 1.77 (m, 6H), 1.73 – 1.51 (m, 8H), 1.42 – 1.30 (m, 6H), 1.18 – 1.11 (m, 2H), 1.07 – 0.99 (m, 2H). HRMS (ESI-QTOF) m/z [M + H]+ calcd for $C_{75}H_{101}N_{14}O_{14}$ 1421.7622; found 1421.7646. Purity *via* HPLC = 82.2%.

IAP-PROTAC-4 (Compound 34, EG-5-61-2)

Synthesized using *General Procedure E* (white solid, mg, %)

^{1}H NMR (600 MHz, d_6-DMSO) δ 9.47 – 9.39 (m, 1H), 8.91 – 8.85 (m, 1H), 8.80 (d, *J* = 7.7 Hz, 2H), 8.51 – 8.41 (m, 2H), 8.35 (d, *J* = 8.4 Hz, 1H), 8.27 – 8.21 (m, 1H), 8.16 – 8.08 (m, 1H), 8.01 (d, *J* = 8.3 Hz, 1H), 7.99 – 7.95 (m, 1H), 7.94 – 7.89 (m, 1H), 7.64 (d, *J* = 7.0 Hz, 1H), 7.58 – 7.51 (m, 4H), 7.39 – 7.26 (m, 6H), 7.17 – 7.05 (m, 3H), 6.26 – 6.15 (m, 1H), 6.10 – 6.02 (m, 1H), 5.57 – 5.51 (m, 1H), 5.06 – 4.89 (m, 4H), 4.50 – 4.40 (m, 4H), 4.40 – 4.30 (m, 4H), 4.07 – 3.99 (m, 1H), 3.89 – 3.41 (m, 28H), 3.14 – 3.05 (m, 2H), 2.80 – 2.64 (m, 2H), 2.45 (t, *J* = 5.4 Hz, 3H), 2.40 – 2.25 (m, 3H), 2.05 – 1.97 (m, 1H), 1.93 – 1.76 (m, 6H), 1.73 – 1.53 (m, 8H), 1.42 – 1.30 (m, 6H), 1.19 – 1.12 (m, 2H), 1.06 – 0.98 (m, 2H). HRMS (ESI-QTOF) m/z [M + Na]+ calcd for $C_{77}H_{104}N_{14}O_{15}Na$ 1487.7703; found 1487.7704. Purity *via* HPLC = 86.8%.

Lenalidomide-PROTAC-1 (Compound 17, EG-5-49)

Synthesized using *General Procedure D* (white solid, 24 mg, 36%)

^{1}H NMR (600 MHz, $CDCl_3$) δ 10.38 – 10.02 (m, 1H), 8.52 – 8.34 (m, 1H), 8.28 – 8.16 (m, 2H), 7.95 – 7.89 (m, 1H), 7.89 – 7.83 (m, 1H), 7.76 – 7.65 (m, 1H), 7.64 – 7.60 (m, 2H), 7.56 – 7.39 (m, 5H), 7.35 – 7.28 (m, 6H), 6.29 – 6.16 (m, 2H), 6.13 – 6.03 (m, 1H), 5.95 – 5.78 (m, 1H), 5.61 – 5.51 (m, 1H), 5.26 – 5.16 (m, 1H), 5.14 – 5.02 (m, 3H), 4.73 – 4.55 (m, 3H), 4.55 – 4.39 (m, 3H), 4.11 – 3.44 (m, 13H), 3.33 – 3.22 (m, 2H), 2.82 – 2.61 (m, 2H), 2.60 – 2.50 (m, 1H), 2.48 – 2.38 (m, 1H), 2.27 – 2.13 (m, 1H), 2.09 – 1.99 (m, 2H), 1.87 – 1.76 (m, 1H), 1.71 – 1.47 (m, 4H), 1.44 – 1.28 (m, 2H). HRMS (ESI-QTOF) m/z [M + Na]+ calcd for $C_{57}H_{64}N_{12}O_{12}Na$ 1131.4664; found 1131.4630. Purity *via* HPLC = 92.1%.

Lenalidomide-PROTAC-2 (Compound 18, EG-5-50)

Synthesized using *General Procedure D* (white solid, 70 mg, 28%)

^{1}H NMR (600 MHz, $CDCl_3$) δ 9.85 – 9.72 (m, 1H), 8.68 – 8.61 (m, 1H), 8.25 (dd, *J* = 6.5, 3.5 Hz, 1H), 7.87 (t, *J* = 7.3 Hz, 1H), 7.84 – 7.80 (m, 1H), 7.78 – 7.69 (m, 2H), 7.67 – 7.58 (m, 3H), 7.50 – 7.45 (m, 3H), 7.44 – 7.36 (m, 2H), 7.34 – 7.27 (m, 5H), 6.56 – 6.27 (m, 1H), 6.25 – 6.17 (m, 1H), 6.11 – 5.91 (m, 2H), 5.57 – 5.47 (m, 1H), 5.21 (t, *J* = 9.5 Hz, 1H), 5.14 – 5.00 (m, 3H), 4.67 – 4.48 (m, 2H), 4.44 – 4.32 (m, 3H), 4.31 – 4.19 (m, 2H), 4.01 – 3.91 (m, 2H), 3.79 – 3.41 (m, 14H), 3.29 – 3.16 (m, 2H), 2.73 – 2.59 (m, 2H), 2.47 – 2.41 (m, 1H), 2.41 – 2.32 (m, 1H), 2.31 – 2.08 (m, 2H), 2.04 – 1.98 (m, 1H), 1.89 – 1.76 (m, 1H), 1.65 – 1.28 (m, 6H). HRMS (ESI-QTOF) m/z [M + Na]+ calcd for $C_{59}H_{68}N_{12}O_{13}Na$ 1175.4927; found 1175.4928. Purity *via* HPLC = 94.5%.

Lenalidomide-PROTAC-3 (Compound 19, EG-5-51)

Synthesized using *General Procedure D* (white solid, 161 mg, 53%)

^{1}H NMR (600 MHz, $CDCl_3$) δ 9.88 – 9.69 (m, 1H), 9.13 – 8.99 (m, 1H), 8.30 – 8.20 (m, 1H), 7.91 – 7.77 (m, 2H), 7.70 – 7.56 (m, 5H), 7.54 – 7.44 (m, 3H), 7.43 – 7.34 (m, 2H), 7.34 – 7.25 (m, 5H), 6.60 – 6.33 (m, 1H), 6.19 (dd, *J* = 17.1, 1.5 Hz, 1H), 6.15 – 5.94 (m, 2H), 5.62 – 5.43 (m, 1H), 5.28 – 5.18 (m, 1H), 5.16 – 5.01 (m, 3H), 4.71 – 4.46 (m, 2H), 4.38 – 4.29 (m, 3H), 4.26 – 4.16 (m, 2H), 4.15 – 4.04 (m, 2H), 3.86 – 3.44 (m, 14H), 3.39 – 3.33 (m, 4H), 3.26 – 3.16 (m, 2H), 2.73 – 2.59 (m, 2H), 2.50 – 2.41 (m, 1H), 2.40 – 2.31 (m, 1H), 2.25 – 2.11 (m, 2H), 2.04 – 1.98 (m, 1H), 1.92 – 1.82 (m, 1H), 1.69 – 1.26 (m, 6H). HRMS (ESI-QTOF) m/z [M + Na]+ calcd for $C_{61}H_{72}N_{12}O_{14}Na$ 1219.5189; found 1219.5166. Purity *via* HPLC = 93.2%.

Lenalidomide-PROTAC-4 (Compound 20, EG-5-52)

Synthesized using *General Procedure D* (white solid, 64 mg, 52%)

^{1}H NMR (600 MHz, $CDCl_3$) δ 9.83 – 9.66 (m, 1H), 9.24 – 9.14 (m, 1H), 8.30 – 8.23 (m, 1H), 7.91 – 7.85 (m, 1H), 7.85 – 7.80 (m, 1H), 7.72 – 7.57 (m, 5H), 7.53 – 7.44 (m, 3H), 7.43 – 7.36 (m, 2H), 7.34 – 7.27 (m, 5H), 6.52 – 6.26 (m, 1H), 6.24 – 6.17 (m, 1H), 6.13 – 6.01 (m, 1H), 5.97 – 5.89 (m, 1H), 5.58 – 5.47 (m, 1H), 5.30 – 5.20 (m, 1H), 5.16 – 5.03 (m, 3H), 4.72 – 4.49 (m, 2H), 4.42 – 4.34 (m, 3H), 4.33 – 4.28 (m, 2H), 4.18 – 4.05 (m, 2H), 3.79 – 3.69 (m, 4H), 3.68 – 3.56 (m, 9H), 3.52 – 3.39 (m, 5H), 3.33 – 3.21 (m, 6H), 2.74 – 2.64 (m, 2H), 2.51 – 2.46 (m, 1H), 2.43 – 2.33 (m, 1H), 2.30 – 2.20 (m, 1H), 2.17 – 2.11 (m, 1H), 2.06 – 1.99 (m, 1H), 1.94 – 1.83 (m, 1H), 1.66 – 1.29 (m, 6H). HRMS (ESI-QTOF) m/z [M + Na]+ calcd for $C_{63}H_{76}N_{12}O_{15}Na$ 1263.5451; found 1263.5486. Purity *via* HPLC = 94.9%.

Supplementary Kinetic Traces:

Compound	Alias	Kinetic Curve	**Estimated k_{inact}/K_I ± SD ($\times 10^3$ $M^{-1}min^{-1}$)
9 (EG-5-35)	VHL PROTAC 1	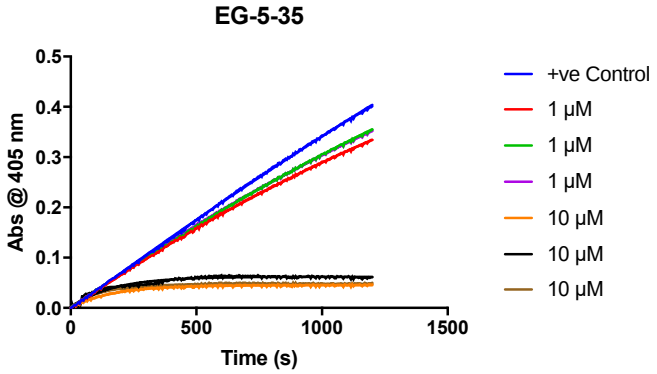	231 ± 35
10 (EG-5-36)	VHL PROTAC 2	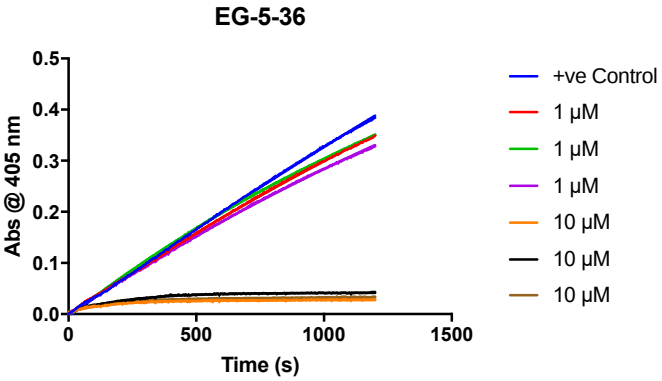	228 ± 71
11 (EG-5-37)	VHL PROTAC 3	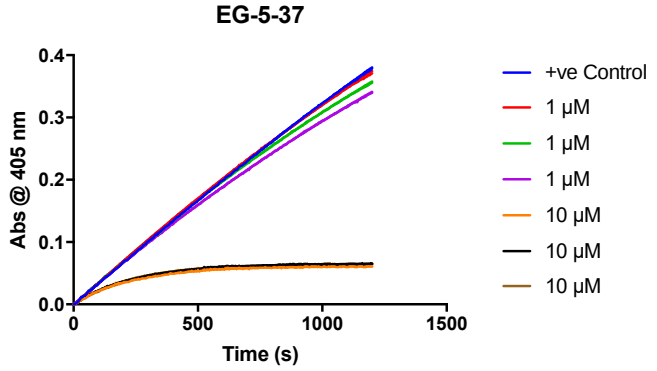	222 ± 32

12 (EG-5-38)	VHL PROTAC 4	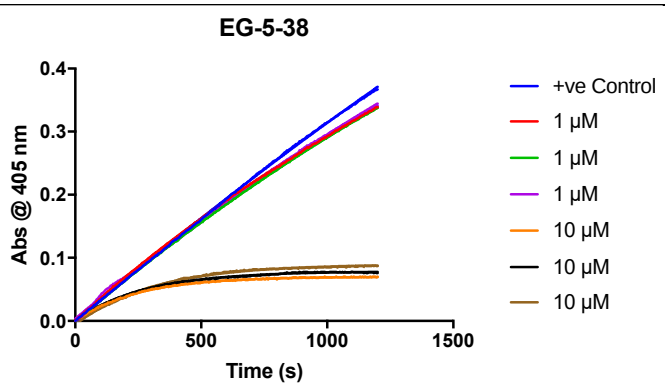	226 ± 51
17 (EG-5-49)	Lenalidomide PROTAC 1	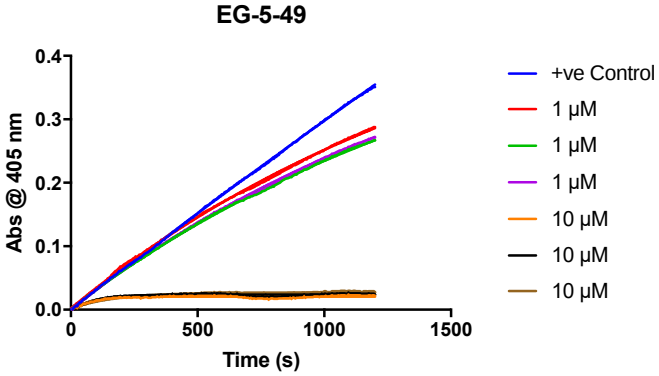	380 ± 14
18 (EG-5-50)	Lenalidomide PROTAC 2	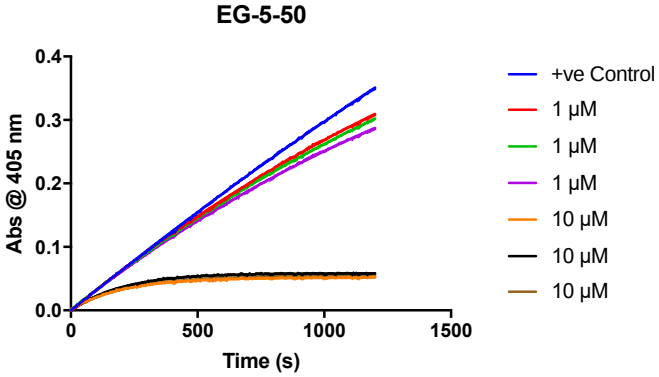	300 ± 27
19 (EG-5-51)	Lenalidomide PROTAC 3	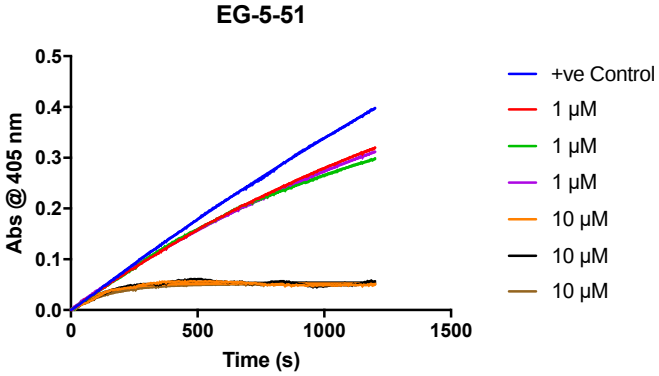	431 ± 115

20 (EG-5-52)	Lenalidomide PROTAC 4	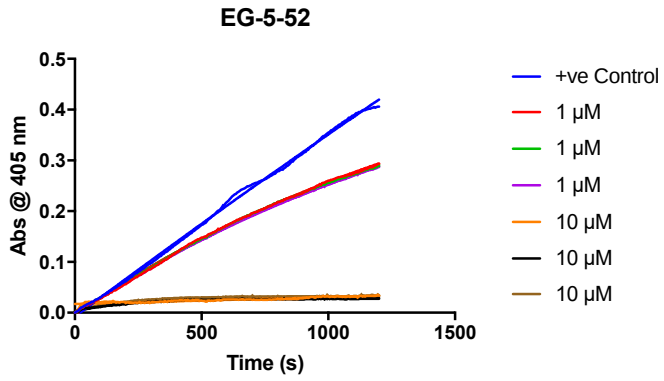	397 ± 10
31 (EG-5-58)	IAP PROTAC 1	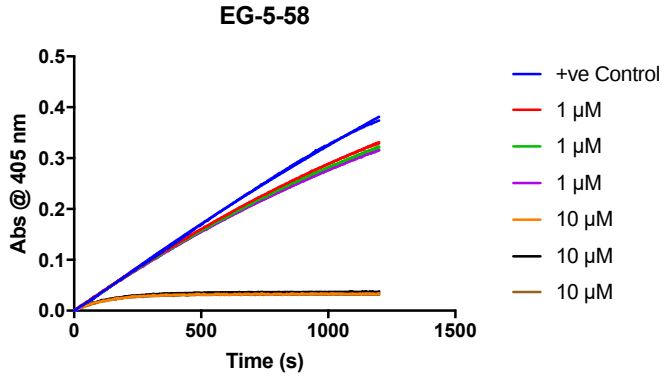	325 ± 14
32 (EG-5-59)	IAP PROTAC 2	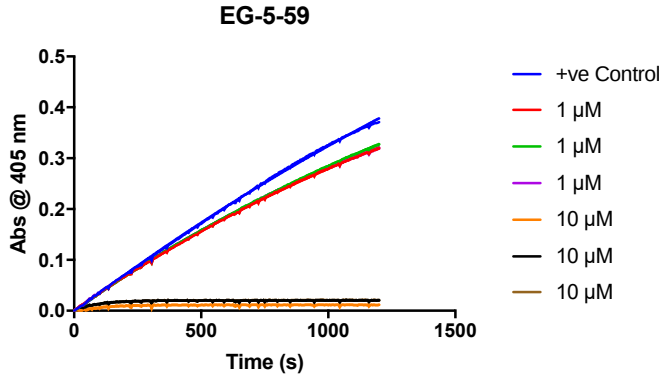	313 ± 21
33 (EG-5-60)	IAP PROTAC 3	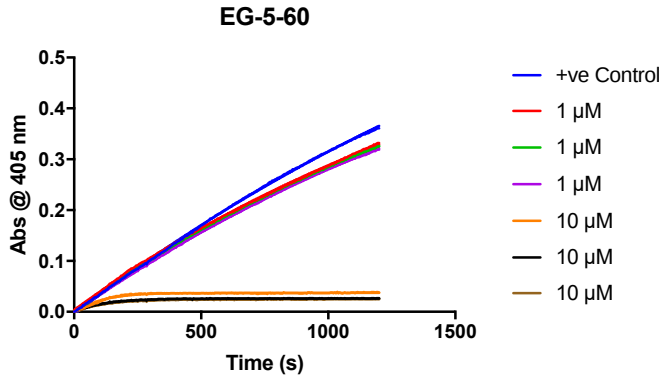	339 ± 19

34 (EG-5-61)	IAP PROTAC 4	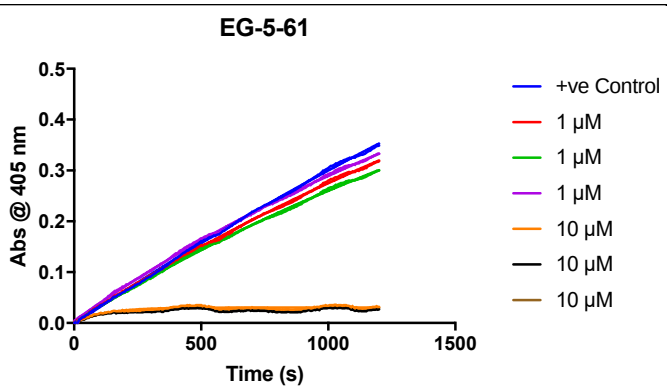	257 ± 33

** k_{inact}/K_I values were approximated by using one low [I] such that [I]<<K_I. This allows for simplification of the formula where $(k_{obs}/[I])(\alpha) = k_{inact}/K_I$. Here, we are assuming that 1 µM <<K_I

NMR Spectra of Intermediates and Final Compounds:

Fmoc Deprotection of IAP Ligand (Compound 22, EG-5-28)*:*

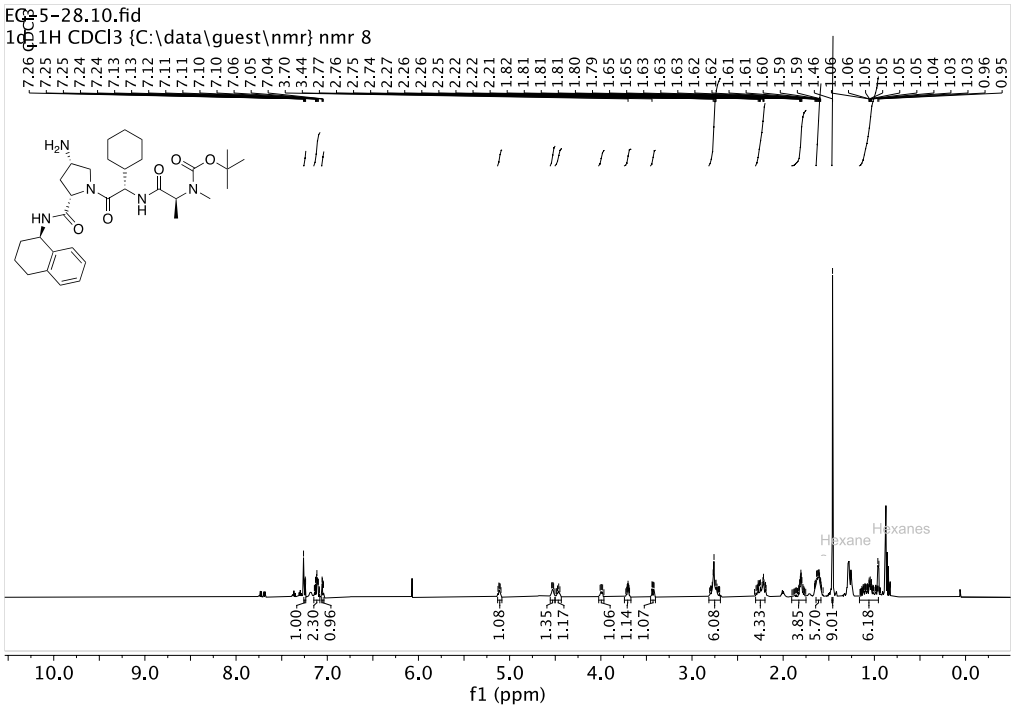

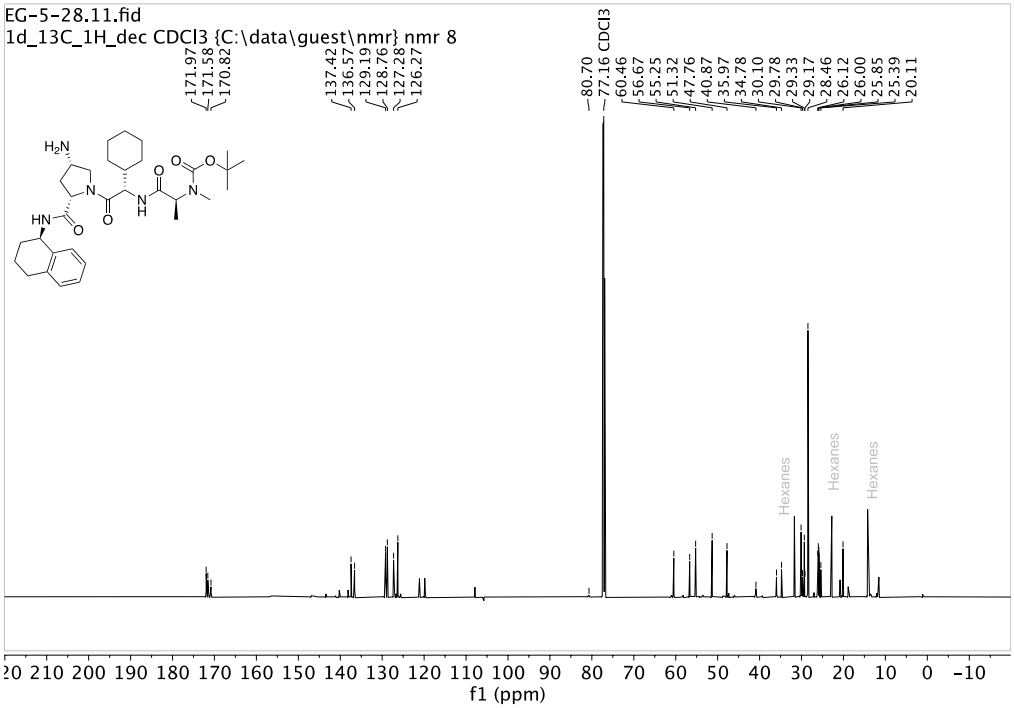

Propargylated Inhibitor (Compound EG-5-34)

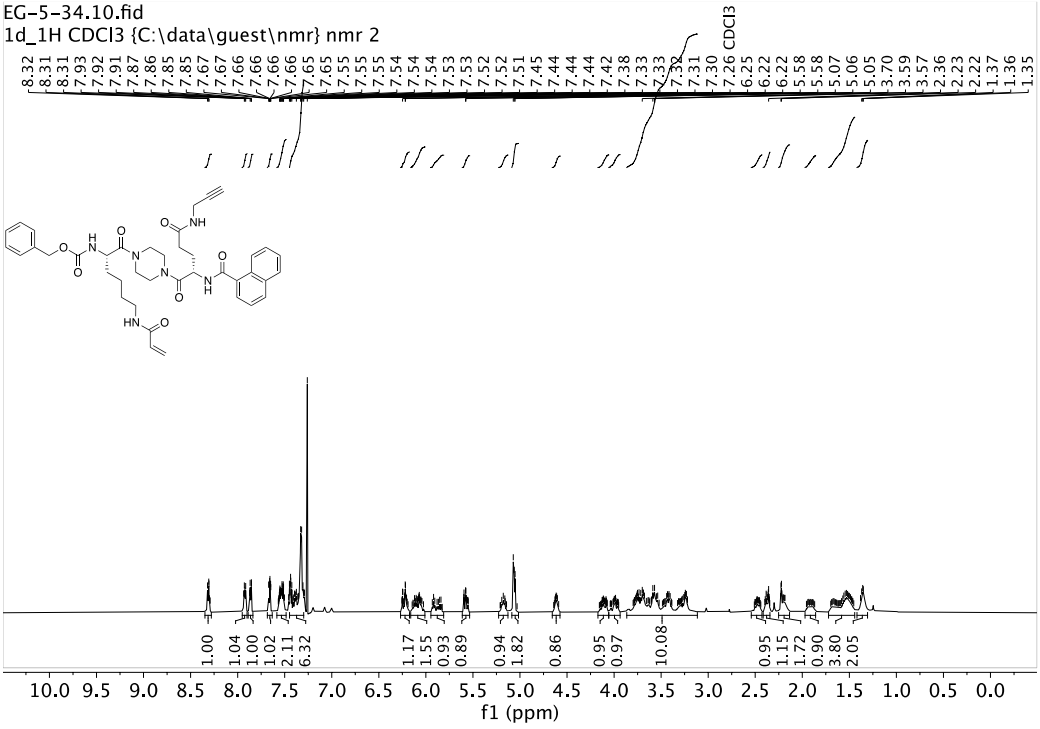

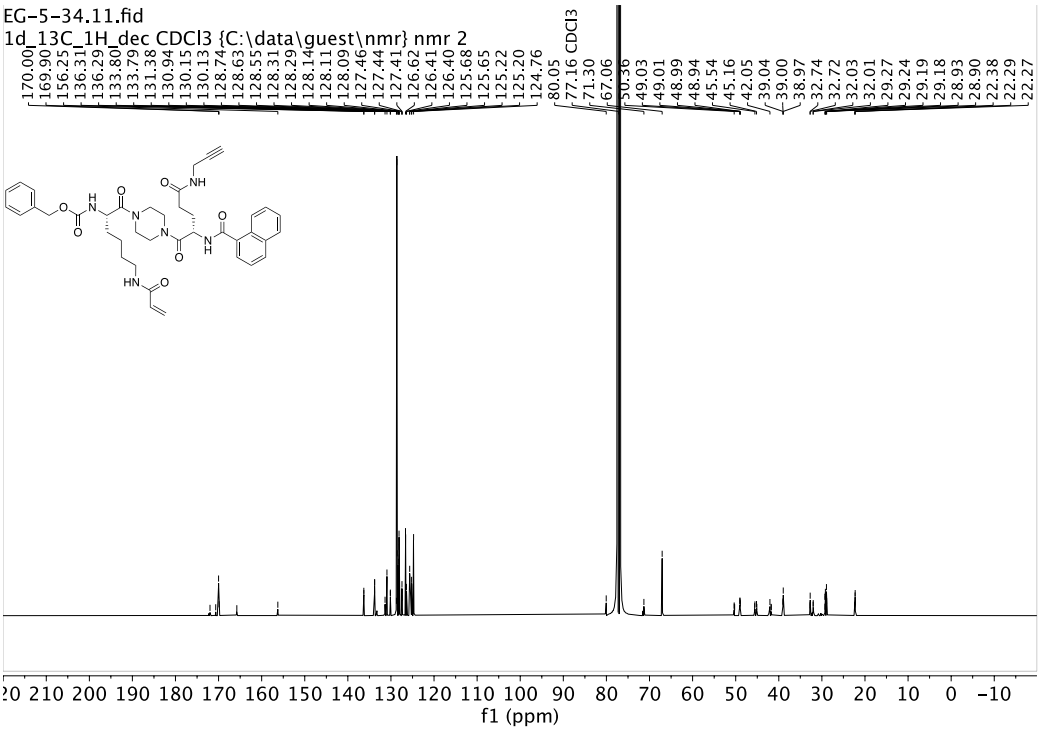

Azide-PEG1-VHL (Compound 5, EG-5-17)

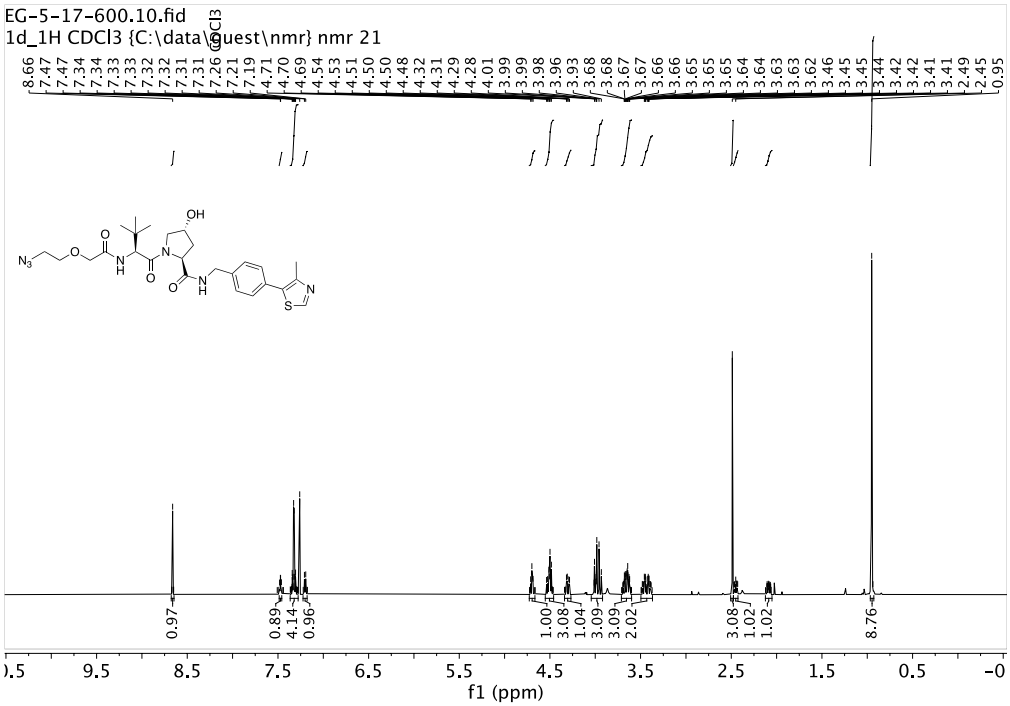

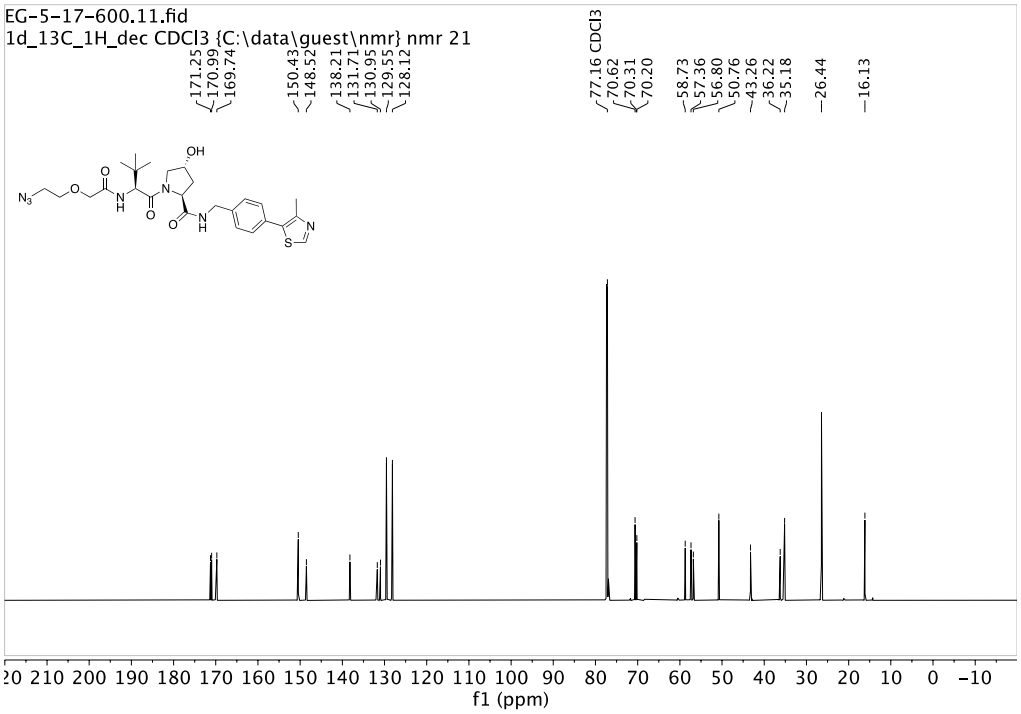

Azide-PEG2-VHL (Compound 6, EG-5-18)

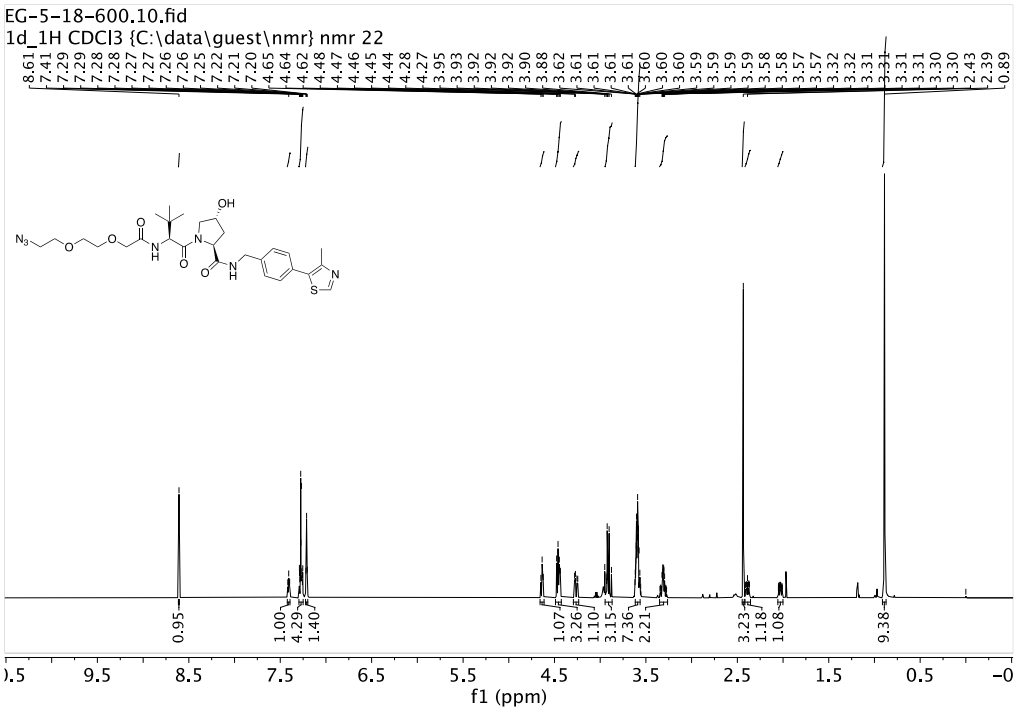

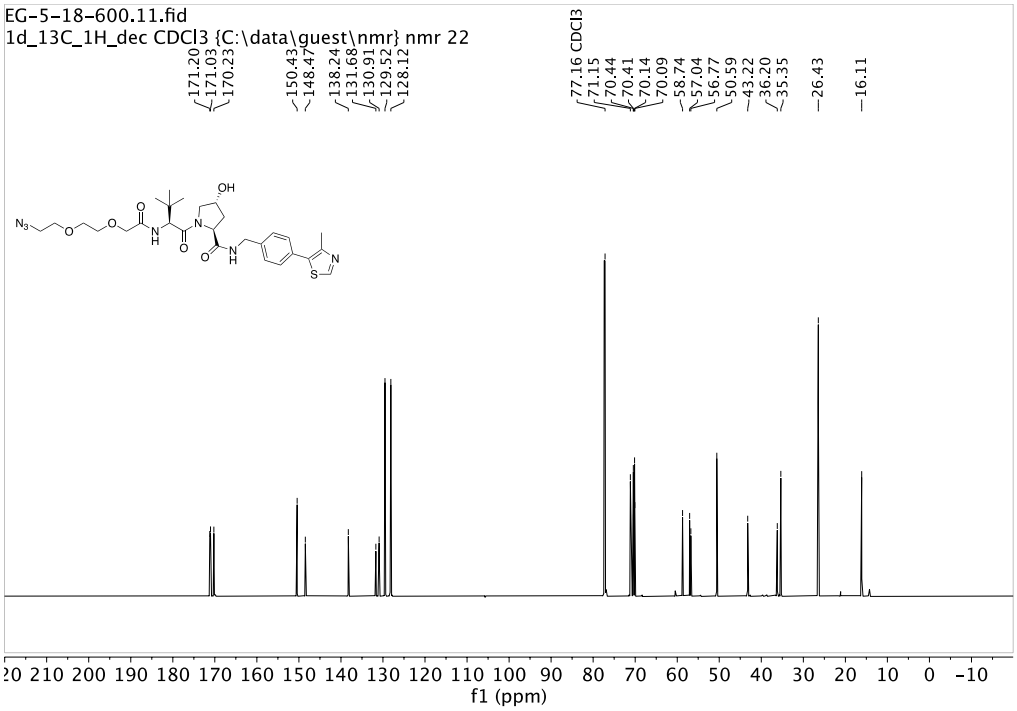

Azide-PEG3-VHL (Compound 7, EG-5-19)

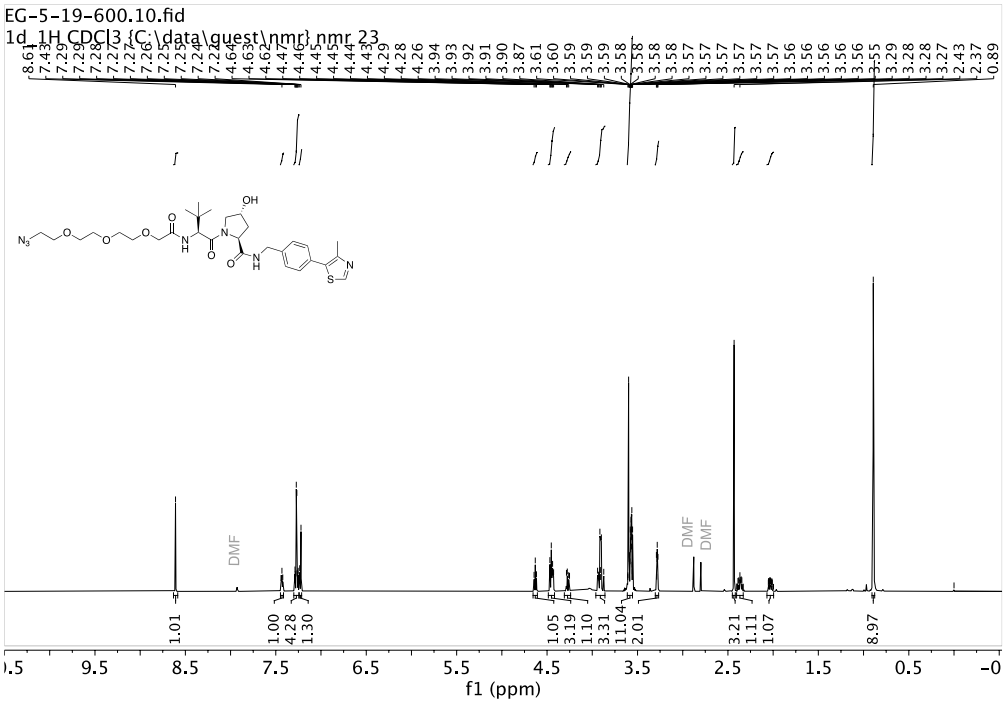

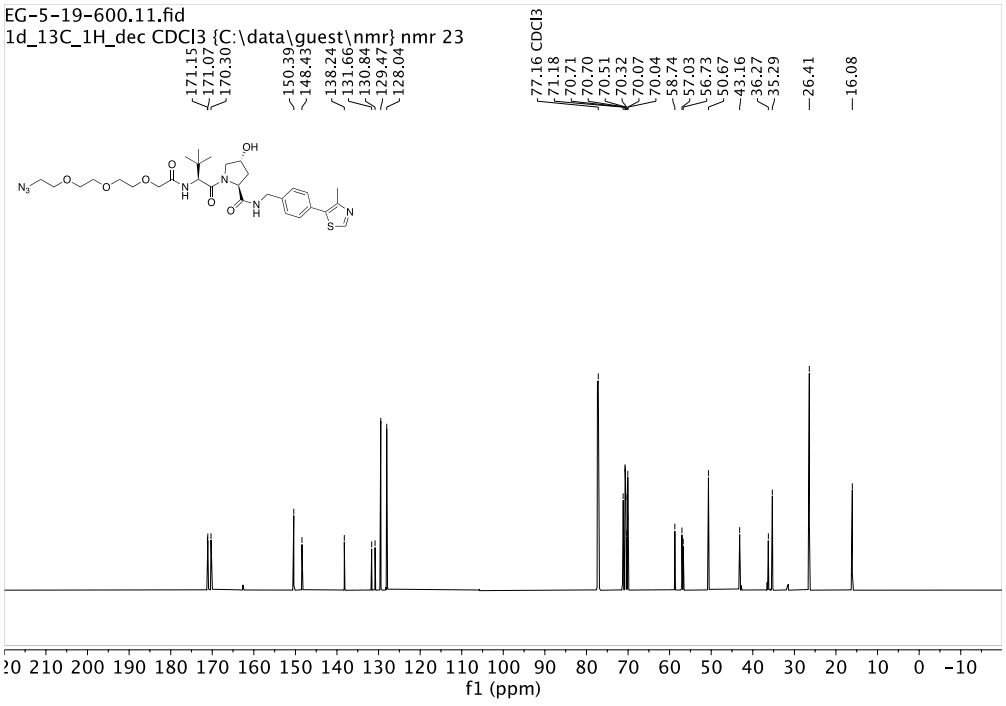

Azide-PEG4-VHL (Compound 8, EG-5-20)

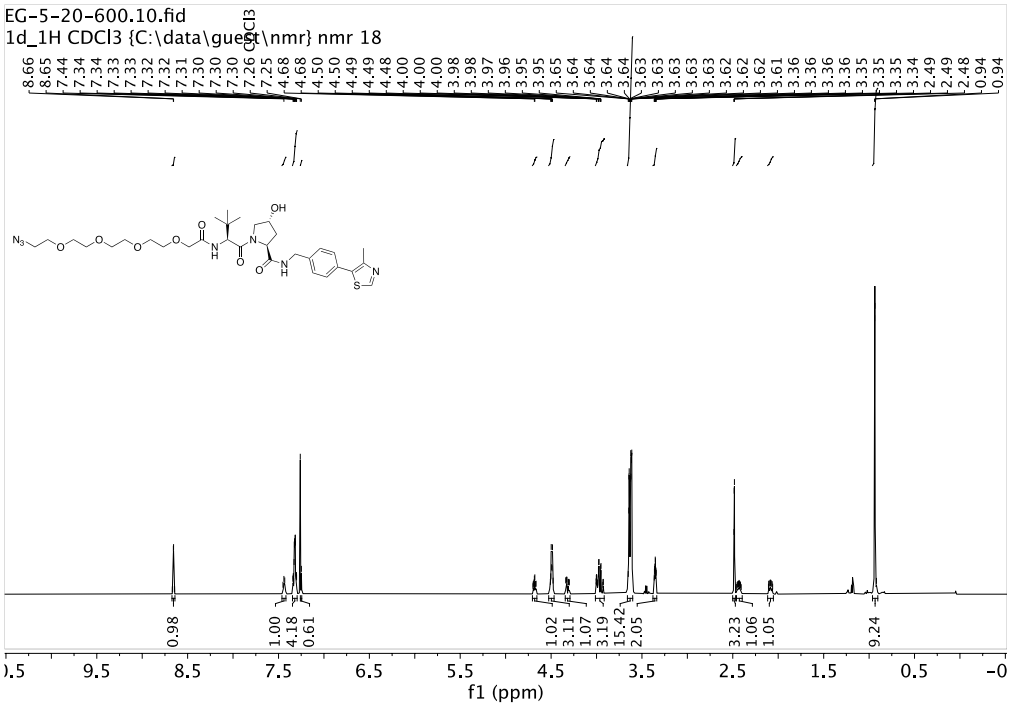

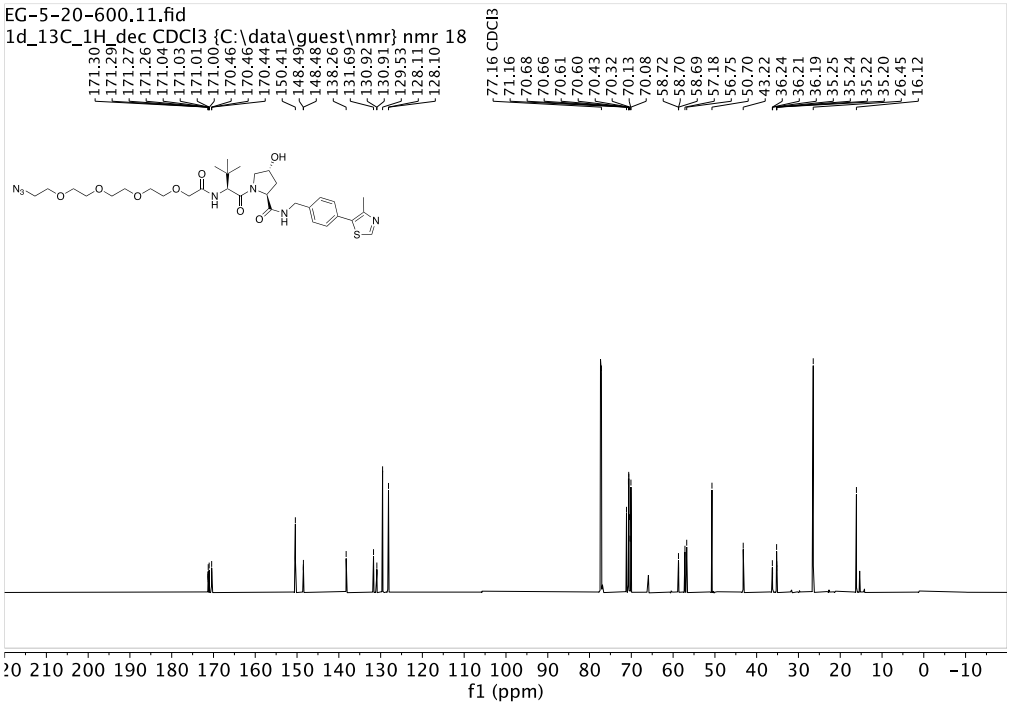

Azide-PEG1-IAP (Compound 23, EG-5-29)

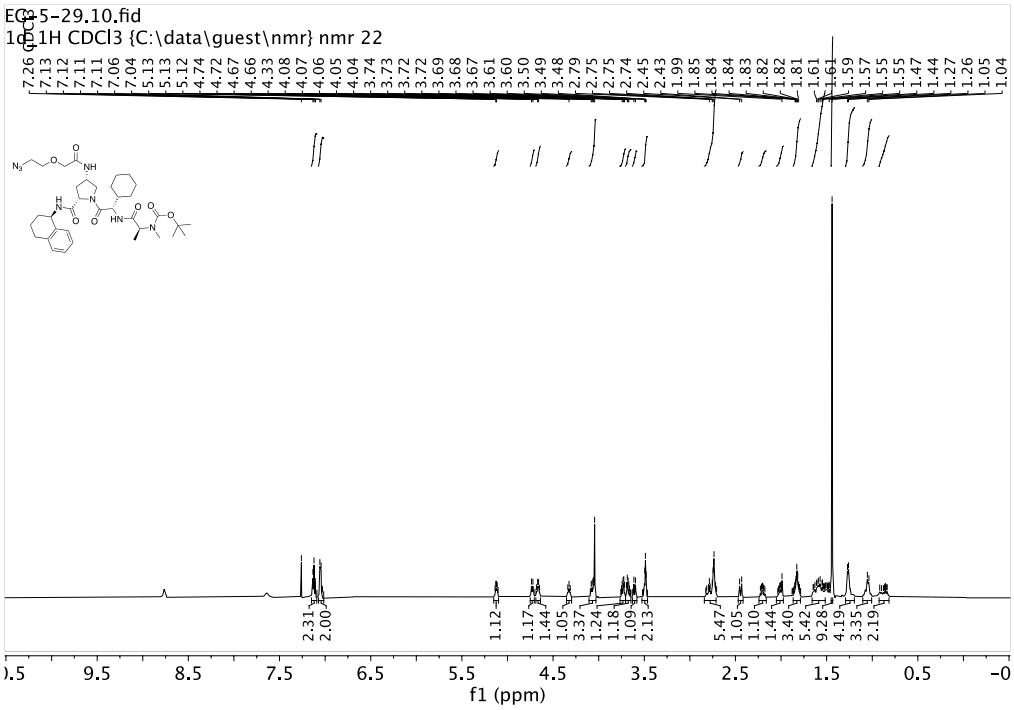

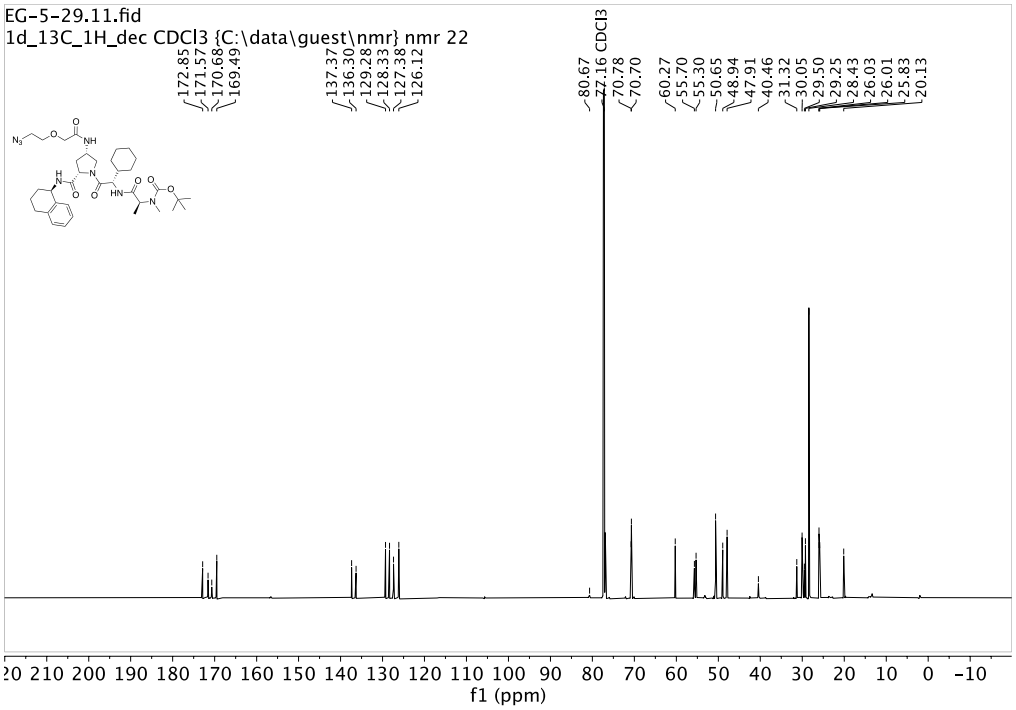

Azide-PEG2-IAP (Compound 24, EG-5-30)

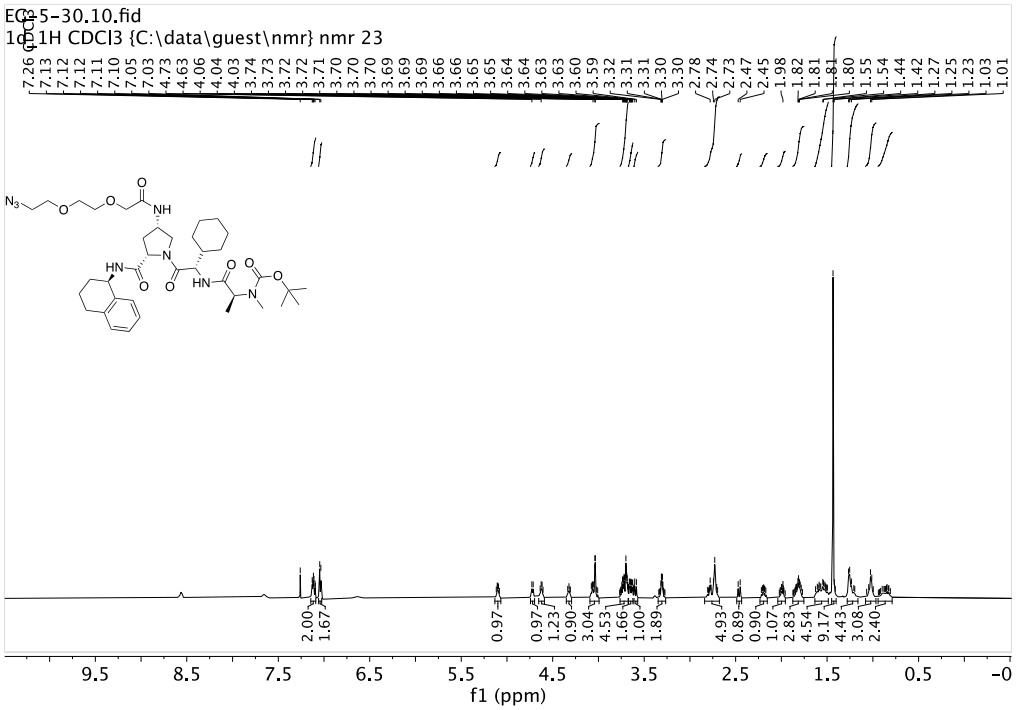

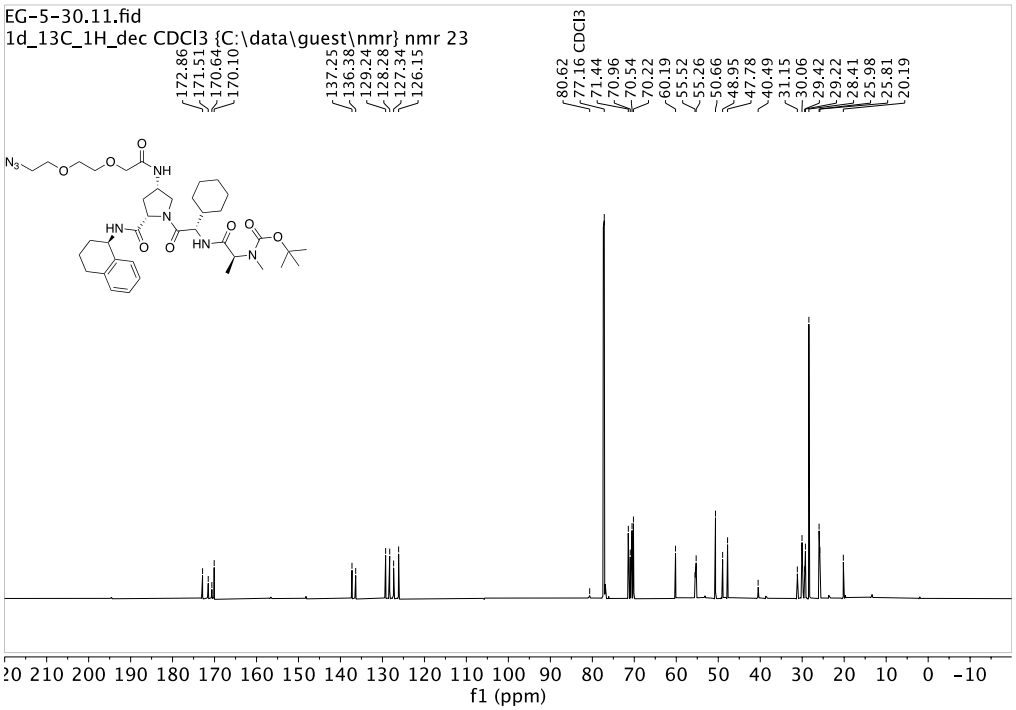

Azide-PEG3-IAP (Compound 25, EG-5-31)

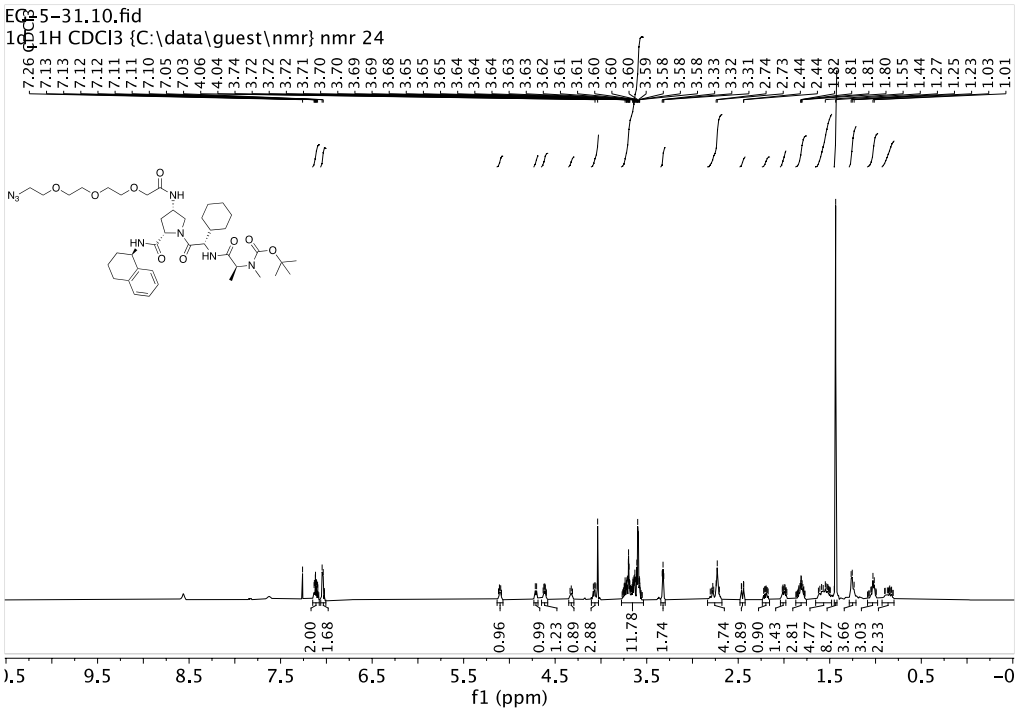

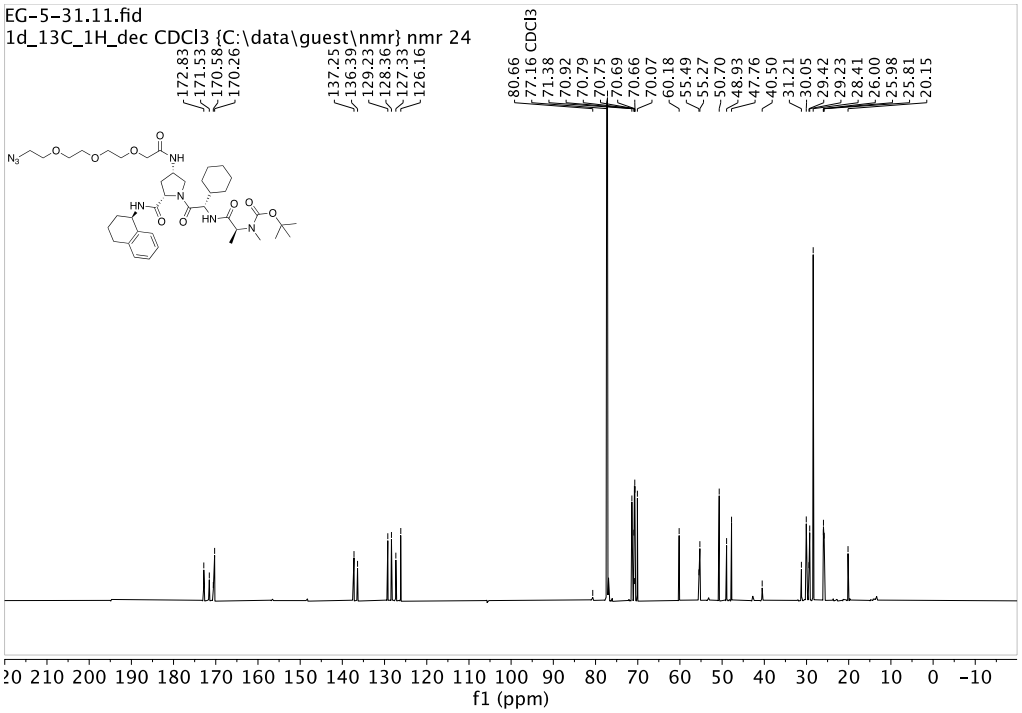

Azide-PEG4-IAP (Compound 26, EG-5-26/EG-5-32)

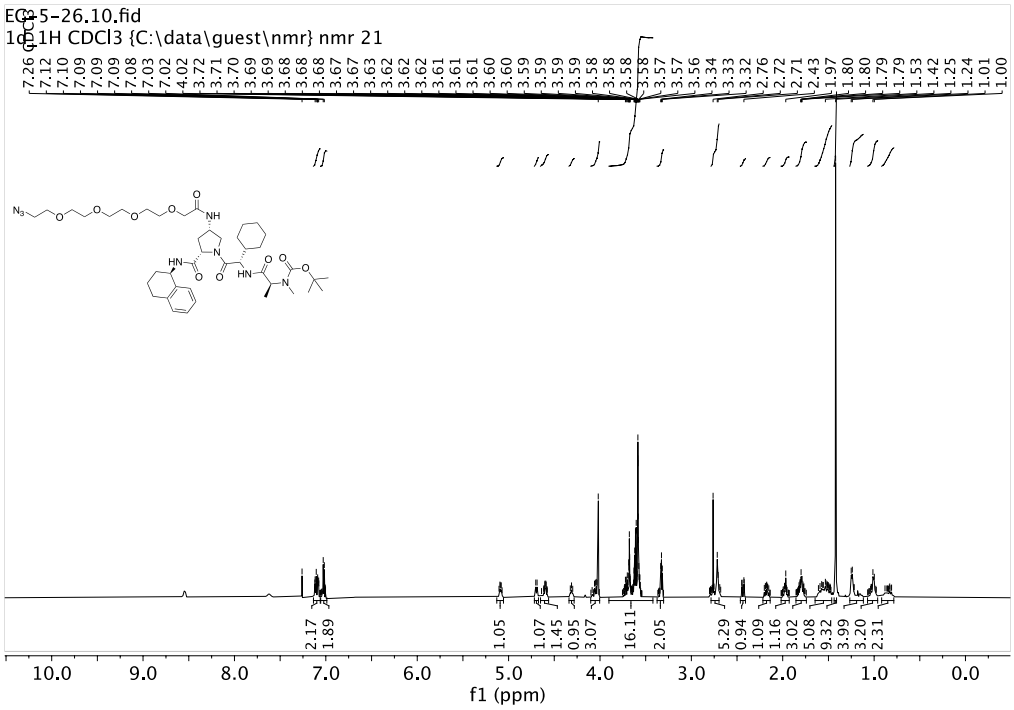

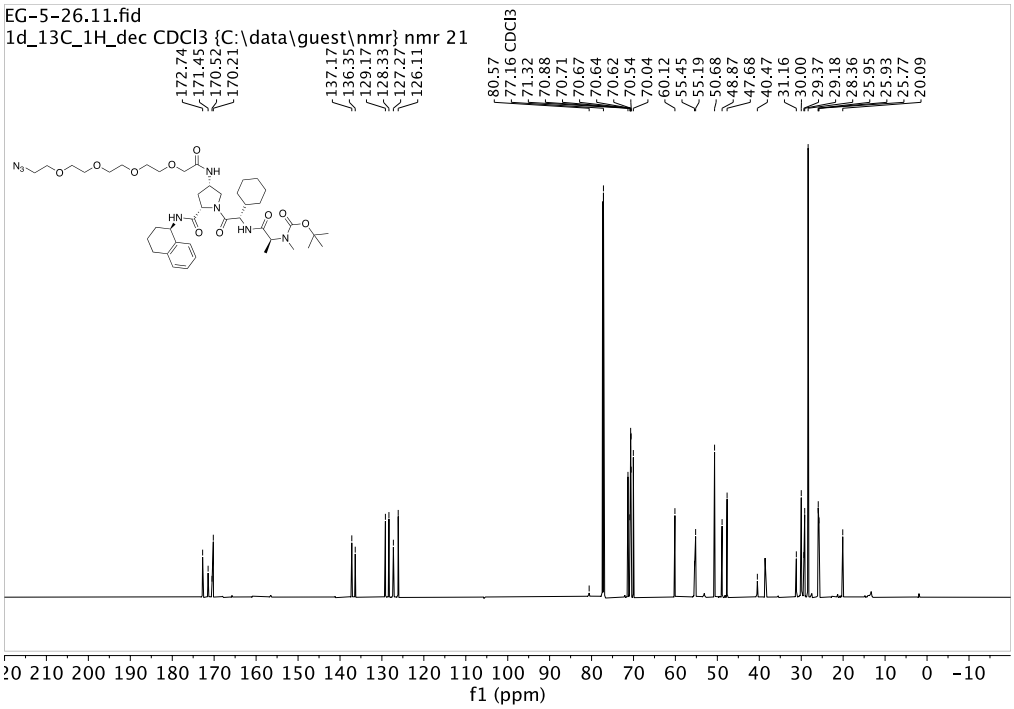

Azide-PEG1-Lenalidomide (Compound 13, EG-5-39)

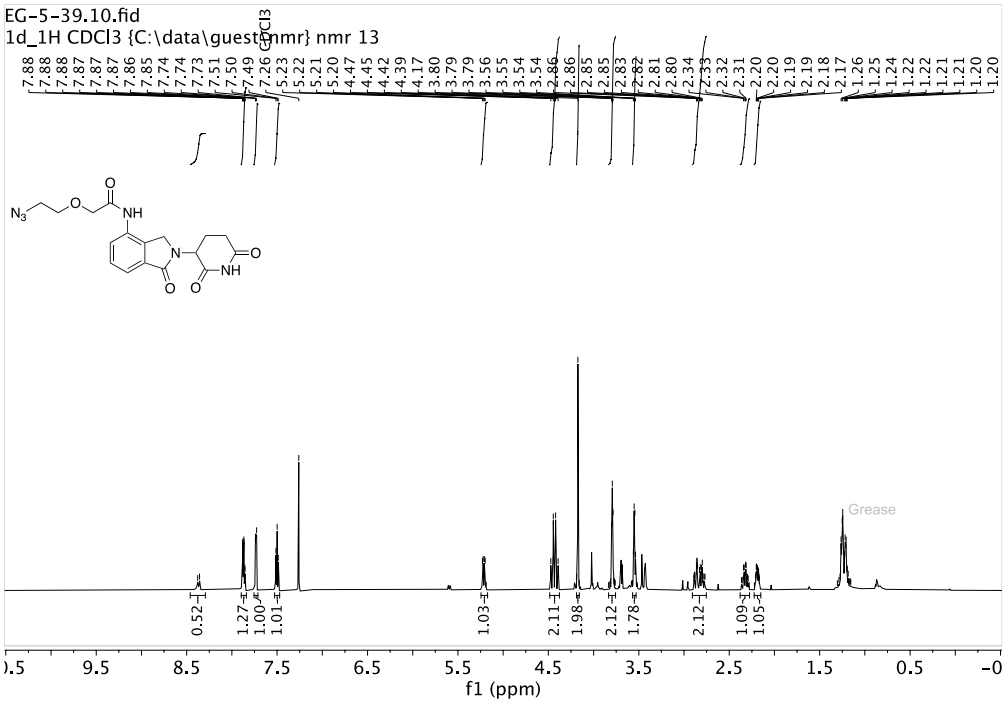

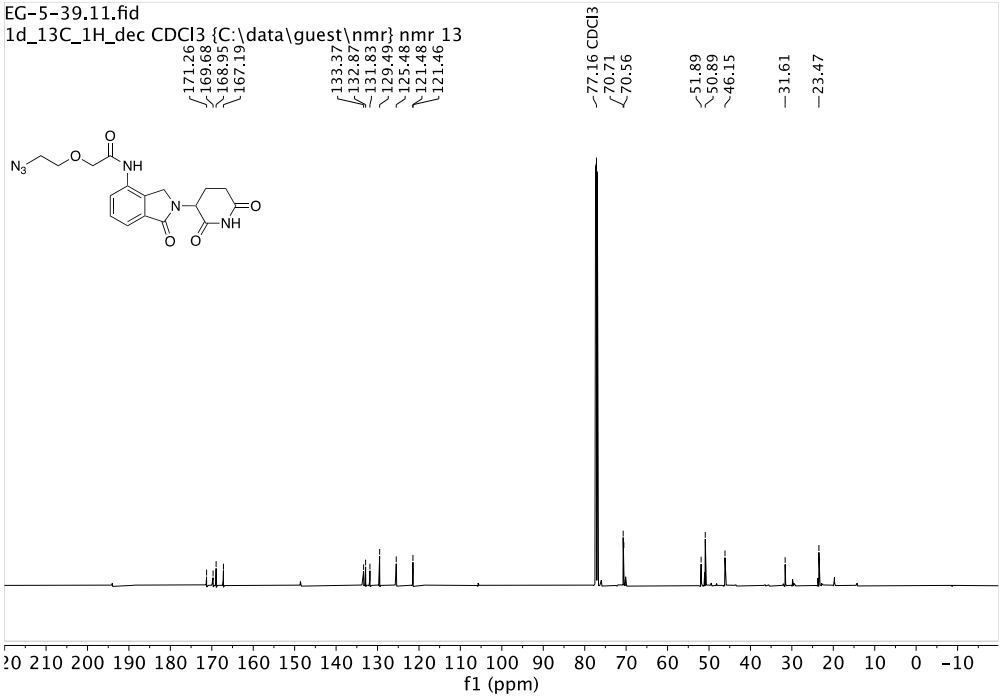

Azide-PEG2-Lenalidomide (Compound 14, EG-5-40)

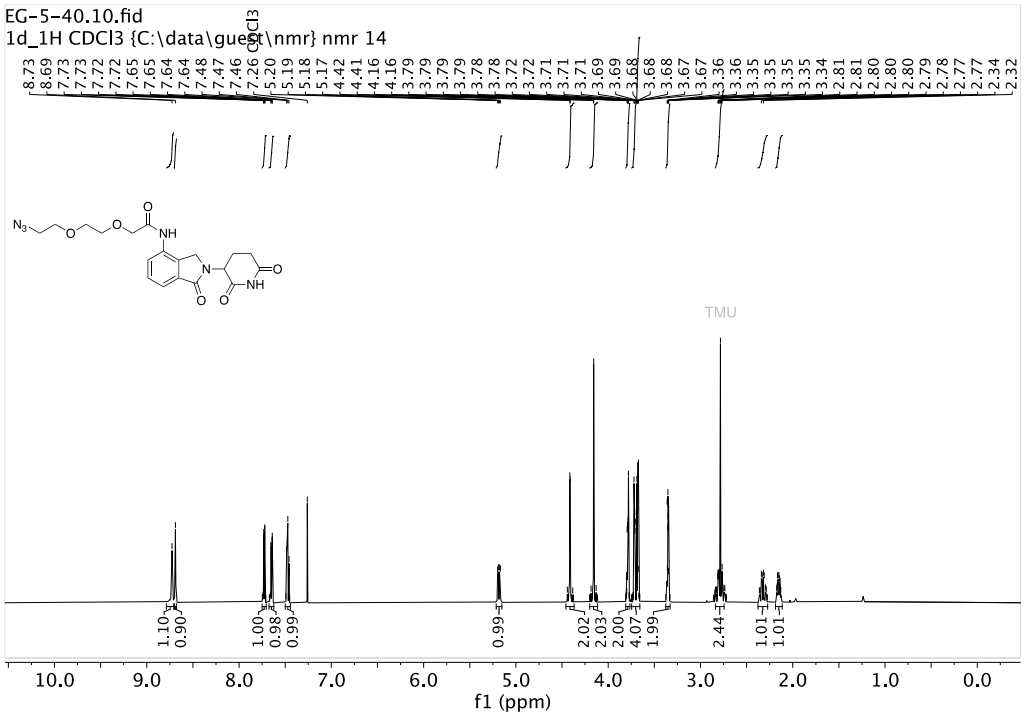

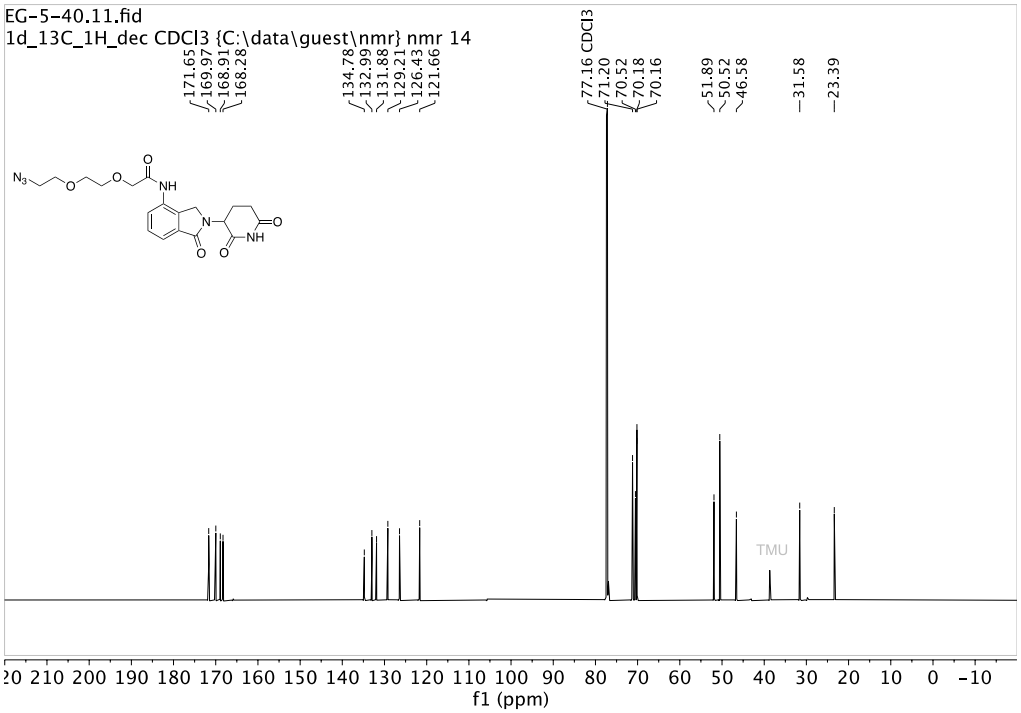

Azide-PEG3-Lenalidomide (Compound 15, EG-5-41)

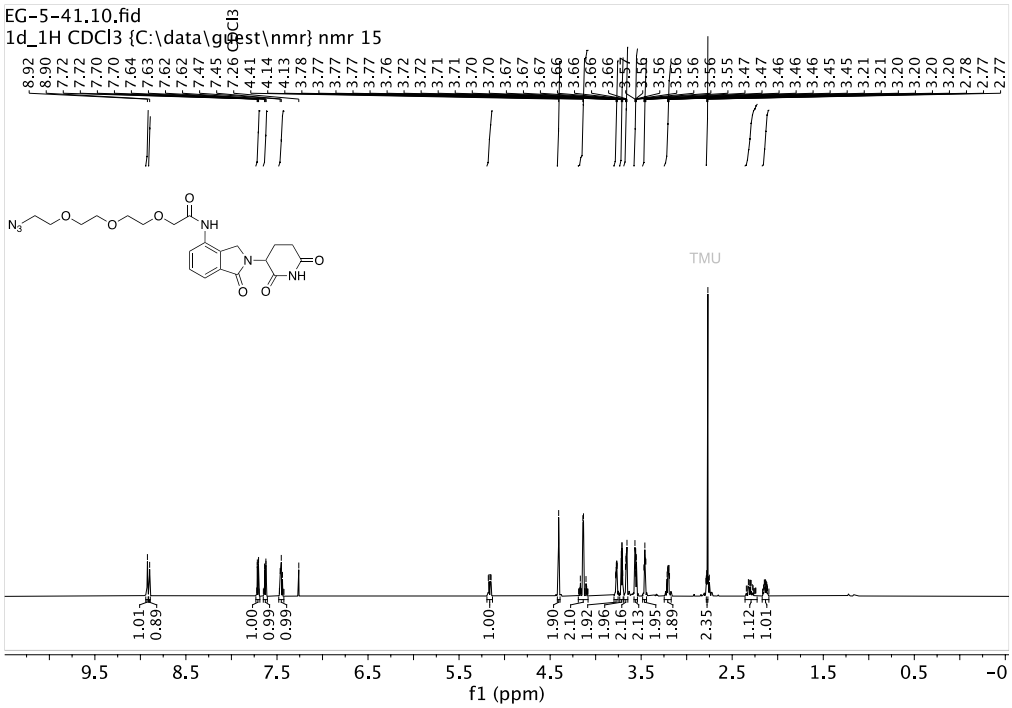

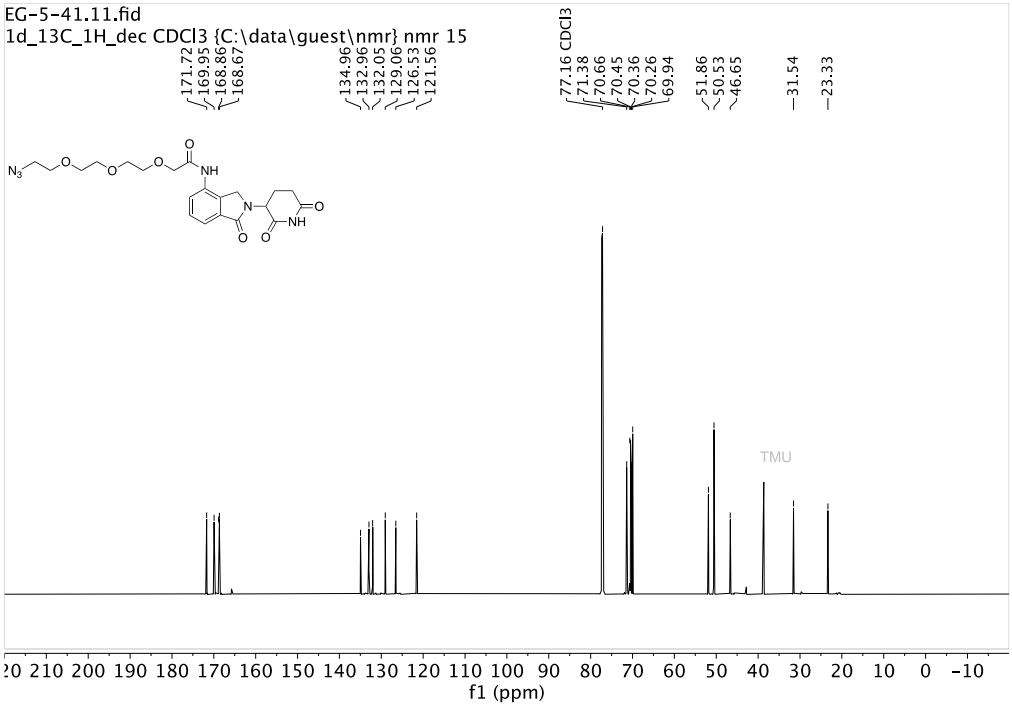

Azide-PEG4-Lenalidomide (Compound 16, EG-5-42)

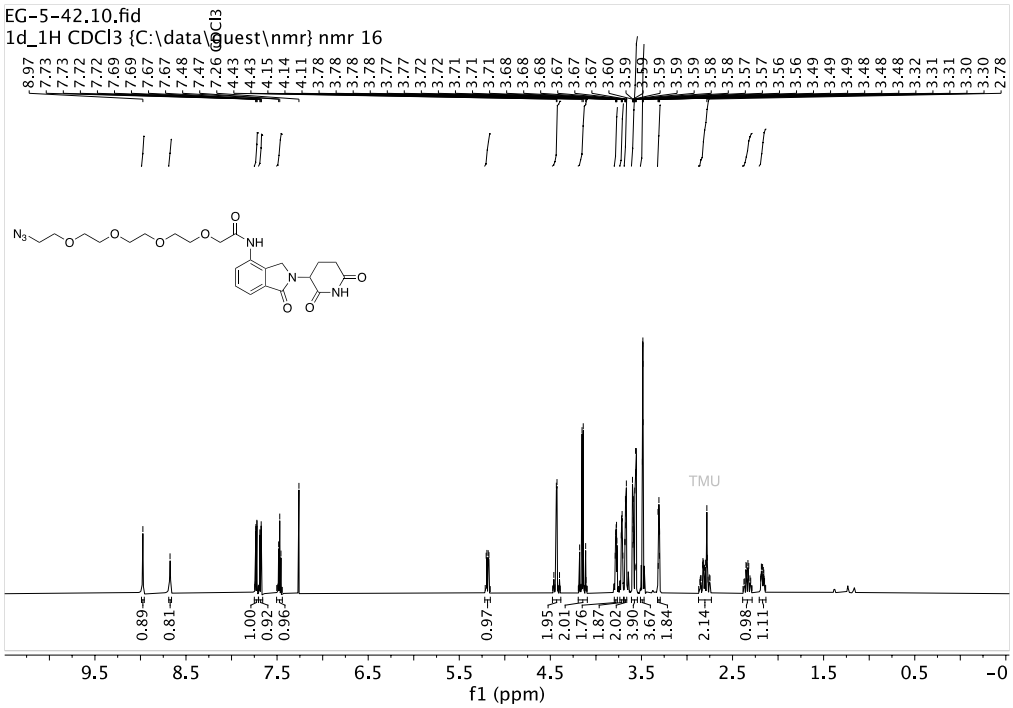

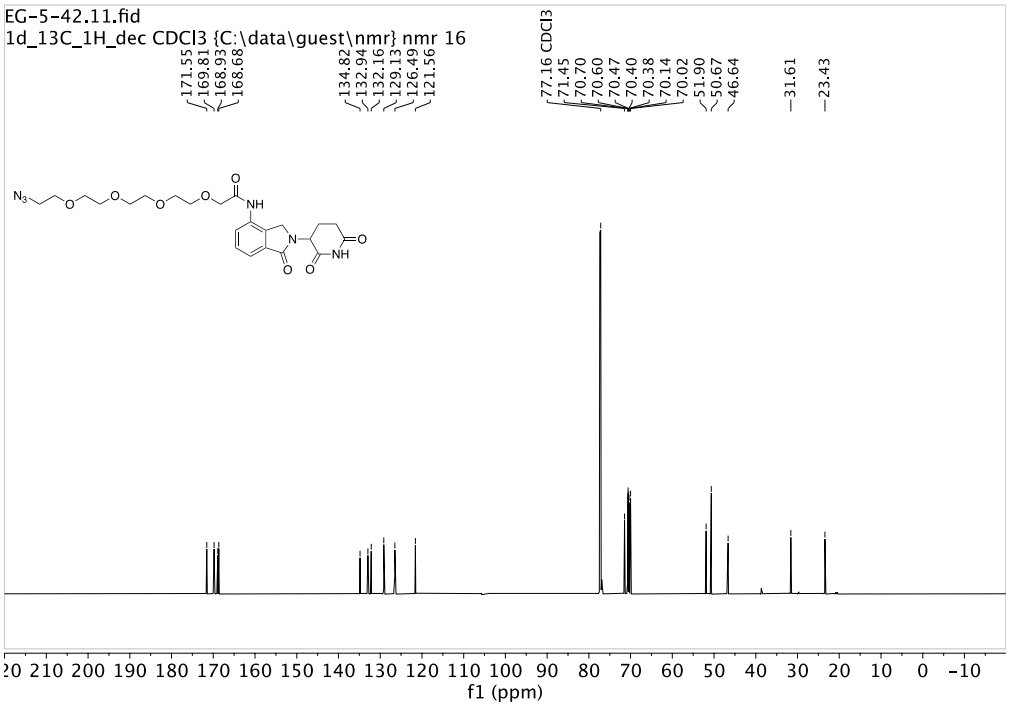

Boc-IAP-PEG1-TG2Ligand (Compound 27, EG-5-43-2)

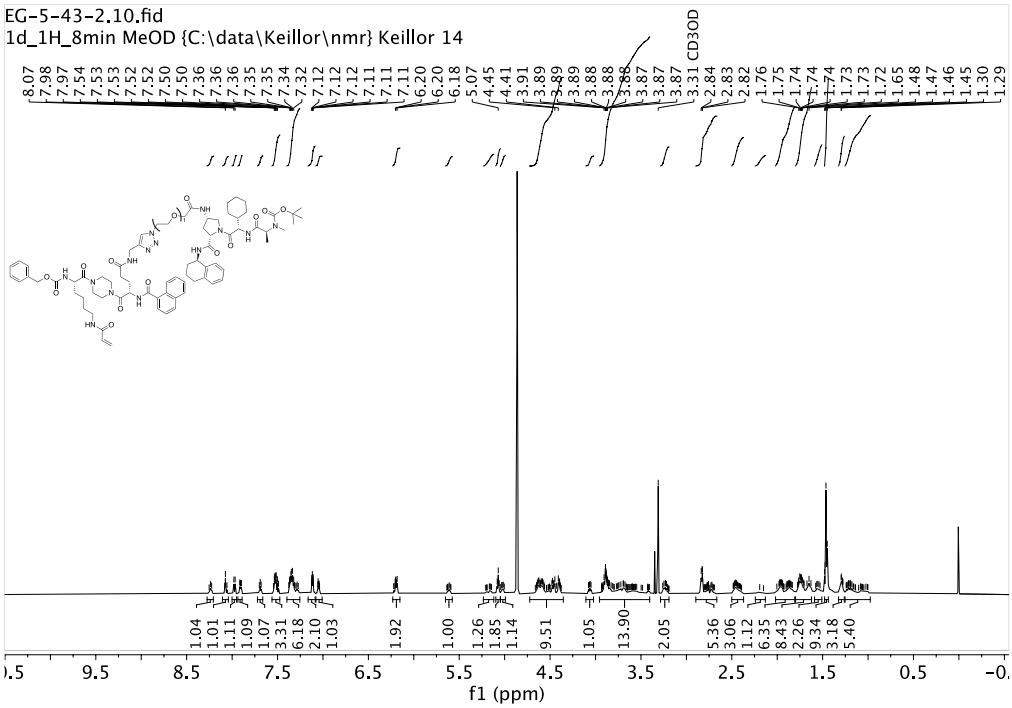

Boc-IAP-PEG2-TG2Ligand (Compound 28, EG-5-44-2)

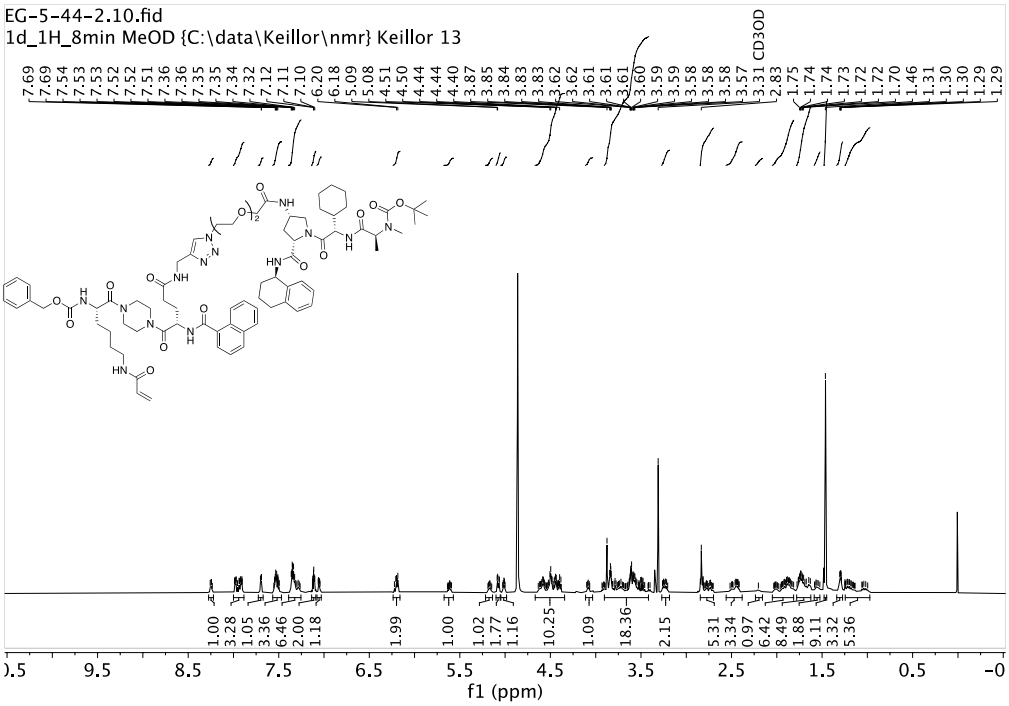

Boc-IAP-PEG3-TG2Ligand (Compound 29, EG-5-45-2)

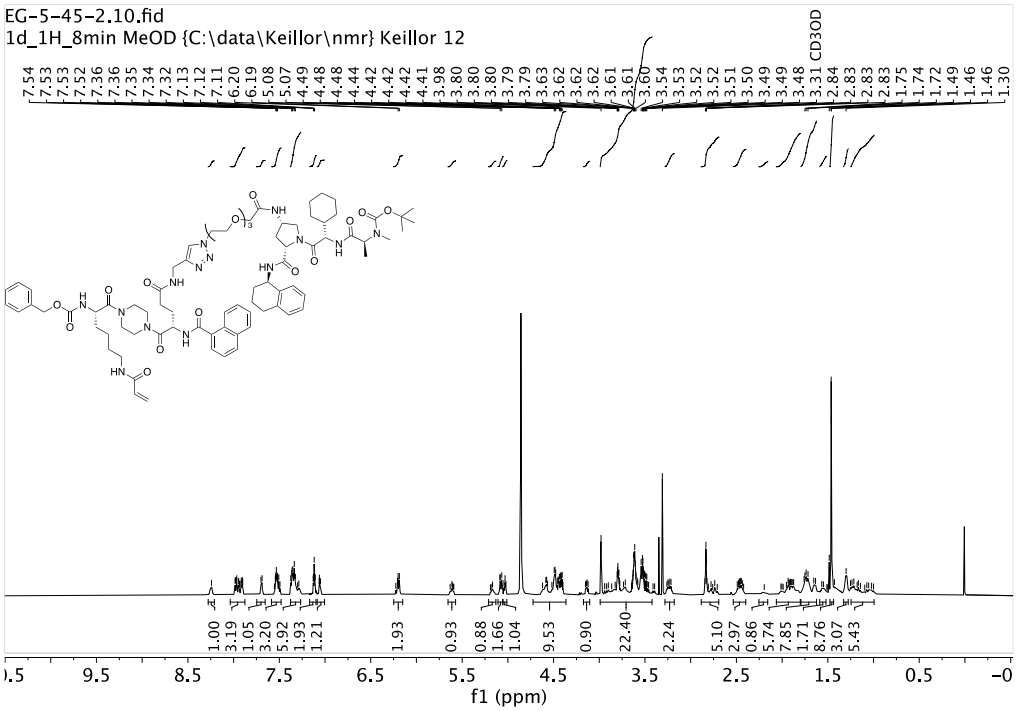

Boc-IAP-PEG4-TG2Ligand (Compound 30, EG-5-46-2)

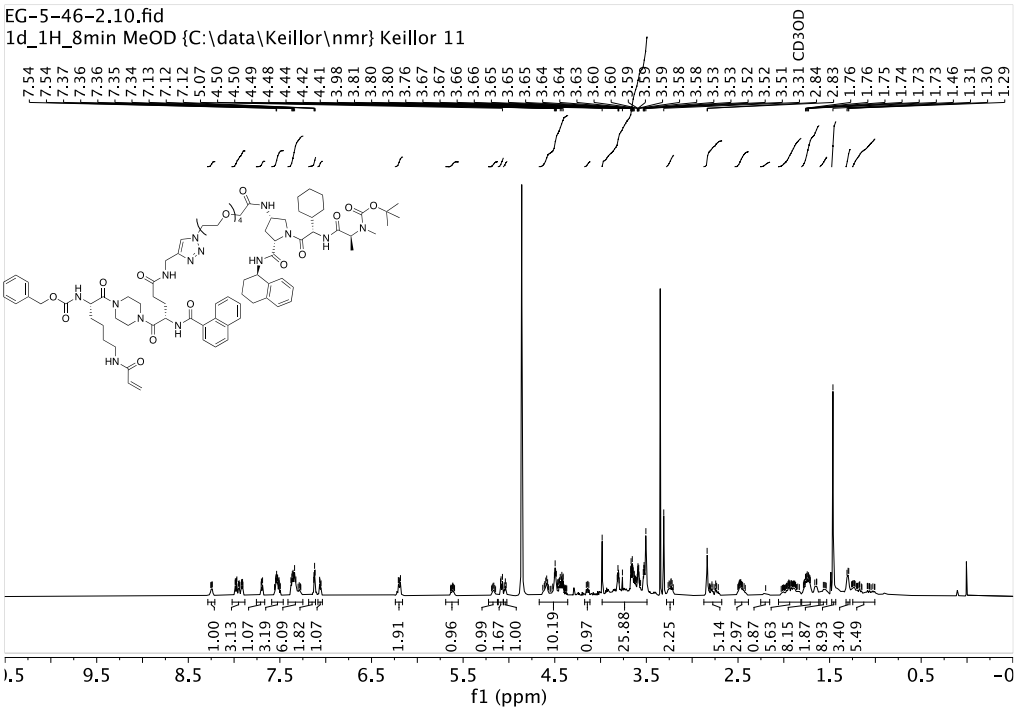

VHL-PROTAC-1 (Compound 9, EG-5-35)

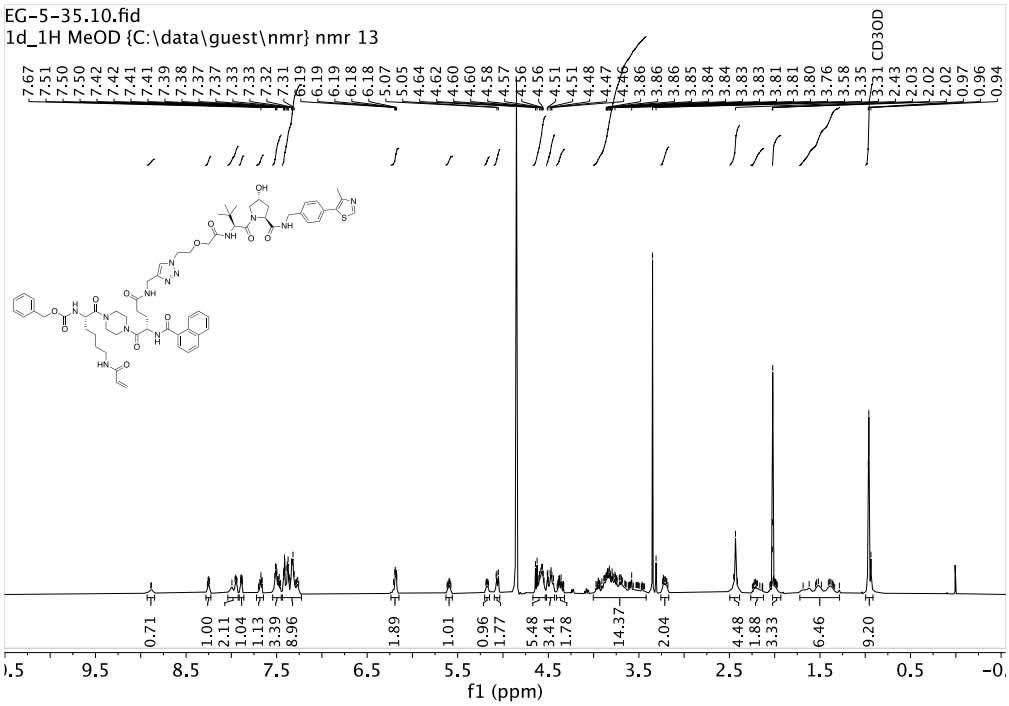

VHL-PROTAC-2 (Compound 10, EG-5-36)

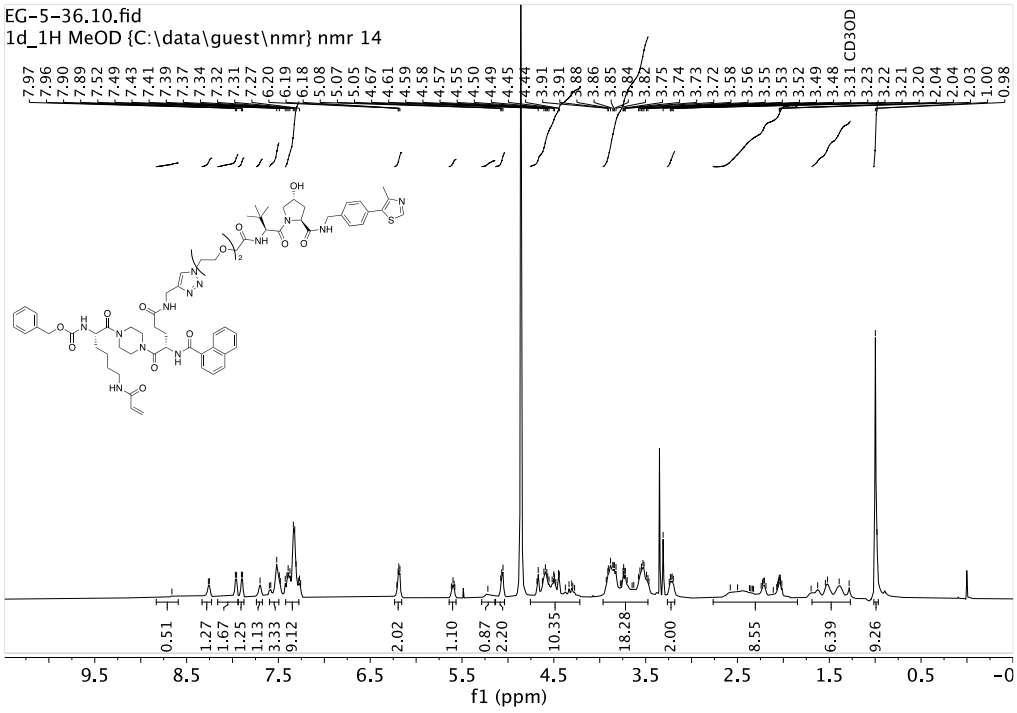

VHL-PROTAC-3 (Compound 11, EG-5-37)

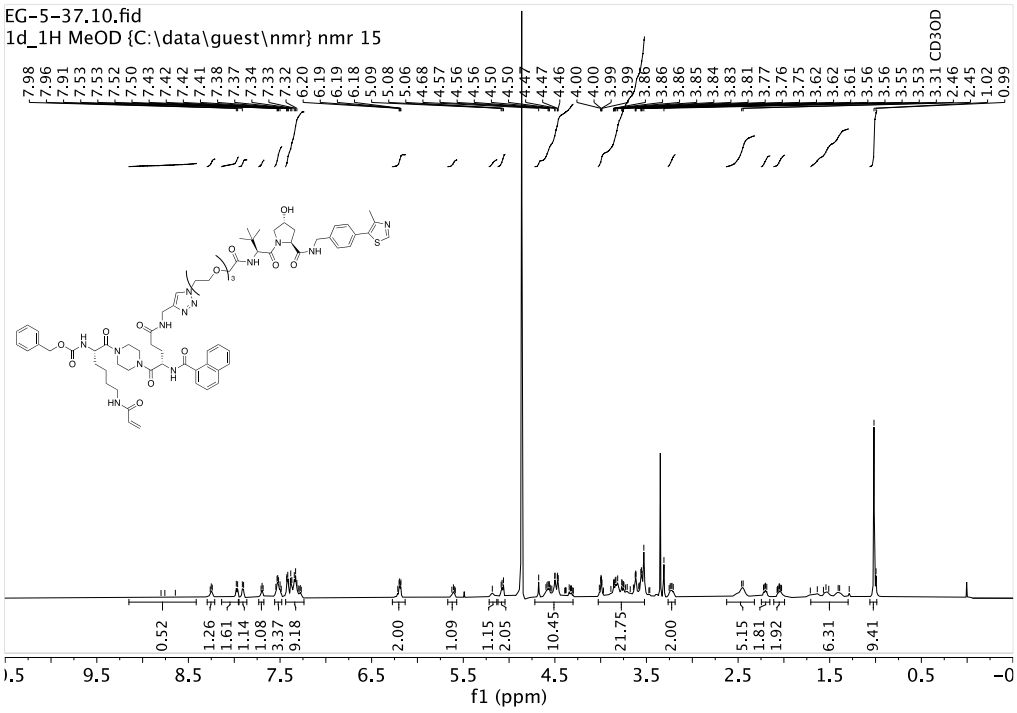

VHL-PROTAC-4 (Compound 12, EG-5-38)

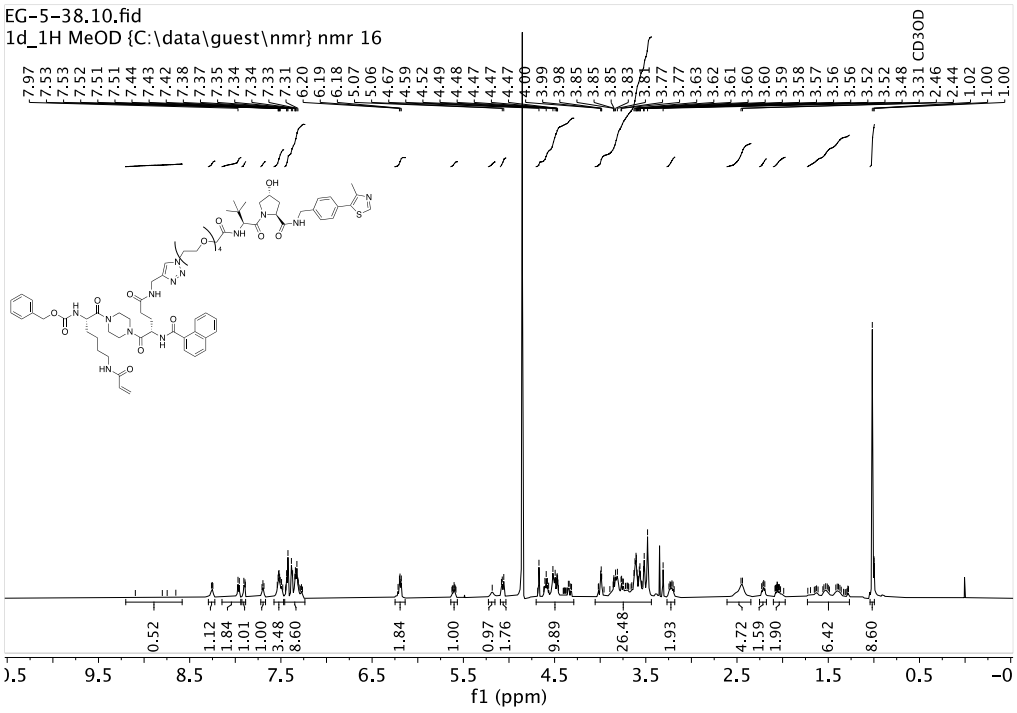

IAP-PROTAC-1 (Compound 31, EG-5-58-2)

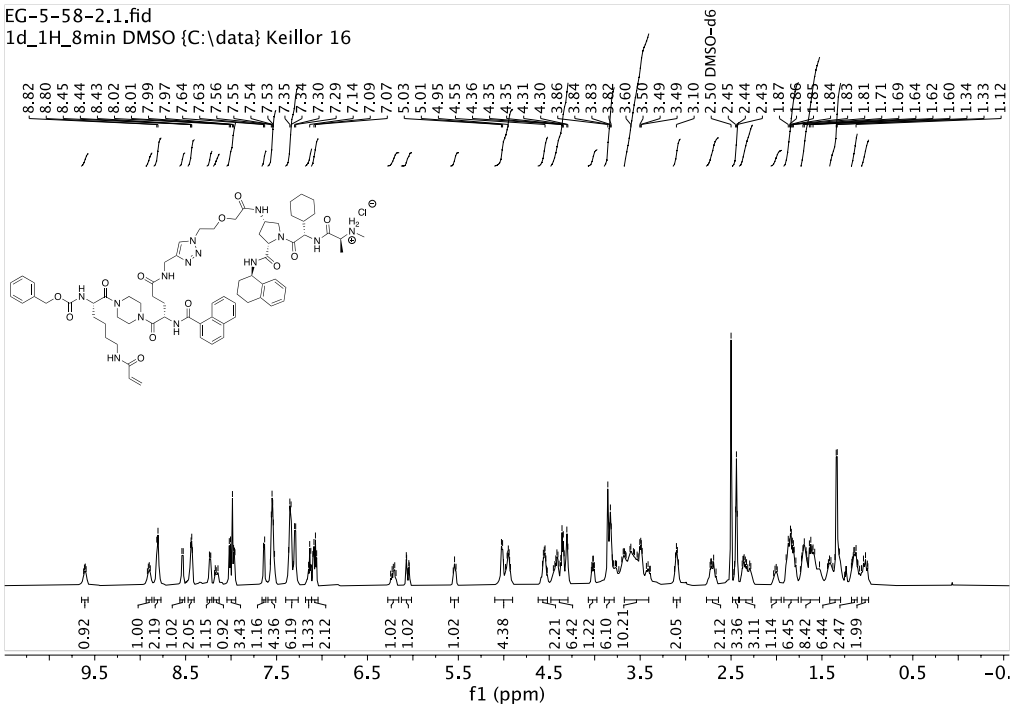

IAP-PROTAC-2 (Compound 32, EG-5-59-2)

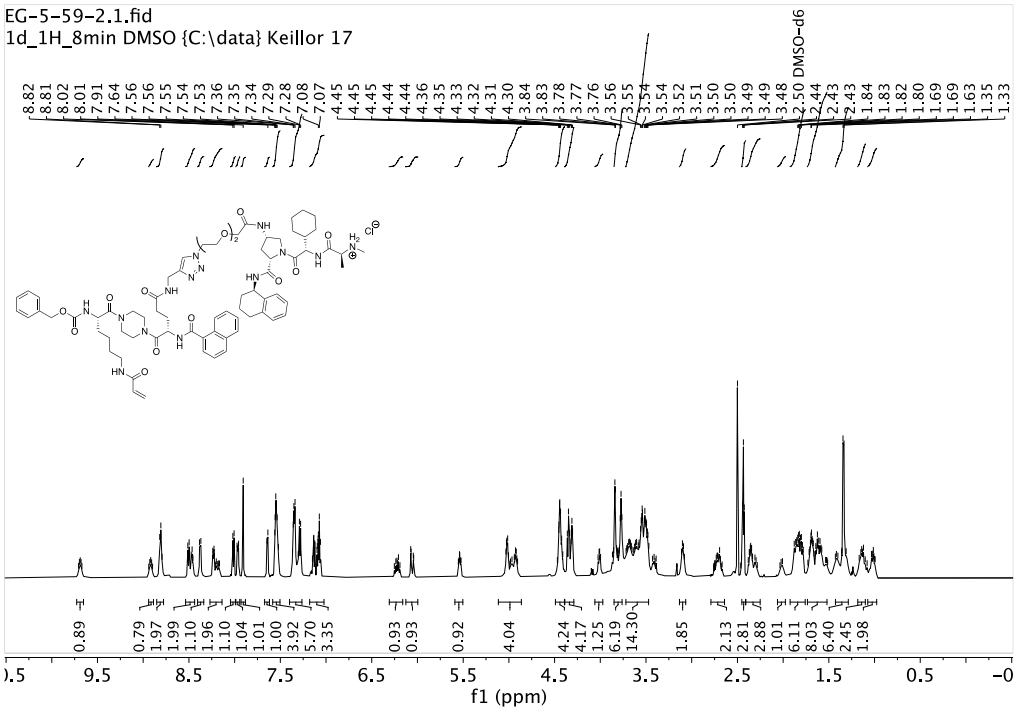

IAP-PROTAC-3 (Compound 33, EG-5-60-2)

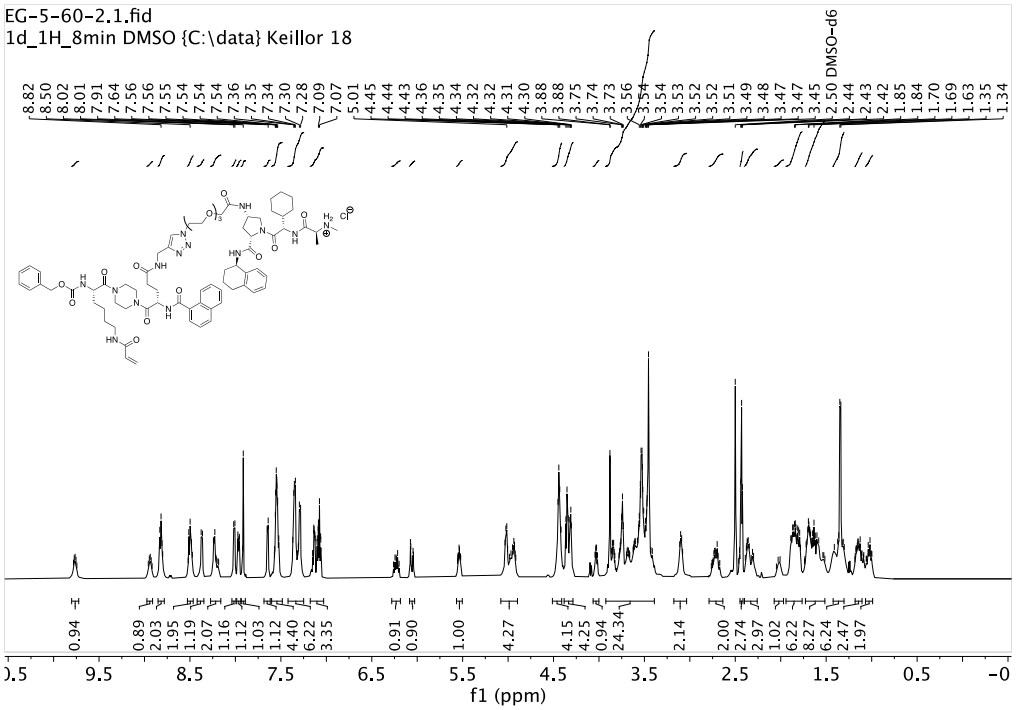

IAP-PROTAC-4 (Compound 34, EG-5-61-2)

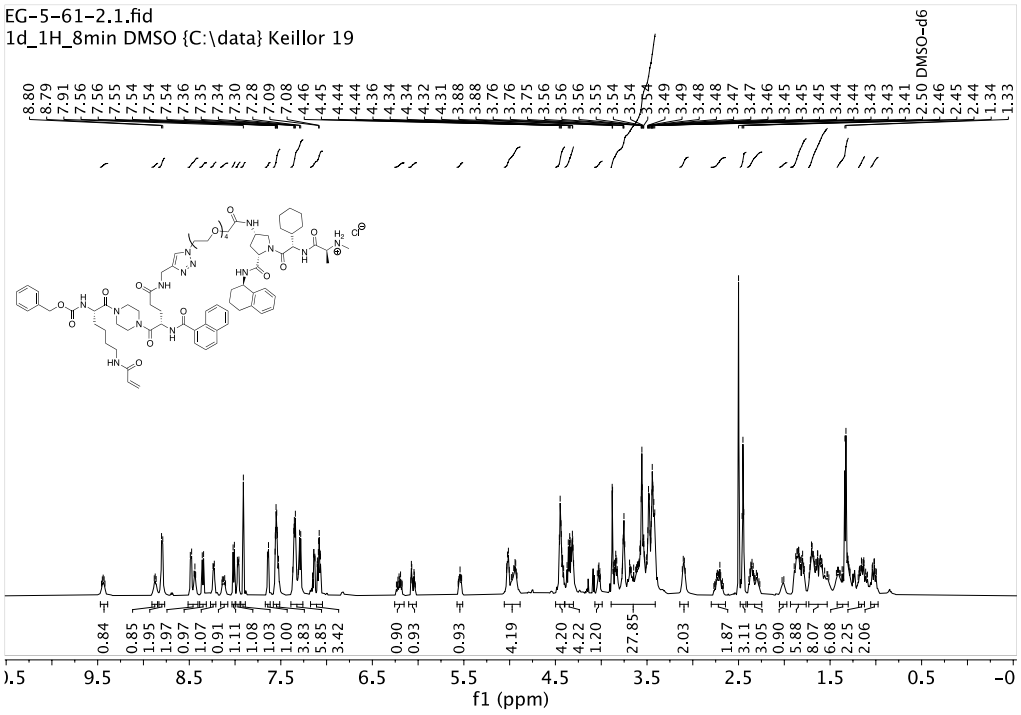

Lenalidomide-PROTAC-1 (Compound 17, EG-5-49)

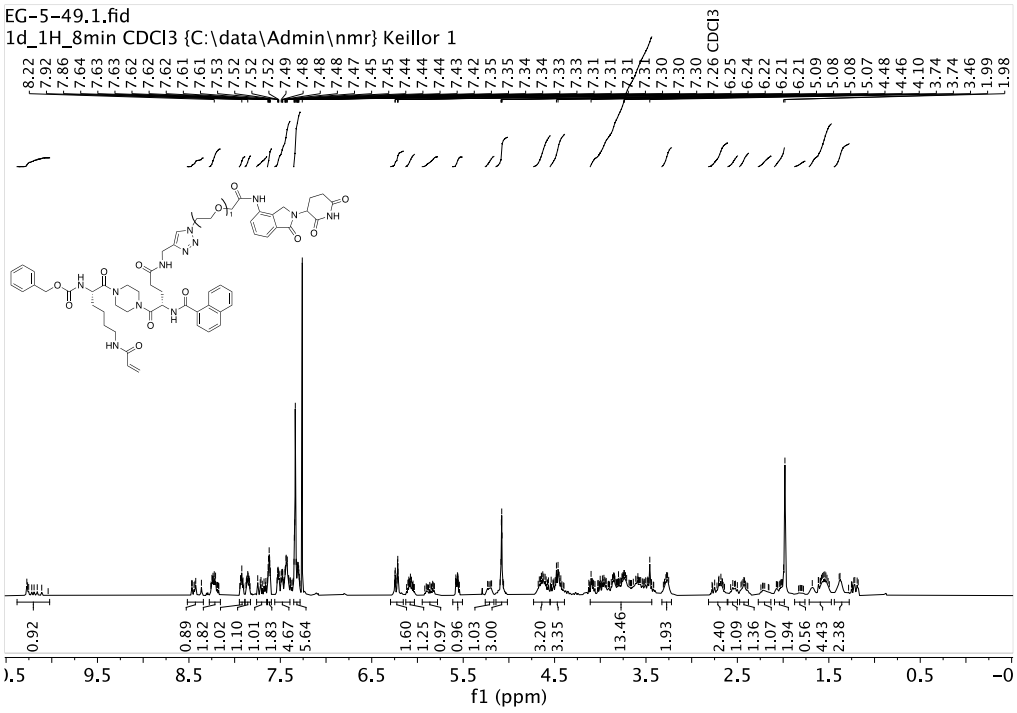

Lenalidomide-PROTAC-2 (Compound 18, EG-5-50)

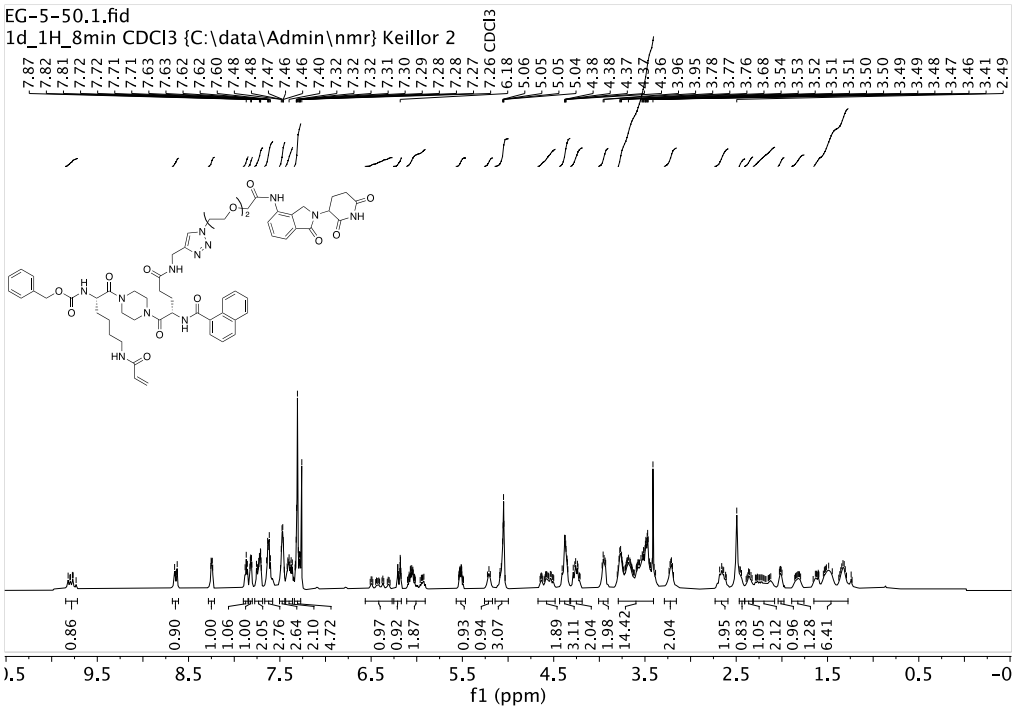

Lenalidomide-PROTAC-3 (Compound 19, EG-5-51)

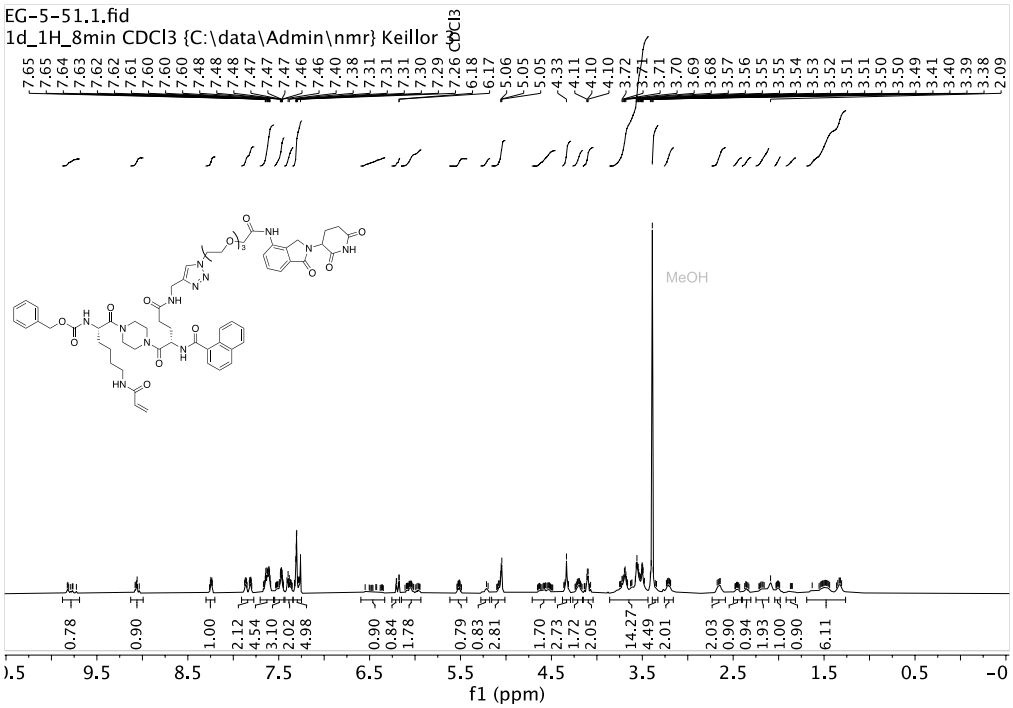

Lenalidomide-PROTAC-4 (Compound 20, EG-5-52)

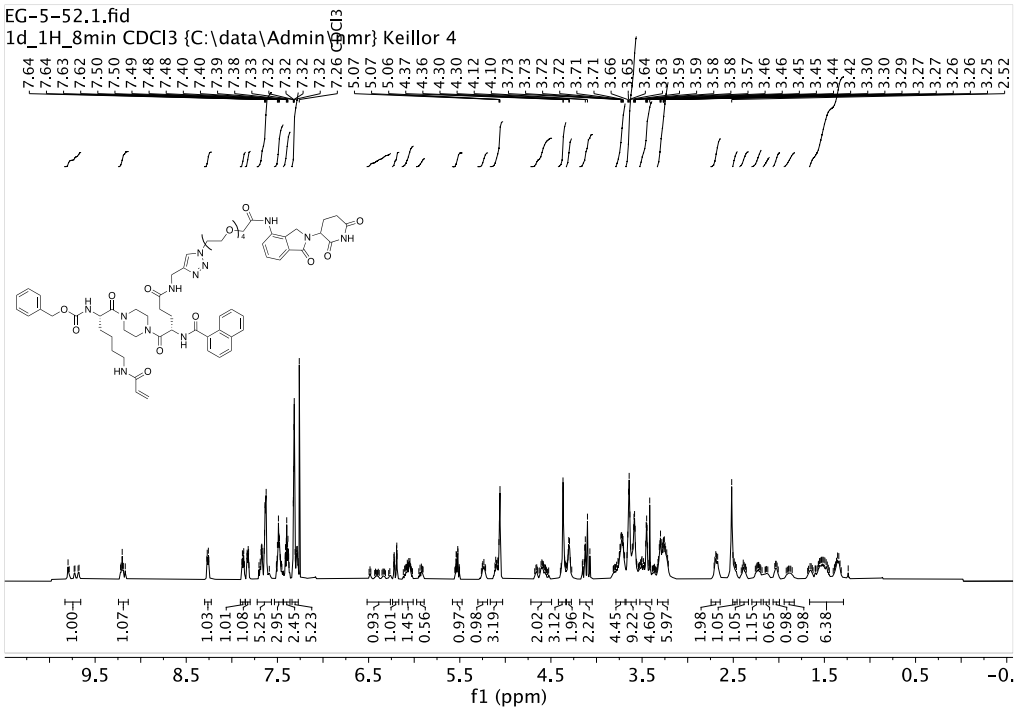

HPLC Traces of Final Compounds:

VHL-PROTAC-1 (Compound 9, EG-5-35)

<Sample Information>

Sample Name	: EG-5-35		
Sample ID	: EG-5-35		
Data Filename	: EG-5-35.lcd		
Method Filename	: 5-95% Method.lcm		
Batch Filename	:		
Vial #	: 0-2	Sample Type	: Unknown
Injection Volume	: 10 uL		
Date Acquired	: 2/3/2023 12:50:32 PM	Acquired by	: Boddy lab
Date Processed	: 2/3/2023 1:11:40 PM	Processed by	: Boddy lab

<Chromatogram>

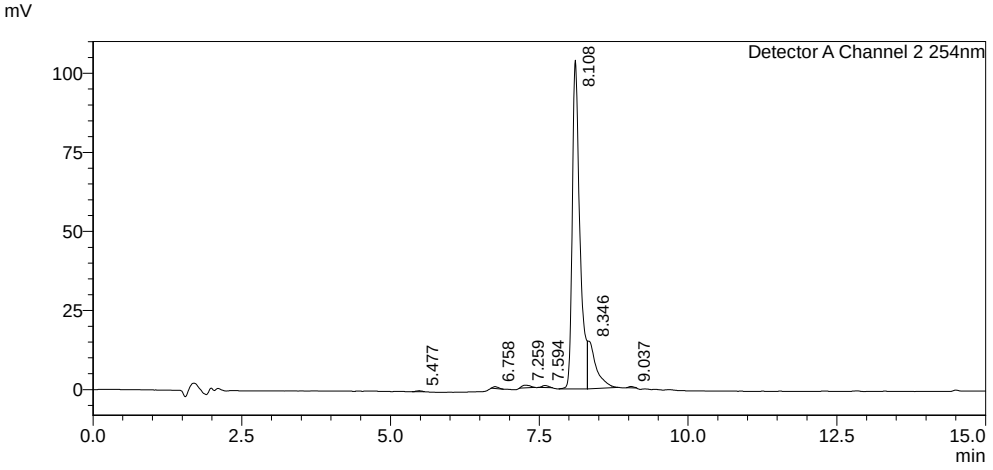

Peak Table

Detector A Channel 2 254nm

Peak#	Ret. Time	Area%
1	5.477	0.167
2	6.758	0.344
3	7.259	0.756
4	7.594	0.472
5	8.108	84.368
6	8.346	13.654
7	9.037	0.239
Total		100.000

VHL-PROTAC-2 (Compound 10, EG-5-36)

<Sample Information>

Sample Name	: EG-5-36		
Sample ID	: EG-5-36		
Data Filename	: EG-5-36_001.lcd		
Method Filename	: 5-95% Method.lcm		
Batch Filename	: EG-5-36-37-38.lcb		
Vial #	: 0-2	Sample Type	: Unknown
Injection Volume	: 10 uL		
Date Acquired	: 2/13/2023 3:42:22 PM	Acquired by	: Boddy lab
Date Processed	: 2/14/2023 12:08:00 PM	Processed by	: Boddy lab

<Chromatogram>

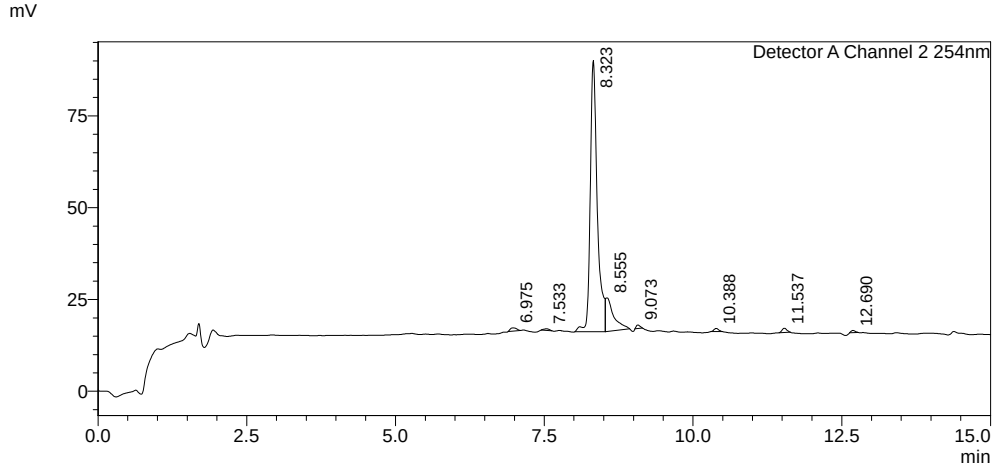

Peak Table

Detector A Channel 2 254nm

Peak#	Ret. Time	Area%
1	6.975	0.891
2	7.533	0.384
3	8.323	84.324
4	8.555	11.902
5	9.073	0.569
6	10.388	0.623
7	11.537	0.897
8	12.690	0.410
Total		100.000

VHL-PROTAC-3 (Compound 11, EG-5-37)

<Sample Information>

Sample Name	: EG-5-37		
Sample ID	: EG-5-37		
Data Filename	: EG-5-37_002.lcd		
Method Filename	: 5-95% Method.lcm		
Batch Filename	: EG-5-36-37-38.lcb		
Vial #	: 0-3	Sample Type	: Unknown
Injection Volume	: 10 uL		
Date Acquired	: 2/13/2023 3:57:54 PM	Acquired by	: Boddy lab
Date Processed	: 2/14/2023 12:13:25 PM	Processed by	: Boddy lab

<Chromatogram>

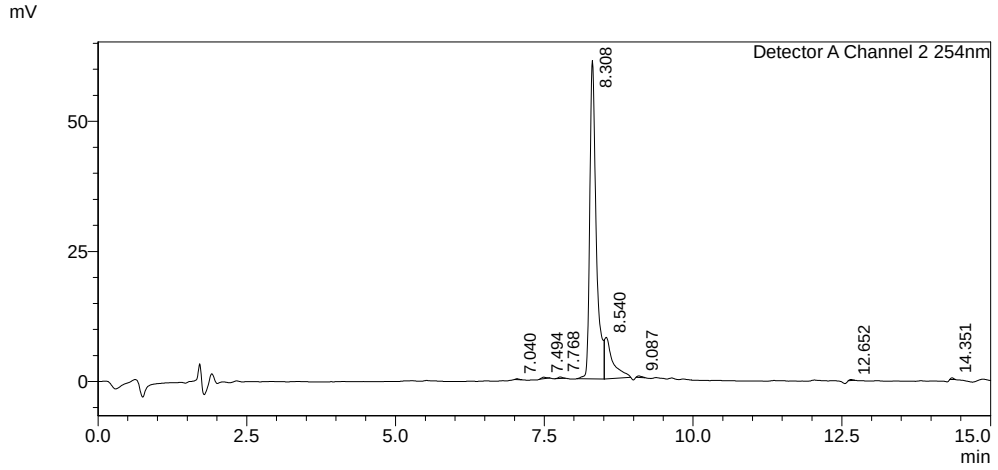

Peak Table

Detector A Channel 2 254nm

Peak#	Ret. Time	Area%
1	7.040	0.099
2	7.494	0.285
3	7.768	0.269
4	8.308	84.944
5	8.540	13.785
6	9.087	0.270
7	12.652	0.163
8	14.351	0.184
Total		100.000

VHL-PROTAC-4 (Compound 12, EG-5-38)

<Sample Information>

Sample Name	: EG-5-38		
Sample ID	: EG-5-38		
Data Filename	: EG-5-38_003.lcd		
Method Filename	: 5-95% Method.lcm		
Batch Filename	: EG-5-36-37-38.lcb		
Vial #	: 0-4	Sample Type	: Unknown
Injection Volume	: 10 uL		
Date Acquired	: 2/13/2023 4:13:30 PM	Acquired by	: Boddy lab
Date Processed	: 2/14/2023 12:17:47 PM	Processed by	: Boddy lab

<Chromatogram>

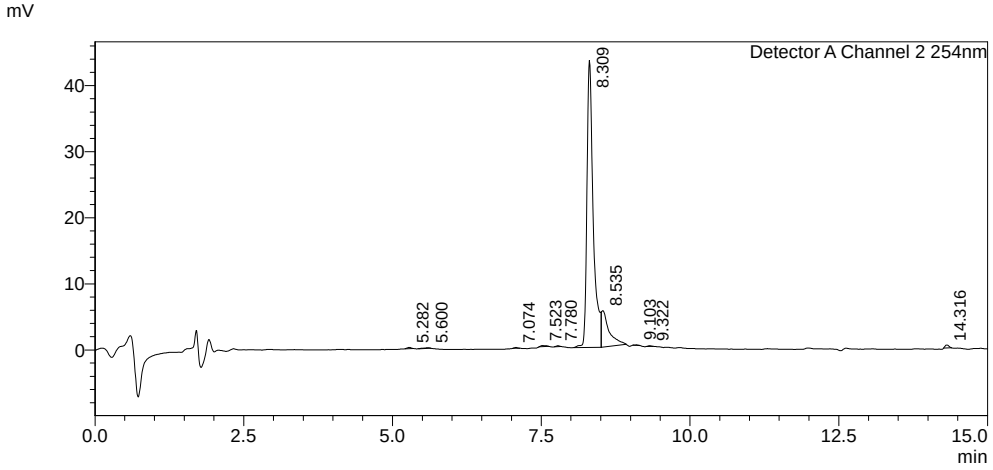

Peak Table

Detector A Channel 2 254nm

Peak#	Ret. Time	Area	Area%
1	5.282	779	0.207
2	5.600	637	0.169
3	7.074	405	0.108
4	7.523	968	0.257
5	7.780	516	0.137
6	8.309	322819	85.655
7	8.535	48302	12.816
8	9.103	273	0.073
9	9.322	329	0.087
10	14.316	1854	0.492
Total		376883	100.000

IAP-PROTAC-1 (Compound 31, EG-5-58-2)

<Sample Information>

Sample Name	: EG-5-58		
Sample ID	: EG-5-58		
Data Filename	: EG-5-58_002.lcd		
Method Filename	: 5-95% Method.lcm		
Batch Filename	: EG-5-58-59-60-61-Purity.lcb		
Vial #	: 0-2	Sample Type	: Unknown
Injection Volume	: 10 uL		
Date Acquired	: 4/4/2023 10:48:18 AM	Acquired by	: Boddy lab
Date Processed	: 4/4/2023 11:43:58 AM	Processed by	: Boddy lab

<Chromatogram>

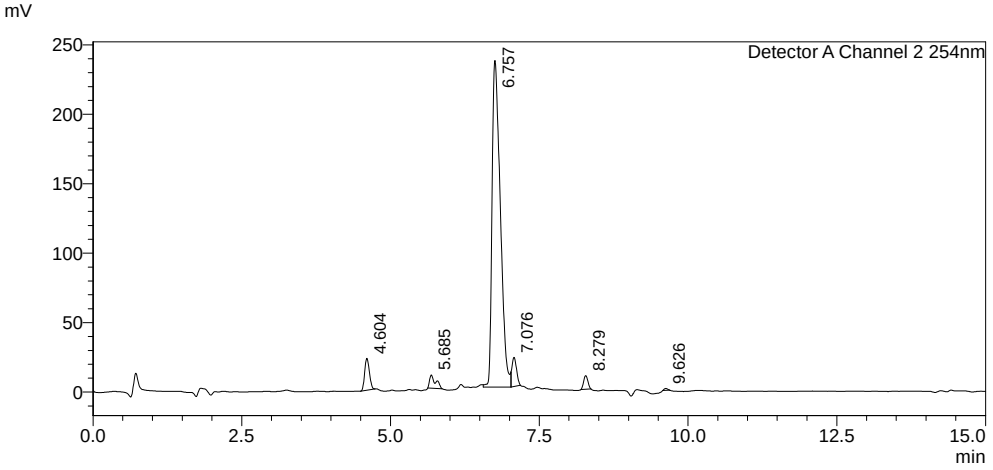

Peak Table
Detector A Channel 2 254nm

Peak#	Ret. Time	Area%
1	4.604	4.904
2	5.685	2.565
3	6.757	86.186
4	7.076	4.239
5	8.279	1.886
6	9.626	0.219
Total		100.000

IAP-PROTAC-2 (Compound 32, EG-5-59-2)

<Sample Information>

Sample Name	: EG-5-59		
Sample ID	: EG-5-59		
Data Filename	: EG-5-59_003.lcd		
Method Filename	: 5-95% Method.lcm		
Batch Filename	: EG-5-58-59-60-61-Purity.lcb		
Vial #	: 0-3	Sample Type	: Unknown
Injection Volume	: 10 uL		
Date Acquired	: 4/4/2023 11:03:53 AM	Acquired by	: Boddy lab
Date Processed	: 4/4/2023 11:48:17 AM	Processed by	: Boddy lab

<Chromatogram>

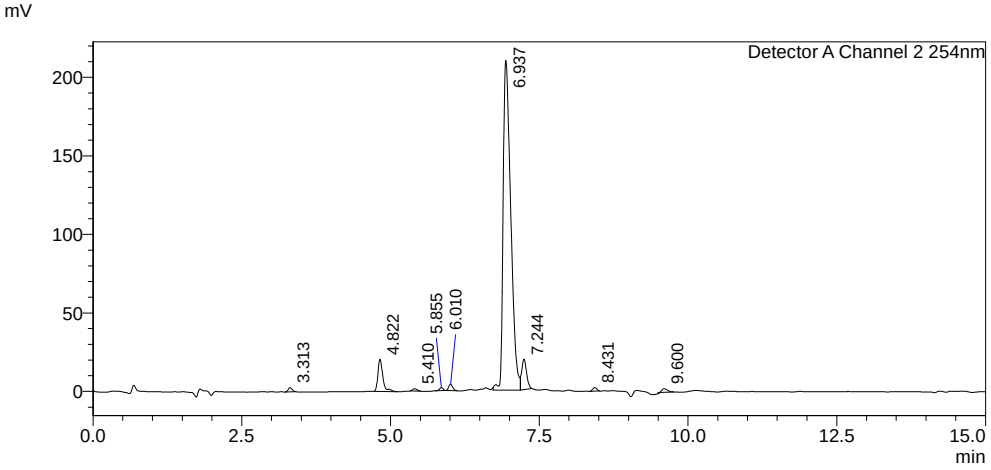

Peak Table

Detector A Channel 2 254nm

Peak#	Ret. Time	Area%
1	3.313	0.526
2	4.822	5.433
3	5.410	0.347
4	5.855	0.384
5	6.010	0.877
6	6.937	86.291
7	7.244	5.016
8	8.431	0.499
9	9.600	0.628
Total		100.000

IAP-PROTAC-3 (Compound 33, EG-5-60-2)

<Sample Information>

Sample Name	: EG-5-60		
Sample ID	: EG-5-60		
Data Filename	: EG-5-60_004.lcd		
Method Filename	: 5-95% Method.lcm		
Batch Filename	: EG-5-58-59-60-61-Purity.lcb		
Vial #	: 0-4	Sample Type	: Unknown
Injection Volume	: 10 uL		
Date Acquired	: 4/4/2023 11:19:28 AM	Acquired by	: Boddy lab
Date Processed	: 4/4/2023 11:52:10 AM	Processed by	: Boddy lab

<Chromatogram>

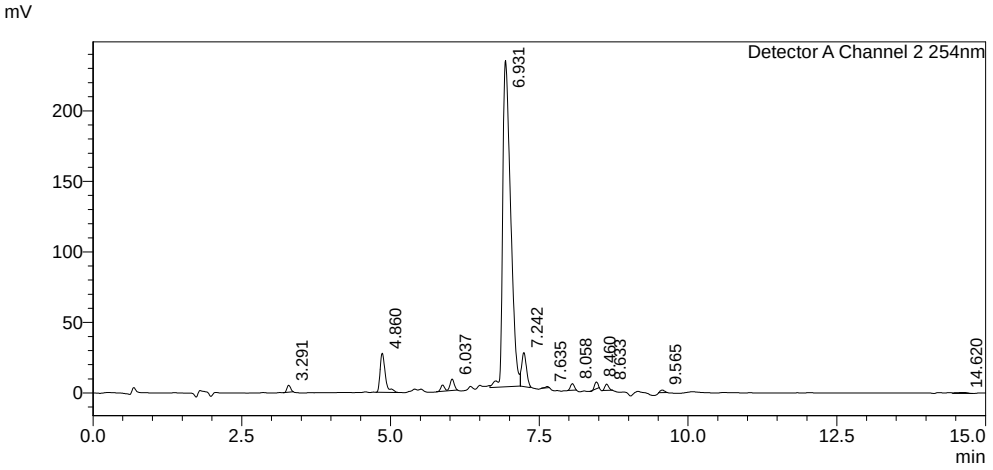

Peak Table

Detector A Channel 2 254nm

Peak#	Ret. Time	Area%
1	3.291	0.825
2	4.860	6.451
3	6.037	2.289
4	6.931	82.174
5	7.242	5.086
6	7.635	0.144
7	8.058	0.803
8	8.460	0.724
9	8.633	0.791
10	9.565	0.341
11	14.620	0.372
Total		100.000

IAP-PROTAC-4 (Compound 34, EG-5-61-2)

<Sample Information>

Sample Name	: EG-5-61		
Sample ID	: EG-5-61		
Data Filename	: EG-5-61_005.lcd		
Method Filename	: 5-95% Method.lcm		
Batch Filename	: EG-5-58-59-60-61-Purity.lcb		
Vial #	: 0-5	Sample Type	: Unknown
Injection Volume	: 10 uL		
Date Acquired	: 4/4/2023 11:35:01 AM	Acquired by	: Boddy lab
Date Processed	: 4/4/2023 11:56:34 AM	Processed by	: Boddy lab

<Chromatogram>

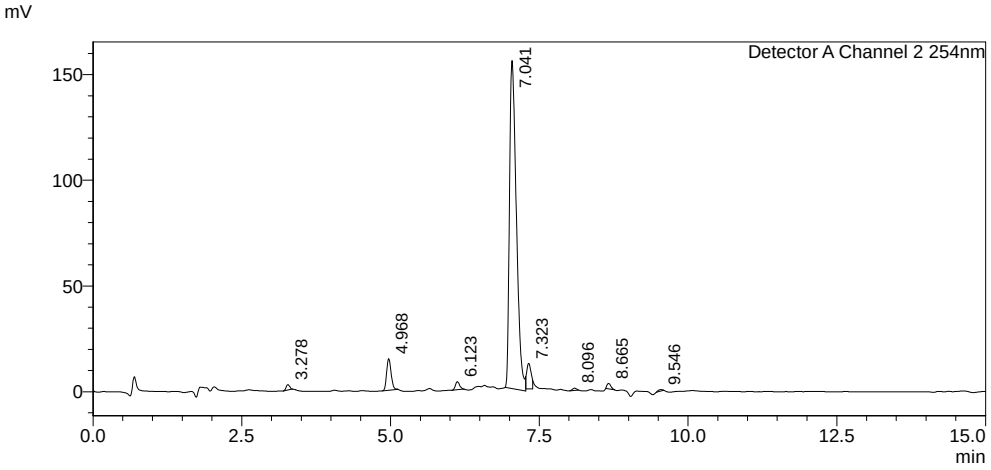

Peak Table
Detector A Channel 2 254nm

Peak#	Ret. Time	Area%
1	3.278	0.755
2	4.968	5.454
3	6.123	1.279
4	7.041	86.800
5	7.323	4.304
6	8.096	0.337
7	8.665	0.800
8	9.546	0.271
Total		100.000

Lenalidomide-PROTAC-1 (Compound 17, EG-5-49)

<Sample Information>

Sample Name	: EG-5-49		
Sample ID	: EG-5-49		
Data Filename	: EG-5-49_002.lcd		
Method Filename	: 5-95% Method.lcm		
Batch Filename	: EG-5-49-50-51-52-Purity.lcb		
Vial #	: 0-2	Sample Type	: Unknown
Injection Volume	: 10 uL		
Date Acquired	: 3/31/2023 1:31:42 PM	Acquired by	: Boddy lab
Date Processed	: 3/31/2023 1:46:44 PM	Processed by	: Boddy lab

<Chromatogram>

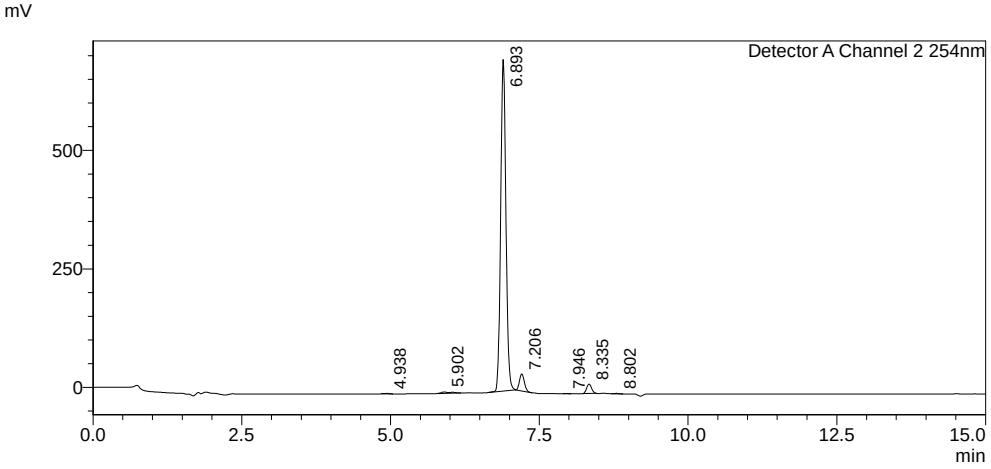

Peak Table
Detector A Channel 2 254nm

Peak#	Ret. Time	Area%
1	4.938	0.083
2	5.902	0.758
3	6.893	92.092
4	7.206	4.398
5	7.946	0.049
6	8.335	2.504
7	8.802	0.116
Total		100.000

Lenalidomide-PROTAC-2 (Compound 18, EG-5-50)

<Sample Information>

Sample Name	: EG-5-50		
Sample ID	: EG-5-50		
Data Filename	: EG-5-50_003.lcd		
Method Filename	: 5-95% Method.lcm		
Batch Filename	: EG-5-49-50-51-52-Purity.lcb		
Vial #	: 0-3	Sample Type	: Unknown
Injection Volume	: 10 uL		
Date Acquired	: 3/31/2023 1:47:14 PM	Acquired by	: Boddy lab
Date Processed	: 3/31/2023 2:02:16 PM	Processed by	: Boddy lab

<Chromatogram>

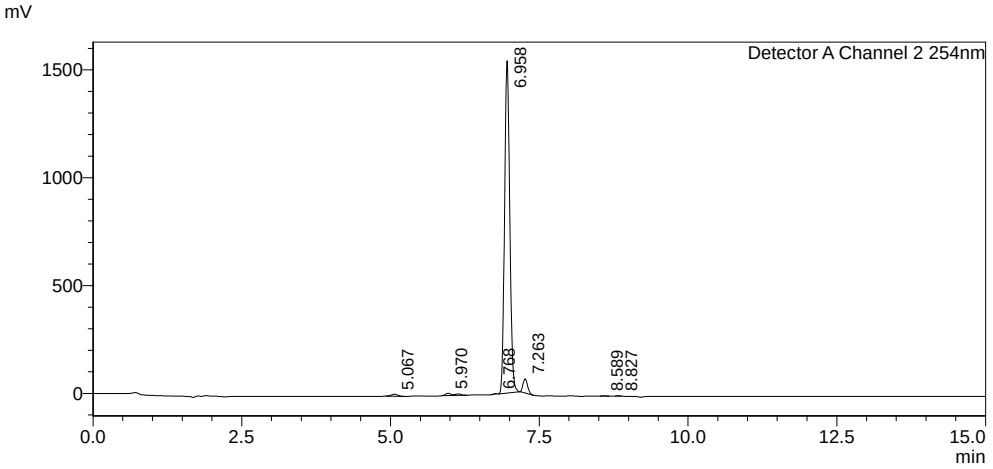

Peak Table
Detector A Channel 2 254nm

Peak#	Ret. Time	Area%
1	5.067	0.656
2	5.970	1.142
3	6.768	0.057
4	6.958	94.503
5	7.263	3.522
6	8.589	0.081
7	8.827	0.040
Total		100.000

Lenalidomide-PROTAC-3 (Compound 19, EG-5-51)

<Sample Information>

Sample Name	: EG-5-51		
Sample ID	: EG-5-51		
Data Filename	: EG-5-51_004.lcd		
Method Filename	: 5-95% Method.lcm		
Batch Filename	: EG-5-49-50-51-52-Purity.lcb		
Vial #	: 0-4	Sample Type	: Unknown
Injection Volume	: 10 uL		
Date Acquired	: 3/31/2023 2:02:45 PM	Acquired by	: Boddy lab
Date Processed	: 3/31/2023 2:17:47 PM	Processed by	: Boddy lab

<Chromatogram>

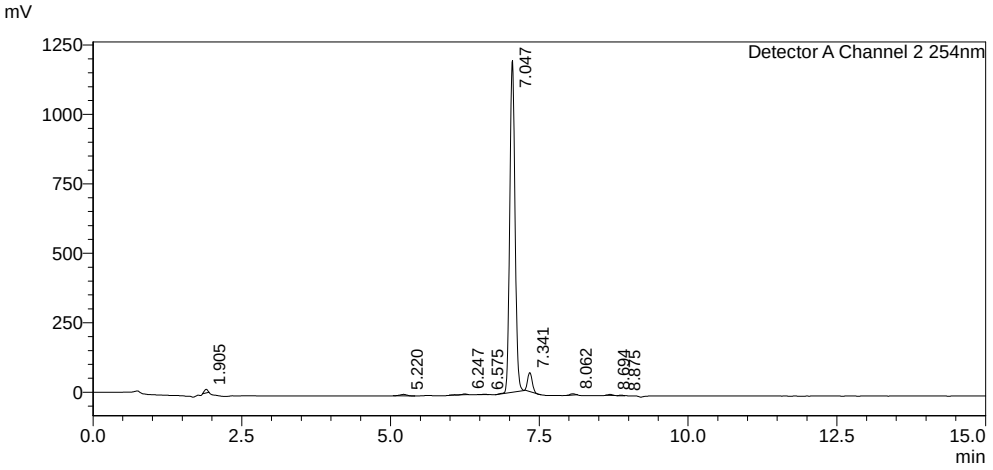

Peak Table

Detector A Channel 2 254nm

Peak#	Ret. Time	Area%
1	1.905	0.659
2	5.220	0.568
3	6.247	0.256
4	6.575	0.055
5	7.047	93.197
6	7.341	4.632
7	8.062	0.339
8	8.694	0.208
9	8.875	0.086
Total		100.000

Lenalidomide-PROTAC-4 (Compound 20, EG-5-52)

<Sample Information>

Sample Name	: EG-5-52		
Sample ID	: EG-5-52		
Data Filename	: EG-5-52_005.lcd		
Method Filename	: 5-95% Method.lcm		
Batch Filename	: EG-5-49-50-51-52-Purity.lcb		
Vial #	: 0-5	Sample Type	: Unknown
Injection Volume	: 10 uL		
Date Acquired	: 3/31/2023 2:18:17 PM	Acquired by	: Boddy lab
Date Processed	: 3/31/2023 2:33:19 PM	Processed by	: Boddy lab

<Chromatogram>

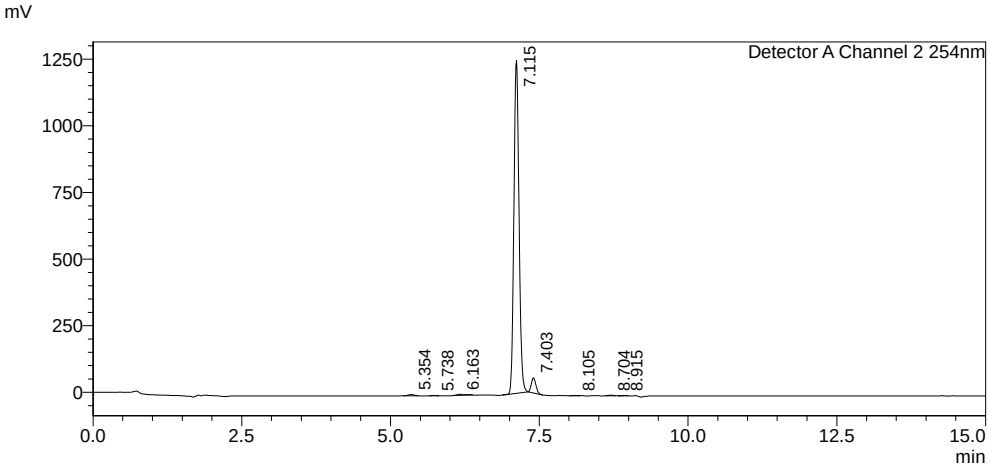

Peak Table
Detector A Channel 2 254nm

Peak#	Ret. Time	Area%
1	5.354	0.382
2	5.738	0.061
3	6.163	0.500
4	7.115	94.911
5	7.403	3.832
6	8.105	0.069
7	8.704	0.143
8	8.915	0.102
Total		100.000

Chapter 6: Conclusions and Future Perspectives

6.1. Chapter 2: Peptidic Inhibitors and a Fluorescent Probe for the Selective Inhibition and Labelling of Factor XIIIa Transglutaminase

6.1.1. Conclusion to Chapter 2

In this chapter we sought to develop first-in-class isozyme selective small molecule inhibitors for FXIIIa. Upon realization that initial compounds were subjects of fluorescence interference, and that the apparent inhibition we were observing was not enzymatic inactivation, we directed our efforts toward optimizing a known peptidic inhibitor, ZED1301. By synthesizing and evaluating a library of 11 peptides, which varied both the warhead itself as well as the length of the methylene linker sidechain, we ultimately discovered that ZED1301 remained as the most potent scaffold, and we reported the first time-independent inhibition parameters for this inhibitor (k_{inact}/K_I = 373 × 10^3 M^{-1} min^{-1}). We then derivatized this scaffold to incorporate a highly fluorescent rhodamine B moiety at the *N*-terminus to produce a probe for active FXIIIa. The probe, KM93, showed excellent potency *in vitro* with a k_{inact}/K_I ratio of 127 × 10^3 M^{-1} min^{-1} and a 6.5-fold selectivity for FXIIIa over TG2. KM93 was also able to label FXIIIa irreversibly both *in vitro* as well as *in cellulo*, making it a cell permeant FXIIIa probe that can be applied to cell culture. Fluorescence microscopy of bone marrow macrophages revealed FXIIIa to be primarily localized in punctate structures, demonstrating the utility of this probe as a new resource in the FXIIIa research toolbox.

6.1.2. Future Perspectives to Chapter 2

Our investigation of novel FXIII inhibitors did not reveal any new leads and moreover confirmed that ZED1301 outcompetes other derivatives that we had hypothesized could show greater reactivity. With this being said, our efforts did produce a first-in-class, highly potent, and efficient probe for FXIIIa, KM93, with desirable photochemical properties. This probe was applied within cell cultures of bone marrow macrophages and will continue to act as an irreversible fluorescent probe of active FXIIIa for future investigations. In particular, it would be interesting to apply KM93 to other cell lines known to express FXIIIa, including chondrocytes and osteoblasts, to enable localization studies within these cell types.

6.2. Chapter 3: Intracellular Human Transglutaminase 2 is Responsible for the Transglutaminase-Associated Cancer Phenotype

6.2.1. Conclusion to Chapter 3

The work presented within this chapter was a multidisciplinary effort to expand our knowledge of the overlapping activities of TG2. More specifically, we designed, synthesized, and evaluated three different classes of chemical biology research tools. Exploiting a recent SAR lead compound, we functionalized the side chain of a glutamate residue to incorporate cargo to facilitate cell impermeability, fluorescent labelling, and biorthogonal chemistry. All of the tools maintained their affinity and reactivity with TG2, and the cell impermeable inhibitors exhibited strong isozyme selectivity. The cell impermeable inhibitors were further validated to be non-cell permeable by directly measuring their permeability and demonstrating that the values fall well below the values that represent acceptable PK parameters. The fluorescent probe, NCEG-RHB, was capable of labelling TG2 *in vitro* and was applied in cell culture of the SH-SY5Y cell line and

visualized *via* fluorescence microscopy. Once visually validated to be cell permeant, NCEG-RHB, as well as the cell impermeable NCEG2, were applied to cancer cell biology studies. Through the analysis we were able to conclude that intracellular TG2 is responsible for both the proliferation of HaCaT, SCC-13, and MDA-MB-436 cells as well as the migration of MDA-MB-436 cells, given that only cell permeable inhibitors could hinder these traits, while the cell impermeable inhibitor failed to provide any significant response compared to controls.

6.2.2. Future Perspectives to Chapter 3

The derivatives developed within this chapter are some of the most broad and all-encompassing chemical biology research tools with isozyme selectivity disclosed to date for TG2. The cell impermeable inhibitors, including NCEG2, are first-in-class scaffolds which can irreversible inhibit specifically extracellular TG2. The cell permeant fluorescent probe, NCEG-RHB, provides a useful visual tool for labelling TG2. The biorthogonal propargylated inhibitor has only gone through a proof of concept in *E. coli* lysate but will be extremely useful in our follow-up mechanism of action studies for our medicinal chemistry efforts. Further, the cell impermeable inhibitors are in high demand by our collaborators as rigorous controls in ongoing studies and will continue to serve this purpose in the future.

6.3. Chapter 4: High Affinity Fluorogenic Substrate for Transglutaminase 2 Reveals Pattern Consistent with Enzymatic Hysteresis

6.3.1. Conclusion to Chapter 4

The manuscript presented in Chapter 4 encompasses our efforts to initially design a novel FXIII fluorogenic activity assay substrate, which ended up resulting in an extremely efficient TG2

substrate. APH7 shows a high degree of affinity for TG2 with a K_M = 3 μM, and a low rate of non-enzymatic background hydrolysis. During our routine analysis of this substrate, we attempted to reproduce the inhibition parameters determined for inhibitor AA9. The data obtained indicated that AA9 appeared to be nearly an order of magnitude more potent when using APH7 than with our classic AL5 substrate. These complexing results led us to several mechanistic experiments before we ultimately concluded that TG2, being a dramatically conformationally flexible enzyme, is vulnerable to patterns of enzymatic hysteresis. Certain substrates, more than others, seem to stabilize a conformation of TG2 that is more susceptible to certain active site inhibitors. These findings are the first evidence that TG2 can undergo this enzymatic phenomenon and through this study we have also provided the field with a sensitive new activity assay.

6.3.2. Future Perspectives to Chapter 4

APH7 is the highest affinity activity assay substrate at the current state in TG2 research. Although this substrate uncovered a pattern of hysteresis with TG2, its usefulness is not hindered by this inherent trait of the enzyme. Our current activity assay utilizing AL5 has been plagued by inconsistencies as the extremely potent inhibitors currently in development in the group have exposed the limitations of the AL5 assay. APH7, on the other hand, exhibits higher affinity for TG2 and negligible background reactivity, which leads us to believe it could be the way forward and the new standard for our research group's evaluation of highly potent TG2 inhibitors. APH7 provides extremely reliable, consistent, and sensitive data with TG2, which highlights its advantages and versatility moving forward.

6.4. Chapter 5: Towards TG2 Active Site Directed PROTACs

6.4.1. Conclusion to Chapter 5

This preliminary work was based on our desire to explore a new route of TG2 therapeutics, by eschewing from traditional small molecule inhibitors and instead targeting the enzyme for proteasomal degradation. By utilizing our known highly tailorable scaffold from Chapter 3, we incorporated various PEG linkers and E3L ligands to create a library of 12 novel compounds. These compounds all exhibited excellent potency versus TG2 with the lead compound having an estimated k_{inact}/K_I efficiency value of 431×10^3 M^{-1} min^{-1}. Furthermore, 10 μM concentrations of these PROTAC candidates completely inhibited the enzyme in less than 100 s in our assay conditions, highlighting their reactivity. The future of this project will rely upon the results from both the primary ELISA screen for TG2 degradation as well as the fully characterized western blot degradation portfolio including efficiency and timeline.

6.4.2. Future Perspectives to Chapter 5

The prospective TG2 active site directed PROTACs have shown that they do indeed bind to the active site irreversibly with a high degree of affinity and reactivity. The next step will be to screen the library *in cellulo* using cancer cell lines that express TG2 at an elevated level, to ensure they serve their purpose and target TG2 for degradation. To design a higher throughput workflow than traditional western blots, the library will first be screened using ELISA of the cell lysate after treatment with the respective PROTAC. The lead compound from this study will then be further evaluated to obtain reliable DC_{50} and D_{max} values by western blot to fully characterize its efficacy and timeline of degradation. Further analysis of the PK portfolio will then be conducted to determine whether this lead candidate could be optimized further from a PK perspective. Future

iterations of these molecules will focus on rigidifying the linker and fine tuning both the PK and PD portfolios in an effort to create a potential TG2 PROTAC with therapeutic applications.